SUPRAMOLECULAR CATALYTIC SYSTEMS: SYNTHESIS, CHARACTERIZATION AND APPLICATION IN CATALYSIS

Ester Iniesta Beteta

UNIVERSITAT ROVIRA i VIRGILI

Supramolecular Catalytic Systems: Synthesis, Characterization and Application in Catalysis

Ester Iniesta Beteta

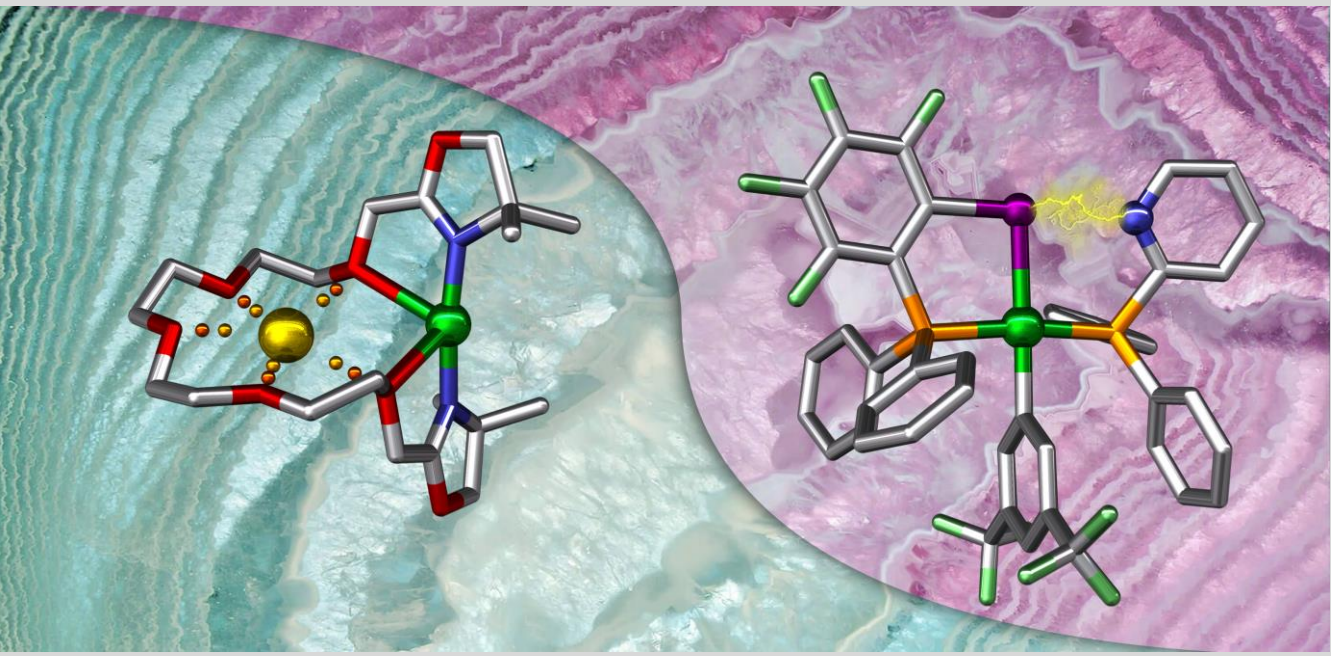

DOCTORAL THESIS
2021

Ester Iniesta Beteta

Supramolecular Catalytic Systems: Synthesis, Characterization and Application in Catalysis

Doctoral Thesis

Supervised by Prof. Dr. Anton Vidal i Ferran

Institute of Chemical Research of Catalonia (ICIQ)

ICIQ
Institut Català d'Investigació Química

UNIVERSITAT ROVIRA i VIRGILI

Tarragona 2021

Institut Català d'Investigació Química

UNIVERSITAT ROVIRA I VIRGILI
DEPARTAMENT DE QUIMICA ANALITICA I QUIMICA ORGANICA
C/ Marcel.lí Domingo s/n
Campus Sescelades
43007 Tarragona

Prof. Dr. Anton Vidal i Ferran, former Group Leader of the Institute of Chemical Research of Catalonia (ICIQ) and Research Professor of the Catalan Institution for Research and Advance Studies (ICREA),

I STATE that the present Doctoral Thesis entitled "**Supramolecular Catalytic Systems: Synthesis, Characterization and Application in Catalysis**" that Ester Iniesta Beteta presents to obtain the PhD degree in chemistry, has been carried out under my supervision, in the corresponding research group at the Institute of Chemical Research of Catalonia (ICIQ).

Tarragona, 3rd March 2021

PhD Thesis Supervisor

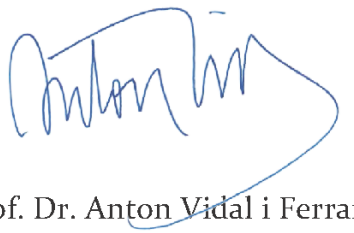

Prof. Dr. Anton Vidal i Ferran

ACKNOWLEDGEMENTS

I would like to thank Prof. Dr. Anton Vidal for giving me the opportunity to pursue my PhD studies in his research group at the Institute of Chemical Research of Catalonia (ICIQ). Thank you for your supervision and your dedication during these four years.

I would like to thank Prof. Kari Rissanen for the opportunity to join his group at the University of Jyväskylä for three months. I would like to thank all the members of his group as well for making me feel comfortable during the stay.

I am also very grateful to the ICIQ Research Support Area for all the services, especially to X-Ray Diffraction Unit, for providing more than support and sharing your knowledge.

I would like to thank all the members of Prof. Vidal′s group current and former members. Thank you Héctor, Jose Luís, Mónica, Rajesh, Laura, Bala, Joan, Lucas, Alicia, Nuria, Andrés, Alba, Juanjo and Paula. Thank you for your support in the bad moments. I would also like to thank all my friends from ICIQ, for every moment shared with them.

Finally, I would like to thank my family and friends, for staying with me every day, despite the distance, and be supportive in every decision and step, during this thesis and in my life.

The research work developed in the present PhD thesis has been possible thanks to the MCINN for a FPI predoctoral fellowship (BES-2015-074962). The ICIQ foundation and the MCINN (CTQ2014-60256-P and CTQ2017-89814-P) are gratefully acknowledged for the financial support provided.

UNIVERSITAT
ROVIRA i VIRGILI

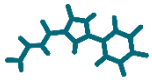

ICIQ
Institut
Català
d'Investigació
Química

A mis padres y a mi hermana

"Después de escalar una gran colina, uno se encuentra sólo con que hay muchas más colinas que escalar"

Nelson Mandela

LIST OF PUBLICATIONS

When this dissertation was submitted, the results contained herein have so far resulted in the following publication:

- "Supramolecularly regulated copper-bisoxazoline catalysts for the efficient insertion of carbenoid species into hydroxyl bonds" Iniesta, E.; Vidal-Ferran, A. *Chem. Commun*. **2020**, *56*, 6364-6367.

Other publications related to the topic covered in the present dissertation in a general way are presented below:

- "Efficient Modular Phosphorus-containing Ligands for Stereoselective Catalysis" (general overview on the research activities of the group) Llorente, N.; Fernández-Pérez, H.; Núñez-Rico, J. L.; Carreras, L.; Martínez-Carrión, A.; Iniesta, E.; Romero-Navarro, A.; Martínez-Bascuñana, A. Vidal-Ferran, A. *Pure Appl. Chem*. **2019**, *91*, 3-15.

TABLE OF CONTENTS

LIST OF ACRONYMS AND ABBREVIATIONS

The acronyms and abbreviations used in this manuscript have been used following the recommendations given by the American Chemical Society in the ACS guidelines for authors (accessed June 2020 (https://pubs.acs.org/doi/10.1021/bk-2006-STYG.ch010). Additional abbreviations and acronyms used in this manuscript are referenced in the list below:

º	angle
Å	angstrom(s)
acac	acetylacetonate or acetylacetonato
AcO	acetate
API	Active Pharmaceutical Ingredient
Ar	aryl
Ar^F	3,5-bis(trifluoromethyl)phenyl
BArF	tetrakis[3,5-bis(trifluoromethyl)phenylborate]
Bn	benzyl
Boc	*(tert*-butoxy)carbonyl
br	broad (spectral)
BSA	N,O-bis(trimethylsilyl)acetamide
Bu	*normal* butyl
^{t}Bu	*tert*-butyl
°C	degrees; Celsius
ca.	*circa* (about)

calcd	calculated
cat.	catalyst
CIF	Crystallographic Information Framework
cm^{-1}	wavenumber(s)
cod	1,5-cyclooctadiene
conv.	conversion
Cy	cyclohexane (solvent)
δ	chemical shift in ppm
d	day(s), doublet (spectral)
DBU	1,8-Diazabicyclo[5.4.0]undec-7-ene
DCM	dichloromethane
DFT	density-functional theory
DOSY	Diffusion Ordered SpectroscopY
dr	diastereomeric ratio
ee	enantiomeric excess
e.g.	*exempli gratia* (for example)
equiv.	equivalent(s)
er	enantiomeric ratio
ESI	electrospray ionization
Et	ethyl
et al.	*et alii* (and coworkers)
EWG	electron-withdrawing groups
EXSY	EXchange SpectroscoPY

FID	flame ionization detector
g	gram(s)
GC	gas chromatography
h	hour(s)
HOMO	highest occupied molecular orbital
HRMS	high resolution mass spectrometry
Hz	hertz
i.e.	*id est* (in other words)
IR	infrared
IS	internal standard
J	coupling constant (expressed in Hz)
LG	ligating group
LUMO	lowest unoccupied molecular orbital
μ	micro- (prefix)
m	multiplet (spectral); milli- (prefix)
M	molar (moles per liter)
M^+	parent molecular ion
Me	methyl
Mes	mesitylene
MHz	megahertz
min.	minute(s)
mL	milliliter
mM	millimolar (millimoles per liter)

mol	mole(s)
MS	mass spectrometry; molecular sieves
MTBE	methyl *tert*-butyl ether
m/z	mass-to-charge ratio
Naph	naphthyl
nbd	norbornadiene
nd	not detected
nm	nanometer(s)
NMR	nuclear magnetic resonance
Nu	nucleophile
Oct	octyl
ORTEP	oak ridge thermal ellipsoid plot program
OTf	triflate
Ph	phenyl
ppm	part(s) per million
q	quartet (spectral)
RA	regulation agent
rac	racemic
ref.	reference
rpm	revolution per minute
rt	room temperature
s	singlet (spectral); second(s)
solv.	solvent

SPS	Solvent Purification System
SSRI	selective serotonin reuptake inhibitors
t	triplet (spectral); time
T	temperature
TBS	*tert*-butyldimethylsilyl
THF	tetrahydrofuran
TMS	tetramethylsilyl; tetramethylsilane
TOF	turnover frequency
vol	volume
vs.	*versus*
v/v	volume per unit volume
XB	halogen bond
XBA	halogen bond acceptor

PROLOGUE

The present doctoral thesis has been divided in three main parts: a general introduction and two chapters on the research activities performed. Each chapter has been divided into the following sections: (1) abstract, (2) introduction, (3) results and discussion, (4) conclusions and (5) experimental section. Compounds have been numbered jointly throughout the thesis. References have been included as footnotes and numbered independently in each chapter.

The general introduction provides an overview of the basic principles in homogeneous supramolecular catalysis and the supramolecular approaches for designing catalysts. A summary of the significant developments in catalysis using regulation strategies and halogen bonding interactions is also included in this section.

Chapter I discloses the design, synthesis and characterization of supramolecular catalytic systems based on regulation strategies and their application to the insertion of carbene species into O–H bonds. The manuscript summarizing the results was published in *Chem. Commun*. **2020**, *56*, 6364-6367.

Chapter II presents the use of halogen bonding interactions as a tool to construct the skeleton of transition metal-based catalysts and the design, synthesis and characterization of these new complexes. The manuscript corresponding to the contents described in Chapter II is under preparation.

INTRODUCTION

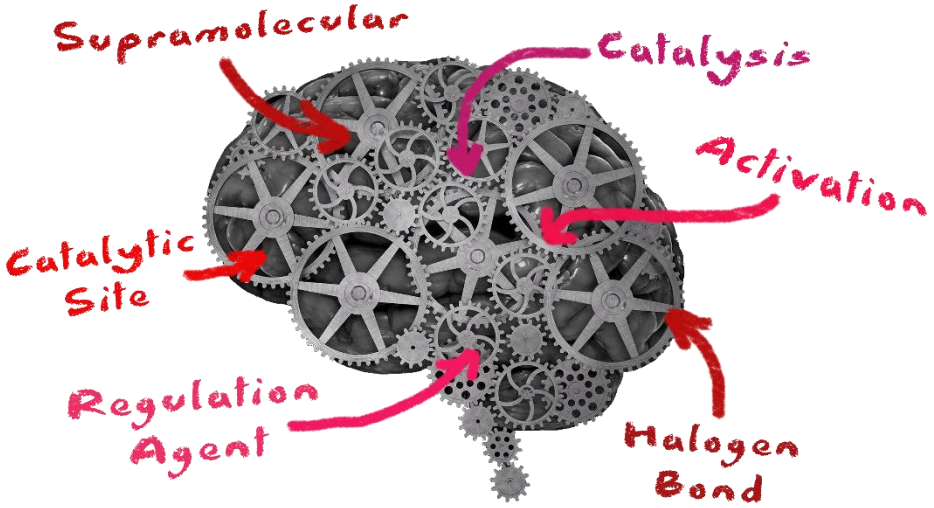

INTRODUCTION

Over the years, catalysis has been used as a synthetic strategy in many transformations. A catalyst[1] provides an energetically favorable pathway for the transformation of simple molecules into more complex structures. The design and synthesis of efficient catalysts have been an appealing objective of remarkable interest for many scientists and are still a challenge for many transformations.

In the past decades, supramolecular homogeneous catalysis has emerged as a promising approach within the field of catalysis and supramolecular chemistry.[2] Proper understanding of enzymatic systems has been the source of inspiration for many researchers aiming to develop new strategies for the synthesis of challenging supramolecular catalysts.[3] The main objective of this field of chemistry is to exploit supramolecular interactions to develop new functional catalysts. These interactions are distinctive for being reversible and non-covalent. Interactions such as the van der Waals forces, dipole-dipole, π-π interactions, anion-π, cation-π, chalcogen bonding, hydrogen bonding, halogen bonding, ion-dipole and ion-ion interaction are included in this context.[4] These interactions have been classified accordingly to their nature and strength (Figure 1). Although metal-ligand interactions have also been exploited in supramolecular chemistry, they cannot be considered non-covalent interactions, though they are reversible.

[1] Catalyst: a substance that increases the rate of a specific reaction without modifying the overall standard Gibbs energy change in the reaction. Adapted from: IUPAC. Laidler, K. J. *Pure Appl. Chem*. **1996**, *68*, 149-192.

[2] Steed, J. W.; Atwood, J. L. *Supramolecular Chemistry, Second Edition*. John Wiley & Sons, Ltd.: Chichester, 2009; p 970.

[3] *Supramolecular Catalysis*; van Leeuwen, P. W. N., Ed.; Wiley-VCH Verlag GmbH & Co.: Weinheim, 2008.

[4] See the following references and those included therein: (a) For chalcogen bonding interactions, see for example: Vogel, L.; Wonner, P.; Huber, S. M. *Angew. Chem., Int. Ed.* **2019**, *58*, 1880-1891. (b) For hydrogen bonding interactions, see: Mote, N. R.; Chikkali, S. H. *Chem.–Asian J.* **2018**, *13*, 3623-3646. (c) For halogen bonding interactions, see: Cavallo, G.; Metrangolo, P.; Milani, R.; Pilati, T.; Priimagi, A.; Resnati, G.; Terraneo, G. *Chem. Rev.* **2016**, *116*, 2478-2601. (d) For anion-π interactions, see: Zhao, Y.; Cotelle, Y.; Liu, L.; López-Andarias, J.; Bornhof, A.-B.; Akamatsu, M.; Sakai, N.; Matile, S. *Acc. Chem. Res.* **2018**, *51*, 2255-2263. (e) For cation-π interactions, see: Kennedy, C. R.; Lin, S.; Jacobsen, E. N. *Angew. Chem., Int. Ed.* **2016**, *55*, 12596-12624. (f) For other interactions, see ref. 2.

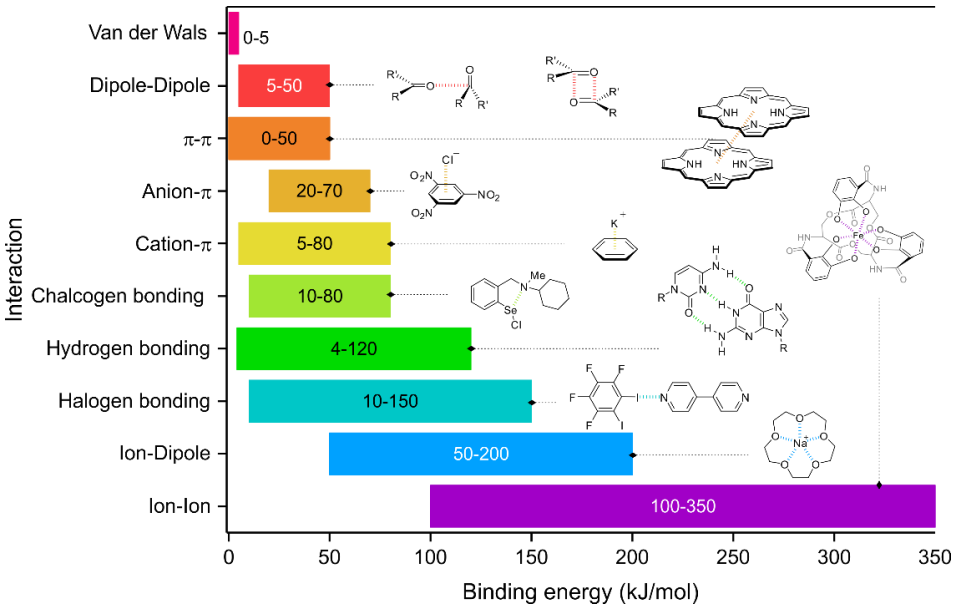

Figure 1. Schematic representation of supramolecular interactions and their strength (supramolecular interactions are highlighted with colored dashed lines).

Due to the extensive literature describing supramolecular catalysis, this introduction will focus on the use of ion-dipole and halogen bonding interactions for the development of catalysts. These two supramolecular interactions are closely related to the topics studied in the present thesis and therefore will be disclosed in detail in this section. The reader is addressed to recent literature describing the exploitation of other supramolecular interactions to design and synthesize functional catalysts.[4]

Ion-dipole interactions are described as electrostatic interactions based on the Coulombic attraction between an ion and a polar neutral molecule. The directional character of this interaction allows designing complex structures under the complementarity principles, achieving self-assembled catalysts in a predictable form.[2] Alternatively, halogen bonding interactions occur when a net attractive interaction between an electrophilic region associated to a halogen atom in the molecular entity and a nucleophilic region (in another or the same molecular entity) takes place.[5]

[5] Desiraju, G. R.; Ho, P. S.; Kloo, L.; Legon, A. C.; Marquardt, R.; Metrangolo, P.; Politzer, P.; Resnati, G.; Rissanen, K. *Pure Appl. Chem.* **2013**, *85*, 1711-1713.

The idea behind the supramolecular catalysis approach[6] relies on bringing together and assembling the diverse entities involved in the catalytic event [*i.e.*, the ligands, the metal (if present), the substrate and other reagents] by supramolecular interactions to perform the catalytic transformation. The term "catalytic system" refers to the combination of all the partners included in the catalytic process. If a metal is present, two different spheres of coordination around the metal center are distinguishable. The first coordination sphere is established by the functional groups of the ligand that are bound directly to the metal center and the solvent molecules. The second sphere of coordination is commonly constituted by the metal counterions (if present), other molecules that interact with the ligands through supramolecular interactions and distal moieties of the ligand.

During the last years, supramolecular homogeneous catalysis has experienced an exponential growth, and many supramolecular catalysts have been designed and synthesized using supramolecular forces.[7] Regarding the diverse design approaches of supramolecular catalysts that can be found in the literature, four general strategies can be depicted (Figure 2):[7a]

- Ligand-ligand interactions:[8] This approach is based on the self-assembly of complementary building blocks by supramolecular interactions to construct the skeleton of the catalyst. Two main strategies have been envisaged for the assembling process. One approach involves the use of a template that displays binding sites for the selective assembly of the same or two different ligands. The second approach entails the functionalization of the ligands with complementary binding motifs.

- Ligand-additive interactions:[9] The second approach is based on the addition of a regulation agent, cofactor or allosteric effector that controls the geometry of the active catalytic site. Consequently, the catalytic response of the reaction can be modified by an external agent.

---

[6] In the present thesis, the term supramolecular catalysis is reserved for those reactions that involve supramolecular interactions that do not take part of the basic catalytic transformation.
[7] For comprehensive reviews see, for example: (a) Ballester, P.; Vidal-Ferran, A.; van Leeuwen, P. W. N. M. *Adv. Catal.* **2011**, *54*, 63-126; (b) Raynal, M.; Ballester, P.; Vidal-Ferran, A.; van Leeuwen, P. W. N. M. *Chem. Soc. Rev.* **2014**, *43*, 1660-1733; (c) Raynal, M.; Ballester, P.; Vidal-Ferran, A.; van Leeuwen, P. W. N. M. *Chem. Soc. Rev.* **2014**, *43*, 1734-1787.
[8] Bellini, R.; van der Vlugt, J. I.; Reek, J. N. H. *Isr. J. Chem.* **2012**, *52*, 613-629.
[9] Bellini, R.; Chikkali, S. H.; Berthon-Gelloz, G.; Reek, J. N. H. *Angew. Chem., Int. Ed.* **2011**, *50*, 7342-7345.

- Catalyst-substrate interactions:[10] The third approach is based on the formation of supramolecular assemblies between the catalyst and the substrate for the control of the reactivity of a substrate, for instance, *via* catalyst encapsulation or substrate orientation.

- Multiple interactions:[11] The fourth approach is based on the multiple supramolecular interactions that could exist between the entities involved in the catalytic transformation (*e.g.*, the metal, the ligand, the substrate, or even the counteranion).

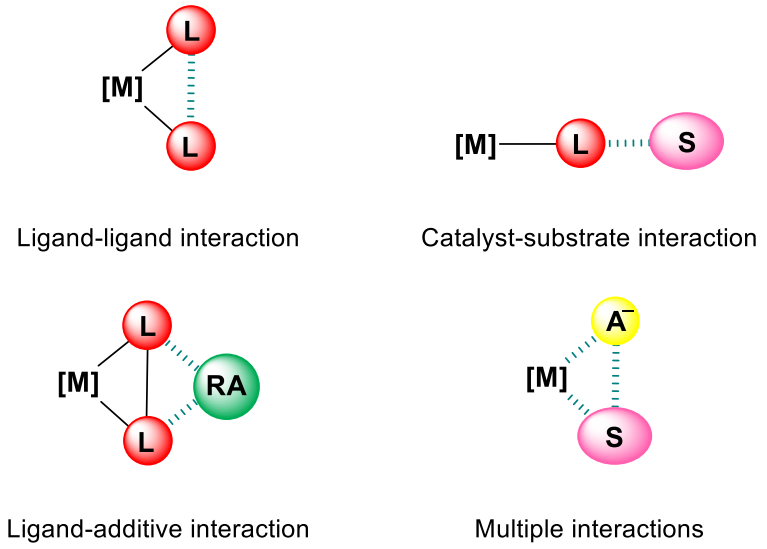

Figure 2. Schematic representation of supramolecular approaches for catalyst design (supramolecular interactions are highlighted with green dashed lines; **L** refers to the ligand, **S** to the substrate, **A** to the anion, and **RA** to the regulation agent).

The use of the abovementioned supramolecular approaches provides several advantages for the construction of a catalyst in comparison to the conventional synthetic methodologies, where the metal catalyst is normally built through standard synthetic protocols. The first benefit is the reduction of the amount of synthetic work. Supramolecular catalytic systems can self-assemble *in situ* by mixing the different building blocks. Furthermore, the steric and electronic properties of the ligand can be tuned by simple modifying one of the components of the catalytic system. Secondly, and probably most importantly, multiple combinations of ligand units enable facile and rapid access to large

[10] Davis, H. J.; Phipps, R. J. *Chem. Sci.* **2017**, *8*, 864-877.
[11] Mukherjee, S.; List, B. *J. Am. Chem. Soc.* **2007**, *129*, 11336-11337.

libraries of catalysts.[7] This is crucial for the catalyst design based on combinatorial methods and high-throughput screening.[12] In catalytic reactions, the selectivity of the transformation is given by energy differences in the transition states smaller than 3 kcal mol^{-1}.[13] Considering that, it has been rationalized that the non-covalent supramolecular interactions could be used to change the activity and selectivity of any catalytic transformation, due to the efficient construction approach that provides several supramolecular catalysts with subtle modifications in their backbones. However, the total control of the self-assembly processes still remains a challenge and the design of effective and efficient catalysts for some transformations remains elusive.

During the sixties, Monod[14] and Koshland[15] introduced the term allosterism, derived from the Greek words *allos*, which means "the other", and *stereos* which means "solid". Allosterism refers to the effects in binding more than one substrate selectively to different binding sites of a receptor. In other words, the binding of an allosteric effector or regulation agent (RA) at a remote allosteric site (or regulation binding site), can cause conformational changes at the active site which alter its reactivity to the substrate(s), resulting in an activating (positive cooperation) or deactivating (negative cooperation) process. (Figure 3).

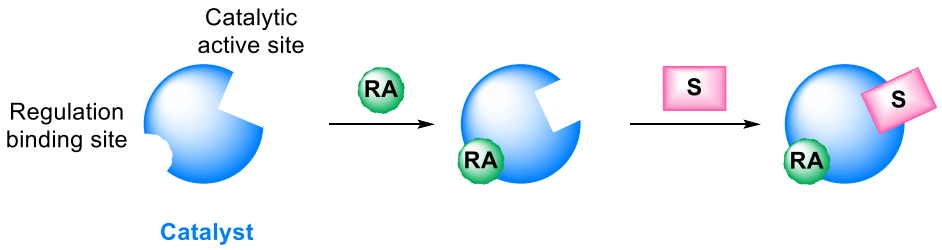

Figure 3. Schematic representation of an allosteric positive regulation process.

This phenomenon is found in Nature in several enzymatic transformations.[16] Interestingly, non-natural allosteric catalysts may provide access to new catalytic systems using supramolecular interactions that can be used in several transformations, where the activity or selectivity can be modulated by a

[12] Crabtree, R. H. *Chem. Commun.* **1999**, 1611-1616.
[13] Knowles, W. S. *Acc. Chem. Res.* **1983**, *16*, 106-112.
[14] Monod, J.; Changeux, J. P.; Jacob, F. *J. Mol. Biol.* **1963**, *6*, 306-329.
[15] Koshland, D. E. Jr.; Némethy, G.; Filmer, D. *Biochemistry* **1966**, *5*, 365-385.
[16] For selected examples, see: (a) Perutz, M. F.; Fermi, G.; Luisi, B.; Shaanan, B.; Liddington, R. C. *Acc. Chem. Res.* **1987**, *20*, 309-321; (b) Grandori, R.; Lavoie, T. A.; Pflumm, M.; Tian, G.; Niersbach, H.; Maas, W. K.; Fairman, R.; Carey, J. *J. Mol. Biol.* **1995**, *254*, 150-162.

regulation agent or cofactor. Moreover, the development of these catalytic systems can be employed as a synthetic model for the better understanding of enzymatic processes, and also, for the development of catalysts for natural enzymatic reactions.

A seminal example of non-natural allosteric catalysts was reported by Shinkai and coworkers, who described the use of histamine-containing methacrylic polymers **3** to catalyze the hydrolysis of carboxylic esters **1** (Scheme 1).[17]

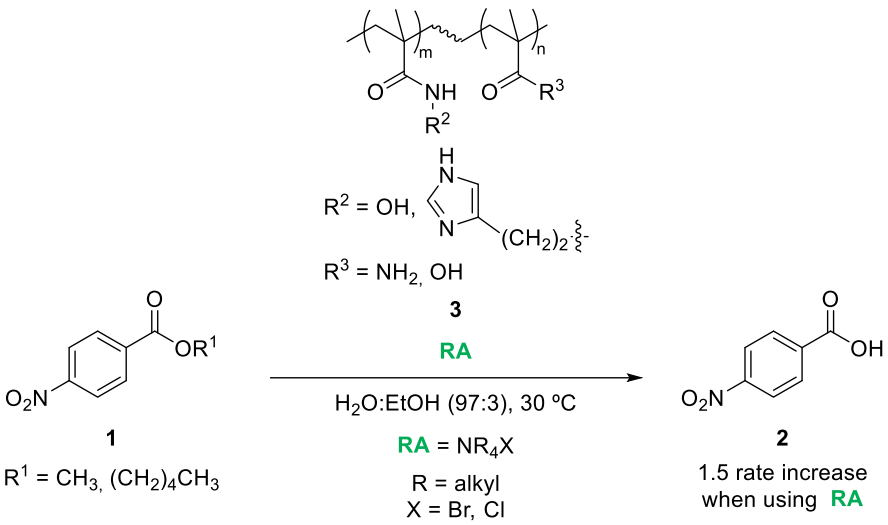

Scheme 1. Hydrolysis of carboxylic esters **1** catalyzed by polymers **3** in the presence of tetraalkylammonium salts as RA.

The authors demonstrated that the addition of tetraalkylammonium salts (regulation agents) to the system enhanced up to 1.5-fold the reaction rate. The authors could demonstrate the allosteric regulation effect, as the addition of salts promoted the binding of the substrate to the catalyst. Shinkai and coworkers followed the investigations in this field by developing systems based on the design of new receptors containing crown ether as regulation sites, expanding the scope of ions that could be used as regulation agents.[18]

[17] Shinkai, S.; Tou, K.; Kunitake, T. *Polym. J.* **1977**, *9*, 381-389.
[18] Takeuchi, M.; Ikeda, M.; Sugasaki, A.; Shinkai, S. *Acc. Chem. Res.* **2001**, *34*, 865-873.

After the pioneering contributions of Shinkai and coworkers in the design of non-natural allosteric catalytic systems, many works emerged in the field of supramolecular catalysis regulated by allosteric mechanisms.[19]

In this area, the contributions of Mirkin and coworkers deserve special mention. In 2003, the authors reported a reversible bistable supramolecular catalyst which could display an *open* or *closed* active site by the effect of an external cofactor at one or more distal binding sites.[20] To build this challenging supramolecular system, Mirkin and coworkers developed the weak-link approach (WLA), which consists of the assembly of flexible multidomain supramolecular scaffolds.[21] The catalytic activity of complex **4** was modified by the interaction between carbon monoxide and chlorido ligands (the allosteric effectors) to each rhodium(I) center (Scheme 2). In other words, the coordination geometry of the transition metal could be easily modified by the addition of small molecules to the distal site of the chromium(II) metal center (the active site). The use of hemilabile ligands allowed building these flexible supramolecular macrocyclic complexes applying the WLA approach for their use in other transformations, for instance, in acyl transfer reactions.[22] Thereafter, Mirkin and coworkers expanded the WLA approach developing a triple layer catalytic system, which could afford three distinct states (fully *open*, *semi-open*, and fully *closed*) through allosteric effectors.[23] More recently, the same group synthesized a new allosterically regulated four-state macrocycle assembled *via* the WLA approach.[24] The complexity of the macrocyclic designs has increased over the years, as much as the use of diverse transition metals or allosteric effectors.[25]

---

[19] For a selected review, see: (a) Kovbasyuk, L.; Krämer, R. *Chem. Rev.* **2004**, *104*, 3161-3187; (b) Kremer, C.; Lützen, A. *Chem.–Eur. J.* **2013**, *19*, 6162-6196; (c) Vaquero, M.; Rovira, L.; Vidal-Ferran, A. *Chem. Commun.* **2016**, *52*, 11038-11051.
[20] Gianneschi, N. C.; Bertin, P. A.; Nguyen, S. T.; Mirkin, C. A.; Zakharov, L. N.; Rheingold, A. L. *J. Am. Chem. Soc.* **2003**, *125*, 10508-10509.
[21] Gianneschi, N. C.; Masar III, M. S.; Mirkin, C. A. *Acc. Chem. Res.* **2005**, *38*, 825-837.
[22] Masar III, M. S.; Gianneschi, N. C.; Oliveri, C. G.; Stern, C. L.; Nguyen, S. T.; Mirkin, C. A. *J. Am. Chem. Soc.* **2007**, *129*, 10149-10158.
[23] Yoon, H. J.; Kuwabara, J.; Kim, J.-H.; Mirkin, C. A. *Science* **2010**, *330*, 66-69.
[24] d'Aquino, A. I.; Cheng, H. F.; Barroso-Flores, J.; Kean, Z. S.; Méndez-Arroyo, J.; McGuirk, C. M.; Mirkin, C. A. *Inorg. Chem.* **2018**, *57*, 3568-3578.
[25] (a) Lifschitz, A. M.; Rosen, M. S.; McGuirk, C. M.; Mirkin, C. A. *J. Am. Chem. Soc.* **2015**, *137*, 7252-7261; (b) Lifschitz, A. M.; Young, R. M.; Méndez-Arroyo, J.; McGuirk, C. M.; Wasielewski, M. R.; Mirkin, C. A. *Inorg. Chem.* **2016**, *55*, 8301-8308.

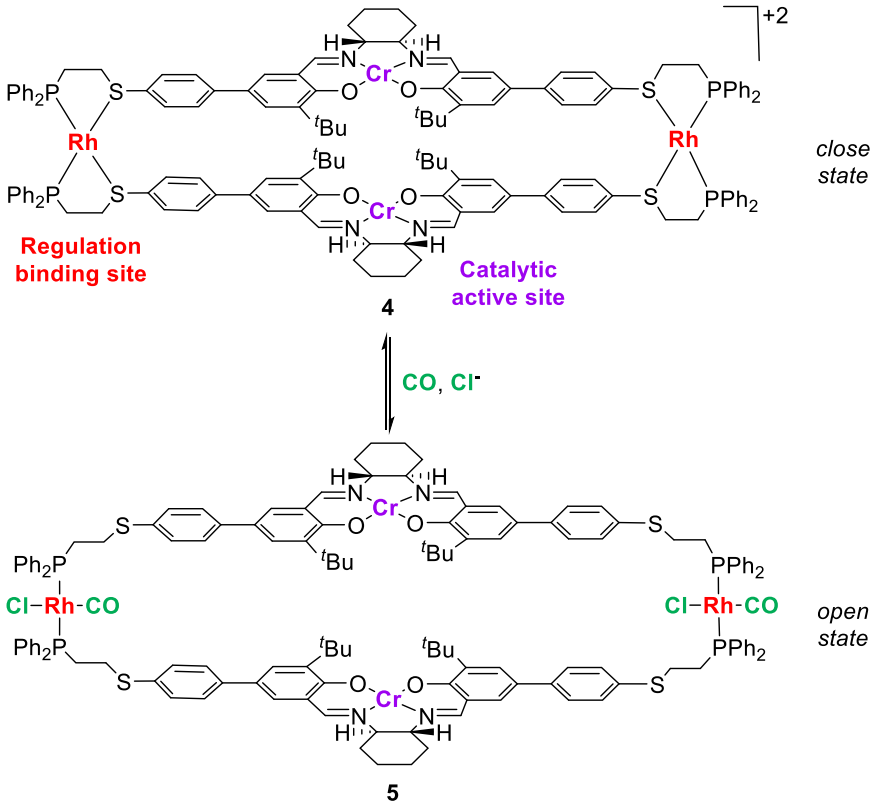

Scheme 2. Mirkin's supramolecular allosteric catalytic system shown in the *close* state **4** and *open* state **5**.

The work of Fan and coworkers must be also included in the discussion of relevant contributions in the field of supramolecular catalysis regulated by allosteric effectors. Fan's group has focused the research activities, among other topics, on the formation of catalytic systems containing bidentate ligands through the presence of ion-dipole interactions.[26] In 2010, Fan and coworkers reported the preparation of the α,ω-bisphosphite polyether ligand **6** (Figure 4). Fan and coworkers pioneered the study of the effect of alkali metals salts as regulation agents in the rhodium-catalyzed enantioselective hydrogenation of α-dehydroamino acid esters.[27] Thus, the authors reported the first example in enantioselective hydrogenation, where the enantioselectivity values were enhanced up to 17% by the addition of a regulation agent.

[26] Li, Y.; Feng, Y.; He, Y.-M.; Chen, F.; Pan, J.; Fan, Q.-H. *Tetrahedron Lett.* **2008**, *49*, 2878-2881.
[27] Li, Y.; Ma, B.; He, Y.; Zhang, F.; Fan, Q.-H. *Chem.–Asian J.* **2010**, *5*, 2454-2458.

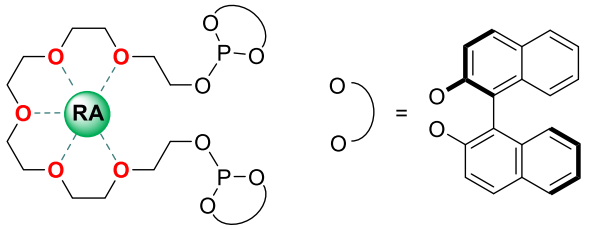

(*S*)-**6**

Figure 4. Fan's supramolecular ligand **6** (supramolecular interactions are highlighted with green dashed lines).

Our research group has also expanded the use of ion-dipole interactions for the construction of supramolecularly regulated catalytic systems. In the following lines of this introduction, the contributions from our research group in supramolecularly regulated catalysis that inspired part of the work of the present thesis will be discussed.

Our group has been developing libraries of supramolecular catalysts based on the allosteric regulation approach.[19c,28] The group developed supramolecular complexes composed by a polyether chain (regulation binding site) displaying functional groups at the α and ω positions of the chain (ligating groups), which were able to coordinate to the metal center (catalytic site). A regulation agent (RA), which is capable of binding to the polyether chain through ion-dipole interactions, brings the ligating groups together due to the template effect that this species exerts (Figure 5). The binding of the RA to the regulation site triggers the regulation mechanism, since this binding event modifies the rigidity and conformation of the catalytic site and results in a change of the activity and selectivity of the catalyst.

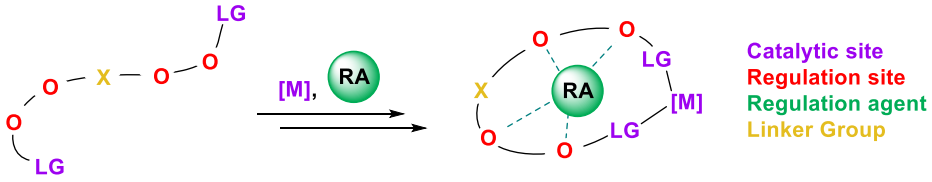

Figure 5. Schematic representation of the supramolecular approach of our research group (supramolecular interactions are highlighted with green dashed lines).

[28] Llorente, N.; Fernández-Pérez, H.; Núñez-Rico, J. L.; Carreras, L.; Martínez-Carrión, A.; Iniesta, E.; Romero-Navarro, A.; Martínez-Bascuñana, A.; Vidal-Ferran, A. *Pure Appl. Chem.* **2019**, *91*, 3-15.

The group has been interested in the use of polyether chains as regulation site for two main reasons.[29] On the one hand, for their ability to strongly bind a large variety of alkali metals salts through ion-dipole interactions. In some examples, a linker group (X) was introduced to endorse additional stereogenic elements or to restrict the flexibility of the polyether motif. On the other hand, due to the well-established protocols that are described in the literature to synthesize this scaffold. Regarding the ligating groups, the group focused its attention on phosphorus-based functional groups. Moreover, these units allowed for the construction of enantiopure catalysts. Concerning the metal center, the group has mainly developed rhodium (I)-,[30] palladium (II)-[31] and gold (I)-[32] supramolecularly regulated catalysts. Finally, a wide range of alkali metal, alkaline earth metal salts, lanthanide, and ammonium salts have been already used by our group as regulation agents.[33]

Initial studies of the group focused on the design and synthesis of an array of P=O disubstituted biphenyl derivatives with appended crown ether moieties (Figure 6). The regulation approach was evaluated in the recognition of dicarboxylic acids.[34]

[29] For selected reviews, see: (a) C. J. Pedersen, *Angew. Chem., Int. Ed. Engl.* **1988**, *100*, 1021-1027; (b) Bajaj, A. V.; Poonia, N. S. *Coord. Chem. Rev*. **1988**, *87*, 55-213; (c) van Veggel, F. C. J. M.; Verboom, W.; Reinhoudt, D. N. *Chem. Rev.* **1994**, *94*, 279-299; (d) Steed, J. W. *Coord. Chem. Rev*. **2001**, *215*, 171-221; (e) Mezei, G.; Zaleski, C. M.; Pecoraro, V. L. *Chem. Rev.* **2007**, *107*, 4933-5003.

[30] (a) Mon, I.; Jose, D. A.; Vidal-Ferran, A. *Chem.–Eur. J.* **2013**, *19*, 2720-2725; (b) Fernández-Pérez, H.; Mon, I.; Frontera, A.; Vidal-Ferran, A. *Tetrahedron* **2015**, *71*, 4490-4494; (c) Rovira, L.; Vaquero, M.; Vidal-Ferran, A. *J. Org. Chem.* **2015**, *80*, 10397-10403; (d) Vidal-Ferran, A.; Mon, I.; Bauzá, A.; Frontera, A.; Rovira, L. *Chem.–Eur. J.* **2015**, *21*, 11417-11426; (e) Martínez-Carrión, A.; Howlett, M. G.; Alamillo-Ferrer, C.; Clayton, A. D.; Bourne, R. A.; Codina, A.; Vidal-Ferran, A.; Adams, R. W.; Burés, J. *Angew. Chem., Int. Ed.* **2019**, *58*, 10189-10193.

[31] Rovira, L.; Fernández-Pérez, H.; Vidal-Ferran, A. *Organometallics* **2016**, *35*, 528-533.

[32] Carreras, L.; Franconetti, A.; Grabulosa, A.; Frontera, A.; Vidal-Ferran, A. *Org. Chem. Front.* **2020**, *7*, 1626-1634.

[33] Carreras, L.; Rovira, L.; Vaquero, M.; Mon, I.; Martin, E.; Benet-Buchholz, J.; Vidal-Ferran, A. *RSC Adv.* **2017**, *7*, 32833-32841.

[34] Jose, D. A.; Mon, I.; Fernández-Pérez, H.; Escudero-Adán, E. C.; Benet-Buchholz, J.; Vidal-Ferran, A. *Org. Lett.* **2011**, *13*, 3632-3635.

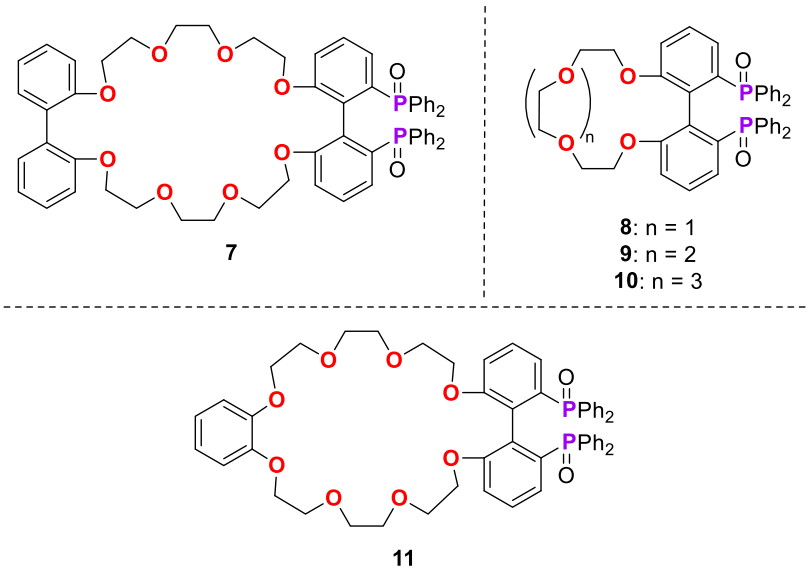

Figure 6. P=O disubstituted biphenyl supramolecular ligands **7**-**11**.

The group demonstrated that the binding event of the regulation agent within the crown ether scaffold *via* ion-dipole interactions induced a conformational change in the ligand, modifying its binding properties towards dicarboxylic acids.

This regulation strategy has been satisfactorily established in the rhodium-catalyzed enantioselective hydroformylation reaction of an array of structurally diverse alkenes **12**.[30a] A set of rhodium complexes derived from ligand **15** were applied in this transformation (Scheme 3). The effects produced by using regulation agents such as alkali metal salts were studied on the catalytic activity and (stereo)selectivity of enantioselective hydroformylation reactions. Positive regulation effects were observed when CsBArF[35] was added as a RA (up to 62%) in the hydroformylation of vinyl acetate, reporting the highest enantioselectivity at that moment for this substrate using a bisphosphite ligand.

[35] BArF = $[B(3,5\text{-}(CF_3)_2C_6H_3)_4]$.

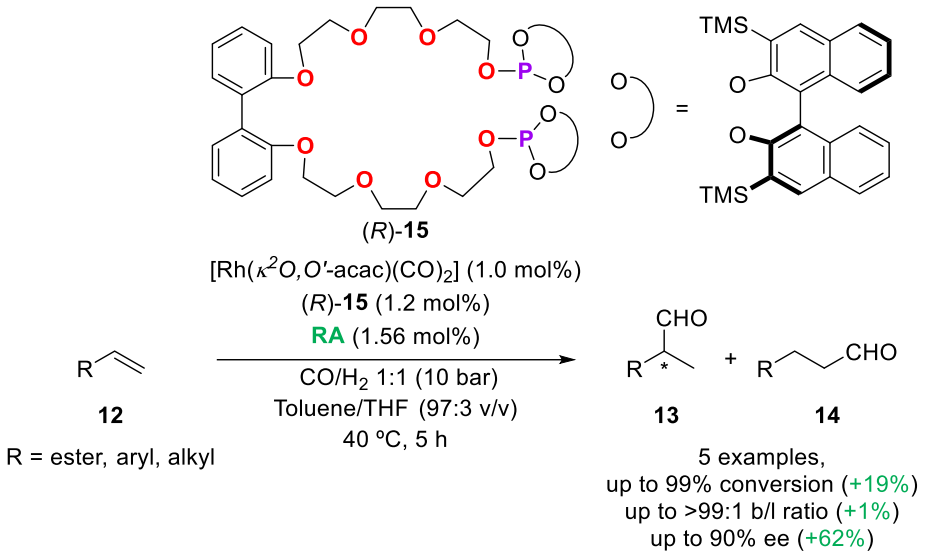

Scheme 3. Enantioselective hydroformylation reactions of alkenes **12** catalyzed by supramolecular rhodium complexes derived from ligand **15**.

A new array of enantiomerically pure supramolecular catalysts incorporating a set of structurally diverse polyether chains, different ligating groups in the catalytic sites, and diverse RAs (alkali metal and ammonium salts) was described.[30d] Binding studies pointed out stronger affinities between the ligands and alkali metal BArF salts than with ammonium BArF salts. The new generation of rhodium catalysts derived from the supramolecular ligand **16** was tested in enantioselective hydroformylation reactions of alkenes **12**. In most cases, a positive allosteric effect was observed when the RA was added to the reaction. Specifically, the highest regulation effect towards the enantioselectivity (increase in the ee up to 96%) was achieved using the ligand **16** and RbBArF as RA in the enantioselective hydroformylation of vinyl benzoate (Scheme 4). Computational studies supported the approach suggesting that the increase of the enantioselectivity provided by RbBArF emerged from the adaptability of the catalytic site to the optimal geometry (*i.e.*, the P–Rh–P bond angle) when RbBArF was added.

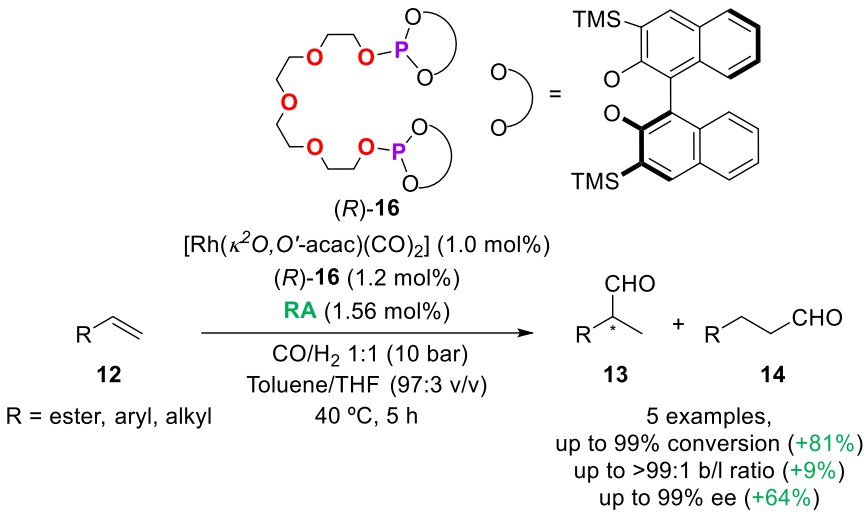

Scheme 4. Enantioselective hydroformylation reaction of alkenes **12** catalyzed by supramolecular rhodium complexes derived from ligand **16**.

A third generation of supramolecular bisphosphite ligands containing a stereogenic element in the regulation site was reported.[30c] The rhodium catalysts derived from the supramolecular ligand **19** were tested in the enantioselective hydroformylation of heterocyclic olefins **17**, which are challenging substrates in this chemistry. The results obtained for five-membered heterocyclic olefins were satisfactory for both the regioselectivities and enantioselectivities when KBArF was used as RA (Scheme 5).

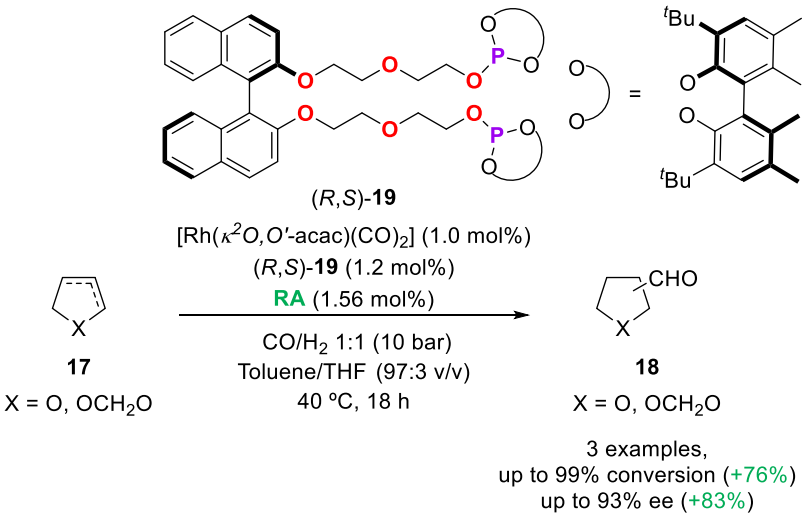

Scheme 5. Hydroformylation of heterocyclic olefins **17** catalyzed by supramolecular rhodium complexes derived from ligand **19**.

After these results, our group expanded the supramolecular approach to palladium-catalyzed enantioselective allylic substitutions.[31] The regulation principle was also demonstrated using a new set of enantiopure bisphosphites ligands **22** (Scheme 6). The selectivity of the reaction could be regulated using alkali metals salts, alkaline earth metal salts or lanthanide metal salts as RA with moderate enhancements of the enantioselectivity being observed (enhancements up to 16% in the ee for benzylamine as the nucleophile and $Mg(OTf)_2$ or $La(OTf)_2$ or $Ho(OTf)_3$ as the regulation agent).

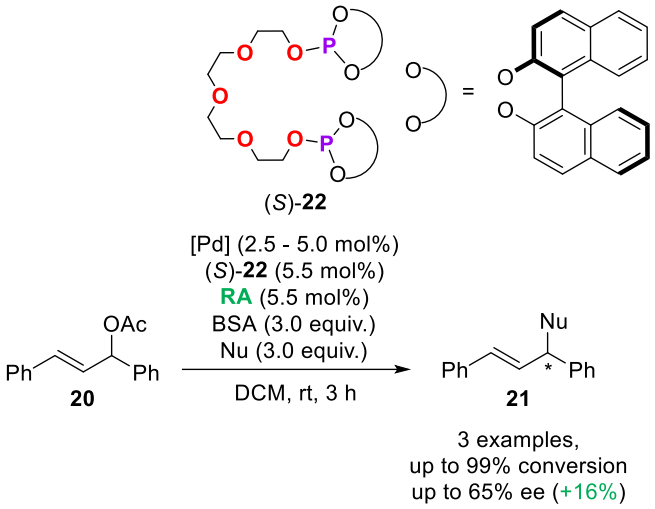

Scheme 6. Allylic substitutions on **20** catalyzed by supramolecular palladium complexes derived from ligand **22**.

A new library of achiral supramolecular ligands, bearing phosphines and phosphites as ligating groups, was developed by our group. These new ligands, in combination with alkali metal BArF salts as RA, were tested in the rhodium-catalyzed hydroformylation of 1,1'-disubtituted allenes **23** (Scheme **7**).[36] The supramolecular rhodium-based complex formed by ligand **25**, KBArF and the rhodium metal center showed an enhancement of the catalytic activity (from 9% in the absence of RA to 69% yield with KBArF as RA) in the hydroformylation of the allene **23** to the corresponding β,γ-unsaturated aldehyde **24**.

[36] Martínez-Carrión, A.; Vidal-Ferran, A.; unpublished results.

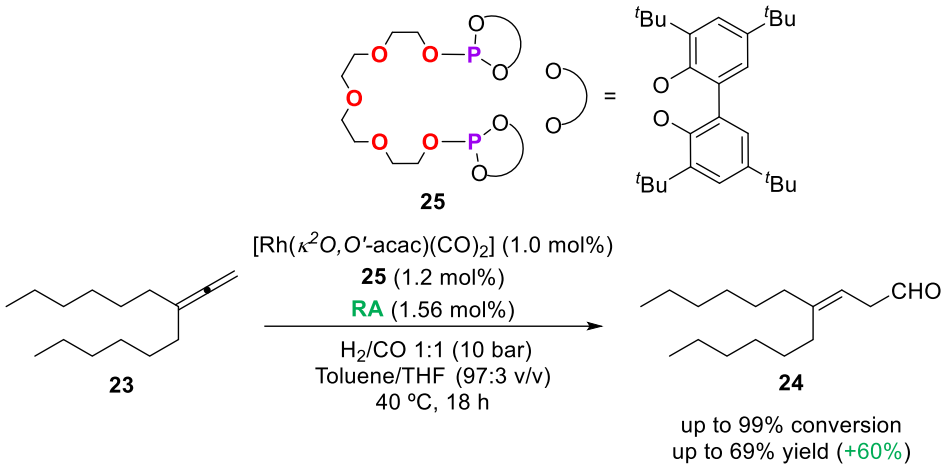

Scheme 7. Hydroformylation of the 1,1'-disubstituted allene **23** catalyzed by supramolecular rhodium complexes derived from ligand **25**.

The enantioselective hydroformylation of aryl vinyl ethers **26** catalyzed by supramolecularly regulated rhodium-based complexes derived from α,ω-bisphosphite ligands **29** and alkali metals BArF salts was also carried out (Scheme 8).[3636] The catalytic activities (from 3-25% conversion in the absence of RA up to 25-99% with the use of a RA) and enantioselectivities (from 57:43-85:15 er in the absence of RA to 47:53-97:3 er) were enhanced using LiBArF as RA.

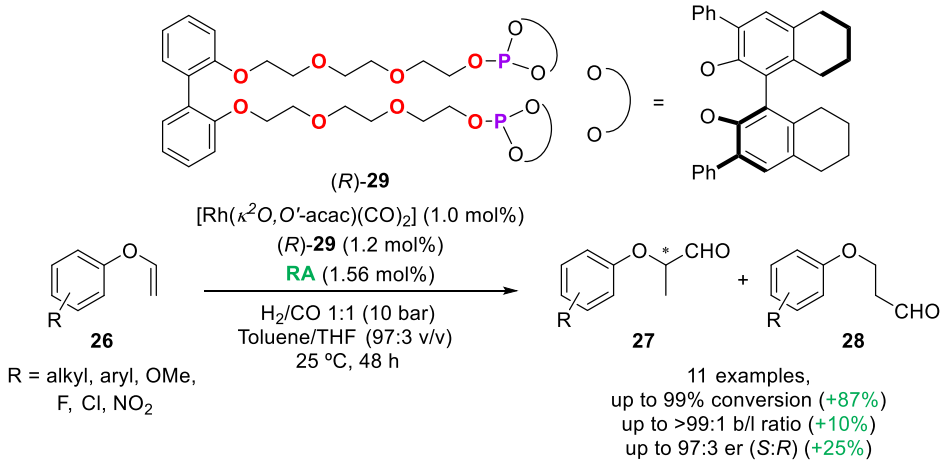

Scheme 8. Enantioselective hydroformylation of aryl vinyl ethers **26** catalyzed by supramolecular rhodium complexes derived from ligand **29**.

More recently, the group described a new set of supramolecularly regulated Au(I) catalysts **34** and successfully used them as catalysts in the selective C–H functionalization of phenols **30** and related derivatives with gold carbenes derived from diazoderivatives **31** (Scheme 9).[32] The regulation strategy provided an enhancement of the activity (from 15-89% yield in the absence of RA to up to 18-99% yield with the use of a RA) and increase of the selectivity of the reaction (from 28:1 to >50:1 in terms of *para*-C_{sp^2}–H *vs.* O–H functionalization products) when $RbBF_4$ or $CsBF_4$ were employed as RAs. DFT calculations were performed to rationalize the catalytic performance of the supramolecularly regulated catalysts. These studies suggested that regulation agents with cations of large size such as $CsBF_4$ or $RbBF_4$ had a positive effect in the insertion of the gold-carbene into the *para*-C_{sp^2}–H bond.

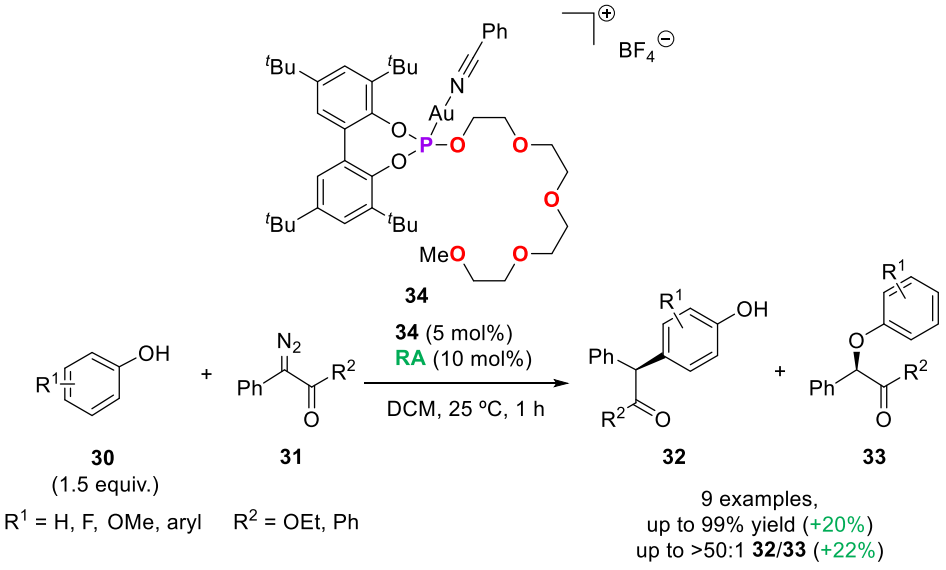

Scheme 9. C–H selective functionalization of phenols **30** catalyzed by supramolecular Au(I) complexes **34**.

As it will be discussed at the time of presenting the objectives of this thesis, all these results encouraged us to expand the regulation principle in supramolecular catalysis by developing a new set of supramolecularly regulated catalysts based on copper(I) as the catalytic metal. The use of copper as a metal precursor picked our interest due to the current concern about using earth abundant metals, rather than precious metals in catalysis.[37]

[37] Zweig, J. E.; Kim, D. E.; Newhouse, T. R. *Chem. Rev.* **2017**, *117*, 11680-11752.

The design and preparation of supramolecular metal complexes derived from bidentate ligands through ligand-ligand interactions is one of the most used strategies over the years.[38] In the first approach, two suitably designed building blocks get assembled to a template through supramolecular interactions, with formation of the target supramolecular metal complex (for a general representation of this assembly process, see Figure 7a). Alternatively, in the second approach within this method, metal complexes derived from bidentate ligands have also been prepared by assembling two building blocks that incorporate the ligating groups for catalysis as well as complementary binding motifs for the assembly process through supramolecular interactions (for a general representation of this assembly process, see Figure 7b).

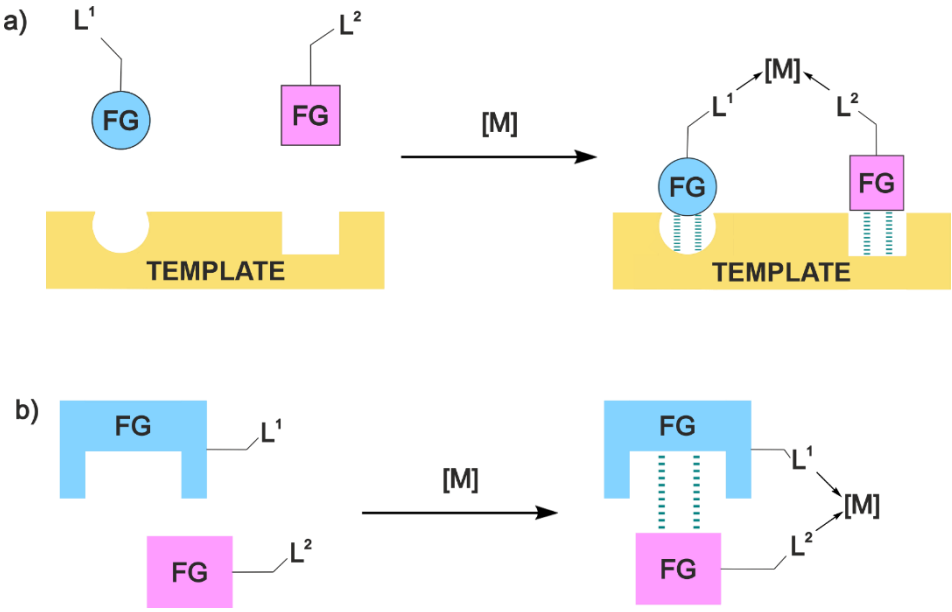

Figure 7. Schematic representation of the two main approaches for the formation of supramolecular metal complexes derived from bidentate ligands by ligand-ligand interactions: a) by using a template; b) by assembling two complementary buildings blocks (supramolecular interactions are highlighted with green dashed lines; **FG** refers to the corresponding functional groups).

The preferred use of monodentate ligands in catalysis is not surprising due to their usually simpler preparation compared to the bidentate ones. Nevertheless, several transformations require the use of chelating bidentate ligands, which is

[38] For selected reviews, see: (a) Wilkinson, M. J.; van Leeuwen, P. W. N. M.; Reek, J. N. H. *Org. Biomol. Chem.* **2005**, *3*, 2371-2383; (b) Breit, B. *Angew. Chem., Int. Ed.* **2005**, *44*, 6816-6825; (c) Meeuwissen, J.; Reek, J. N. H. *Nat. Chem.* **2010**, *2*, 615-621.

attributed to the more rigid environment that they can provide in the surroundings of the metal coordination sphere.[39] Not surprisingly, supramolecular chemistry offers strategies to selectively construct complex systems by the assembly of suitably designed building blocks that incorporate the required ligating groups for catalysis and the required functionalities for the assembly process.[38] The applicability of this principle in homogeneous catalysis implied a breakthrough for the preparation of catalysts when compared with standard covalent chemistry. Furthermore, this supramolecular synthetic strategy allowed for the fast development of combinatorial approaches and its application in the formation of supramolecular catalysts.

During the last years, the assembly of bidentate ligands through Lewis acid-Lewis base interactions,[40] hydrogen bonding,[41] ionic[42] or metal-ligand interactions[43] has become the focus of multiple research activities, as the groups of Breit, van Leeuwen, Reek and Takacs, among others, have elegantly demonstrated.

In 2001, van Leeuwen and Reek demonstrated that using coordinate covalent bonds, supramolecular ligands could also be constructed by the assembly of pyridyl functionalized ligands **35** and a Zn-porphyrin complex **36** *via* a template strategy. The metal catalyst **37** could be structurally varied by changing either the Zn-porphyrin unit or the pyridyl-containing phosphine ligand (Scheme 10).[44]

---

[39] For selected reviews, see: (a) Goudriaan, P. E.; van Leeuwen, P. W. N. M.; Birkholz, M.-N.; Reek, J. N. H. *Eur. J. Inorg. Chem.* **2008**, 2939-2958; (b) Durand, D. J.; Fey, N. *Chem. Rev.* **2019**, *119*, 6561-6594.

[40] Denmark, S. E.; Beutner, G. L. In *Lewis Base Catalysis in Organic Synthesis*; Vedejs, E.; Denmark, S. E., Eds.; Wiley-VCH Verlag GmbH & Co.: Weinheim, 2016; Vol. 1, pp 31-54.

[41] Arunan, E.; Desiraju, G. R.; Klein, R. A.; Sadlej, J.; Scheiner, S.; Alkorta, I.; Clary, D. C.; Crabtree, R. H.; Dannenberg, J. J.; Hobza, P.; Kjaergaard, H. G.; Legon, A. C.; Mennucci, B.; Nesbitt, D. J. *Pure Appl. Chem.* **2011**, *83*, 1619-1636.

[42] Gulyás, H.; Benet-Buchholz, J.; Escudero-Adán, E. C.; Freixa, Z.; van Leeuwen, P. W. N. M. *Chem.–Eur. J.* **2007**, *13*, 3424-3430.

[43] Uflyand, I. E.; Dzhardimalieva, G. I. *J. Coord. Chem.* **2018**, *71*, 1272-1356.

[44] Slagt, V. F.; Reek, J. N. H.; Kamer, P. C. J.; van Leeuwen, P. W. N. M. *Angew. Chem., Int. Ed.* **2001**, *40*, 4271-4274.

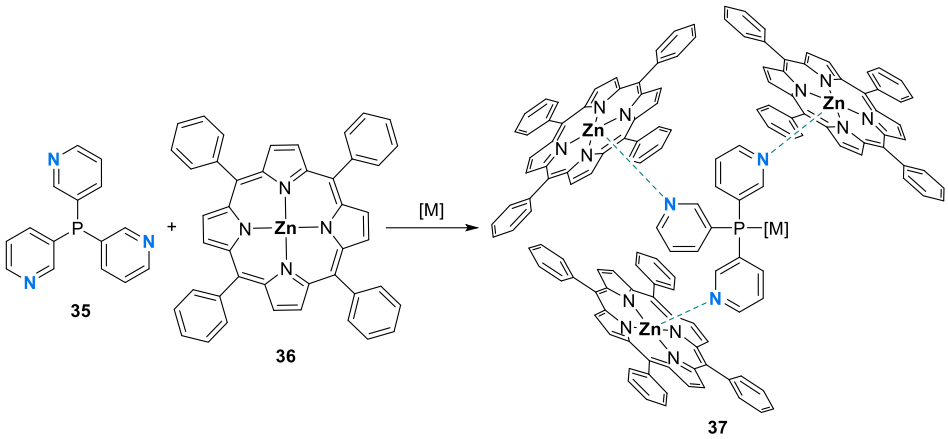

Scheme 10. Formation of supramolecular metal catalysts **37** by the assembly of the pyridyl functionalized ligands **35** and Zn-porphyrin complex **36** (supramolecular interactions are highlighted with green dashed lines).

Some years later, the same authors developed a supramolecular approach to prepare efficient libraries of structurally diverse bidentate ligands named SUPRAPhos.[45] These ligands were constructed by simply mixing two monomeric phosphorus-based ligands in solution, each one incorporating complementary binding groups: a Zn-porphyrin in the building block **38**-**39** and a pyridyl unit in **40**-**41** (Scheme 11). The bidentate ligands were formed *via* self-assembly of the two starting materials.

[45] (a) Slagt, V. F.; Röder, M.; Kamer, P. C. J.; van Leeuwen, P. W. N. M.; Reek, J. N. H. *J. Am. Chem. Soc.* **2004**, *126*, 4056-4057; (b) Jiang, X.-B.; Lefort, L.; Goudriaan, P. E.; de Vries, A. H. M.; van Leeuwen, P. W. N. M.; de Vries, J. G.; Reek, J. N. H. *Angew. Chem., Int. Ed.* **2006**, *45*, 1223-1227.

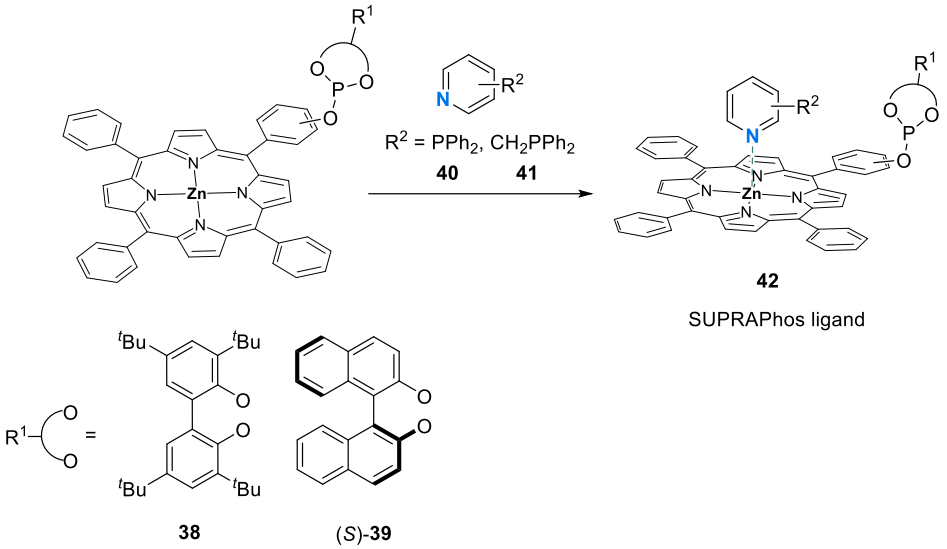

Scheme 11. Formation of supramolecular bidentate ligands SUPRAPhos **42** by using Zn-porphyrin building blocks **38**-**39** and pyridyl units **40**-**41** (supramolecular interactions are highlighted with green dashed lines).

After this work, the authors developed different libraries of catalysts based on the same principle than SUPRAPhos (*e.g.*, UREAPhos,[46] METAMORPhos,[47] LEUPhos,[48] etc.). This methodology provided access to large libraries of bidentate ligands that were used, for instance, in enantioselective rhodium hydrogenations of numerous functionalized alkenes, obtaining excellent enantioselectivities (up to 96% ee using UREAPhos ligands for dimethyl 2-methylenesuccinate as substrate).[46,49] These supramolecular catalysts were also used in the enantioselective rhodium hydroformylations of olefins, achieving moderate results in terms of activity and enantioselectivity (up to 76% ee using SUPRAPhos ligands for styrene as substrate).[50]

---

[46] Sandee, A. J.; van der Burg, A. M.; Reek, J. N. H. *Chem. Commun.* **2007**, 864-866.
[47] Patureau, F. W.; Kuil, M.; Sandee, A. J.; Reek, J. N. H. *Angew. Chem., Int. Ed.* **2008**, *47*, 3180-3183.
[48] Breuil, P.-A. R.; Patureau, F. W.; Reek, H. N. H. *Angew. Chem., Int. Ed.* **2009**, *48*, 2162-2165.
[49] For selected examples, see: (a) Meeuwissen, J.; Kuil, M.; van der Burg, A. M.; Sandee, A. J.; Reek, J. N. H. *Chem.–Eur. J.* **2009**, *15*, 10272-10279; (b) Patureau, F. W.; de Boer, S.; Kuil, M.; Meeuwissen, J.; Breuil, P.-A. R.; Siegler, M. A.; Spek, A. L.; Sandee, A. J.; de Bruin, B.; Reek, J. N. H. *J. Am. Chem. Soc*. **2009**, *131*, 6683-6685; (c) Meeuwissen, J.; Detz, R.; Sandee, A. J.; de Bruin, B.; Siegler, M. A.; Spek, A. L.; Reek, J. N. H. *Eur. J. Inorg. Chem.* **2010**, 2992-2997.
[50] For selected examples, see: (a) Goudriaan, P. E.; Jang, X.-B.; Kuil, M.; Lemmens, R.; van Leeuwen, P. W. N. M.; Reek, J. N. H. *Eur. J. Org. Chem.* **2008**, 6079-6092; (b) Goudriaan, P. E.; Kuil, M.; Jiang, X.-B.; van Leeuwen, P. W. N. M.; Reek, J. N. H. *Dalton Trans.* **2009**, 1801-1805; (c) Meeuwissen, J.; Sandee, A. J.; de Bruin, B.; Siegler, M. A.; Spek, A. L.; Reek, J. N. H. *Organometallics* **2010**, *29*, 2413-2421.

In 2003, Breit and coworkers developed a new concept to build bidentate ligands by the self-assembly of monodentate ligands such as 6-diphenylphosphanyl-2-pyridone (6-DPPon) **43** through hydrogen bonding interactions (Scheme 12).[51] The catalytic system was tested in the rhodium-catalyzed hydroformylation of terminal alkenes. The supramolecular catalyst **45** led to increased regioselectivities towards the terminal (or linear) aldehydes (up to 97:3 l/b ratio in the hydroformylation of 6-bromo-1-hexene and methyl 10-undecenoate).

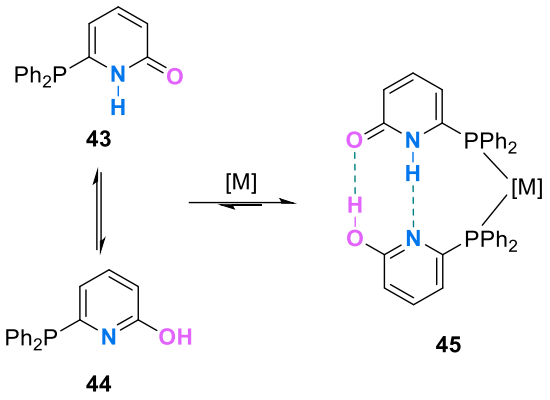

Scheme 12. Supramolecular complex **45** formed by the self-assembly of ligand **43** and **44** through hydrogen bonding interactions (supramolecular interactions are highlighted with green dashed lines).

After demonstrating the viability of constructing bidentate ligands by a self-assembly process as shown for 6-DPPon **43**, the same group reported the formation of libraries of metal complexes derived from homo- and hetero-dimeric bidentate phosphine ligands (Scheme 13). By designing functionalized adenosine and thymidine analogues (compounds **46** and **47**, respectively), the authors developed an elegant strategy to exclusively synthesize heterodimeric metal complexes **50**: the highly favorable hydrogen bonding interactions between the ligands containing adenosine- and thymidine-based hydrogen bonding motifs shifted the equilibrium towards the formation of heterodimeric complexes **50** (Scheme 13). With this strategy, the authors generated a large library of heterodimeric metal catalysts derived from bidentate ligands.[52] The

[51] Breit, B.; Seiche, W. *J. Am. Chem. Soc.* **2003**, *125*, 6608-6609.
[52] Waloch, C.; Wieland, J.; Keller, M.; Breit, B. *Angew. Chem., Int. Ed.* **2007**, *46*, 3037-3039.

applicability of these supramolecular catalysts was tested in diverse transformations, such as rhodium-catalyzed hydroformylation reactions.[53]

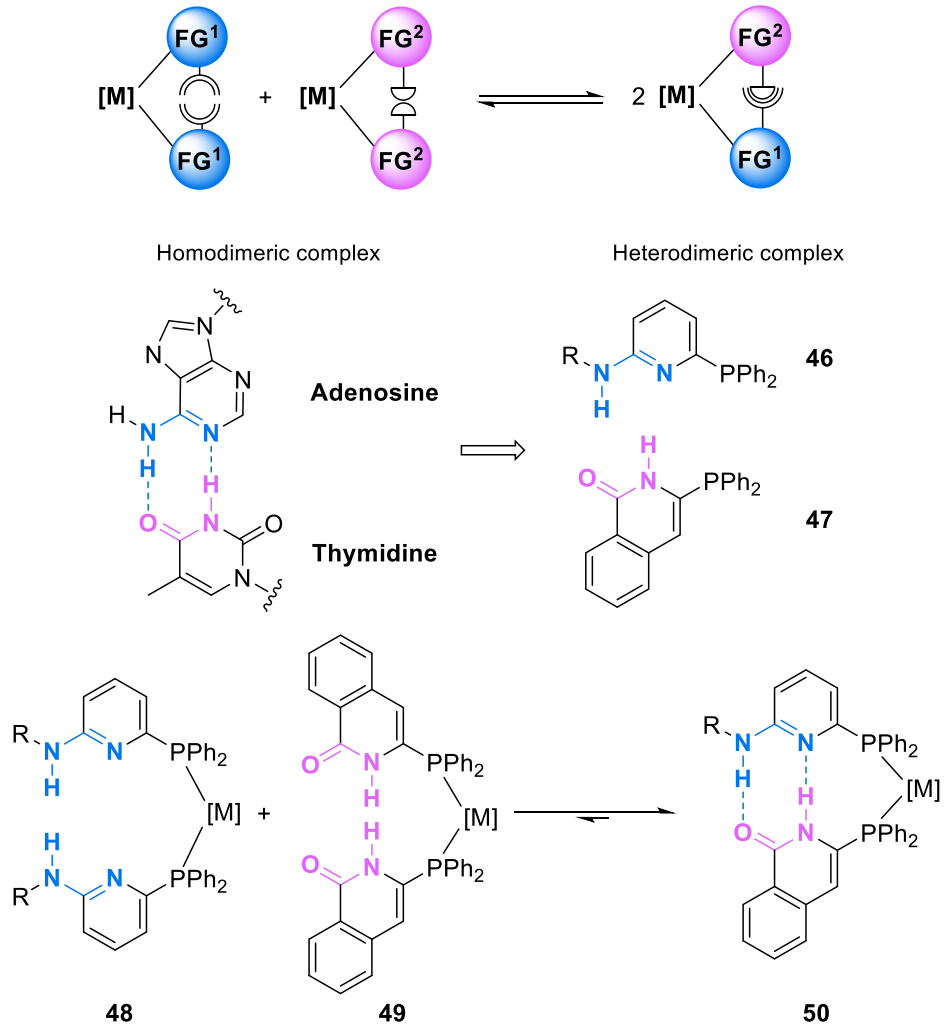

Scheme 13. Schematic representation for the formation of libraries of heterodimeric complexes of bidentate ligands (supramolecular interactions are highlighted with green dashed lines).

In 2004, Takacs and coworkers reported a new approach to construct bidentate ligands using metal-ligand interactions. In the bimetallic catalyst derived from the ligand **53** and the corresponding palladium precursor, the zinc metal center

[53] For selected examples, see: (a) Smejkal, T.; Breit, B. *Angew. Chem., Int. Ed.* **2008**, *47*, 311-315; (b) Köpfer, A.; Breit, B. *Angew. Chem., Int. Ed.* **2015**, *54*, 6913-6917; (c) Fang, W.; Breit, B. *Angew. Chem., Int. Ed.* **2018**, *57*, 14817-14821.

was used to assemble the bidentate ligand, while the other metal center (*e.g.*, palladium) was responsible of the catalytic activity.[54] Using this approach, the authors developed a library of enantiopure bisphosphite ligands *via* metal-directed self-assembly of two anionic bisoxazoline-containing ligands around a zinc(II) metal center. Each moiety presented a conformationally labile aryl-based linker and a second set of ligating groups to bind the second metal center to form the catalytic site (Scheme 14). By modifying the ligand's scaffold, easy access to a structurally diverse library of catalytic systems (over 50 different structures) was achieved. This strategy was used in the palladium-catalyzed allylic amination reaction of substrate **51** and other analogues (Scheme 14). Moreover, the same ligand library provided selective catalysts for rhodium-catalyzed enantioselective hydrogenations[55] and for rhodium-catalyzed enantioselective hydroborations.[56]

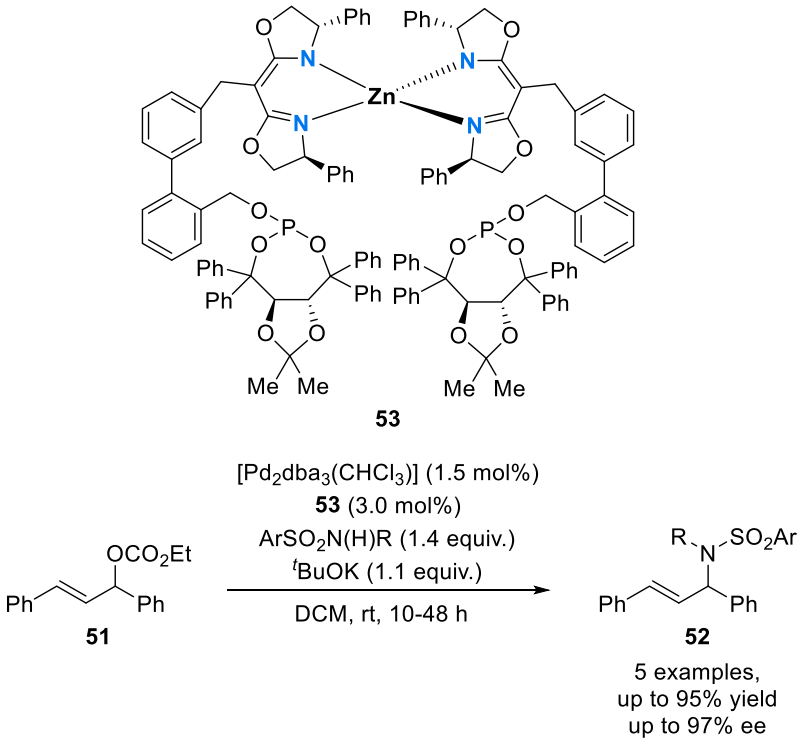

Scheme 14. Allylic amination reaction of **51** catalyzed by supramolecular palladium complexes derived from ligand **53**.

[54] Takacs, J. M.; Reddy, D. S.; Moteki, S. A.; Wu, D.; Palencia, H. *J. Am. Chem. Soc.* **2004**, *126*, 4494-4495.
[55] Takacs, J. M.; Chaiseeda, K.; Moteki, S. A.; Reddy, D. S.; Wu, D.; Chandra, K. *Pure Appl. Chem.* **2006**, *78*, 501-509.
[56] Moteki, S. A.; Takacs, J. M. *Angew. Chem., Int. Ed.* **2008**, *47*, 894-897.

Since the initial works of Breit, Reek, van Leeuwen and Takacs, extensive contributions involving new approaches for the construction of bidentate ligands by ligand-ligand supramolecular interactions have been reported.[38]

More recently, an elegant strategy has emerged to form supramolecular catalysts by self-assembling two complementary building blocks *via* halogen bonding interactions.[4,57]

The halogen bond (XB) results from a net attractive interaction between a region of low electron density associated with a halogen atom in a molecular entity (R–X motif; also referred to as the halogen bond donor) and a high electron density region in another, or the same, molecular entity (XBA motif; also known as the halogen bond acceptor) (Figure 8).

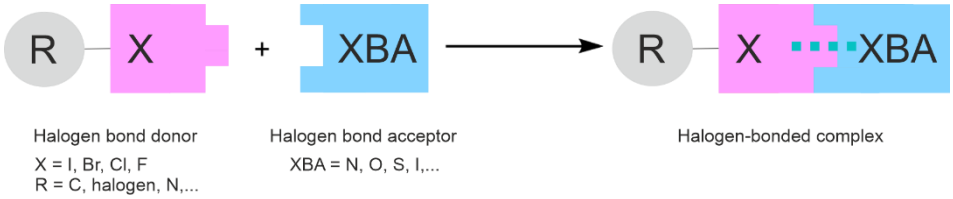

Figure 8. Schematic representation of the halogen bonding interaction.

The halogen bonding interaction can be generally explained through two main concepts in chemistry: electrostatics and orbital interactions.[58] Politzer *et al.* introduced the σ-hole concept, which represents the most accepted model to rationalize halogen bonding.[59] The anisotropic charge distribution around the covalent R–X bond reveals two different regions: on the one hand, a ring orthogonal to the covalent R–X bond with high electron density and, on the other hand, a localized region of low electron density and positive electrostatic potential centered on the R–X bond and placed at the outermost region of the halogen's electrostatic potential surface (σ-hole).[60] This σ-hole can form attractive interactions with electron-rich molecular entities, such as Lewis bases (Figure 9a).

---

[57] For selected reviews, see: (a) Gilday, L. C.; Robinson, S. W.; Barendt, T. A.; Langton, M. J.; Mullaney, B. R.; Beer, P. D. *Chem. Rev.* **2015**, *115*, 7118-7195; (b) Bulfield, D.; Huber, S. M. *Chem.–Eur. J.* **2016**, *22*, 14434-14450.
[58] Oliveira, V.; Kraka, E.; Cremer, D. *Phys. Chem. Chem. Phys.* **2016**, *18*, 33031-33046.
[59] Brinck, T.; Murray, J. S.; Politzer, P. *Int. J. Quantum Chem., Quantum Biol. Symp.* **1992**, *19*, 57-64.
[60] (a) Politzer, P.; Lane, P.; Concha, M. C.; Ma, Y.; Murray, J. S. *J. Mol. Model.* **2007**, *13*, 305-311; (b) Clark, T.; Hennemann, M.; Murray, J. S.; Politzer, P. *J. Mol. Model.* **2007**, *13*, 291-296.

Molecular orbital theory, according to Mulliken's concept, provides a deeper understanding to halogen bonding.[61] Concretely, the attractive force arises from a $n \rightarrow \sigma^*$ partial electron transfer from a non-bonding orbital of the XB acceptor (*i.e.*, Lewis base) into the antibonding orbital of the R–X bond. In other words, the LUMO of the R–X bond interacts with the electron pair of the halogen bond acceptor (HOMO) leading to a stabilizing HOMO-LUMO interaction (Figure 9b).[62]

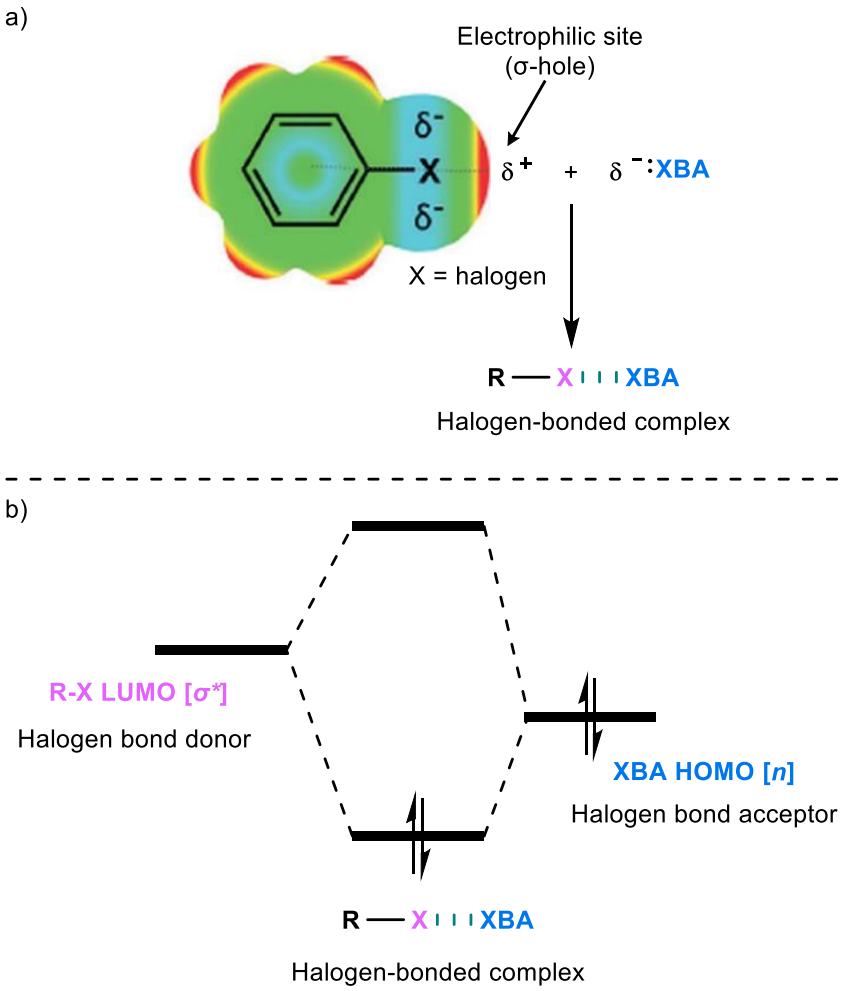

Figure 9. Rationalization of halogen bonding: a) electrostatics and b) orbital interaction.

[61] Mulliken, R. S. *J. Phys. Chem.* **1952**, *56*, 801-822.
[62] (a) Reed, A. E.; Weinhold, F.; Weiss, R.; Macheleid, J. *J. Phys. Chem.* **1985**, *89*, 2688-2694; (b) Wang, C.; Danovich, D.; Mo, Y.; Shaik, S. *J. Chem. Theory Comput.* **2014**, *10*, 3726-3737.

Even though classically hydrogen bonding has been the most studied non-covalent interaction,[63] in the last decades, halogen bonding has emerged as a useful functional tool in supramolecular chemistry.[57,64] The main characteristics of halogen bonding compared to other supramolecular interactions include the high directionality[65] of the interaction (*e.g.*, linear arrangement of the resulting R–X···XBA entity, with a *ca.* 180° bond angle when the XBA is nitrogen), the strength of the interaction,[66] the polarizability of the halogen atoms involved[67] and the lower dependence of the strength of the interaction with the polarity of the solvent.[68] Previous investigations suggested that halogen bond donors have a higher acidic character as Lewis acids in the order X = F < Cl < Br < I, which is in line with the polarizability of the halogen atom. Another strategy to increase the Lewis acidity of the halogen bond donors is increasing the electronegativity of the R substituent.[69]

Owing to the weak and reversible character of the halogen bonds, these interactions have been studied more commonly in the solid estate.[57] The first example of a complex through halogen bonding appeared in the literature two centuries ago, when J. J. Colin discovered serendipitously the $I_2 \cdots NH_3$ halogen-bonded complex.[70] However, the use of halogen bonding interactions in homogeneous catalysis remained unexplored for many years. It was only recently that the groups of Ritter,[71a] Postigo[71b] and Studer[71c] reported the activation of a R–X bond by using a halogen bond acceptor in a stoichiometric ratio. In an analogous manner, the activation of molecules that include a halogen

[63] Juanes, M.; Saragi, R. T.; Caminati, W.; Lesarri, A. *Chem.–Eur. J.* **2019**, *25*, 11402-11411.
[64] (a) Metrangolo, P.; Meyer, F.; Pilati, T.; Resnati, G.; Terraneo, G. *Angew. Chem., Int. Ed.* **2008**, *47*, 6114-6127; (b) Sutar, R. L.; Huber, S. M. *ACS Catal.* **2019**, *9*, 9622-9639; (c) Yang, H.; Wong, M. W. *Molecules* **2020**, *25*, 1045.
[65] Huber, S. M.; Scanlon, J. D.; Jiménez-Izal, E.; Ugalde, J. M.; Infante, I. *Phys. Chem. Chem. Phys.* **2013**, *15*, 10350-10357.
[66] Corradi, E.; Meille, S. V.; Messina; M. T.; Metrangolo; P.; Resnati, G. *Angew. Chem., Int. Ed. Engl.* **2000**, *39*, 1782-1786.
[67] Ibrahim, M. A. A.; Hasb, A. A. M. *Theor. Chem. Acc.* **2019**, *138*, 1-12.
[68] Sarwar, M. G.; Dragisic, B.; Salsberg, L. J.; Gouliaras, C.; Taylor, M. S. *J. Am. Chem. Soc.* **2010**, *132*, 1646-1653.
[69] (a) Metrangolo, P.; Murray, J. S.; Pilati, T.; Politzer, P.; Resnati, G.; Terraneo, G. *CrystEngComm* **2011**, *13*, 6593-6596; (b) Nepal, B.; Scheiner, S. *J. Phys. Chem. A.* **2015**, *119*, 13064-13073.
[70] Colin, J.-J. *Ann. Chim.* **1814**, *91*, 252-272.
[71] (a) Sladojevich, F.; McNeill, E.; Börgel, J.; Zheng, S.-L.; Ritter, T. *Angew. Chem., Int. Ed.* **2015**, *54*, 3712-3716; (b) Yerien, D. E.; Conde, R.; Barata-Vallejo, S.; Camps, B.; Lantano, B.; Postigo, A. *RSC Adv.* **2017**, *7*, 266-274; (c) Tang, X.; Studer, A. *Angew. Chem., Int. Ed.* **2018**, *57*, 814-817.

bond acceptor by using stoichiometric amounts of a halogen bond donor has been illustrated by Huber[72a] and Takemoto.[72b]

The discussion that follows will summarize the application of halogen bonding interactions in catalytic transformations. One strategy consists of the activation of substrates that contain a halogen bond acceptor moiety with a catalyst containing one or multiple halogen bond donor groups. The examples that follow encompass this catalytic strategy.

In 2008, Bolm *et al.* published a seminal work applying halogen bonding interactions for catalysis with a low catalyst loading.[73] The authors described the reduction of quinoline derivatives **54** with the Hantzsch ester **56** catalyzed by perfluoro-1-iodooctane **57** (Scheme 15). The authors demonstrated that the substrate activation took place through the formation of halogen bonding between the iodo group of the catalyst and the quinoline nitrogen of the substrate. With this strategy, the reduced products were obtained in yields up to 98% in a selective manner. In 2014, Tan and coworkers demonstrated that the use of a catalyst, which was based on the 1,1'-(1,3-phenylenebis(methylene))bis(2-iodo-3-methyl-4,5-dihydro-1*H*-imidazol-3-ium) motif and contained two halogen bond donors, led to excellent yields (up to 99%) in the reduction of C=N bonds from quinolines and imines with Hantzsch esters.[74]

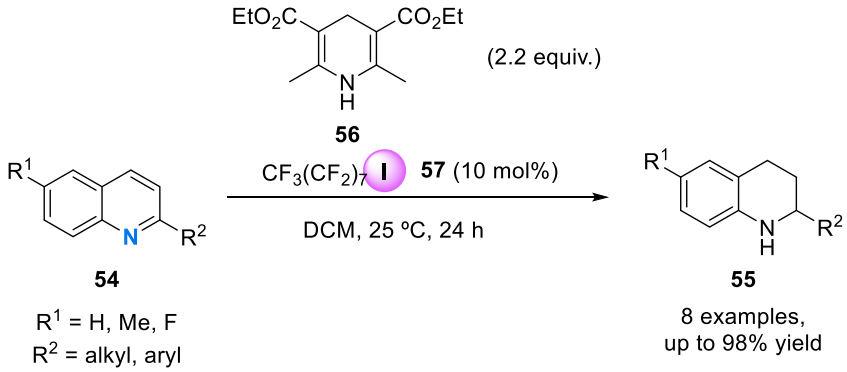

Scheme 15. Reduction of quinoline derivatives **54** with the Hantzsch ester **56** catalyzed by perfluoro-1-iodooctane **57**.

[72] (a) Kniep, F.; Walter, S. M.; Herdtweck, E.; Huber, S. M. *Chem.–Eur. J.* **2012**, *18*, 1306-1310; (b) Tsuji, N.; Kobayashi, Y.; Takemoto, Y. *Chem. Commun.* **2014**, *50*, 13691-13694.
[73] Bruckmann, A.; Pena, M. A.; Bolm, C. *Synlett* **2008**, 900-902.
[74] He, W.; Ge, Y.-C.; Tan, C.-H. *Org. Lett.* **2014**, *16*, 3244-3247.

Huber and coworkers have also contributed to this area of research with numerous elegant examples of application of halogen bonding in catalysis. In 2011, the group published the first example of activation of organic halides by halogen bonding.[75] The authors reported the use of bis(imidazolium)-based halogen bond donors **61** as catalysts in Ritter-type reactions on the carbocation derived from benzhydryl bromide **58** (Scheme 16). Since the bromo group in **58** is a reasonably good halogen bond acceptor in the presence of the iodo groups from the catalyst, the authors demonstrated that halogen bonding facilitated the formation of the carbocation derived from **58**. This reaction intermediate **59** was subsequently trapped by acetonitrile leading to the Ritter-type reaction product **60**.

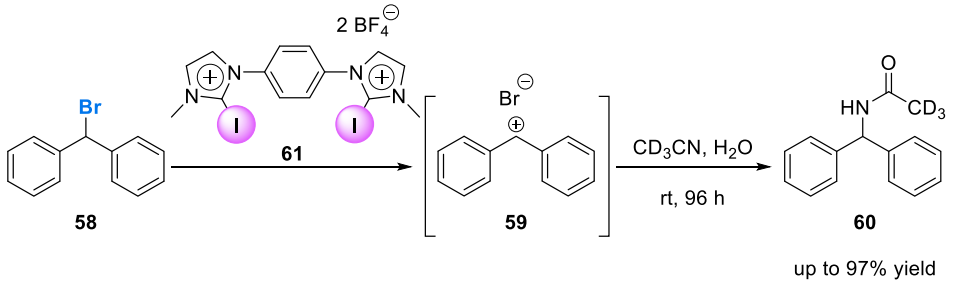

Scheme 16. Ritter reaction on diarylmethylium cations **59** catalyzed by bis(imidazolium)-based catalysts **61**.

Later, Huber *et al.* reported the first example of halogen bond-induced C–C bond formation catalyzed by the neutral multidentate halogen bond donor **65**.[76] The reaction between the carbocation derived from 1-chloroisochroman **62**, after halide abstraction, with the silyl ketene acetal **63** led to product **64** in high yield (up to 91% yield) (Scheme 17). The formation of halogen bonding interactions between the catalyst and the substrate activates the C–Cl bond towards halide abstraction. It is interesting to note that the analogous catalysts of **65** without iodo groups in the backbone of the catalyst does not lead to the ester **64**. Moreover, the authors demonstrated that the catalytic activity depends on the number and orientation of iodine substituents. This observation was proofed by synthetizing a set of catalysts with iodo groups at different positions, which turned out to be less reactive than **65** in this transformation.[77]

[75] Walter, S. M.; Kniep, F.; Herdtweck, E.; Huber, S. M. *Angew. Chem., Int. Ed.* **2011**, *50*, 7187-7191.
[76] Kniep, F.; Jungbauer, S. H.; Zhang, Q.; Walter, S. M.; Schindler, S.; Schnapperelle, I.; Herdtweck, E.; Huber, S. M. *Angew. Chem., Int. Ed.* **2013**, *52*, 7028-7032.
[77] Jungbauer, S. H.; Huber, S. M. *J. Am. Chem. Soc.* **2015**, *137*, 12110-12120.

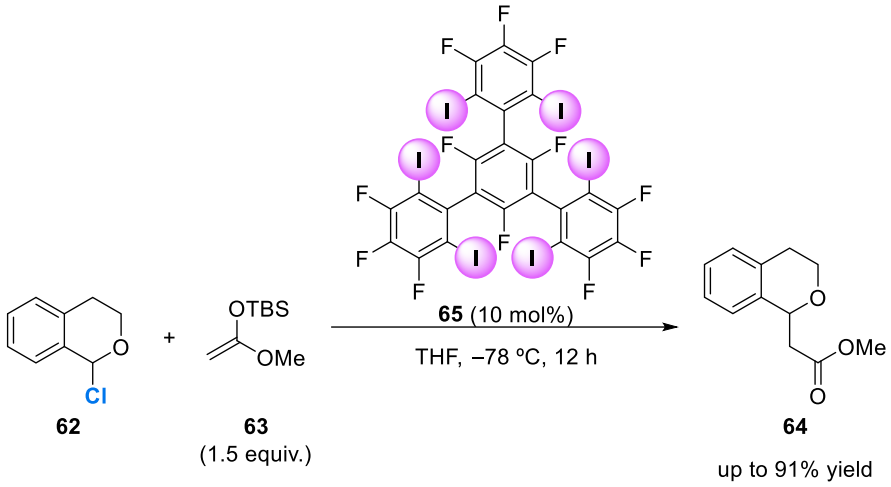

Scheme 17. C–C bond formation between **62** and **63** catalyzed by neutral multidentate halogen bond donor **65**.

In 2014, Huber and coworkers demonstrated that dicationic halogen bond donors **69**, with non-coordinating counteranions such as BArF, activated neutral carbonyl substrates **67** (halogen bond acceptors) towards Diels-Alder reactions (Scheme 18).[78] In this study, the bidentate halogen bond donor catalyst **69** catalyzed the formation of the product in good yields (63% yield). Monodentate halogen bond donors were also tested and afforded the product in 28% yield. These results pointed out that bidentate halogen bond donor catalysts are more efficient for the Diels-Alder reaction than the monodentate analogues.

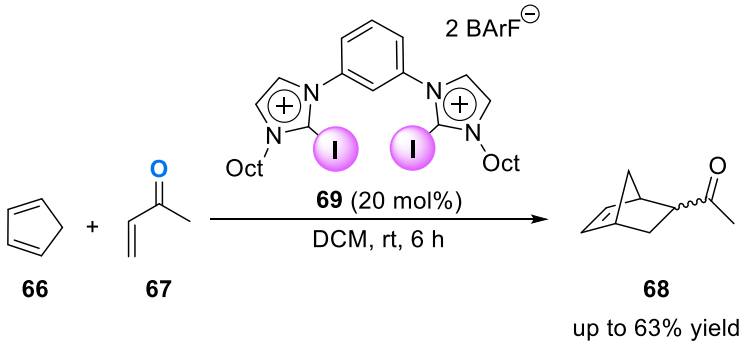

Scheme 18. Diels-Alder reaction activated by dicationic XB donor **69**.

[78] Jungbauer, S. H.; Walter, S. M.; Schindler, S.; Rout, L.; Kniep, F.; Huber, S. M. *Chem. Commun.* **2014**, *50*, 6281-6284.

In 2017, the same group also described the activation of Michael acceptors through monodentate and bidentate benzimidazolium-based halogen bond donor **73** as catalyst between indoles **70** and *trans*-crotonophenone **71** (Scheme 19).[79] The study concluded that when the halogen bond donor atom was bromide or chloride, the product was obtained in poor yields (9-32% yield). On the contrary, when using iodine as halogen bond donor, the yield increased up to 57-68%.

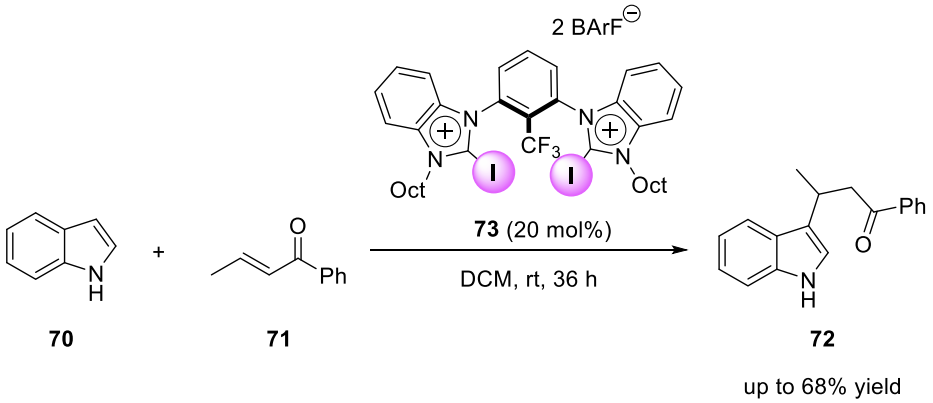

Scheme 19. Michael addition reaction catalyzed by bidentate halogen bond donor **73**.

Takeda *et al.* reported that the aza-Diels-Alder reaction of aldimines **74** with the Danishefsky's diene **75a** was efficiently catalyzed by 2-iodoimidazolium salts **77** (Scheme 20).[80] The necessity of strong halogen bond interactions between the imines and the catalyst for the reaction to take place was demonstrated, as catalysts without iodo substituents in their backbones, or their neutral analogues, did not catalyze the reaction. The studies showed that the stronger the halogen bond interaction was, the higher the yield (up to 74% yield). Fukuzawa and coworkers also studied another aza-Diels-Alder reaction employing 2-siloxy-1,3-butadiene **75b** as diene and a iodotriazolium-based catalyst **78** as halogen bond donor (Scheme 20).[81] The authors demonstrated that these catalysts efficiently mediated the formation of the aza-Diels-Alder adduct (up to 90% yield).

[79] Gliese, J.-P.; Jungbauer, S. H.; Huber, S. M. *Chem. Commun.* **2017**, *53*, 12052-12055.
[80] Takeda, Y.; Hisakuni, D.; Lin, C.-H.; Minakata, S. *Org. Lett.* **2015**, *17*, 318-321.
[81] Haraguchi, R.; Hoshino, S.; Sakai, M.; Tanazawa, S.-g.; Morita, Y.; Komatsu, T.; Fukuzawa, S.-i. *Chem. Commun.* **2018**, *54*, 10320-10323.

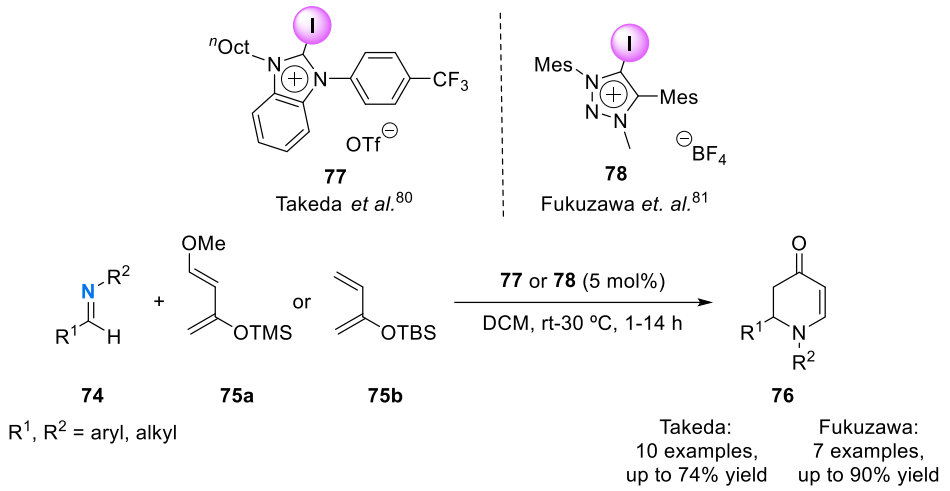

Scheme 20. Aza-Diels-Alder reaction of aldimines **74** with diene **75** catalyzed by 2-iodomidazolium salt **77** and iodotriazolium derivative **78** as catalysts.

Arai *et al.* described a new activation mode for [4+2] cycloaddition reactions based on the formation of a halogen bond between the π-system of the substrate **79** as halogen bond acceptor and a iodo-containing catalyst **81** that provided the halogen bond donor.[82] Experimental and *in silico* studies suggested that the activation of **79** was achieved by C–I···π halogen bonding between the catalyst and the substrate (Scheme 21). Interestingly, the yield of the dimerization reaction increased from 25% in the absence of a halogen-containing catalyst to 99% when catalyst **81** was used.

[82] Kuwano, S.; Suzuki, T.; Yamanaka, M.; Tsutsumi, R.; Arai, T. *Angew. Chem., Int. Ed.* **2019**, *58*, 10220-10224.

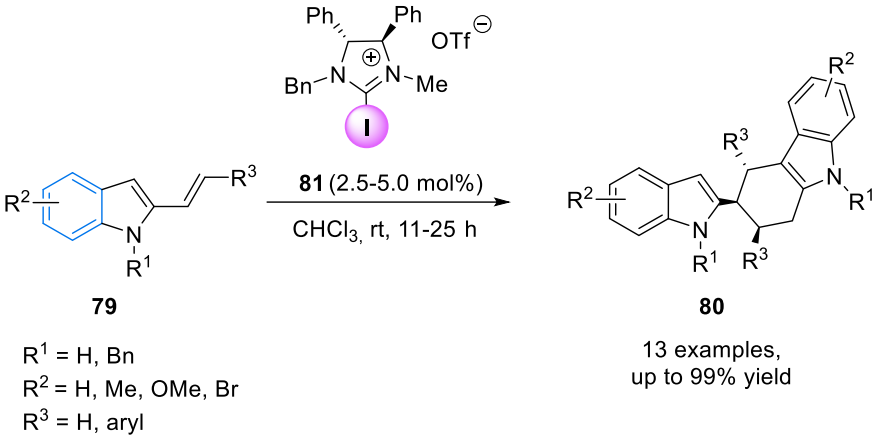

Scheme 21. [4+2] cycloaddition reaction of 2-alkenylindoles **79** catalyzed by XB donor catalyst **81**.

Huber and coworkers also developed designs of halogen bond donors as catalysts based on hypervalent iodine species (see structure **82** in Figure 10). The hypervalent iodolium derivative **82** behaved as an efficient catalyst in the solvolysis reactions of an analogue of benzhydryl chloride (compound **58**, see Scheme 16; up to 80% yield) and the Diels-Alder reaction between **66** and **67** (see Scheme 18; up to 95% yield).[83]

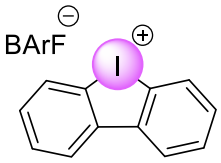

82

Figure 10. Iodolium derivative **82**.

Takemoto and coworkers reported the use of the halogen bond donor **86** to activate iodine, which in turn, is responsible for the activation of the hydroxyl group (OH) of **83** towards the direct dehydroxylative coupling reaction with nucleophiles **87** (Scheme 22).[84]

[83] Heinen, F.; Engelage, E.; Dreger, A.; Weiss, R.; Huber, S. M. *Angew. Chem., Int. Ed.* **2018**, *57*, 3830-3833.
[84] Saito, M.; Tsuji, N.; Kobayashi, Y.; Takemoto, Y. *Org. Lett.* **2015**, *17*, 3000-3003.

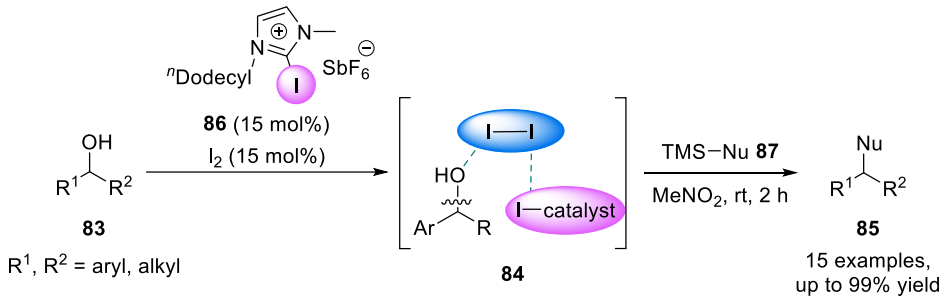

Scheme 22. Activation of the OH group of **83** induced by XB donor **86** (supramolecular interactions are highlighted with green dashed lines).

Inspired by the results previously discussed, Yeung and coworkers recently reported the halogen bond-catalyzed functionalization of N,O-containing substrates **88**.[85] After elimination of the acetoxy group from the substrate with chlorotrimethylsilane, the authors claimed that the chloride anion interacted with catalyst **91** to undergo an anion-metathesis process, yielding the highly reactive *N*-acyliminium triflate **92**, which was subsequently attacked by nucleophile **94** to yield the product **89** (Scheme 23).

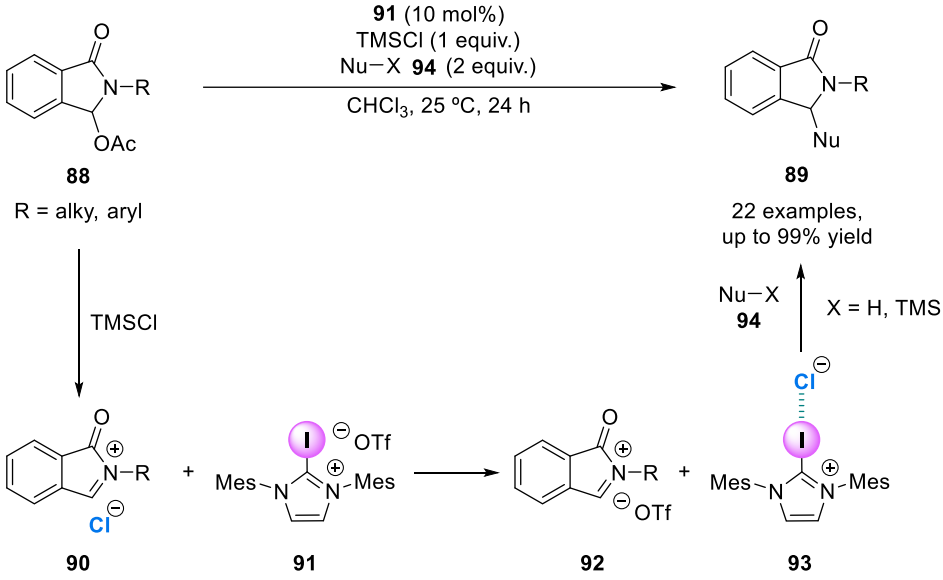

Scheme 23. Functionalization of **88** catalyzed by XB donor **91**.

Although catalytic transformations through halogen bonding interactions have been gradually attracting interest, it is interesting to note that the use of halogen

[85] Chan, Y.-C.; Yeung, Y.-Y. *Org. Lett.* **2019**, *21*, 5665-5669.

bond catalysts in enantioselective transformations is still understudied.[86,87] Owing to the size of the halogen substituents and the high directionality of the halogen bonds, the design of enantioselective catalysts capable of biasing the stereochemical outcome of the reaction by interacting with the reagents through halogen bonding is challenging.

One relevant example was developed by Arai and coworkers, who described excellent enantioselectivities (up to 98% ee) in the Mannich reaction between malononitrile **95** and *N*-Boc aldimines **96** using an enantiopure quinidine-based catalyst **98** equipped with a iodo group as halogen bond donor (Scheme 24).[88]

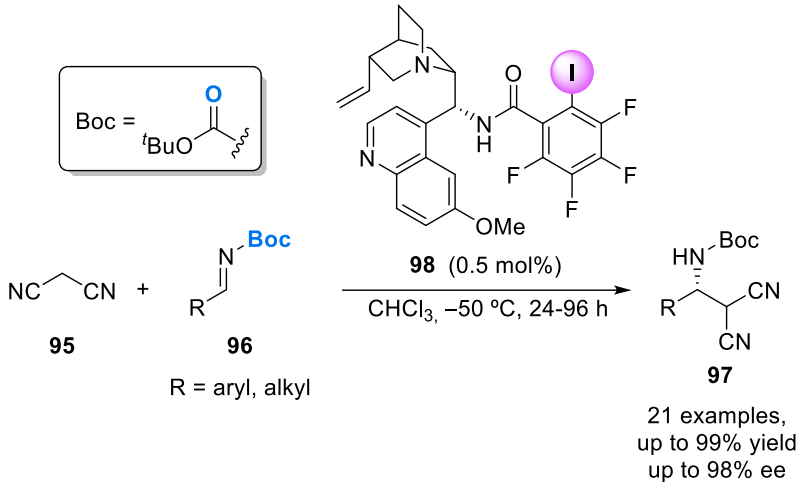

Scheme 24. Mannich reaction between **95** and **96** catalyzed by **98**.

Tan and coworkers have recently described the enantioconvergent nucleophilic substitution reaction of activated tertiary bromides **99** with thiocarboxylates **100** as nucleophiles through halogen bonding interactions. The halogenophilic S_N2X[89] mechanism started due to the presence of a σ-hole in the halogen atom of **99**, which interacts with the nucleophile **100** through halogen bonding (complex **103**). The generation of the carbanion **105** and a new electrophilic intermediate **106** was achieved. Thereafter, the carbanion **105** displaced the bromide group from the new intermediate **106** to generate the desired substitution product **101** in excellent yields (up to 98%) and with excellent enantioselectivities (up to 97% ee). The catalyst **102** was responsible for the

[86] Zong, L.; Ban, X.; Kee, C. W.; Tan, C.-H. *Angew. Chem., Int. Ed.* **2014**, *53*, 11849-11853.
[87] Arai, T.; Suzuki, T.; Inoue, T.; Kuwano, S. *Synlett* **2017**, *28*, 122-127.
[88] Kuwano, S.; Suzuki, T.; Hosaka, Y.; Arai, T. *Chem. Commun.* **2018**, *54*, 3847-3850.
[89] Sazonov, P. K.; Artamkina, G. A.; Beletskaya, I. P. *Russ. Chem. Rev.* **2012**, *81*, 317-335.

creation of an environment that induced enantioselectivity to the product during the nucleophilic attack to the *in situ* generated electrophile **106** (Scheme 25).[90]

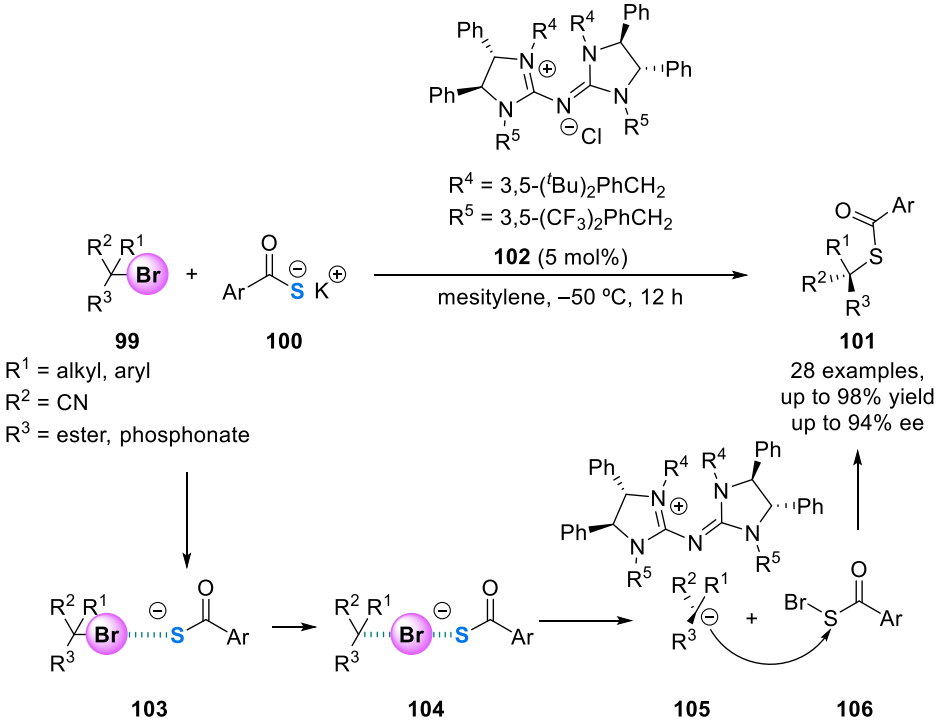

Scheme 25. Enantioconvergent substitution reaction of activates tertiary bromides **99** catalyzed by **102**.

Last year, Huber and coworkers, described the synthesis of enantiopure bidentate dicationic halogen bond donors **110** containing two iodoimidazolium groups derived from enantiopure (1*R*,2*S*)-1-amino-2,3-dihydro-1*H*-inden-2-ol (Scheme 26). The enantioselective Mukaiyama aldol reaction between ethyl glyoxylate **107** and TMS-enolate **108** was catalyzed by **110** obtaining moderated enantiomeric excesses that ranged from 2 to 33% ee.[91]

[90] Zhang, X.; Ren, J.; Tan, S. M.; Tan, D.; Lee, R.; Tan, C.-H. *Science* **2019**, *363*, 400-404.
[91] Sutar, R. L.; Engelage, E.; Stoll, R.; Huber, S. M. *Angew. Chem., Int. Ed.* **2020**, *59*, 6806-6810.

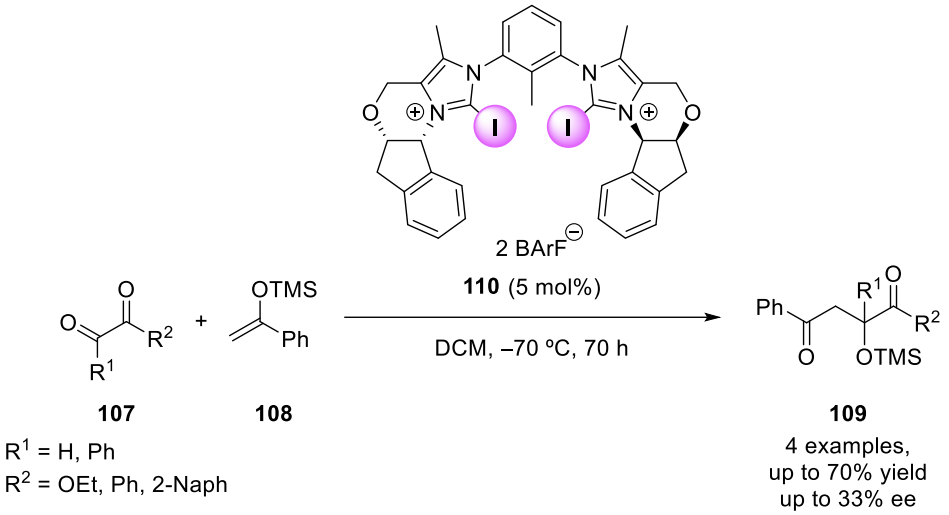

Scheme 26. Mukaiyama aldol reaction catalyzed by dicationic halogen bond donor **110**.

The use of the halogen bonding interactions to control the rigidity of the enantioselective catalyst is another strategy that has been scarcely studied in the literature. Charette and coworkers used halogen bonding to induce rigidity to an enantiopure catalyst in solution. The authors hypothesized that intramolecular halogen bonding interactions between the chloro and carbonyl groups in the catalyst would lead to a highly ordered structure in solution with increased rigidity. These authors reported the enantioselective cyclopropanation of alkenes **111** with α-nitrodiazoketones **112** catalyzed by halogenated rhodium carboxylate **114** (Scheme 27).[92] The tetrachlorinated catalyst showed higher enantioselectivities compared to those observed with the unchlorinated catalyst (80-98% ee *vs.* 2-43% ee, respectively).

[92] Lindsay, V. N. G.; Nicolas, C.; Charette, A. B. *J. Am. Chem. Soc.* **2011**, *133*, 8972-8981.

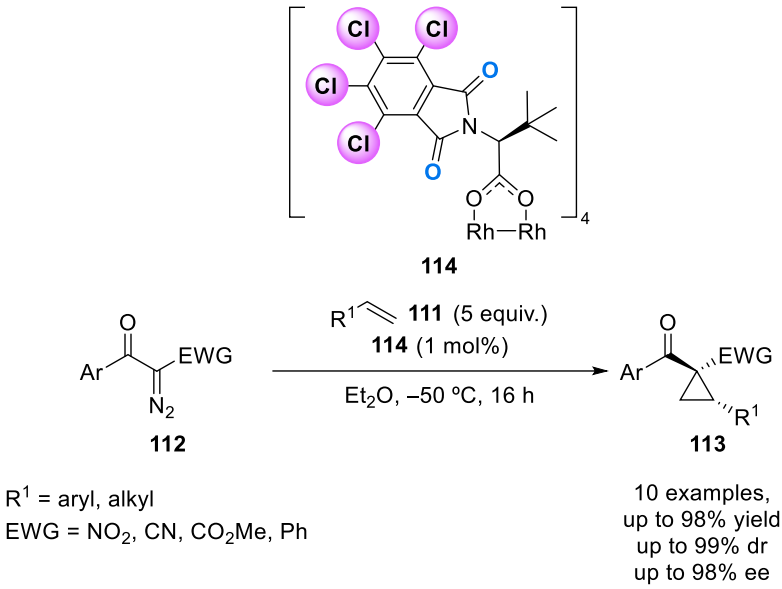

Scheme 27. Enantioselective cyclopropanation of alkenes **111** with α-nitrodiazoketones **112** catalyzed by **114**.

Our group introduced for the first time the use of halogen bonding as a tool to construct rhodium complexes derived from supramolecular bisphosphines. This approach consisted of the formation of metal complexes by self-assembling two complementary building blocks (halogen bond donor and acceptor) that incorporated phosphino groups as coordinating moieties to the transition metal. In this case, the template effect exerted by the metal center was crucial for the formation of the complex **116** (Scheme 28).

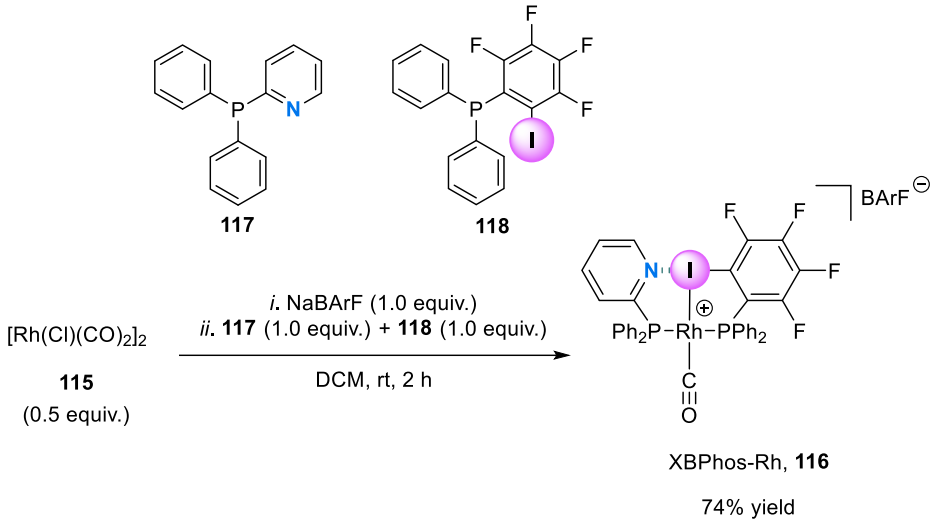

Scheme 28. Formation of the supramolecular rhodium complex XBPhos-Rh **116**.

The resulting rhodium complex XBPhos-Rh **116** was successfully synthesized and used as a supramolecular catalyst for the hydroboration of terminal alkynes **119** (Scheme 29).[93]

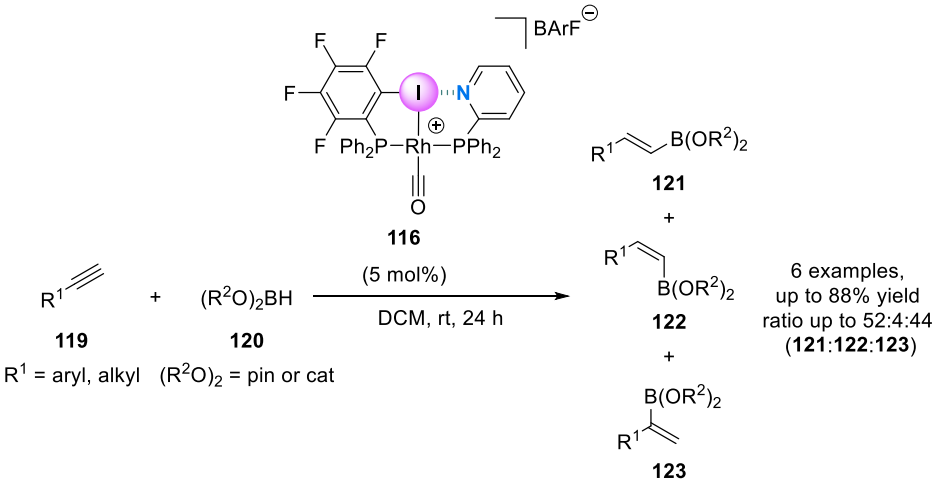

Scheme 29. Hydroboration of terminal alkynes **119** catalyzed by halogen-bonded complex **116** (the supramolecular interaction is highlighted with green dashed lines).

Our group continued the investigation in this research area with the expansion of the catalyst design employing diverse rhodium precursors.[94] When

[93] Carreras, L.; Serrano-Torné, M.; van Leeuwen, P. W. N. M.; Vidal-Ferran, A. *Chem. Sci.* **2018**, *9*, 3644-3648.

$[Rh(nbd)_2]BF_4$ was used as a precursor, the octahedral final complex **124** exhibited a P–Rh–P angle of 95.31(5)°. Consequently, the halogen bonding was not favored in an octahedral environment due to the high directionality required (Figure 11a). The use of [Rh(κ^2*O,O'*-acac)$(C_2H_4)_2$] as rhodium precursor led to the formation of the complex **125**, which incorporated both phosphines, the acetylacetonato ligand, together with a cyclometallated motif and a iodido ligand bonded to a rhodium(III) center. With this rhodium precursor, oxidative addition of the C–I bond in **125** had taken place under very mild conditions (*i.e.*, room temperature (Figure 11b)). The authors reasoned that a transient N···I–C alignment *via* halogen bonding with simultaneous coordination of the I-atom to the rhodium center could be taking place, ultimately favoring the oxidative addition of the C–I bond to the electron-rich rhodium center.

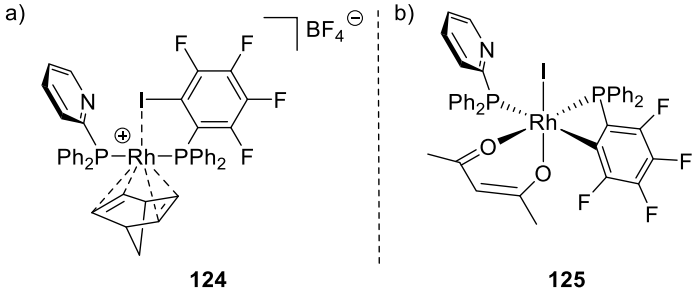

Figure 11. Rhodium complexes **124** and **125** derived from pyridyl and iodo-containing ligands.

Inspired by these results, we reasoned that the platinum- and palladium-analogues of XBPhos-Rh **116** were good candidates to be prepared following an analogous synthetic methodology to that used for XBPhos-Rh **116**.

[94] Carreras, L.; Benet-Buchholz, J.; Franconetti, A.; Frontera, A.; van Leeuwen, P. W. N. M.; Vidal-Ferran, A. *Chem. Commun.* **2019**, *55*, 2380-2383.

OBJECTIVES

As we previously summarized in the introduction, the need of efficient catalysts capable of performing well in a number of transformations and for a structurally diverse array of substrates has been a concern over the years. Supramolecular chemistry has evolved as a useful tool aiming to contribute to the development of such high-performing catalysts.[7] Our group has developed supramolecularly regulated catalysts.[19c] These catalytic systems are well established for a number of transformations, such as enantioselective hydroformylation,[30a,c,d] hydrogenation,[30b,d] allylic substitutions[31] and C–H functionalization of electron rich aromatic derivatives.[32] Moreover, the construction of supramolecular metal complexes derived from halogen-bonded diphosphine ligands has proven to be an interesting strategy in stereoselective hydroborations of alkynes.[93] Inspired by the excellent results obtained in both areas of research, the expansion of these supramolecular strategies for synthesizing stereoselective catalysts may contribute to the development of new and efficient catalytic tools for new chemistries.

Therefore, the objectives of the present thesis are:

1. Design, preparation and application of efficient catalytic systems based on the supramolecularly regulated approach developed by our research group. Development of efficient supramolecularly regulated catalytic systems for the insertion of copper carbenoids into O–H bonds of structurally diverse alcohols. Evaluation of the activity of the supramolecularly regulated catalysts on benchmark model substrates as well as on starting materials leading to advanced synthetic intermediates of biologically relevant molecules.

2. Design, preparation and characterization of palladium(II) and platinum(II) complexes incorporating halogen-bonded supramolecular bisphosphines. Carrying out mechanistic studies on the formation of these supramolecular complexes and preliminary studies on the use of these platinum(II) complexes as catalysts in transformations of interest.

CHAPTER I

Supramolecularly Regulated Copper-Bisoxazoline Catalysts for the Efficient Insertion of Carbenoid Species into Hydroxyl Bonds

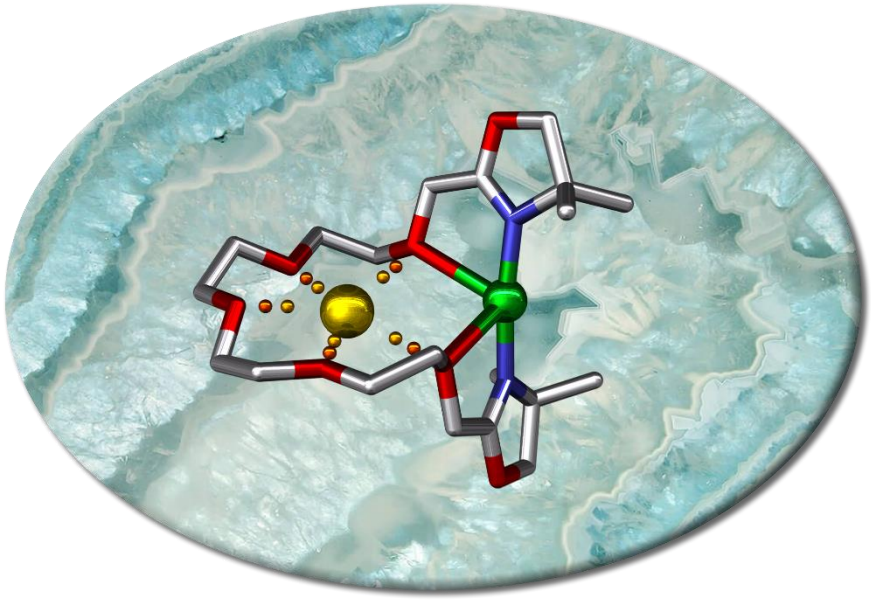

Supramolecularly Regulated Copper-Bisoxazoline Catalysts for the Efficient Insertion of Carbenoid Species into Hydroxyl Bonds

Chem. Commun. **2020**, *56*, 6364-6367

Ester Iniesta[a,b] and Anton Vidal-Ferran[*c,d]

a Universitat Rovira i Virgili, Departament de Química Analítica i Química Orgànica, C. Marcel·lí Domingo 1, 43007, Tarragona, Spain.

b Institut Català d'Investigació Química (ICIQ) & Barcelona Institute of Science and Technology (BIST), Av. Països Catalans 16, 43007 Tarragona, Spain.

c Institució Catalana de Recerca i Estudis Avançats (ICREA), Pg. Lluís Companys 23, 08010, Barcelona, Spain.

d Universitat de Barcelona, Departament de Química Inorgànica i Química Orgànica, C. Martí i Franquès 1-11, 08028 Barcelona, Spain.

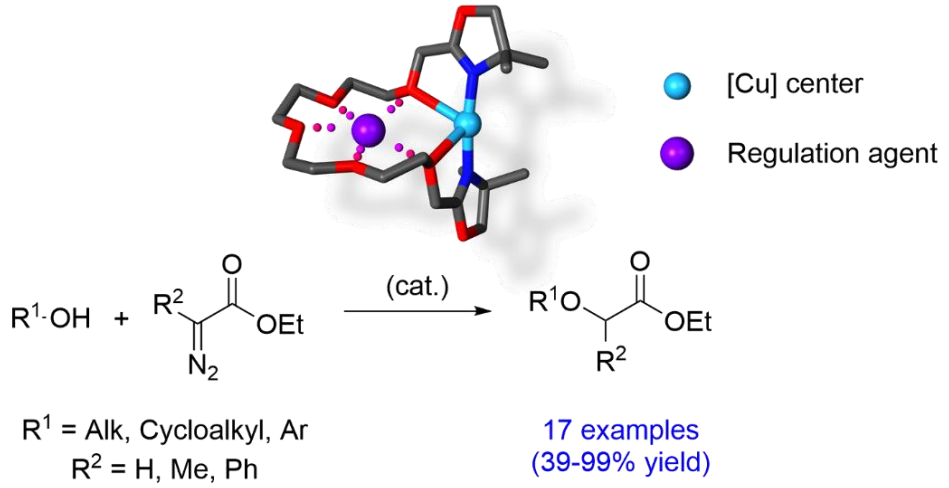

1.1. ABSTRACT

The catalytic insertion of copper carbenoids into O–H bonds affords synthetically useful α-alkyl/aryl-α-alkoxy/aryloxy derivatives. Herein, the design, preparation, and application of supramolecularly regulated copper(I) complexes of bisoxazoline ligands is reported. We have demonstrated that the catalytic performance of these systems can be modulated by the use of an external molecule (*i.e.*, the regulation agent), which interacts with the polyethyleneoxy chain on the ligand (*i.e.*, the regulation site) *via* supramolecular interactions. This approach has been applied to an array of structurally diverse alcohols (cycloalkyl, alkyl and aryl derivatives). Moreover, we have used this methodology to synthesize advanced synthetic intermediates of biologically relevant compounds.

1.2. INTRODUCTION

Pressure is increasing on chemists to replace expensive noble metal catalysts with earth abundant metals. Although the number of papers describing the use of such metals (*i.e.*, Fe, Co, Ni or Cu) in catalysis is growing, many synthetic transformations lack efficient catalysts of this type.[1] α-Alkyl/aryl, α-alkoxy/aryloxy carboxylate moieties are very common in biologically active compounds[2] and their preparation by earth abundant metal-carbene insertion into O–H bonds has gained research attention.[3] Early studies by Yates *et al.*[4] showed the catalytic insertion of copper carbenoid derivatives, which were prepared *in situ* from diazo derivatives, into O–H bonds (Figure 12a). Following

[1] For example, see: (a) Bauer, E. B. *Curr. Org. Chem.* **2008**, *12*, 1341-1369. (b) Gandeepan, P.; Cheng, C.-H. *Acc. Chem. Res.* **2015**, *48*, 1194-1206. (c) Humphries, T. D.; Sheppard, D. A.; Buckley, C. E. *Coord. Chem. Rev.* **2017**, *342*, 19-33. (d) Gandeepan, P.; Mueller, T.; Zell, D.; Cera, G.; Warratz, S.; Ackermann, L. *Chem. Rev.* **2019**, *119*, 2192-2452.

[2] For example, see: (a) Nagai, K.; Sunazuka, T.; Omura, S. *Tetrahedron Lett.* **2004**, *45*, 2507-2509. (b) Bambi-Nyanguile, S.-M.; Hanson, J.; Ooms, A.; Alpan, L.; Kolh, P.; Dogné, J.-M.; Pirotte, B. *Eur. J. Med. Chem.* **2013**, *65*, 32-40. (c) Shahzad, D.; Faisal, M.; Rauf, A.; Huang, J.-H. *Org. Process Res. Dev.* **2017**, *21*, 1705-1731.

[3] For reviews on this topic, see: (a) Zhu, S.-F.; Zhou, Q.-L. *Acc. Chem. Res.* **2012**, *45*, 1365-1377. (b) Zhao, X.; Zhang, Y.; Wang, J. *Chem. Commun.* **2012**, *48*, 10162-10173. (c) Gillingham, D.; Fei, N. *Chem. Soc. Rev.* **2013**, *42*, 4918-4931. (d) Ford, A.; Miel, H.; Ring, A.; Slattery, C. N.; Maguire, A. R.; McKervey, M. A. *Chem. Rev.* **2015**, *115*, 9981-10080. (e) Ren, Y.-Y.; Zhu, S.-F.; Zhou, Q.-L. *Org. Biomol. Chem.* **2018**, *16*, 3087-3094.

[4] Yates, P. *J. Am. Chem. Soc.* **1952**, *74*, 5376-5381.

this seminal work, several studies were published,[5] with the enantioselective copper catalysts developed by Fu[6] and Zhou[7] deserving mention (Figure 12b). Although high enantioselectivities were obtained with these catalysts, the scope of the reaction was limited: reactions between phenyldiazoacetates and substituted phenols were understudied,[3] and carbenoid insertions into electron-deficient phenols or cycloalkyl alcohols were unreported.[8]

Inspired by Nature, non-natural allosteric catalysts have been developed in past years.[9] Our research group has contributed to this area of research by reporting supramolecularly regulated catalysts[10] containing linear polyethyleneoxy chains as regulation sites and stereogenic phosphite motifs as ligating groups for catalysis.[10a,d-h] Our regulation mechanism is triggered by the addition of a regulation agent (RA) capable of interacting with the regulation site *via* supramolecular interactions. The choice of regulation agent determines the rigidity and conformational flexibility of the whole catalytic system, which ultimately translates into a modulation of the (stereo)selectivity in the

[5] For selected examples of Cu-catalyzed transformation, see: (a) Liang, Y.; Zhou, H.; Yu, Z.-X. *J. Am. Chem. Soc.* **2009**, *131*, 17783-17785. (b) Osako, T.; Panichakul, D.; Uozumi, Y. *Org. Lett.* **2012**, *14*, 194-197. (c) Nicolle, S. M.; Lewis, W.; Hayes, C. J.; Moody, C. J. *Angew. Chem., Int. Ed.* **2015**, *54*, 8485-8489. (d) Le Maux, P.; Carrié, D.; Jéhan, P.; Simonneaux, G. *Tetrahedron* **2016**, *72*, 4671-4675. (e) Wang, X.; Zhang, C.; Ma, Q.; Xiao, W.; Guo, L.; Wu, Y. *Tetrahedron Lett.* **2018**, *59*, 280-283.

[6] Maier, T. C.; Fu, G. C. *J. Am. Chem. Soc.* **2006**, *128*, 4594-4595.

[7] (a) Chen, C.; Zhu, S.-F.; Liu, B.; Wang, L.-X.; Zhou, Q.-L. *J. Am. Chem. Soc.* **2007**, *129*, 12616-12617. (b) Zhu, S.-F.; Chen, C.; Cai, Y.; Zhou, Q.-L. *Angew. Chem., Int. Ed.* **2008**, *47*, 932-934. (c) Zhu, S.-F.; Song, X.-G.; Li, Y.; Cai, Y.; Zhou, Q.-L. *J. Am. Chem. Soc.* **2010**, *132*, 16374-16376.

[8] Insertions of Cu-carbenoids into the OH groups of cycloalkanols are difficult, as ring-opening products can be obtained. For example, see: (a) Zhang, H.; Wu, G.; Yi, H.; Sun, T.; Wang, B.; Zhang, Y.; Dong, G.; Wang, J. *Angew. Chem., Int. Ed.* **2017**, *56*, 3945-3950. (b) Wu, X.; Zhu, C. *Chem. Rec.* **2018**, *18*, 587-598.

[9] For selected reviews, see: (a) Breit, B. *Angew. Chem., Int. Ed.* **2005**, *44*, 6816-6825; (b) Joyce, L. A.; Shabbir, S. H.; Anslyn, E. V. *Chem. Soc. Rev.* **2010**, *39*, 3621-3632; (c) Vaquero, M.; Rovira, L.; Vidal-Ferran, A. *Chem. Commun.* **2016**, *52*, 11038-11051; (d) Yoo, C.; Dodge, H. M.; Miller, A. J. M. *Chem. Commun.* **2019**, *55*, 5047-5059.

[10] (a) Mon, I.; Jose, D. A.; Vidal-Ferran, A. *Chem.–Eur. J.* **2013**, *19*, 2720-2725. (b) Raynal, M.; Ballester, P.; Vidal-Ferran, A.; van Leeuwen, P. W. N. M. *Chem. Soc. Rev.* **2014**, *43*, 1660-1733. (c) Raynal, M.; Ballester, P.; Vidal-Ferran, A.; van Leeuwen, P. W. N. M. *Chem. Soc. Rev.* **2014**, *43*, 1734-1787. (d) Fernández-Pérez, H.; Mon, I.; Frontera, A.; Vidal-Ferran, A. *Tetrahedron* **2015**, *71*, 4490-4494. (e) Rovira, L.; Vaquero, M.; Vidal-Ferran, A. *J. Org. Chem.* **2015**, *80*, 10397-10403. (f) Vidal-Ferran, A.; Mon, I.; Bauzà, A.; Frontera, A.; Rovira, L. *Chem.–Eur. J.* **2015**, *21*, 11417-11426. (g) Rovira, L.; Fernández-Pérez, H.; Vidal-Ferran, A. *Organometallics* **2016**, *35*, 528-533. (h) Martínez-Carrión, A.; Howlett, M. G.; Alamillo-Ferrer, C.; Clayton, A. D.; Bourne, R. A.; Codina, A.; Vidal-Ferran, A.; Adams, R. W.; Burés, J. *Angew. Chem., Int. Ed.* **2019**, *58*, 10189-10193.

transformation of interest. Given the efficacy of supramolecular regulation in previous transformations, we postulated that this strategy could be implemented to improve the earth abundant copper-catalyzed insertion of carbenoids into O–H bonds. In particular, an oxazoline[11] group, regularly used in copper catalysis, could act as a coordinating motif while the polyethyleneoxy motif is maintained in the regulation site. Our catalyst design incorporates two oxazoline units linked by a polyethyleneoxy chain at the alpha and omega positions (Figure 12c).[12]

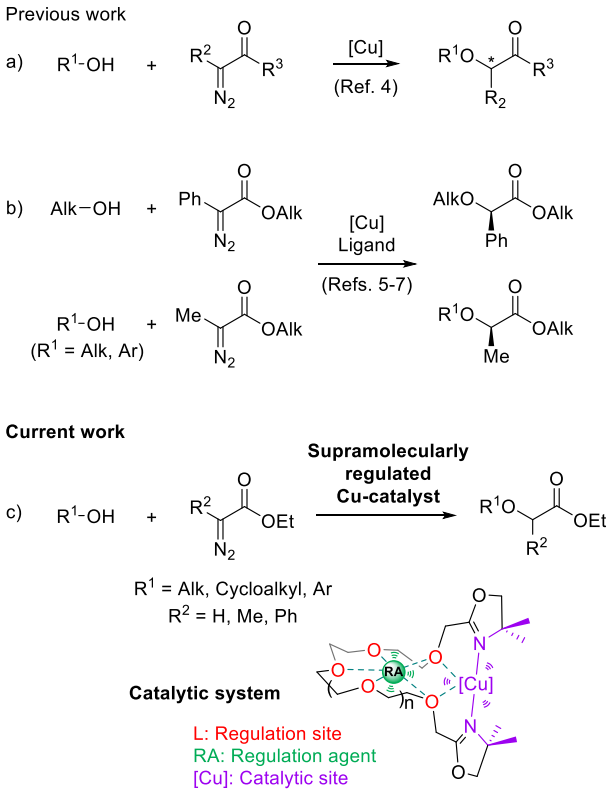

Figure 12. (a) Insertion of Cu-carbenoids into O–H bonds. (b) Enantioselective transformations. (c) Supramolecularly regulated insertion of Cu-carbenoids into O–H bonds (our approach).

[11] It has been reported that bisoxazoline ligands are optimal for metal carbenoid insertions into O–H bonds (see ref. 3) and other transformations. See also: (a) Desimoni, G.; Faita, G.; Jørgensen, K. A. *Chem. Rev.* **2011**, *111*, PR284-PR437 ; (b) Liao, S.; Sun, X.-L.; Tang, Y. *Acc. Chem. Res.* **2014**, *47*, 2260-2272.

[12] For others examples of supramolecular bisoxazoline ligands with no regulation site, see: (a) Takacs, J. M.; Reddy, D. S.; Moteki, S. A.; Wu, D.; Palencia, H. *J. Am. Chem. Soc.* **2004**, *126*, 4494-4495. (b) Durini, M.; Russotto, E.; Pignataro, L.; Reiser, O.; Piarulli, U. *Eur. J. Org. Chem.* **2012**, *2012*, 5451-5461.

We envisaged that the binding of the regulation agent by the polyethyleneoxy moiety would not only serve as a template to bring together the two terminal ligating groups, but would also serve to modify the geometry and flexibility of the associated catalytic site. With regard to the regulation agent, alkali metal BArF derivatives[13] (BArF = [B(3,5-$(CF_3)_2C_6H_3)_4$]) were selected due to their good performance as regulation agents in our previous studies.[10]

Herein, we report the results of the synthesis of copper-bisoxazoline complexes that can be structurally modified by an external regulation agent. We also describe the application of these supramolecularly regulated catalysts for the insertion of copper carbenoids into O–H bonds, affording synthetically useful α-alkyl/aryl-α-alkoxy/aryloxy derivatives.

1.3. RESULTS AND DISCUSSION

Our investigations began with the preparation of the ligands and desired supramolecular complexes. The first step in the synthesis of the ligand was the preparation of the hydroxymethyl-substituted oxazoline derivative **128**. Following the well-established and already reported in the literature[14] synthetic protocol from 2-amino-2-methyl-1-propanol **126** and glycolic acid **127**, the target oxazoline derivative **128** was obtained in 60% yield (Scheme 30a).

Bisoxazoline ligands **L1** and **L2** were straightforwardly synthesized from an oxazoline derivative **128** and the commercially available bistosylated polyethyleneoxy derivatives **129**-**130**. The nucleophilic attack of the alkoxide group in the oxazoline **128** to the bistosylated polyethyleneoxy afforded the desired ligands **L1** and **L2** in 60% and 64% yield, respectively (Scheme 30b).

Supramolecular complexes between ligands **L1** and **L2** and NaBArF were prepared by addition of substoichiometric quantities of ligand to NaBArF (Scheme 30c).

[13] For the preparation of alkali metal BArF salts, see: Carreras, L.; Rovira, L.; Vaquero, M.; Mon, I.; Martin, E.; Benet-Buchholz, J.; Vidal-Ferran, A. *RSC Adv.* **2017**, *7*, 32833-32841.
[14] de Mello, M. B. M.; Clososki, G. C.; Piovan, L.; de Oliveira, A. R. M. *J. Organomet. Chem.* **2015**, *794*, 11-16.

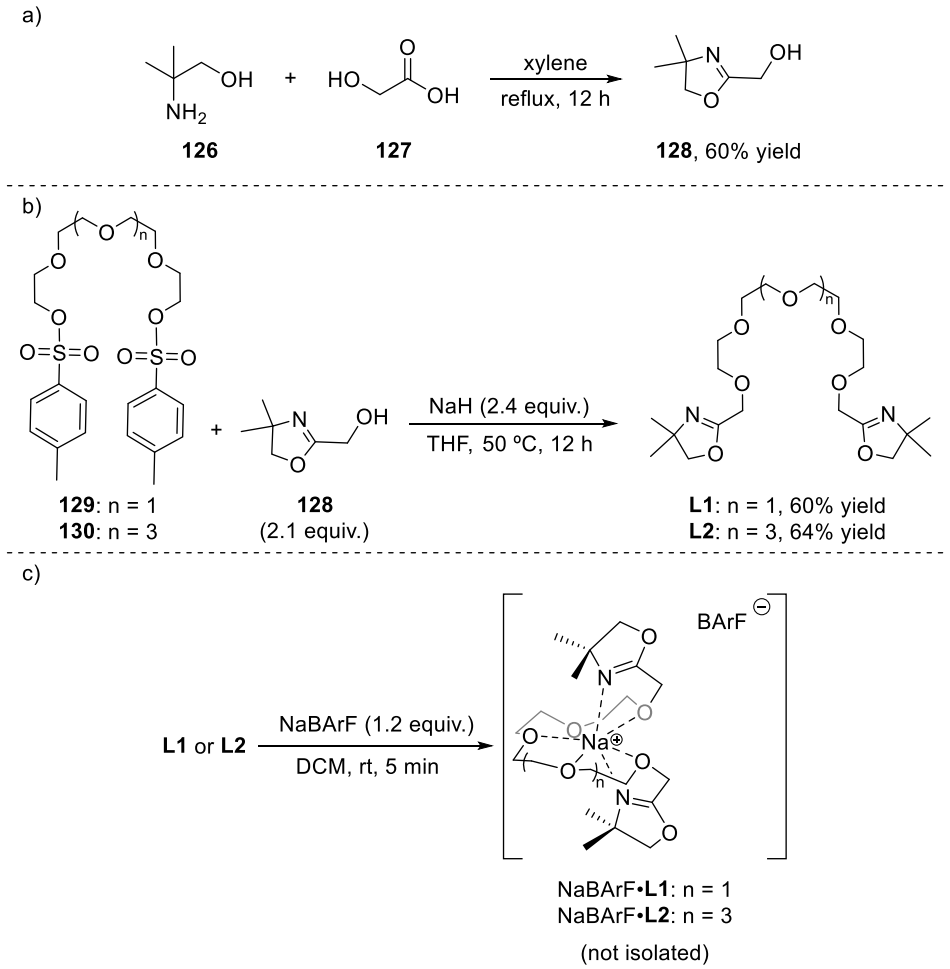

Scheme 30. General procedure for the synthesis of a) the oxazoline derivative **128**, b) ligands **L1** and **L2** and c) complexes NaBArF•**L1** and NaBArF•**L2**.

The regulation approach proposed by our group relies on the binding of suitable metal or ammonium salts (the regulation agents) into the polyethyleneoxy chain (the regulation site) by supramolecular interactions (ion-dipole interactions) (Figure 13).

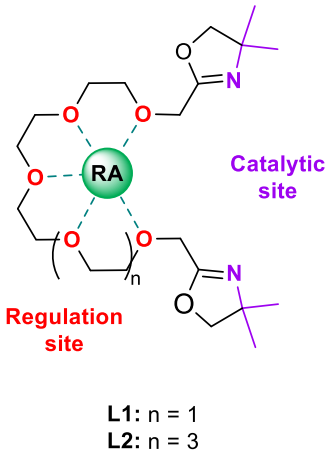

L1: n = 1
L2: n = 3

Figure 13. Supramolecular ligands **L1** and **L2**.

Thus, preliminary NMR studies were performed to estimate the binding affinities between the ligands already synthesized and the regulation agents. A solution of ligand **L1** (*ca.* 1 x 10^{-3} M) in $CDCl_3$ was prepared and, at the same time, a solution of the BArF salt (*ca.* 1 x 10^{-3} M) was also prepared in the same solvent. The titration was carried out adding at 25 ºC incremental amounts of the regulation agent (*i.e.*, guest) to the **L1** solution. Polyethyleneoxy chain signals suffered considerable changes in the chemical shift in the NMR spectra upon addition of increasing RA amounts, indicating that the polyethyleneoxy chain was the binding site (Figure 14). Binding constants for **L1** and BArF salts were calculated by nonlinear curve fitting[15] of the NMR titration data assuming a 1 : 1 binding model. Binding constants were found to be $K > 10^3$ M^{-1} at 25 ºC in $CDCl_3$ for all the BArF salts tested using **L1** as ligand.

[15] NMR titration data were analyzed by using Specfit software (Version 3.0; Spectra Software Associates), see: (a) Gampp, H.; Maeder, M.; Meyer, C. J.; Zuberbühler, A. D. *Talanta* **1985**, *32*, 95-101. (b) Gampp, H.; Maeder, M.; Meyer, C. J.; Zuberbühler, A. D. *Talanta* **1986**, *33*, 943-951.

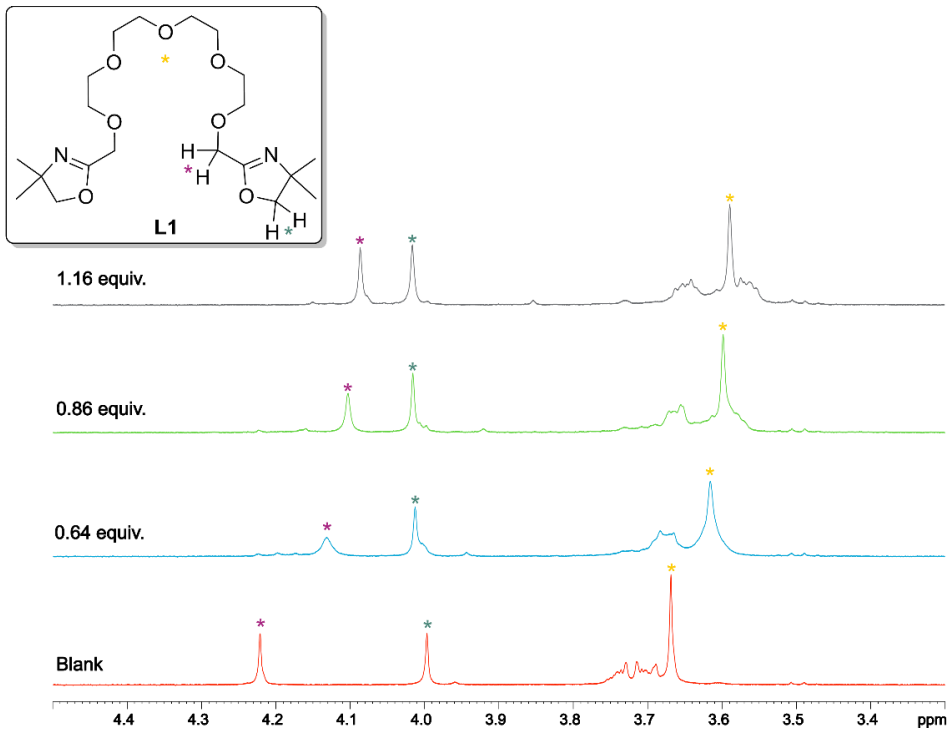

Figure 14. Changes in the ^{1}H NMR (400 MHz, $CDCl_3$) spectra acquired at 25 ºC during the titration of **L1** (2.54×10^{-3} M) with NaBArF.

Single crystal X-ray diffraction confirmed the complexation of NaBArF to the polyethyleneoxy motif in NaBArF•**L1**, with the BArF anion being located at the metal coordination outer-sphere (Figure 15).

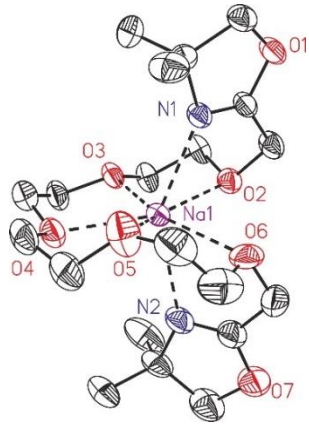

Figure 15. ORTEP drawing (thermal ellipsoids drawn at a 50% probability level) of the crystal structure of NaBArF•**L1**. The BArF anion and hydrogen atoms have been omitted for clarity. Color scheme: C: black, O: red, N: dark blue, Na: purple.

Further research activities aimed at synthesizing and characterizing supramolecularly regulated copper(I) complexes derived from **L1** and **L2** that could be used as catalysts in the insertion of Cu-carbenoids into O–H bonds. We hypothesized that these complexes could be straightforwardly prepared by mixing the adequate relative amounts of a copper(I) precursor, the ligand and the regulation agent.[10d-g] To prevent anion exchange processes between the copper(I) precursor and the regulation agent, we deemed it necessary to synthesize the $[Cu(MeCN)_4]BArF$[16] complex. Therefore, this copper(I) precursor was synthesized by the exchange of the BF_4 anion from the copper complex $[Cu(MeCN)_4]BF_4$ by the BArF anion from the sodium salt in an organic solvent (Scheme 31). We envisaged that the lack of solubility of sodium tetrafluoroborate in dichloromethane would be the driving force for the anion exchange reaction to take place. Indeed, the target copper(I) complex was straightforwardly isolated in 70% yield.

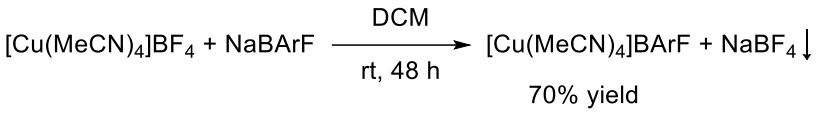

Scheme 31. General procedure for the synthesis of $[Cu(MeCN)_4]BArF$.

The target copper(I) complexes bearing the supramolecular bisoxazoline ligands and the regulation agent were prepared from pre-synthesized NaBArF•**L1** or NaBArF•**L2** and $[Cu(MeCN)_4]BArF$ and characterized with standard spectroscopic techniques (Scheme 32).

[16] Zhang, Y.; Sun, W.; Freund, C.; Santos, A. M.; Herdtweck, E.; Mink, J.; Kühn, F. E. *Inorg. Chim. Acta* **2006**, *359*, 4723-4729.

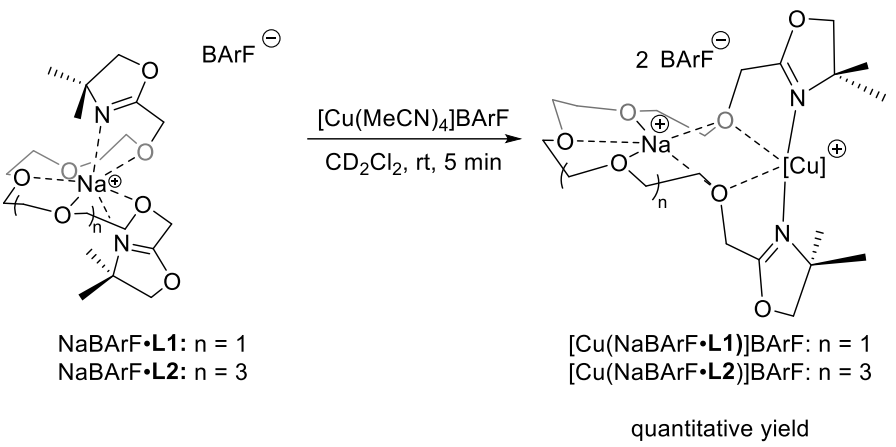

NaBArF•**L1:** n = 1
NaBArF•**L2:** n = 3

[Cu(NaBArF•**L1**)]BArF: n = 1
[Cu(NaBArF•**L2**)]BArF: n = 3

quantitative yield

Scheme 32. Preparation and isolation of complexes [Cu(NaBArF•**L1**)]BArF and [Cu(NaBArF•**L2**)]BArF.

The stacked plot of the spectra of ligands **L1** or **L2**, the corresponding supramolecular complexes NaBArF•**L1** or NaBArF•**L2** and [Cu(NaBArF•**L1**)]BArF or [Cu(NaBArF•**L2**)]BArF exhibited significant changes in the chemical shifts in the NMR spectra, suggesting important conformational changes in their structures when moving from the ligand alone, to the ligand and regulation agent complex and to the final copper complexes (see Figure 16 for the ^{1}H NMR spectra of compounds related to **L1**, Figure 17 for the ^{13}C{^{1}H} NMR spectra of compounds related to **L1**, Figure 18 for the ^{1}H NMR spectra of compounds related to **L2**, and Figure 19 for the ^{13}C{^{1}H} NMR spectra of compounds related to **L2**). Notably, one signal for each magnetically inequivalent nucleus was observed in the ^{13}C{^{1}H} NMR spectra of [Cu(NaBArF•**L1**)]BArF and [Cu(NaBArF•**L2**)]BArF, which may be attributed to the rigidity and stability of these compounds.

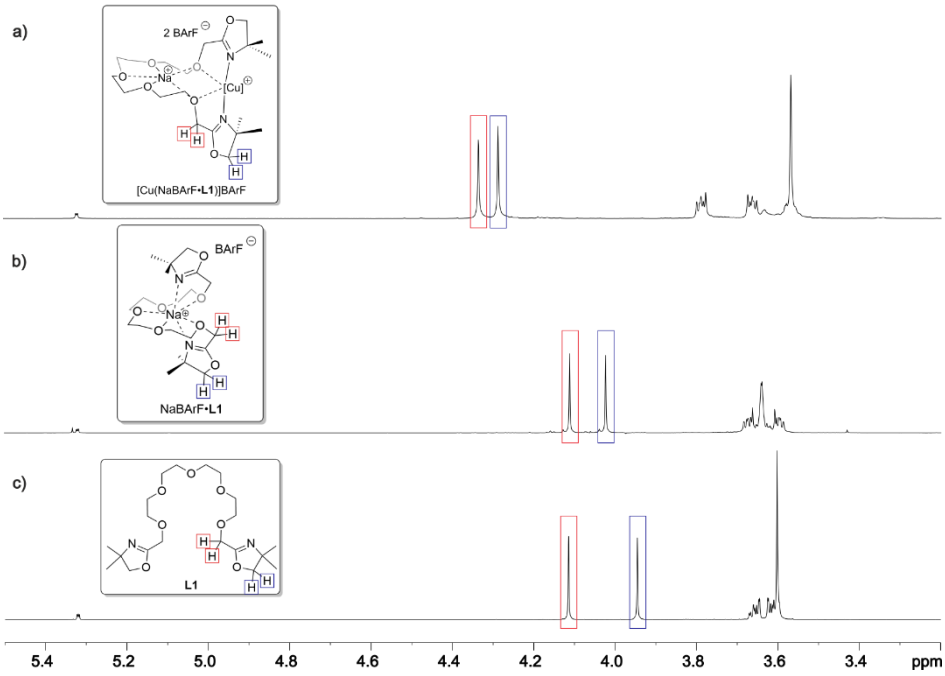

Figure 16. Aliphatic region of the ^{1}H NMR spectra (400 MHz, CD_2Cl_2) acquired at 25 ºC of **L1** (c), NaBArF•**L1** (b), and [Cu(NaBArF•**L1**)]BArF (a) (*ca.* 0.08 M).

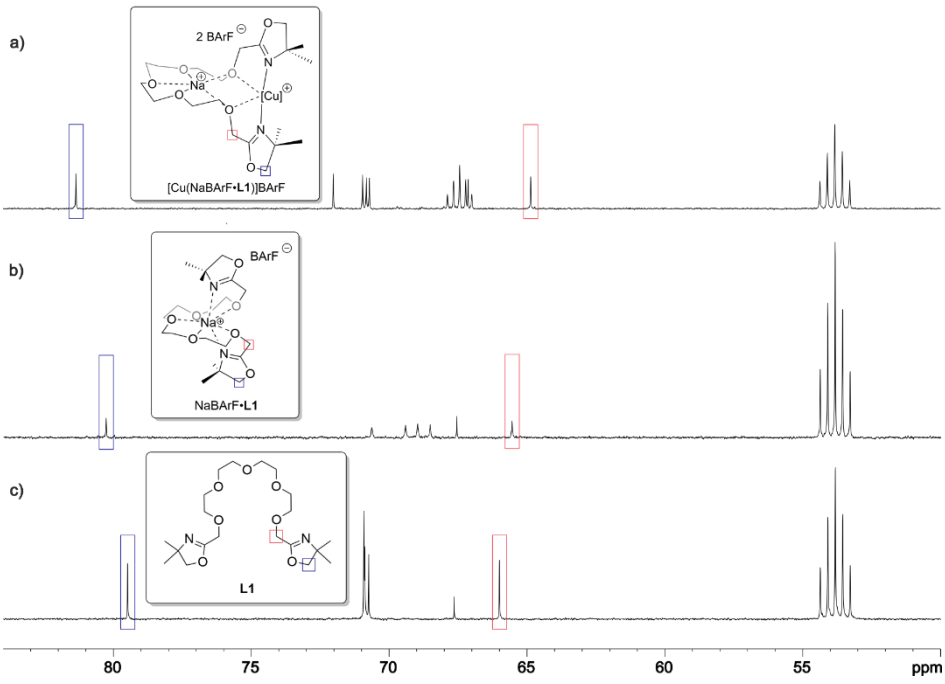

Figure 17. Aliphatic region of the $^{13}C\{^{1}H\}$ NMR spectra (101 MHz, CD_2Cl_2) acquired at 25 ºC of **L1** (c), NaBArF•**L1** (b), and [Cu(NaBArF•**L1**)]BArF (a) (*ca.* 0.08 M).

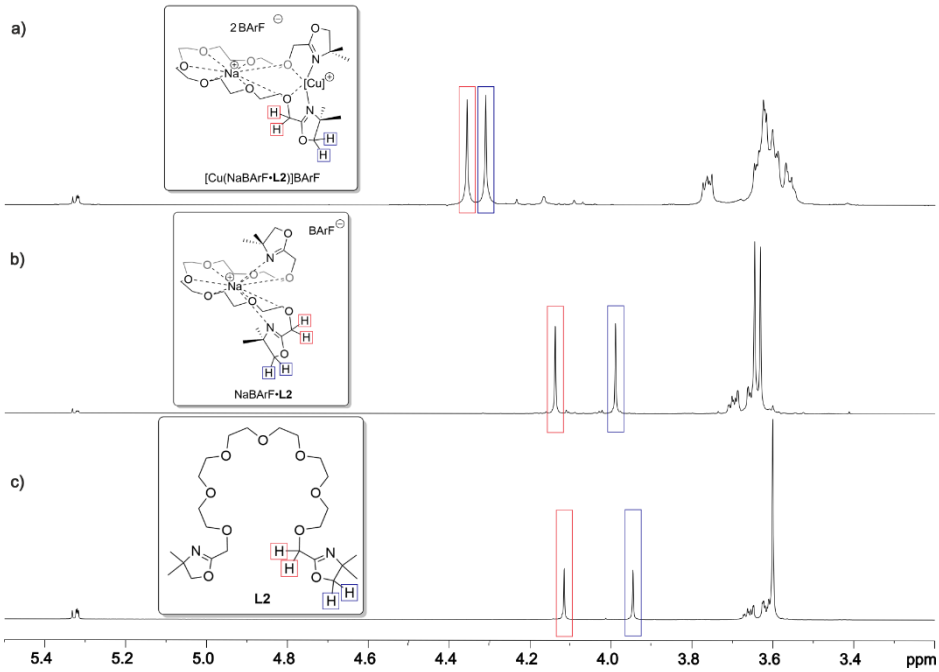

Figure 18. Aliphatic region of the ^{1}H NMR spectra (400 MHz, CD_2Cl_2) acquired at 25 ºC of **L2** (c), NaBArF•**L2** (b), and [Cu(NaBArF•**L2**)]BArF (a) (*ca.* 0.08 M).

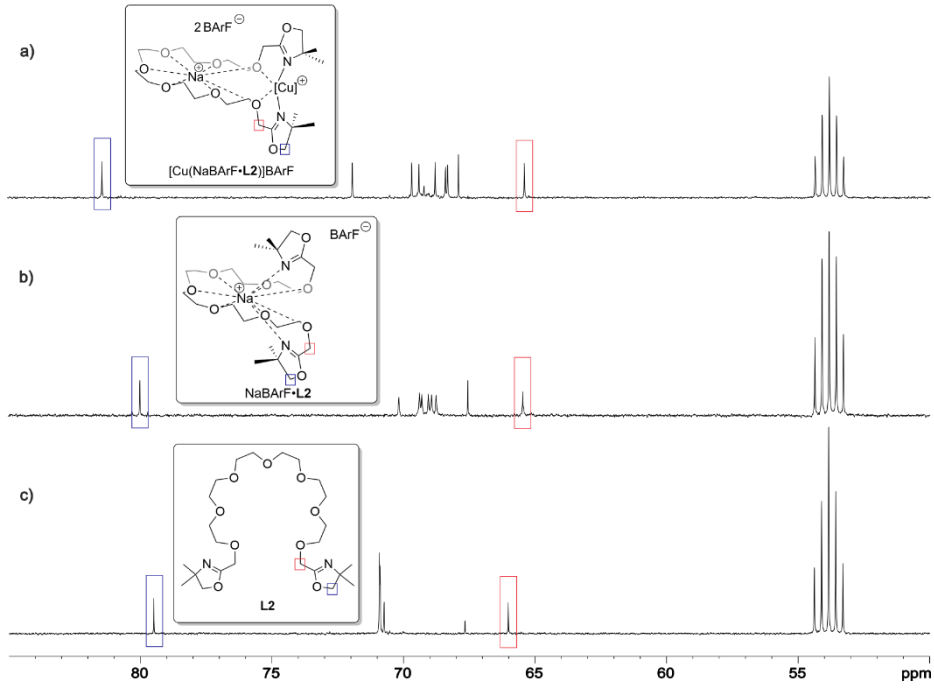

Figure 19. Aliphatic region of the $^{13}C\{^{1}H\}$ NMR spectra (101 MHz, CD_2Cl_2) acquired at 25 ºC of **L2** (c), NaBArF•**L2** (b), and [Cu(NaBArF•**L2**)]BArF (a) (*ca.* 0.08 M).

Unfortunately, single crystals of [Cu(NaBArF•**L1**)]BArF or [Cu(NaBArF•**L2**)]BArF were not obtained. However, when the synthetic protocol indicated in Scheme 30 and Scheme 32 was followed with PF_6 derivatives, single crystals of the corresponding complexes were obtained. X-ray analysis confirmed the coordination of both oxazoline units to the copper center and the coordination of sodium within the metallacrown structure (see Figure 20 for **L1** and Figure 21 for **L2**).

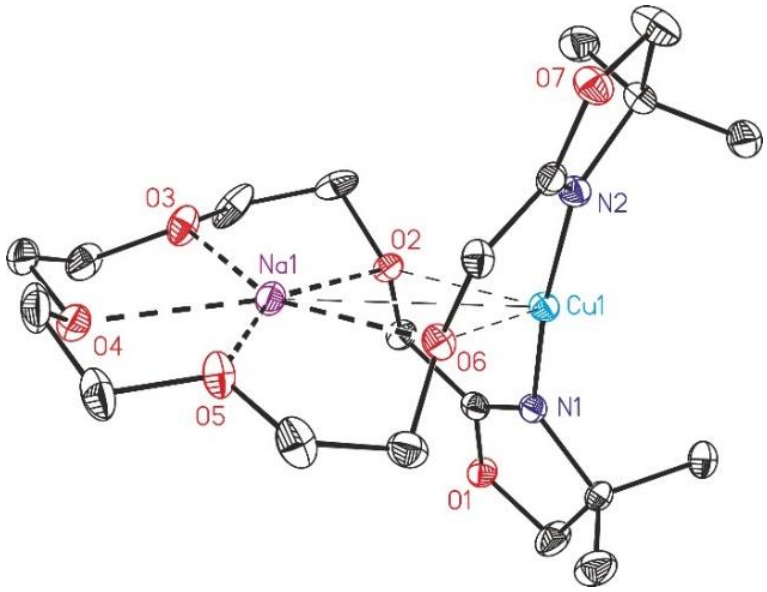

Figure 20. ORTEP drawing (thermal ellipsoids drawn at 50% probability level) of the crystal structure of [Cu($NaPF_6$•**L1**)]PF_6. Hydrogen atoms and PF_6 groups have been omitted for clarity. Color scheme: C: black, O: red, N: dark blue, Na: purple, Cu: light blue.

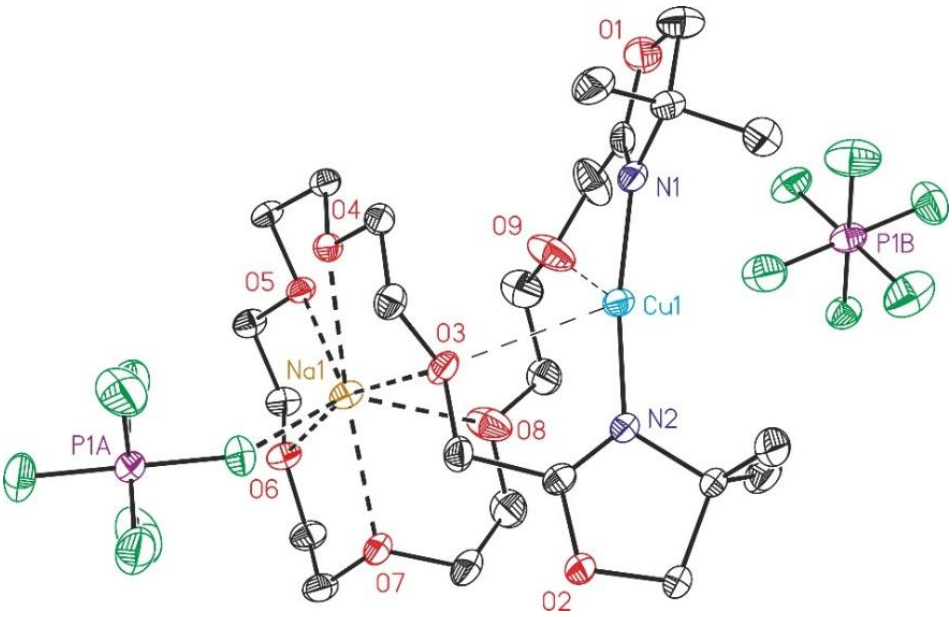

Figure 21. ORTEP drawing (thermal ellipsoids drawn at a 50% probability level) showing the structure of [Cu(NaPF$_6$•**L2**)]PF$_6$. Hydrogen atoms have been omitted for clarity. Color scheme: C: black, O: red, N: dark blue, Na: light brown, Cu: light blue, F: green, P: purple.

With a method for the preparation of supramolecular copper(I) catalysts in hand, we set about evaluating their activity and selectivity in the insertion of copper carbenoids into O–H bonds. The model substrates selected were phenol **131a** and the diazocompound **132a** to afford the O–H insertion product **133a,a**. Following a synthetic protocol already reported in the literature[17] from 4-acetamidobenzenesulfonyl azide **134** and ethyl 2-phenylacetoacetate **135a**, the target diazocompound **132a** was obtained in 57% yield (Scheme 33).

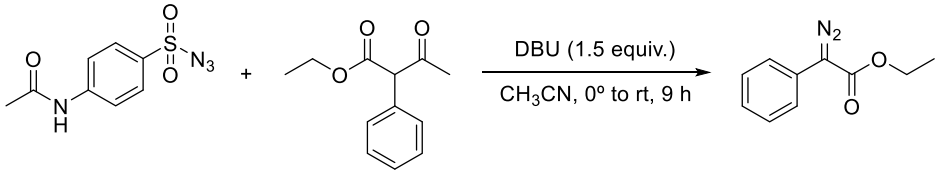

Scheme 33. General procedure for the synthesis of diazocompound **132a**.

[17] Tyagi, V.; Alwaseem, H.; O'Dwyer, K. M.; Ponder, J.; Li, Q. Y.; Jordan, C. T.; Fasan, R. *Bioorg. Med. Chem.* **2016**, *24*, 3876-3886.

The insertion reactions of Cu-carbenoids into O–H bonds were performed generating the copper catalysts *in situ* from 5 mol% of $[Cu(MeCN)_4]BArF$, 6 mol% of the bisoxazoline ligand **L1** or **L2** and 8 mol% of NaBArF as the RA[18] prior to substrate addition. The experimental conditions employed in this study, together with the results obtained, are summarized in Table 1, Table 2 and Table 3.

Although our initial experiments showed that NaBArF did not play a role as a modulator of the reaction between **131a** and **132a** (see entries 1 and 2 in Table 1), these initial experiments demonstrated that copper complexes derived from **L1** catalyze the insertion of the carbenoid species formed from **132a** into the O–H bond of **131a** in the absence of the RA in 67% yield or in presence of NaBArF as RA in 66% yield. The diazoester **132a** was fully consumed and no C–H insertion products were detected in the crude reaction mixtures. In order to decouple activation effects that were not related to the envisioned regulation mechanism, several control experiments were performed (Table 1). For instance, NaBArF or **L1** displayed negligible activity in the reaction (see entries 5 and 6 in Table 1). The effects in the reaction of the $[Cu(MeCN)_4]BArF$ alone (Table 1, entry 4) or in combination with two equivalents of the monodentate 4,4-dimethyl-4,5-dihydrooxazole ligand were also studied, with the O–H product **133a,a** being obtained in lower yield (*ca.* 47%, Table 1, entry 11) than with the Cu(I)-complex derived from **L1** (67%, Table 1, entry 2). Furthermore, the effect of the molecular sieves on the outcome of the reaction was also studied and when this material was added to the reaction mixture, the product **133a,a** was obtained in slightly higher yields (compare entries 1 and 9 in Table 1) than without it.

[18] The rationale for this ratio of copper precursor, ligand and RA was to ensure efficient formation of the supramolecular copper complex with no copper centers remaining uncoordinated to the ligand and with the RA being fully bound to the ligand.

Table 1. Background experiments for the copper-catalyzed carbene insertion into O–H bonds.

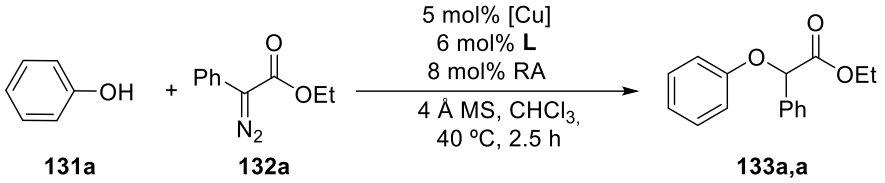

131a **132a** **133a,a**

Entry	[Cu]	**L**	RA	Molecular sieves	Yield [%][a]
1	$[Cu(MeCN)_4]BArF$	**L1**	NaBArF	yes,[b]	66
2	$[Cu(MeCN)_4]BArF$	**L1**	--	yes,[b]	67
3	--	--	--	yes,[b]	<1
4	$[Cu(MeCN)_4]BArF$	--	--	--	48
5	--	**L1**	--	--	<1
6	--	--	NaBArF	--	<1
7	--	**L1**	NaBArF	--	<1
8	$[Cu(MeCN)_4]BArF$	--	NaBArF	--	51
9	$[Cu(MeCN)_4]BArF$	**L1**	NaBArF	--	64
10	$[Cu(MeCN)_4]BArF$	--	NaBArF	yes,[b]	53
11	$[Cu(MeCN)_4]BArF$	Ox[c]	--	yes,[b]	47

Reactions were performed employing a **131a** : [Cu] : **L1** : RA : **132a** ratio equal to 500 : 5 : 6 : 8 : 100. [a] Yields were determined by ^1H NMR using 1,3,5-trimethoxybenzene as the internal standard. [b] 4 Å molecular sieves were used in a 95:5 weight ratio with respect to **132a**. [c] 2.0 equiv. of 4,4-dimethyl-4,5-dihydrooxazole were added.

A screening of the temperature, solvent and source of copper was also carried out for the copper-catalyzed carbene insertion into O–H bonds using **131a** and **132a** as substrates. The results are summarized in Table 2. Temperature affected the yield of the reaction, with an increase from 42% at 0 °C to 66% at 40 °C (compare entries 1-3 in Table 2). The yield of **133a,a** was also affected by the solvent, with chloroform at 40 °C providing the highest yields (compare entries 1, 4-6 in Table 2). Besides, another copper precursor with a different counterion was used to form the supramolecular copper catalyst and it was observed that $[Cu(MeCN)_4]BF_4$ provided the product **133a,a** in lower yields (compare entries 1 and 7 in Table 2).

Table 2. Screening of the temperature, solvent, and copper precursor for the copper-catalyzed carbene insertion into O–H bonds.

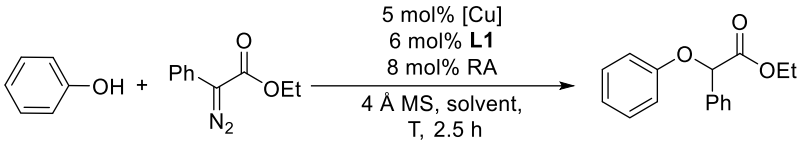

131a **132a** **133a,a**

Entry	[Cu]	RA	Solvent	T (ºC)	Yield [%][a]
1	$[Cu(MeCN)_4]BArF$	NaBArF	$CHCl_3$	40	66
2[b]	$[Cu(MeCN)_4]BArF$	NaBArF	$CHCl_3$	0	42
3	$[Cu(MeCN)_4]BArF$	NaBArF	$CHCl_3$	rt	64
4	$[Cu(MeCN)_4]BArF$	NaBArF	CH_2Cl_2	40	62
5[c]	$[Cu(MeCN)_4]BArF$	NaBArF	PhMe	40	47
6	$[Cu(MeCN)_4]BArF$	NaBArF	PhCl	40	59
7	$[Cu(MeCN)_4]BF_4$	$NaBF_4$	$CHCl_3$	40	15

Reactions were performed employing a **131a** : [Cu] : **L1** : RA : **132a** ratio equal to 500 : 5 : 6 : 8 : 100. 4 Å molecular sieves were used in a 95:5 weight ratio with respect to **132a**. [a] Yields were determined by ^1H NMR using 1,3,5-trimethoxybenzene as the internal standard. [b] Reaction time was 5 h. [c] The reaction was performed adding a 3% (v/v) of THF to the reaction mixture.

We next evaluated whether the use of different RAs would translate into improved yields of the desired ester **133a,a**. The effects produced by alkali metal BArF salts on the catalytic activity of copper complexes derived from **L1** and **L2** have been summarized in Table 3. Of all the RAs tested for **131a**, the catalyst incorporating RbBArF ([Cu(RbBArF•**L1**)]BArF) gave the best results (85% yield, Table 3, entry 5), even though LiBArF ([Cu(LiBArF•**L1**)]BArF) provided similar yield (Table 3, entry 2). It is interesting to highlight the ease with which a library of Cu-catalysts was generated with our strategy of adding an alkali metal BArF salt, allowing the straightforward identification of the optimal catalyst.

Moreover, we set out to determine the optimal length of the polyethyleneoxy chain (Table 3). The results demonstrated that the length of the polyethyleneoxy chains in the regulation site of ligands **L1** and **L2** had little effect on the yield of the insertion product (compare entries 1-6 and 7-12 in Table 3). Copper

catalysts derived from **L2** provided lower yields than those obtained with ligand **L1**. Moreover, high selectivity towards the formation of the O–H insertion product rather than the C–H insertion product **136** was achieved with the use of **L1** in the system. Thus, ligand **L1** was used in subsequent catalytic studies.

Table 3. Study of the performance of copper catalysts derived from ligands **L1** and **L2** using the complete set of alkali metal BArF salts as RA.

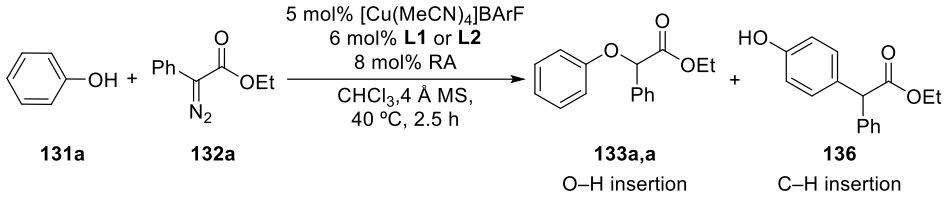

Entry	**L**	RA	**133a,a** yield [%][a]	**136** yield [%][a]
1	**L1**	None	67	nd[b]
2		LiBArF	84	nd
3		NaBArF	66	nd
4		KBArF	77	nd
5		RbBArF	85 (81)[c]	nd
6		CsBArF	65	nd
7	**L2**	None	50	6
8		LiBArF	77	5
9		NaBArF	64	nd
10		KBArF	79	4
11		RbBArF	71	nd
12		CsBArF	60	14

Reactions were performed employing a **131a** : [Cu] : **L** : RA : **132a** ratio equal to 500 : 5 : 6 : 8 : 100. 4 Å molecular sieves were used in a 95:5 weight ratio with respect to **132a**. [a] Yields were determined by ^{1}H NMR using 1,3,5-trimethoxybenzene as the internal standard. [b] Not detected. [c] Isolated yield.

The optimization study of diverse reaction parameters allowed determining the optimal conditions for the copper-catalyzed carbene insertion into O–H bonds between **131a** and **132a**. Therefore, the use of [Cu(MeCN)$_4$]BArF as copper precursor, **L1** as ligand, the addition of 4 Å molecular sieves in a 95:5 weight

ratio with respect to **132a**, and the use of $CHCl_3$ as solvent at 40 ºC gave the O–H insertion product **133a,a** in the highest yield.

A monitoring study of the reaction between **132a** and phenol **131a** by ^1H NMR at different reaction times was performed following the general procedure (see section 1.5.10), in the absence and in the presence of RbBArF as RA. The yields for **132a**, **133a,a**, **137** and **138** (for the structures of byproducts **137** and **138**, see Figure 25) were quantified by ^1H NMR using 1,3,5-trimethoxybenzene as internal standard.

Yield curves for the O–H insertion product derived from **131a** and **132a** were calculated from ^1H NMR data at different reactions times (Figure **22**) and then used to calculate turnover frequency numbers at *ca.* 50% conversion ($TOF_{1/2}$). Interestingly, a comparison of the $TOF_{1/2}$ numbers in the presence ($TOF_{1/2}$ = 400 h^{-1}, Figure 23) or absence ($TOF_{1/2}$ = 34 h^{-1}, Figure 24) of RA demonstrate the rate acceleration effects induced by RbBArF in the reaction between **131a** and **132a**.

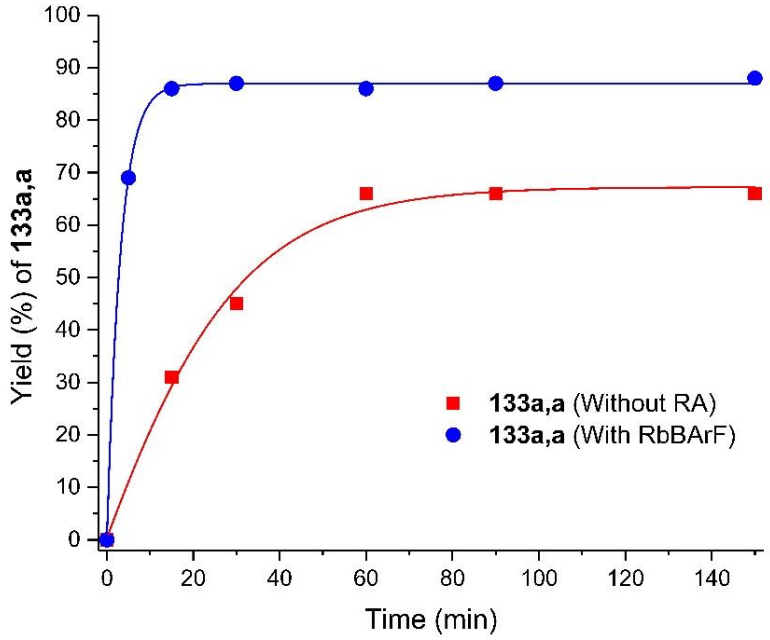

Figure 22. Yield for product **133a,a** plotted against reaction time (solid lines correspond to eye guidelines).

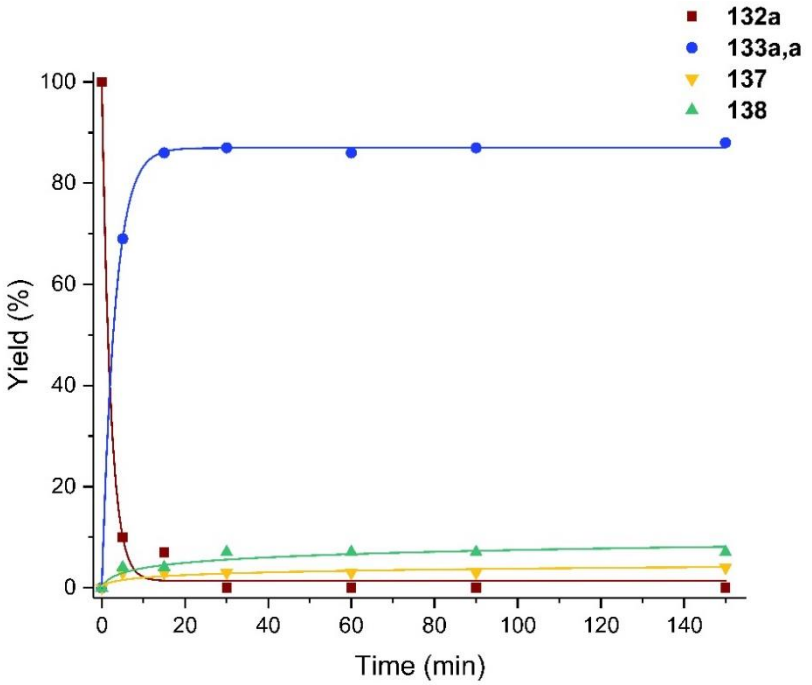

Figure 23. Reaction monitoring in the presence of RbBArF as RA (solid lines correspond to eye guidelines).

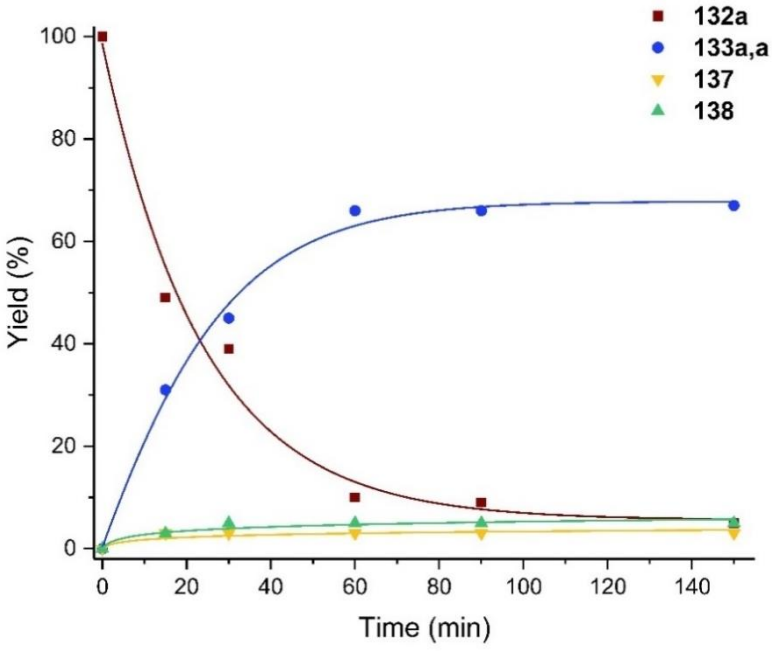

Figure 24. Reaction monitoring in the absence of RA (solid lines correspond to eye guidelines).

Byproducts **137** and **138** (Figure 25) were identified in low yields (<5%) in the crude mixture of the O–H insertion reaction. Azine **137** and diethyl fumarate or maleate **138** were formed through a homocoupling reaction between two molecules of diazocompound **132a**.[19]

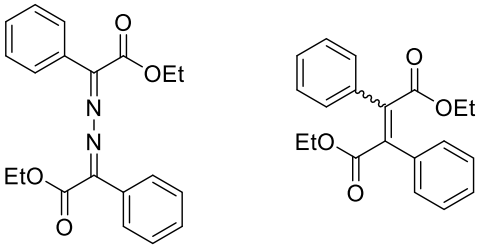

137 **138**

Figure 25. Byproducts **137** and **138** in the O–H insertion reaction.

To determine the catalyst stability during the O–H insertion reaction and the selectivity of the catalyst towards the O–H insertion product, an additional ^{1}H NMR reaction monitoring study was carried out. Two independents reactions, one without RA and the other with RbBArF as regulation agent, were carried out following the general procedure between **131a** and **132a** as substrates (see section 1.5.10). After two and a half hours, a second batch of **131a** and **132a** (the same amounts than before) were added to each reaction mixture. It should be mentioned that no amounts of ligand, copper precursor or regulation agent were added to the reaction mixtures at this point. The formation of **133a,a** as a function of time was monitored by ^{1}H NMR analysis of the corresponding reaction mixtures using 1,3,5-trimethoxybenzene as internal standard. The resulting plots are shown in Figure 26 and Figure 27.

[19] For the formation of the azine product **137**, see: Glaser, R.; Chen, G. S.; Barnes, C. L. *J. Org. Chem.* **1993**, *58*, 7446-7455. For the formation of diethyl fumarate or maleate homocoupling products **138**, see: Barluenga, J.; Riesgo, L.; López, L. A.; Rubio, E.; Tomás, M. *Angew. Chem., Int. Ed.* **2009**, *48*, 7569-7572.

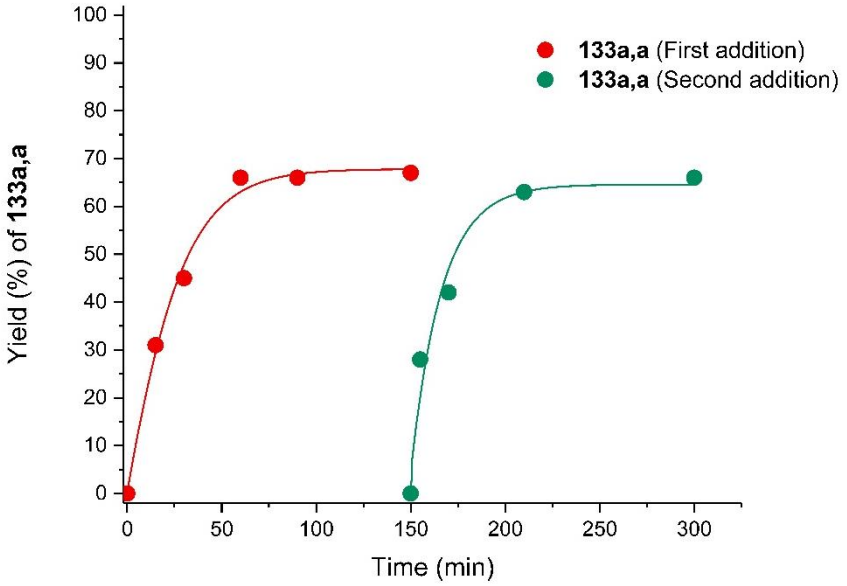

Figure 26. Reaction monitoring of two reaction cycles in the absence of RA. The red line corresponds to the yield towards the **133a,a** product for the first reaction cycle (from 0 to 150 min) and the green one for the second reaction cycle (from 150 to 300 min; solid lines correspond to eye guidelines).

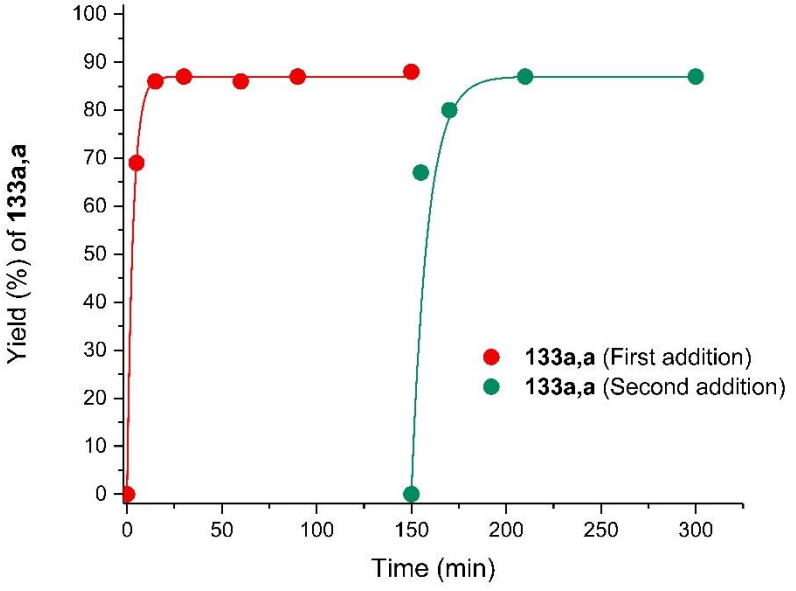

Figure 27. Reaction monitoring of two reaction cycles with RbBArF as RA. The red line corresponds to the yield towards the **133a,a** product for the first reaction cycle (from 0 to 150 min) and the green one for the second reaction cycle (from 150 to 300 min; solid lines correspond to eye guidelines).

As it can be observed in the conversion curves in Figure 26 and Figure 27, the rate of formation of product **133a,a** during the first (from 0 to 150 min) and second (from 150 to 300 min) reaction cycles are very similar. These experiments demonstrate that the catalytic species survive the first reaction cycle and remain active to transform a second batch of reagents into the corresponding product with very similar catalytic efficiency. Hence, these experiments rule out deactivation processes of the catalyst, as the supramolecular catalytic system remains active in solution.

Having determined optimal reactions conditions for this transformation with phenol, and having demonstrated that the yield of the reaction involving reaction partners **131a** and **132a** can be maximized by the choice of the RA, we decided to explore the substrate scope of the reaction with an array of structurally and electronically diverse phenols. An additional diazocompound **132b** was selected to be included in the expansion of the scope of the reaction. Substrate **132b** was synthesized following a reported procedure (Scheme 34).[17]

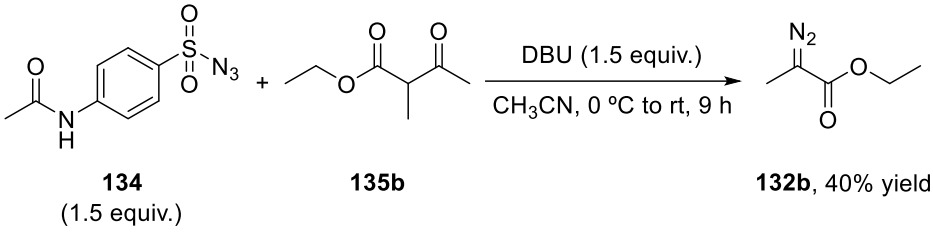

Scheme 34. General procedure for the synthesis of diazocompound **132b**.

Reaction partners that are typically challenging, such as phenols substituted with electron-withdrawing groups were also included in this study. In order to determine which RA was the most favorable for each phenol, the complete set of alkali metal BArF salts was tested, with the yield indicated in Scheme 35 being the highest one (the whole set of results with the regulation effects induced by each RA on each substrate is described in Section 1.5.12.3).

In terms of position effects, yields were higher for products with substituents at the *para* position with respect to the *meta* and *ortho* analogues (87%, 69% and 59% for compounds **133d,a**; **133c,a** and **133b,a**). Pronounced electronic effects were observed, with the lowest yield within the series obtained for the most electron-deficient phenols (41% yield for the formation of **133f,a** from *p*-nitrophenol in the absence of RA). Rapid tailoring of the catalyst system to each substrate was achieved through the RA approach, with yields being improved by the addition of a regulation agent in most cases. The greatest

improvements were observed for the *p*-fluoro-substituted product **133d,a** with an increase from 32% with no RA to 87% when NaBArF was used as the RA. We also performed an analogous study with ethyl 2-diazopropanoate **132b** as the carbenoid precursor and obtained similar outcomes and conclusions to those described for **132a** (Scheme 35).

Scheme 35. Supramolecularly regulated insertions of copper carbenoids into phenolic O–H bonds.

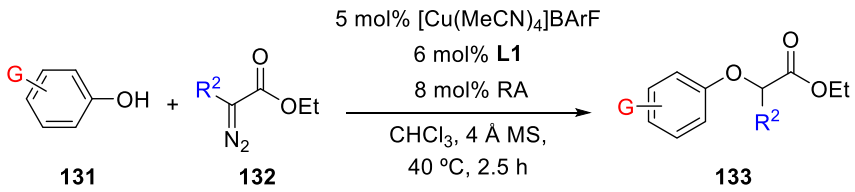

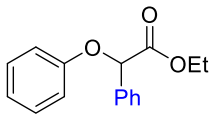

133a,a
No RA, 67% yield
RbBArF, 85 (81)[a] % yield

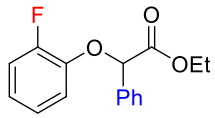

133b,a
No RA, 49% yield
RbBArF, 59 (55)[a] % yield

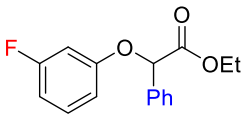

133c,a
No RA, 54% yield
CsBArF, 69 (64)[a] % yield

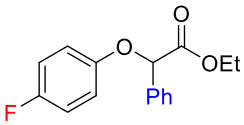

133d,a
No RA, 32% yield
NaBArF, 87 (80)[a] % yield

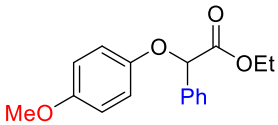

133e,a
No RA, 70% yield
NaBArF, 99 (91)[a] % yield

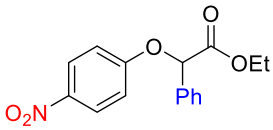

133f,a
No RA, 41 (38)[a] % yield
NaBArF, 99 (91)[a] % yield

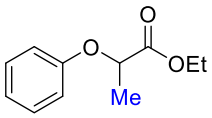

133a,b
No RA, 66% yield
KBArF, 77 (75)[a] % yield

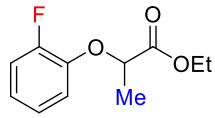

133b,b
No RA, 54% yield
NaBArF, 69 (63)[a] % yield

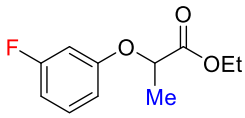

133c,b
No RA, 44% yield
NaBArF, 62 (60)[a] % yield

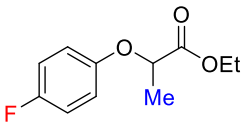

133d,b
No RA, 64% yield
NaBArF, 74 (68)[a] % yield

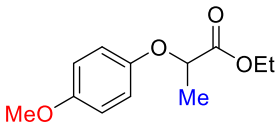

133e,b
No RA, 50% yield
RbBArF, 74 (71)[a] % yield

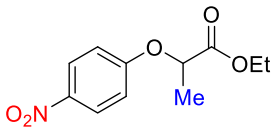

133f,b,
No RA 19% yield
KBArF, 42 (29)[a] % yield

Reactions were performed employing a **131** : [Cu] : **L1** : RA : **132** ratio equal to 500 : 5 : 6 : 8 : 100. 4 Å molecular sieves were used in a 95:5 weight ratio with respect to **132**. Yields were determined by ^{1}H NMR using 1,3,5-trimethoxybenzene as the internal standard. [a] Isolated yields.

The results obtained in this study indicate that the catalysts derived from **L1** mediate the formation of the O–H insertion products for all the substrates studied, regardless of the nature of the substituents. Moreover, these results confirm the validity of our catalyst regulation strategy for extending this transformation to the synthesis of a number of challenging and synthetically useful α-methyl-α-aryloxy derivatives.

The practicality of our catalytic system was further demonstrated by the preparation of the insertion products derived from several tertiary cycloalkanols previously synthesized following a reported procedure (Scheme 36).[20]

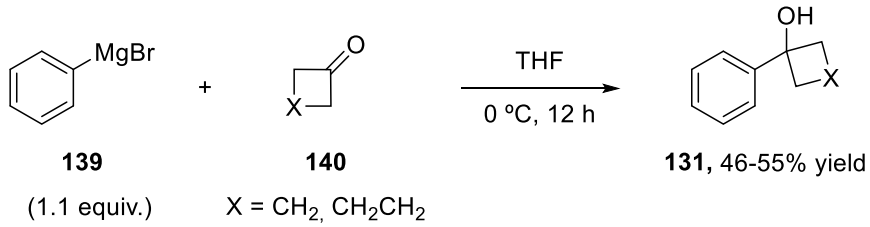

Scheme 36. General procedure for the preparation of cycloalkanol substrates.

This is a challenging transformation, as insertions of Cu-carbenoids into the O–H groups of cycloalkanols are limited and with ring opening products generally being obtained instead.[8] In our case, the use of NaBArF maximized the yield of the target compounds **133g,a** (64%, Scheme 37) and **133i,a** (39%, Scheme 37), while LiBArF enhanced the yield of **133h,a** (85%, Scheme 37). Cycloalkanol fragments are frequently present in drug candidates, and this reaction gives efficient access to potential pharmacophores.[21]

The preparation of advanced synthetic intermediates of biologically relevant compounds was also studied. Substrates **133j,a** and **133k,c** were selected to access advanced synthetic intermediates of fluoxetine or Prozac® (an SSRI antidepressant,[22] which is marketed as a racemate[23]) and Benadryl® (an antihistaminic drug[24]), respectively. Regarding the preparation of fluoxetine

[20] For the preparation of 1-phenylcyclopropan-1-ol **131g**, see: Elek, G. Z.; Borovkov, V.; Lopp, M.; Kananovich, D. G. *Org. Lett.* **2017**, *19*, 3544-3547. For the preparation of 1-phenylcyclobutan-1-ol **131h** and 1-phenylcyclopentan-1-ol **131i**, see: Sun, Y.; Huang, X.; Li, X.; Luo, F.; Zhang, L.; Chen, M.; Zheng, S.; Peng, B. *Adv. Synth. Catal.* **2018**, *360*, 1082-1087.
[21] (a) Talele, T. T. *J. Med. Chem.* **2016**, *59*, 8712-8756. (b) Pagar, V. V.; RajanBabu, T. V. *Science* **2018**, *361*, 68-72.
[22] Calow, A. D. J.; Fernández, E.; Whiting, A. *Org. Biomol. Chem*. **2014**, *12*, 6121-6127.
[23] Cotton, S. *Educ. Chem*. **2004**, *41*, 123-125.
[24] Snead, D. R.; Jamison, T. F. *Chem. Sci.* **2013**, *4*, 2822-2827.

precursor **133j,a**, the reaction between 4-(trifluoromethyl)phenol and **132a** under our optimized reaction conditions afforded the corresponding O–H insertion product in good yield (Scheme 37). For this particular substrate, the absence of regulation agent gave the best yield of the product. Subsequent reduction of the ester group with $LiAlH_4$ afforded the corresponding alcohol **141** (Scheme 38), whose transformation into fluoxetine has been reported in the literature.[25] Thus, the preparation of precursor **133j,a** *via* copper-catalyzed insertion of carbenoids into an O–H bond constitutes a new formal synthesis of fluoxetine.

In an analogous manner for Benadryl®, an advanced synthetic intermediate **133k,c** was efficiently synthesized by reacting diphenylmethanol and ethyl diazoacetate **132c** in the presence of the catalytic system derived from **L1** and NaBArF. The reduction of **133k,c** with $LiAlH_4$ afforded the corresponding alcohol **141** (Scheme 38), which can be transformed into Benadryl® following an already published synthetic protocol.[26] Our chemistry therefore constitutes a new formal synthesis of this active pharmaceutical ingredient.

[25] Devine, P. N.; Heid, R. M., Jr.; Tschaen, D. M. *Tetrahedron* **1997**, *53*, 6739-6746.
[26] Hamid, M. H. S. A.; Allen, C. L.; Lamb, G. W.; Maxwell, A. C.; Maytum, H. C.; Watson, A. J. A.; Williams, J. M. J. *J. Am. Chem. Soc.* **2009**, *131*, 1766-1774.

Scheme 37. Extension of the supramolecular regulation strategy.

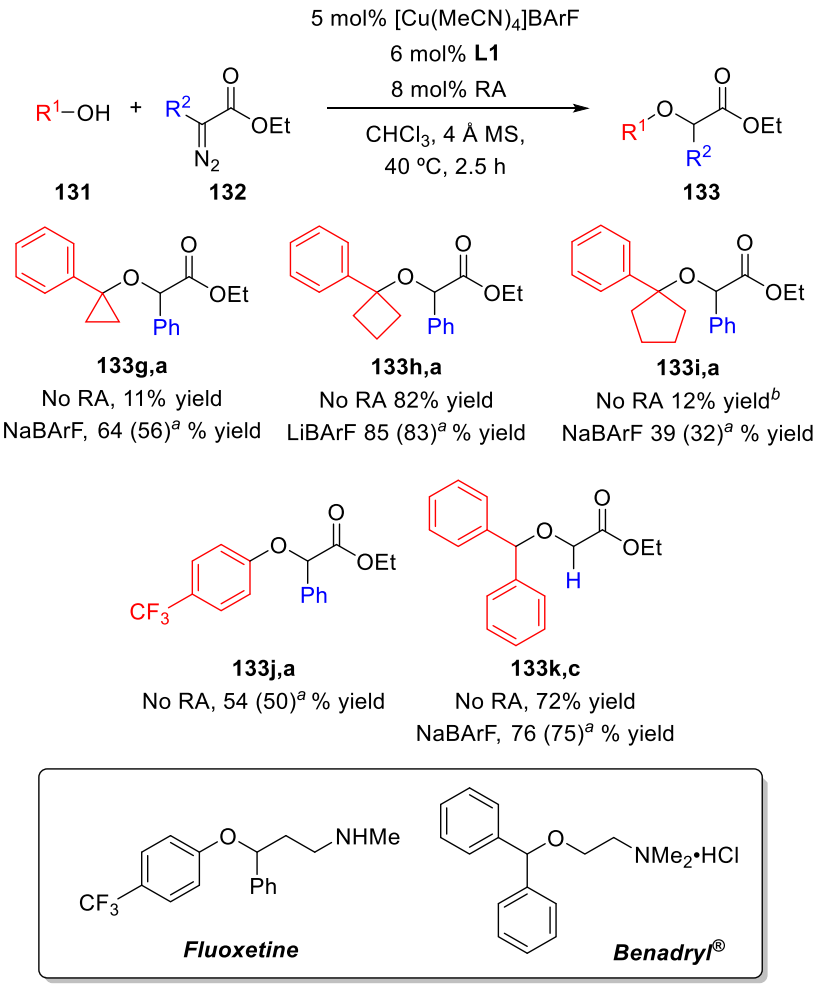

Reactions were performed employing a **131** : [Cu] : **L1** : RA : **132** ratio equal to 500 : 5 : 6 : 8 : 100. 4 Å molecular sieves were used in a 95:5 weight ratio with respect to **132**. Yields were determined by ^{1}H NMR using 1,3,5-trimethoxybenzene as the internal standard. [a] Isolated yields. [b] Reaction time was 24 h.

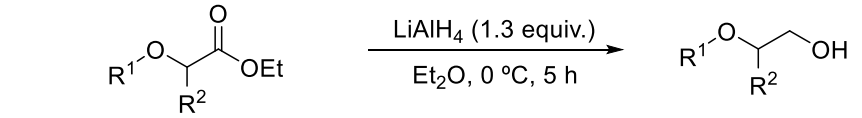

133j,a: R^1 = (4-CF_3)C_6H_4, R^2 = Ph
133k,c: R^1 = $CH(Ph)_2$, R^2 = H

141j,a, 50% yield
141k,c, 49% yield

Scheme 38. General synthesis for products **141**.

1.4. CONCLUSIONS

In conclusion, catalysts containing linear polyethyleneoxy chains as supramolecular regulation sites and oxazoline units as coordinating groups for copper(I) centers have been designed, prepared and characterized. These supramolecular copper complexes have found application in the catalyzed insertion of copper carbenoids into the O–H groups of an array of structurally diverse alcohols to afford synthetically useful α-alkyl/aryl-α-alkoxy/aryloxy derivatives in yields ranging from 39% to 99% (seventeen examples). Our regulation approach, which consists of screening a set of regulation agents to obtain the highest yield for the substrate of interest, has been demonstrated. The rapid tailoring of the catalyst system to each substrate has been achieved and the practicality of this transformation employing our supramolecularly regulated catalysts has been expanded by preparing advanced synthetic intermediates of relevant APIs.

1.5. Experimental section

1.5.1. General considerations

All syntheses were carried out using chemicals as purchased from commercial sources unless otherwise stated. Air- and moisture-sensitive manipulations or reactions were run under inert atmosphere, either in a N_2-filled glove box or with standard Schlenk techniques. Glassware was dried *in vacuo* before use with a hot air gun. All solvents were dried with a Solvent Purification System (SPS) and thoroughly deoxygenated by freeze-pump-thaw cycles. Silica gel 60 Å (230 - 400 mesh particle size) was used for column chromatography, unless otherwise stated. NMR spectra were recorded at room temperature in 400 MHz or 500 MHz spectrometers in $CDCl_3$ or CD_2Cl_2, unless otherwise mentioned. ^{1}H and $^{13}C\{^{1}H\}$ NMR chemical shifts are quoted in ppm relative to residual solvent peaks. $^{11}B\{^{1}H\}$ NMR chemical shifts are quoted in ppm relative to $BF_3{\cdot}(CH_3)_2O$ in $CDCl_3$. $^{19}F\{^{1}H\}$ NMR chemical shifts are quoted in ppm relative to $CFCl_3$ in $CDCl_3$. High resolution mass spectra (HRMS) were recorded by using ESI ionization in positive mode. IR spectra were recorded using Attenuated Total Reflection (ATR) technique, unless otherwise cited.

1.5.2. Synthesis of the hydroxymethyl-substituted oxazoline derivative 128

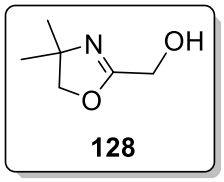

128

The preparation of **128** was performed adapting a reported procedure.[14] In a flame-dried 100 mL flask, 2-amine-2-methyl-1-propanol (15.00 mmol, 1.3 g) was dissolved in xylene (50.0 mL). Glycolic acid (15.00 mmol, 1.1 g) was added and the resulting solution was refluxed for 5 hours. After that, water was removed for 12 hours using a Dean-Stark apparatus. After the stated time, the solvent was distilled off and the resulting dark-yellow oil was distilled under vacuum (1.33×10^{-3} mbar, 110 °C). The product **128** was obtained as a white crystalline solid (1.2 g, 60% yield). Spectroscopic data were in agreement with those previously reported.[14] ^{1}H NMR (500 MHz, $CDCl_3$) δ: 4.21 (s, 2H), 4.02 (s, 2H) and 1.30 (s, 6H) ppm; $^{13}C\{^{1}H\}$ NMR (126 MHz, $CDCl_3$) δ: 166.4 (C), 80.1 (CH_2), 66.9 (C), 57.4 (CH_2) and 28.4 (CH_3) ppm.

1.5.3. Synthesis of bisoxazoline ligands L1 and L2

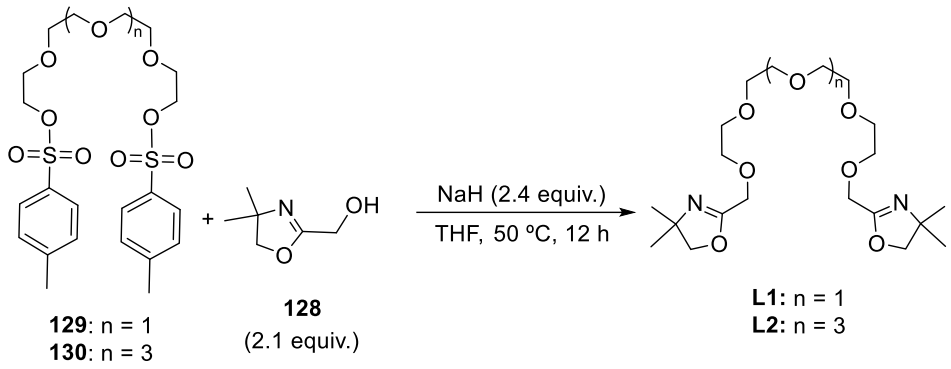

Scheme 39. General procedure for the synthesis of ligands **L1** and **L2**.

In a flame-dried 100 mL flask, a slurry of NaH (4.78 mmol) in dry THF (4.0 mL) was prepared under inert atmosphere and cooled at 0 ºC. A solution of (2,2-dimethyl-2,5-dihydrooxazol-4-yl)methanol **128** (4.18 mmol) in dry THF (4.0 mL) was slowly syringed into the NaH suspension at 0 ºC. The resulting mixture was allowed to reach room temperature and stirred for further 30 minutes. Then, a solution of polyethylene glycol ditosylate (1.99 mmol) in dry THF (4.0 mL) was syringed into the reaction mixture at room temperature. The resulting reaction mixture was heated at 50 ºC and stirred for 12 hours. Solvent was removed under reduced pressure. The residue obtained was dissolved in CH_2Cl_2 (20.0 mL) and filtered on Celite®. The filtrate was evaporated *in vacuo* and the residue was finally purified by silica gel column chromatography using EtOAc/MeOH (95:5 v/v) as the eluent to provide the corresponding bisoxazoline ligands as yellowish oils.

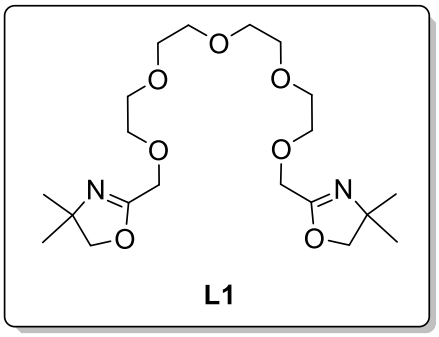

Ligand **L1** was synthesized following the general procedure from tetraethylene glycol bistosylate **129** (1.99 mmol, 1.0 g), NaH (4.78 mmol, 121.0 mg), and (2,2-dimethyl-2,5-dihydrooxazol-4-yl)methanol **128** (4.18 mmol, 540.0 mg). After purification by silica gel column chromatography, ligand **L1** was obtained as a yellowish oil (500.0 mg, 60% yield). ^{1}H NMR (400 MHz, $CDCl_3$) δ: 4.19 (s, 4H), 3.97 (s, 4H), 3.73 - 3.64 (m, 16H) and 1.29 (s, 12H) ppm; $^{13}C\{^1H\}$ NMR (101 MHz,

$CDCl_3$) δ: 162.4 (C), 79.3 (CH_2), 70.68 (CH_2), 70.66 (CH_2), 70.65 (CH_2), 70.56 (CH_2), 67.3 (C), 65.9 (CH_2) and 28.4 (CH_3) ppm; IR (neat): 2965, 2868, 1666, 1461, 1349, 1294, 1253, 1101, 980, 924, 876 and 815 cm^{-1}; HRMS (ESI) *m/z*: calcd for $C_{20}H_{36}N_2O_7Na$ $[M+Na]^+$ 439.2415, found 439.2417.

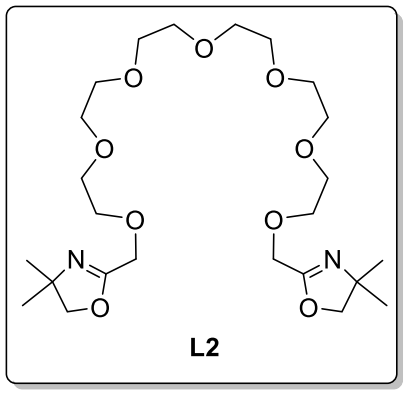

Ligand **L2** was synthesized following the general procedure from hexaethylene glycol bistosylate **130** (1.64 mmol, 1.0 g), NaH (3.94 mmol, 99.6 mg), and (2,2-dimethyl-2,5-dihydrooxazol-4-yl)methanol **128** (3.28 mmol, 424.0 mg). After purification by silica gel column chromatography, ligand **L2** was obtained as a yellowish oil (527.0 mg, 64% yield). ^1H NMR (400 MHz, $CDCl_3$) δ: 4.19 (s, 4H), 3.97 (s, 4H), 3.75 - 3.64 (m, 24H) and 1.29 (s, 12H) ppm; $^{13}C\{^1H\}$ NMR (101 MHz, $CDCl_3$) δ: 162.4 (C), 79.4 (CH_2), 70.74 (CH_2), 70.73 (CH_2), 70.71 (CH_2), 70.6 (CH_2), 67.3 (C), 65.9 (CH_2) and 28.5 (CH_3) ppm; IR (neat): 3390, 2868, 1665, 1527, 1460, 1349, 1295, 1251, 1098 and 981 cm^{-1}; HRMS (ESI) *m/z*: calcd for $C_{24}H_{45}N_2O_9$ $[M+H]^+$ 505.3120, found 505.3102.

1.5.4. Synthesis of regulation agents: alkali metal BArF salts

NaBArF was purchased from a commercial supplier, dried under vacuum (10^{-2} mbar, 120 ºC, 18 h) and used afterwards. LiBArF, KBArF, RbBArF and CsBArF were synthesized following reported procedures.[13]

1.5.5. Preparation and characterization of copper(I)-complexes derived from NaBArF and ligands L1 or L2

1.5.5.1. Complexation of L1 and L2 with NaBArF

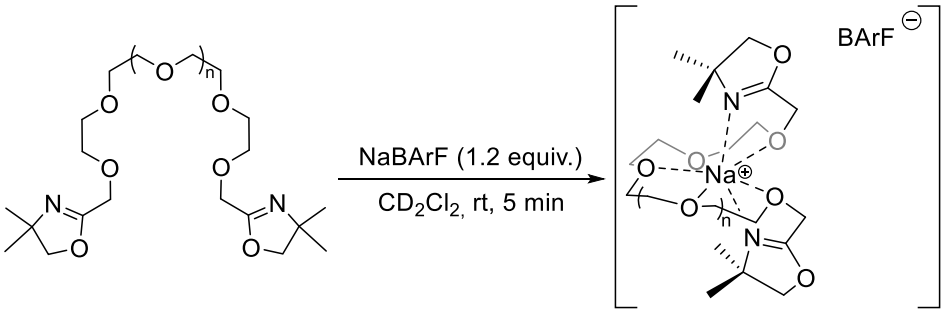

Scheme 40. Preparation of NaBArF•**L1** and NaBArF•**L2**.

In a N_2-filled glove box, a solution of NaBArF (0.06 mmol) in CD_2Cl_2 (0.5 mL) was prepared. Then, a solution of the desired ligand (0.05 mmol) in CD_2Cl_2 (0.4 mL) was added dropwise to the previous solution. The resulting mixture was stirred for 5 minutes at room temperature. NMR characterization studies were made directly with this solution, which was subsequently concentrated under reduced pressure to isolate the complex as a solid in a quantitative manner.

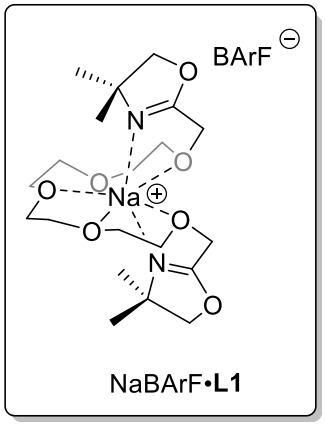

Complex NaBArF•**L1** was prepared following the general procedure from ligand **L1** (0.05 mmol, 20.8 mg) and NaBArF (0.06 mmol, 48.7 mg). The complex NaBArF•**L1** was obtained as a whitish foamy solid (78.1 mg, quantitative yield). ^{1}H NMR (400 MHz, CD_2Cl_2) δ: 7.74 - 7.73 (m, 8H), 7.58 - 7.57 (m, 4H), 4.11 (s, 4H), 4.02 (s, 4H), 3.68 - 3.59 (m, 16H) and 1.27 (s, 12H) ppm; ^{13}C{^{1}H} NMR (101 MHz, CD_2Cl_2) δ: 164.7 (C), 162.2 (q, $^1J_{C-B}$ = 50.2 Hz, C), 135.2 (CH), 129.8 - 128.8 (C), 125.0 (q, $^1J_{C-F}$ = 272.4 Hz, C) 118.1 - 117.7 (CH), 80.3 (CH_2), 70.6 (CH_2), 69.4 (CH_2), 69.0 (CH_2), 68.5 (CH_2), 67.5 (C), 65.5 (CH_2) and 28.6 (CH_3) ppm; ^{19}F{^{1}H} NMR (376 MHz, CD_2Cl_2)

δ: −63.0 ppm; $^{11}B\{^1H\}$ NMR (128 MHz, CD_2Cl_2) δ: −6.6 ppm; IR (neat): 2929, 1673, 1612, 1353, 1275, 1113, 944, 888, 839, 745, 715, 681 and 668 cm^{-1}; HRMS (ESI) *m/z*: calcd for $C_{20}H_{36}N_2NaO_7$ $[M]^+$ 439.2415, found 439.2401.

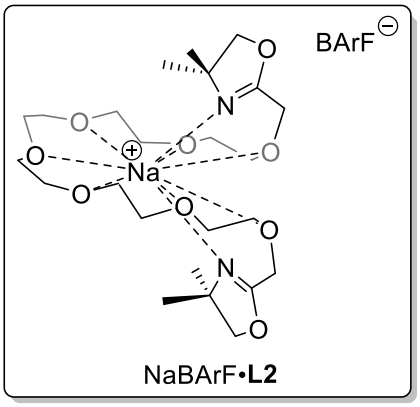

Complex NaBArF•**L2** was prepared following the general procedure from ligand **L2** (0.05 mmol, 25.2 mg) and NaBArF (0.06 mmol, 48.7 mg). The complex NaBArF•**L2** was obtained as a yellowish foamy solid (83.2 mg, quantitative yield). ^1H NMR (400 MHz, CD_2Cl_2) δ: 7.74 - 7.73 (m, 8H), 7.59 - 7.57 (m, 4H), 4.14 (s, 4H), 3.99 (s, 4H), 3.71 - 3.63 (m, 24H) and 1.25 (s, 12H) ppm; $^{13}C\{^1H\}$ NMR (101 MHz, CD_2Cl_2) δ: 163.7 (C), 162.2 (q, $^1J_{C-B}$ = 49.8 Hz, C), 135.2 (CH), 129.8 - 128.9 (C), 125.0 (q, $^1J_{C-F}$ = 272.6 Hz, C), 118.1 - 117.7 (CH), 80.0 (CH_2), 70.2 (CH_2), 69.4 (CH_2), 69.3 (CH_2), 69.0 (CH_2), 68.9 (CH_2), 68.7 (CH_2), 67.5 (C), 65.5 (CH_2) and 28.5 (CH_3) ppm; $^{19}F\{^1H\}$ NMR (376 MHz, CD_2Cl_2) δ: −63.0 ppm; $^{11}B\{^1H\}$ NMR (128 MHz, CD_2Cl_2) δ: −6.6 ppm; IR (neat): 2920, 1673, 1611, 1464, 1353, 1273, 1114, 947, 886, 839, 745, 713, 682 and 669 cm^{-1}; HRMS (ESI) *m/z*: calcd for $C_{24}H_{44}N_2NaO_9$ $[M]^+$ 527.2939, found 527.2922.

1.5.5.2. Synthesis of [Cu(MeCN)$_4$]BArF

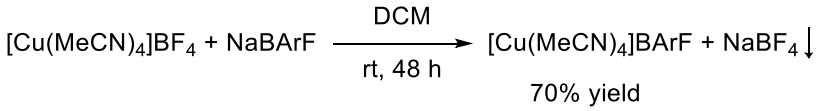

Scheme 41. General procedure for the preparation of [Cu(MeCN)$_4$]BArF.

In a N_2-filled glove box, a solution of [Cu(MeCN)$_4$]BF_4 (0.32 mmol) in CH_2Cl_2 (4.0 mL) was prepared at room temperature and stirred for 72 h. After the stated time, NaBArF (0.32 mmol) was added and the resulting mixture was stirred for 24 h at room temperature. The solution was filtered and concentrated under reduced pressure to isolate the complex as a solid in a 70% yield.

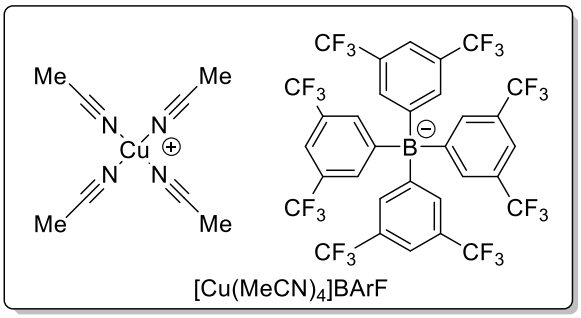

Complex [Cu(MeCN)$_4$]BArF was synthesized following the general procedure from [Cu(MeCN)$_4$]BF$_4$ (0.32 mmol, 103.4 mg) and NaBArF (0.32 mmol, 284.0 mg). The complex [Cu(MeCN)$_4$]BArF was obtained as a yellowish solid (255.2 mg, 70% yield). Spectroscopic data were in agreement with those previously reported.[16] ^{1}H NMR (400 MHz, $CDCl_3$) δ: 7.73 - 7.69 (m, 8H), 7.57 - 7.55 (m, 4H) and 2.06 (s, 12H) ppm; $^{13}C\{^1H\}$ NMR (101 MHz, $CDCl_3$) δ: 160.5 (q, $^1J_{C-B}$ = 50.2 Hz, C), 133.8 (CH), 128.2 (qm, $^2J_{C-F}$ = 31.5 Hz, C), 123.6 (q, $^1J_{C-F}$ = 272.2 Hz, C), 116.9 - 116.6 (CH), 115.4 (C) and 0.9 (CH_3) ppm; $^{19}F\{^1H\}$ NMR (376 MHz, $CDCl_3$) δ: −62.6 ppm; $^{11}B\{^1H\}$ NMR (128 MHz, $CDCl_3$) δ: −6.7 ppm.

1.5.5.3. Complexation of NaBArF•L1 and NaBArF•L2 with [Cu(MeCN)$_4$]BArF

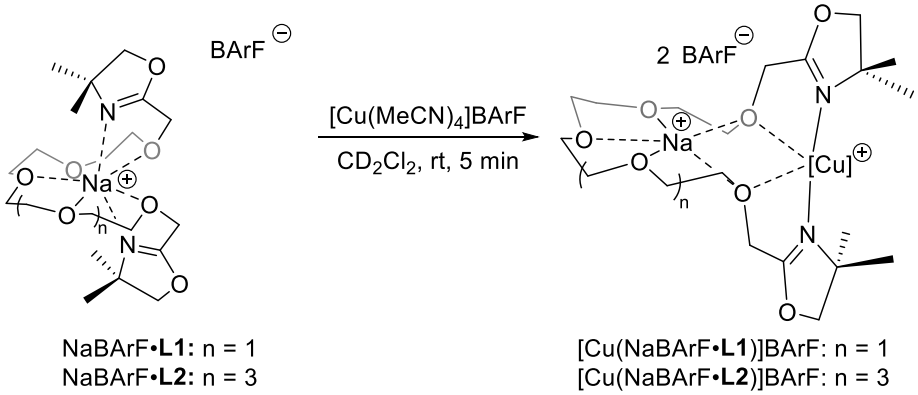

Scheme 42. Preparation of complexes [Cu(NaBArF•**L1**)]BArF and [Cu(NaBArF•**L2**)]BArF.

In a N_2-filled glove box, a solution of [Cu(MeCN)$_4$]BArF (0.05 mmol) in CD_2Cl_2 (0.3 mL) was prepared at room temperature. A solution of NaBArF•**L1** (0.05 mmol) in CD_2Cl_2 (0.9 mL) was prepared as indicated in Section 1.5.5.1 and added dropwise to the solution containing the copper precursor. NMR characterization studies were made directly with this solution, which was

subsequently concentrated under reduced pressure to isolate the complex as a solid in a quantitative manner.

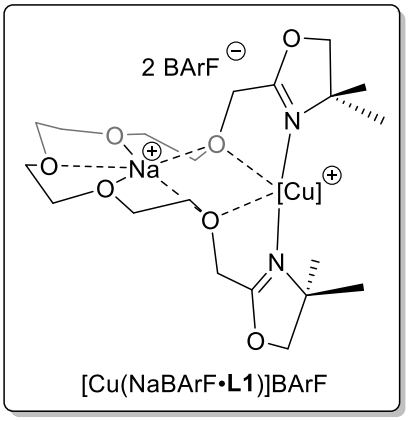

[Cu(NaBArF•**L1**)]BArF

Complex [Cu(NaBArF•**L1**)]BArF was synthesized following the general procedure from [Cu(MeCN)$_4$]BArF (0.05 mmol, 56.8 mg), NaBArF (0.06 mmol, 48.7 mg), and ligand **L1** (0.05 mmol, 20.8 mg). The complex [Cu(NaBArF•**L1**)]BArF was obtained as a yellowish foamy solid (132.9 mg, quantitative yield). ^{1}H NMR (400 MHz, CD_2Cl_2) δ: 7.75 - 7.74 (m, 16H), 7.59 - 7.57 (m, 8H), 4.34 (s, 4H), 4.29 (s, 4H), 3.80 - 3.57 (m, 16H), 1.99 (s, 12H) and 1.37 (s, 12H) ppm; ^{13}C{^{1}H} NMR (101 MHz, CD_2Cl_2) δ: 171.6 (C), 162.4 (q, $^1J_{C–B}$ = 49.8 Hz, C), 135.3 (CH), 130.0 - 129.1 (C), 125.1 (q, $^1J_{C–F}$ = 272.0 Hz, C), 118.1 - 117.8 (CH), 117.0 (C), 81.4 (CH_2), 72.0 (CH_2), 71.0 (CH_2), 70.8 (CH_2), 70.7 (CH_2), 67.1 (C), 64.9 (CH_2), 28.8 (CH_3) and 1.8 (CH_3) ppm; ^{19}F{^{1}H} NMR (376 MHz, CD_2Cl_2) δ: −63.1 ppm; ^{11}B{^{1}H} NMR (128 MHz, CD_2Cl_2) δ: −6.6 ppm; IR (neat): 2932, 1667, 1611, 1354, 1274, 1111, 945, 886, 838, 712, 681 and 669 cm^{-1}; HRMS (ESI) *m/z*: calcd for $C_{20}H_{36}CuN_2O_7$ [M−Na]$^+$ 479.1813, found 479.1819.

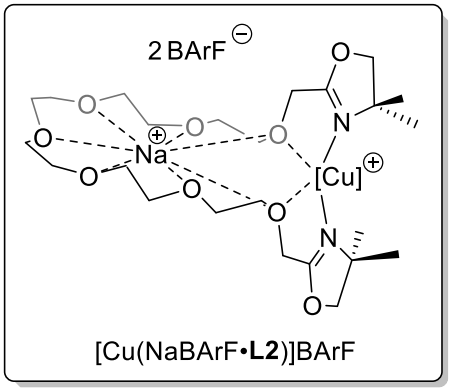

[Cu(NaBArF•**L2**)]BArF

Complex [Cu(NaBArF•**L2**)]BArF was synthesized following the general procedure from [Cu(MeCN)$_4$]BArF (0.05 mmol, 56.8 mg), NaBArF (0.06 mmol, 48.7 mg), and ligand **L2** (0.05 mmol, 25.2 mg). The complex [Cu(NaBArF•**L2**)]BArF was obtained as a yellowish foamy solid (138.7 mg, quantitative yield). ^{1}H NMR (400 MHz, CD_2Cl_2) δ: 7.76 - 7.73 (m, 16H), 7.60 - 7.58 (m, 8H), 4.36 (s, 4H), 4.31 (s, 4H), 3.77 - 3.56 (m, 24H), 2.01 (s, 12H) and 1.40 (s, 12H) ppm; ^{13}C{^{1}H} NMR (101 MHz, CD_2Cl_2) δ: 171.2 (C), 162.2 (q, $^1J_{C–B}$ = 49.6 Hz, C), 135.3 (CH), 129.9 - 128.9 (C), 125.0 (q, $^1J_{C–F}$ = 272.0 Hz, C), 118.1 - 117.8(CH), 117.2 (C), 81.4 (CH_2), 71.9 (CH_2), 69.7 (CH_2), 69.4 (CH_2), 68.8 (CH_2), 68.4 (CH_2), 68.3 (CH_2), 67.9 (C), 65.4 (CH_2), 29.0 (CH_3) and 1.8 (CH_3) ppm;

$^{19}F\{^{1}H\}$ NMR (376 MHz, CD_2Cl_2) δ: −62.9 ppm; $^{11}B\{^{1}H\}$ NMR (128 MHz, CD_2Cl_2) δ: −6.7 ppm; IR (neat): 2932, 1657, 1354, 1274, 1115, 886, 839, 712 and 669 cm^{-1}; HRMS (ESI) *m/z*: calcd for $C_{24}H_{44}CuN_2O_9$ $[M–Na]^+$ 567.2337, found 567.2354.

1.5.6. NMR titrations and measurement of binding constants by NMR

1.5.6.1. Qualitative titrations

Titrations were carried out on a 400 MHz spectrometer by using a solution of ligand **L1** (*ca.* 1 x 10^{-3} M) in $CDCl_3$ and adding aliquots of a solution of the corresponding regulation agent at 25 ºC.

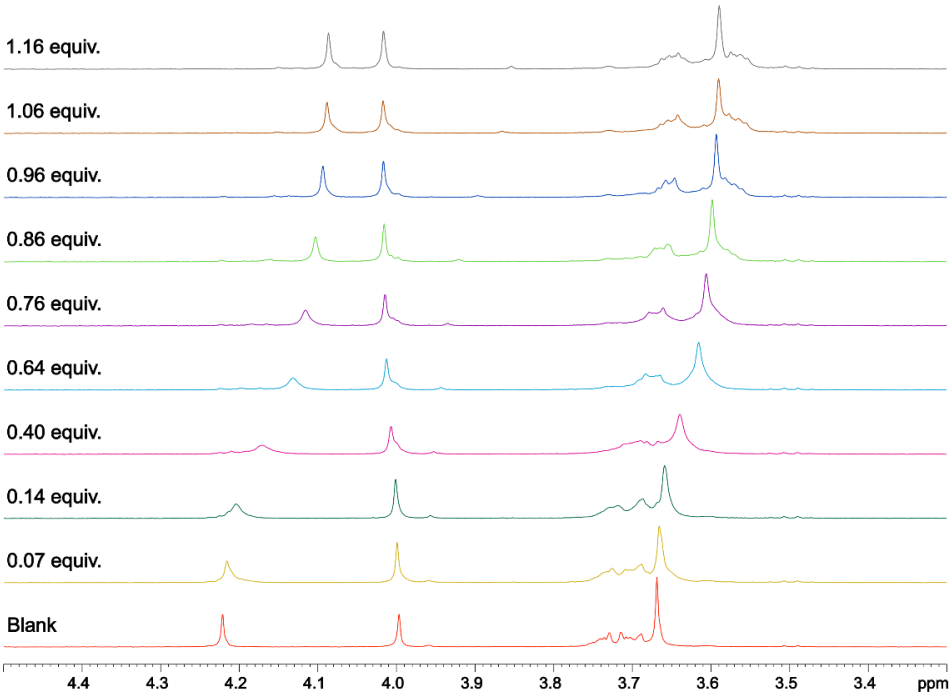

Figure 28. Changes in the ^{1}H NMR (400 MHz, $CDCl_3$) spectra acquired at 25 ºC during the titration of **L1** (2.54 x 10^{-3} M) with NaBArF.

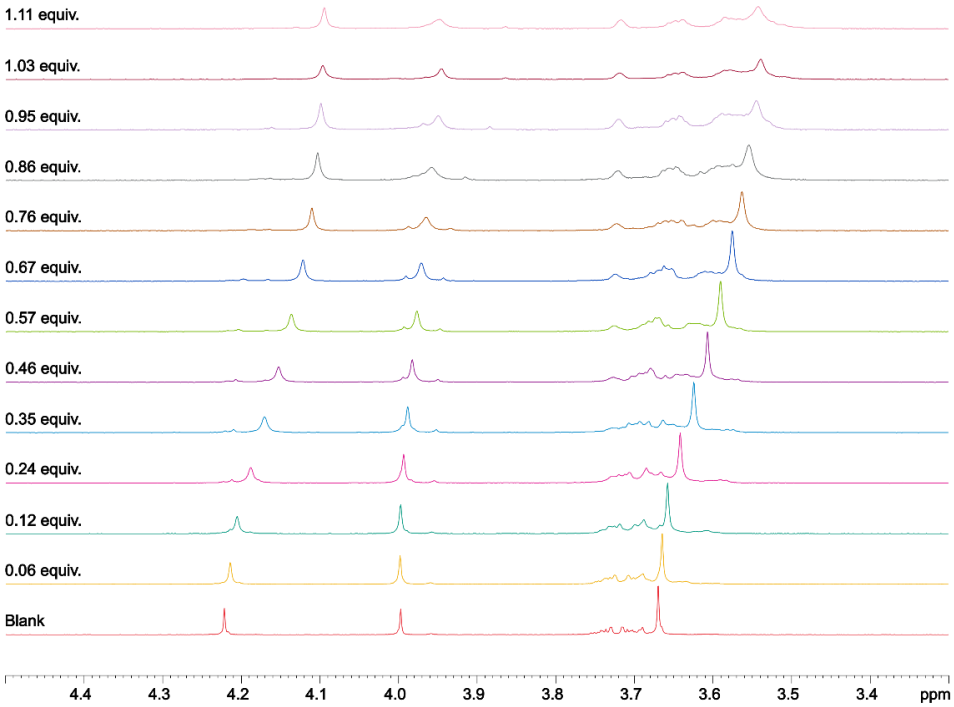

Figure 29. Changes in the ^{1}H NMR (400 MHz, $CDCl_3$) spectra acquired at 25 ºC during the titration of **L1** (2.51 x 10^{-3} M) with RbBArF.

1.5.6.2. Measurement of binding constants by NMR spectroscopy

A solution of ligand **L1** (*ca.* 1 x 10^{-3} M) in $CDCl_3$ was prepared. Solutions of NaBArF and RbBArF (*ca.* 1 x 10^{-3} M) were also prepared in the same solvent. The host solution (0.5 mL) was placed in a NMR tube. The titration was carried out adding at 25 ºC incremental amounts of guest (NaBArF or RbBArF) to the host (**L1**) solution. This process led to changes in the chemical shift in the NMR spectra. Binding constants were calculated by multivariate factor analysis of the ^{1}H NMR chemical shift values, considering a 1:1 binding model in the fast exchange-limit. The SPECFIT software (Version 3.0; Spectra Software Associates)[15] was used.

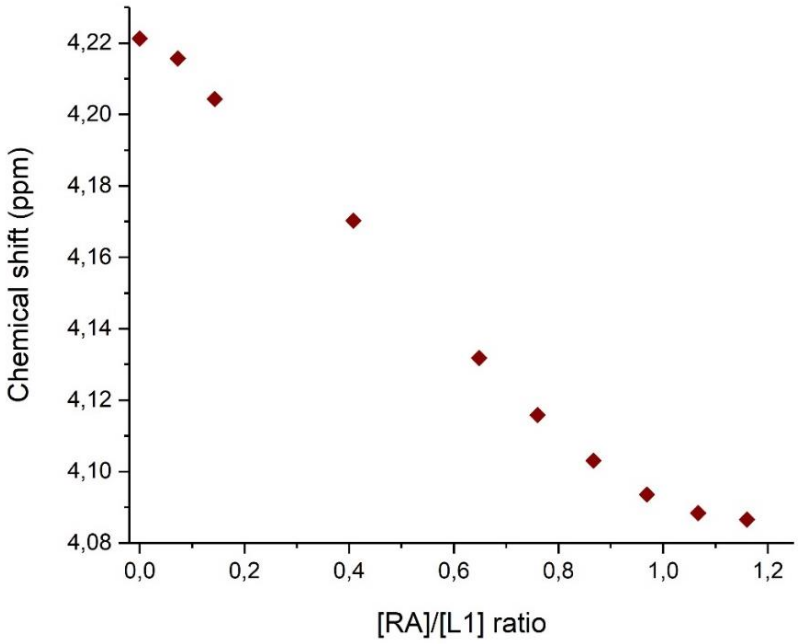

Figure 30. NMR titration to measure the binding constant between **L1** (2.54×10^{-3} M) and NaBArF as RA. Changes (ppm) in the ^{1}H NMR (400 MHz, $CDCl_3$) upon addition of NaBArF (14.0×10^{-3} M).

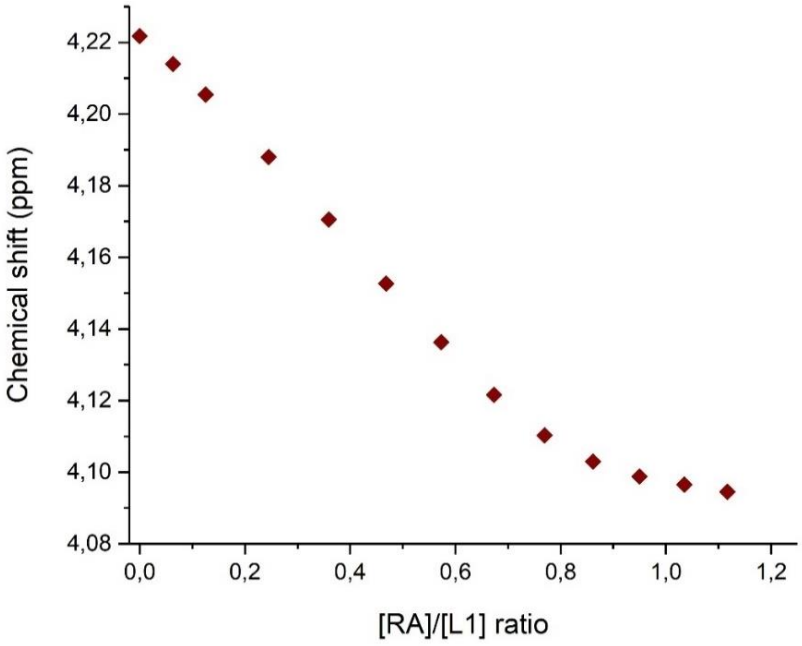

Figure 31. NMR titration to measure the binding constant between **L1** (2.51×10^{-3} M) and RbBArF as RA. Changes (ppm) in the ^{1}H NMR (400 MHz, $CDCl_3$) upon addition of RbBArF (13.4×10^{-3} M).

1.5.7. Preparation of [Cu(NaPF$_6$•L1)]PF$_6$ and [Cu(NaPF$_6$•L2)]PF$_6$

Complexes [Cu(NaPF$_6$•**L1**)]PF$_6$ and [Cu(NaPF$_6$•**L2**)]PF$_6$ were prepared following analogous synthetic protocols to those indicated in sections 1.5.5.1 and 1.5.5.3, employing the corresponding molar amounts of NaPF$_6$ instead of NaBArF. The resulting solids were dissolved in CH_2Cl_2 and Et_2O was carefully layered on top of the previous solution. Single crystals were obtained by allowing Et_2O to slowly diffuse into the CH_2Cl_2 solution.

1.5.8. Single crystal X-ray structure determinations

Crystal preparation: Crystals of NaBArF•**L1**, [Cu(NaPF$_6$•**L1**)]PF$_6$ and [Cu(NaPF$_6$•**L2**)]PF$_6$ were grown by slow diffusion of Et_2O in CH_2Cl_2. The crystals used for X-ray measurements were selected using a Zeiss stereomicroscope using polarized light and prepared under inert conditions immersed in perfluoropolyether as protecting oil for manipulation.

Data collection: Crystal structure determination for samples NaBArF•**L1**, [Cu(NaPF$_6$•**L1**)]PF$_6$ and [Cu(NaPF$_6$•**L2**)]PF$_6$ were carried out using a Apex DUO Kappa 4-axis goniometer equipped with an APPEX 2 4K CCD area detector, a Microfocus Source E025 IμS using MoK$_\alpha$ radiation, Quazar MX multilayer Optics as monochromator and an Oxford Cryosystems low temperature device Cryostream 700 plus (T = −173 °C). Full-sphere data collection was used with ω and φ scans. *Programs used:* Bruker Device: Data collection APEX-2,[27] data reduction Bruker Saint[28] V/.60A and absorption correction SADABS.[29]

Structure Solution and Refinement: Crystal structure solution was achieved using the computer program SHELXT.[30] Visualization was performed with the

[27] Data collection with APEX II version 2013.4-1. Bruker (2007). Bruker AXS Inc., Madison, Wisconsin, USA.
[28] Data reduction with Bruker SAINT version 8.30c. Bruker (2007). Bruker AXS Inc., Madison, Wisconsin, USA.
[29] SADABS: V2012/1 Bruker (2001). Bruker AXS Inc., Madison, Wisconsin, USA. See the following reference: Blessing, R. H. *Acta Crystallogr*. **1995**, *A51*, 33-38.
[30] SHELXT. V2014/4 (Sheldrick 2014). See the following reference: Sheldrick, G. M. *Acta Crystallogr*. **2008**, *A64*, 112-122.

program SHELXle.[31] Missing atoms were subsequently located from difference Fourier synthesis and added to the atom list. Least-squares refinement on F^2 using all measured intensities was carried out using the program SHELXL 2015.[32] All non-hydrogen atoms were refined including anisotropic displacement parameters.

Comments to the structure of NaBArF•L1: The asymmetric unit contains one molecule of the cationic sodium complex and one molecule of the BArF anion. The central part of the ligand in the sodium complex is disordered in two orientations. Also, the CF_3 groups in the BArF anion are disordered in different orientations.

(a) (b)

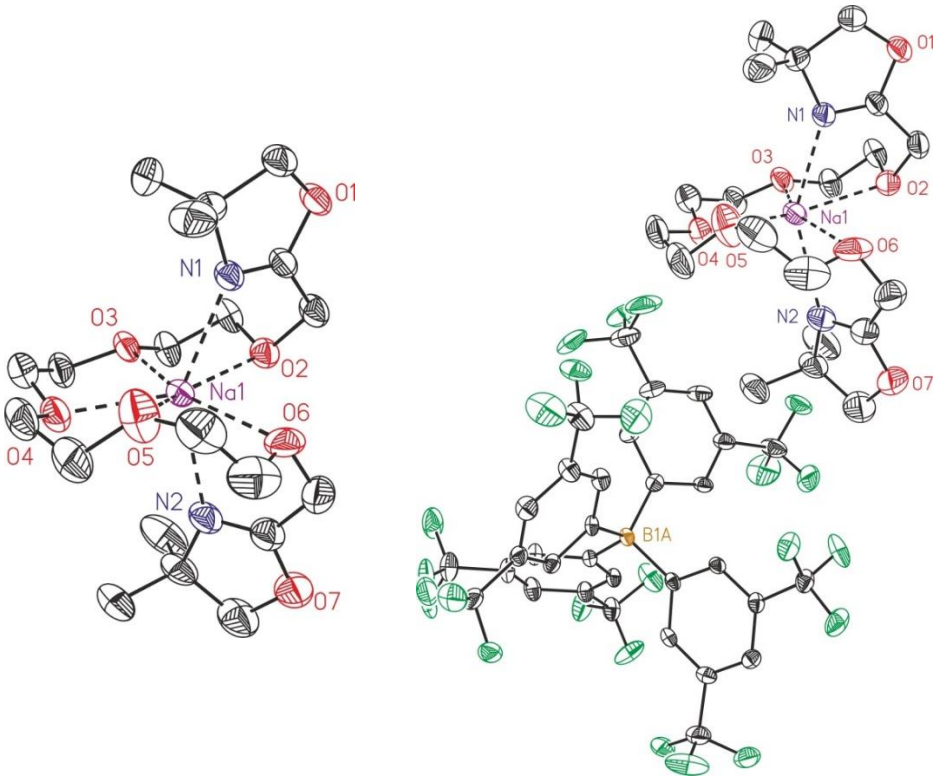

Figure 32. ORTEP drawing (thermal ellipsoids drawn at a 50% probability level) showing the structure of NaBArF•**L1**. (a) The BArF anion and hydrogen atoms have been omitted for clarity; (b) hydrogen atoms have been omitted for clarity. Color scheme: C: black, O: red, N: dark blue, Na: purple, F: green, B: light brown.

[31] SHELXle; See the following reference: Hübschle, C. B.; Sheldrick, G. M.; Dittrich, B. *J. Appl. Crystallogr.* **2011**, *44*, 1281-1284.
[32] SHELXL; SHELXL-2014/7 (Sheldrick 2014). See the following reference: Sheldrick, G.M. *Acta Crystallogr.* **2015**, *C71*, 3-8.

Table 4. Crystal data and structural parameters for complex NaBArF•**L1**.

Compound	NaBArF•**L1**
Formula	$C_{52}H_{48}BF_{24}N_2NaO_7$
Solvent	CH_2Cl_2
Formula weight	1302.72
Crystal size (mm^3)	0.10 x 0.10 x 0.06
Temperature (K)	100(2)
Wavelength (Å)	0.71073
Crystal system	Monoclinic
Space group	P2(1)/c
a (Å)	12.7633(4)
b (Å)	18.5020(6)
c (Å)	24.5224(8)
α (º)	90
β (º)	96.5057(10)
γ (º)	90
Volume ($Å^3$)	5753.6(3)
Z	4
ρ ($g \cdot cm^{-3}$)	1.504
μ (mm^{-1})	0.157
θ_{max} (º)	28.154
Reflections collected	68048
Independent reflections	14080 [R(int) = 0.0549]
Absorption correction	Multi-Scan
Data / restraints /Parameters	14080/ 1502/ 1169
R1/wR2 [I>2σ(I)]	0.0680/0.1701
R1/wR2 (all data)	0.1199/0.2003
Goodness-of-fit (F^2)	1.030
Peak/hole ($e/Å^{-3}$)	0.801/−0.535

Table 5. Selected bond lengths (Å) for complex NaBArF•**L1**.

Entry	Atoms	Length (Å)	Entry	Atoms	Length (Å)
1	Na1-O5'	2.298(19)	9	Na1-N2	2.557(3)
2	Na1-O3'	2.32(3)	10	Na1-O4'	2.566(11)
3	Na1-O3	2.376(10)	11	Na1-C13'	3.074(13)
4	Na1-O5	2.433(6)	12	Na1-C14'	3.127(13)
5	Na1-O4	2.433(3)	13	B1A-C9A	1.630(6)
6	Na1-O6	2.481(3)	14	B1A-C25A	1.637(4)
7	Na1-N1	2.488(3)	15	B1A-C1A	1.638(4)
8	Na1-O2	2.523(2)	16	B1A-C17A	1.641(3)

Table 6. Selected bond angles (°) for complex NaBArF•**L1**.

Entry	Atoms	Angles (°)	Entry	Atoms	Angles (°)
1	O5'-Na1-O3'	126.8(5)	20	O4-Na1-O2	136.94(11)
2	O3-Na1-O5	132.5(2)	21	O6-Na1-O2	86.03(10)
3	O3-Na1-O4	68.05(15)	22	N1-Na1-O2	68.19(8)
4	O5-Na1-O4	70.33(14)	23	O5'-Na1-N2	87.2(4)
5	O5'-Na1-O6	74.4(4)	24	O3'-Na1-N2	102.9(7)
6	O3'-Na1-O6	157.3(5)	25	O3-Na1-N2	107.2(2)
7	O3-Na1-O6	155.36(16)	26	O5-Na1-N2	96.01(16)
8	O5-Na1-O6	72.00(14)	27	O4-Na1-N2	91.91(11)
9	O4-Na1-O6	134.15(12)	28	O6-Na1-N2	67.05(9)
10	O5'-Na1-N1	102.4(4)	29	N1-Na1-N2	146.95(10)
11	O3'-Na1-N1	96.4(7)	30	O2-Na1-N2	91.73(9)
12	O3-Na1-N1	90.7(2)	31	O5'-Na1-O4'	61.2(4)
13	O5-Na1-N1	91.39(15)	32	O3'-Na1-O4'	68.8(5)
14	O4-Na1-N1	120.81(11)	33	O6-Na1-O4'	133.9(3)
15	O6-Na1-N1	84.98(9)	34	N1-Na1-O4'	92.3(3)
16	O5'-Na1-O2	159.2(4)	35	O2-Na1-O4'	135.2(3)
17	O3'-Na1-O2	73.6(4)	36	N2-Na1-O4'	119.5(3)
18	O3-Na1-O2	69.92(14)	37	O5'-Na1-C13'	27.2(3)
19	O5-Na1-O2	151.47(13)	38	O3'-Na1-C13'	151.9(4)

Table 7. Selected torsion angles (°) for complex NaBArF•**L1**.

Entry	Atoms	Torsion Angles (°)	Entry	Atoms	Torsion Angles (°)
1	Na1-N1-C1-C3	−66.3(4)	8	Na1-O3-C8-C7	−54.4(6)
2	Na1-N1-C1-C4	55.6(4)	9	Na1-O3-C9-C10	43.9(7)
3	Na1-N1-C1-C2	176.0(3)	10	Na1-O4-C10-C9	48.1(6)
4	Na1-N1-C5-O1	178.5(2)	11	Na1-O4-C11-C12	−38.8(6)
5	Na1-N1-C5-C6	0.2(4)	12	Na1-O5-C12-C11	−55.5(5)
6	Na1-O2-C6-C5	−39.1(3)	13	Na1-O5-C13-C14	−41.7(7)
7	Na1-O2-C7-C8	−43.2(4)	14	Na1-O6-C14-C13	−46.8(6)

Comments to the structure of [Cu(NaPF$_6$•L1)]PF$_6$: The asymmetric unit contains one molecule of the metal complex (with a copper and a sodium atom), two PF_6 anions and a half diethyl ether molecule. The two PF_6 anions are located in three positions with a ratio 1:0.5:0.5. The two half PF_6 anions are shared with neighboring symmetry equivalent units. The sodium cation is coordinated to two of the PF_6 anions forming a two dimensional chain. One of the PF_6 anions is disordered in three rotated orientations with a ratio of 55:30:15. The half diethyl ether molecule is disordered in two orientations also shared with a neighboring symmetry equivalent unit.

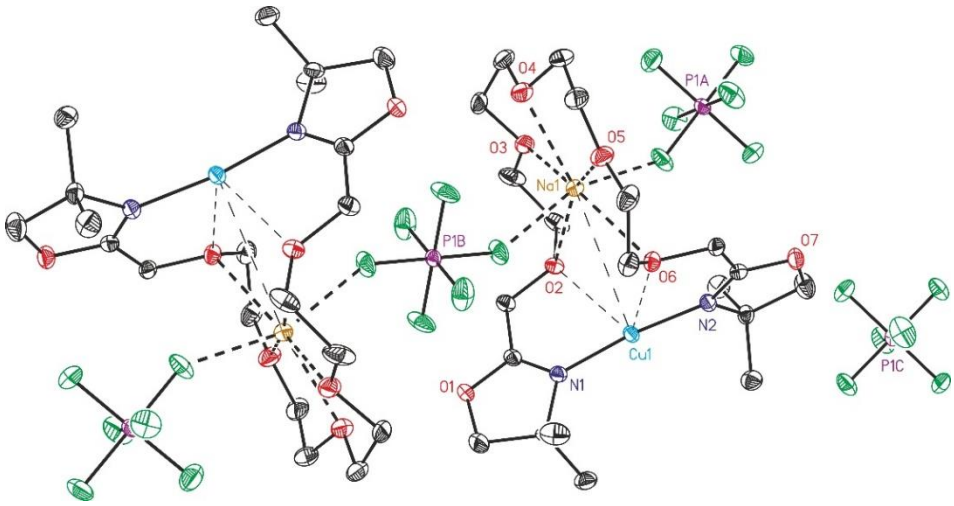

Figure 33. ORTEP drawing (thermal ellipsoids drawn at a 50% probability level) showing the structure of [Cu(NaPF$_6$•**L1**)]PF$_6$. Hydrogen atoms have been omitted for clarity. Color scheme: C: black, O: red, N: dark blue, Na: light brown, Cu: light blue, F: green, P: purple.

Table 8. Crystal data and structural parameters for complex [Cu(NaPF$_6$•**L1**)]PF$_6$.

Compound	[Cu(NaPF$_6$•**L1**)]PF$_6$
Formula	$C_{44}H_{82}ClCu_2F_{24}N_4Na_2O_{15}P_4$
Solvent	CH_2Cl_2
Formula weight	1660.07
Crystal size (mm^3)	0.10 x 0.05 x 0.05
Temperature (K)	100(2)
Wavelength (Å)	0.71073
Crystal system	Monoclinic
Space group	P2(1)/n
a (Å)	10.5906(5)
b (Å)	25.0689(13)
c (Å)	12.4435(6)
α (º)	90
β (º)	92.9669(17)
γ (º)	90
Volume (Å^3)	3299.3(3)
Z	2
ρ (g·cm^{-3})	1.671
μ (mm^{-1})	0.885
θ_{max} (º)	30.191
Reflections collected	33599
Independent reflections	8553[R(int) = 0.0439]
Absorption correction	Multi-Scan
Data / restraints /Parameters	8553/ 238/ 526
R1/wR2 [I>2σ(I)]	0.0424/0.0911
R1/wR2 (all data)	0.0608/0.0976
Goodness-of-fit (F^2)	1.049
Peak/hole (e/Å^{-3})	0.909/−0.334

Table 9. Selected bond length (Å) for complex [Cu($NaPF_6$•**L1**)]PF_6.

Entry	Atoms	Length (Å)	Entry	Atoms	Length (Å)
1	Cu1-N1	1.8674(18)	6	Na1-O5	2.3464(19)
2	Cu1-N2	1.8764(18)	7	Na1-O3	2.3567(19)
3	Cu1-Na1	3.5807(9)	8	Na1-O4	2.4798(19)
4	Na1-F1B	2.2828(16)	9	Na1-O6	2.6020(18)
5	Na1-F2A	2.3198(16)	10	Na1-O2	2.7857(18)

Table 10. Selected bond angles (°) for complex [Cu($NaPF_6$•**L1**)]PF_6.

Entry	Atoms	Angles (°)	Entry	Atoms	Angles (°)
1	N1-Cu1-N2	172.19(8)	48	N1-Cu1-N2	172.19(8)
2	N1-Cu1-Na1	97.00(6)	49	N1-Cu1-Na1	97.00(6)
3	N2-Cu1-Na1	90.48(6)	50	N2-Cu1-Na1	90.48(6)
25	F1B-Na1-Cu1	76.15(4)	72	F1B-Na1-Cu1	76.15(4)
26	F2A-Na1-Cu1	81.82(4)	73	F2A-Na1-Cu1	81.82(4)
27	O5-Na1-Cu1	111.25(5)	74	O5-Na1-Cu1	111.25(5)
28	O3-Na1-Cu1	113.78(5)	75	O3-Na1-Cu1	113.78(5)
29	O4-Na1-Cu1	171.01(5)	76	O4-Na1-Cu1	171.01(5)
30	O6-Na1-Cu1	46.48(4)	77	O6-Na1-Cu1	46.48(4)
31	O2-Na1-Cu1	47.27(4)	78	O2-Na1-Cu1	47.27(4)
32	C3-N1-Cu1	125.32(16)	79	C3-N1-Cu1	125.32(16)
33	C1-N1-Cu1	126.49(15)	80	C1-N1-Cu1	126.49(15)
34	C14-N2-Cu1	126.84(16)	81	C14-N2-Cu1	126.84(16)
35	C16-N2-Cu1	124.60(15)	82	C16-N2-Cu1	124.60(15)

Table 11. Selected torsion angles (°) for complex [Cu($NaPF_6$•**L1**)]PF_6.

Entry	Atoms	Torsion Angles (°)	Entry	Atoms	Torsion Angles (°)
1	Na1-Cu1-N1-C3	53.02(19)	4	Na1-Cu1-N2-C16	−133.78(17)
2	Na1-Cu1-N1-C1	−133.50(17)	5	Cu1-N1-C1-C17	62.0(2)
3	Na1-Cu1-N2-C14	52.6(2)	6	Cu1-N1-C1-C18	−60.3(2)

Table 11 cont.

Entry	Atoms	Torsion Angles (°)	Entry	Atoms	Torsion Angles (°)
7	Cu1-N1-C1-C2	−178.78(16)	11	Cu1-N2-C14-C13	−7.3(3)
8	Cu1-N1-C3-O1	175.04(15)	12	Cu1-N2-C16-C19	68.1(2)
9	Cu1-N1-C3-C4	−4.3(3)	13	Cu1-N2-C16-C20	−53.8(2)
10	Cu1-N2-C14-O7	172.40(15)	14	Cu1-N2-C16-C15	−172.52(16)

Comments to the structure of [Cu(NaPF$_6$•L2)]PF$_6$: The asymmetric unit contains one molecule of the metal complex (Cu and Na) and two PF_6 anions. The atoms belonging to the ether part with the free oxygen atom (not coordinated to the sodium atom) are disordered in two orientations with an occupancy of 67:33.

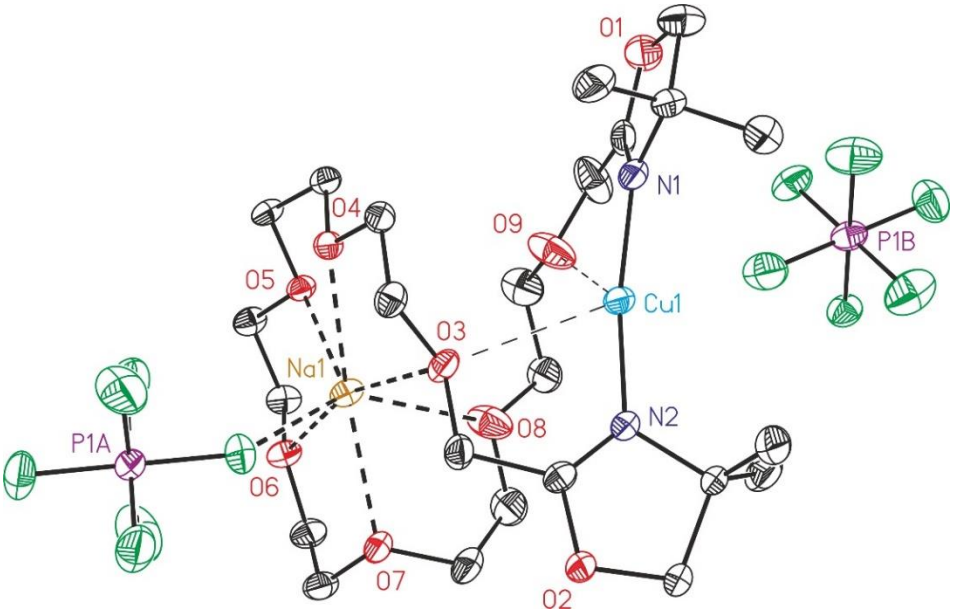

Figure 34. ORTEP drawing (thermal ellipsoids drawn at a 50% probability level) showing the structure of [Cu(NaPF$_6$•**L2**)]PF$_6$. Hydrogen atoms have been omitted for clarity. Color scheme: C: black, O: red, N: dark blue, Na: light brown, Cu: light blue, F: green, P: purple.

Table 12. Crystal data and structural parameters for complex [Cu(NaPF$_6$•**L2**)]PF$_6$.

Compound	[Cu(NaPF$_6$•**L2**)]PF$_6$
Formula	$C_{24}H_{44}CuF_{12}N_2NaO_9P_2$
Solvent	CH_2Cl_2
Formula weight	881.08
Crystal size (mm^3)	0.20 x 0.10 x 0.05
Temperature (K)	100(2)
Wavelength (Å)	0.71073
Crystal system	Triclinic
Space group	P−1
a (Å)	11.2430(9)
b (Å)	12.5262(10)
c (Å)	14.6345(10)
α (º)	64.708(2)
β (º)	87.283(2)
γ (º)	73.184(2)
Volume (Å^3)	1776.8(2)
Z	2
ρ (g·cm^{-3})	1.647
μ (mm^{-1})	0.829
θ_{max} (º)	28.353
Reflections collected	16935
Independent reflections	8406 [R(int) = 0.0579]
Absorption correction	Multi-Scan
Data / restraints /Parameters	8406/ 111/ 492
R1/wR2 [I>2σ(I)]	0.0500/0.1226
R1/wR2 (all data)	0.0736/0.1377
Goodness-of-fit (F^2)	1.021
Peak/hole (e/Å^{-3})	0.941 /−0.804

Table 13. Selected bond lengths (Å) for complex [Cu($NaPF_6$•**L2**)]PF_6.

Entry	Atoms	Length (Å)	Entry	Atoms	Length (Å)
1	Cu1A-N2A	1.882(2)	6	Na1A-O7A	2.455(2)
2	Cu1A-N1A	1.885(2)	7	Na1A-O6A	2.457(2)
3	Cu1A-O9'	2.405(10)	8	Na1A-O5A	2.473(2)
4	Na1A-F1B	2.378(2)	9	Na1A-O8A	2.538(3)
5	Na1A-O4A	2.453(2)	10	Na1A-O3A	2.653(2)

Table 14. Selected bond angles (°) for complex [Cu($NaPF_6$•**L2**)]PF_6.

Entry	Atoms	Angles (°)	Entry	Atoms	Angles (°)
1	N2A-Cu1A-N1A	167.56(11)	6	C10A-N2A-Cu1A	127.1(2)
2	N2A-Cu1A-O9'	114.6(2)	7	C6A-N2A-Cu1A	124.32(18)
3	N1A-Cu1A-O9'	75.9(2)	8	C23'-O9'-Cu1A	127.8(8)
4	C1A-N1A-Cu1A	124.4(2)	9	C25A-O9'-Cu1A	108.0(5)
5	C3A-N1A-Cu1A	127.25(19)			

Table 15. Selected torsion angles (°) for complex [Cu($NaPF_6$•**L2**)]PF_6.

Entry	Atoms	Torsion Angles (°)	Entry	Atoms	Torsion Angles (°)
1	N2A-Cu1A-N1A-C1A	146.0(4)	32	Cu1A-O9'-C23'-C22'	110.0(10)
2	O9'-Cu1A-N1A-C1A	−3.3(3)	33	Cu1A-O9'-C25A-C1A	1.4(6)
3	N2A-Cu1A-N1A-C3A	−26.8(6)	38	N2A-Cu1A-N1A-C1A	146.0(4)
4	O9'-Cu1A-N1A-C3A	−176.0(4)	39	O9'-Cu1A-N1A-C1A	−3.3(3)
5	N1A-Cu1A-N2A-C10A	121.0(5)	40	N2A-Cu1A-N1A-C3A	−26.8(6)
6	O9'-Cu1A-N2A-C10A	−92.0(4)	41	O9'-Cu1A-N1A-C3A	−176.0(4)
7	N1A-Cu1A-N2A-C6A	−45.9(6)	42	N1A-Cu1A-N2A-C10A	121.0(5)
8	O9'-Cu1A-N2A-C6A	101.1(4)	43	O9'-Cu1A-N2A-C10A	−92.0(4)
9	Cu1A-N1A-C1A-O1A	−173.4(2)	44	N1A-Cu1A-N2A-C6A	−45.9(6)
10	Cu1A-N1A-C1A-C25A	6.0(5)	45	O9'-Cu1A-N2A-C6A	101.1(4)
11	Cu1A-N1A-C3A-C4A	50.8(3)	16	Cu1A-N2A-C6A-C9A	−177.11(18)
12	Cu1A-N1A-C3A-C5A	−71.7(3)	17	Cu1A-N2A-C10A-O2A	−173.10(19)
13	Cu1A-N1A-C3A-C2A	169.1(2)	18	Cu1A-N2A-C10A-C11A	7.0(4)
14	Cu1A-N2A-C6A-C7A	−58.3(3)	69	Cu1A-O9'-C23'-C22'	110.0(10)

CCDC 1900983-1900985 contain the supplementary crystallographic data for this section of the thesis. These data can be obtained free of charge from "The Cambridge Crystallographic Data Centre" *via* www.ccdc.cam.ac.uk/data_request/cif.

1.5.9. Synthesis of substrates 131g, 131h, 131i, 132a and 132b

1.5.9.1. Synthesis of 1-phenylcyclopropan-1-ol, 131g

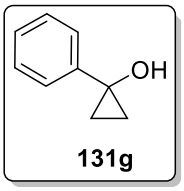

The preparation of **131g** was performed adapting a reported procedure.[20] In a flame-dried Schlenk under inert atmosphere, MeMgBr (3 M in Et_2O, 10.0 mL, 30.00 mmol) was added dropwise to a solution of titanium isopropoxide (6.1 mL, 20.00 mmol) in anhydrous Et_2O (20.0 mL). The resulting yellow solution was cooled to 0 ºC and a solution of methyl benzoate (2.6 mL, 20.00 mmol) in Et_2O (20.0 mL) was then added. A second fraction of EtMgBr (3 M in Et_2O, 10.0 mL, 30.00 mmol) was then added dropwise and the resulting reaction mixture was allowed to warm to room temperature and then stirred for an additional hour. The reaction was quenched at 0 ºC by careful addition of an ice-cooled 10% H_2SO_4 solution (80.0 mL), and extracted with Et_2O (3 x 20.0 mL). The combined organic layers were washed with saturated $NaHCO_3$ solution (60.0 mL), brine (60.0 mL) and dried ($MgSO_4$). After removal of the solvent under reduced pressure and purification on silica gel column chromatography using Cy/EtOAc (10:1) as the eluent, **131g** was isolated as a colorless oil (1.3 g, 50% yield). Spectroscopic data were in agreement with those previously reported.[20] ^{1}H NMR (500 MHz, $CDCl_3$) δ: 7.36 - 7.30 (m, 4H), 7.25 - 7.22 (m, 1H), 2.44 (broad signal, 1H), 1.28 - 1.25 (m, 2H) and 1.06 - 1.04 (m, 2H) ppm; $^{13}C\{^1H\}$ NMR (101 MHz, $CDCl_3$) δ: 144.4 (C), 128.5 (CH), 126.5 (CH), 124.5 (CH), 56.8 (C) and 18.0 (CH_2) ppm.

1.5.9.2. Synthesis of 1-phenylcyclobutan-1-ol, 131h

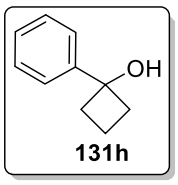

The preparation of **131h** was performed adapting a reported procedure.[20] In a flame-dried Schlenk under inert atmosphere, a solution of cyclobutanone (0.9 mL, 12.20 mmol) in dry THF (25.0 mL) was cooled to 0 ºC. C_6H_5MgBr (2.8 M in Et_2O, 4.8 mL, 13.40 mmol) was added dropwise with stirring at the

same temperature. The mixture was allowed to warm to room temperature, stirred for 12 hours and quenched with a sat. NH_4Cl solution (25.0 mL). The aqueous layer was extracted with EtOAc (3 x 40.0 mL). The combined organic layers were dried over anhydrous Na_2SO_4, filtered, and concentrated under reduced pressure. The crude mixture was purified by silica gel column chromatography using Cy/EtOAc (10:1) as the eluent to yield **131h** as yellow solid (852.2 mg, 46% yield). Spectroscopic data were in agreement with those previously reported.[20] ^1H NMR (500 MHz, $CDCl_3$) δ: 7.53 - 7.49 (m, 2H), 7.40 - 7.37 (m, 2H), 7.30 - 7.27 (m, 1H), 2.61 - 2.55 (m, 2H), 2.41 - 2.35 (m, 2H), 2.06 - 2.02 (m, 2H) and 1.73 - 1.67 (m, 1H) ppm; $^{13}C\{^1H\}$ NMR (101 MHz, $CDCl_3$) δ: 146.4 (C), 128.6 (CH), 127.4 (CH), 125.1 (CH), 77.4 (C) 37.0 (CH_2) and 13.1 (CH_2) ppm.

1.5.9.3. Synthesis of 1-phenylcyclopentan-1-ol, 131i

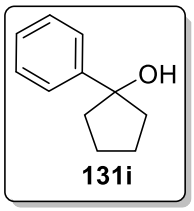

131i

The preparation of **131i** was performed adapting a reported procedure.[20] In a flame-dried Schlenk under inert atmosphere, a solution of cyclopentanone (1.3 mL, 14.50 mmol) in dry THF (25.0 mL) was cooled to 0 ºC. C_6H_5MgBr (2.8 M in Et_2O, 10.4 mL, 29.10 mmol) was added dropwise with stirring at the same temperature. The mixture was allowed to warm to room temperature, stirred for 12 hours and quenched with a sat. NH_4Cl solution (25.0 mL). The aqueous layer was extracted with EtOAc (3 x 40.0 mL). The combined organic layers were dried over anhydrous Na_2SO_4, filtered, and concentrated under reduced pressure. The crude mixture was purified by silica gel column chromatography using Cy/EtOAc (10:1) as the eluent to yield **131i** as yellow oil (1.3 g, 55% yield). Spectroscopic data were in agreement with those previously reported.[20] ^1H NMR (500 MHz, $CDCl_3$) δ: 7.52 - 7.50 (m, 2H), 7.37 - 7.34 (m, 2H), 7.30 - 7.26 (m, 1H), 2.02 - 1.98 (m, 6H), 1.91 - 1.84 (m, 2H) and 1.58 (broad signal, 1H) ppm; $^{13}C\{^1H\}$ NMR (126 MHz, $CDCl_3$) δ: 147.2 (C), 128.4 (CH), 126.9 (CH), 125.2 (CH), 83.6 (C), 42.0 (CH_2) and 24.0 (CH_2) ppm.

1.5.9.4. Synthesis of phenyl diazoacetate (PhEDA), 132a

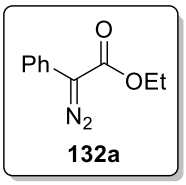

132a

The preparation of **132a** was performed adapting a reported procedure.[17] A solution of 1,8-diazabicyclo[5.4.0]undec-7-ene (DBU, 1.2 g, 7.78 mmol) in dry CH_3CN (20.0 mL) was added dropwise at 0 ºC to a solution of methyl 2-phenylacetoacetate (1.1 g, 5.19 mmol) and *p*-acetamidobenzenesulfonylazide (*p*-ABSA, 1.9 g, 7.78 mmol) in dry CH_3CN (50.0 mL). The mixture was then stirred at 0 ºC for 1 hour, allowed to reach room temperature and then stirred for 8 hours. The reaction was quenched by addition of water (50.0 mL) and Et_2O (100.0 mL). The two layers were separated and the aqueous layer was extracted with Et_2O (2 x 50.0 mL). The combined organic layers were dried over $MgSO_4$, filtered and concentrated *in vacuo*. The product was purified by silica gel column chromatography using Cy/EtOAc (30:1) as the eluent to yield **132a** as an orange oil (560.4 mg, 57% yield). Spectroscopic data were in agreement with those previously reported.[17] ^{1}H NMR (400 MHz, $CDCl_3$) δ: 7.50 - 7.48 (m, 2H), 7.41 - 7.36 (m, 2H), 7.20 - 7.16 (m, 1H), 4.34 (q, *J* = 7.1 Hz, 2H) and 1.35 (t, *J* = 7.1 Hz, 3H) ppm; $^{13}C\{^1H\}$ NMR (101 MHz, $CDCl_3$) δ: 165.4 (C), 129.1 (C), 125.9 (CH), 125.8 (CH), 124.1 (CH), 63.4 (C), 61.1 (CH_2) and 14.6 (CH_3) ppm.

1.5.9.5. Synthesis of methyl diazoacetate (MeEDA), 132b

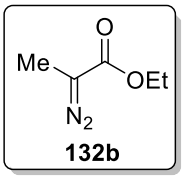

132b

The preparation of **132b** was performed adapting a reported procedure.[17] A solution of DBU (1.7 g, 11.30 mmol) in dry CH_3CN (20.0 mL) was added dropwise at 0 ºC to a solution of 2-methyl-3-oxo-butyric acid ethyl ester (1.1 g, 7.50 mmol) and *p*-ABSA (2.8 g, 11.30 mmol) in dry CH_3CN (20.0 mL). Then, the reaction mixture was stirred at 0 ºC for 1 hour, allowed to reach room temperature and then stirred for 8 hours. The reaction was quenched by addition of water (25.0 mL) and Et_2O (50.0 mL). The two layers were separated and the aqueous layer was extracted with Et_2O (2 x 25.0 mL). The combined organic layers were dried over $MgSO_4$, filtered and concentrated *in vacuo*. The product was purified by silica gel column chromatography using pentane/Et_2O (20:1) as the eluent to yield **132b** as a yellowish liquid (379.0 mg, 40% yield). Spectroscopic data were in agreement with those previously reported.[17,33] ^{1}H NMR (400 MHz, $CDCl_3$) δ: 4.20 (q, *J* = 7.1 Hz, 2H), 1.95 (s, 3H) and 1.26

[33] Keipour, H.; Ollevier, T. *Org. Lett.* **2017**, *19*, 5736-5739.

(t, J = 7.1 Hz, 3H) ppm; $^{13}C\{^{1}H\}$ NMR (101 MHz, $CDCl_3$) δ: 168.1 (C), 62.8 (C), 60.9 (CH_2), 14.6 (CH_3) and 8.5 (CH_3) ppm.

1.5.10. General procedure for the Cu-catalyzed insertion of carbenoid species into hydroxyl bonds and characterization of the resulting insertion products 133

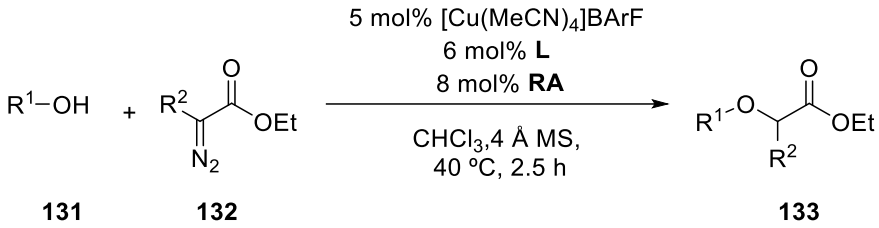

Scheme 43. General procedure for the catalyzed insertion of copper-carbenoids into O–H bonds.

In a flame-dried Schlenk under inert atmosphere, a solution of the corresponding BArF salt[13] (0.02 mmol) was prepared in dry and deoxygenated $CHCl_3$ (0.5 mL). A solution of ligand (0.01 mmol) in $CHCl_3$ (0.5 mL) was added to the previous solution and the mixture was stirred for 5 min at room temperature. This mixture was then added dropwise to a solution of $[Cu(MeCN)_4]BArF$ (0.01 mmol) in $CHCl_3$ (0.5 mL) and, subsequently, 770.0 mg of 4 Å molecular sieves (powder) were added. After stirring for 5 min at room temperature, a solution of substrate **131** (1.0 mmol) in $CHCl_3$ (0.5 mL) was added dropwise and the mixture was stirred for another 5 minutes. Then, the corresponding diazoderivative **132** (0.20 mmol) was added dropwise (an intense bubbling was observed due to N_2 release) and the resulting mixture was stirred for 2.5 h at 40 ºC. After the stated time, the crude mixture was filtered, the residue was washed with 1.0 mL of $CHCl_3$ and the combined organic solutions were evaporated *in vacuo*. The resulting mixture was analyzed by ^{1}H NMR using 1,3,5-trimethoxybenzene as internal standard to quantify the amount of O–H insertion product.[34] For the best catalytic result for a given substrate **131** and diazoderivative **132**, the residue after evaporating the organic solvent was purified by silica gel column chromatography using Cy/EtOAc

[34] The *para*-C–H insertion product **136** was formed in low amounts when **L2** was used as the ligand and was identified according to previous reports in the literature. See: (a) Yu, Z.; Ma, B.; Chen, M.; Wu, H.-H.; Liu, L.; Zhang, J. *J. Am. Chem. Soc.* **2014**, *136*, 6904-6907. (b) Xi, Y.; Su, Y.; Yu, Z.; Dong, B.; McClain, E. J.; Lan, Y.; Shi, X. *Angew. Chem., Int. Ed.* **2014**, *53*, 9817-9821.

(98:2) as the eluent, unless otherwise stated. The target product was obtained as a yellowish oil.

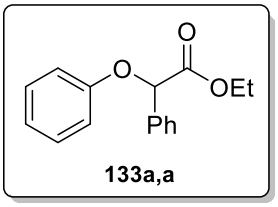

133a,a

Compound 133a,a: This compound was synthesized following the general procedure indicated at the beginning of this section from phenol **131a** (94.0 mg, 1.00 mmol) and diazo compound **132a** (35 μL, 0.20 mmol) as substrates, using [Cu(MeCN)$_4$]BArF (11.4 mg, 0.01 mmol), **L1** (5.0 mg, 0.01 mmol) and RbBArF (15.2 mg, 0.02 mmol) to generate *in situ* the supramolecular catalyst. After purification by silica gel column chromatography, product **133a,a** was obtained as a yellowish oil (46.1 mg, 81% yield). Spectroscopic data were in agreement with those previously reported.[35] ^{1}H NMR (400 MHz, $CDCl_3$) δ: 7.60 - 7.58 (m, 2H), 7.43 - 7.34 (m, 3H), 7.29 - 7.25 (m, 2H), 7.00 - 6.95 (m, 3H), 5.63 (s, 1H), 4.27 - 4.13 (m, 2H) and 1.21 (t, J = 7.1 Hz, 3H) ppm; ^{13}C{^{1}H} NMR (101 MHz, $CDCl_3$) δ: 170.1 (C), 157.5 (C), 135.7 (C), 129.7 (CH), 129.0 (CH), 128.9 (CH), 127.2 (CH), 121.9 (CH), 115.6 (CH), 78.8 (CH), 61.7 (CH_2) and 14.2 (CH_3) ppm.

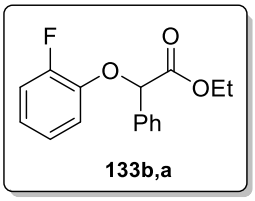

133b,a

Compound 133b,a: This compound was synthesized following the general procedure indicated at the beginning of this section from 2-fluorophenol **131b** (112.0 mg, 1.00 mmol) and diazo compound **132a** (35 μL, 0.20 mmol) as substrates, using [Cu(MeCN)$_4$]BArF (11.4 mg, 0.01 mmol), **L1** (5.0 mg, 0.01 mmol) and RbBArF (15.2 mg, 0.02 mmol) to generate *in situ* the supramolecular catalyst. After purification by silica gel column chromatography, product **133b,a** was obtained as a yellowish oil (30.3 mg, 55% yield). ^{1}H NMR (400 MHz, $CDCl_3$) δ: 7.60 - 7.58 (m, 2H), 7.42 - 7.36 (m, 3H), 7.12 - 7.07 (m, 1H), 7.00 - 6.94 (m, 3H), 5.65 (s, 1H), 4.25 - 4.16 (m, 2H) and 1.20 (t, J = 7.1 Hz, 3H) ppm; ^{13}C{^{1}H} NMR (101 MHz, $CDCl_3$) δ: 169.7 (C), 153.5 (d, $^1J_{C–F}$ = 246.9 Hz, C), 145.4 (d, $^2J_{C–F}$ = 10.3 Hz, C), 135.3 (C), 129.2 (CH), 128.9 (CH), 127.3 (CH), 124.4 (d, $^3J_{C–F}$ = 4.1 Hz, CH), 123.0 (d, $^3J_{C–F}$ = 7.1 Hz, CH), 117.9 (d, $^4J_{C–F}$ = 1.3 Hz, CH), 116.8 (d, $^2J_{C–F}$ = 18.6 Hz, CH), 80.3 (CH), 61.8 (CH_2) and 14.1 (CH_3) ppm; ^{19}F{^{1}H} NMR (376 MHz, $CDCl_3$) δ: −132.2 ppm; IR (neat): 3069, 2989, 2925. 2853, 1734, 1613, 1592, 1506,

[35] Berglund, P.; Vallikivi, I.; Fransson, L.; Dannacher, H.; Holmquist, M.; Martinelle, M.; Bjorkling, F.; Parve, O.; Hult, K. *Tetrahedron: Asymmetry* **1999**, *10*, 4191-4202.

1258, 1212, 1178, 1110, 1055, 1019 and 752 cm^{-1}. HRMS (ESI) *m/z*: calcd for $C_{16}H_{15}FO_3Na$ $[M+Na]^+$ 297.0897, found 297.0887.

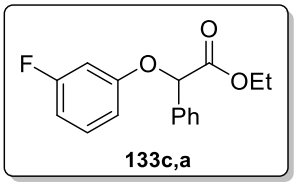

133c,a

Compound 133c,a: This compound was synthesized following the general procedure indicated at the beginning of this section from 3-fluorophenol **131c** (114.0 mg, 1.00 mmol) and diazo compound **132a** (35 µL, 0.20 mmol) as substrates, using $[Cu(MeCN)_4]BArF$ (11.4 mg, 0.01 mmol), **L1** (5.0 mg, 0.01 mmol) and CsBArF (15.9 mg, 0.02 mmol) to generate *in situ* the supramolecular catalyst. After purification by silica gel column chromatography, product **133c,a** was obtained as a yellowish oil (35.0 mg, 64% yield). ^1H NMR (500 MHz, $CDCl_3$) δ: 7.58 - 7.57 (m, 2H), 7.43 - 7.36 (m, 3H), 7.24 - 7.19 (m, 1H), 6.75 - 6.68 (m, 3H), 5.60 (s, 1H), 4.27 - 4.15 (m, 2H) and 1.21 (t, *J* = 7.1 Hz, 3H) ppm; $^{13}C\{^1H\}$ NMR (126 MHz, $CDCl_3$) δ: 169.6 (C), 163.6 (d, $^1J_{C-F}$ = 245.9 Hz, C), 158.7 (d, $^3J_{C-F}$ = 10.6 Hz, C), 135.2 (C), 130.4 (d, $^3J_{C-F}$ = 10.2 Hz, CH), 129.2 (CH), 129.0 (CH), 127.2 (CH), 111.2 (d, $^4J_{C-F}$ = 2.7 Hz, CH), 108.8 (d, $^2J_{C-F}$ = 21.7 Hz, CH), 103.6 (d, $^2J_{C-F}$ = 24.9 Hz, CH), 79.0 (CH), 61.9 (CH_2) and 14.1 (CH_3) ppm; $^{19}F\{^1H\}$ NMR (376 MHz, $CDCl_3$) δ: −111.3 ppm; IR (neat): 2982, 1751, 1610, 1594, 1488, 1261, 1182, 1165, 1134, 1024 and 695 cm^{-1}; HRMS (ESI) *m/z*: calcd for $C_{16}H_{15}FO_3Na$ $[M+Na]^+$ 297.0897, found 297.0890.

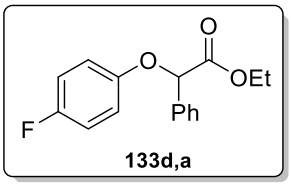

133d,a

Compound 133d,a: This compound was synthesized following the general procedure indicated at the beginning of this section from 4-fluorophenol **131d** (112.0 mg, 1.00 mmol) and diazo compound **132a** (35 µL, 0.20 mmol) as substrates, using $[Cu(MeCN)_4]BArF$ (11.4 mg, 0.01 mmol), **L1** (5.0 mg, 0.01 mmol) and NaBArF (14.2 mg, 0.02 mmol) to generate *in situ* the supramolecular catalyst. After purification by silica gel column chromatography, product **133d,a** was obtained as a yellowish oil (43.7 mg, 80% yield). ^1H NMR (500 MHz, $CDCl_3$) δ: 7.58 - 7.56 (m, 2H), 7.42 - 7.35 (m, 3H), 6.97 - 6.89 (m, 4H), 5.55 (s, 1H), 4.24 - 4.16 (m, 2H) and 1.21 (t, *J* = 7.1 Hz, 3H) ppm; $^{13}C\{^1H\}$ NMR (126 MHz, $CDCl_3$) δ: 170.0 (C), 158.0 (d, $^1J_{C-F}$ = 239.6 Hz, C), 153.7 (d, $^4J_{C-F}$ = 1.8 Hz, C), 135.6 (C), 129.2 (CH), 129.0 (CH), 127.3 (CH), 117.1 (d, $^3J_{C-F}$ = 7.9 Hz, CH), 116.2 (d, $^2J_{C-F}$ = 23.1 Hz, CH), 79.7 (CH), 61.9 (CH_2) and 14.2 (CH_3) ppm; $^{19}F\{^1H\}$ NMR (376 MHz, $CDCl_3$) δ:

−122.5 ppm; IR (neat): 3072, 2996, 2963, 1736, 1504, 1186, 1153, 1091, 1061, 830 and 728 cm^{-1}; HRMS (ESI) *m/z*: calcd for $C_{16}H_{15}FO_3Na$ $[M+Na]^+$ 297.0897, found 297.0897.

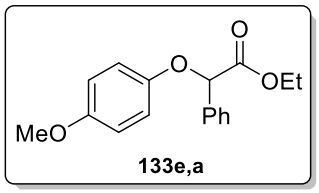

133e,a

Compound 133e,a: This compound was synthesized following the general procedure indicated at the beginning of this section from 4-methoxyphenol **131e** (124.0 mg, 1.00 mmol) and diazo compound **132a** (35 μL, 0.20 mmol) as substrates, using $[Cu(MeCN)_4]BArF$ (11.4 mg, 0.01 mmol), **L1** (5.0 mg, 0.01 mmol) and NaBArF (14.2 mg, 0.02 mmol) to generate *in situ* the supramolecular catalyst. After purification by silica gel column chromatography, product **133e,a** was obtained as a yellowish oil (52.0 mg, 91% yield). Spectroscopic data were in agreement with those previously reported.[36] ^1H NMR (500 MHz, $CDCl_3$) δ: 7.58 - 7.56 (m, 2H), 7.41 - 7.34 (m, 3H), 6.92 - 6.89 (m, 2H), 6.82 - 6.79 (m, 2H), 5.54 (s, 1H), 4.25 - 4.15 (m, 2H), 3.75 (s, 3H) and 1.21 (t, *J* = 7.1 Hz, 3H) ppm; $^{13}C\{^1H\}$ NMR (126 MHz, $CDCl_3$) δ: 170.3 (C), 154.8 (C), 151.7 (C), 136.0 (C), 129.1 (CH), 128.9 (CH), 127.3 (CH), 117.1 (CH), 114.9 (CH), 80.0 (CH), 61.8 (CH_2), 55.9 (CH_3) and 14.3 (CH_3) ppm.

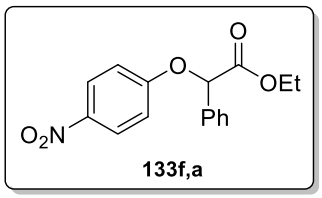

133f,a

Compound 133f,a: This compound was synthesized following the general procedure indicated at the beginning of this section from 4-nitrophenol **131f** (139.0 mg, 1.00 mmol) and diazo compound **132a** (35 μL, 0.20 mmol) as substrates, using $[Cu(MeCN)_4]BArF$ (11.4 mg, 0.01 mmol) and **L1** (5.0 mg, 0.01 mmol) to generate *in situ* the supramolecular catalyst. After purification by silica gel column chromatography using a mixture of Cy/EtOAc that ranged from 98:2 to 90:10 (v/v), product **133f,a** was obtained as a yellowish oil (23.1 mg, 38% yield). ^1H NMR (400 MHz, $CDCl_3$) δ: 8.20 - 8.18 (m, 2H), 7.58 - 7.56 (m, 2H), 7.43 - 7.41 (m, 3H), 7.04 - 7.00 (m, 2H), 5.70 (s, 1H), 4.29 - 4.15 (m, 2H) and 1.22 (t, *J* = 7.1 Hz, 3H) ppm; $^{13}C\{^1H\}$ NMR (101 MHz, $CDCl_3$) δ: 168.8 (C), 162.2 (C), 142.4 (C), 134.3 (C), 129.6 (CH), 129.1 (CH), 127.2 (CH), 126.0 (CH), 115.5 (CH), 79.0 (CH), 62.2 (CH_2) and 14.1 (CH_3) ppm; IR (neat): 2983, 1748, 1591, 1513, 1493, 1455, 1370, 1341,

[36] Miller, E. J.; Zhao, W.; Herr, J. D.; Radosevich, A. T. *Angew. Chem., Int. Ed.* **2012**, *51*, 10605-10609.

1299, 1247, 1183, 1111, 1051, 913, 843, 751, 729, 695 and 663 cm^{-1}; HRMS (ESI) *m/z*: calcd for $C_{16}H_{15}NO_5Na$ $[M+Na]^+$ 324.0842, found 324.0840.

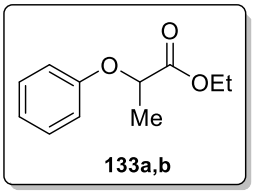

133a,b

Compound 133a,b: This compound was synthesized following the general procedure indicated at the beginning of this section from phenol **131a** (94.0 mg, 1.00 mmol) and diazo compound **132b** (25.6 mg, 0.20 mmol) as substrates, using $[Cu(MeCN)_4]BArF$ (11.4 mg, 0.01 mmol), **L1** (5.0 mg, 0.01 mmol) and KBArF (14.4 mg, 0.02 mmol) to generate *in situ* the supramolecular catalyst. After purification by silica gel column chromatography, product **133a,b** was obtained as a yellowish oil (29.2 mg, 75% yield). Spectroscopic data were in agreement with those previously reported.[7a] ^1H NMR (500 MHz, $CDCl_3$) δ: 7.26 - 7.22 (m, 2H), 6.96 - 6.92 (m, 1H), 6.86 - 6.84 (m, 2H), 4.72 (q, *J* = 6.8 Hz, 1H), 4.19 (q, *J* = 7.1 Hz, 2H), 1.59 (d, *J* = 6.8 Hz, 3H) and 1.22 (t, *J* = 7.1 Hz, 3H) ppm; $^{13}C\{^1H\}$ NMR (126 MHz, $CDCl_3$) δ: 172.4 (C), 157.7 (C), 129.7 (CH), 121.7 (CH), 115.2 (CH), 72.8 (CH), 61.4 (CH_2), 18.7 (CH_3) and 14.3 (CH_3) ppm.

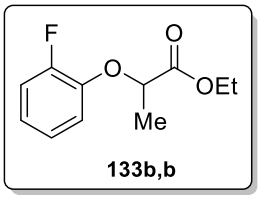

133b,b

Compound 133b,b: This compound was synthesized following the general procedure indicated at the beginning of this section from 2-fluorophenol **131b** (112.0 mg, 1.00 mmol) and diazo compound **132b** (25.6 mg, 0.20 mmol) as substrates, using $[Cu(MeCN)_4]BArF$ (11.4 mg, 0.01 mmol), **L1** (5.0 mg, 0.01 mmol) and NaBArF (14.2 mg, 0.02 mmol) to generate *in situ* the supramolecular catalyst. After purification by silica gel column chromatography, product **133b,b** was obtained as a yellowish oil (26.7 mg, 63% yield). ^1H NMR (400 MHz, $CDCl_3$) δ: 7.11 - 6.90 (m, 4H), 4.76 (q, *J* = 6.8 Hz, 1H), 4.27 - 4.18 (m, 2H), 1.65 (d, *J* = 6.8 Hz, 3H) and 1.25 (t, *J* = 7.1 Hz, 3H) ppm; $^{13}C\{^1H\}$ NMR (101 MHz, $CDCl_3$) δ: 171.8 (C), 153.3 (d, $^1J_{C-F}$ = 245.8 Hz, C), 145.7 (d, $^2J_{C-F}$ = 10.3 Hz, C), 124.3 (d, $^3J_{C-F}$ = 4.0 Hz, CH), 122.7 (d, $^3J_{C-F}$ = 6.5 Hz, CH), 117.5 (d, $^4J_{C-F}$ = 1.8 Hz, CH), 116.7 (d, $^2J_{C-F}$ = 18.9 Hz, CH), 74.7 (CH), 61.4 (CH_2), 18.7 (CH_3) and 14.2 (CH_3) ppm; $^{19}F\{^1H\}$ NMR (376 MHz, $CDCl_3$) δ: −132.9 ppm; IR (neat): 2987, 1750, 1504, 1257, 1191, 1132, 1095, 1049 and 744 cm^{-1}; HRMS (ESI) *m/z*: calcd for $C_{11}H_{13}FO_3Na$ $[M+Na]^+$ 235.0741, found 235.0737.

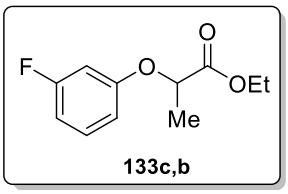

133c,b

Compound 133c,b: This compound was synthesized following the general procedure indicated at the beginning of this section from 3-fluorophenol **131c** (114.0 mg, 1.00 mmol) and diazo compound **132b** (25.6 mg, 0.20 mmol) as substrates, using $[Cu(MeCN)_4]BArF$ (11.4 mg, 0.01 mmol), **L1** (5.0 mg, 0.01 mmol) and NaBArF (14.2 mg, 0.02 mmol) to generate *in situ* the supramolecular catalyst. After purification by silica gel column chromatography, product **133c,b** was obtained as a yellowish oil (25.5 mg, 60% yield). ^{1}H NMR (400 MHz, $CDCl_3$) δ: 7.24 - 7.18 (m, 1H), 6.70 - 6.58 (m, 3H), 4.72 (q, *J* = 6.8 Hz, 1H), 4.22 (q, *J* = 7.1 Hz, 2H), 1.62 (d, *J* = 6.8 Hz, 3H) and 1.25 (t, *J* = 7.1 Hz, 3H) ppm; $^{13}C\{^1H\}$ NMR (101 MHz, $CDCl_3$) δ: 171.9 (C), 163.6 (d, $^1J_{C-F}$ = 245.8 Hz, C), 159.0 (d, $^3J_{C-F}$ = 10.9 Hz, C), 130.4 (d, $^3J_{C-F}$ = 9.9 Hz, CH), 110.8 (d, $^4J_{C-F}$ = 3.9 Hz, CH), 108.5 (d, $^2J_{C-F}$ = 21.9 Hz, CH), 103.2 (d, $^2J_{C-F}$ = 24.8 Hz, CH), 73.0 (CH), 61.5 (CH_2), 18.6 (CH_3) and 14.2 (CH_3) ppm; $^{19}F\{^1H\}$ NMR (376 MHz, $CDCl_3$) δ: −111.5 ppm; IR (neat): 2988, 1752, 1593, 1489, 1278, 1197, 1168, 1134, 1094, 1049, 978, 766 and 680 cm^{-1}; HRMS (ESI) *m/z*: calcd for $C_{11}H_{13}FO_3Na$ $[M+Na]^+$ 235.0741, found 235.0742.

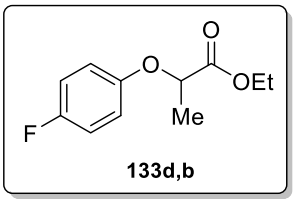

133d,b

Compound 133d,b: This compound was synthesized following the general procedure indicated at the beginning of this section from 4-fluorophenol **131d** (112.0 mg, 1.00 mmol) and diazo compound **132b** (25.6 mg, 0.20 mmol) as substrates, using $[Cu(MeCN)_4]BArF$ (11.4 mg, 0.01 mmol), **L1** (5.0 mg, 0.01 mmol) and NaBArF (14.2 mg, 0.02 mmol) to generate *in situ* the supramolecular catalyst. After purification by silica gel column chromatography, product **133d,b** was obtained as a yellowish oil (28.7 mg, 68% yield). ^{1}H NMR (400 MHz, $CDCl_3$) δ: 6.98 - 6.92 (m, 2H), 6.85 - 6.81 (m, 2H), 4.67 (q, *J* = 6.8 Hz, 1H), 4.21 (q, *J* = 7.1 Hz, 2H), 1.60 (d, *J* = 6.8 Hz, 3H) and 1.25 (t, *J* = 7.1 Hz, 3H) ppm; $^{13}C\{^1H\}$ NMR (101 MHz, $CDCl_3$) δ: 172.2 (C), 157.8 (d, $^1J_{C-F}$ = 239.6 Hz, C), 153.9 (d, $^4J_{C-F}$ = 2.3 Hz, C), 116.6 (d, $^3J_{C-F}$ = 8.0 Hz, CH), 116.1 (d, $^2J_{C-F}$ = 23.5 Hz, CH), 73.6 (CH), 61.4 (CH_2), 18.7 (CH_3) and 14.3 (CH_3) ppm; $^{19}F\{^1H\}$ NMR (376 MHz, CDCl3) δ: −122.9 ppm; IR (neat): 2987, 1750, 1503, 1196, 1132, 1095, 1050, 827 and 746 cm^{-1}; HRMS (ESI) *m/z*: calcd for $C_{11}H_{13}FO_3Na$ $[M+Na]^+$ 235.0741, found 235.0749.

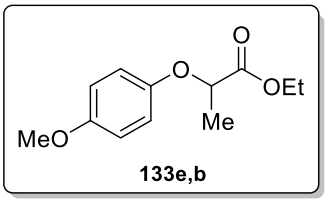

133e,b

Compound 133e,b: This compound was synthesized following the general procedure indicated at the beginning of this section from phenol **131e** (124.0 mg, 1.00 mmol) and diazo compound **132b** (25.6 mg, 0.20 mmol) as substrates, using [Cu(MeCN)$_4$]BArF (11.4 mg, 0.01 mmol), **L1** (5.0 mg, 0.01 mmol) and RbBArF (15.2 mg, 0.02 mmol) to generate *in situ* the supramolecular catalyst. After purification by silica gel column chromatography, product **133e,b** was obtained as yellowish oil (31.8 mg, 71% yield). Spectroscopic data were in agreement with those previously reported.[7a] ^{1}H NMR (400 MHz, $CDCl_3$) δ: 6.87 - 6.65 (m, 4H), 4.65 (q, *J* = 6.8 Hz, 1H), 4.21 (q, *J* = 7.2 Hz, 2H), 3.76 (s, 3H), 1.59 (d, *J* = 6.8 Hz, 3H) and 1.25 (t, *J* = 7.1 Hz, 3H) ppm; ^{13}C{^{1}H} NMR (101 MHz, $CDCl_3$) δ: 172.6 (C), 154.6 (C), 151.9 (C), 116.7 (CH), 116.2 (CH), 115.0 (CH), 114.8 (CH), 73.8 (CH), 61.3 (CH_2), 55.8 (CH_3), 18.8 (CH_3) and 14.3 (CH_3) ppm.

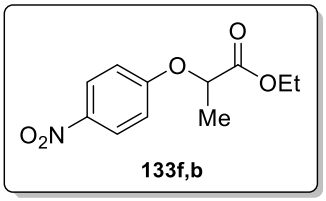

133f,b

Compound 133f,b: This compound was synthesized following the general procedure indicated at the beginning of this section from 4-nitrophenol **131f** (139.0 mg, 1.00 mmol) and diazo compound **132b** (25.6 mg, 0.20 mmol) as substrates, using [Cu(MeCN)$_4$]BArF (11.4 mg, 0.01 mmol), **L1** (5.0 mg, 0.01 mmol) and KBArF (14.9 mg, 0.02 mmol) to generate *in situ* the supramolecular catalyst. After purification by silica gel column chromatography using a mixture of Cy/EtOAc that ranged from 98:2 to 90:10 (v/v), product **133f,b** was obtained as a yellowish oil (13.8 mg, 29% yield). ^{1}H NMR (500 MHz, $CDCl_3$) δ: 8.21 - 8.15 (m, 2H), 6.94 - 6.91 (m, 2H), 4.84 (q, *J* = 6.8 Hz, 1H), 4.24 (q, *J* = 7.1 Hz, 2H), 1.67 (d, *J* = 6.8 Hz, 3H) and 1.26 (d, *J* = 7.1 Hz, 3H) ppm; ^{13}C{^{1}H} NMR (126 MHz, $CDCl_3$) δ: 171.1 (C), 162.7 (C), 142.2 (C), 126.1 (CH), 115.1 (CH), 73.1 (CH), 61.9 (CH_2), 18.5 (CH_3) and 14.3 (CH_3) ppm; IR (neat): 2919, 2850, 1745, 1592, 1513, 1494, 1342, 1257, 1198, 1094, 1048, 1016, 845, 751 and 654 cm^{-1}; HRMS (ESI) *m/z*: calcd for $C_{11}H_{13}NO_5Na$ $[M+Na]^+$ 262.0686, found 262.0688.

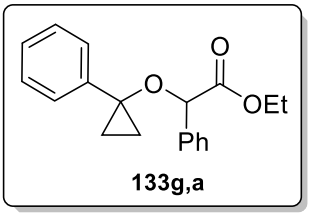

133g,a

Compound 133g,a: This compound was synthesized following the general procedure indicated at the beginning of this section from compound **131g** (134.0 mg, 1.00 mmol) and diazo compound **132a** (35 μL, 0.20 mmol) as substrates, using [Cu(MeCN)$_4$]BArF (11.4 mg, 0.01 mmol), **L1** (5.0 mg, 0.01 mmol) and NaBArF (14.2 mg, 0.02 mmol) to generate *in situ* the supramolecular catalyst. After purification by silica gel column chromatography, product **133g,a** was obtained as a yellowish oil (33.2 mg, 56% yield). ^{1}H NMR (400 MHz, $CDCl_3$) δ: 7.37 - 7.23 (m, 10H), 4.97 (s, 1H), 4.10 - 3.97 (m, 2H), 1.42 - 1.38 (m, 1H), 1.18 - 1.16 (m, 1H), 1.14 (t, *J* = 7.1 Hz, 3H) and 0.99 - 0.89 (m, 2H) ppm; ^{13}C{^{1}H} NMR (101 MHz, $CDCl_3$) δ: 171.6 (C), 140.5 (C), 137.5 (C), 128.6 (CH), 128.48 (CH), 128.45 (CH), 127.51 (CH), 127.49 (CH), 127.1 (CH), 79.2 (CH), 64.9 (C), 61.2 (CH_2), 14.43 (CH_2), 14.36 (CH_2) and 14.1 (CH_3) ppm; IR (neat): 2981, 1748, 1453, 1230, 1203, 1173, 1088, 1063, 1024 and 696 cm^{-1}. HRMS (ESI) *m/z*: calcd for $C_{19}H_{20}O_3Na$ [M+Na]$^+$ 319.1305, found 319.1294.

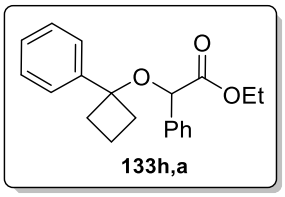

133h,a

Compound 133h,a: This compound was synthesized following the general procedure indicated at the beginning of this section from compound **131h** (156.0 mg, 1.00 mmol) and diazo compound **132a** (35 μL, 0.20 mmol) as substrates, using [Cu(MeCN)$_4$]BArF (11.4 mg, 0.01 mmol), **L1** (5.0 mg, 0.01 mmol) and LiBArF (16.3 mg, 0.02 mmol) to generate *in situ* the supramolecular catalyst. After purification by silica gel column chromatography, product **133h,a** was obtained as a yellowish oil (40.2 mg, 83% yield). ^{1}H NMR (400 MHz, $CDCl_3$) δ: 7.48 - 7.46 (m, 2H), 7.37 - 7.26 (m, 8H), 4.65 (s, 1H), 4.00 - 3.90 (m, 2H), 2.65 - 2.58 (m, 1H), 2.48 - 2.38 (m, 2H), 2.37 - 2.28 (m, 1H), 1.96 - 1.92 (m, 1H), 1.64 - 1.59 (m, 1H) and 1.10 (t, *J* = 7.1 Hz, 3H) ppm; ^{13}C{^{1}H} NMR (101 MHz, $CDCl_3$) δ: 171.8 (C), 142.6 (C), 138.0 (C), 128.5 (CH), 128.3 (CH), 128.2 (CH), 127.8 (CH), 127.1 (CH), 127.0 (CH), 83.3 (C), 75.7 (CH), 61.0 (CH_2), 34.2 (CH_2), 33.3 (CH_2), 14.1 (CH_3) and 13.5 (CH_2) ppm; IR (neat): 2982, 2946, 1749, 1172, 1095, 1057, 1026 and 696 cm^{-1}. HRMS (ESI) *m/z*: calcd for $C_{20}H_{22}O_3Na$ [M+Na]$^+$ 333.1461, found 333.1454.

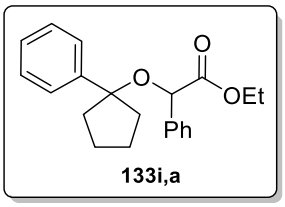

133i,a

Compound 133i,a: This compound was synthesized following the general procedure indicated at the beginning of this section from compound **131i** (171.0 mg, 1.00 mmol) and diazo compound **132a** (35 μL, 0.20 mmol) as substrates, using [Cu(MeCN)$_4$]BArF (11.4 mg, 0.01 mmol), **L1** (5.0 mg, 0.01 mmol) and NaBArF (14.4 mg, 0.02 mmol) to generate *in situ* the supramolecular catalyst. After purification by silica gel column chromatography, product **133i,a** was obtained as a yellowish oil (31.7 mg, 32% yield). ^{1}H NMR (500 MHz, $CDCl_3$) δ: 7.50 - 7.37 (m, 2H), 7.35 - 7.21 (m, 8H), 4.67 (s, 1H), 4.05 - 3.87 (m, 2H), 2.40 - 2.29 (m, 1H), 2.22 - 2.10 (m, 1H), 2.10 - 1.97 (m, 1H), 1.95 - 1.88 (m, 2H), 1.82 - 1.62 (m, 3H) and 1.09 (t, *J* = 7.1 Hz, 3H) ppm; ^{13}C{^{1}H} NMR (126 MHz, $CDCl_3$) δ: 172.1 (C), 142.9 (C), 138.6 (C), 128.4 (CH), 128.2 (CH), 128.0 (CH), 127.7 (CH), 127.5 (CH), 126.8 (CH), 91.2 (C), 75.6 (CH), 60.9 (CH_2), 38.2 (CH_2), 36.7 (CH_2), 23.2 (CH_2), 23.1 (CH_2) and 14.1 (CH_3) ppm; IR (neat): 2961, 2873, 1750, 1171, 1091, 1066, 1029 and 698 cm^{-1}. HRMS (ESI) *m/z*: calcd for $C_{21}H_{24}O_3Na$ $[M+Na]^+$ 347.1618, found 347.1616.

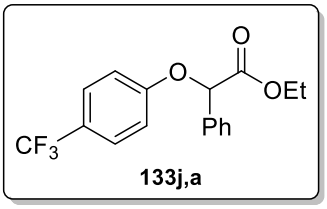

133j,a

Compound 133j,a: This compound was synthesized following the general procedure indicated at the beginning of this section from 4-(trifluoromethyl)phenol **131j** (166.0 mg, 1.00 mmol) and diazo compound **132a** (35 μL, 0.20 mmol) as substrates, using [Cu(MeCN)$_4$]BArF (11.4 mg, 0.01 mmol) and **L1** (5.0 mg, 0.01 mmol) to generate *in situ* the supramolecular catalyst. After purification by silica gel column chromatography, product **133j,a** was obtained as a yellowish oil (32.3 mg, 50% yield). ^{1}H NMR (500 MHz, $CDCl_3$) δ: 7.59 - 7.53 (m, 4H), 7.44 - 7.39 (m, 3H), 7.05 - 7.01 (m, 2H), 5.66 (s, 1H), 4.28 - 4.15 (m, 2H) and 1.21 (t, *J* = 7.1 Hz, 3H) ppm; ^{13}C{^{1}H} NMR (101 MHz, $CDCl_3$) δ: 169.4 (C), 159.8 (C), 134.9 (C), 129.4 (CH), 129.0 (CH), 127.2 (CH), 127.1 (q, $^3J_{C-F}$ = 3.5 Hz, CH), 124.4 (q, $^1J_{C-F}$ = 270.0 Hz, C), 124.1 (q, $^2J_{C-F}$ = 33.3 Hz, C), 115.5 (CH), 78.8 (CH), 62.0 (CH_2) and 14.1 (CH_3) ppm; ^{19}F{^{1}H} NMR (471 MHz, $CDCl_3$) δ: –61.8 ppm; IR (neat): 2992, 1733, 1614, 1520, 1326, 1253, 1213, 1192, 1152, 1106, 1069, 1054, 1021, 873, 727, 694 and 648 cm^{-1}; HRMS (ESI) *m/z*: calcd for $C_{17}H_{15}F_3O_3Na$ $[M+Na]^+$ 347.0865, found 347.0862.

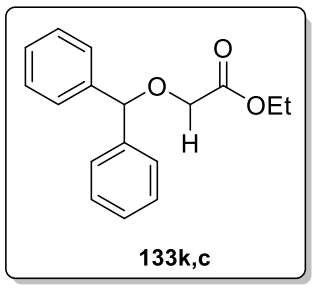

133k,c

Compound 133k,c: This compound was synthesized following the general procedure indicated at the beginning of this section from diphenylmethanol **131k** (185.0 mg, 1.00 mmol) and the commercial available ethyl 2-diazoacetate **132c** (24 μL, 0.20 mmol) as substrates, using $[Cu(MeCN)_4]BArF$ (11.4 mg, 0.01 mmol) and **L1** (5.0 mg, 0.01 mmol) and NaBArF (14.2 mg, 0.02 mmol) to generate *in situ* the supramolecular catalyst. After purification by silica gel column chromatography, product **133k,c** was obtained as a yellowish oil (40.7 mg, 75% yield). Spectroscopic data were in agreement with those previously reported.[37] ^1H NMR (500 MHz, $CDCl_3$) δ: 7.37 - 7.35 (m, 4H), 7.32 - 7.29 (m, 4H), 7.26 - 7.23 (m, 2H), 5.56 (s, 1H), 4.19 (q, *J* = 7.1 Hz, 2H), 4.07 (s, 2H) and 1.25 (t, *J* = 7.1 Hz, 3H) ppm; $^{13}C\{^1H\}$ NMR (126 MHz, $CDCl_3$) δ: 170.6 (C), 141.2 (C), 128.6 (CH), 127.9 (CH), 127.5 (CH), 83.7 (CH), 66.1 (CH_2), 60.9 (CH_2) and 14.3 (CH_3) ppm.

[37] Krishna, P. R.; Prapurna, Y. L.; Alivelu, M. *Tetrahedron Lett.* **2011**, *52*, 3460-3462.

1.5.11. Transformation of O–H insertion products into advanced synthetic intermediates of APIs

1.5.11.1. General procedure for the reduction of an ester group into the corresponding primary alcohol 141

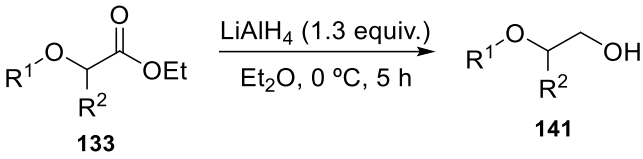

Scheme 44. General synthesis for products **141**.

To a flame-dried Schlenk flask, $LiAlH_4$ (19.1 mg, 0.50 mmol) was added, suspended in anhydrous Et_2O (0.5 mL) and cooled at 0 °C. Then, a solution of **133** (100.0 mg, 0.37 mmol) in anhydrous Et_2O (0.5 mL) was slowly cannulated into the $LiAlH_4$ suspension. The reaction mixture was allowed to reach room temperature and stirred for 4.5 hours. The reaction was then cooled down to 0 °C, diluted with Et_2O (0.5 mL), and carefully quenched with a saturated aqueous solution (1.0 mL) of Rochelle salt (*i.e.*, sodium potassium L(+)-tartrate tetrahydrate). The biphasic mixture was vigorously stirred overnight at room temperature. The two phases were then separated and the aqueous phase was extracted with Et_2O (2 x 5.0 mL). The combined organic phases were washed with brine (1 x 5.0 mL), dried over $MgSO_4$, filtered, and concentrated *in vacuo*. The desired product was obtained after purification by silica gel column chromatography using Cy/EtOAc (98:2) as eluent.

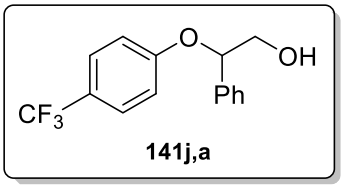

Compound **141j,a** was synthesized following the general procedure from $LiAlH_4$ (0.42 mmol, 15.9 mg) and **133j,a** (0.31 mmol, 100.0 mg). After purification by silica gel column chromatography, product **141j,a** was obtained as a colorless oil (43.2 mg, 50% yield). Spectroscopic data were in agreement with those previously reported.[25] ^{1}H NMR (400 MHz, $CDCl_3$) δ: 7.47 - 7.44 (m, 2H), 7.39 - 7.30 (m, 5H), 6.95 - 6.93 (m, 2H), 5.32 (dd, *J* = 8.1, 3.6 Hz, 1H), 3.97 (dd, *J* = 12.1, 8.1 Hz, 1H), 3.85 (dd, *J* = 12.1, 3.6 Hz, 1H) and 2.32 (broad signal, 1H) ppm; $^{13}C\{^1H\}$ NMR (101 MHz, $CDCl_3$) δ: 160.3 (C), 137.1 (C), 129.1 (CH), 128.6 (CH), 127.0 (q, $^3J_{C–F}$ = 3.7 Hz, CH), 126.4 (CH), 124.5 (q,

$^{1}J_{C-F}$ = 270.8 Hz, C), 123.5 (q, $^{2}J_{C-F}$ = 32.8 Hz, C), 116.0 (CH), 81.6 (CH) and 67.5 (CH_2) ppm; $^{19}F\{^{1}H\}$ NMR (376 MHz, $CDCl_3$) δ: −61.7 ppm.

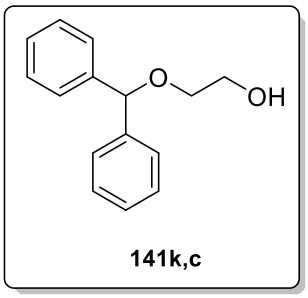

141k,c

Compound **141k,c** was synthesized following the general procedure from $LiAlH_4$ (0.50 mmol, 19.1 mg) and **133k,c** (0.37 mmol, 100.0 mg). After purification by silica gel column chromatography, product **141k,c** was obtained as a colorless oil (41.0 mg, 49% yield). Spectroscopic data were in agreement with those previously reported.[26] ^{1}H NMR (500 MHz, $CDCl_3$) δ: 7.37 - 7.24 (m, 10H), 5.41 (s, 1H), 3.79 (broad multiplet, 2H), 3.61 - 3.59 (m, 2H) and 2.01 (broad signal, 1H) ppm; $^{13}C\{^{1}H\}$ NMR (126 MHz, $CDCl_3$) δ: 142.0 (C), 128.6 (CH), 127.8 (CH), 127.1 (CH), 84.2 (CH) , 70.5 (CH_2) and 62.2 (CH_2) ppm.

1.5.12. Complete set of results for catalyzed insertion of copper-carbenoids into O–H bonds

1.5.12.1. Background experiments

A full set of experiments on the optimization of the reaction conditions, as well as background experiments, is summarized below (Table 16). See section 1.5.10 for the general procedure and experimental details to carry out the O–H insertion reactions.

131a **132a** **133a,a**

Table 16. Optimization for the copper-catalyzed carbene insertion into O−H bonds.

Entry	[Cu]	L	RA	MS	Solv.	T (ºC)	Yield [%][a]
1	--	--	--	yes,[b]	$CHCl_3$	40	<1
2	$[Cu(MeCN)_4]BArF$	--	--	--	$CHCl_3$	40	48
3	--	**L1**	--	--	$CHCl_3$	40	<1
4	--	--	NaBArF	--	$CHCl_3$	40	<1
5	--	**L1**	NaBArF	--	$CHCl_3$	40	<1
6	$[Cu(MeCN)_4]BArF$	--	NaBArF	--	$CHCl_3$	40	51
7	$[Cu(MeCN)_4]BArF$	**L1**	NaBArF	--	$CHCl_3$	40	64
8	$[Cu(MeCN)_4]BArF$	--	NaBArF	yes,[b]	$CHCl_3$	40	53
9	$[Cu(MeCN)_4]BArF$	**L1**	NaBArF	yes,[b]	$CHCl_3$	40	66
10	$[Cu(MeCN)_4]BArF$	**L1**	--	yes,[b]	$CHCl_3$	40	67
11	$[Cu(MeCN)_4]BArF$	**Ox**[c]	--	yes,[b]	$CHCl_3$	40	47
12	$[Cu(MeCN)_4]BArF$	**L1**	NaBArF	yes,[b]	CH_2Cl_2	40	62
13[d]	$[Cu(MeCN)_4]BArF$	**L1**	NaBArF	yes,[b]	PhMe	40	47
14	$[Cu(MeCN)_4]BArF$	**L1**	NaBArF	yes,[b]	PhCl	40	59
15[e]	$[Cu(MeCN)_4]BArF$	**L1**	NaBArF	yes,[b]	$CHCl_3$	0	42
16	$[Cu(MeCN)_4]BArF$	**L1**	NaBArF	yes,[b]	$CHCl_3$	rt	64
17	$[Cu(MeCN)_4]BF_4$	**L1**	$NaBF_4$	yes,[b]	$CHCl_3$	40	15

[a] Yields were determined by ^1H NMR using 1,3,5-trimethoxybenzene as the internal standard. [b] 4 Å molecular sieves were used in a 95:5 weight ratio with respect to **132a**. [c] 2.0 equiv. of 4,4-dimethyl-4,5-dihydrooxazole were added. [d] The reaction was performed adding a 3% of THF. [e] Reaction time was 5 h.

1.5.12.2. Comparative study of the reactivity of L1 and L2

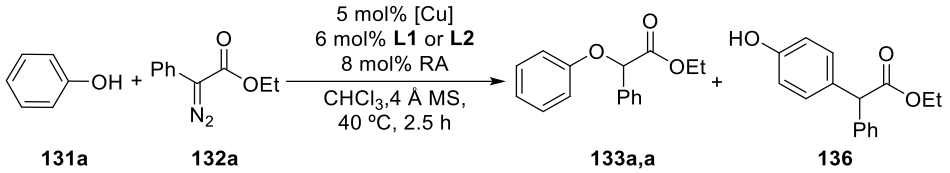

131a **132a** **133a,a** **136**

Table 17. Study of the performance of copper catalysts derived from ligands **L1** and **L2** using all the set of alkali metal BArF salts as RA.

Entry	Substrate 131	Substrate 132	L	RA	133 yield [%][a]	136 yield [%][a]
1	**131a**	**132a**	**L1**	None	67	nd[b]
2				LiBArF	84	nd
3				NaBArF	66	nd
4				KBArF	77	nd
5				RbBArF	85 (81)[c]	nd
6				CsBArF	65	nd
7	**131a**	**132a**	**L2**	None	50	6
8				LiBArF	77	5
9				NaBArF	64	nd
10				KBArF	79	4
11				RbBArF	71	nd
12				CsBArF	60	14

[a] Yields were determined by ^{1}H NMR using 1,3,5-trimethoxybenzene as the internal standard. [b] Not detected. [c] Isolated yield.

1.5.12.3. Full set of results for the catalyzed insertion of copper-carbenoids into the O–H bonds of compounds 131a-i

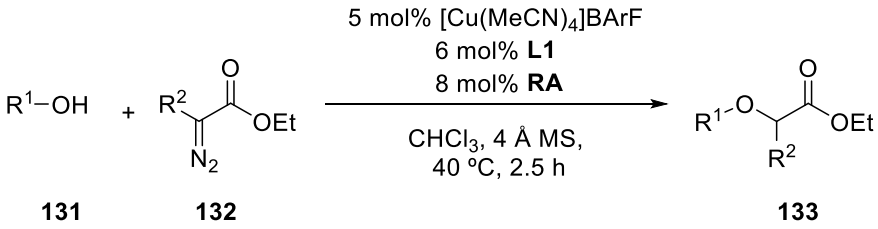

131 **132** **133**

See section 1.5.10 for the general procedure and experimental details to carry out the O–H insertion reactions.

Table 18. Catalyzed insertion of copper-carbenoids into the O–H bonds of compounds **131a-i**.

Entry	Substrate 131	Substrate 132	RA	133 yield [%][a]
1	**131b**	**132a**	None	49
2			LiBArF	52
3			NaBArF	56
4			KBArF	50
5			RbBArF	59 (55)[b]
6			CsBArF	51
7	**131c**	**132a**	None	54
8			LiBArF	53
9			NaBArF	55
10			KBArF	51
11			RbBArF	61
12			CsBArF	69 (64)[b]

Table 18 cont.

Entry	Substrate 131	Substrate 132	RA	133 yield [%][a]
13	**131d**	**132a**	None	32
14			LiBArF	82
15			NaBArF	87 (80)[b]
16			KBArF	82
17			RbBArF	83
18			CsBArF	80
19	**131e**	**132a**	None	70
20			LiBArF	98
21			NaBArF	99 (91)[b]
22			KBArF	97
23			RbBArF	88
24			CsBArF	80
25	**131f**	**132a**	None	41 (38)[b]
26			LiBArF	28
27			NaBArF	30
28			KBArF	20
29			RbBArF	24
30			CsBArF	17
31[c]			NaBArF	10
32	**131a**	**132b**	None	66
33			LiBArF	70
34			NaBArF	72
35			KBArF	77 (75)[b]
36			RbBArF	77
37			CsBArF	72

Table 18 cont.

Entry	Substrate 131	Substrate 132	RA	133 yield [%][a]
38	**131b**	**132b**	None	54
39			LiBArF	21
40			NaBArF	69 (63)[b]
41			KBArF	65
42			RbBArF	53
43			CsBArF	58
44	**131c**	**132b**	None	44
45			LiBArF	61
46			NaBArF	62 (60)[b]
47			KBArF	62
48			RbBArF	59
49			CsBArF	62
50	**131d**	**132b**	None	64
51			LiBArF	72
52			NaBArF	74 (68)[b]
53			KBArF	65
54			RbBArF	19
55			CsBArF	43
56	**131e**	**132b**	None	50
57			LiBArF	59
58			NaBArF	63
59			KBArF	58
60			RbBArF	74 (71)[b]
61			CsBArF	72

Table 18 cont.

Entry	Substrate 131	Substrate 132	RA	133 yield [%][a]
62	**131f**	**132b**	None	19
63			LiBArF	16
64			NaBArF	38
65			KBArF	42 (29)[b]
66			RbBArF	25
67			CsBArF	34
68	**131g**	**132a**	None	11
69			LiBArF	57
70			NaBArF	64 (56)[b]
71			KBArF	61
72			RbBArF	61
73			CsBArF	59
74	**131h**	**132a**	None	82
75			LiBArF	85 (83)[b]
76			NaBArF	80
77			KBArF	81
78			RbBArF	71
79			CsBArF	71
80[d]	**131i**	**132a**	None	12
81			LiBArF	36
82			NaBArF	39 (32)[b]
83			KBArF	38
84			RbBArF	37
85			CsBArF	38

Table 18 cont.

Entry	Substrate 131	Substrate 132	RA	133 yield [%][a]
86	**131j**	**132a**	None	54 (50)[b]
87			LiBArF	43
88			NaBArF	35
89			KBArF	35
90			RbBArF	54
91			CsBArF	52
92	**131k**	**132c**	None	72
93			LiBArF	69
94			NaBArF	76 (75)[b]
95			KBArF	75
96			RbBArF	68
97			CsBArF	73

[a] Yields were determined by ^{1}H NMR using 1,3,5-trimethoxybenzene as the internal standard. [b] Isolated yield. [c] Addition time of **132a** was 6 h and reaction time 24 h. [d] Reaction time was 24 h.

1.5.13. Characterization of products 137 and 138

Products **137** and **138** were identified in the crude mixture. Both compounds were independently synthesized.

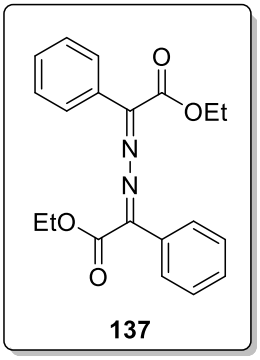

137

Product **137** was prepared reacting PhEDA **132a** (0.26 mmol) with $AgBF_4$ (10 mol%) in 2 mL of CH_2Cl_2 for 1 hour. After evaporation, the reaction crude mixture was purified by column chromatography using silica gel and Cy/AcOEt (30:1) as the eluents, to afford **137** as a yellow solid (9.1 mg, 10% yield). Spectroscopic data were in agreement with those previously reported.[19] ^{1}H NMR (400 MHz, $CDCl_3$) δ: 7.81 - 7.78 (m, 4H), 7.50 - 7.41 (m, 6H), 4.50 (q, J = 7.1 Hz, 4H) and 1.42 (t, J = 7.1 Hz, 6H) ppm; ^{13}C{^{1}H}

NMR (101 MHz, $CDCl_3$) δ: 165.3 (C), 162.3 (C), 132.1 (C), 131.4 (CH), 128.9 (CH), 128.0 (CH), 61.7 (CH_2) and 14.5 (CH_3) ppm.

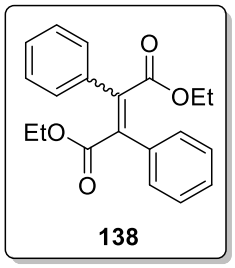

138

Product **138** was prepared reacting PhEDA **132a** (0.26 mmol) with $AgBF_4$ (10 mol%) in 2 mL of CH_2Cl_2 for 1 hour. After evaporation, the reaction crude mixture was purified by column chromatography using silica gel and Cy/AcOEt (30:1) as the eluents, to afford **138** as a pale yellow oil (18.3 mg, 22% yield). Spectroscopic data were in agreement with those previously reported.[38] ^1H NMR (400 MHz, $CDCl_3$) δ: 7.45 - 7.34 (m, 10H), 4.00 (q, J = 7.1 Hz, 4H) and 0.94 (t, J = 7.1 Hz, 6H) ppm; $^{13}C\{^1H\}$ NMR (101 MHz, $CDCl_3$) δ: 168.2 (C), 137.8 (C), 135.7 (C), 128.8 (CH), 128.5 (CH), 128.3 (CH), 61.5 (CH_2) and 13.7 (CH_3) ppm.

[38] The *E*- or *Z*-configuration could not be unequivocally assigned according to previous reports. See the following references: (a) Zhou, C.; Larock, R. C. *J. Org. Chem.* **2005**, *70*, 3765-3777. (b) Zhou, L.; Zhang, W.; Jiang, H. *Sci. China, Ser. B: Chem.* **2008**, *51*, 241-247.

1.5.14. Copies of NMR spectra

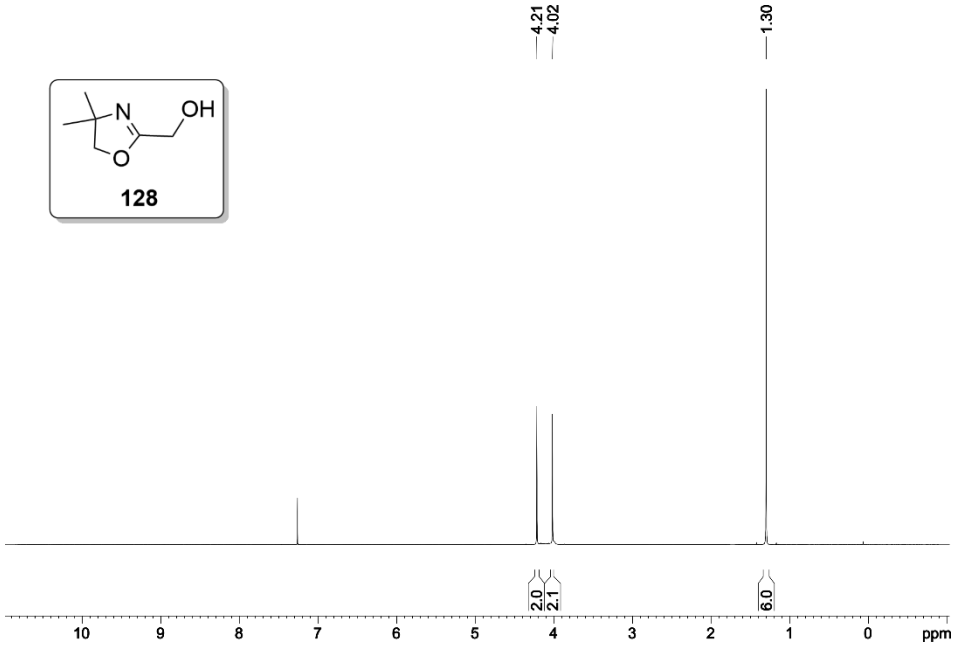

Figure 35. ^{1}H NMR spectrum (500 MHz, $CDCl_3$) of **128**.

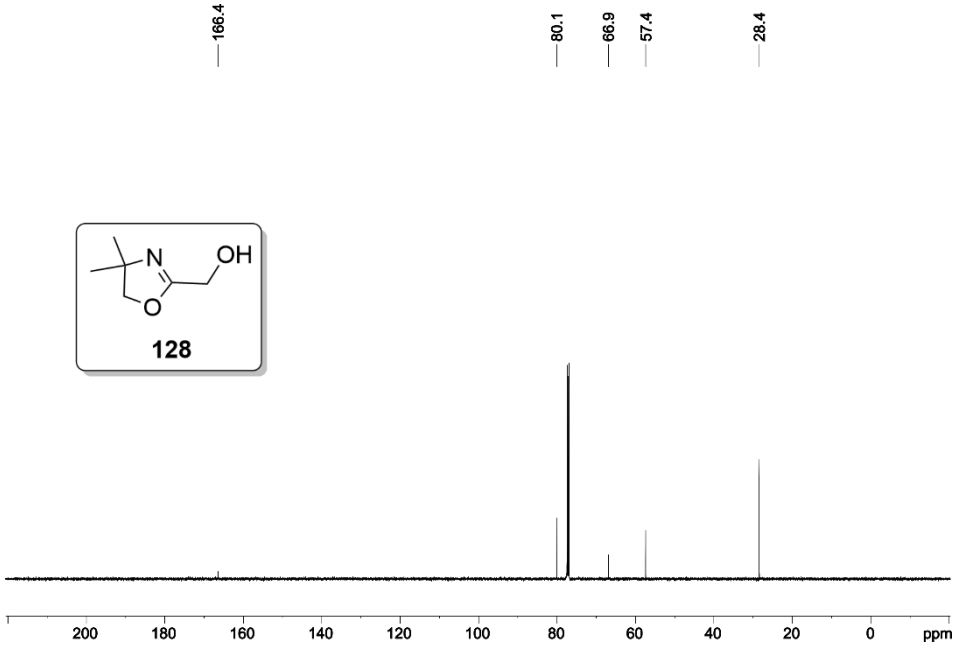

Figure 36. $^{13}C\{^{1}H\}$ NMR spectrum (126 MHz, $CDCl_3$) of **128**.

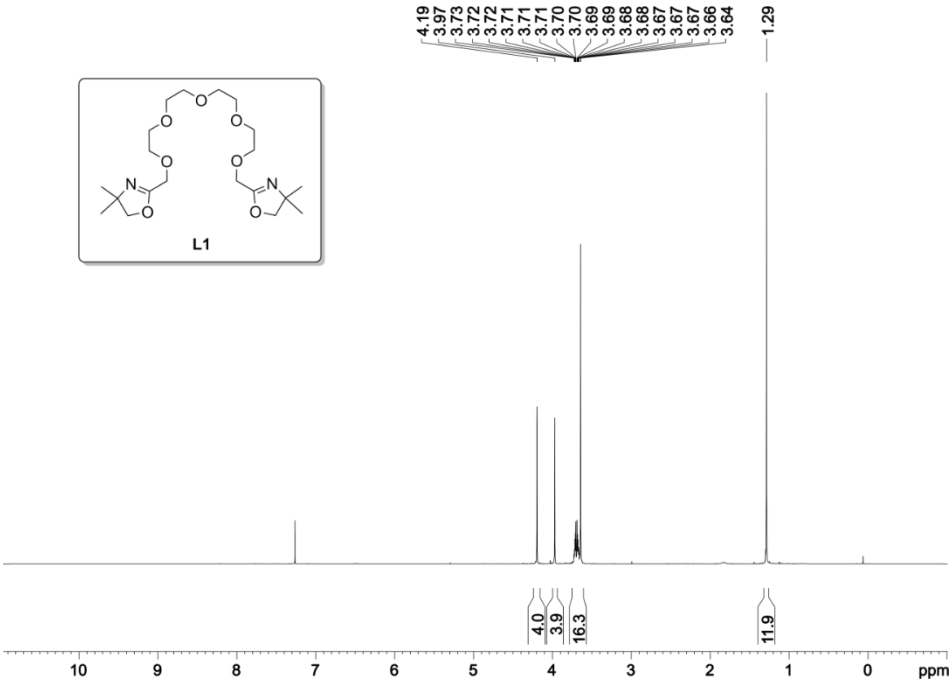

Figure 37. ^{1}H NMR spectrum (400 MHz, $CDCl_3$) of **L1**.

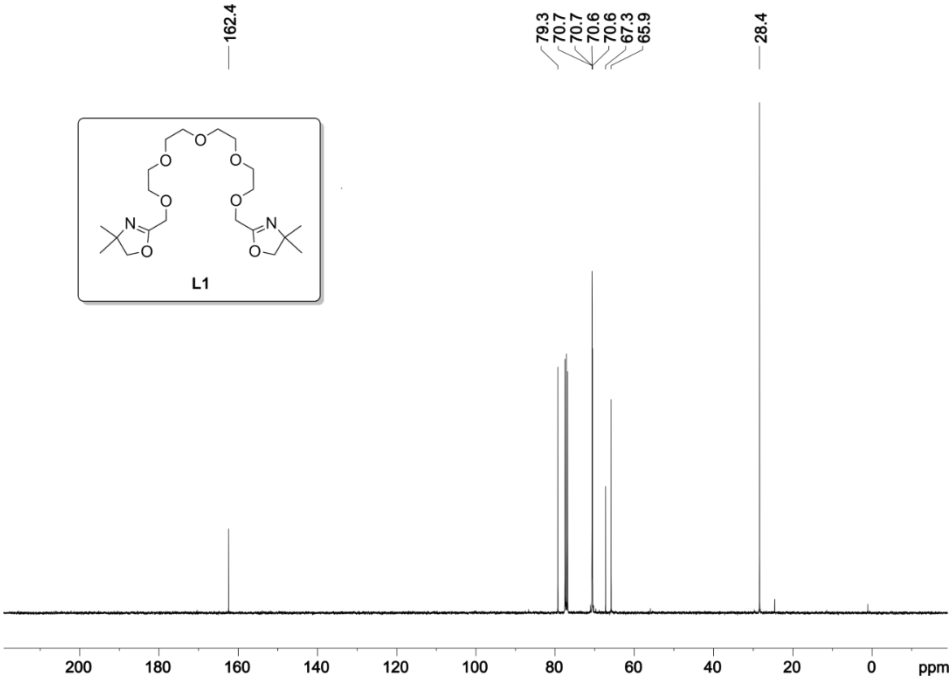

Figure 38. $^{13}C\{^{1}H\}$ NMR spectrum (101 MHz, $CDCl_3$) of **L1**.

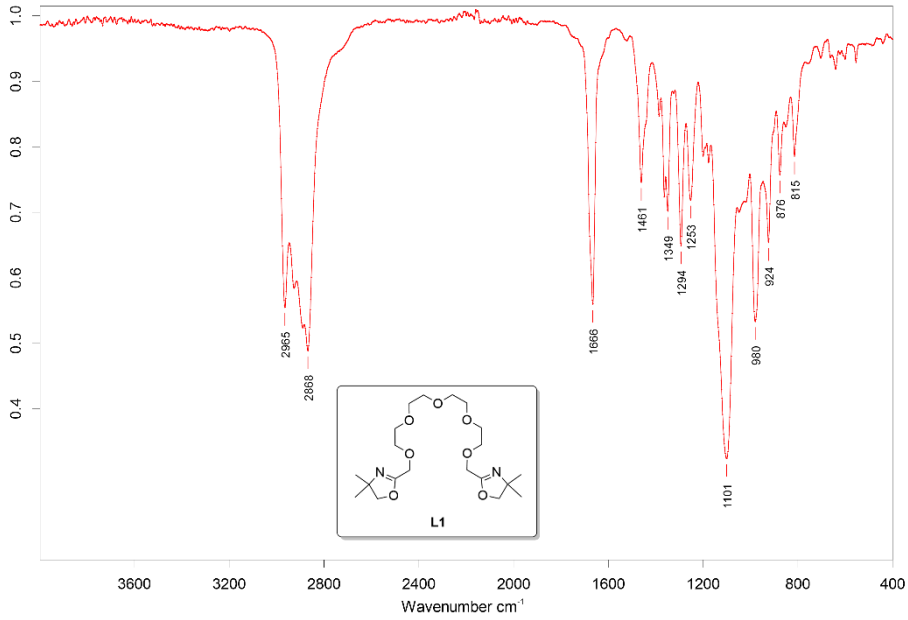

Figure 39. IR spectrum of **L1**.

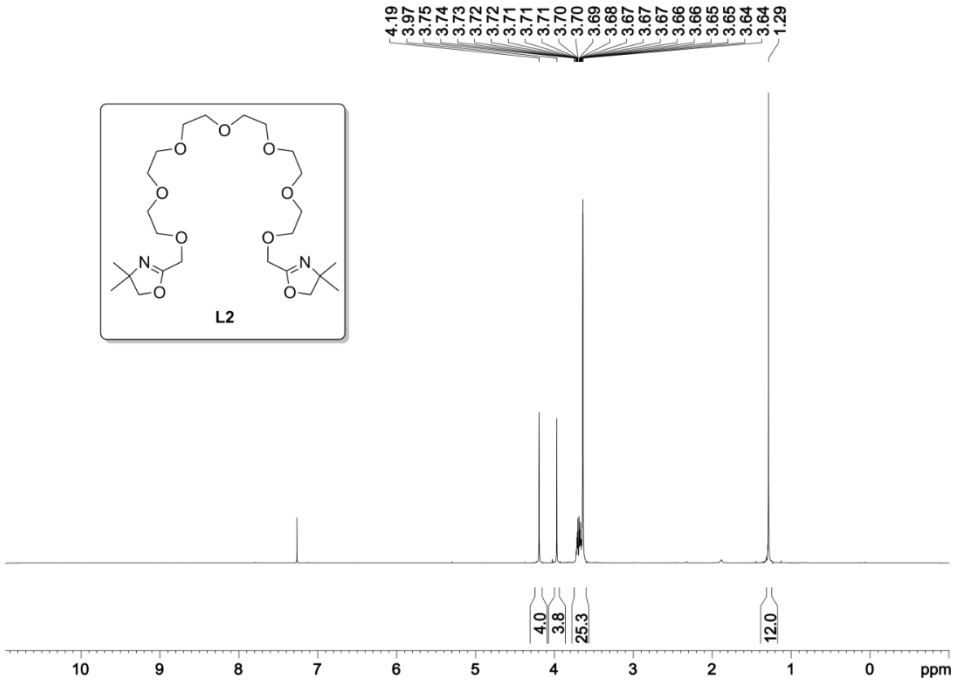

Figure 40. ^{1}H NMR spectrum (400 MHz, $CDCl_3$) of **L2**.

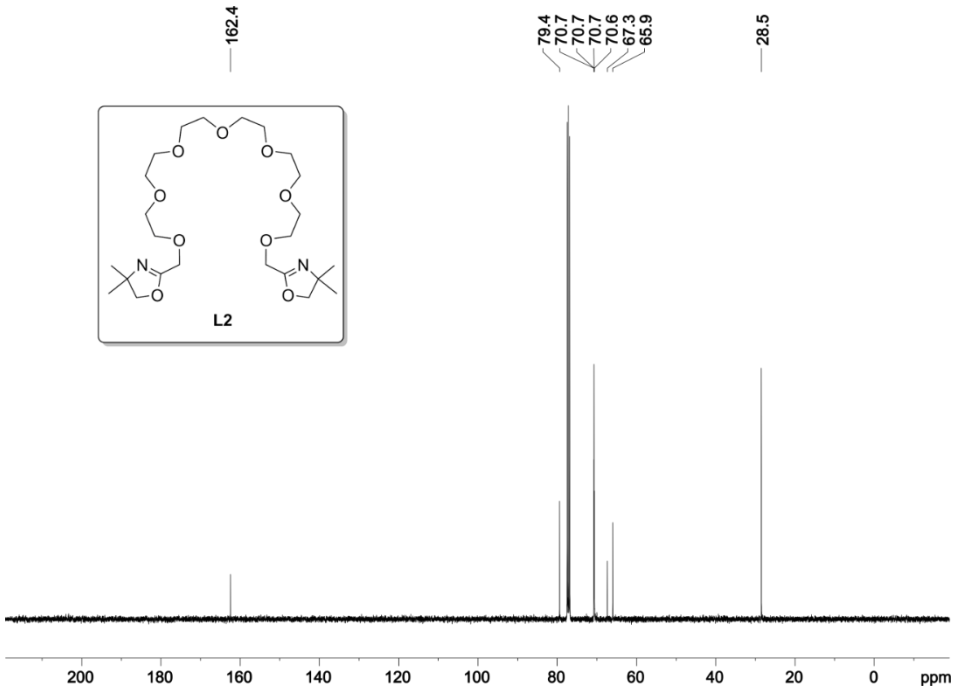

Figure 41. $^{13}C\{^{1}H\}$ NMR spectrum (101 MHz, $CDCl_3$) of **L2**.

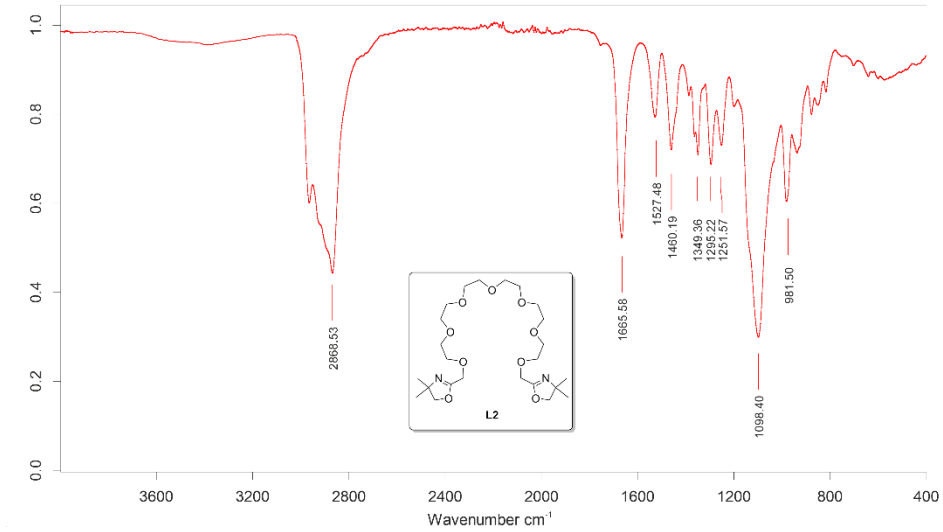

Figure 42. IR spectrum of **L2**.

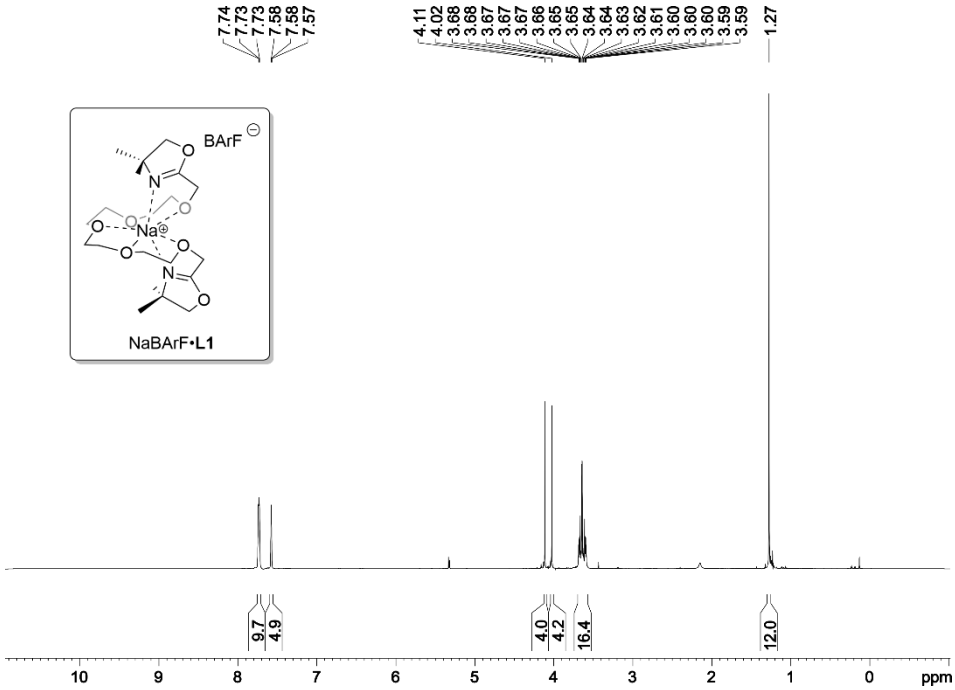

Figure 43. ^{1}H NMR spectrum (400 MHz, CD_2Cl_2) of NaBArF•**L1**.

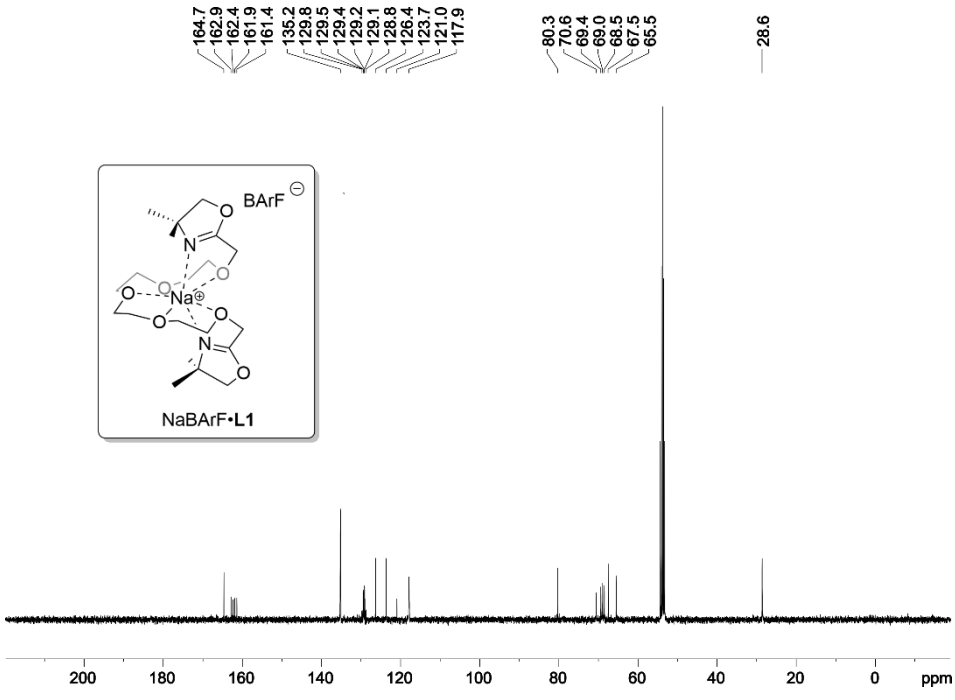

Figure 44. $^{13}C\{^{1}H\}$ NMR spectrum (101 MHz, CD_2Cl_2) of NaBArF•**L1**.

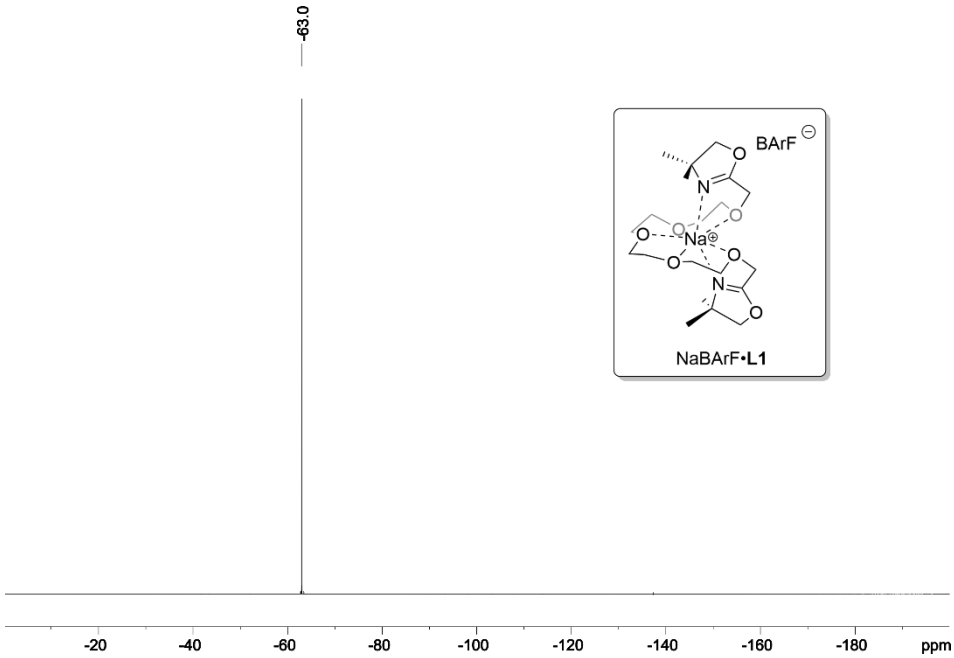

Figure 45. $^{19}F\{^{1}H\}$ NMR spectrum (376 MHz, CD_2Cl_2) of NaBArF•**L1**.

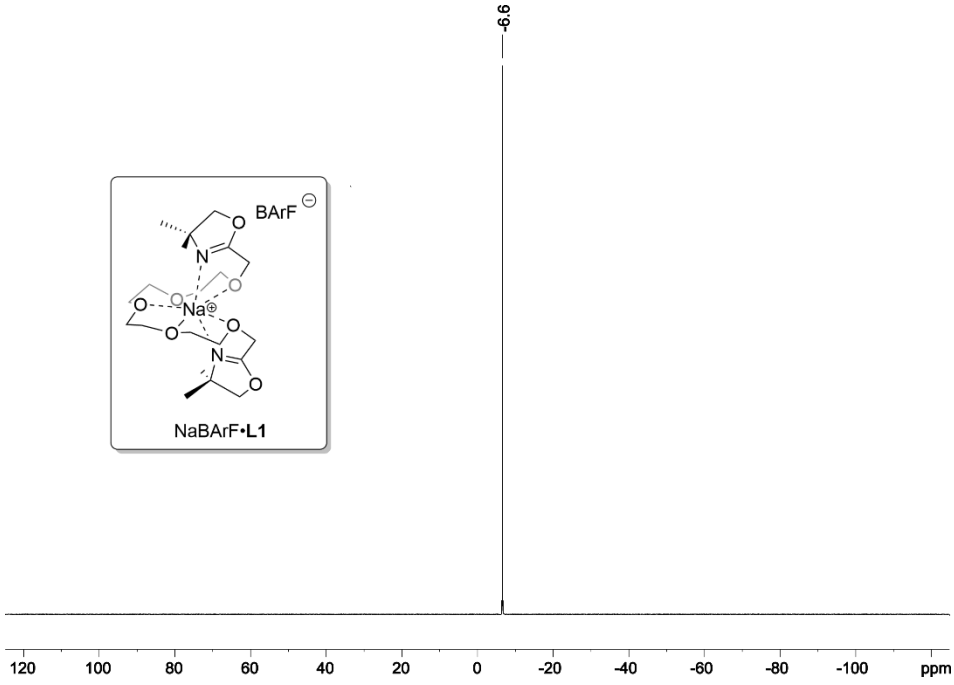

Figure 46. $^{11}B\{^{1}H\}$ NMR spectrum (128 MHz, CD_2Cl_2) of NaBArF•**L1**.

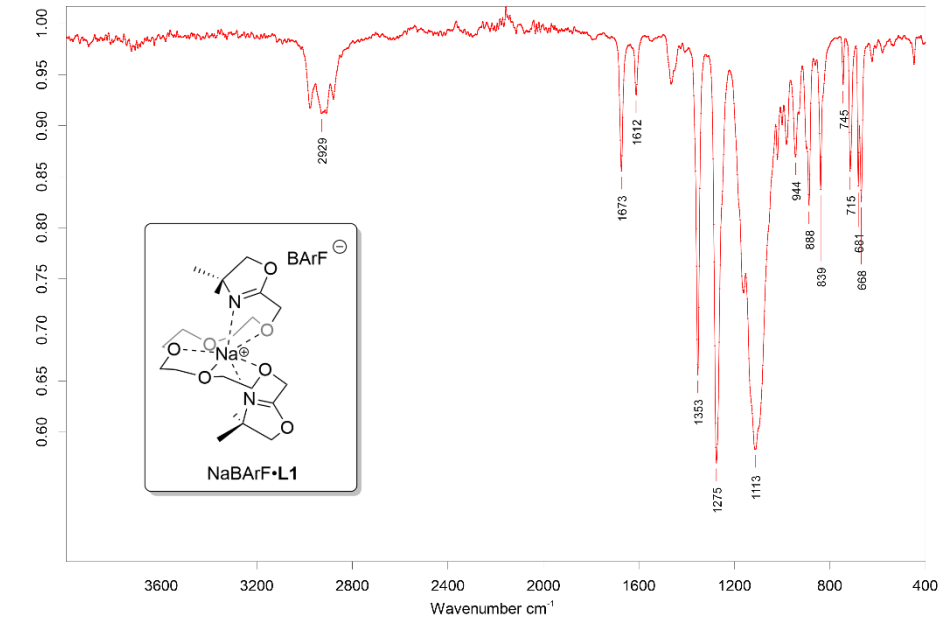

Figure 47. IR spectrum of NaBArF•**L1**.

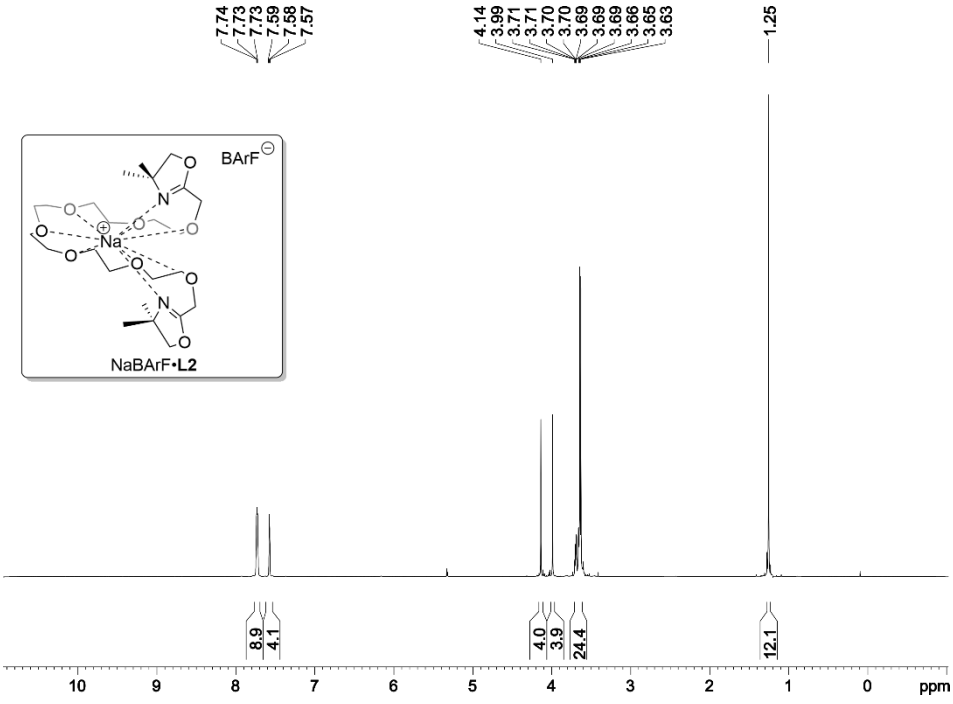

Figure 48. ^{1}H NMR spectrum (400 MHz, CD_2Cl_2) of NaBArF•**L2**.

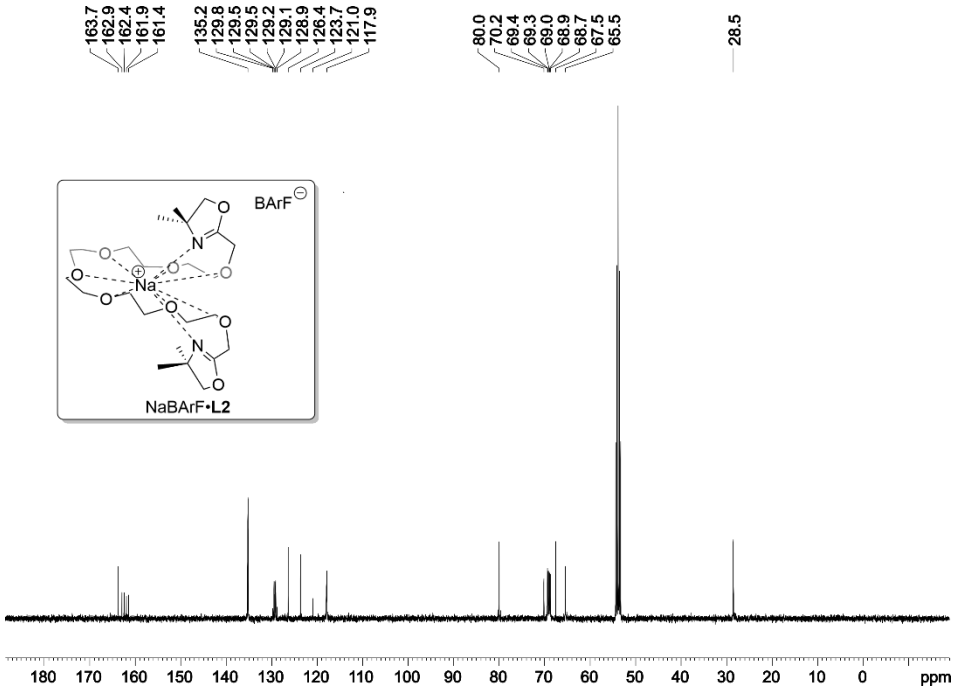

Figure 49. $^{13}C\{^{1}H\}$ NMR spectrum (101 MHz, CD_2Cl_2) of NaBArF•**L2**.

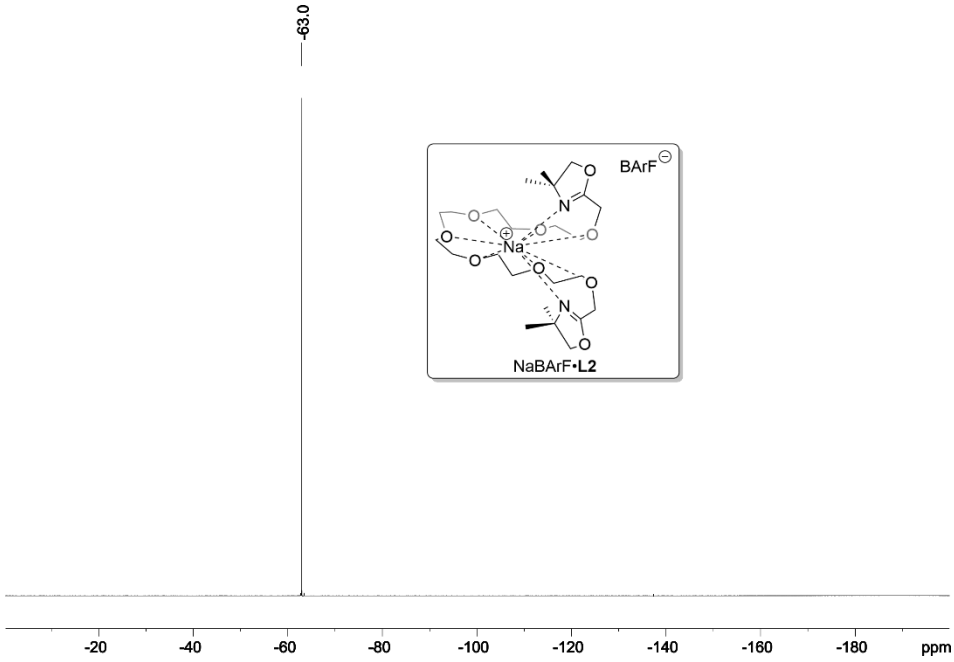

Figure 50. $^{19}F\{^{1}H\}$ NMR spectrum (376 MHz, CD_2Cl_2) of NaBArF•**L2**.

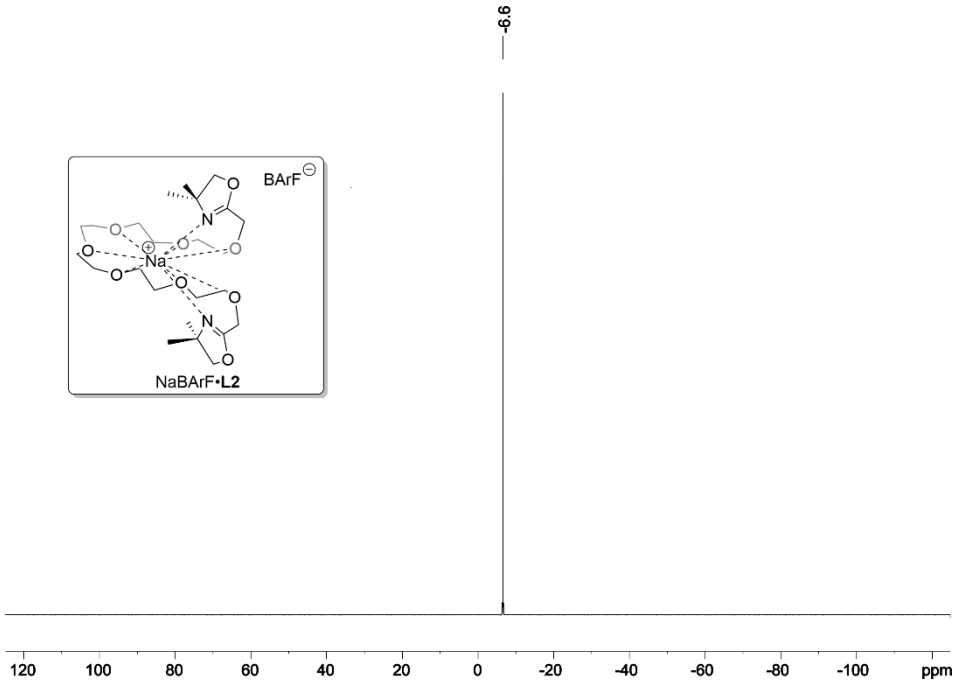

Figure 51. $^{11}B\{^{1}H\}$ NMR spectrum (128 MHz, CD_2Cl_2) of NaBArF•**L2**.

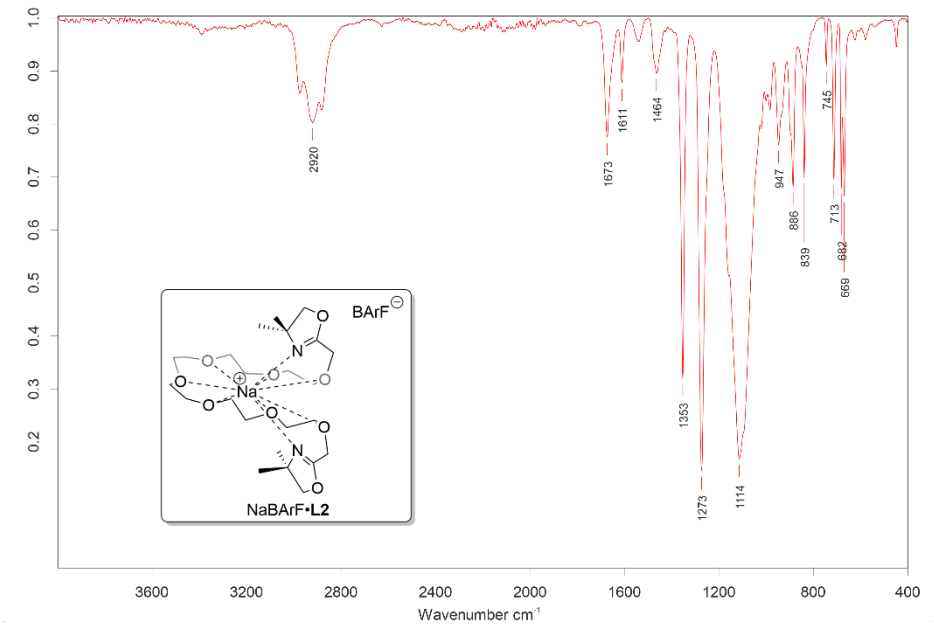

Figure 52. IR spectrum of NaBArF•**L2**.

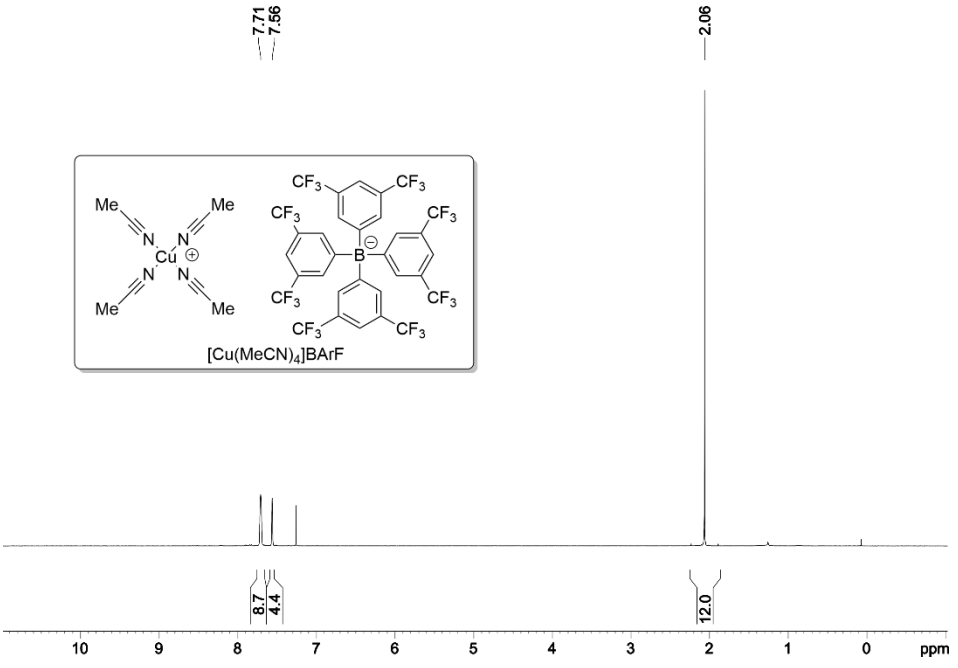

Figure 53. ^{1}H NMR spectrum (400 MHz, $CDCl_3$) of $[Cu(MeCN)_4]BArF$.

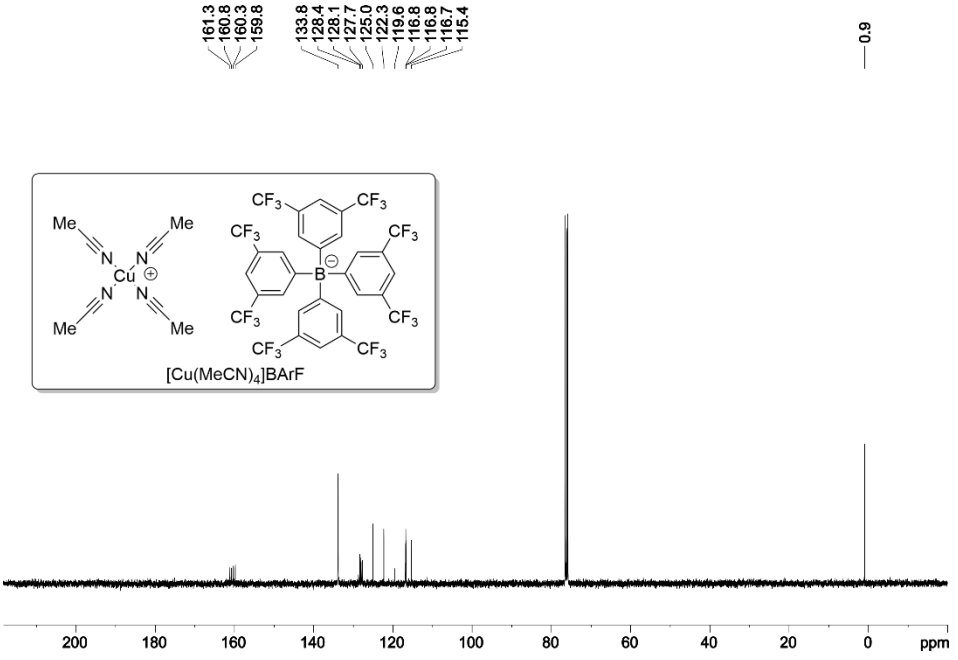

Figure 54. $^{13}C\{^{1}H\}$ NMR spectrum (101 MHz, $CDCl_3$) of $[Cu(MeCN)_4]BArF$.

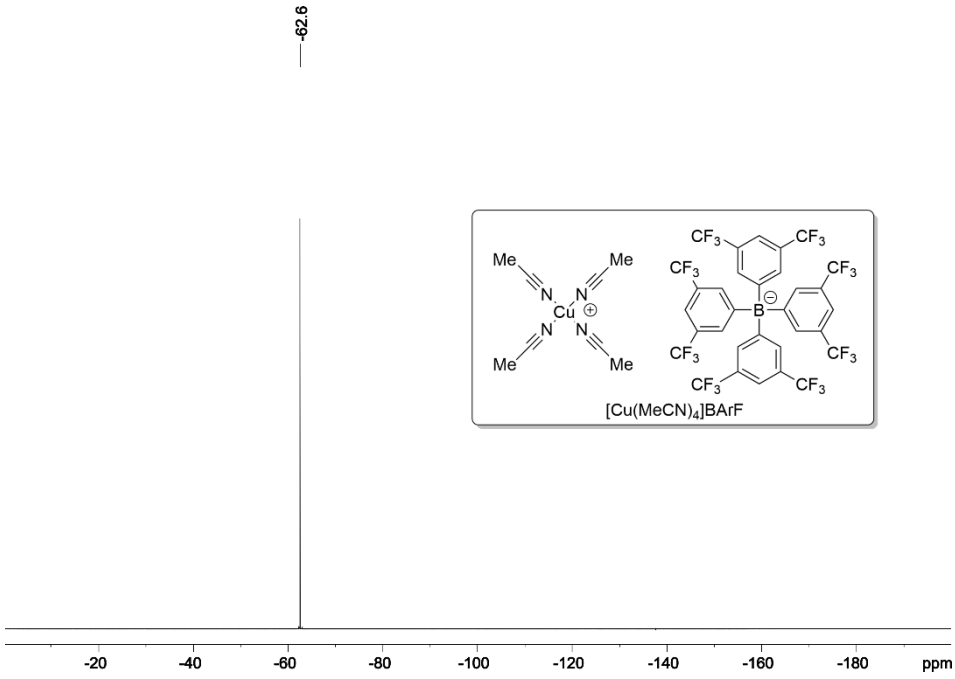

Figure 55. $^{19}F\{^{1}H\}$ NMR spectrum (376 MHz, $CDCl_3$) of $[Cu(MeCN)_4]BArF$.

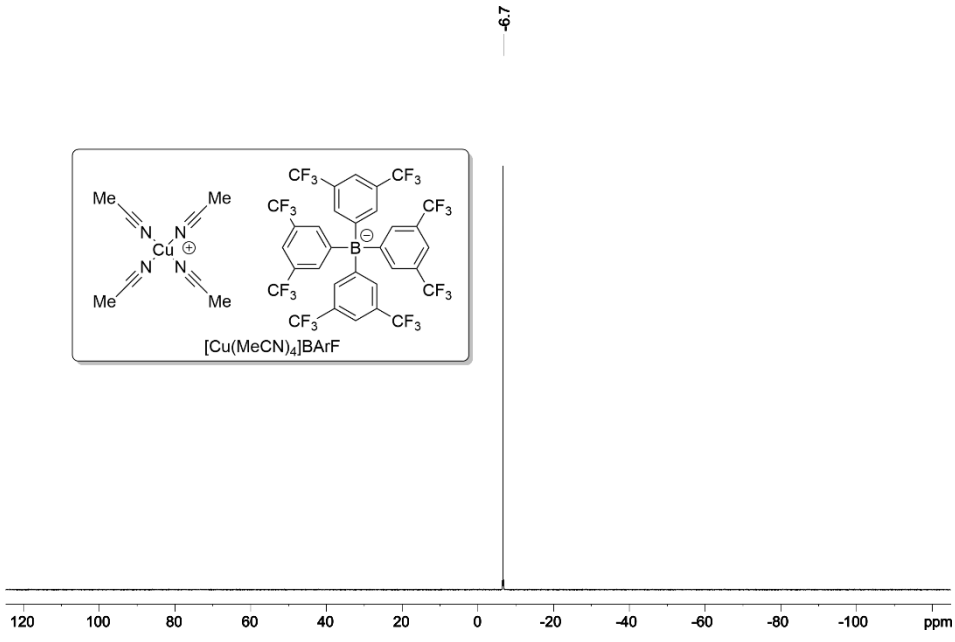

Figure 56. $^{11}B\{^{1}H\}$ NMR spectrum (128 MHz, $CDCl_3$) of $[Cu(MeCN)_4]BArF$.

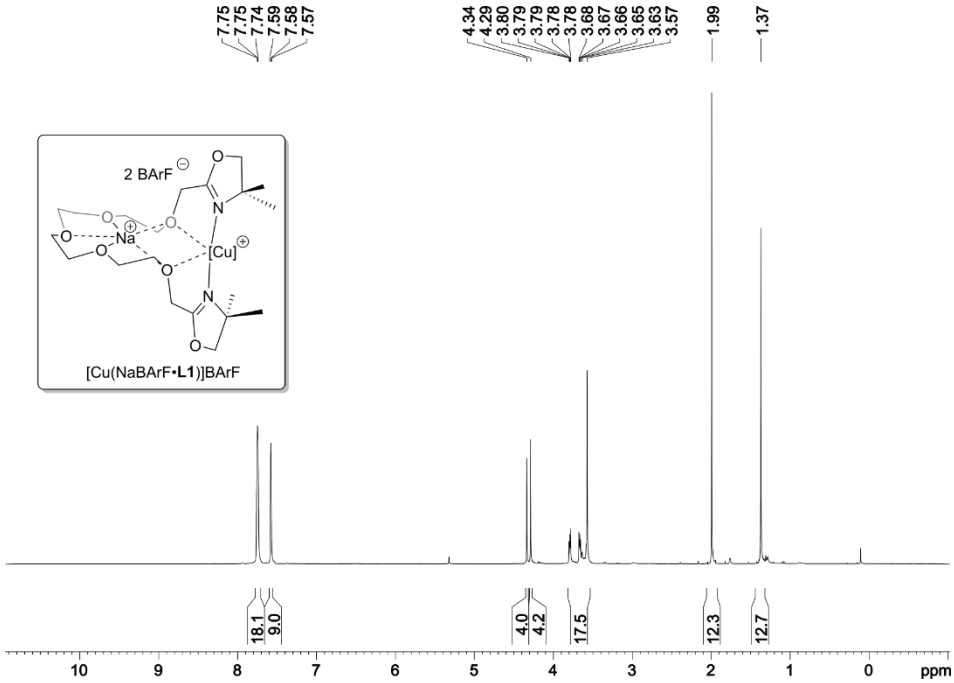

Figure 57. ^{1}H NMR spectrum (400 MHz, CD_2Cl_2) of [Cu(NaBArF•**L1**)]BArF.

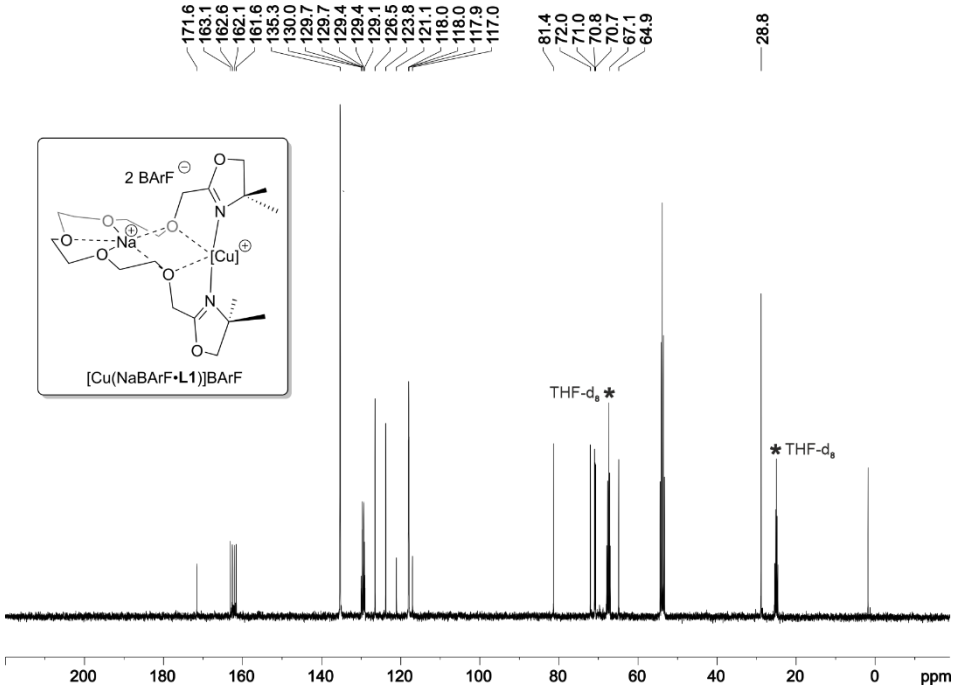

Figure 58. $^{13}C\{^{1}H\}$ NMR spectrum (101 MHz, CD_2Cl_2) of [Cu(NaBArF•**L1**)]BArF.

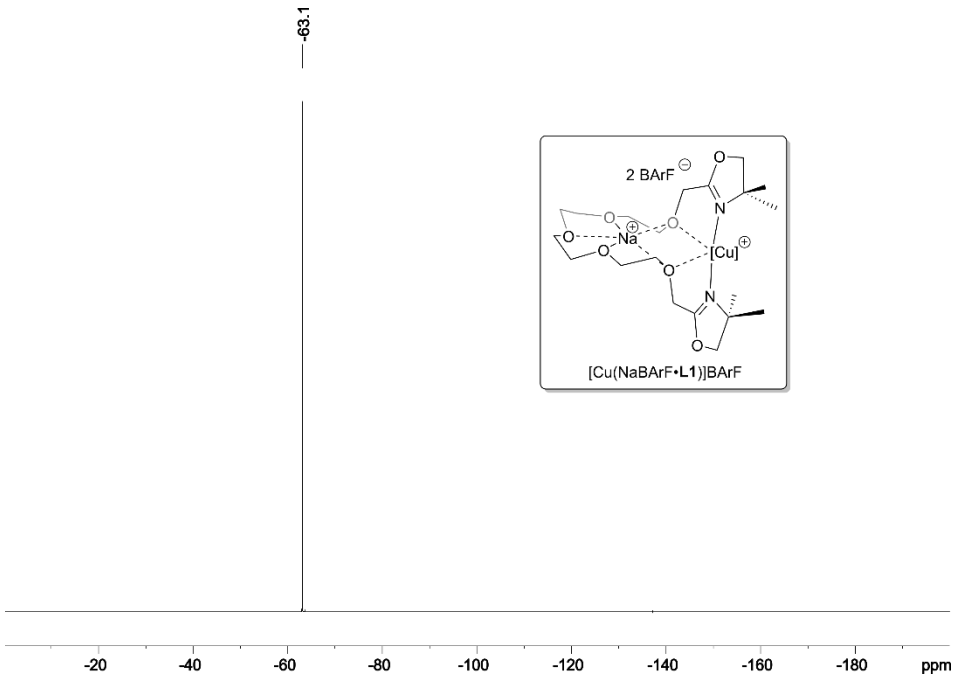

Figure 59. $^{19}F\{^{1}H\}$ NMR spectrum (376 MHz, CD_2Cl_2) of [Cu(NaBArF•**L1**)]BArF.

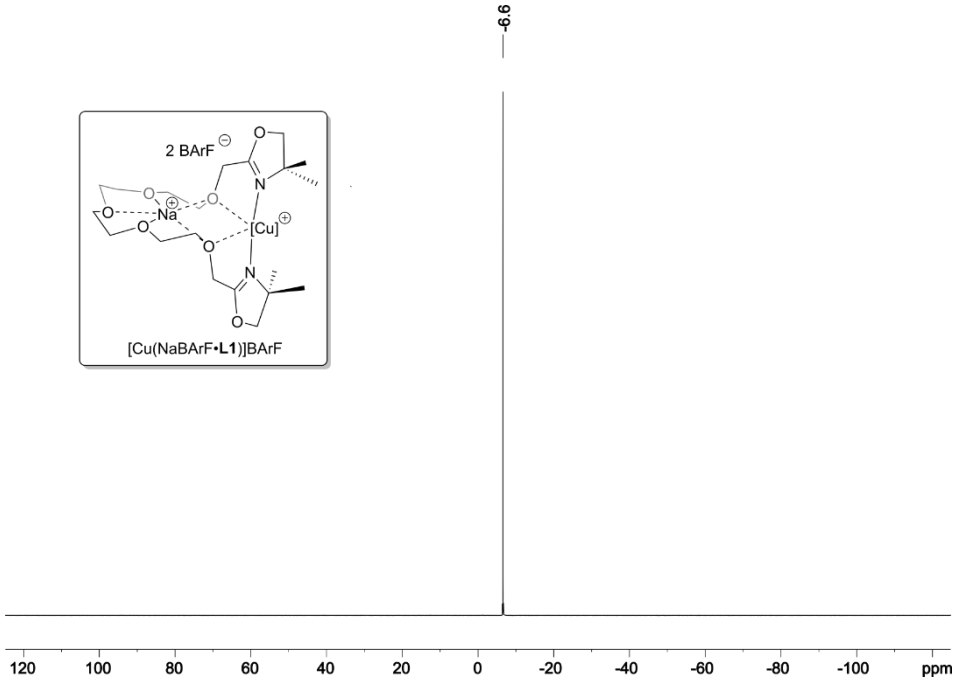

Figure 60. $^{11}B\{^{1}H\}$ NMR spectrum (128 MHz, CD_2Cl_2) of [Cu(NaBArF•**L1**)]BArF.

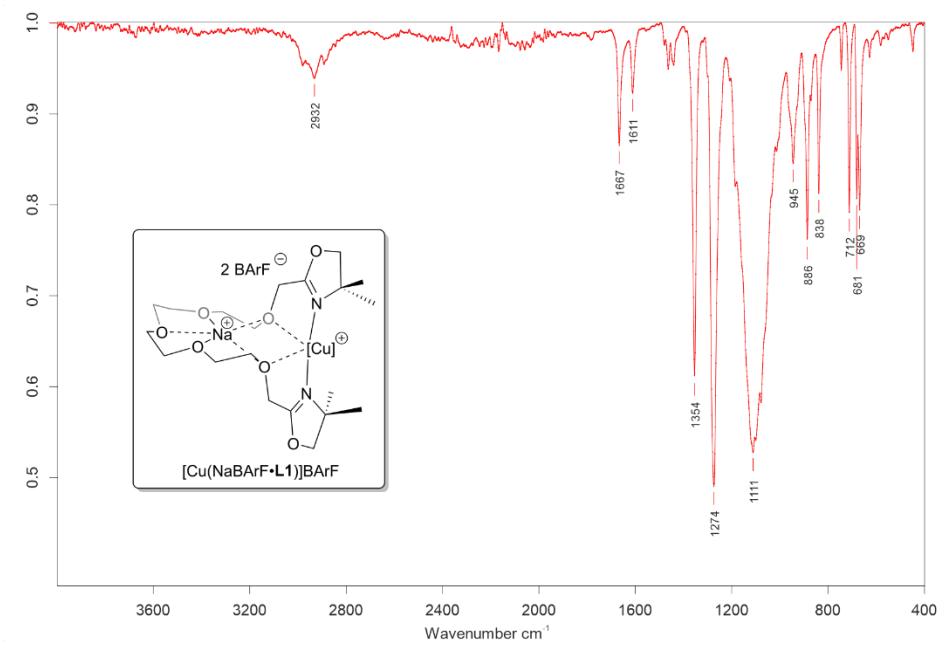

Figure 61. IR spectrum of [Cu(NaBArF•**L1**)]BArF.

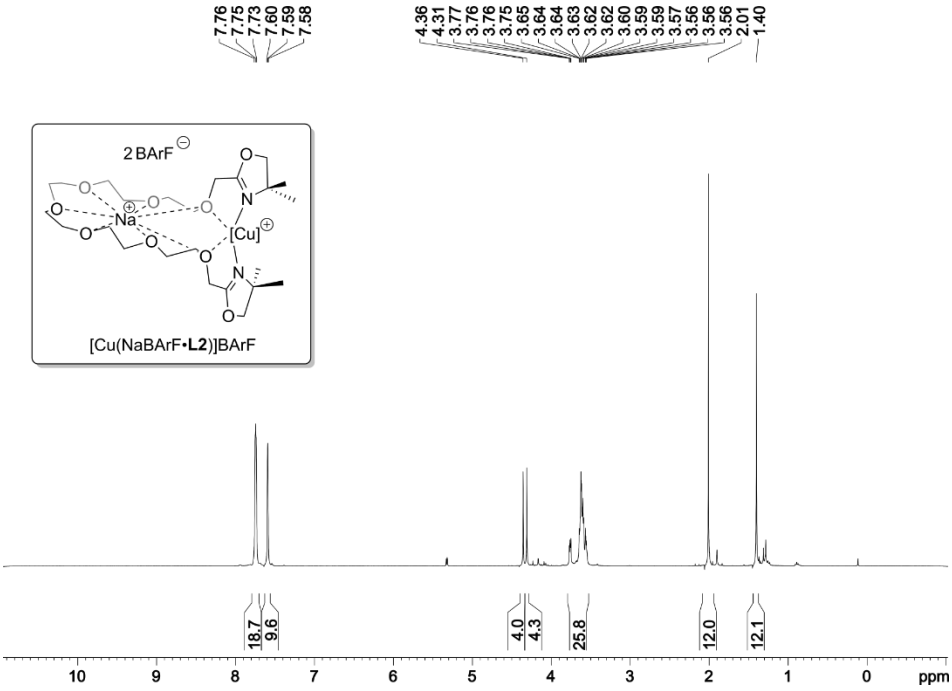

Figure 62. ^{1}H NMR spectrum (400 MHz, CD_2Cl_2) of [Cu(NaBArF•**L2**)]BArF.

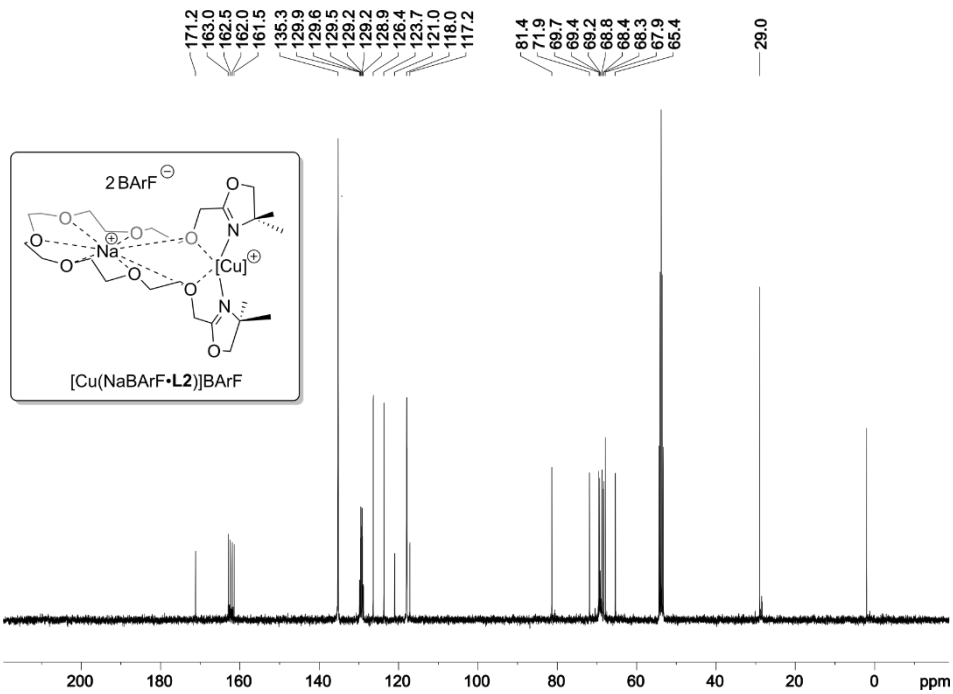

Figure 63. $^{13}C\{^{1}H\}$ NMR spectrum (101 MHz, CD_2Cl_2) of [Cu(NaBArF•**L2**)]BArF.

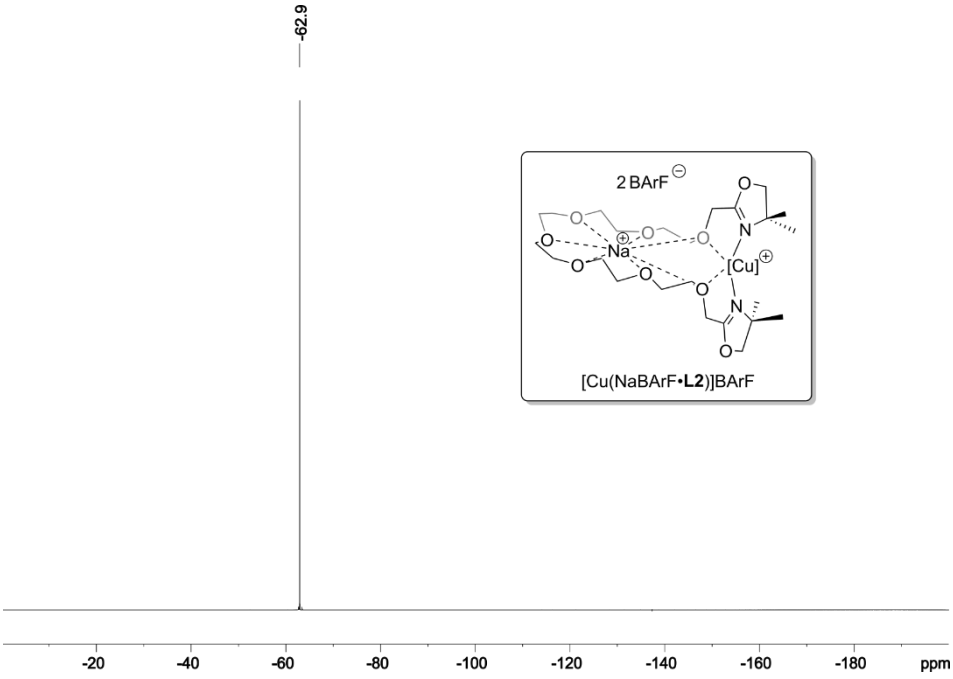

Figure 64. $^{19}F\{^{1}H\}$ NMR spectrum (376 MHz, CD_2Cl_2) of [Cu(NaBArF•**L2**)]BArF.

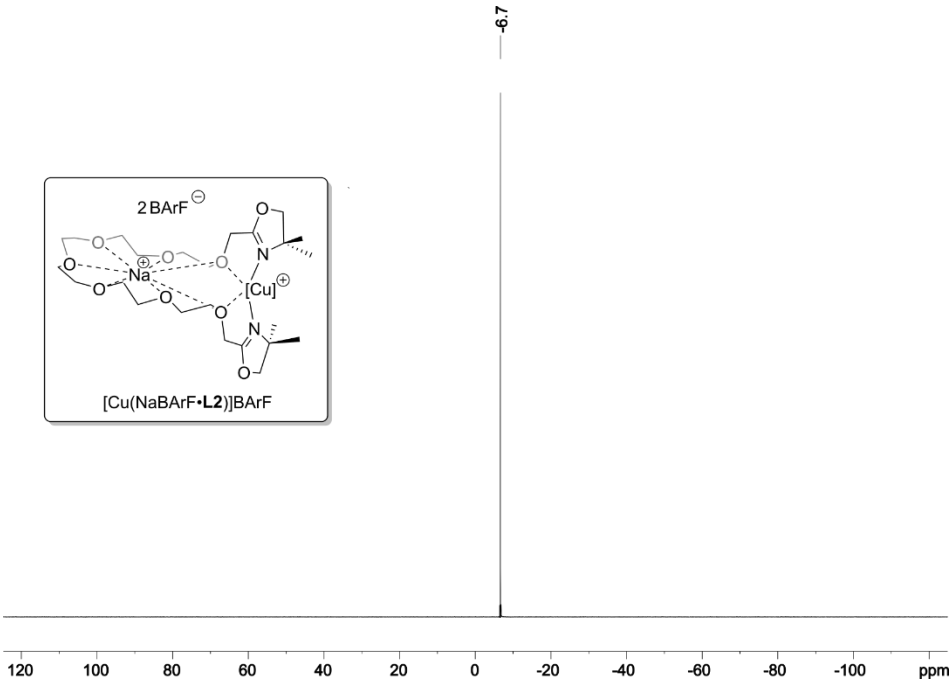

Figure 65. $^{11}B\{^{1}H\}$ NMR spectrum (128 MHz, CD_2Cl_2) of [Cu(NaBArF•**L2**)]BArF.

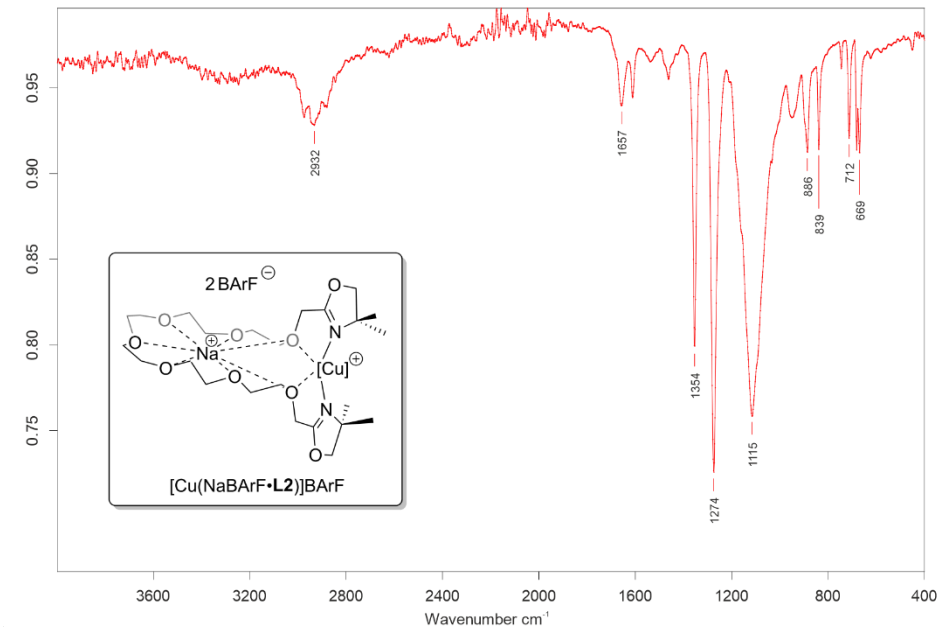

Figure 66. IR spectrum of [Cu(NaBArF•**L2**)]BArF.

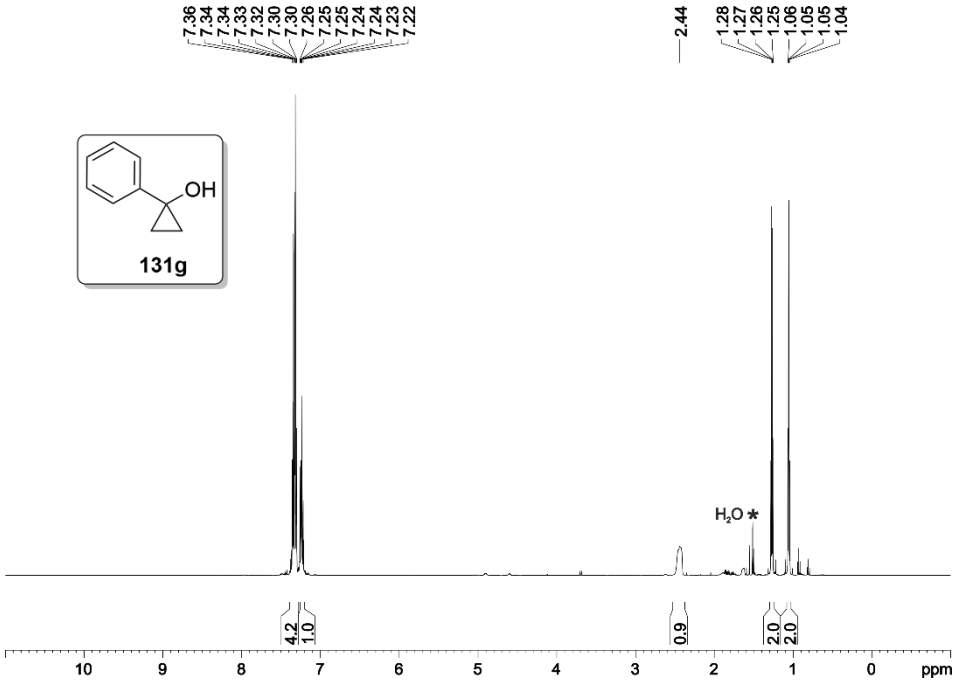

Figure 67. ^{1}H NMR spectrum (500 MHz, $CDCl_3$) of **131g**.

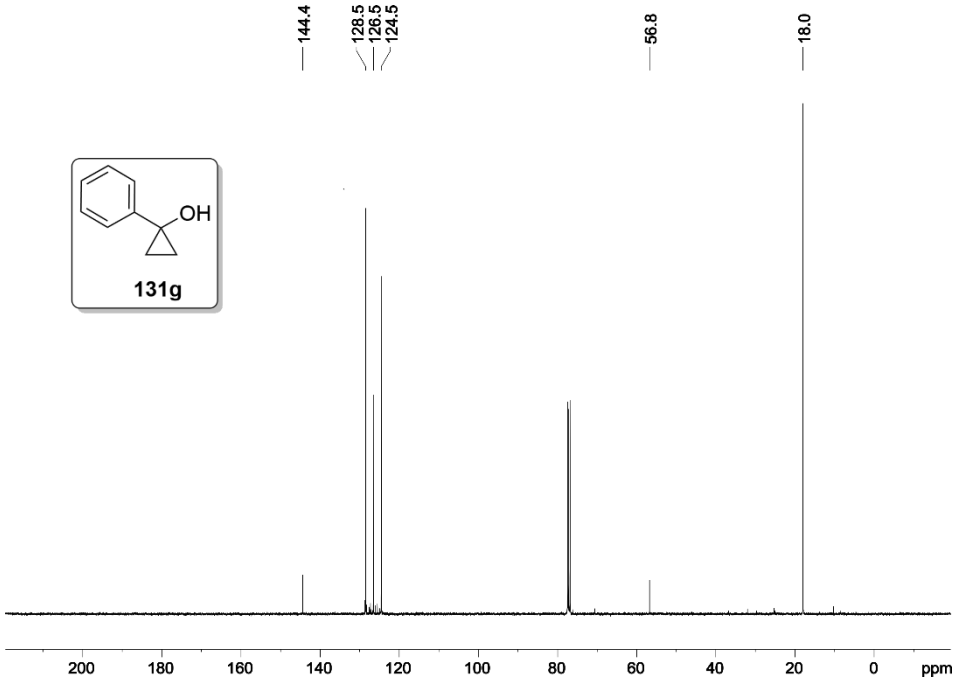

Figure 68. $^{13}C\{^{1}H\}$ NMR spectrum (101 MHz, $CDCl_3$) of **131g**.

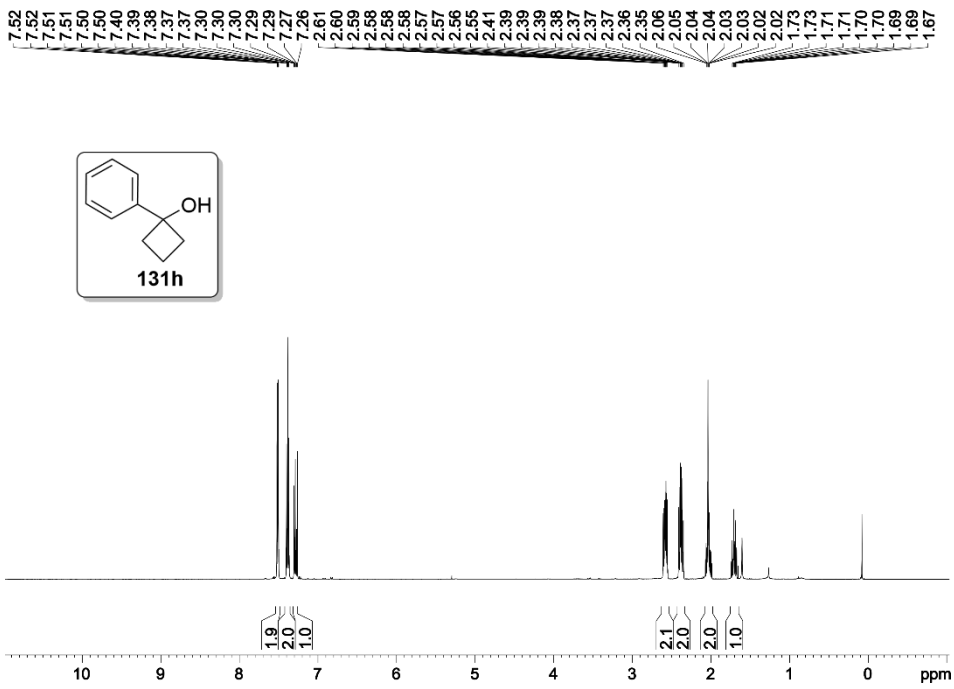

Figure 69. ^{1}H NMR spectrum (500 MHz, $CDCl_3$) of **131h**.

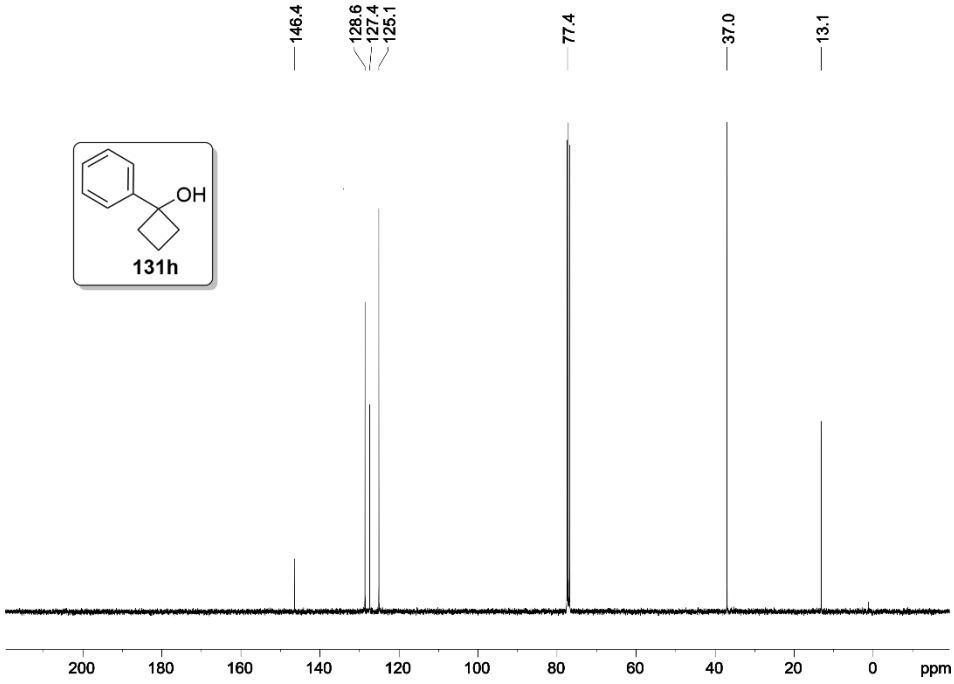

Figure 70. $^{13}C\{^{1}H\}$ NMR spectrum (101 MHz, $CDCl_3$) of **131h**.

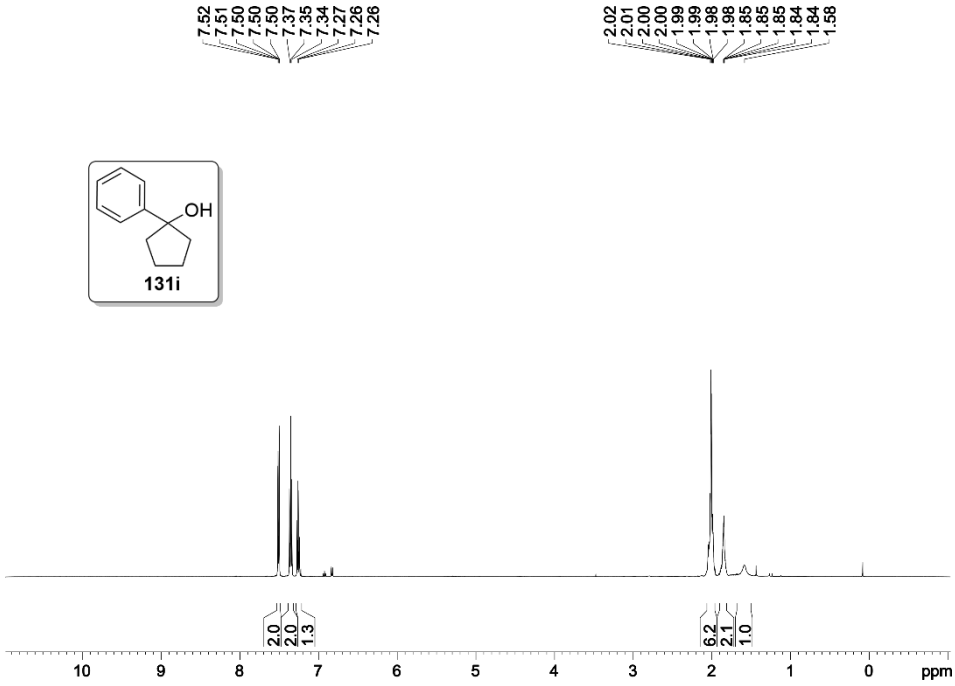

Figure 71. ^{1}H NMR spectrum (500 MHz, $CDCl_3$) of **131i**.

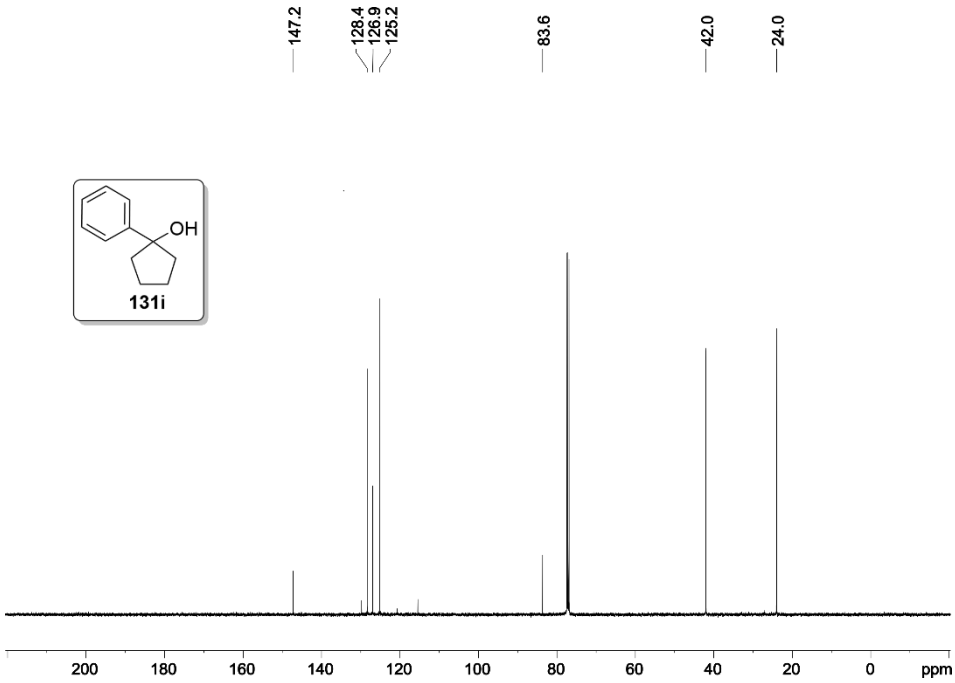

Figure 72. $^{13}C\{^{1}H\}$ NMR spectrum (126 MHz, $CDCl_3$) of **131i**.

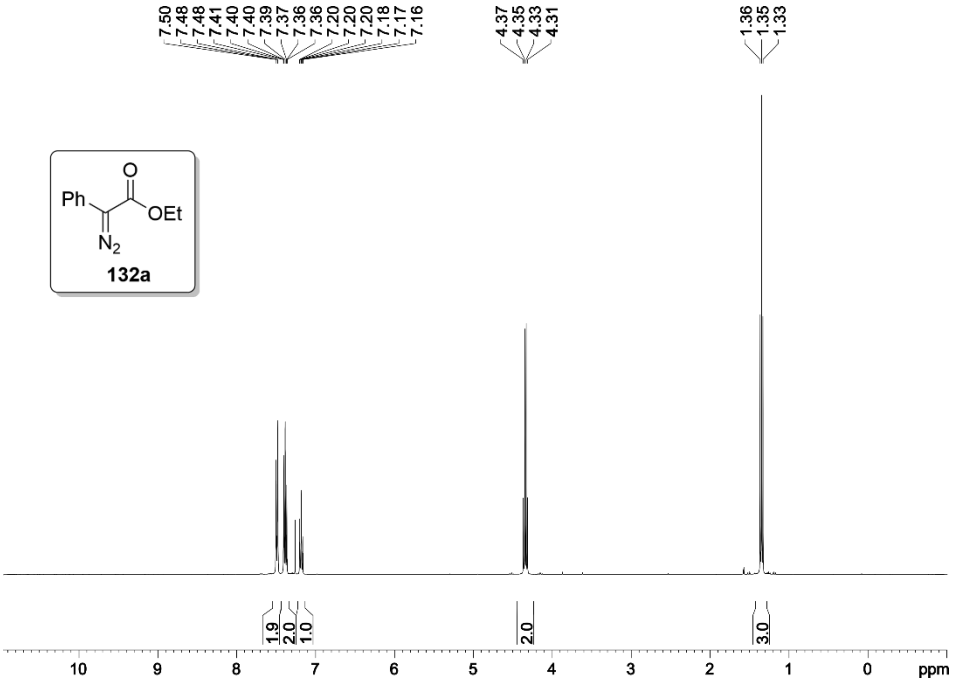

Figure 73. ^{1}H NMR spectrum (400 MHz, $CDCl_3$) of **132a**.

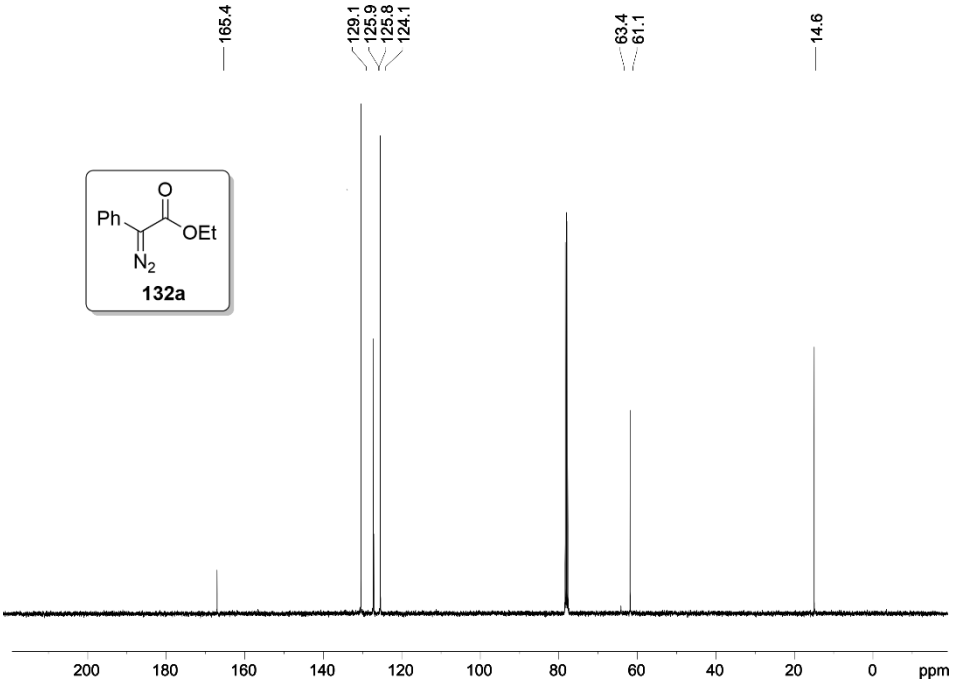

Figure 74. $^{13}C\{^{1}H\}$ NMR spectrum (101 MHz, $CDCl_3$) of **132a**.

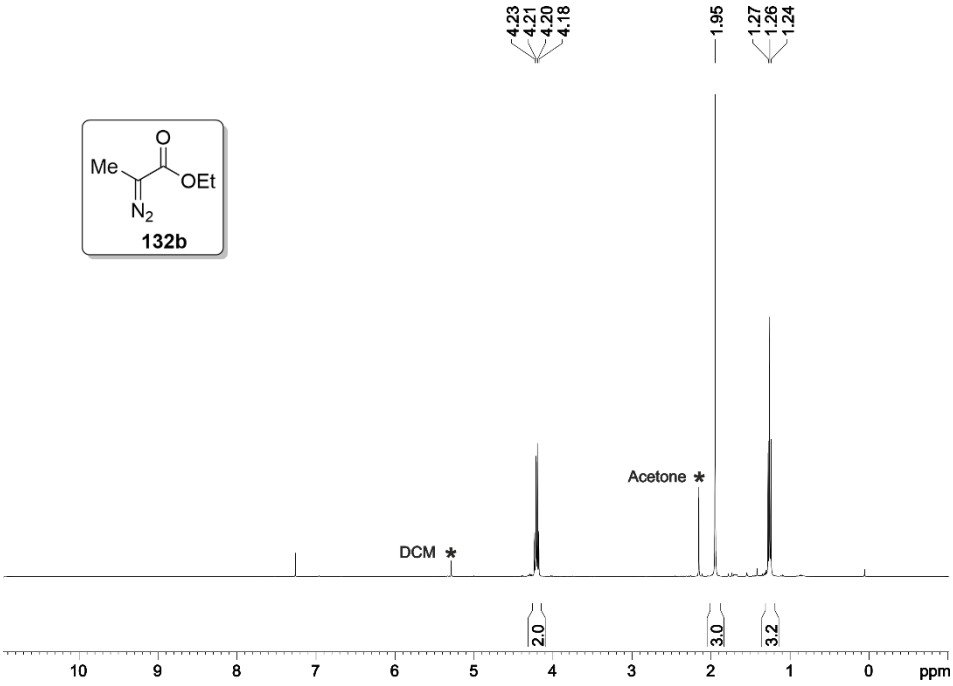

Figure 75. ^{1}H NMR spectrum (400 MHz, $CDCl_3$) of **132b**.

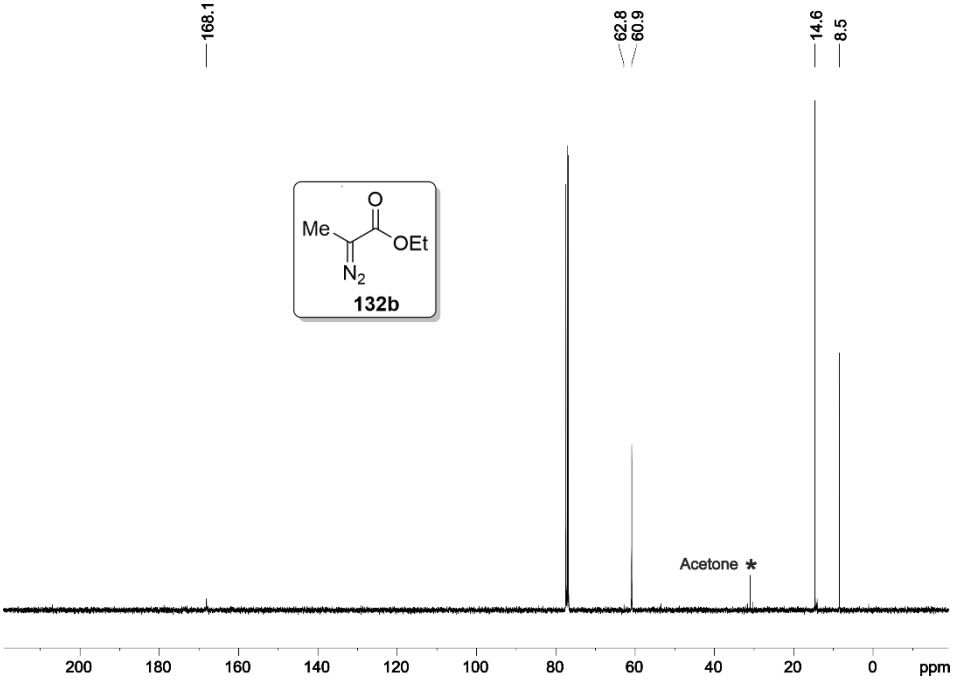

Figure 76. $^{13}C\{^{1}H\}$ NMR spectrum (101 MHz, $CDCl_3$) of **132b**.

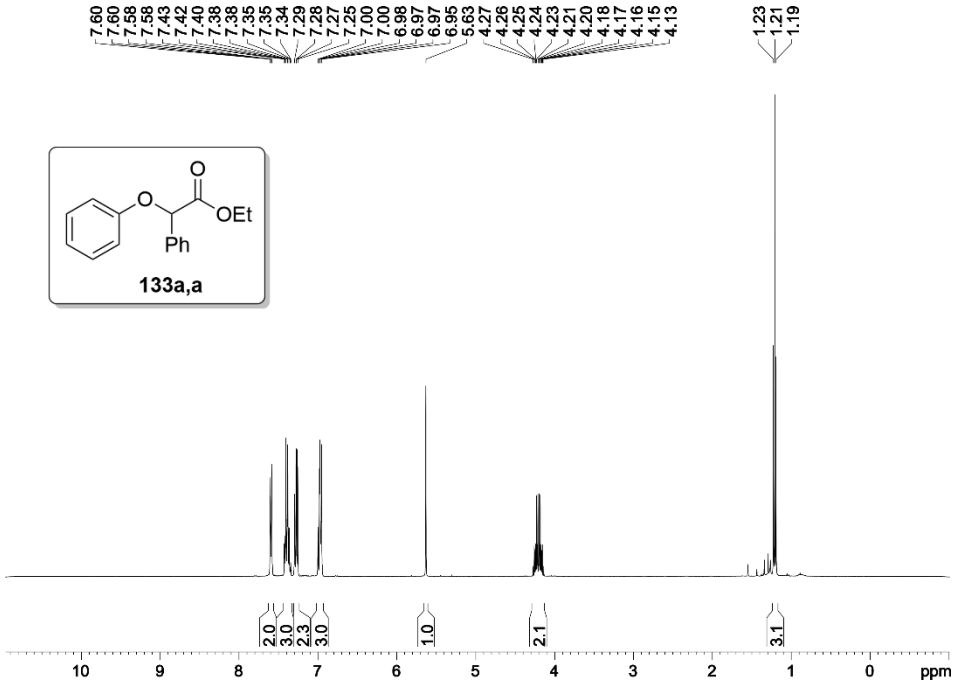

Figure 77. ^{1}H NMR spectrum (400 MHz, $CDCl_3$) of **133a,a**.

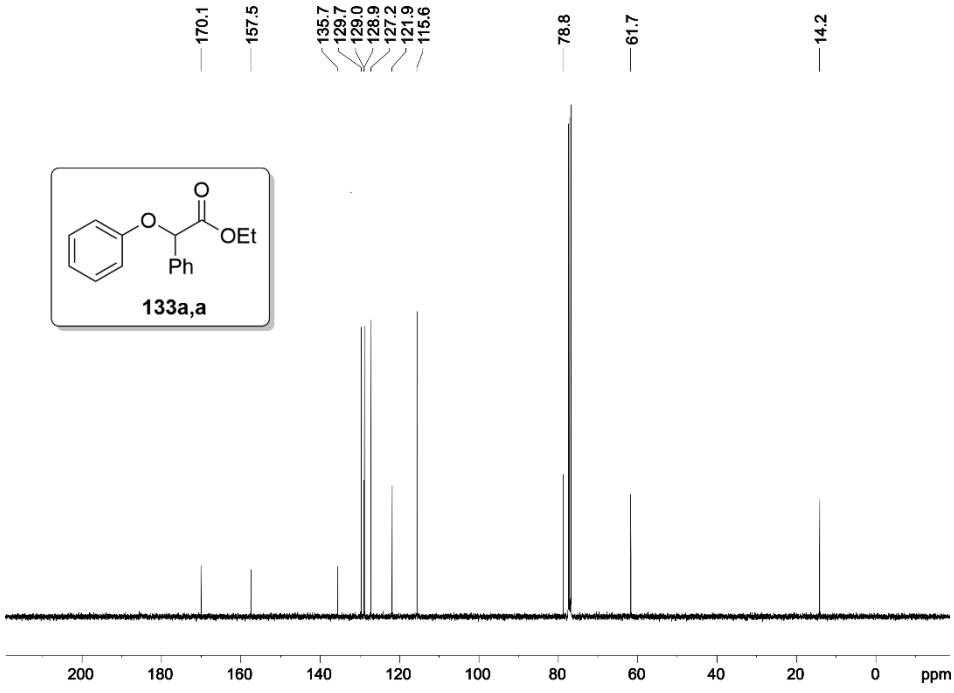

Figure 78. $^{13}C\{^{1}H\}$ NMR spectrum (101 MHz, $CDCl_3$) of **133a,a**.

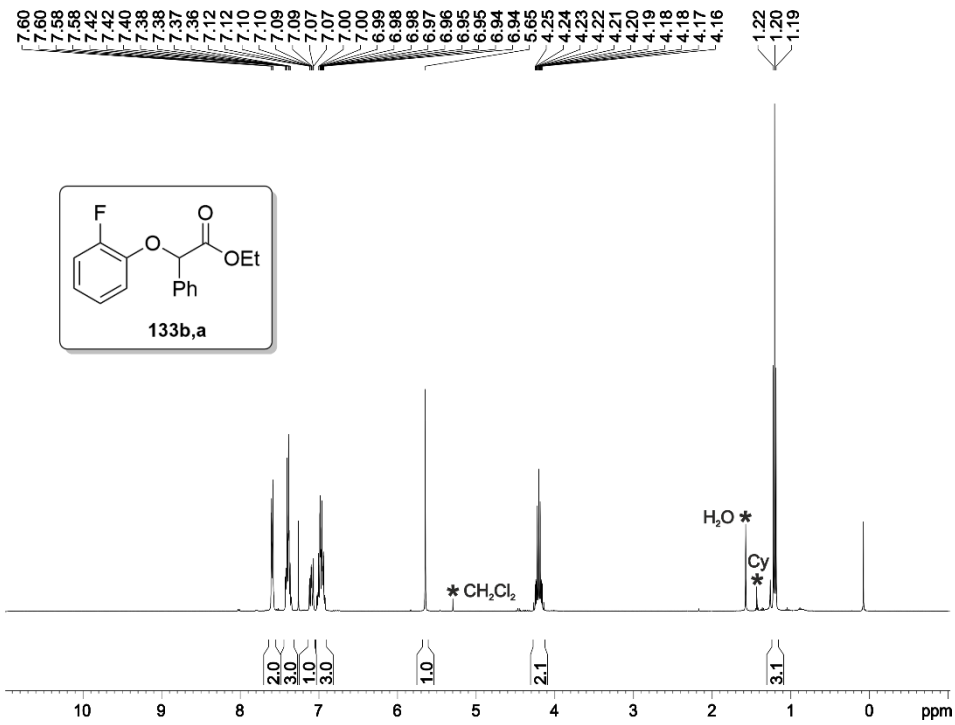

Figure 79. ^{1}H NMR spectrum (400 MHz, $CDCl_3$) of **133b,a**.

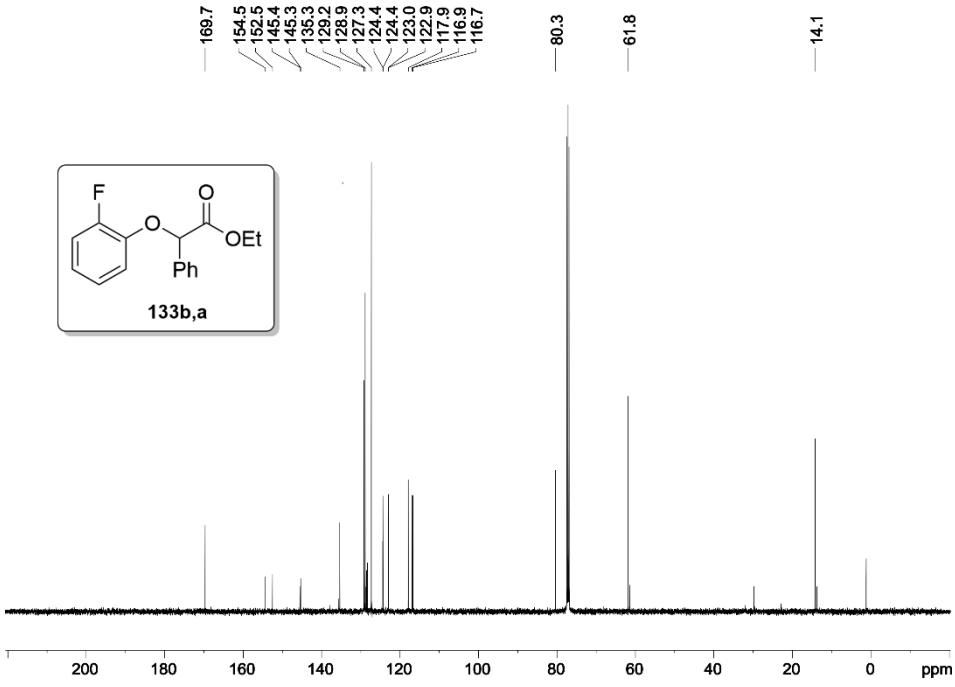

Figure 80. $^{13}C\{^{1}H\}$ NMR spectrum (101 MHz, $CDCl_3$) of **133b,a**.

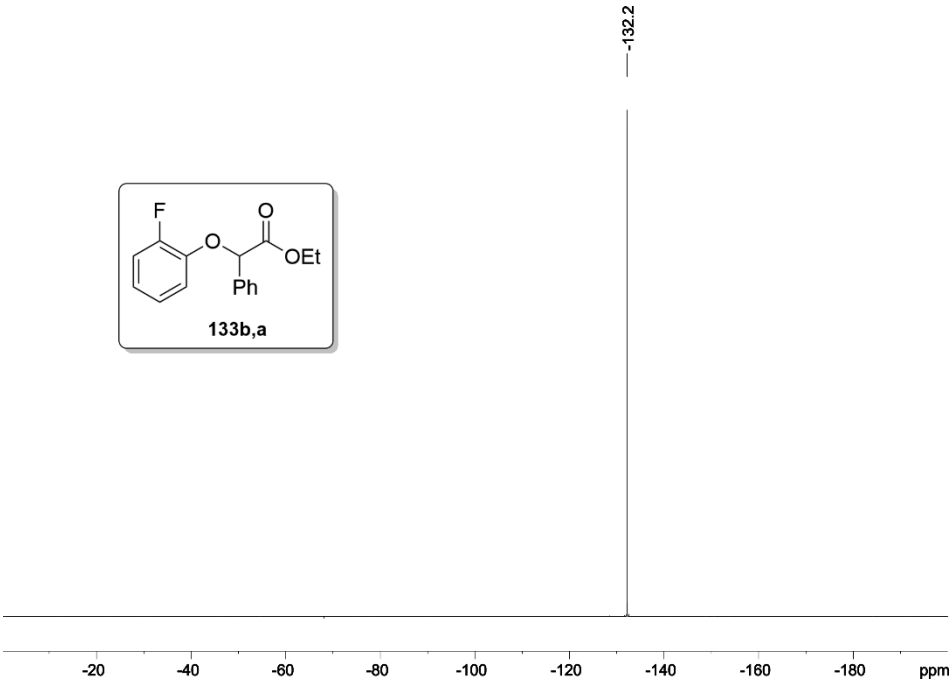

Figure 81. $^{19}F\{^{1}H\}$ NMR spectrum (376 MHz, $CDCl_3$) of **133b,a**.

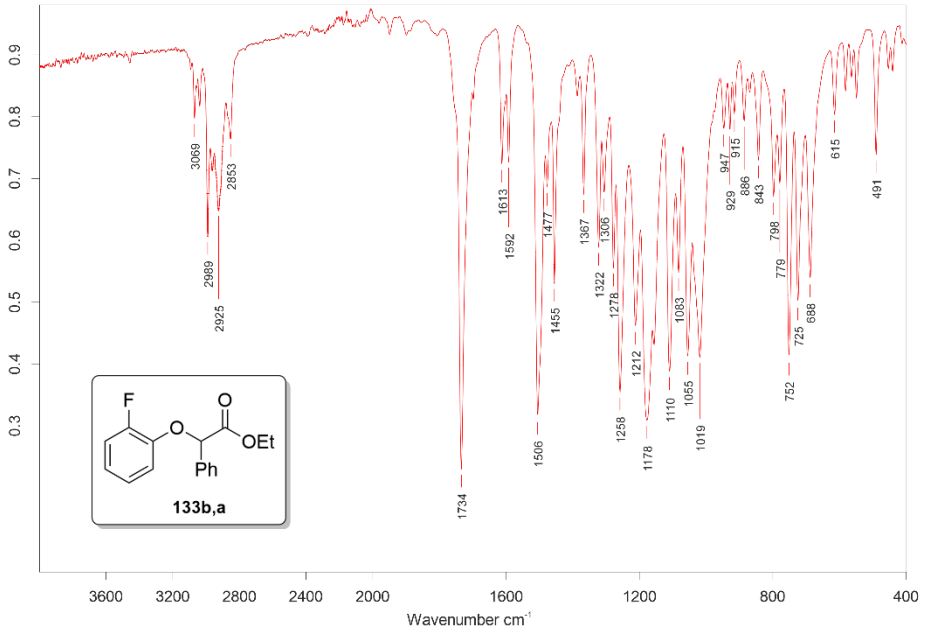

Figure 82. IR spectrum of **133b,a**.

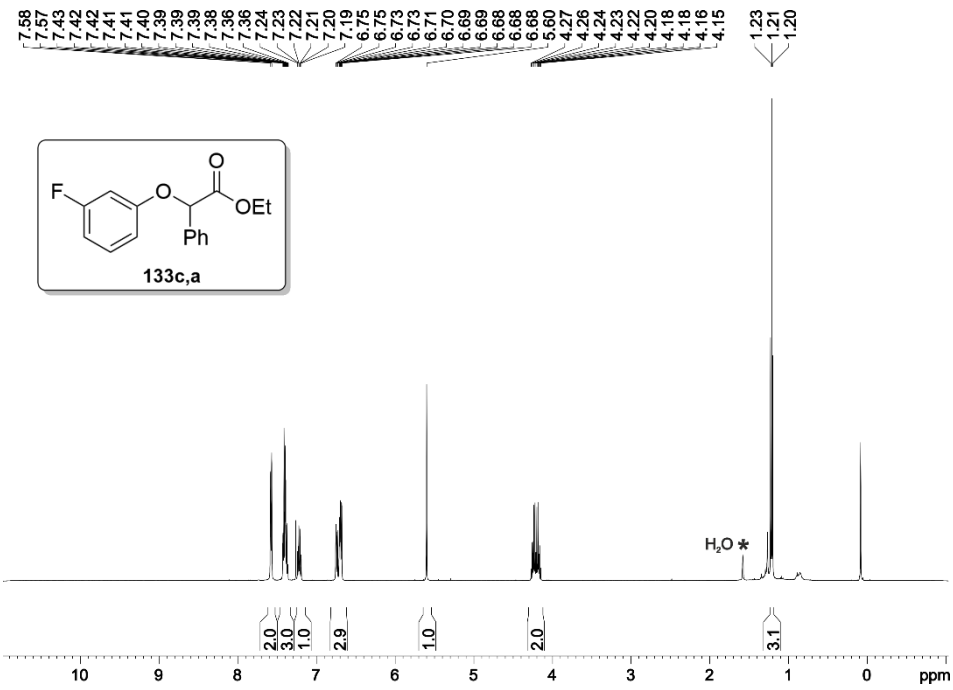

Figure 83. ^{1}H NMR spectrum (500 MHz, $CDCl_3$) of **133c,a**.

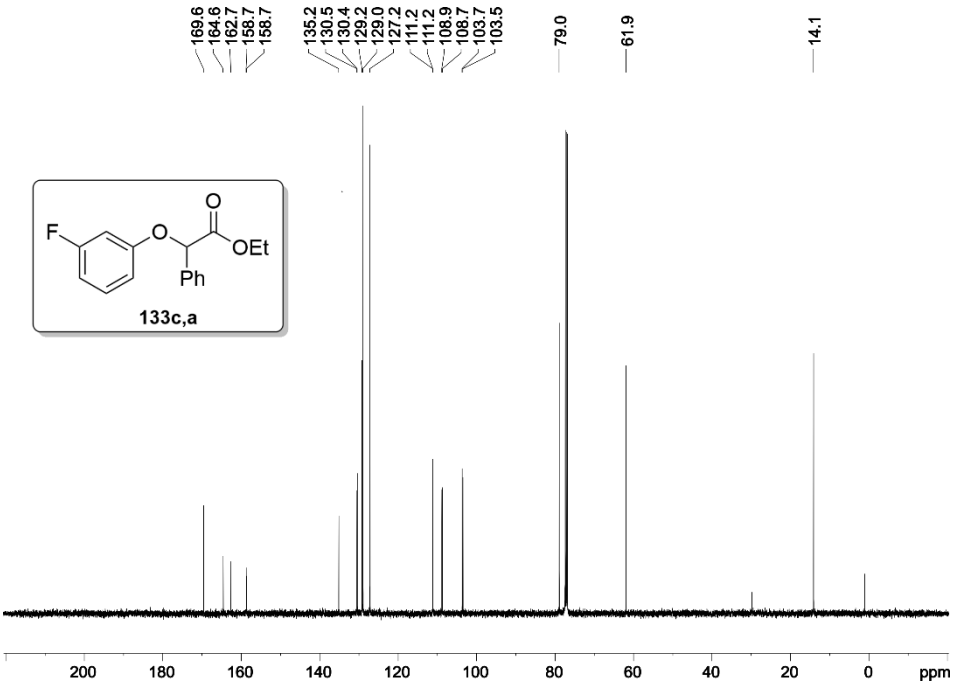

Figure 84. $^{13}C\{^{1}H\}$ NMR spectrum (126 MHz, $CDCl_3$) of **133c,a**.

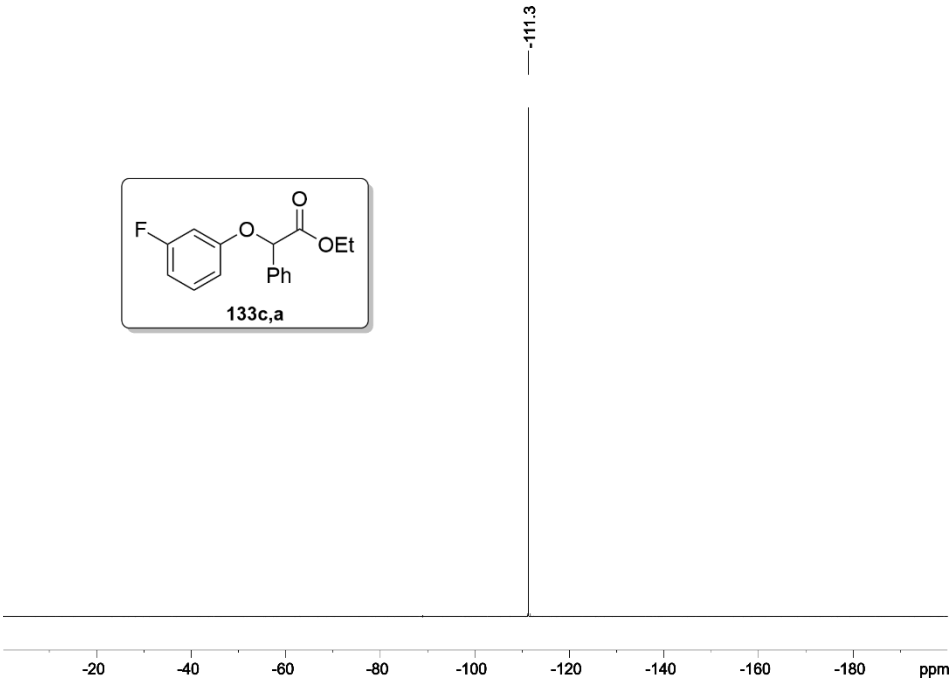

Figure 85. $^{19}F\{^{1}H\}$ NMR spectrum (376 MHz, $CDCl_3$) of **133c,a**.

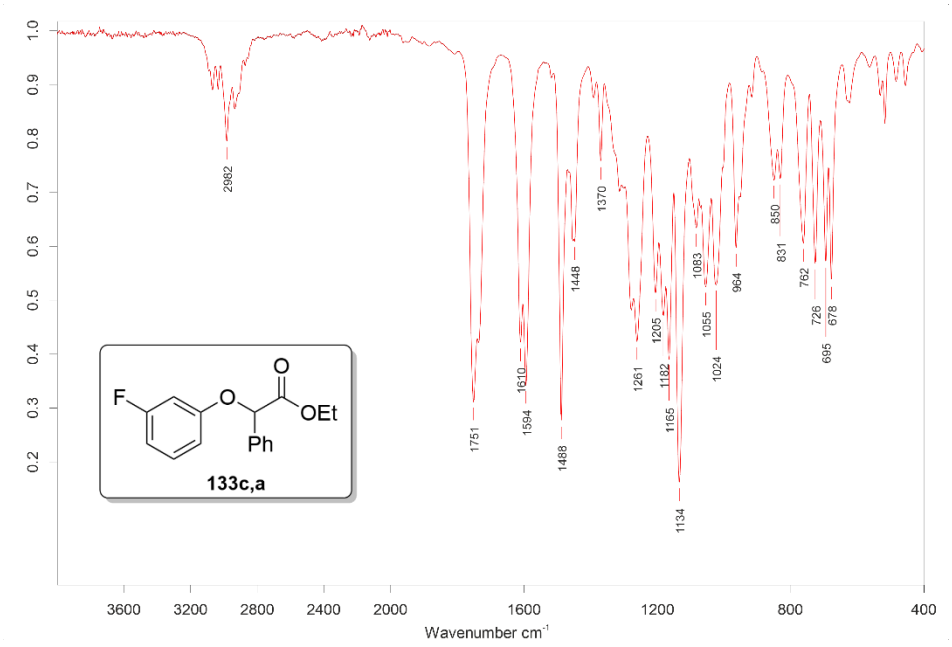

Figure 86. IR spectrum of **133c,a**.

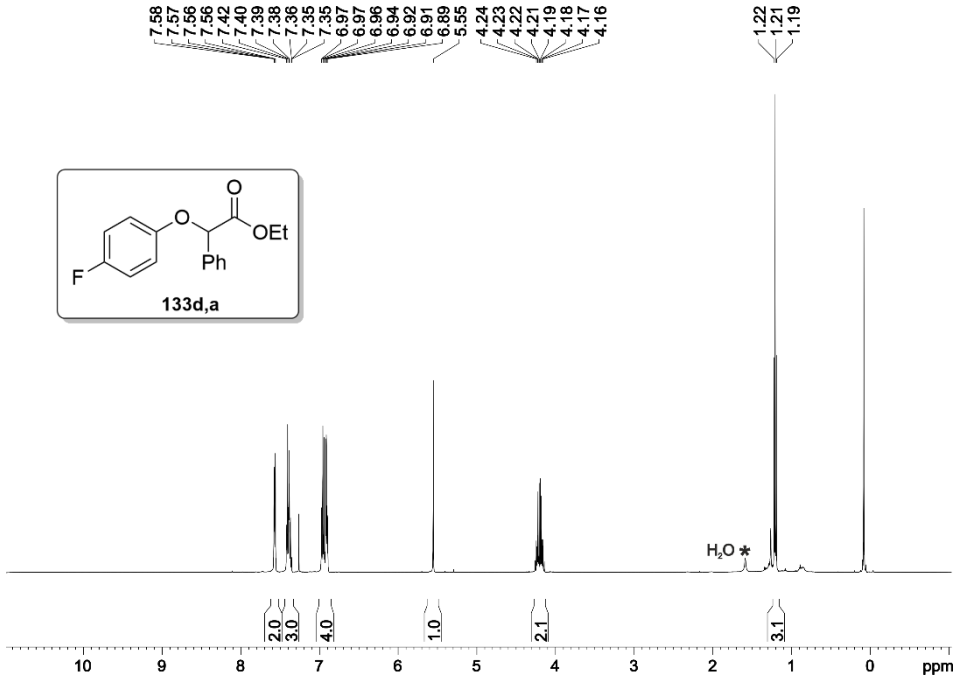

Figure 87. ^{1}H NMR spectrum (500 MHz, $CDCl_3$) of 133d,a.

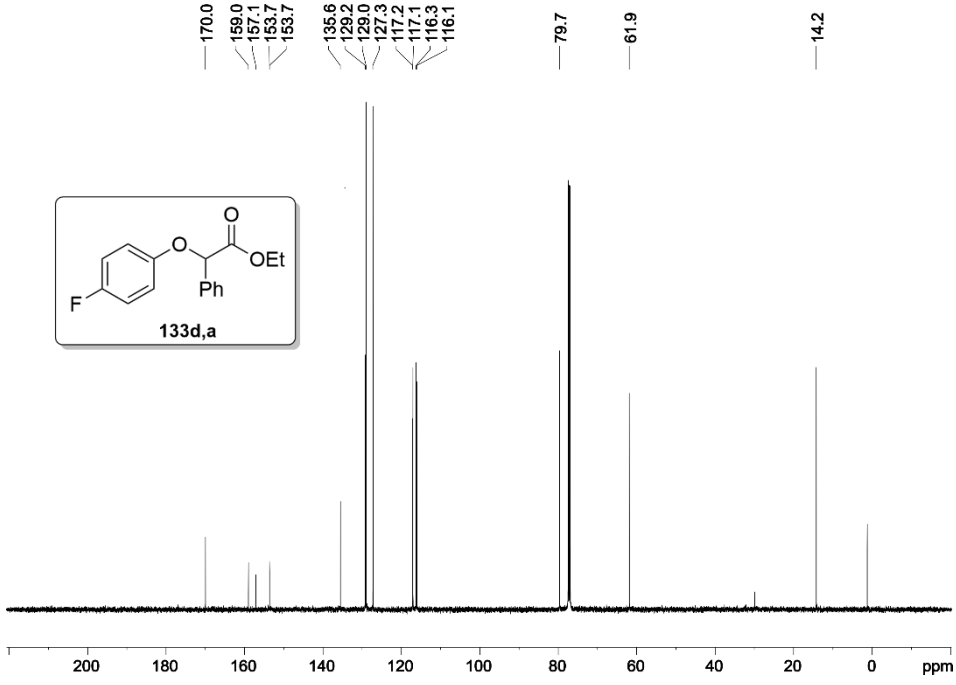

Figure 88. $^{13}C\{^{1}H\}$ NMR spectrum (126 MHz, $CDCl_3$) of **133d,a**.

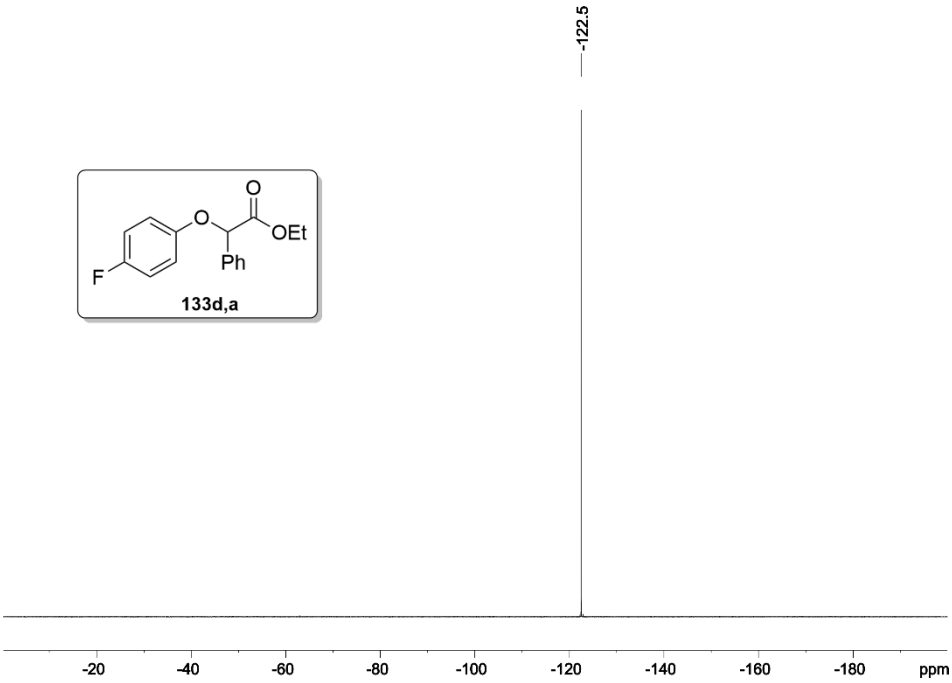

Figure 89. $^{19}F\{^{1}H\}$ NMR spectrum (376 MHz, $CDCl_3$) of **133d,a**.

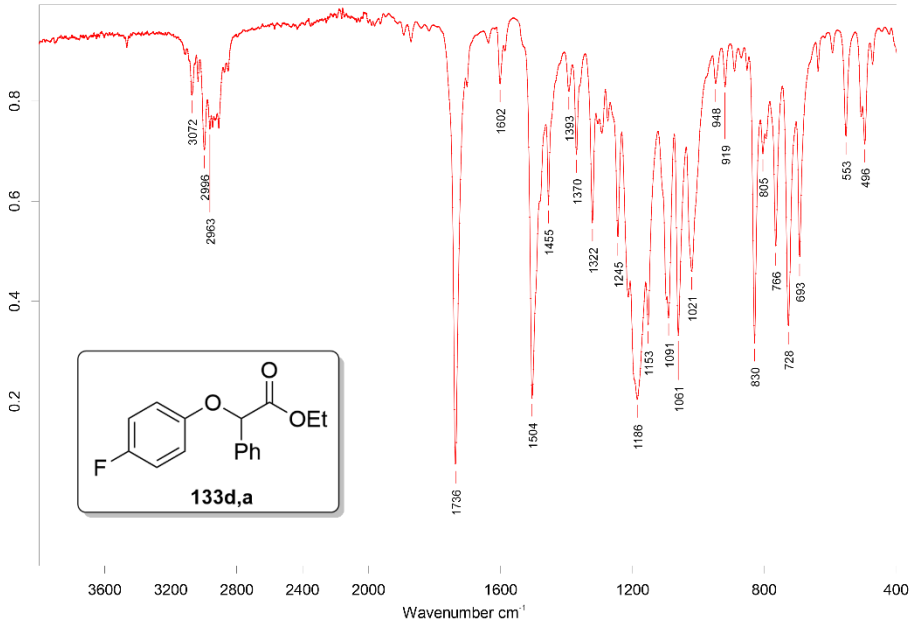

Figure 90. IR spectrum of **133d,a**.

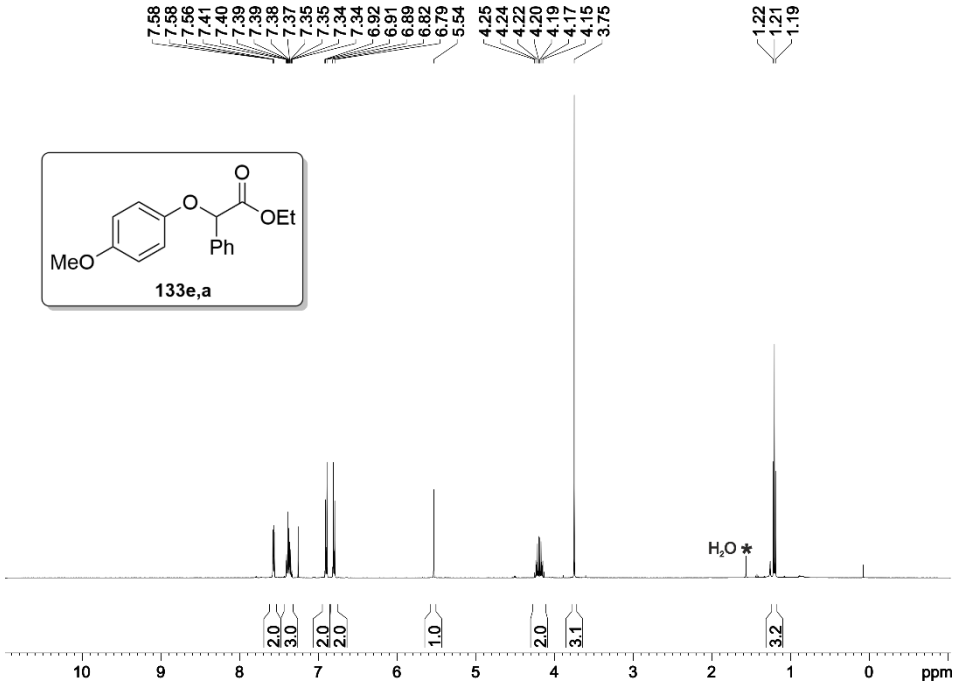

Figure 91. ^{1}H NMR spectrum (500 MHz, $CDCl_3$) of **133e,a**.

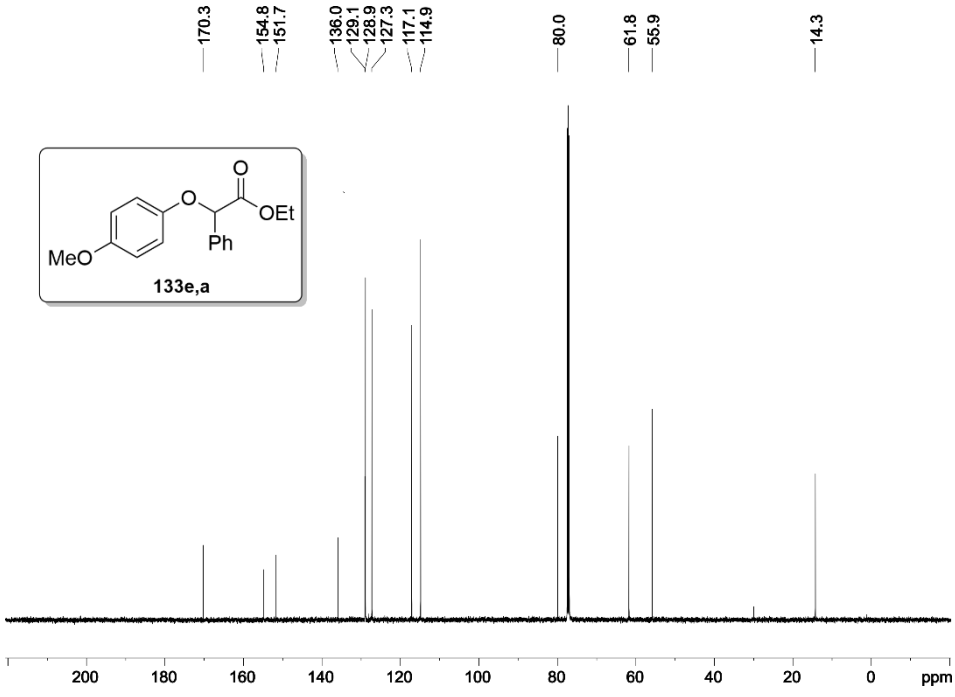

Figure 92. $^{13}C\{^{1}H\}$ NMR spectrum (126 MHz, $CDCl_3$) of **133e,a**.

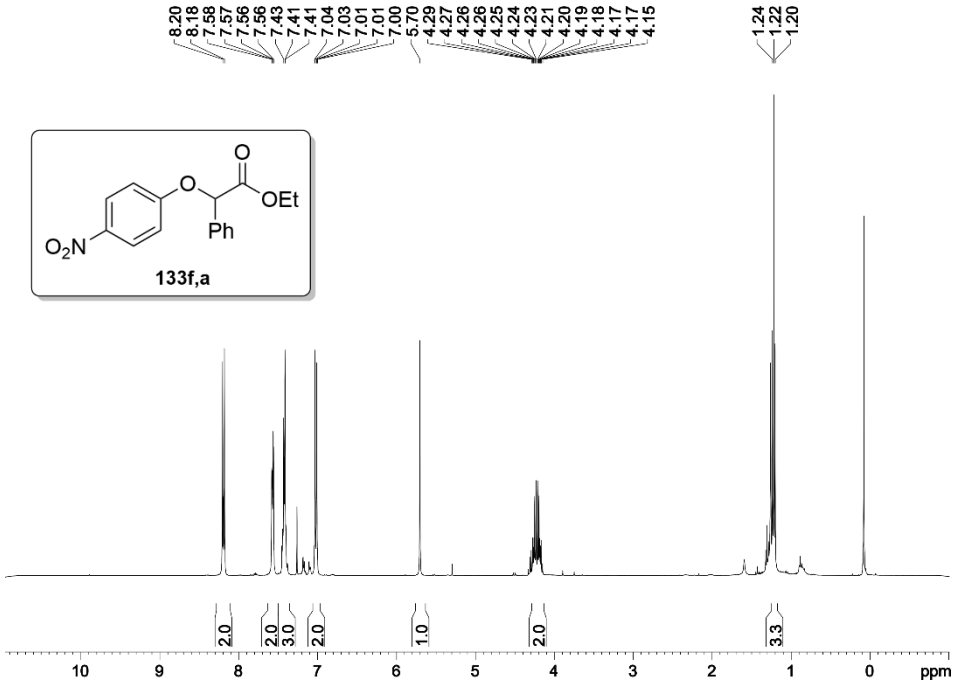

Figure 93. ^{1}H NMR spectrum (400 MHz, $CDCl_3$) of **133f,a**.

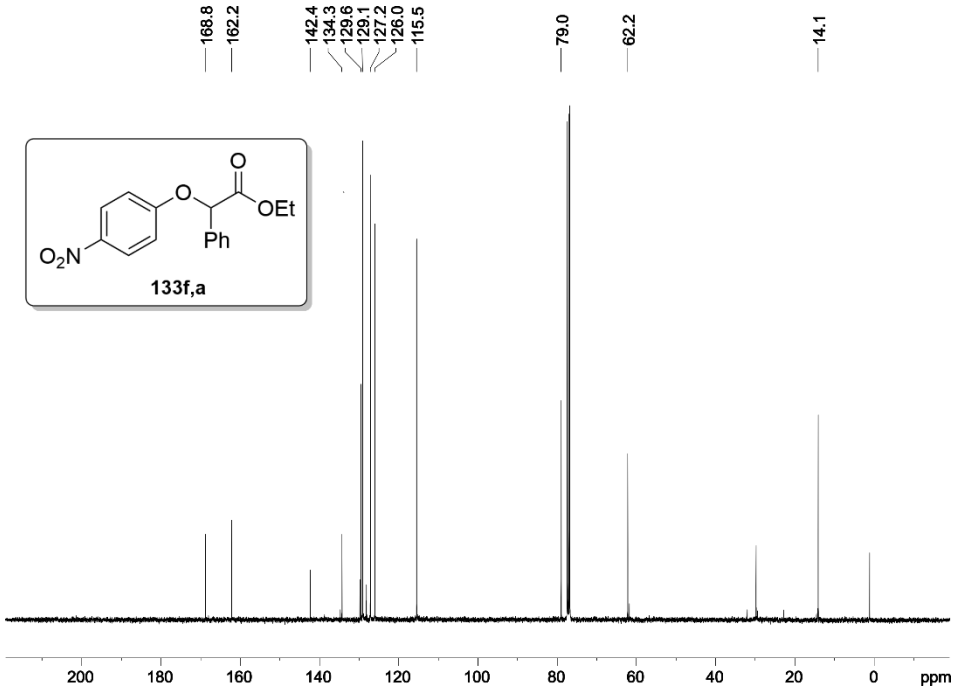

Figure 94. $^{13}C\{^{1}H\}$ NMR spectrum (101 MHz, $CDCl_3$) of **133f,a**.

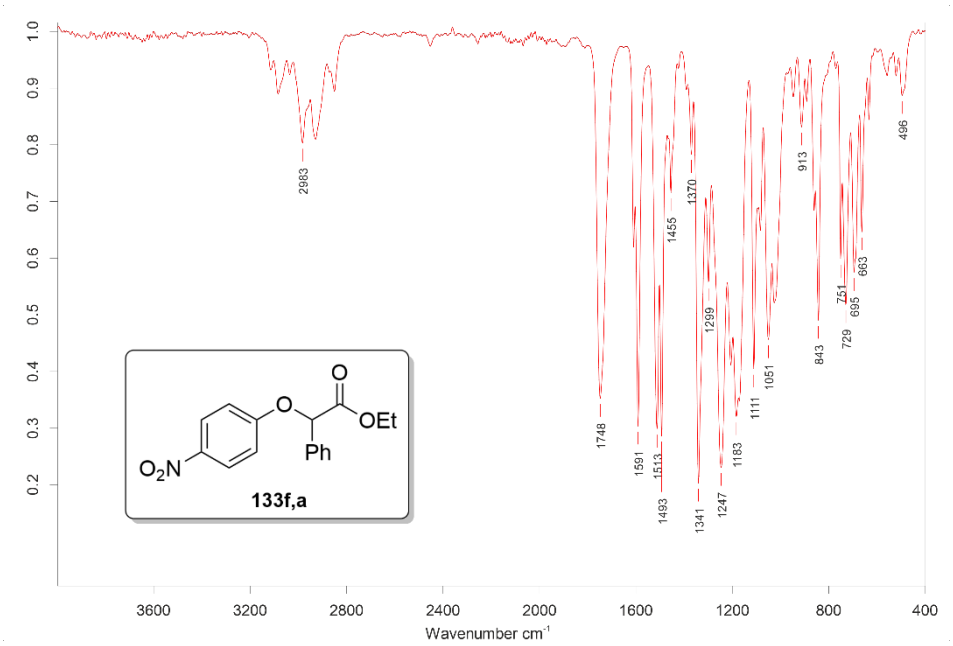

Figure 95. IR spectrum of **133f,a**.

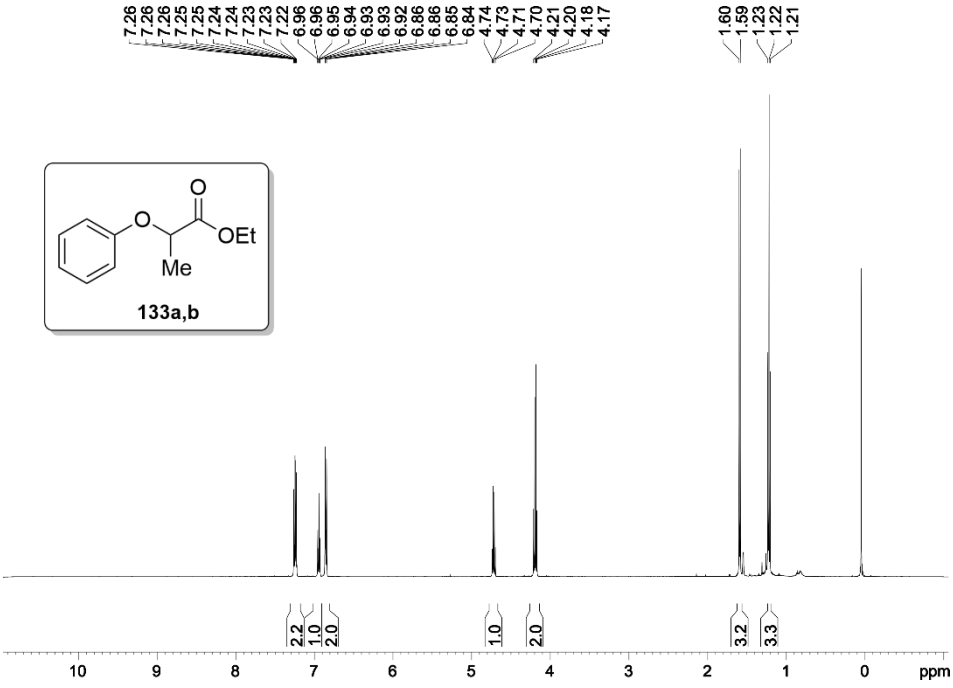

Figure 96. ^{1}H NMR spectrum (500 MHz, $CDCl_3$) of **133a,b**.

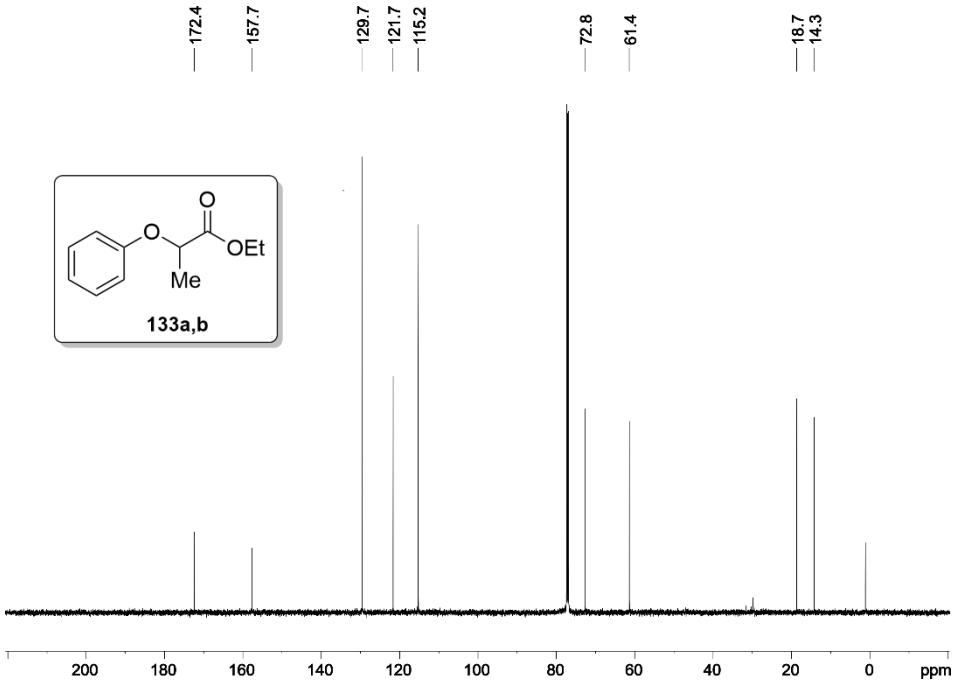

Figure 97. $^{13}C\{^{1}H\}$ NMR spectrum (126 MHz, $CDCl_3$) of **133a,b**.

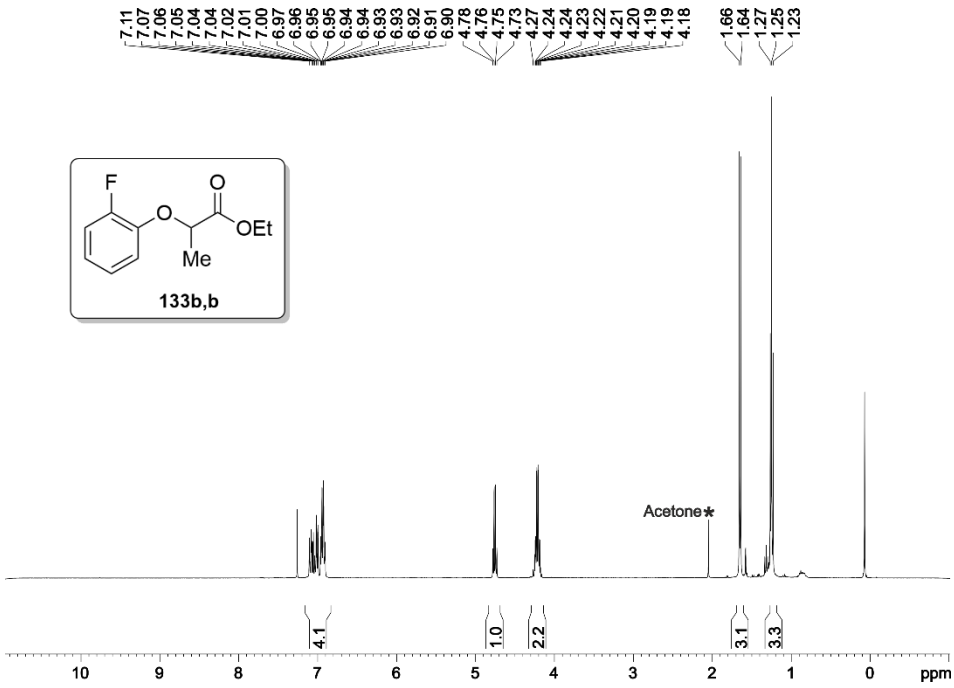

Figure 98. ^{1}H NMR spectrum (400 MHz, $CDCl_3$) of **133b,b**.

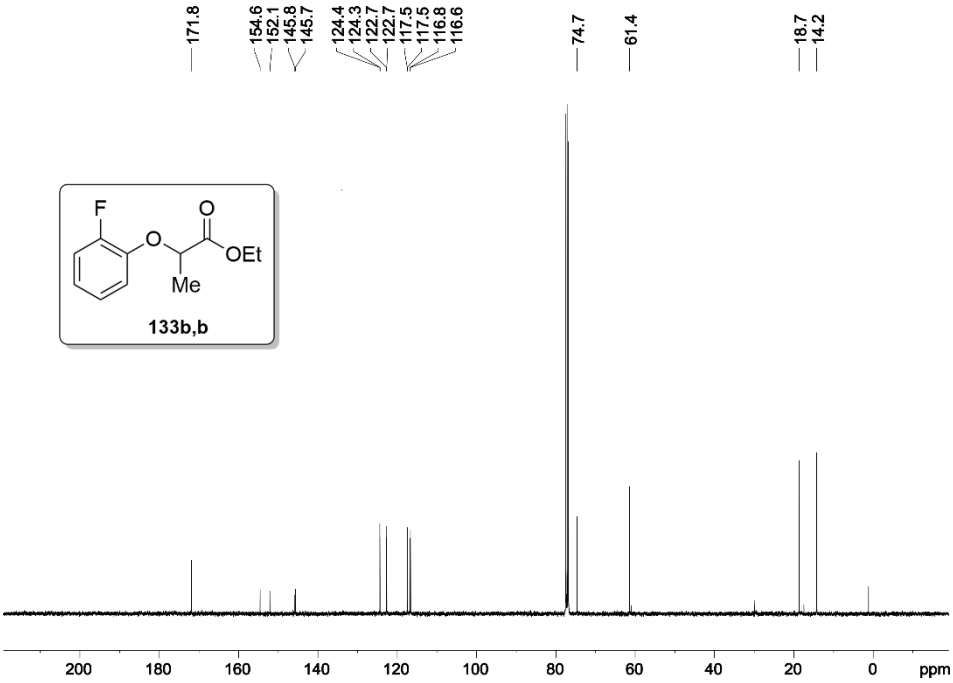

Figure 99. $^{13}C\{^{1}H\}$ NMR spectrum (101 MHz, $CDCl_3$) of **133b,b**.

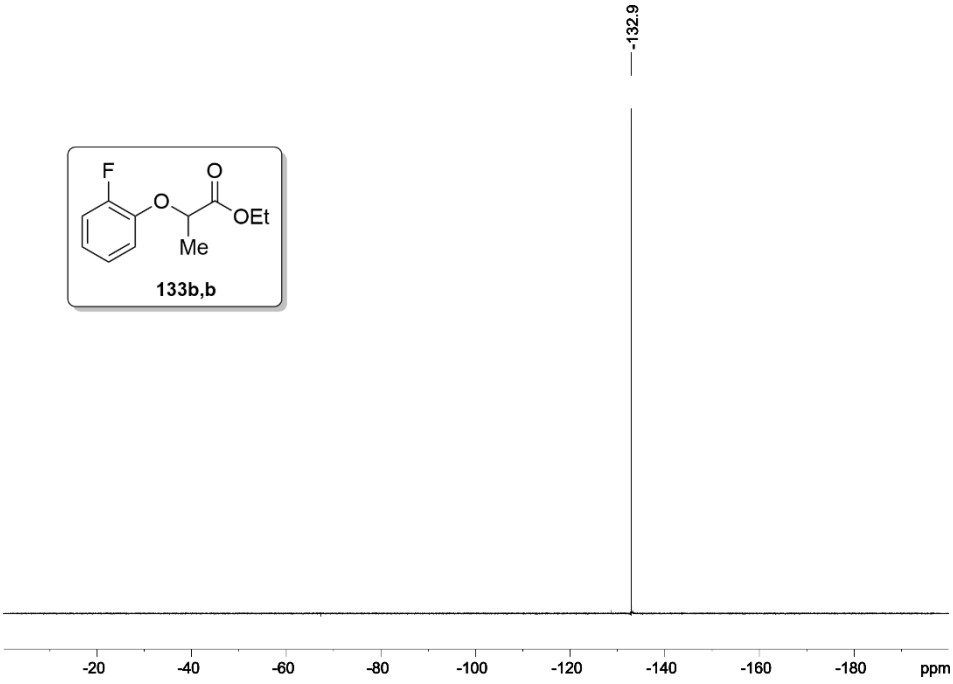

Figure 100. $^{19}F\{^{1}H\}$ NMR spectrum (376 MHz, $CDCl_3$) of **133b,b**.

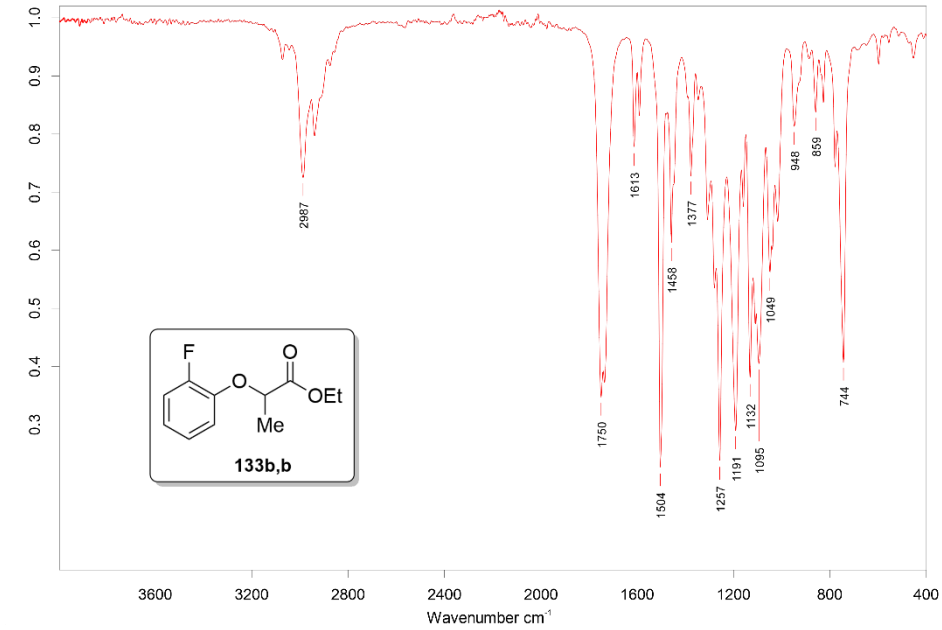

Figure 101. IR spectrum of **133b,b**.

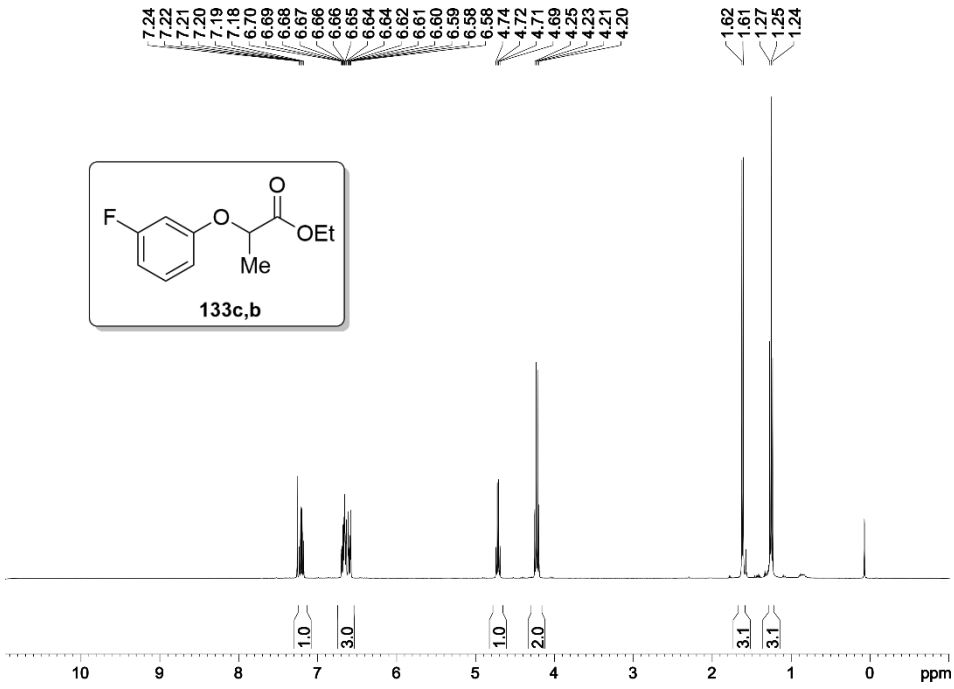

Figure 102. ^{1}H NMR spectrum (400 MHz, $CDCl_3$) of **133c,b**.

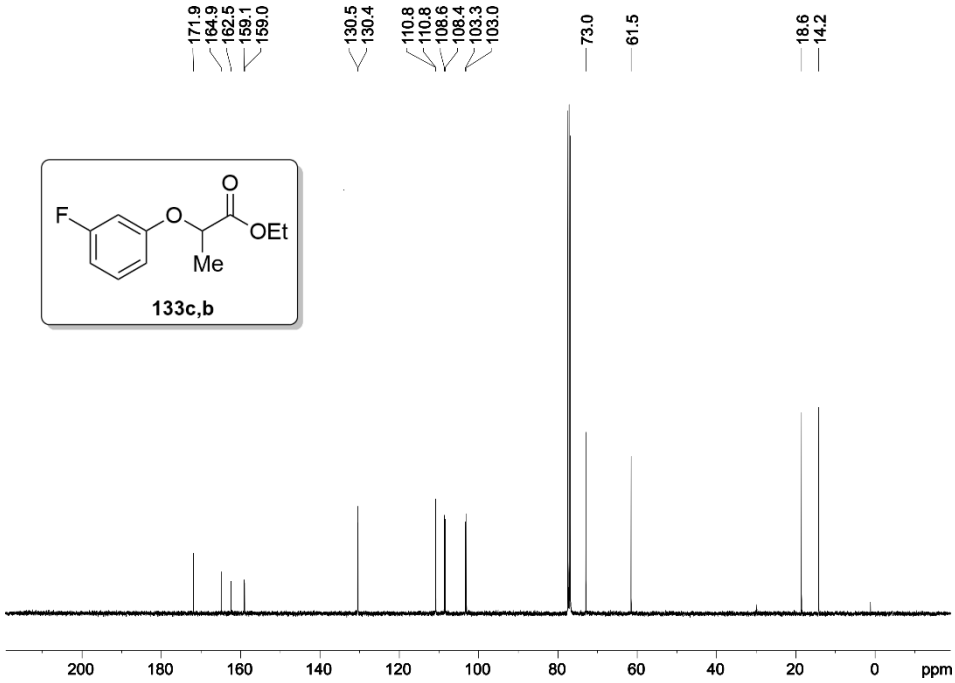

Figure 103. $^{13}C\{^{1}H\}$ NMR spectrum (101 MHz, $CDCl_3$) of **133c,b**.

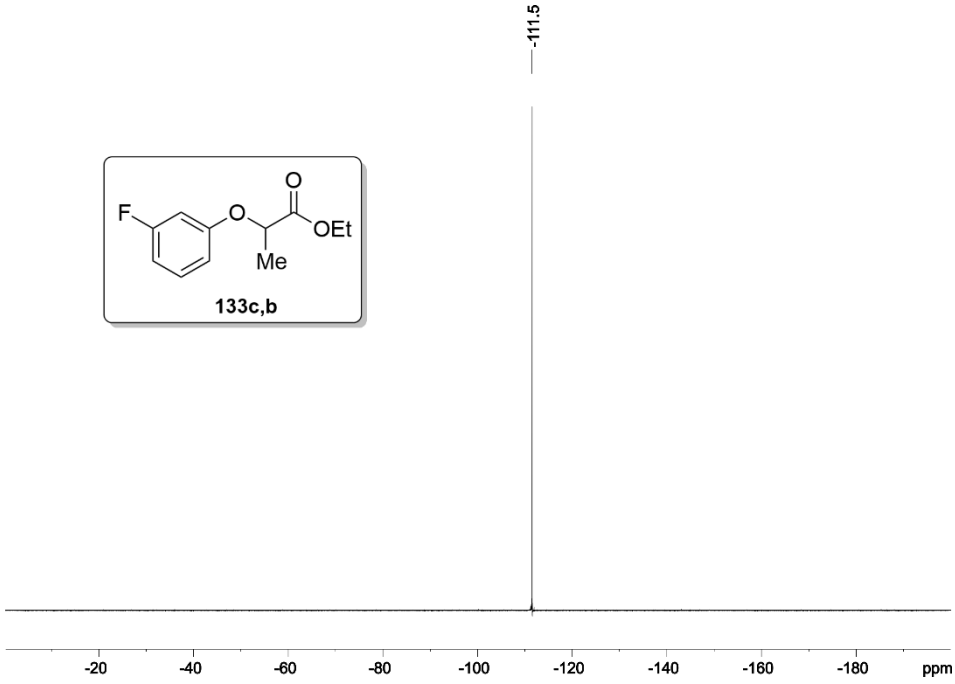

Figure 104. $^{19}F\{^{1}H\}$ NMR spectrum (376 MHz, $CDCl_3$) of **133c,b**.

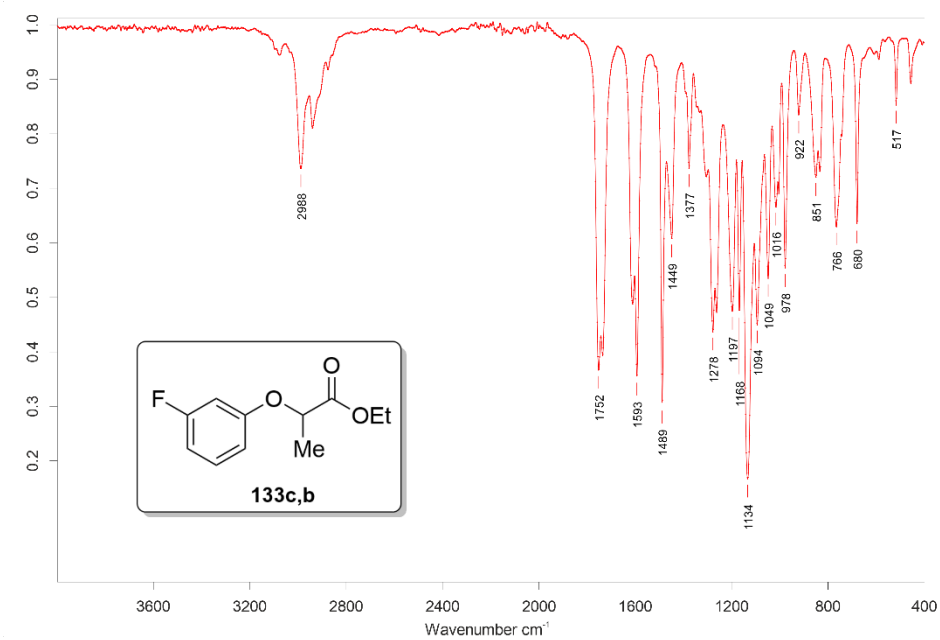

Figure 105. IR spectrum of **133c,b**.

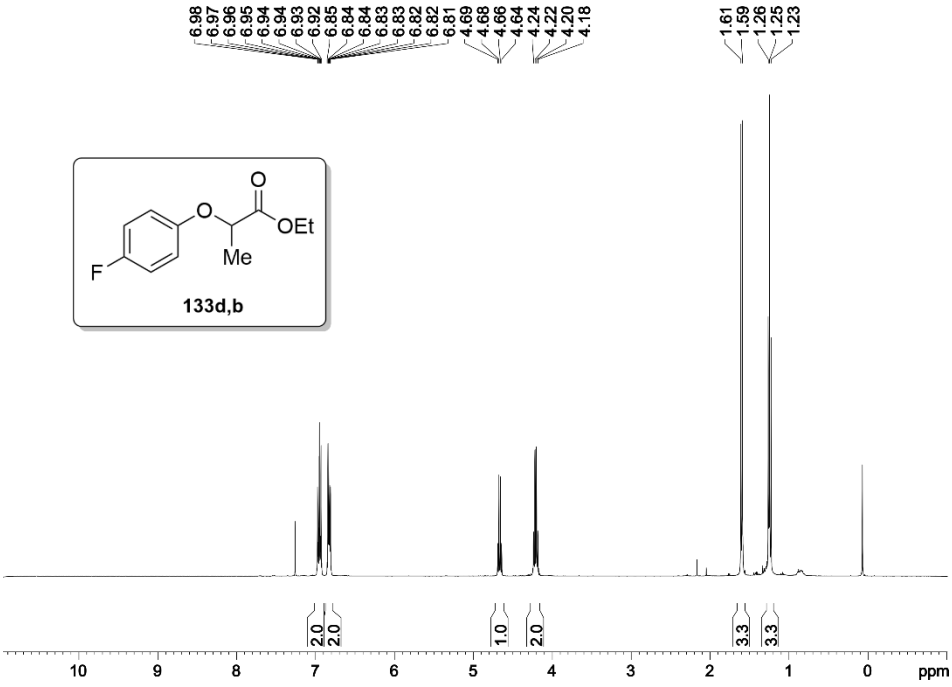

Figure 106. ^{1}H NMR spectrum (400 MHz, $CDCl_3$) of **133d,b.**

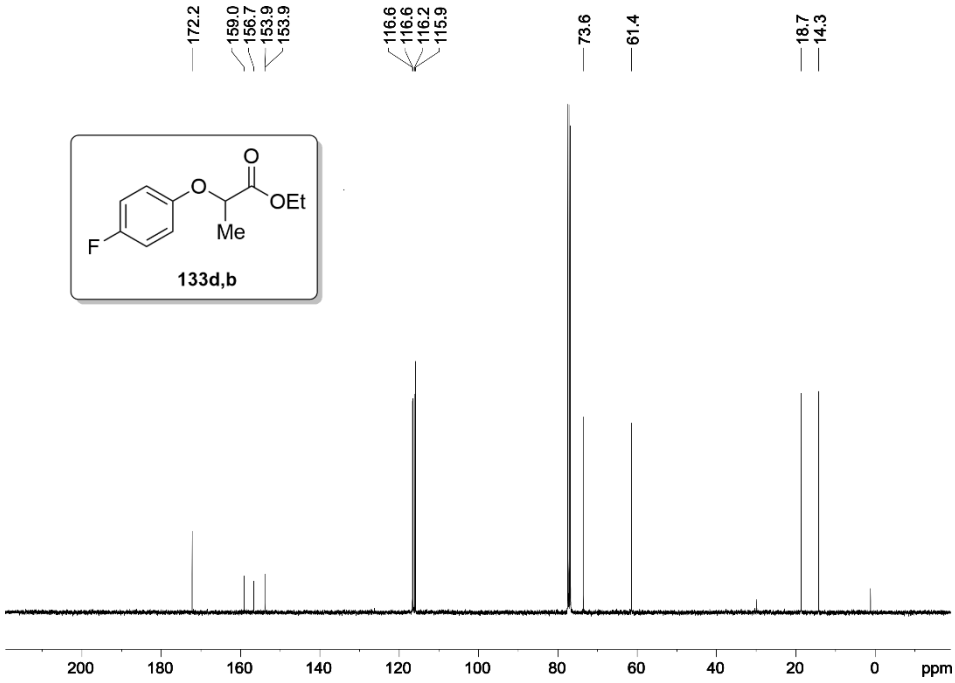

Figure 107. $^{13}C\{^{1}H\}$ NMR spectrum (101 MHz, $CDCl_3$) of **133d,b**.

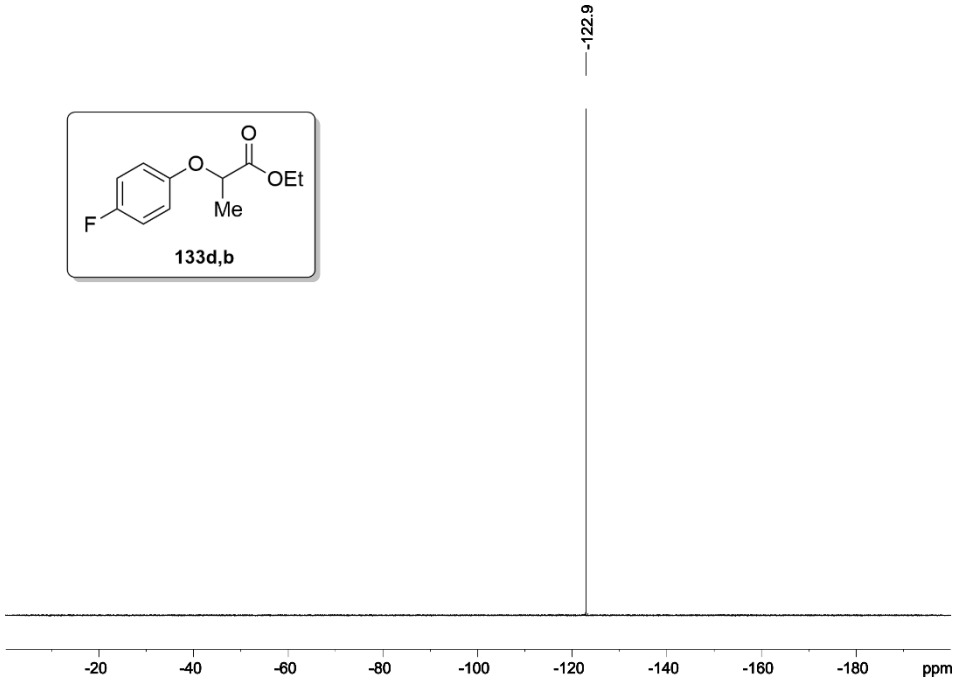

Figure 108. $^{19}F\{^{1}H\}$ NMR spectrum (376 MHz, $CDCl_3$) of **133d,b**.

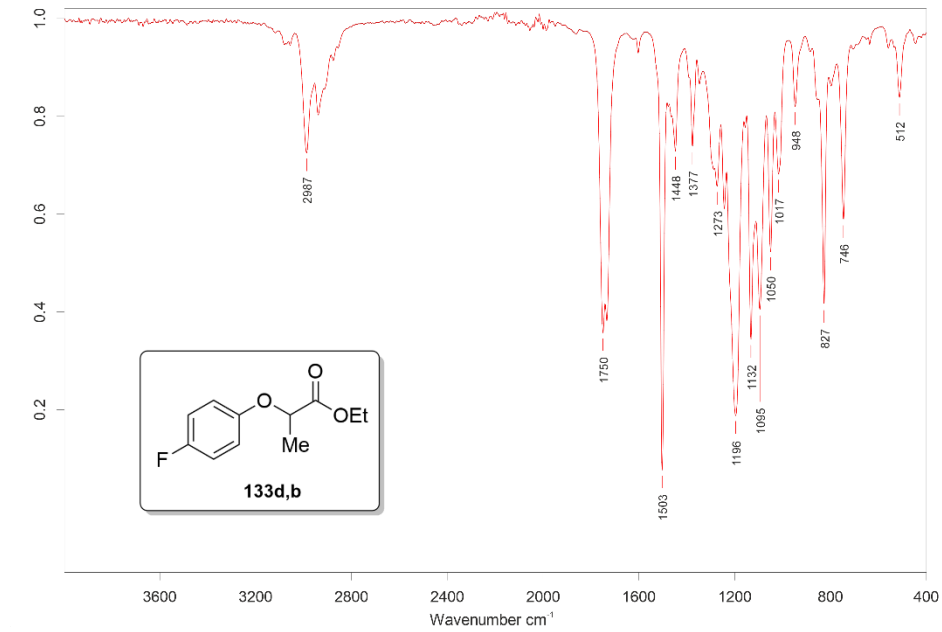

Figure 109. IR spectrum of **133d,b**.

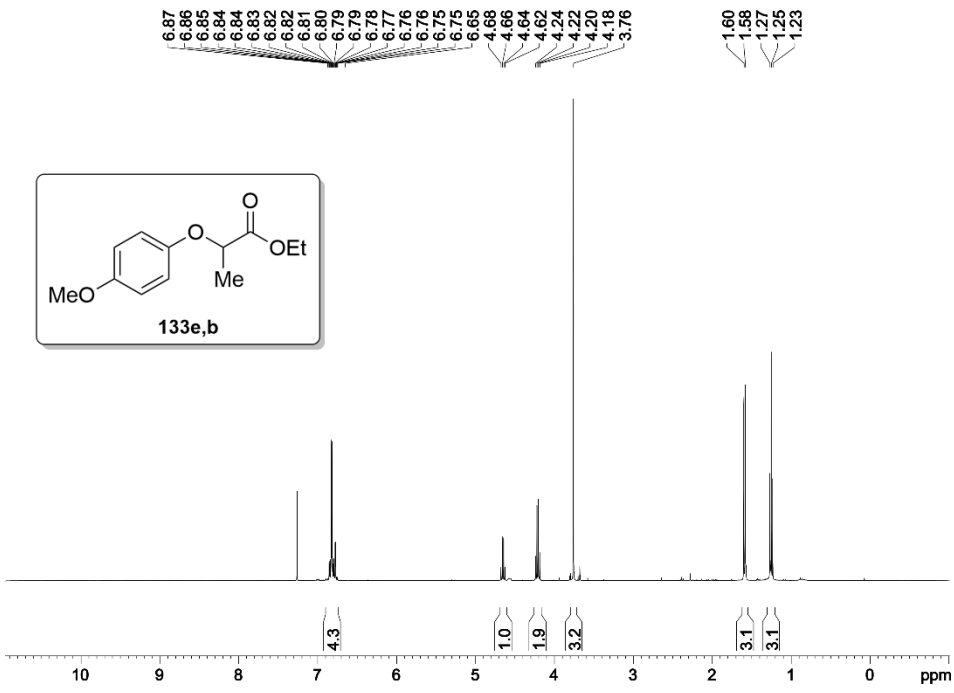

Figure 110. ^{1}H NMR spectrum (400 MHz, $CDCl_3$) of **133e,b**.

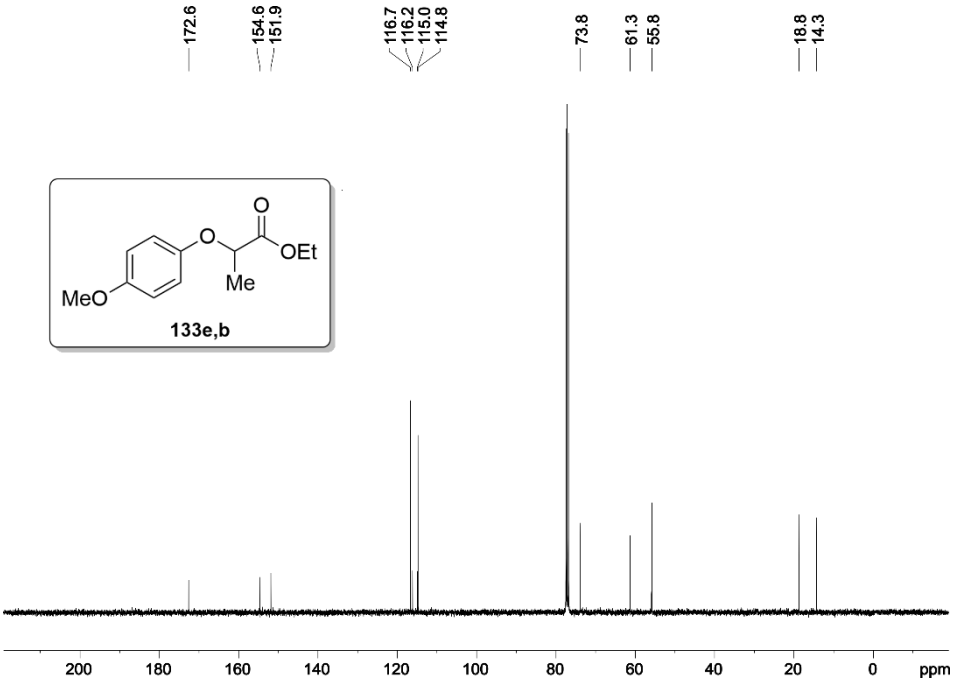

Figure 111. $^{13}C\{^{1}H\}$ NMR spectrum (101 MHz, $CDCl_3$) of **133e,b**.

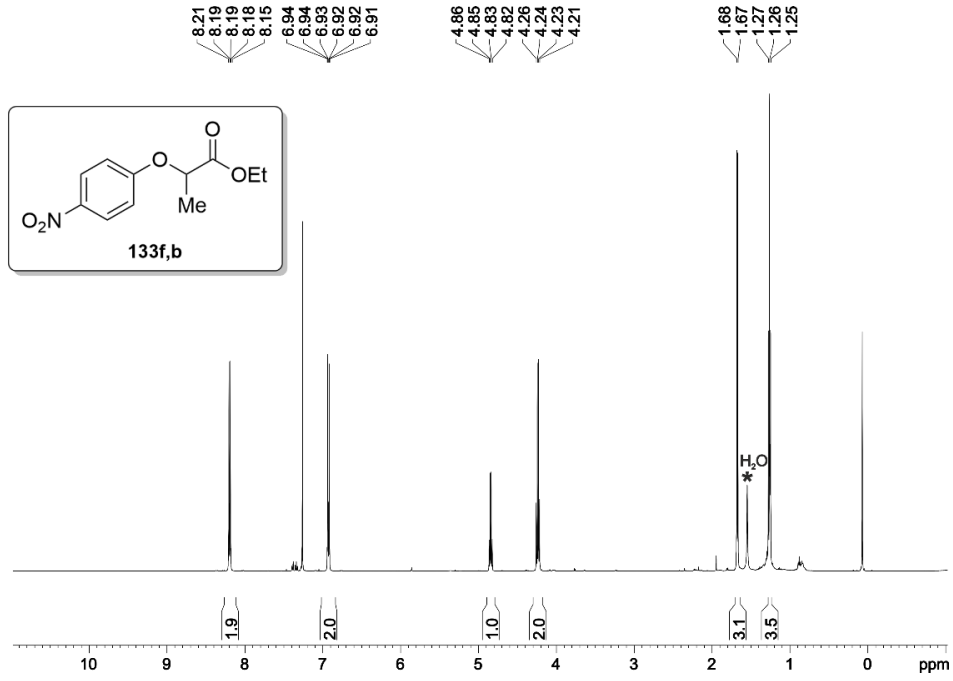

Figure 112. ^{1}H NMR spectrum (500 MHz, $CDCl_3$) of **133f,b**.

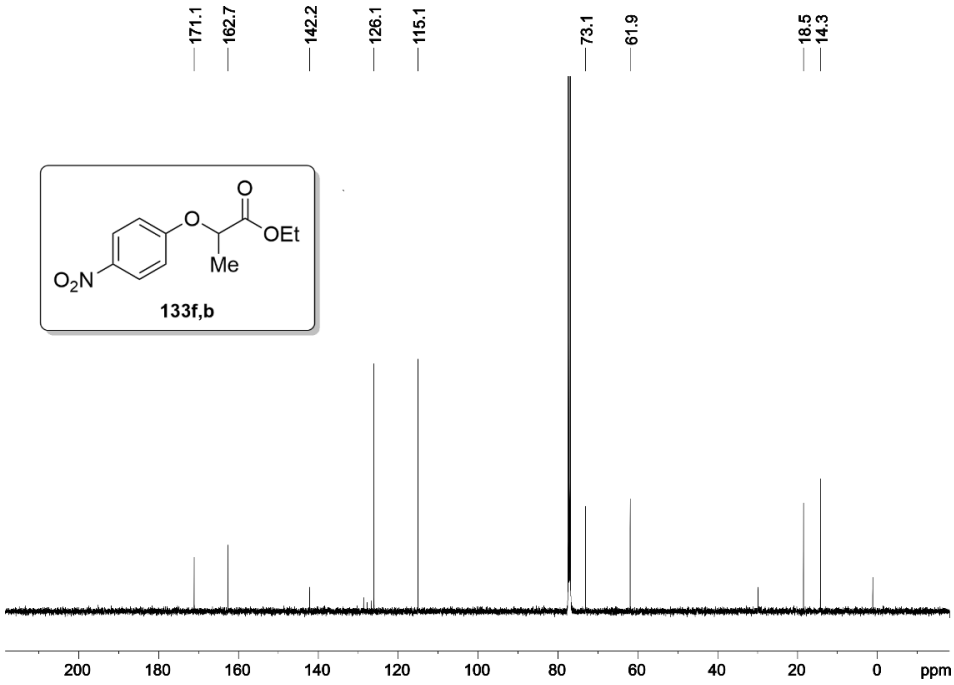

Figure 113. $^{13}C\{^{1}H\}$ NMR spectrum (126 MHz, $CDCl_3$) of **133f,b**.

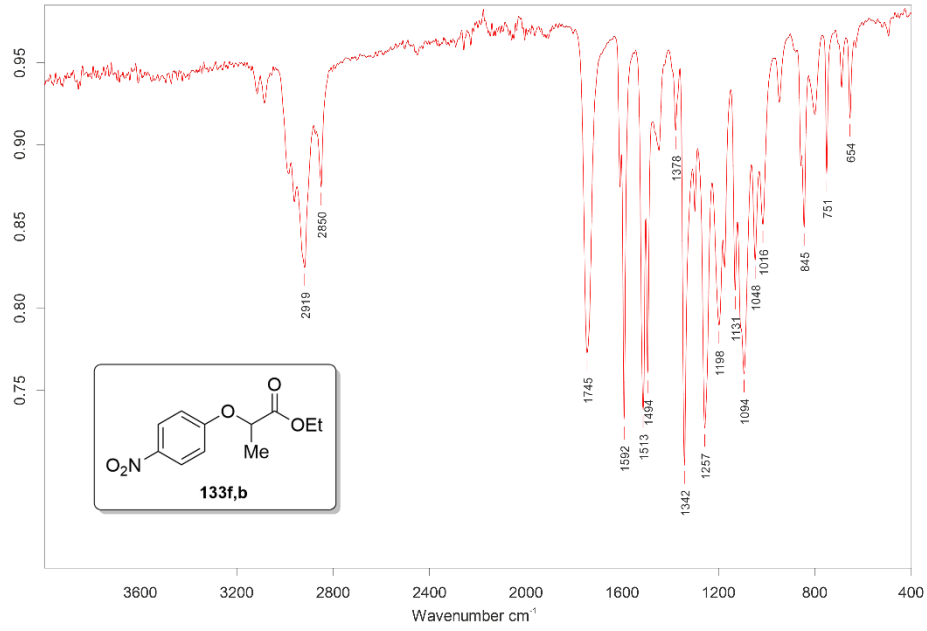

Figure 114. IR spectrum of **133f,b**.

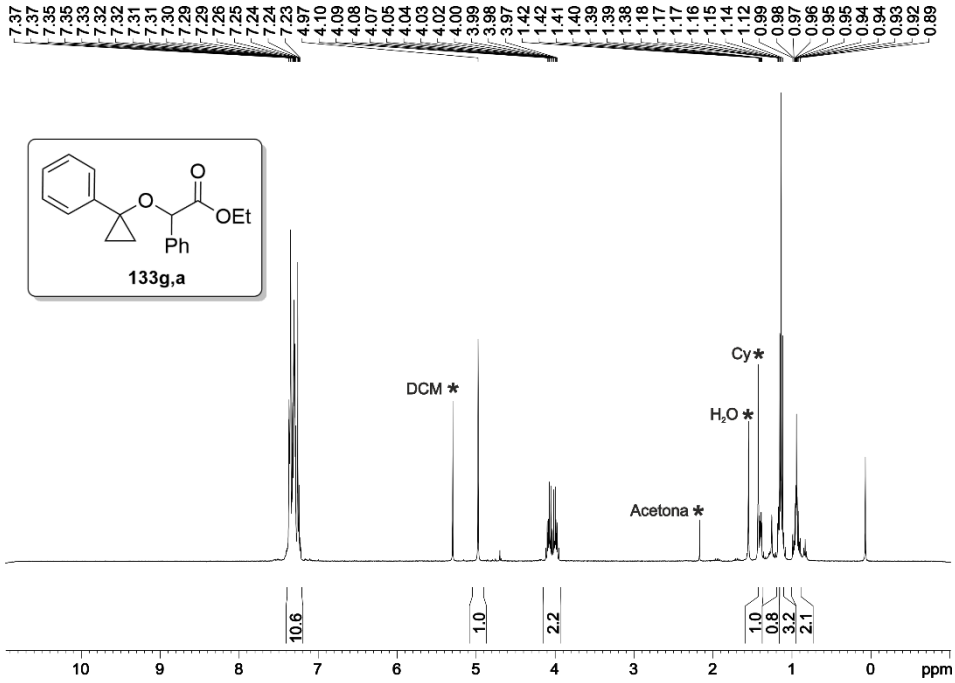

Figure 115. ^{1}H NMR spectrum (400 MHz, $CDCl_3$) of **133g,a**.

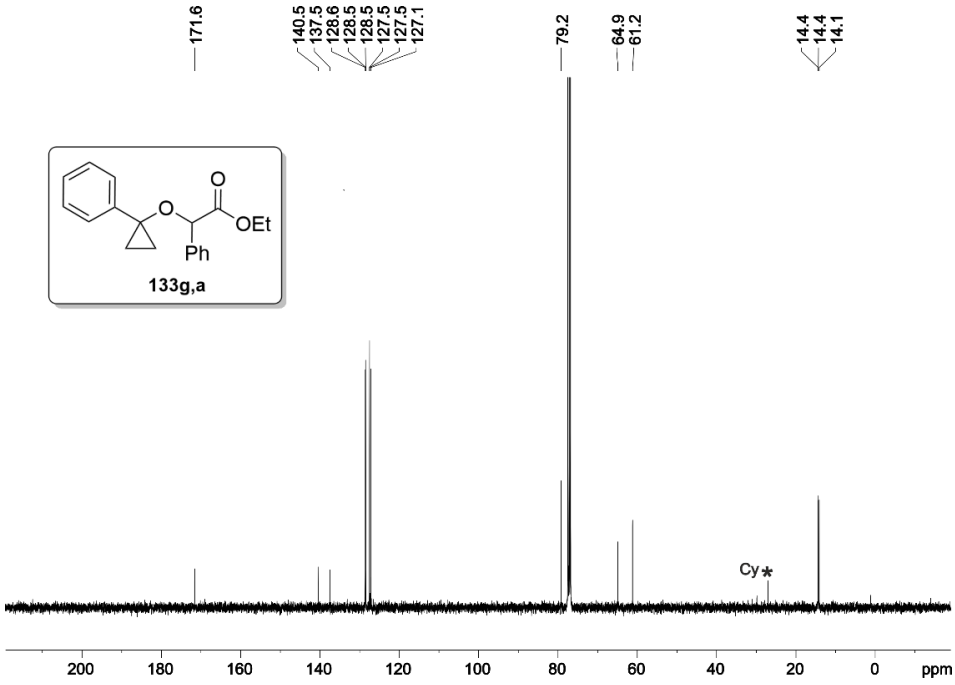

Figure 116. $^{13}C\{^{1}H\}$ NMR spectrum (101 MHz, $CDCl_3$) of **133g,a**.

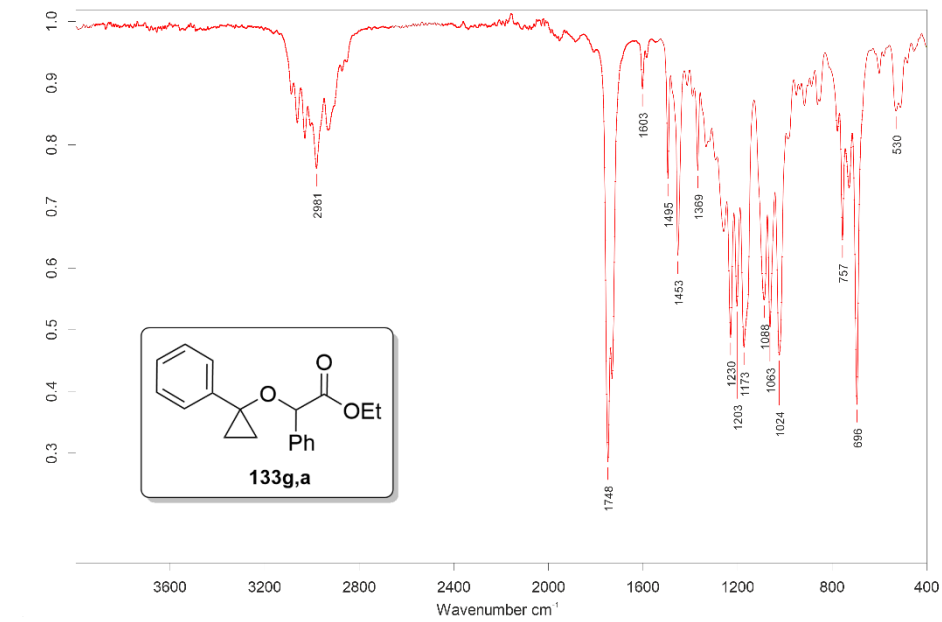

Figure 117. IR spectrum of **133g,a**.

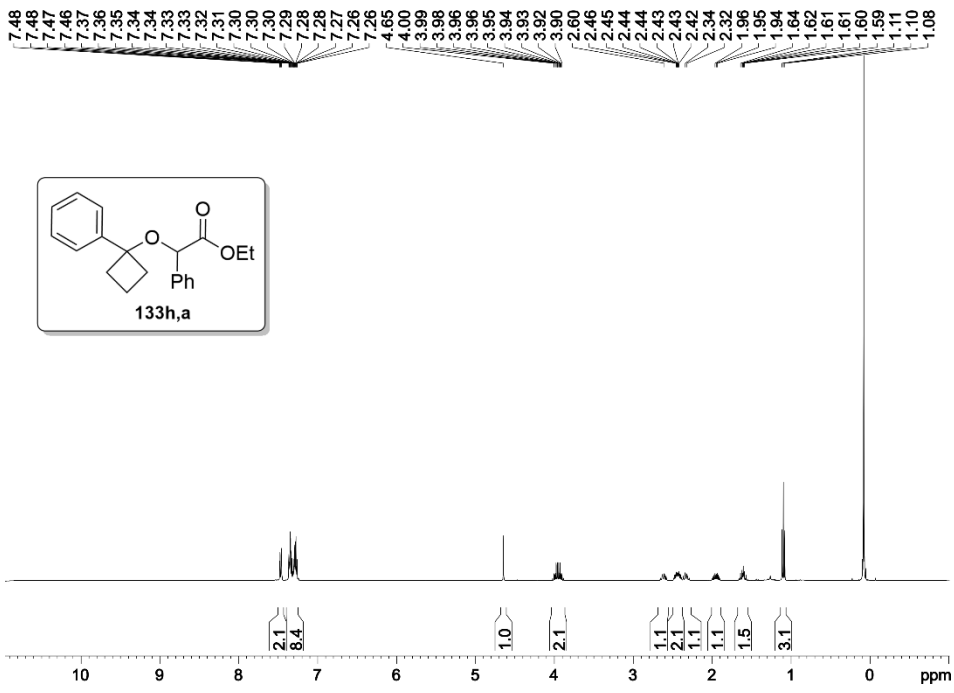

Figure 118. ^{1}H NMR spectrum (400 MHz, $CDCl_3$) of **133h,a**.

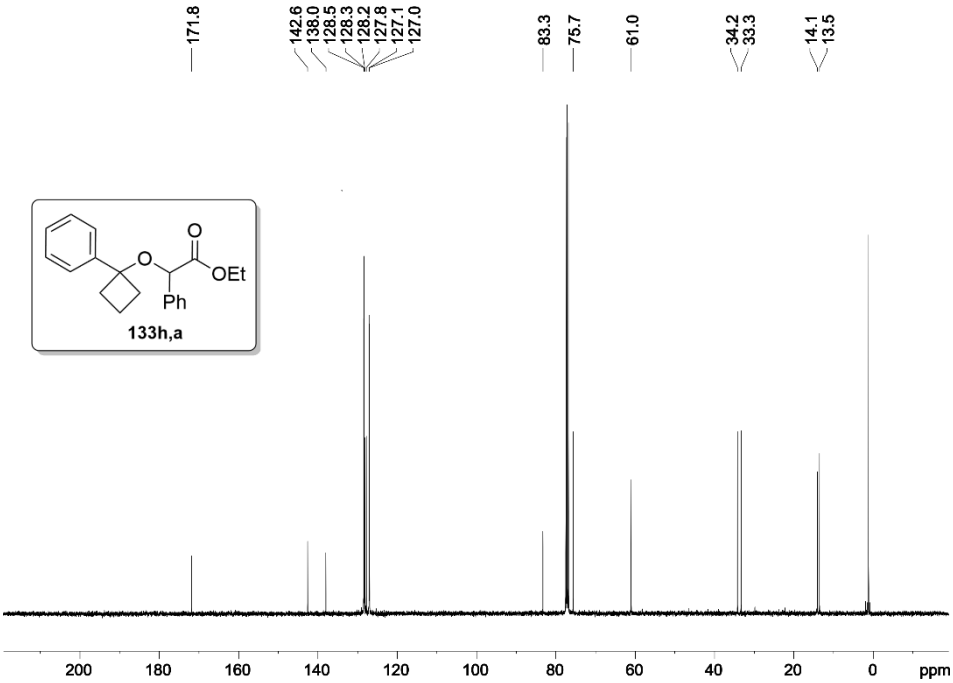

Figure 119. $^{13}C\{^{1}H\}$ NMR spectrum (101 MHz, $CDCl_3$) of **133h,a**.

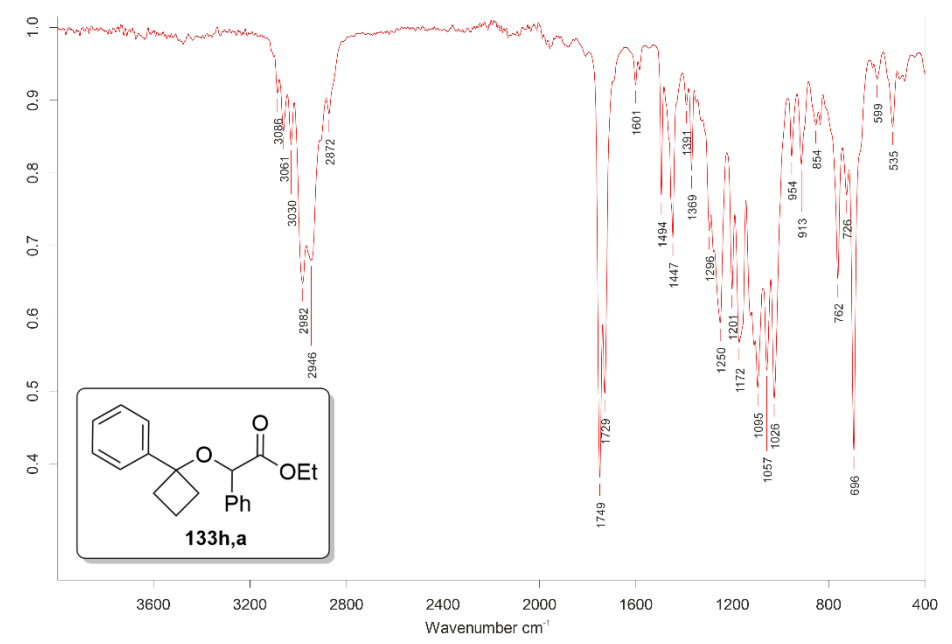

Figure 120. IR spectrum of **133h,a**.

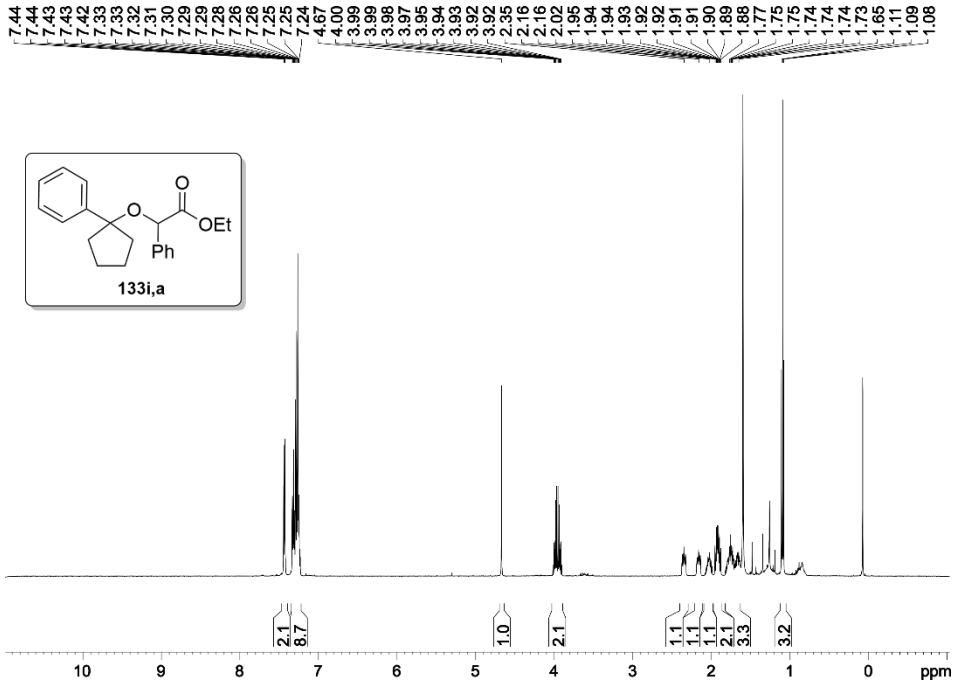

Figure 121. ^{1}H NMR spectrum (500 MHz, $CDCl_3$) of **133i,a**.

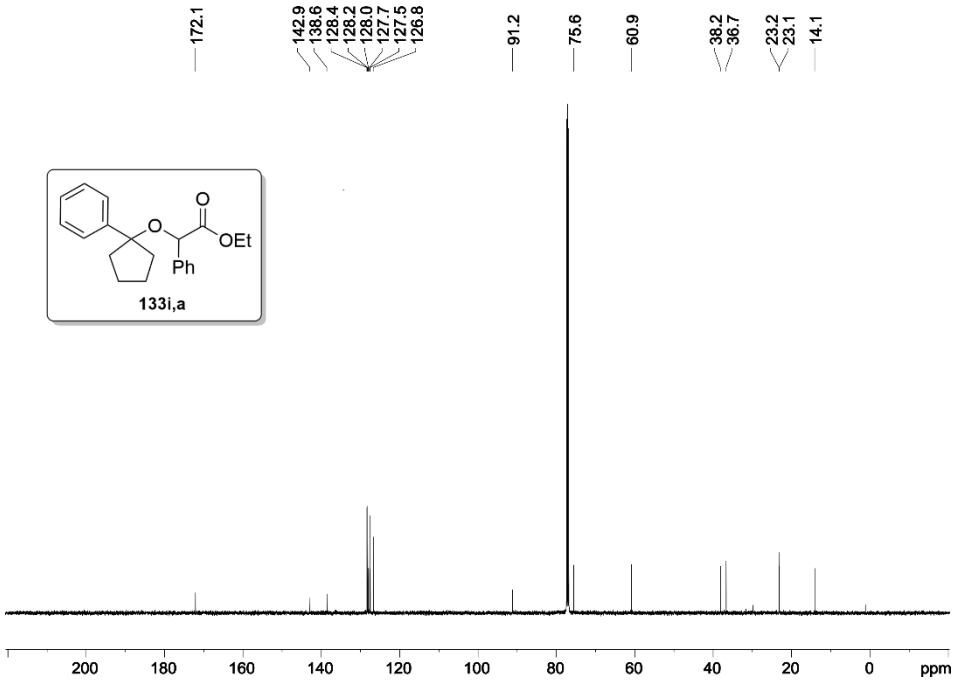

Figure 122. $^{13}C\{^{1}H\}$ spectrum (101 MHz, $CDCl_3$) of **133i,a**.

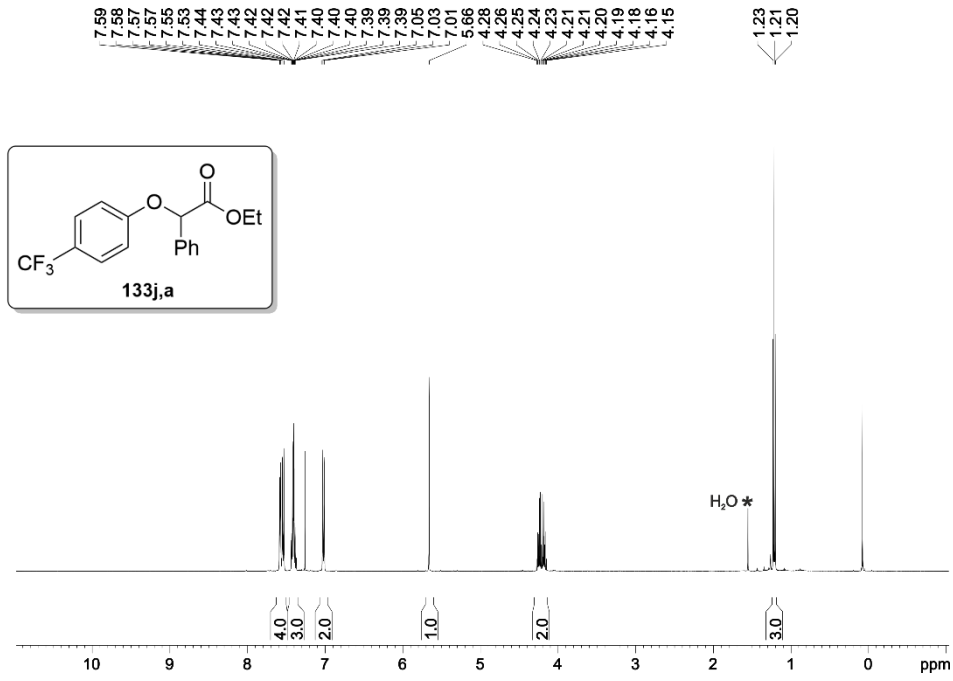

Figure 123. ^{1}H NMR spectrum (500 MHz, $CDCl_3$) of **133j,a**.

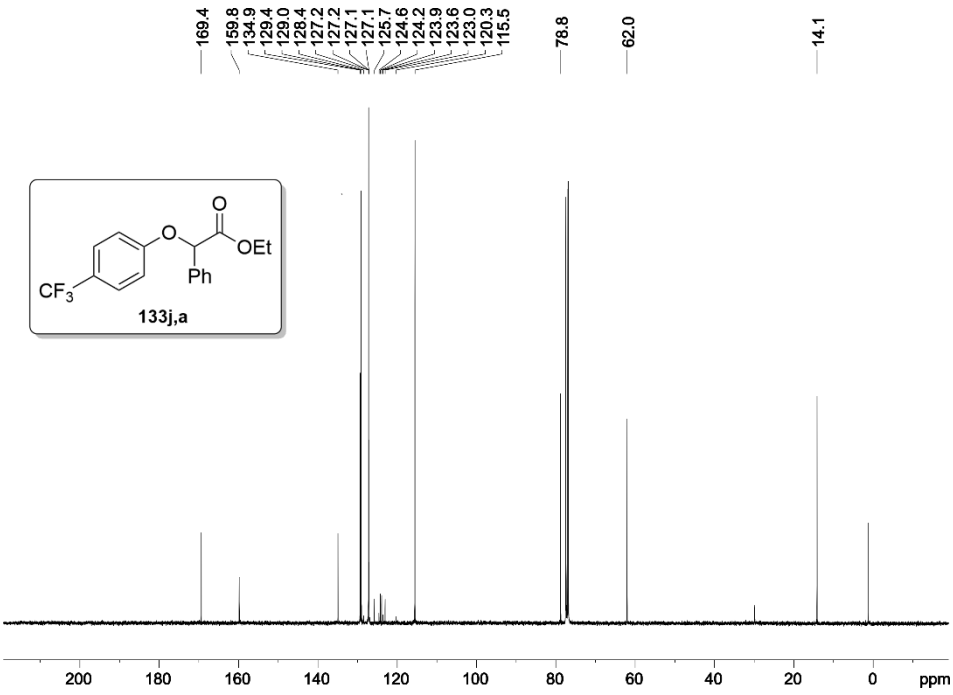

Figure 124. $^{13}C\{^{1}H\}$ NMR spectrum (101 MHz, $CDCl_3$) of **133j,a**.

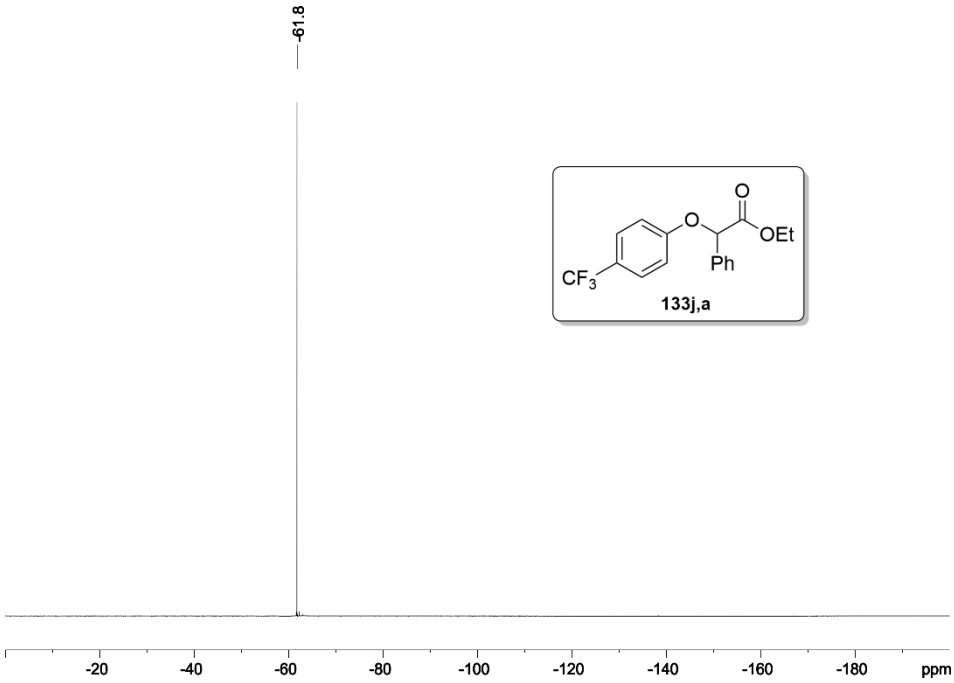

Figure 125. $^{19}F\{^{1}H\}$ NMR spectrum (471 MHz, $CDCl_3$) of **133j,a**.

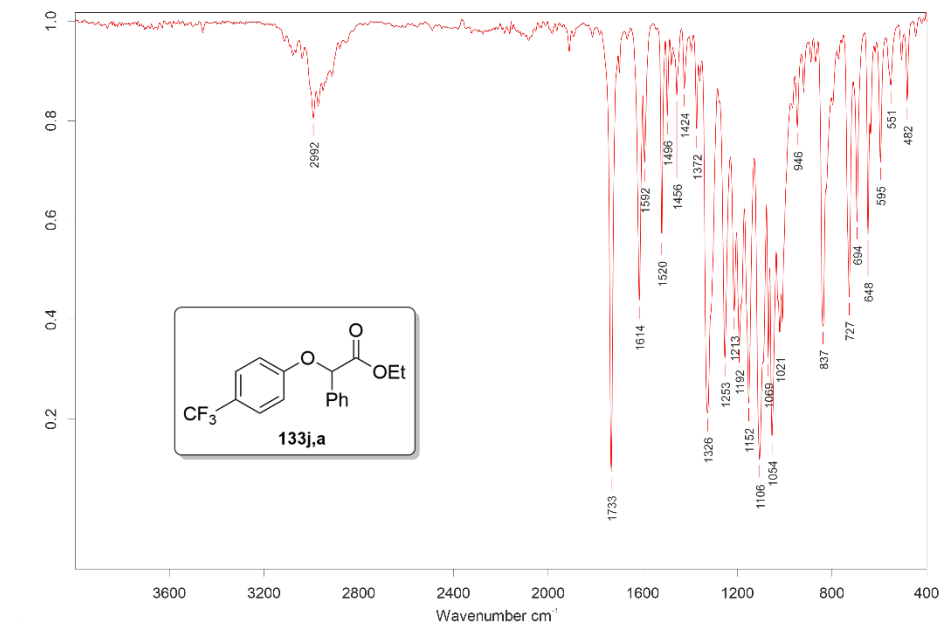

Figure 126. IR spectrum of **133j,a**.

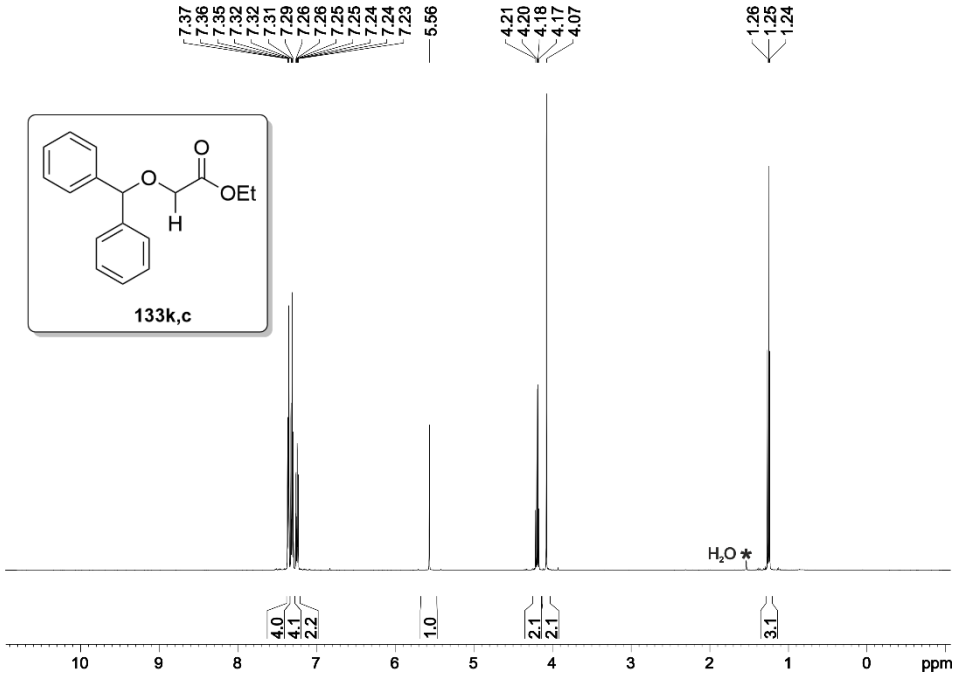

Figure 127. ^{1}H NMR spectrum (500 MHz, $CDCl_3$) of **133k,c**.

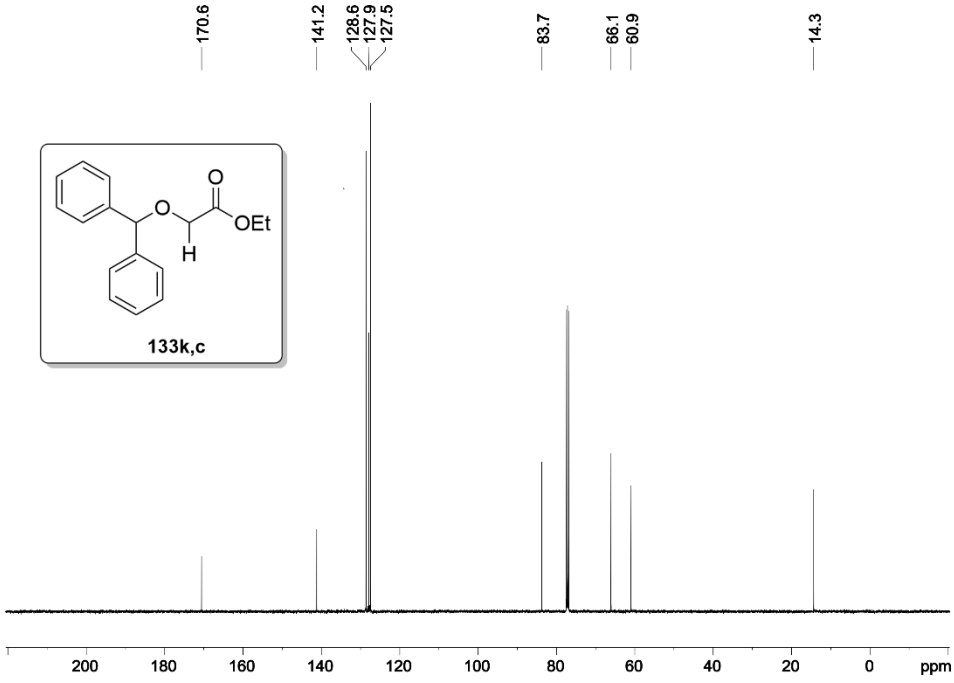

Figure 128. $^{13}C\{^{1}H\}$ NMR spectrum (126 MHz, $CDCl_3$) of **133k,c**.

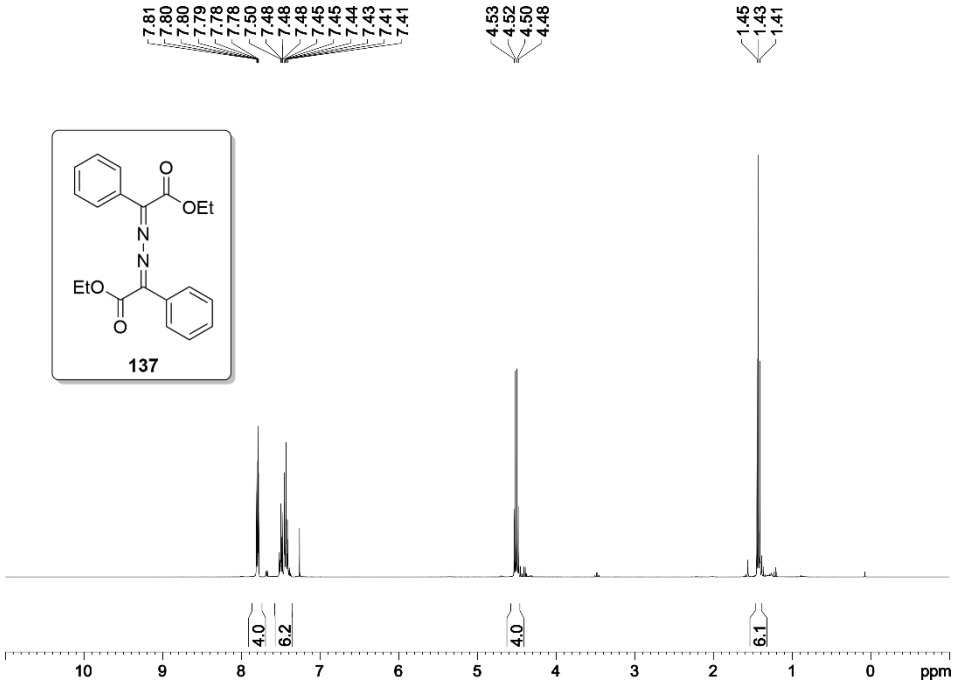

Figure 129. ^{1}H NMR spectrum (400 MHz, $CDCl_3$) of **137**.

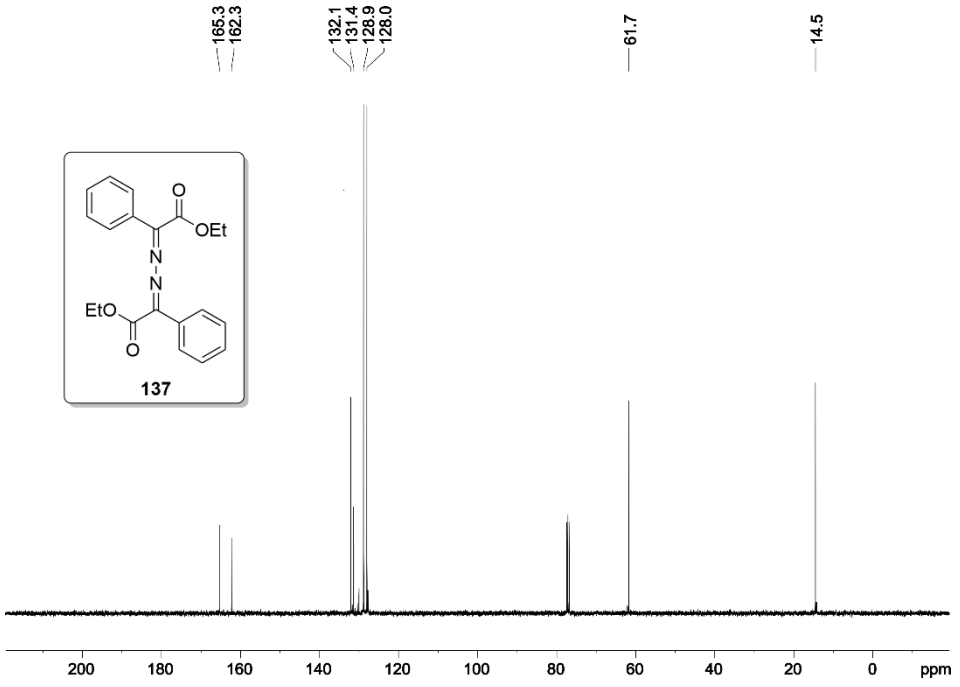

Figure 130. $^{13}C\{^{1}H\}$ NMR spectrum (101 MHz, $CDCl_3$) of **137**.

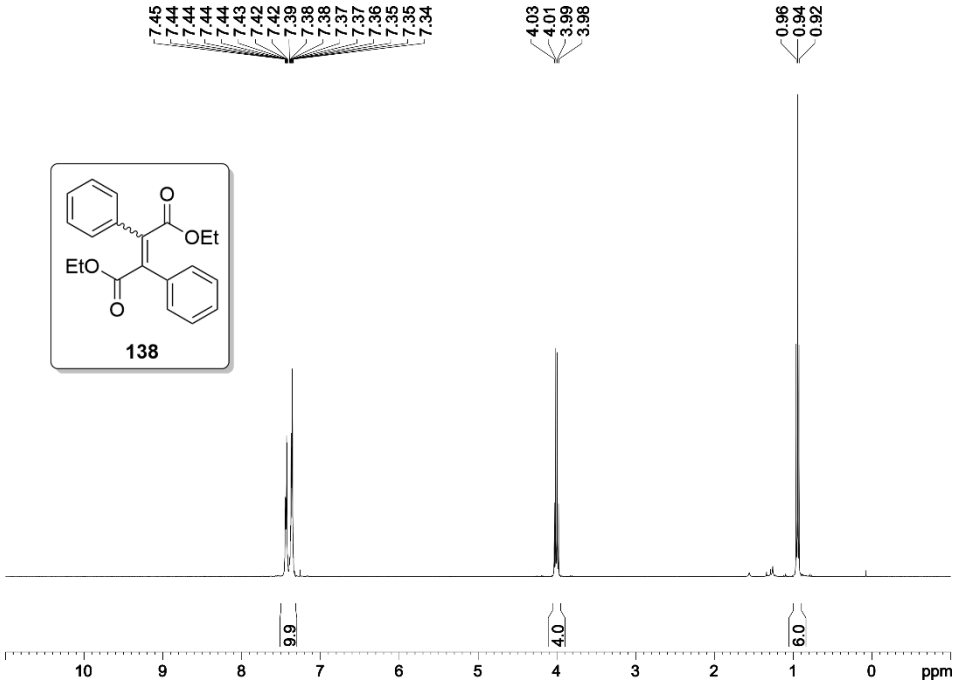

Figure 131. ^{1}H NMR spectrum (400 MHz, $CDCl_3$) of **138**.

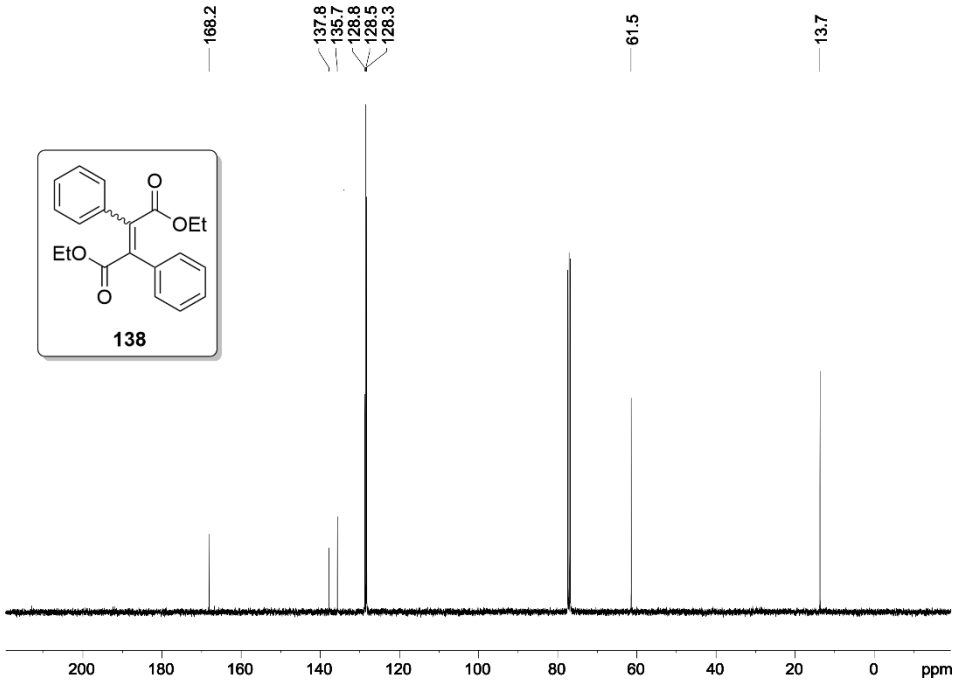

Figure 132. $^{13}C\{^{1}H\}$ NMR spectrum (101 MHz, $CDCl_3$) of **138**.

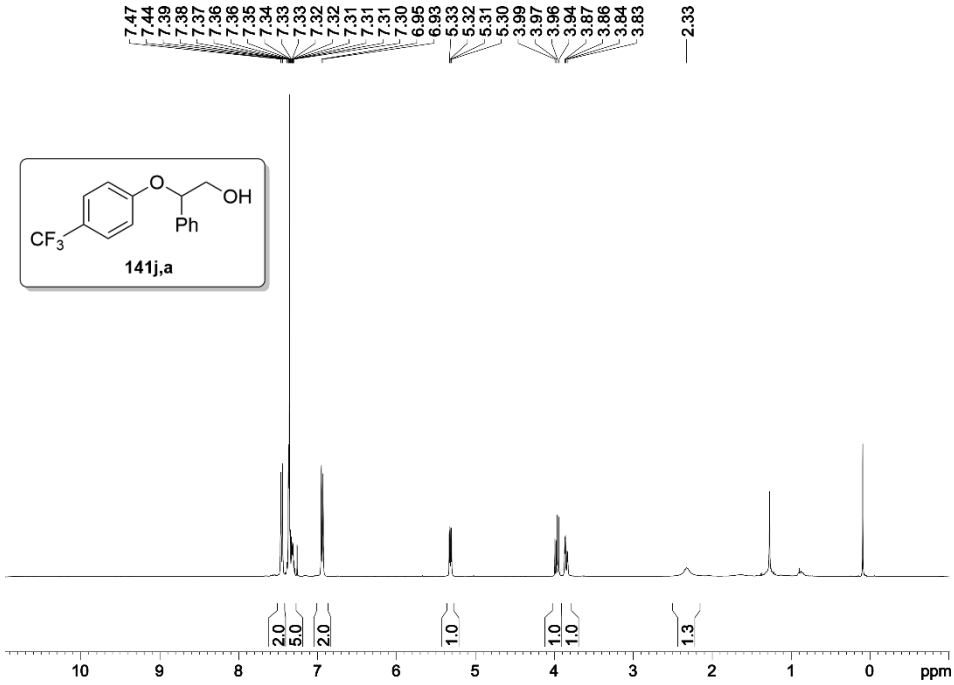

Figure 133. ^{1}H NMR spectrum (400 MHz, $CDCl_3$) of **141j,a**.

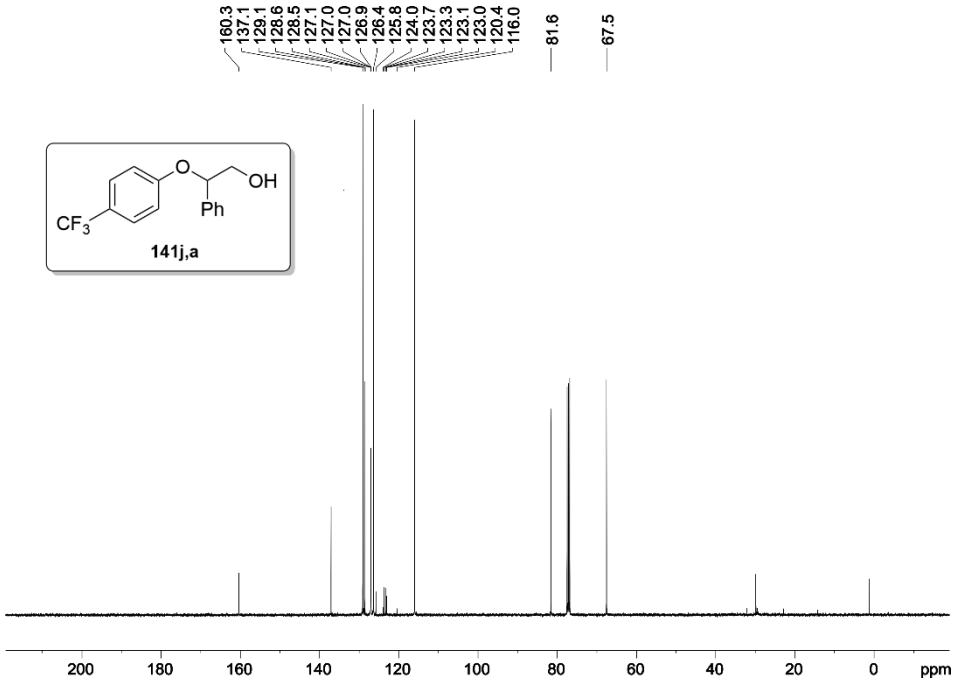

Figure 134. $^{13}C\{^{1}H\}$ NMR spectrum (101 MHz, $CDCl_3$) of **141j,a**.

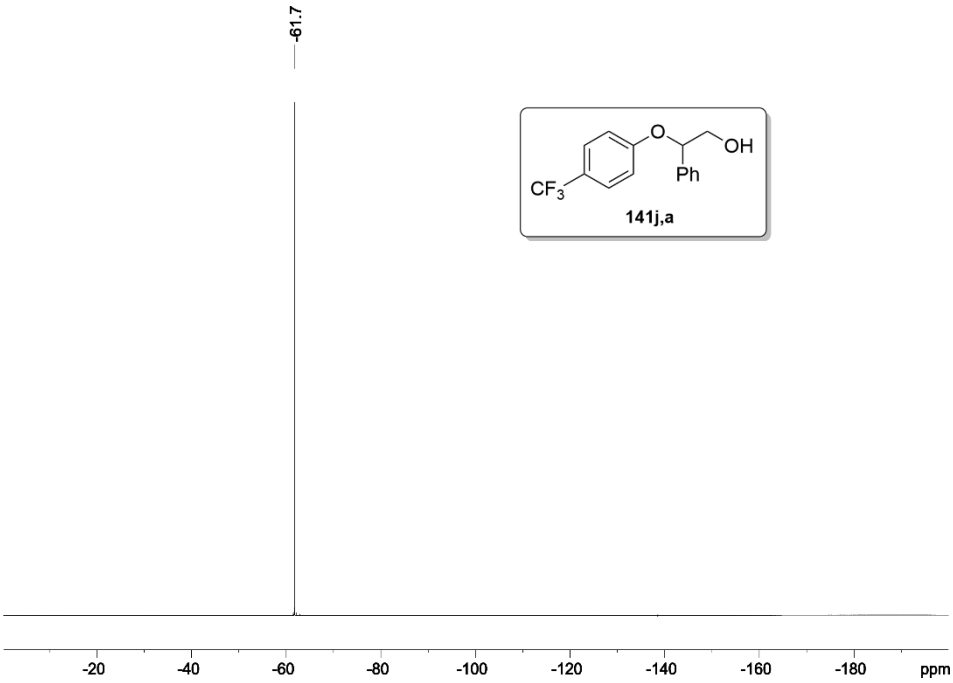

Figure 135. $^{19}F\{^{1}H\}$ NMR spectrum (376 MHz, $CDCl_3$) of **141j,a**.

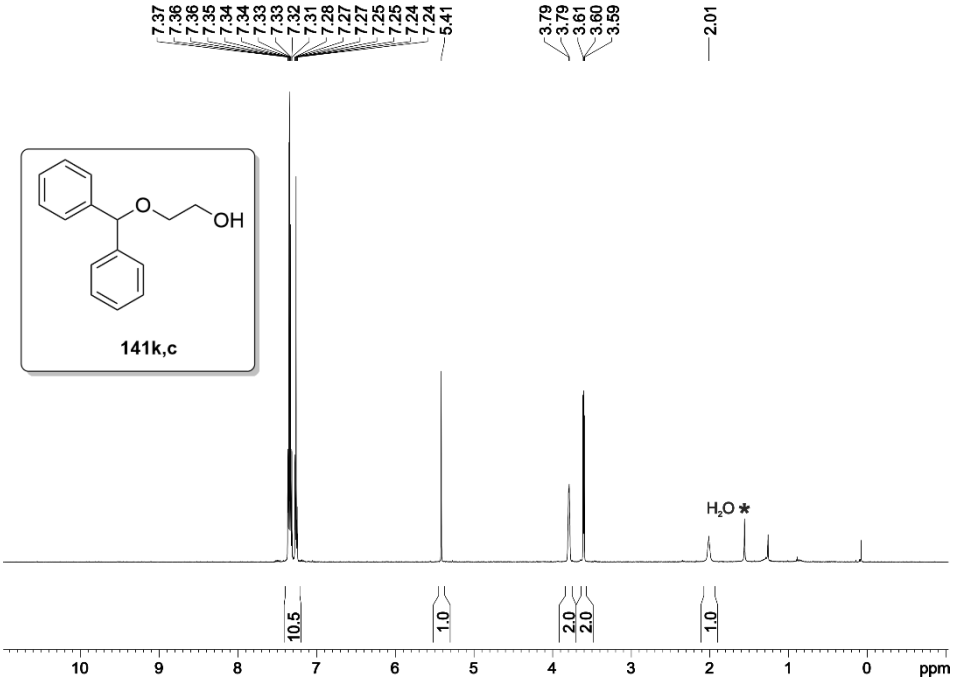

Figure 136. ^{1}H NMR spectrum (500 MHz, $CDCl_3$) of **141k,c**.

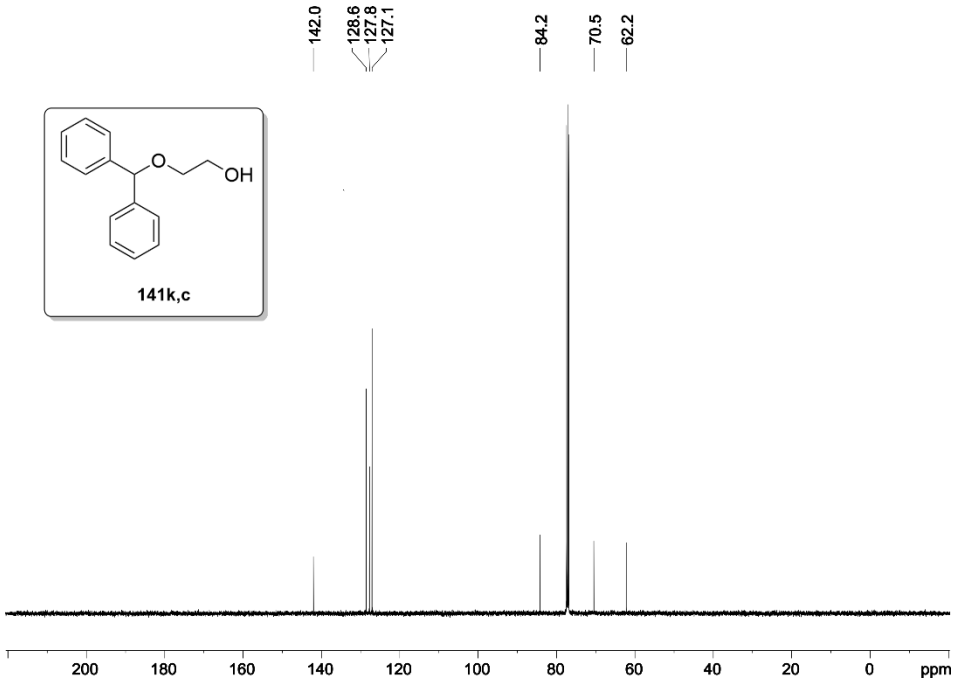

Figure 137. $^{13}C\{^{1}H\}$ NMR spectrum (126 MHz, $CDCl_3$) of **141k,c**.

CHAPTER II

Synthesis and Characterization of Pt(II) and Pd(II) Supramolecular Complexes Derived from Halogen-Bonded Diphosphines

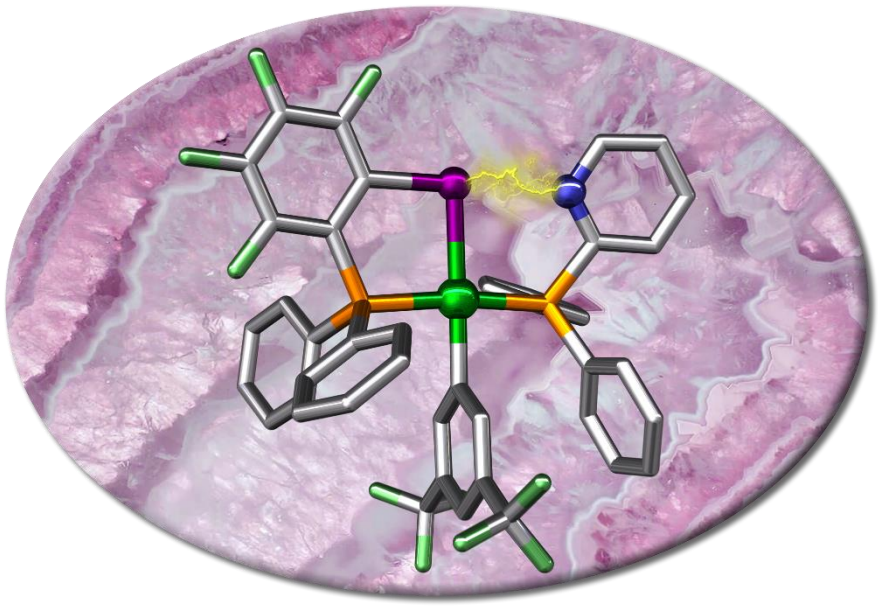

Synthesis and Characterization of Pt(II) and Pd(II) Supramolecular Complexes Derived from Halogen-Bonded Diphosphines

(Unpublished results)

Ester Iniesta[a,b] and Anton Vidal-Ferran[*c,d]

a Universitat Rovira i Virgili, Departament de Química Analítica i Química Orgànica, C. Marcel·lí Domingo 1, 43007, Tarragona, Spain.

b Institut Català d'Investigació Química (ICIQ) & Barcelona Institute of Science and Technology (BIST), Av. Països Catalans 16, 43007 Tarragona, Spain.

c Institució Catalana de Recerca i Estudis Avançats (ICREA), Pg. Lluís Companys 23, 08010, Barcelona, Spain.

d Universitat de Barcelona, Departament de Química Inorgànica i Química Orgànica, C. Martí i Franquès 1-11, 08028 Barcelona, Spain.

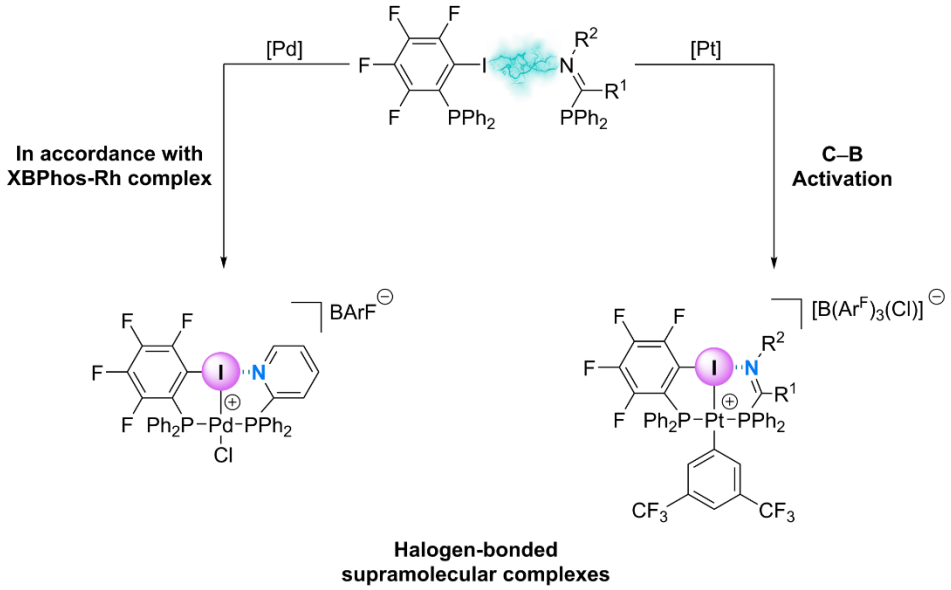

2.1. ABSTRACT

The design and synthesis of new supramolecular platinum(II) and palladium(II) complexes by assembling two building blocks that incorporate phosphines as ligating groups, as well as complementary binding motifs for the assembly process through halogen bonding interactions, are reported. A set of structurally diverse platinum and palladium complexes derived from (halogen-bonded) diphosphines has been characterized in solution and in the solid state. A broad study of the reaction intermediates that led to platinum(II) complexes has been performed. A tentative mechanistic rationalization for the formation of the platinum complexes derived from halogen-bonded diphosphines is proposed (oxidative addition of a B–C bond from the BArF counterion to $[Pt(Cl)_2(cod)]$, subsequent B–Cl reductive elimination, coordination of the phosphine ligands with concomitant displacement of the cod ligand and NaCl elimination). The complex XBPhos-Pt has proved to be unreactive as a supramolecular catalyst in carbocyclizations of enynes and the hydrophenylation of ethylene. Strategies towards the activation of the complex XBPhos-Pt and analogues for new chemistries are presented.

2.2. INTRODUCTION

The broad applicability and versatility of metal complexes as efficient catalysts for a wide variety of chemical transformations such as the synthesis of fine chemicals with added value or molecules with biological activity has been historically established.[1] In this field, catalysts based on noble metals are, still nowadays, one of the most powerful synthetic tools. Specifically, the use of platinum and/or palladium catalysts has been constantly growing.[2] Although these metals have been studied in supramolecular chemistry, examples of the

[1] For example, see: (a) Hoyos, P.; Pace, V.; Alcántara, A. R. *Adv. Synth. Catal.* **2012**, *354*, 2585-2611. (b) Choy, P. Y.; Wong, S. M.; Kapdi, A.; Kwong, F. Y. *Org. Chem. Front.* **2018**, *5*, 288-321. (c) Blaszczyk, S. A.; Glazier, D. A.; Tang, W. *Acc. Chem. Res.* **2020**, *53*, 231-243. (d) Diccianni, J.; Lin, Q.; Diao, T. *Acc. Chem. Res.* **2020**, *53*, 906-919. (e) Lichtenberg, C. *Chem.–Eur. J.* **2020**, *26*, 9674-9687.

[2] For example, see: (a) Belskaya, O. B.; Duplyakin, V. K.; Likholobov, V. A. *Kinet. Catal.* **2019**, *60*, 761-775. (b) Chuentragool, P.; Kurandina, D.; Gevorgyan, V. *Angew. Chem., Int. Ed.* **2019**, *58*, 11586-11598. (c) Mascareñas, J. L.; Varela, I.; López, F. *Acc. Chem. Res.* **2019**, *52*, 465-479. (d) Oliveira, B. L.; Stenton, B. J.; Unnikrishnan, V. B.; de Almeida, C. R.; Conde, J.; Negrão, M.; Schneider, F. S. S.; Cordeiro, C.; Ferreira, M. G.; Caramori, G. F.; Domingos, J. B.; Fior, R.; Bernardes, G. J. L. *J. Am. Chem. Soc.* **2020**, *142*, 10869-10880.

construction of the skeleton of ligands for these metals through supramolecular interactions remain scarce in the literature.[3]

During the last decades, supramolecular chemistry has emerged as a highly efficient strategy for the design and synthesis of challenging metal-based catalysts.[4a] Elegant examples of supramolecular metal complexes entail the construction of their framework through supramolecular interactions by self-assembly of complementary building blocks that also display ligating groups for the metal center.[4b,c] One important advantage of this supramolecular strategy is that the difficulties in the synthesis of the ligands or catalysts, often encountered by conventional covalent synthesis, can be overcome.[4]

Recently, halogen bonding has emerged within the field of supramolecular chemistry as an efficient and versatile non-covalent interaction that has been used in catalysis.[5] The great potential of halogen bonding compared to other supramolecular interactions relies on its high directionality[6] and strength,[7] together with the polarizability[8] of the halogen atoms involved. The halogen bonding interaction contains two electronically different entities: the first is the electron-deficient moiety (halogen bond donor), which contains the so-called σ-hole (*i.e.*, a region of positive electrostatic potential in a halogen atom, which is placed on the outermost portion of the halogen's potential surface and centred on the R–halogen axis). The second entity is a nucleophilic moiety (halogen bond acceptor), which interacts with the σ-hole to form the halogen bonding interaction (Figure 138).

---

[3] (a) McGuirk, C. M.; Stern, C. L.; Mirkin, C. A. *J. Am. Chem. Soc.* **2014**, *136*, 4689-4696. (b) Kaphan, D. M.; Levin, M. D.; Bergman, R. G.; Raymond, K. N.; Toste, F. D. *Science* **2015**, *350*, 1235-1238. (c) Rao, M.; Kanagaraj, K.; Fan, C.; Ji, J.; Xiao, C.; Wei, X.; Wu, W.; Yang, C. *Org. Lett.* **2018**, *20*, 1680-1683.

[4] For example, see: (a) *Supramolecular Catalysis*; van Leeuwen, P. W. N., Ed.; Wiley-VCH Verlag GmbH & Co.: Weinheim, 2008. (b) Raynal, M.; Ballester, P.; Vidal-Ferran, A.; van Leeuwen, P. W. N. M. *Chem. Soc. Rev.* **2014**, *43*, 1660-1733. (c) Raynal, M.; Ballester, P.; Vidal-Ferran, A.; van Leeuwen, P. W. N. M. *Chem. Soc. Rev.* **2014**, *43*, 1734-1787.

[5] (a) Metrangolo, P.; Meyer, F.; Pilati, T.; Resnati, G.; Terraneo, G. *Angew. Chem., Int. Ed.* **2008**, *47*, 6114-6127. (b) Gilday, L. C.; Robinson, S. W.; Barendt, T. A.; Langton, M. J.; Mullaney, B. R.; Beer, P. D. *Chem. Rev.* **2015**, *115*, 7118-7195. (c) Cavallo, G.; Metrangolo, P.; Milani, R.; Pilati, T.; Priimagi, A.; Resnati, G.; Terraneo, G. *Chem. Rev.* **2016**, *116*, 2478-2601.

[6] Huber, S. M.; Scanlon, J. D.; Jiménez-Izal, E.; Ugalde, J. M.; Infante, I. *Phys. Chem. Chem. Phys.* **2013**, *15*, 10350-10357.

[7] Corradi, E.; Meille, S. V.; Messina, M. T.; Metrangolo, P.; Resnati, G. *Angew. Chem., Int. Ed. Engl.* **2000**, *39*, 1782-1786.

[8] Ibrahim, M. A. A.; Hasb, A. A. M. *Theor. Chem. Acc.* **2019**, *138*, 1-12.

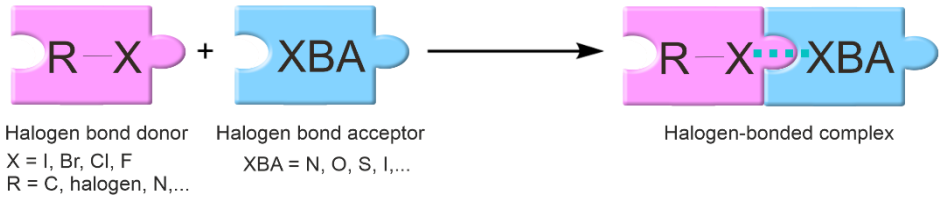

Figure 138. Schematic representation of the halogen bonding interaction.

Our group pioneered the use of the halogen bonding as a tool to construct the backbone of catalytic rhodium chelates derived from halogen-bonded diphosphines. [9] The approach consisted of the formation of supramolecular metal complexes by self-assembling two complementary building blocks (halogen bond donor and acceptor) that incorporated phosphino groups as ligating moieties to the rhodium center (Figure 139). The choice of phosphino groups as ligating groups was mainly for two reasons: (i) the well-known activity of these ligands in homogeneous catalysis[10] and (ii) the versatility that they offer in terms of functionalization.[11] The described rhodium complex XBPhos-Rh **116** was successfully used as supramolecular catalyst for the hydroboration of terminal alkynes.[9a]

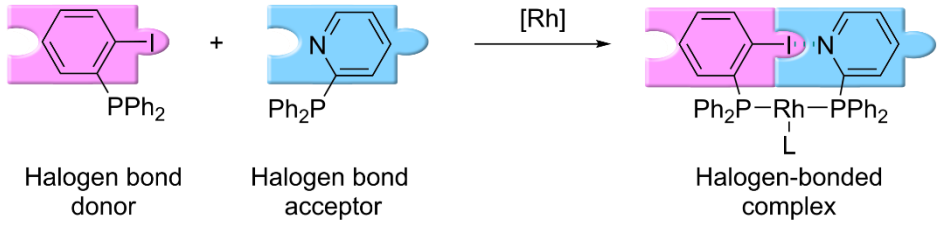

Figure 139. Schematic representation of the approach for synthesizing XBPhos-Rh **116**: The halogen bond donor and acceptor (left), that displayed P-ligating groups, by self-assembly with a metal center (Rh) to form the halogen-bonded complex (right). The halogen bonding interaction is highlighted with a green dashed line.

[9] (a) Carreras, L.; Serrano-Torné, M.; van Leeuwen, P. W. N. M.; Vidal-Ferran, A. *Chem. Sci.* **2018**, *9*, 3644-3648. (b) Carreras, L.; Benet-Buchholz, J.; Franconetti, A.; Frontera, A.; van Leeuwen, P. W. N. M.; Vidal-Ferran, A. *Chem. Commun.* **2019**, *55*, 2380-2383.

[10] *Phosphorus(III) Ligands in Homogeneous Catalysis: Design and Synthesis*; Kamer, P. C. J., van Leeuwen, P. W. N. M., Eds.; John Wiley & Sons Ltd.: United Kingdom, 2012.

[11] Fernández-Pérez, H.; Etayo, P.; Panossian, A.; Vidal-Ferran, A. *Chem. Rev.* **2011**, *111*, 2119-2176.

Inspired by these results, we envisaged that platinum(II) and palladium(II), as the metal centers, were good candidates to expand the XBPhos approach by synthesizing the corresponding XBPhos-metal supramolecular complexes.

Herein, we report the formation of supramolecular platinum(II) and palladium(II) complexes by assembling two complementary halogen bond donor and acceptor molecules containing phosphine ligands. Mechanistic studies on the formation of these complexes have also been performed. Moreover, their use as catalysts in several transformations of interest has also been studied.

2.3. RESULTS AND DISCUSSION

2.3.1. Preparation of group-10 analogues of XBPhos-Rh

Our studies began with the synthesis of XBPhos-Pt complex **142** by employing an analogous methodology to that developed for the synthesis of XBPhos-Rh **116**.[9a] The first step in the synthesis of the platinum complex was the preparation of the ligand that incorporates the halogen bond donor (*i.e.*, 2-iodo-3,4,5,6-tetrafluorophenyldiphenylphosphine **L3**). Following the synthetic protocols reported in the literature[12] from 1,2,3,4-tetrafluoro-5,6-diiodobenzene **143** and chlorodiphenylphosphine **144**, the compound **L3** was obtained in 68% yield (Scheme 45). The second building block required for preparing complex **142** (*i.e.*, the halogen bond acceptor 2-pyridyldiphenylphosphine **L4**) is commercially available.

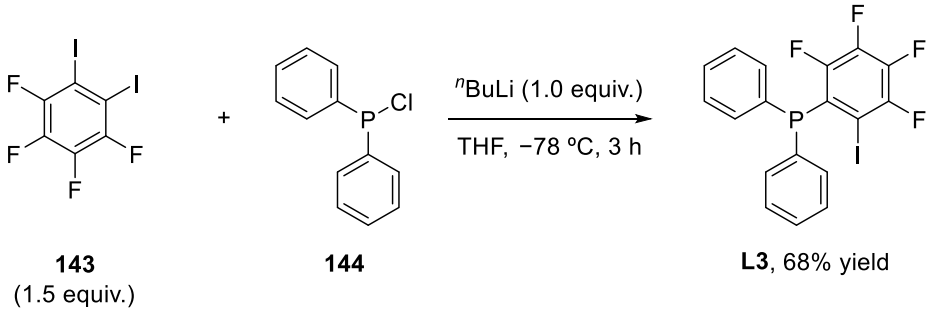

Scheme 45. Synthesis of 2-iodo-3,4,5,6-tetrafluorophenyldiphenylphosphine **L3**.

[12] Eller, P. G.; Meek, D. W. *J. Organometal. Chem.* **1970**, *22*, 631-636.

We hypothesized that the use of $[Pt(Cl)_2(cod)]$ along with a halide scavenger would render a putative $[Pt(Cl)(cod)]^+$ intermediate that should react with phosphines **L3** and **L4**. Following an analogous synthetic procedure to that developed for XBPhos-Rh, NaBArF was used as the halide scavenger. After mixing $[Pt(Cl)_2(cod)]$ and NaBArF in toluene, a white precipitate (*i.e.*, NaCl) was progressively formed, which led us to assume that platinum(II) complex $[Pt(Cl)(cod)]^+$ had been formed. We then allowed the reaction of this platinum intermediate with phosphine ligands **L3** and **L4**. A new platinum complex was isolated from the reaction mixture, whose structure was at first sight in agreement with that expected for complex XBPhos-Pt (Scheme 46).

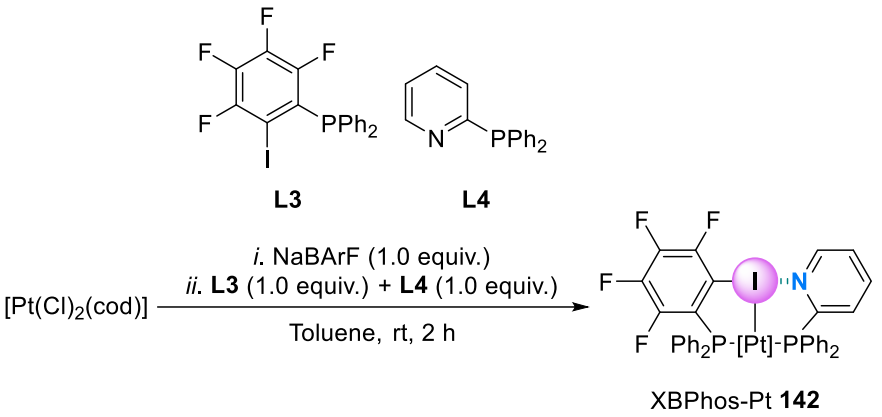

Scheme 46. Synthesis of the supramolecular complex XBPhos-Pt **142**.

The $^{31}P\{^1H\}$ NMR spectrum showed two complex multiplets, which have been grouped under the splitting pattern diagrams marked in blue and red in Figure 140. The ^{195}Pt satellite signals[13] were split due to the ^{195}Pt–^{31}P coupling through one bond ($^1J_{Pt–P}$ = 1368.2 and 1416.4 Hz). A high value $^2J_{P–P}$ coupling constant (*i.e.*, 376.2 Hz) was calculated for the phosphorus atoms. According to the literature reviewed, this high value $^2J_{P–P}$ coupling constant indicated a *trans*-spanning diphosphine coordinated to the platinum center.[14] As for the other ligands on the first coordination sphere of platinum, the presence of the cyclooctadiene ligand was ruled out by ^1H NMR spectroscopy. Moreover, the aromatic region of the ^1H NMR spectrum contained unexpected signals and did not have the expected intensity for the $[Pt(\mathbf{L3}•\mathbf{L4})](BArF)_2$ complex. ESI-MS

[13] Robertson, G. P.; Odell, B.; Kuprov, I.; Dixon, D. J.; Claridge, T. D. W. *Angew. Chem., Int. Ed.* **2018**, *57*, 7498-7502.
[14] (a) Still, B. M.; Kumar, P. G. A.; Aldrich-Wright, J. R.; Price, W. S. *Chem. Soc. Rev.* **2007**, *36*, 665-686 . (b) Freixa, Z.; van Leeuwen, P. W. N. M. *Coord. Chem. Rev.* **2008**, *252*, 1755-1786.

analysis did not identify the fragments [Pt(**L3•L4**)]$^{2+}$ or [Pt(Cl)(**L3•L4**)]$^{+}$, but signals at a higher *m/z* ratio (*m/z* for the base peak = 1131).

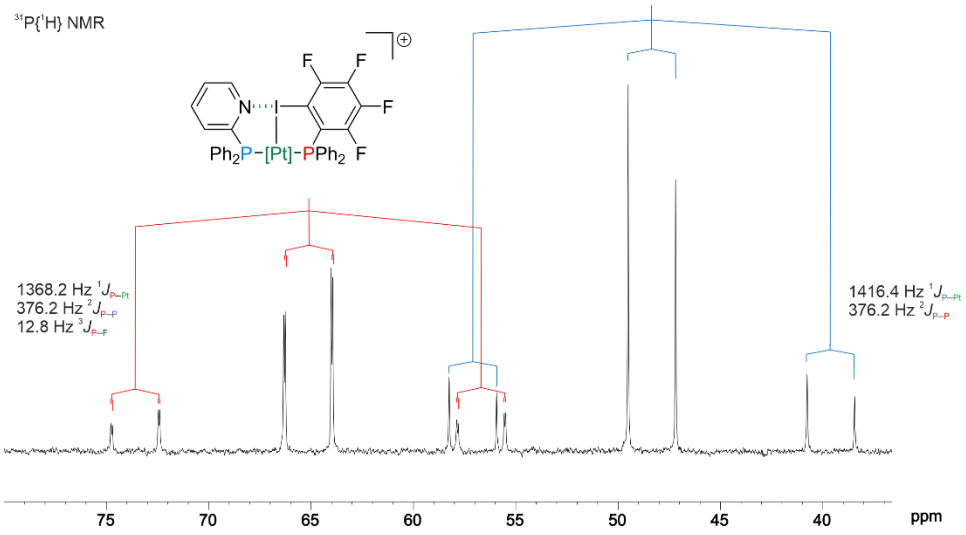

Figure 140. $^{31}P\{^{1}H\}$ NMR (162 MHz, CD_2Cl_2) of XBPhos-Pt **142**.

Crystals suitable for X-ray diffraction analysis were grown for the platinum complex derived from ligand **L3** and **L4** and this technique revealed the structure for XBPhos-Pt **142** (Figure 141). X-Ray analysis evidenced a halogen bonding interaction between the iodine (halogen bond donor) and the nitrogen (halogen bond acceptor). The iodine and the nitrogen atoms were aligned with a I···N distance of 2.7210(2) Å and with a C–I···N bond angle of 172.94(5)°. The iodine atom was coordinated to the metal center (Pt–I distance = 2.6134(5) Å) resulting in a P–I–P pincer-type complex, as it was observed for the rhodium complex XBPhos-Rh **116**.[15]

[15] *Pincer and Pincer-Type Complexes: Applications in Organic Synthesis and Catalysis;* Szabó, K. J., Wendt, O. F., Eds.; Wiley-VCH Verlag GmbH & Co.: Weinheim, 2014.

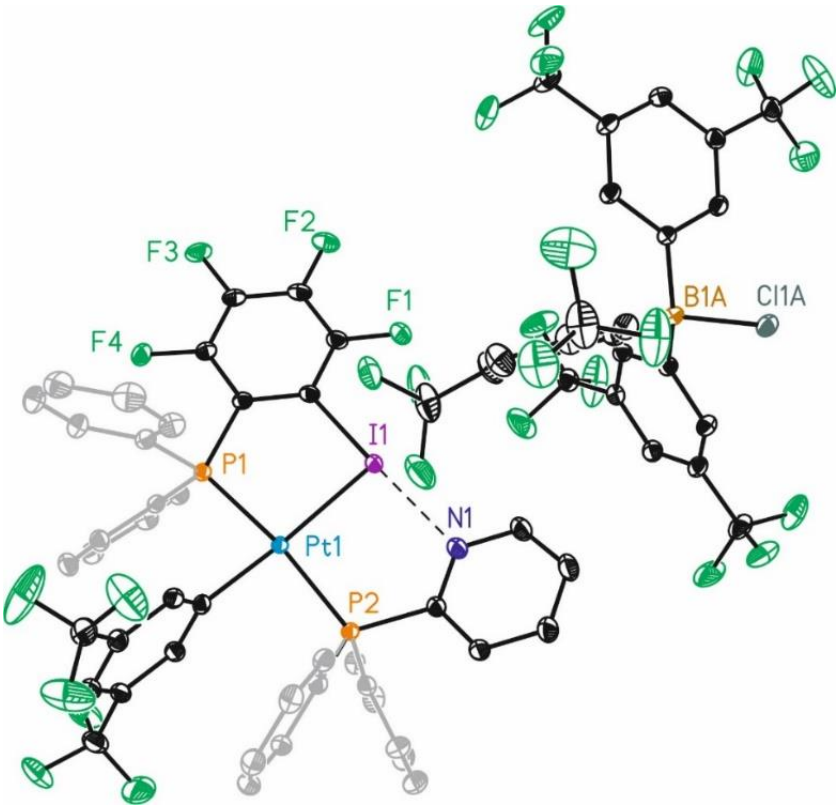

Figure 141. ORTEP drawing (thermal ellipsoids drawn at a 50% probability level) of the crystal structure of XBPhos-Pt **142**. Hydrogen atoms have been omitted for clarity. Color scheme: C: black and grey, N: dark blue, P: orange, B: light brown, Cl: dark green, F: light green, I: purple, Pt: light blue.

Furthermore, the R_{XB}[16] value that gives information about the strength of the halogen bonding interaction was calculated.[17] In our case, the halogen bonding interaction displayed a R_{XB} value of *ca*. 0.77, which is in accordance with the expected value for strong halogen bonding interactions (*i.e.*, values of R_{XB} between 0.75 and 0.90). Interestingly, X-ray analysis indicated that a 3,5-bis(trifluoromethyl)phenyl ligand was bound to the platinum center, resulting in a monocationic complex, whose charge was compensated by the tris(3,5-bis(trifluoromethyl)phenyl)chloroborate anion (see Figure 141 for the ORTEP drawing and Figure 142 for the chemical structure).

[16] Normalized interaction ratio (R_{XB}); $R_{XB} = d_{XB}/(X_{vdW} + B_{vdW})$, where d_{XB} [Å] refers to the distance between the donor atom (X) and the acceptor atom (B); vdW refers to the van der Waals radius [Å]; X to the halogen bond donor atom and B to the halogen bond acceptor atom.

[17] Puttreddy, R.; Jurcek, O.; Bhowmik, S.; Mäkelä, T.; Rissanen, K. *Chem. Commun.* **2016**, *52*, 2338-2341.

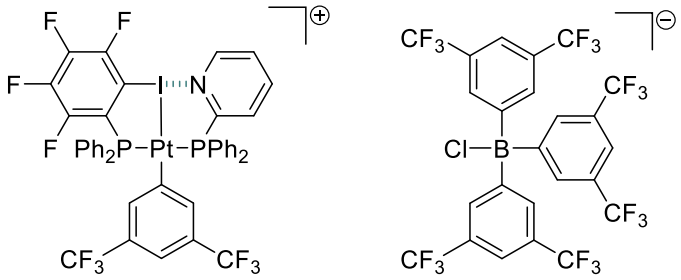

XBPhos-Pt **142**
[Pt(Ar^F)(κ^3*I,P,P*-(**L3**•**L4**))][B(Ar^F)$_3$(Cl)]
(Ar^F= 3,5-bis(trifluoromethyl)phenyl)

Figure 142. Chemical structure of complex XBPhos-Pt **142**.

The fragmentation of the BArF anion during the formation of platinum complexes derived from a halogen-bonded diphosphine was not in agreement with the results obtained in the synthesis of XBPhos-Rh **116**, in which this C–B bond cleavage process was not observed. With the aim of determining the generality of this cleavage process, we selected a structurally different halogen bond acceptor (phosphinoimine ligand **L5**) to study its reactivity towards [Pt(Cl)$_2$(cod)] in the presence of **L3** for the preparation of supramolecular platinum complexes incorporating a halogen-bonded diphosphorus ligand. The P-containing building block **L5** was readily prepared from diphenylphosphine **148** and (*N*-phenyl)(phenyl)carbonitrilium triflate **147**, following the synthetic procedure developed by Lammertsma *et al.*[18] (Scheme 47).

[18] (a) van Dijk, T.; Burck, S.; Rong, M. K.; Rosenthal, A. J.; Nieger, M.; Slootweg, J. C.; Lammertsma, K. *Angew. Chem., Int. Ed.* **2014**, *53*, 9068-9071. (b) van Dijk, T.; Burck, S.; Rosenthal, A. J.; Nieger, M.; Ehlers, A. W.; Slootweg, J. C.; Lammertsma, K. *Chem.–Eur. J.* **2015**, *21*, 9328-9331.

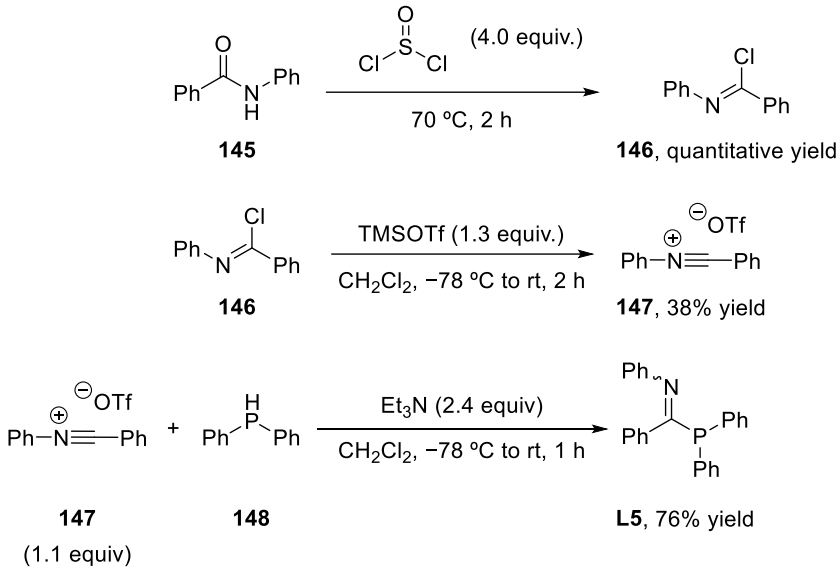

Scheme 47. General procedure for the preparation of **L5**.

The previously discussed synthetic methodology for the preparation of platinum complexes was followed using ligand **L3** and ligand **L5**. As a result, complex **149** was obtained in a 42 % yield (Scheme 48)

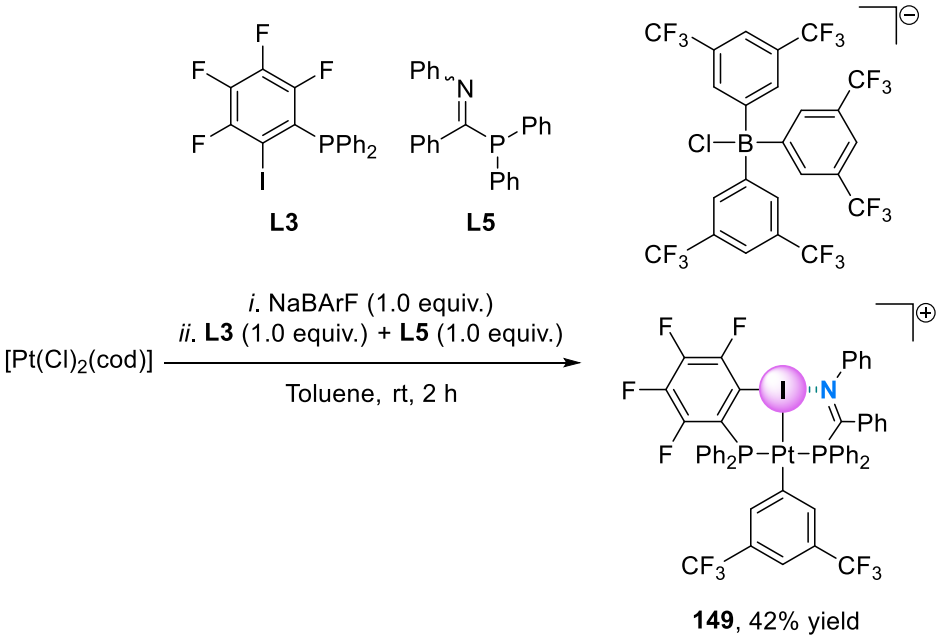

Scheme 48. General procedure for the formation of complex **149**.

Standard spectroscopic techniques pointed to the formation of platinum complex [Pt(Ar^F)(κ^3*I,P,P*-(**L3•L5**))][B(Ar^F)$_3$(Cl)] **149** (Scheme 48), with the same relevant structural features than XBPhos-Pt **142**. It is interesting to note the high $^2J_{P-P}$ coupling constant (*i.e.*, 376.5 Hz), which was in agreement with a *trans*-coordination fashion of the P-ligating groups.[14] The structure of the complex was unequivocally established by single crystal X-ray diffraction analysis (Figure 143), which indicated that a C–B bond cleavage process in NaBArF had again taken place during the formation of **149**. The complex presented a halogen bonding interaction between the iodine and the nitrogen with a I···N distance of 2.6544 Å and with a C–I···N bond angle of 178.17°. In this case, a R_{XB} value of *ca.* 0.75 was calculated, which is consistent with a strong halogen bonding interaction. The metal center was again coordinated to the iodine (Pt–I distance = 2.6063 Å). The complex **149** presented a shorter halogen bond distance and a higher R_{XB} value than XBPhos-Pt **142**.

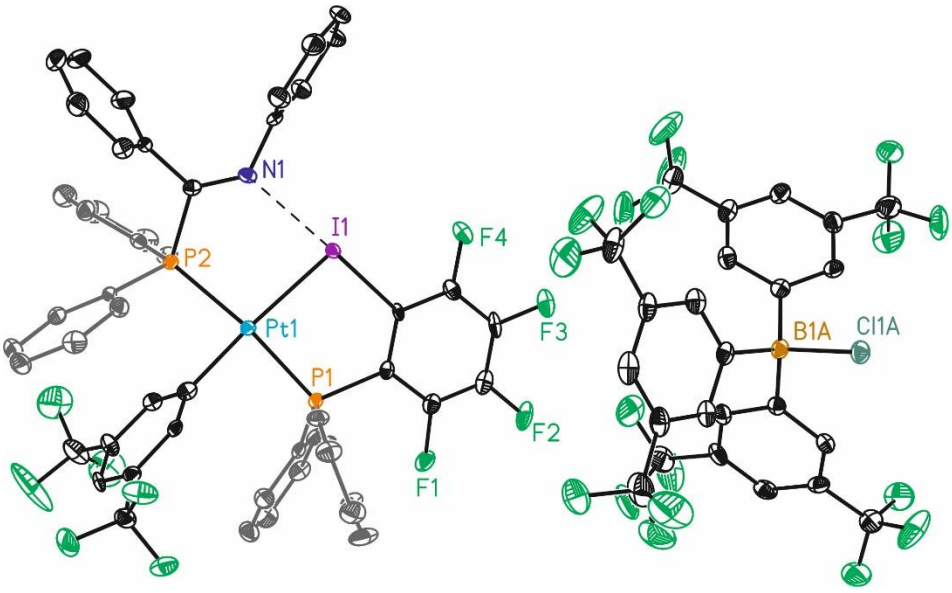

Figure 143. ORTEP drawing (thermal ellipsoids drawn at a 50% probability level) of the crystal structure of complex **149**. Hydrogen atoms have been omitted for clarity. Color scheme: C: black and grey, N: dark blue, P: orange, B: light brown, Cl: dark green, F: light green, I: purple, Pt: light blue.

These results indicate that cleavage of a B–C bond in the BArF anion took place irrespective of the nature of the halogen bond acceptor and resulted in the transfer of a 3,5-bis(trifluoromethyl)phenyl group (referred to as Ar^F in this discussion) to the platinum center and a transfer of a chloride group to the

boron-based anion. A similar behavior of the BArF anion was first reported by Kubas *et al*.[19] in 1999, where the non-coordinating anion reacted in the presence of an electrophilic platinum center (Scheme 49) leading to arylated platinum-complexes. The study of the mechanism of this arylation reaction performed by Kubas and coworkers demonstrated the formation of the products $B(Ar^F)_3$ and HAr^F, along with several other boron-containing species, as a consequence of the decomposition of the BArF group in the presence of a platinum(II) center.

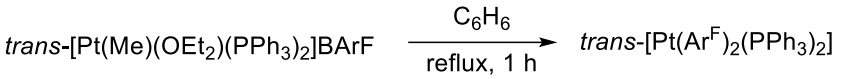

Scheme 49. Arylation reaction by Kubas *et al*.[19]

The fact that the BArF anion decomposed during the formation of the XBPhos-Pt was not in agreement with the results obtained for XBPhos-Rh, which presents the BArF anion located in the outer coordination sphere of the metal. At this point of the research activities, we hypothesized that palladium, the second-row analogue of platinum, would be less prone to promote the cleavage of C–B bond in the BArF anion.

Thus, we then studied the reaction between $[Pd(Cl)_2(cod)]$, NaBArF and ligands **L3** and **L4** following and analogous procedure to that used for XBPhos-Rh **116**. Elimination of one chlorido ligand from $[Pd(Cl)_2(cod)]$ was successfully achieved with 1.0 equiv. of NaBArF and the resulting palladium complex was allowed to react with an equimolar mixture of phosphines **L3** and **L4**. Interestingly, the desired complex XBPhos-Pd **150** was successfully prepared in a 30% yield (Scheme 50).

[19] Konze, W. V.; Scott, B. L.; Kubas, G. J. *Chem. Commun*. **1999**, 1807-1808.

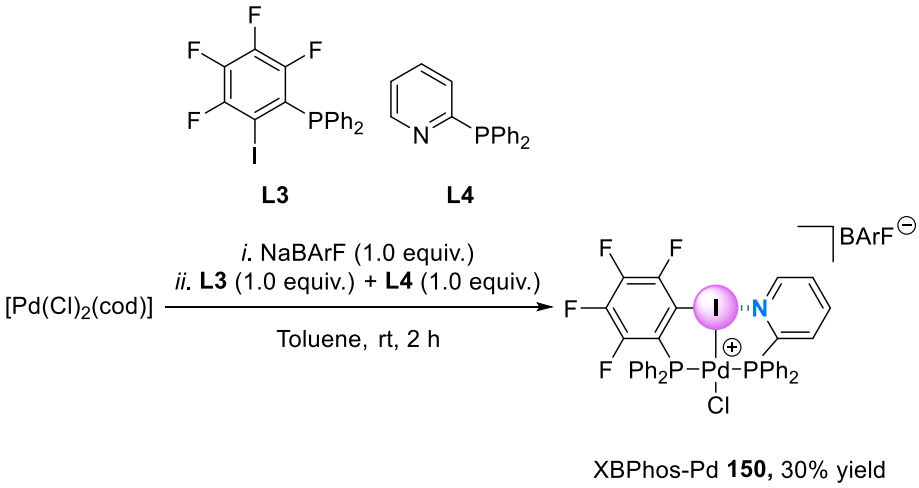

Scheme 50. Synthesis of the supramolecular complex XBPhos-Pd **150**.

The complex XBPhos-Pd **150** was characterized by standard spectroscopic studies, with the $^{31}P\{^{1}H\}$ NMR exhibiting two groups of signals (see the splitting pattern diagrams in Figure 144). A high value $^{2}J_{P-P}$ coupling constant (*i.e.*, 488.2 Hz) was calculated. According to the literature reviewed, this high value $^{2}J_{P-P}$ coupling constant indicated a *trans*-spanning diphosphine coordinated to the palladium center.[14] In the $^{19}F\{^{1}H\}$ NMR spectrum, a characteristic signal of BArF anion at −63.0 ppm was observed, which indicated that the BArF anion did not undergo any cleavage process during the formation of XBPhos-Pd **150**.

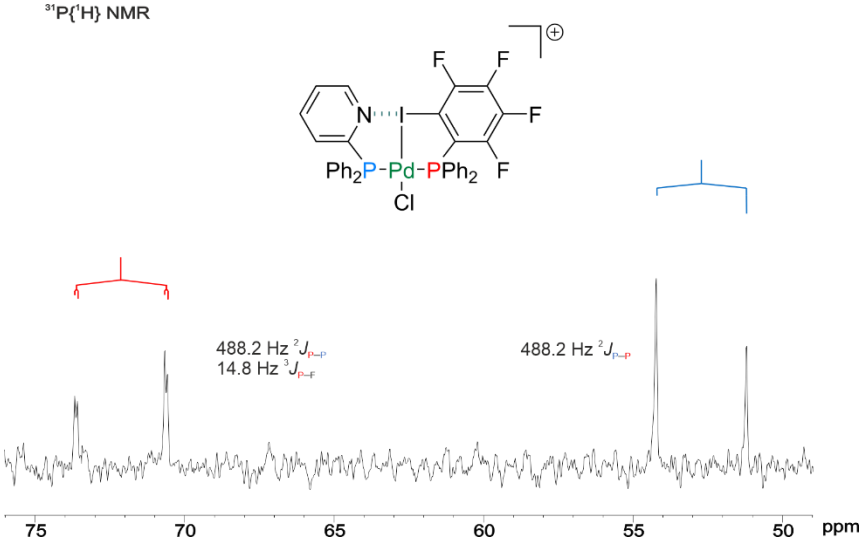

Figure 144. $^{31}P\{^{1}H\}$ NMR (162 MHz, CD_2Cl_2) of XBPhos-Pd **150**.

The structure of the XBPhos-Pd **150** complex was univocally confirmed by X-ray diffraction analysis of a single crystal (Figure 145).

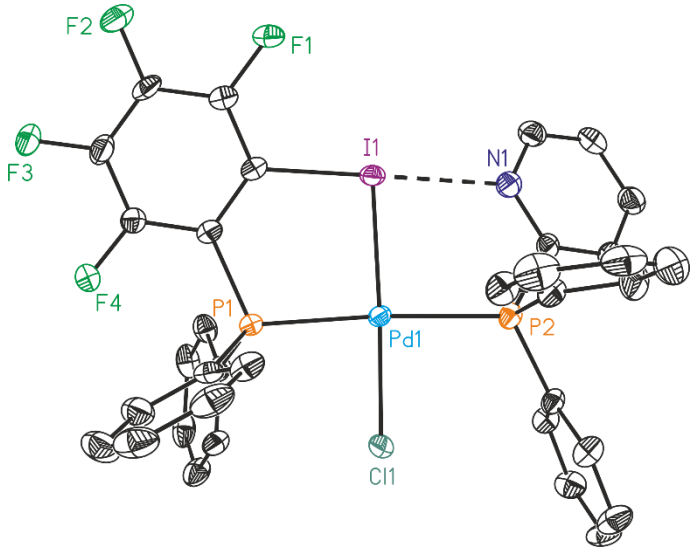

Figure 145. ORTEP drawing (thermal ellipsoids drawn at a 50% probability level) of the crystal structure of complex XBPhos-Pd **150**. Hydrogen atoms and the BArF anion have been omitted for clarity. Color scheme: C: black, N: dark blue, P: orange, Cl: dark green, F: light green, I: purple, Pd: light blue.

The complex showed the halogen bonding interaction between the iodine and the nitrogen atoms which were aligned with a I···N distance of 2.705(6) Å and with a C–I···N bond angle of 169.74(2)°. The value of R_{XB} was *ca.* 0.76, displaying a strong halogen bonding interaction. The structure of the palladium complex presents chlorido (Pd–Cl distance = 2.3342(8) Å) and iodido (Pd–I distance = 2.5478(3) Å) ligands bound to the metal center and a regular BArF counteranion. This behavior was in accordance with the previous results obtained in the group for the XBPhos-Rh **116**.[9]

2.3.2. Rationalization of the results obtained in the preparation of platinum complexes derived from halogen-bonded P-ligating groups

Subsequent research activities aimed at determining whether the C–B bond cleavage process was taking place during the elimination process of one chlorido ligand from the starting platinum complex (*i.e.*, [$Pt(Cl)_2$(cod)]) or at latter stages of the synthetic sequence towards XBPhos-Pt, once **L3** and/or **L4** were coordinated to the platinum center. To this purpose, the reaction mixture

obtained after stirring for one hour an equimolar mixture of $[Pt(Cl)_2(cod)]$ and NaBArF in toluene (Scheme 51) was analyzed by standard spectroscopic techniques. Analysis by NMR spectroscopy indicated that the reaction evolved to multiple platinum complexes.

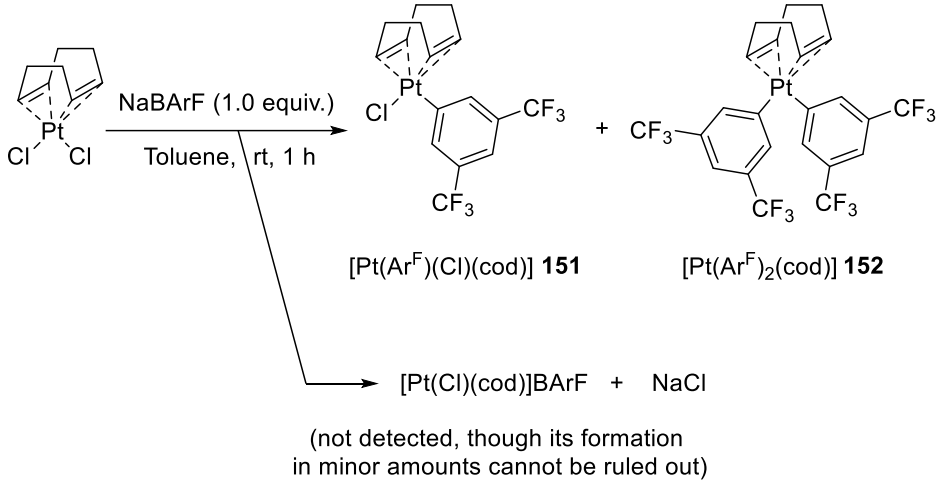

Scheme 51. General procedure for the synthesis of platinum intermediates **151** and **152**.

The ^{1}H NMR spectrum of the reaction mixture showed several signals attributable to the olefinic protons of the cod ligand in different platinum complexes. For instance, ^{1}H NMR showed that minor amounts of the starting platinum complex remained in solution after having been allowed to react with NaBArF for one hour (9%, see signal labelled with a green asterisk in Figure 146). The major product of the reaction contained a cod ligand in an asymmetric chemical environment, as two groups of olefin protons with different chemical shifts were observed (66%, see signals labelled with a blue asterisk in Figure 146). This observation pointed to an asymmetrically substituted square planar platinum(II) complex incorporating the cod ligand, for which we suggested structure **151**. A third cod-containing platinum complex was observed with all the olefin protons from the cod ligand having the same chemical shift (25%, see signals labelled with a red asterisk in Figure 146), for which we suggested structure **152**.

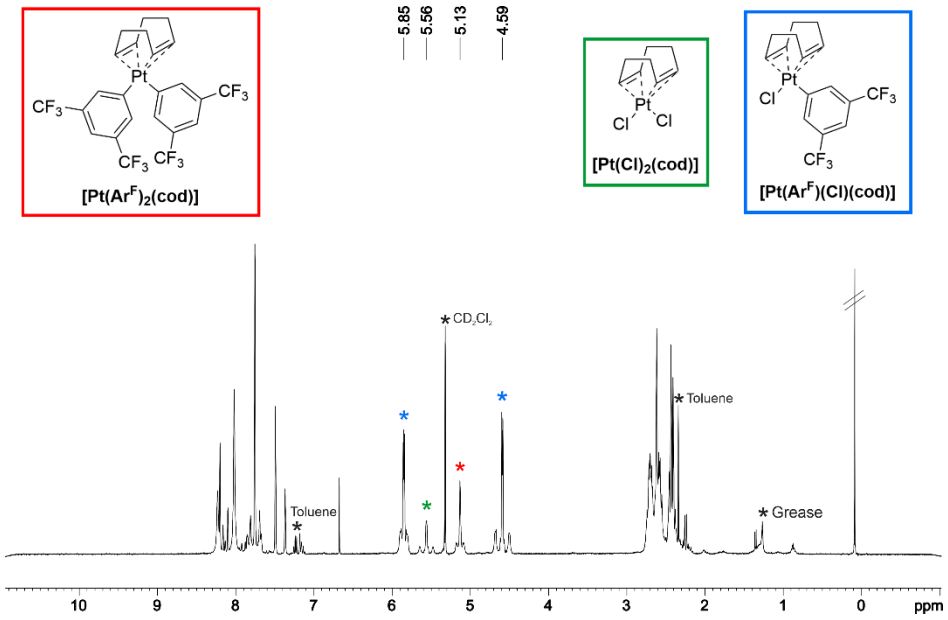

Figure 146. ^{1}H NMR spectrum (400 MHz, CD_2Cl_2) of the reaction intermediate mixture.

The $^{19}F\{^{1}H\}$ NMR spectrum exhibited several signals with chemical shifts similar to those observed for the BArF anion (*ca.* −63.0 ppm). An assignation of the different signals is indicated in Figure 147.

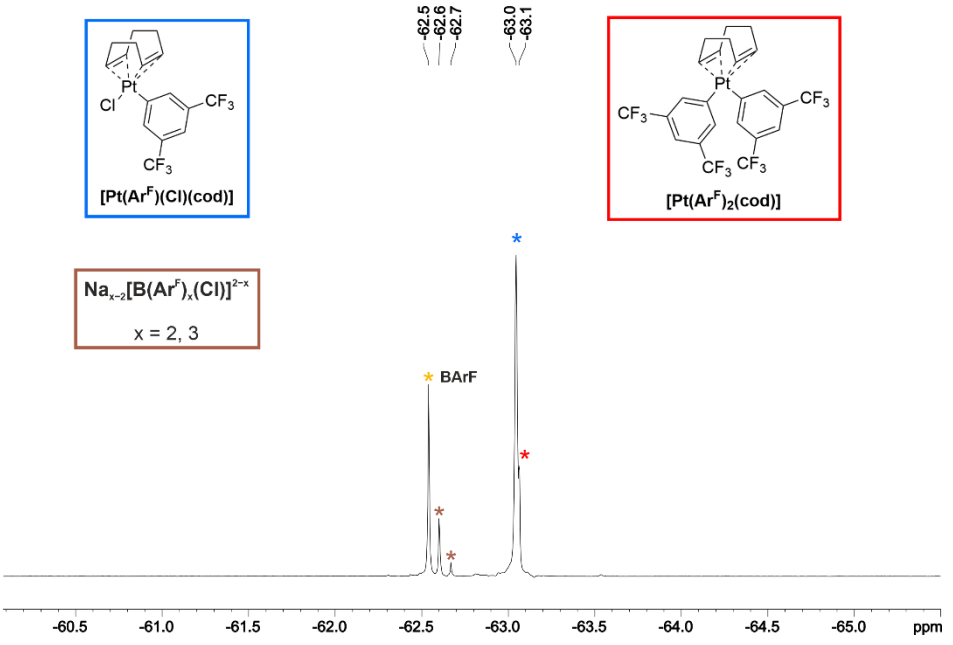

Figure 147. $^{19}F\{^{1}H\}$ NMR spectrum (376 MHz, CD_2Cl_2) of the reaction intermediate mixture.

The ^{195}Pt NMR spectrum of the mixture exhibited three signals at 1168.4, 1144.5 and 870.5 ppm, which were in agreement with the [Pt(Cl)$_2$(cod)], [Pt(Ar^F)(Cl)(cod)] **151** and [Pt(Ar^F)$_2$(cod)] **152** platinum complexes, respectively (Figure 148).

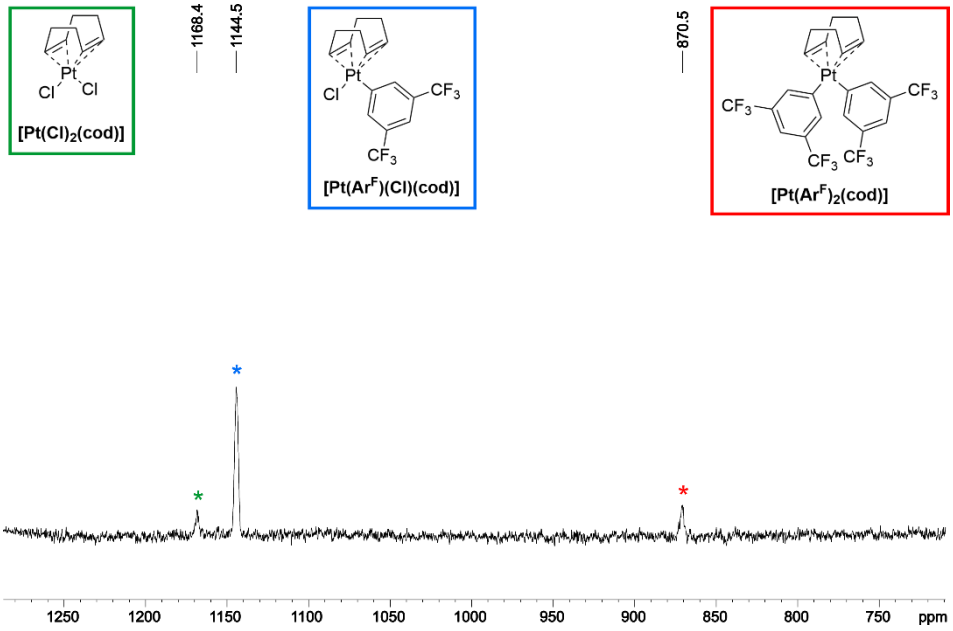

Figure 148. ^{195}Pt NMR spectrum (86 MHz, CD_2Cl_2) of the reaction intermediate mixture.

Unfortunately, mass spectrometry spectra of the reaction mixture employing the available ionization techniques (ESI) were not diagnostic, as they did not provide information on the molecular ions of the different cationic complexes.

As regards the rationalization of the formation of supramolecular platinum complexes **142** and **149**, the results obtained with NMR studies suggested that the C–B bonds were cleaved and the Ar^F moieties transferred from the BArF anion to the platinum centers prior to the addition of the phosphine ligands, as complexes [Pt(Ar^F)(Cl)(cod)] **151** and [Pt(Ar^F)$_2$(cod)] **152** were formed in the absence of phosphine ligands.

The structures of complexes **151** and **152** were confirmed by X-ray analysis, as crystals suitable for X-ray diffraction of these complexes could be picked from the solution (Figure 149). Single crystals of the complex [Pt(Cl)$_2$(cod)] were also detected in the same reaction mixture, though its structure has not

been included in the present thesis because it is already reported in the literature.[20]

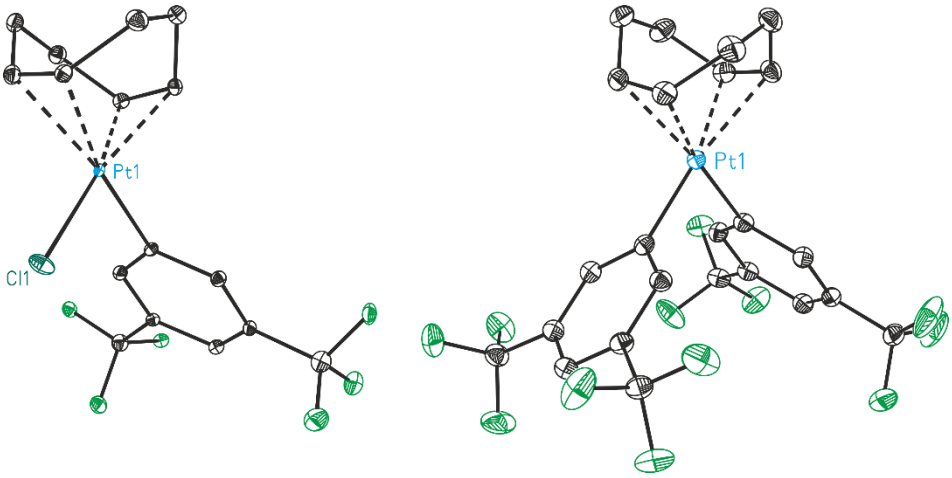

Figure 149. ORTEP drawing (thermal ellipsoids drawn at a 50% probability level) of the crystal structure of the **151** (left), and the **152** (right). Hydrogen atoms have been omitted for clarity. Color scheme: C: black, Cl: dark green, F: light green, Pt: light blue.

NMR spectra of the crystals subjected to X-ray analysis were recorded and the spectroscopic NMR data from the diffracted crystals were in agreement with the previously described NMR data (compare Figure 146 with Figure 198 and Figure 200).

Finally, the formation of XBPhos-Pt **142** was monitored by $^{19}F\{^{1}H\}$ NMR spectroscopy. In this study, the consumption of BArF and the formation of new species were analyzed. The first spectrum of the monitoring study (t = 0 min) exhibited the BArF anion signal at −62.5 ppm. After 15 minutes, the upfield signals observed (−62.9 - −63.6 ppm) corresponded to the platinum complexes **151** and **152** (see Figure 149). In one hour, the intensity of the signals of these complexes increased substantially with the $^{19}F\{^{1}H\}$ signal of $[Pt(Ar^F)_2(cod)]$ **152** being observed as a shoulder in the $^{19}F\{^{1}H\}$ NMR signal of **151**. Concurrently, from 15 minutes of reaction onward, signals in the downfield region of the $^{19}F\{^{1}H\}$ NMR spectrum (from −62.4 to −62.7 ppm) were observed. These signals were attributed to boron derivatives generated by decomposition of the BArF anion. Apart of the corresponding signal for the untransformed BArF anion, signals in agreement with the $Na[B(Ar^F)_3(Cl)]$ and $[B(Ar^F)_2(Cl)]$ derivatives were observed, as well as other weak signals that could not be

[20] Syed, A.; Stevens, E. D.; Cruz, S. G. *Inorg. Chem.* **1984**, *23*, 3673-3674.

unequivocally assigned. After allowing to react this mixture for one hour, phosphine ligands **L3** and **L4** were added and a $^{19}F\{^{1}H\}$ NMR spectrum was recorded one hour after (t = 120 min). $^{19}F\{^{1}H\}$ NMR analysis indicated that platinum complex [Pt(Ar^F)(κ^3*I,P,P*-(**L3•L4**))][$B(Ar^F)_3$(Cl)] **142** was formed, that complex **151** was consumed by reaction with phosphine ligands **L3** and **L4** and that complex **152** remained unreacted in solution. (Figure 150).

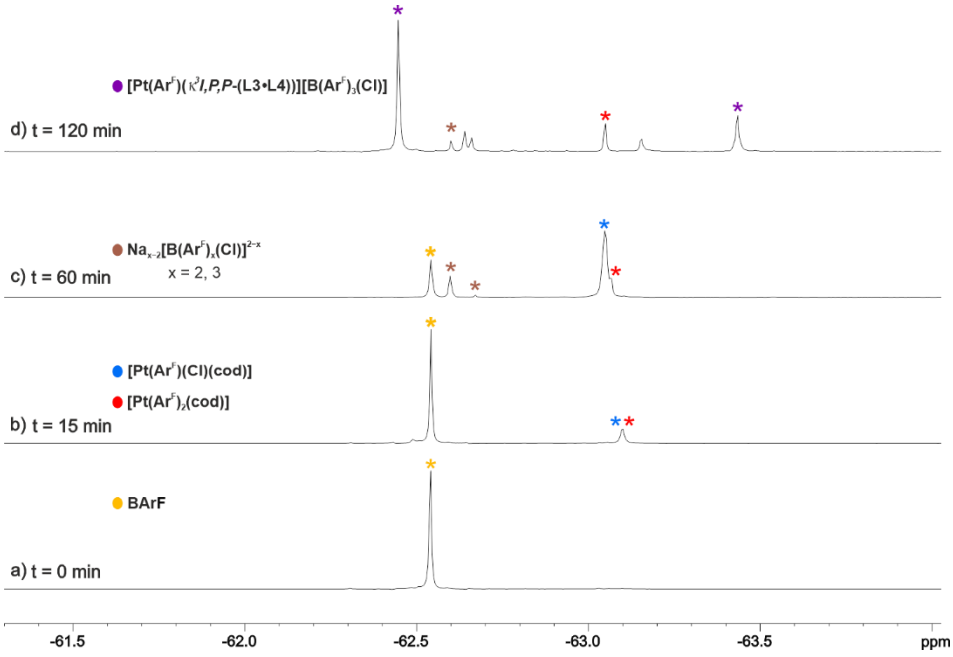

Figure 150. Stacked plot of the $^{19}F\{^{1}H\}$ NMR (376 MHz, CD_2Cl_2) spectra for the formation of XBPhos-Pt **142** at different reaction times: a) t = 0 min; b) t = 15 min; c) t = 60 min; d) t = 120 min, this spectrum was recorded one hour after adding ligands **L3** and **L4**.

Additional 2D NMR experiments (DOSY and EXSY) were recorded on the reaction mixture and ruled out the possibility of formation of monomeric or dimeric platinum species in equilibrium (see Figure 161 and Figure 162).

To rule out the possibility that complex **152** was involved in the formation of halogen-bonded complex XBPhos-Pt **142**, it was envisioned that platinum complex **152** could be selectively prepared by using two equivalents of NaBArF with respect to [$Pt(Cl)_2$(cod)] (Scheme 52).

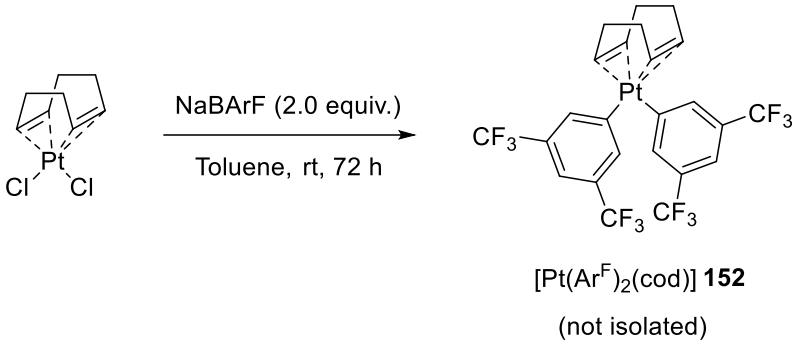

Scheme 52. Synthesis of complex **152**.

^{1}H and ^{195}Pt NMR spectra after 72 hours showed that [Pt(Ar^F)$_2$(cod)] **152** had been formed as the major product, without observing the formation of **151** (compare Figure 151 and Figure 152 with Figure 200 and Figure 148).

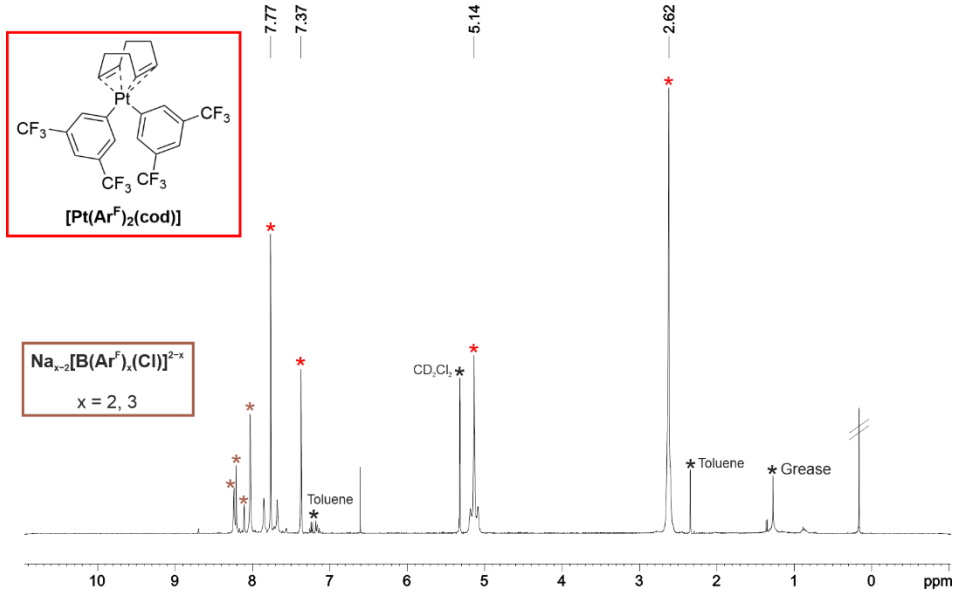

Figure 151. ^{1}H NMR spectrum (400 MHz, CD_2Cl_2) of the reaction mixture at 72 h.

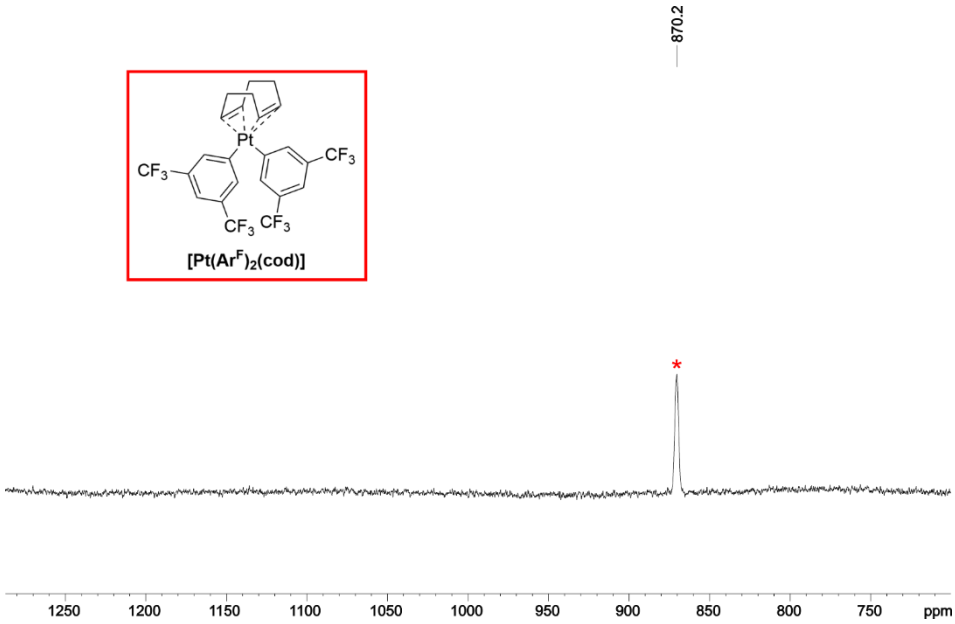

Figure 152. ^{195}Pt NMR spectrum (86 MHz, CD_2Cl_2) of the reaction mixture at 72 h.

After this time, and having **152** as the major product, ligands **L3** and **L4** were added to the mixture. The solution was stirred for 1 hour. The desired complex **142** was obtained in trace amounts, indicating that the formation of XBPhos-Pt **142** was not favorable from complex **152**.

With all these results in hand, we can conclude that complex XBPhos-Pt **142** is formed from complex [Pt(Ar^F)(Cl)(cod)] **151** in good yields. The presence of the platinum complex [Pt(Cl)(cod)]BArF (*i.e.*, the expected complex that should be formed from [Pt(Cl)$_2$(cod)] and equimolar amounts of NaBArF by elimination of NaCl) has not been detected in any of the reaction mixtures studied. However, it should be noted that minor peaks in the reaction mixture between [Pt(Cl)$_2$(cod)] and 1.0 equiv. of NaBArF remain unassigned (see Figure 150), which does not allow to rule out its formation, though this must be in minor amounts.

In the case of the XBPhos-Pt complex, monodentate ligands **L3** and **L4** function as a *trans*-spanning bidentate ligand due to their preorganization by halogen bonding.[21] Further research activities in this section aimed at confirming that a *trans*-coordination preference of the ligand had an effect in the outcome of the complexation reaction. To this purpose, we attempted the

[21] This behavior has also been observed in rhodium complexes. For example, see ref. 9b.

preparation of the Xantphos-Pt complex **153**, starting from the well-known *trans*-spanning diphosphine Xantphos[22] **L6** and by following an analogous synthetic methodology to that developed for XBPhos-Pt. Interestingly, the Xantphos-Pt complex **153** was obtained in good yield (71% yield) after following the synthetic methodology summarized in Scheme 53. The formation of the product was confirmed by standard spectroscopic techniques, which revealed analogous structural features to those observed for XBPhos-Pt **142**.

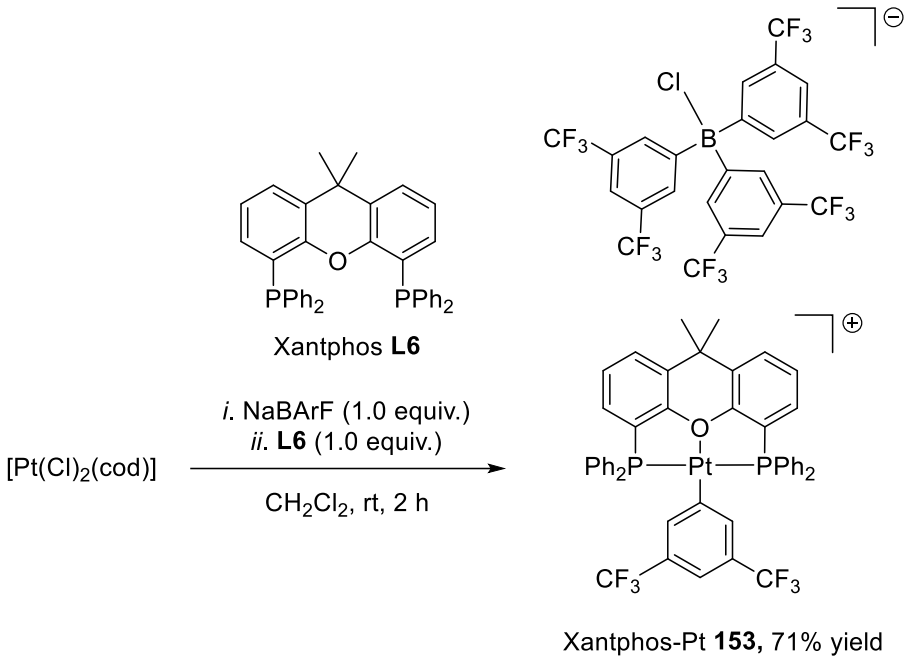

Scheme 53. General procedure for the synthesis of Xantphos-Pt **153**.

Moreover, the structure of the complex was unequivocally confirmed by single crystal X-ray diffraction. Xantphos-Pt **153** presented the oxygen bonded to the platinum center (Pt–O distance = 2.1700(1) Å), with a pincer-type structure for the resulting complex. Again, a C–B bond cleavage from NaBArF took place during the formation of Xantphos-Pt **153**, which incorporated an Ar^F moiety bound to the platinum center (Figure 153). These results confirmed that the C–B bond cleavage step is inherent to the platinum center rather than being due to the halogen bonding interactions involved in the formation of platinum complexes when ligands **L3**, **L4** and **L5** were used.

[22] Xantphos = 9,9'-Dimethyl-4,5-bis(diphenylphosphino)xanthene. For example, see the following reference: van Leeuwen, P. W. N. M.; Kamer, P. C. J. *Catal. Sci. Technol*. **2018**, *8*, 26-113.

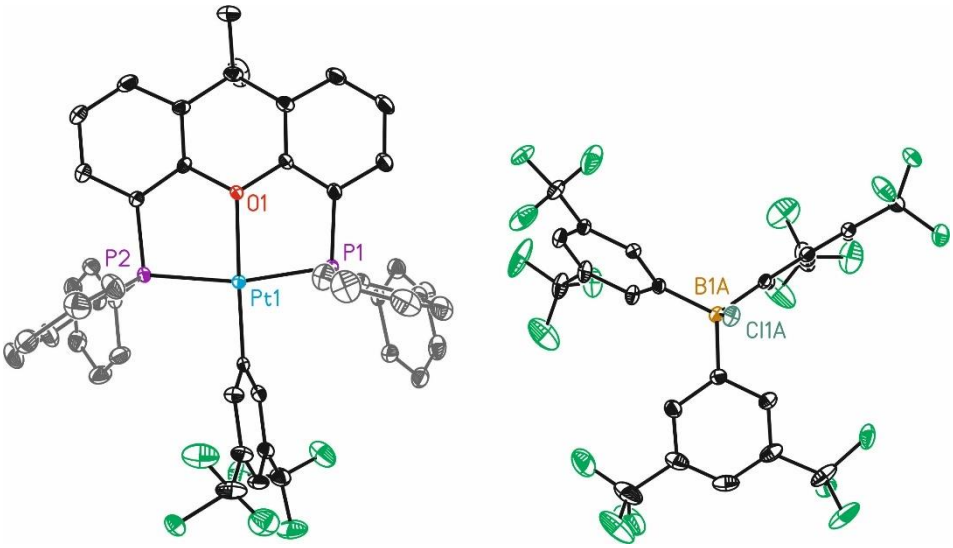

Figure 153. ORTEP drawing (thermal ellipsoids drawn at a 50% probability level) of the crystal structure of Xantphos-Pt **153** complex. Hydrogen atoms have been omitted for clarity. Color scheme: C: black and grey, O: red, P: purple, B: light brown, Cl: dark green, F: light green, Pt: light blue.

To conclude this section, we propose a tentative mechanistic rationalization for the formation of the of platinum(II) complex **142** (Scheme 54). We have demonstrated that the first step is the formation of the platinum intermediate [Pt(Ar^F)(Cl)(cod)] **151** along with the boron derivative Na[B(Ar^F)$_3$(Cl)] **155**. Relevant reaction intermediates were isolated and characterized from the reaction mixture and we hypothesized that these products were generated by oxidative addition of a B–C bond from the BArF counterion to the platinum metal center followed by B–Cl reductive elimination. Subsequent coordination of the phosphine ligands **L3** and **L4**, which contain complementary halogen bonding motifs, to the platinum complex **151** followed by concomitant displacement of the cod ligand and elimination of NaCl led to XBPhos-Pt **142**. It is interesting to recall at this point that the spectroscopic studies revealed that the halogen-bonded diphosphine **L3•L4** is coordinated in XBPhos-Pt **142** in a *trans*-fashion.

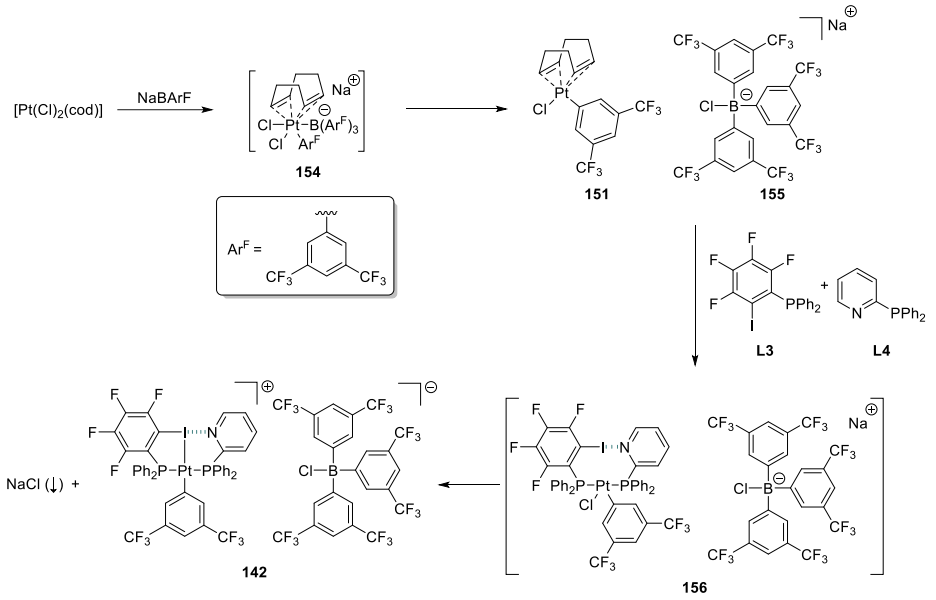

Scheme 54. Tentative mechanistic rationalization for the formation of the of platinum(II) complex **142**.

2.3.3. Attempted applications of platinum complexes derived from halogen-bonded diphosphines in catalysis

With platinum complexes derived from halogen-bonded phosphines in hand (*e.g.*, XBPhos-Pt **142**), we set about evaluating its activity as catalyst in several transformations of interest.[23]

As for potential applications of XBPhos-Pt as catalyst, we turned initially our attention to the cyclization of enynes. Our motivation was based on the fact that the platinum complex XBPhos-Pt **142** presents some similarities with complex **161**, which has been used in the Pt-catalyzed cyclization of **157** to highly functionalized cyclization products (structures **158**, **159** and **160**, which were obtained in 81% yield and in a 0.9:1:0.2 ratio, respectively; Scheme 55).

[23] Ríos, P.; Rodríguez, A.; Conejero, S. *Chem. Commun.* **2020**, *56*, 5333-5349.

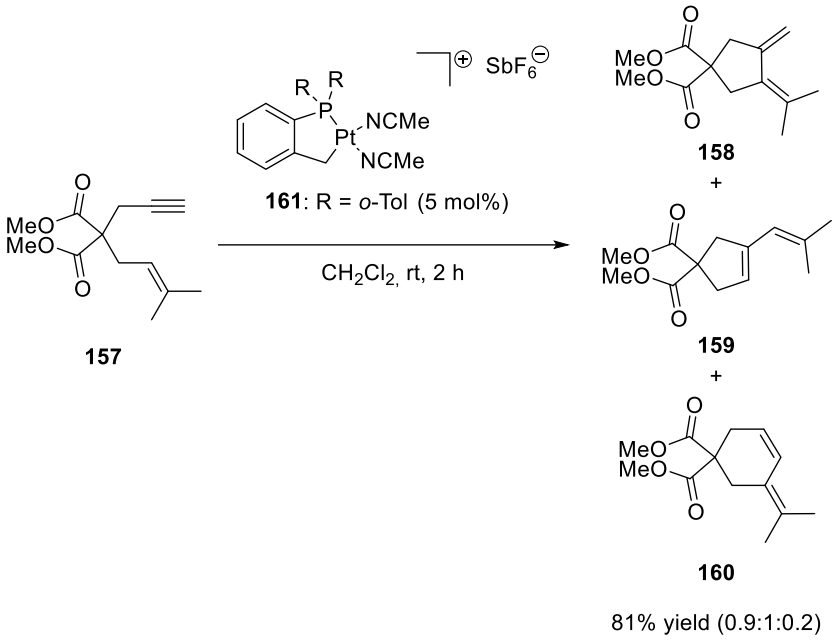

Scheme 55. Platinum(II)-catalyzed cyclization of 1,6-enynes reported by Echavarren *et al.*[24]

Despite the structural differences between complexes **142** and **161** (complex **161** derived from a monophosphine ligand and incorporated two labile CH_3CN ligands), we hypothesized that XBPhos-Pt **142** complex could be active in catalyzing the cyclization of 1,6-enynes (Scheme 56). To this purpose, we selected dimethyl 2-allyl-2-(prop-2-yn-1-yl)malonate **162** as model substrate, which was prepared following a well-established synthetic protocol reported in the literature[25] from dimethyl 2-(prop-2-yn-1-yl)malonate and allyl bromide.

[24] Ferrer, C.; Raducan, M.; Nevado, C.; Claverie, C. K.; Echavarren, A. M. *Tetrahedron* **2007**, *63*, 6306-6316.
[25] Benedetti, E.; Simonneau, A.; Hours, A.; Amouri, H.; Penoni, A.; Palmisano, G.; Malacria, M.; Goddard, J.-P.; Fensterbank, L. *Adv. Synth. Catal.* **2011**, *353*, 1908-1912.

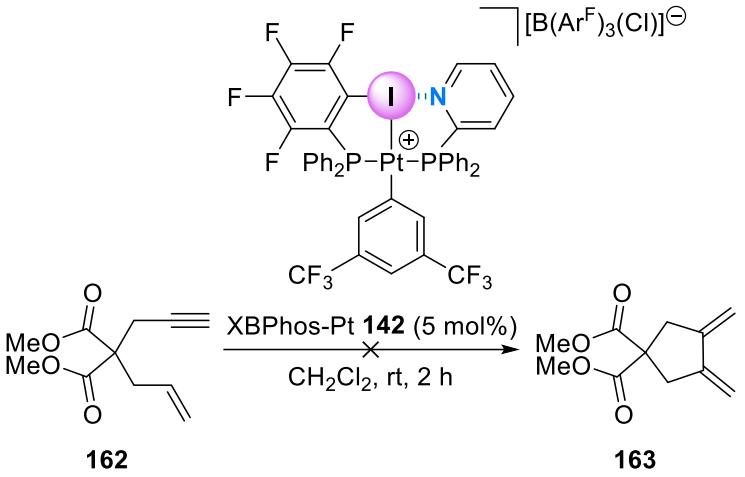

162 **163**

Scheme 56. Attempted cyclizations of 1,6-enynes employing XBPhos-Pt **142**.

To our dismay, the cyclization was not successful, recovering only unreacted starting material from the crude. No changes in the outcome of the reaction were detected when the reaction time was extended (up to 24 h) and the temperature was increased (up to 60 ºC).

Interestingly, Sabat and coworkers reported that the platinum(II) complex **168** was highly active in the hydrophenylation of ethylene towards aromatic products **165**, **166** and **167**. The mechanism of this challenging transformation entailed the coordination of ethylene to the platinum(II) center, subsequent insertion of ethylene into the Pt–phenyl bond followed by benzene C–H activation to afford the products **165**, **166** and **167**, which were obtained in 89% yield and in a 1:0.22:0.02 ratio, respectively (Scheme 57).[26]

[26] McKeown, B. A.; González, H. E.; Friedfeld, M. R.; Gunnoe, T. B.; Cundari, T. R.; Sabat, M. *J. Am. Chem. Soc.* **2011**, *133*, 19131-19152.

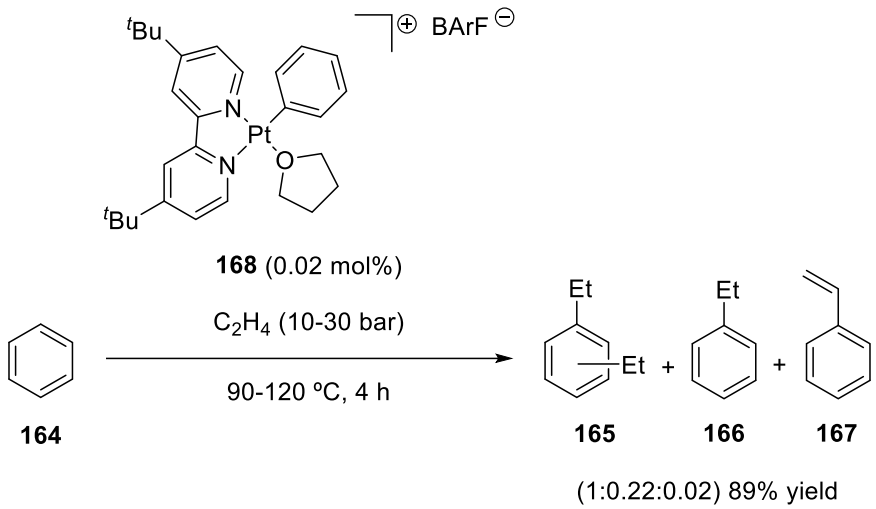

Scheme 57. Platinum(II)-catalyzed hydrophenylation of ethylene by Sabat *et al*.[26]

Due to the similarities between the platinum catalyst **168** and XBPhos-Pt **142**, we hypothesized that ethylene could react first with the Ar^F group in **142** with concomitant formation of a coordination vacant and re-entry of the resulting platinum complex into the hydrophenylation catalytic cycle. We performed the reaction in an autoclave reactor and the crude mixture was analyzed by GC-MS (Scheme 58). Unfortunately, no reaction product was detected, perhaps due to the fact that the reported reaction temperatures cannot be used with XBPhos-Pt due to a lack of stability of XBPhos-Pt at temperatures higher than 60 ºC.

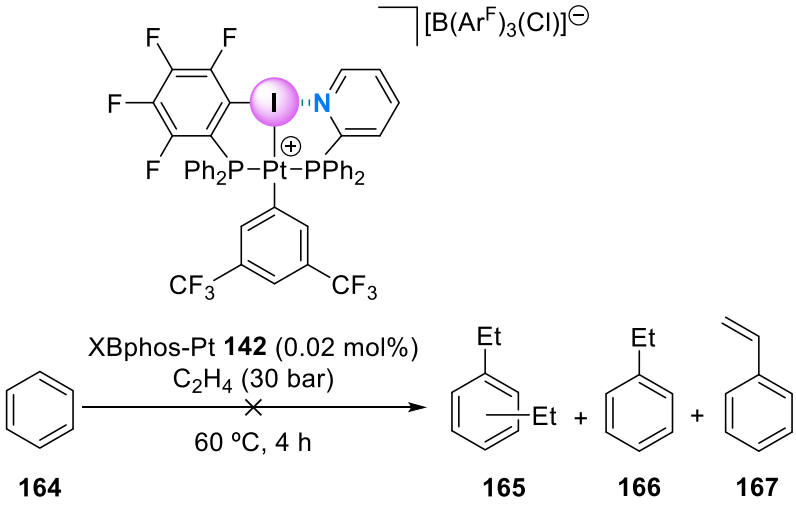

Scheme 58. Attempted ethylene hydrophenylation employing XBPhos-Pt **142**.

As complex XBPhos-Pt **142** proved to be unreactive in the above mentioned chemistries, we reasoned that the coordination of the Ar^F ligand to the platinum center could stay at the origin of the lack of reactivity. It is reported in the literature that one of the phenyl ligands in platinum complex **169** was cleaved with *in situ* generated HCl with formation of a Pt–Cl bond (Scheme 59).[27]

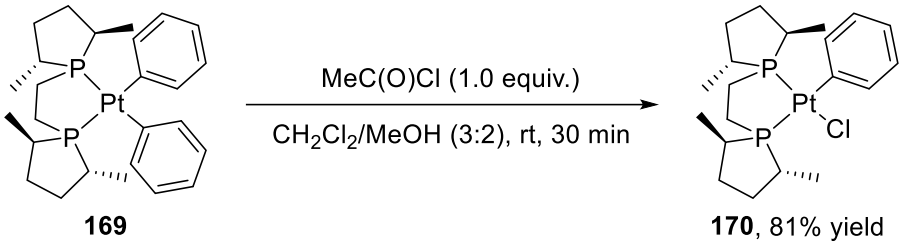

169 **170**, 81% yield

Scheme 59. Cleavage of a Pt–Ar bond with HCl reported by Rheingold *et al*.[27]

Unfortunately, under the reported reaction conditions, the Pt-complex **142** evolved to a complex mixture of platinum complexes.

The use of electrophilic fluorinating agents, such as **174** (Scheme 60), was also considered a good strategy to cleave the Ar^F-group in XBPhos-Pt **142** with the generation of a coordination vacant at the platinum center and formation of the $F–Ar^F$ product.

Interestingly, Gagné and coworkers reported the efficient transformation of Pt-complex **171** into a new platinum complex **172** along with the fluorinated product **173** (Scheme 60).[28] Unfortunately, under the same reaction conditions, complex XBPhos-Pt **142** evolved to a complex mixture of unidentified platinum derivatives.

[27] Guino-o, M. A.; Zureick, A. H.; Blank, N. F.; Anderson, B. J.; Chapp, T. W.; Kim, Y.; Glueck, D. S.; Rheingold, A. L. *Organometallics* **2012**, *31*, 6900-6910.
[28] Zhao, S.-B.; Becker, J. J.; Gagné, M. R. *Organometallics* **2011**, *30*, 3926-3929.

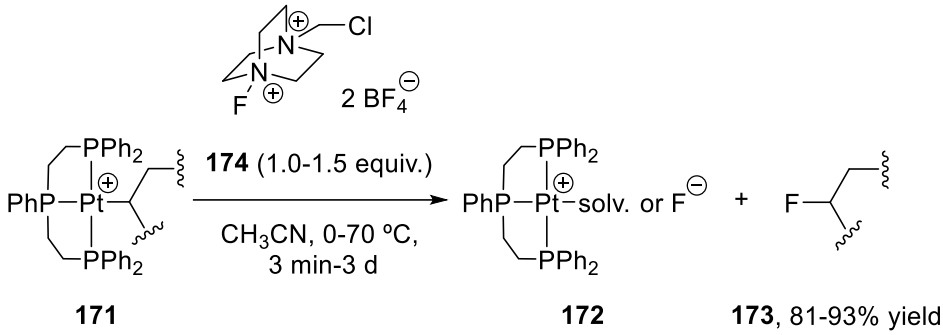

Scheme 60. Cleavage of the Pt–C bond in **171** using **174** reported by Gagné *et al.*[28]

Further attempts for generating a coordination vacant by cleaving the Pt–Ar^F bond involved the use of CO as reagent. It has been described in the literature that the *trans*-P-disubstituted platinum complex **175** reacted with CO to afford the platinum complex **176** by CO insertion into Pt–aryl or Pt–alkyl bonds (Scheme 61).[29]

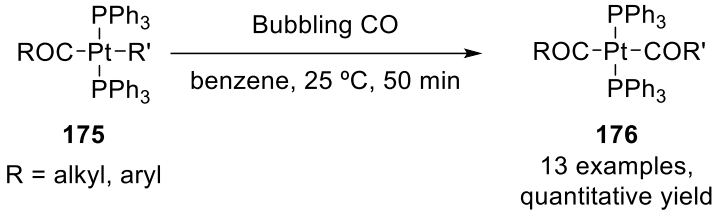

Scheme 61. CO insertion reaction reported by Chen *et al.*[29]

We considered that this chemistry could open the opportunity of transforming XBPhos-Pt into the corresponding carbonylated analogue **177**, which contains a more reactive Pt–$COAr^F$ bond than the Pt–Ar^F bond in XBPhos **142**. Interestingly, the reaction of XBPhos-Pt with CO at 60 ºC under high pressure (80 bar) translated into the formation of the desired complex with *ca.* 51% conversion[30] (Scheme 62).

[29] Chen, J.-T.; Yeh, Y.-S.; Yang, C.-S.; Tsai, F.-Y.; Huang, G.-L.; Shu, B.-C.; Huang, T.-M.; Chen, Y.-S.; Lee, G.-H.; Cheng, M.-C.; Wang, C.-C.; Wang, Y. *Organometallics* **1994**, *13*, 4804-4824.
[30] Calculated from the MS-ESI data.

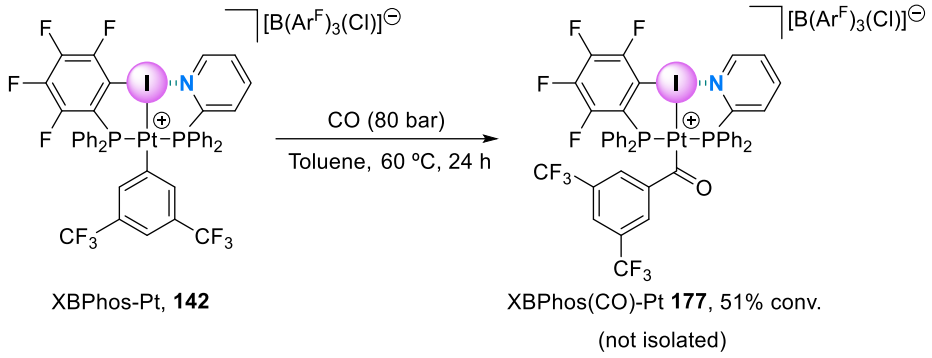

Scheme 62. General procedure for the carbonylation reaction of XBPhos-Pt **142**.

The analysis of the crude mixture by MS exhibited a peak at *m/z* = 1158.8 with the expected molecular ion for XBPhos(CO)-Pt **177** (*m/z*: calcd for $C_{44}H_{27}F_{10}INOP_2Pt$ $[M]^+$ 1159.0; Figure 154). Further experiments are required to optimize the yield of this transformation.

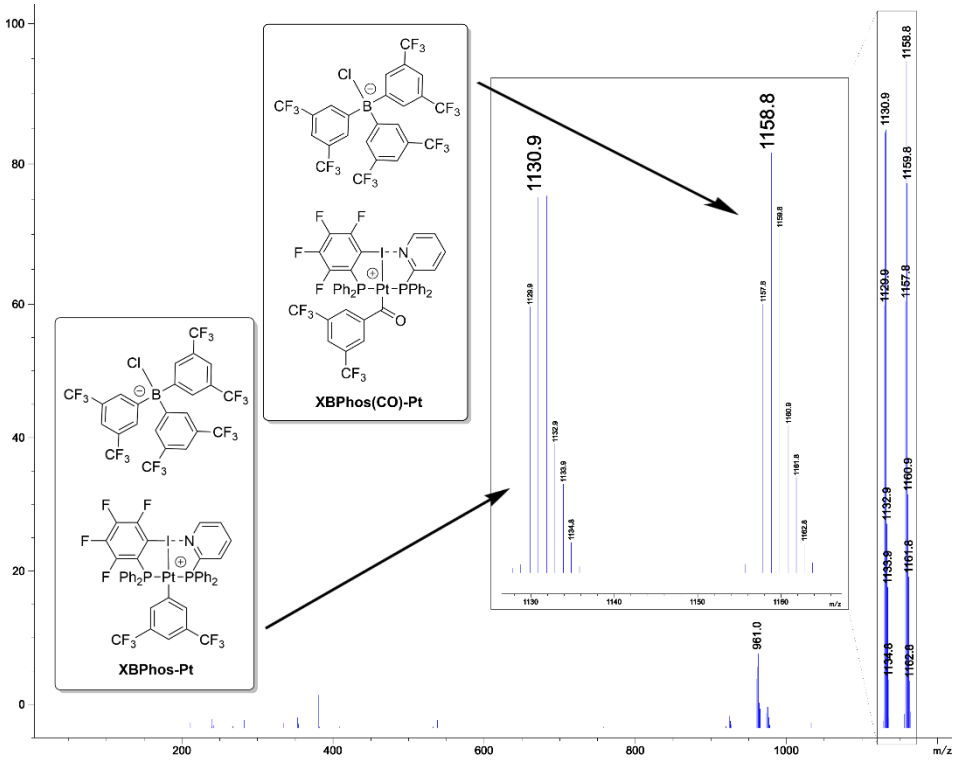

Figure 154. MS spectra of the reaction mixture arising from the carbonylation of XBPhos-Pt **142**.

To conclude, we would like to note that this strategy paves the way to the successful application of XBPhos-Pt **142** as catalyst for new transformations of interest (for instance, hydroformylations,[31] hydroborations,[9a,32] etc.).

[31] Boerner, A.; Franke, R. Metals in Hydroformylation. *Hydroformylation: Fundamentals, Processes, and Applications in Organic Synthesis*; Wiley-VCH Verlag GmbH & Co.: Weinheim, 2016; Volume 1, pp 5-72.

[32] Yu, X.-H.; Cao, K.; Huang, Y.; Yang, J.; Li, J.; Chang, G. *Chem. Commun.* **2014**, *50*, 4585-4587.

2.4. CONCLUSIONS

In conclusion, the design, synthesis and characterization of new supramolecular platinum(II) and palladium(II) complexes derived from halogen-bonded diphosphines are described. The assembly of two building blocks that incorporate P-containing ligating groups, as well as complementary binding motifs for the assembly process through halogen bonding, efficiently led to new supramolecular platinum(II) and palladium(II) complexes. These new complexes were thoroughly characterized in solution (standard spectroscopic techniques) and in the solid state (single crystal X-ray diffraction). In contrast to the analogous supramolecular rhodium complexes previously reported by our group, the supramolecular platinum complexes prepared (*i.e.*, [Pt(Ar^F)(κ^3*I,P,P*-(**L3•L4**))][B(Ar^F)$_3$(Cl)] and [Pt(Ar^F)(κ^3*I,P,P*-(**L3•L5**))][B(Ar^F)$_3$(Cl)]) incorporated an Ar^F (3,5-bis(trifluoromethyl)phenyl) ligand, which arose from the BArF counterion through a platinum mediated B–Ar^F bond cleavage. A broad study of the reaction intermediates and reaction pathway that led to the final platinum(II) complexes has been performed. A tentative mechanistic rationalization for the formation of the platinum(II) complex **142** is proposed (oxidative addition of a B–C bond from the BArF counterion to [Pt(Cl)$_2$(cod)], subsequent B–Cl reductive elimination, coordination of the phosphine ligands with concomitant displacement of the cod ligand and NaCl elimination). The complex XBPhos-Pt has proved to be unreactive as a supramolecular catalyst in carbocyclizations of enynes and the hydrophenylation of ethylene. Strategies towards the activation of the complex XBPhos-Pt and analogues for new chemistries are presented.

2.5. Experimental section

2.5.1. General consideration

All syntheses were carried out using chemicals as purchased from commercial sources unless otherwise stated. Air- and moisture-sensitive manipulations or reactions were performed under inert atmosphere, either in a N_2-filled glove box or with standard Schlenk techniques. Glassware was dried *in vacuo* before use with a hot air gun. All solvents were dried and deoxygenated by using a Solvent Purification System (SPS). Silica gel 60 Å (230 - 400 mesh particle size) was used for column chromatography, unless otherwise stated. NMR spectra were recorded at room temperature in 400 MHz or 500 MHz spectrometers in $CDCl_3$ or CD_2Cl_2, unless otherwise mentioned. ^{1}H and $^{13}C\{^{1}H\}$ NMR chemical shifts are quoted in ppm relative to residual solvent peaks. $^{11}B\{^{1}H\}$ NMR chemical shifts are quoted in ppm relative to $BF_3{\cdot}(CH_3)_2O$ in $CDCl_3$. $^{19}F\{^{1}H\}$ NMR chemical shifts are quoted in ppm relative to $CFCl_3$ in $CDCl_3$. $^{31}P\{^{1}H\}$ NMR chemical shifts are quoted in ppm relative to 85% phosphoric acid in water. High resolution mass spectra (HRMS) were recorded using ESI ionization method in positive mode. GC-MS analyses were performed using electron ionization (EI). GC analyses were performed with a flame ionization detector (FID). IR spectra were recorded using Attenuated Total Reflection (ATR) technique, unless otherwise cited.

2.5.2. Single crystal X-ray structure determinations

Crystal preparation: Crystals of [Pt(Ar^F)(Cl)(cod)] **151**, [Pt(Ar^F)$_2$(cod)] **152**, XBPhos-Pt **142**, complex **149**, XBPhos-Pd **150** and Xantphos-Pt **153** were grown by slow diffusion of pentane in toluene or CH_2Cl_2. The crystals used for structure determination were selected using a Zeiss stereomicroscope using polarized light and prepared under inert conditions immersed in perfluoropolyether as protecting oil for manipulation.

Data collection: Crystal structure determination for samples [Pt(Ar^F)(Cl)(cod)] **151**, [Pt(Ar^F)$_2$(cod)] **152**, XBPhos-Pt **142**, complex **149**, XBPhos-Pd **150** and Xantphos-Pt **153** was carried out using a Apex DUO Kappa 4-axis goniometer equipped with an APPEX 2 4K CCD area detector, a Microfocus Source E025 IuS using MoK_α radiation, Quazar MX multilayer Optics as monochromator and an Oxford Cryosystems low temperature device

Cryostream 700 plus (T = −173 °C). Full-sphere data collection was used with ω and φ scans. *Programs used*: Data collection APEX-2,[33] data reduction Bruker Saint[34] V/.60A and absorption correction SADABS[35] or TWINABS[36] (complex **149**).

Structure Solution and Refinement: Crystal structure solution was achieved using the computer program SHELXT.[37] Visualization was performed with the program SHELXle.[38] Missing atoms were subsequently located from difference Fourier synthesis and added to the atom list. Least-squares refinement on F^2 using all measured intensities was carried out using the program SHELXL 2015.[39] All non-hydrogen atoms were refined including anisotropic displacement parameters.

Comments to the structure of [Pt(Ar^F)(Cl)(cod)] 151: The asymmetric unit contains one molecule of metal complex. Several large residual densities were observed surrounding the platinum atom, which were attributed to the presence of the mentioned heavy atom. The structure was checked for unaccounted twinning, wrongly assigned atom types and other model errors, and is sound. Absorption correction was performed choosing strong absorber but only a week improvement was observed. The structure was considered sound for structure identification and publication (A- and B-alerts related to the high densities observed have been addressed in the CIF-file).

---

[33] Data collection with APEX II version 2013.4-1. Bruker (2007). Bruker AXS Inc., Madison, Wisconsin, USA.

[34] Data reduction with Bruker SAINT version 8.30c. Bruker (2007). Bruker AXS Inc., Madison, Wisconsin, USA.

[35] SADABS: V2012/1 Bruker (2001). Bruker AXS Inc., Madison, Wisconsin, USA. See the following reference: Blessing, R. H. *Acta Crystallogr*. **1995**, *A51*, 33-38.

[36] TWINABS Version 2008/4 Bruker AXS. See the following reference: Blessing, R. H. *Acta Crystallogr*. **1995**, *A51*, 33-38.

[37] SHELXT. V2014/4 (Sheldrick 2014). See the following reference: Sheldrick, G. M. *Acta Crystallogr*. **2008**, *A64*, 112-122.

[38] SHELXle; See the following reference: Hübschle, C. B.; Sheldrick, G. M.; Dittrich, B. *J. Appl. Crystallogr*. **2011**, *44*, 1281-1284.

[39] SHELXL; SHELXL-2014/7 (Sheldrick 2014). See the following reference: Sheldrick, G. M. *Acta Crystallogr*. **2015**, *C71*, 3-8.

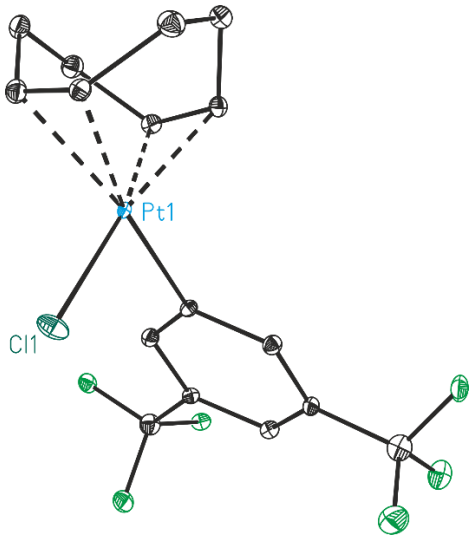

Figure 155. ORTEP drawing (thermal ellipsoids drawn at a 50% probability level) showing the structure of [Pt(Ar^F)(Cl)(cod)] **151**. Hydrogen atoms have been omitted for clarity. Color scheme: C: black, Cl: dark green, F: light green, Pt: light blue.

Table 19. Crystal data and structural parameters for complex [Pt(Ar^F)(Cl)(cod)] **151**.

Compound	**151**
Formula	$C_{32}H_{30}Cl_2F_{12}Pt_2$
Solvent	CH_2Cl_2
Formula weight	1103.64
Crystal size (mm^3)	0.50 x 0.50 x 0.05
Temperature (K)	100(2)
Wavelength (Å)	0.71073
Crystal system	Monoclinic
Space group	P21/n
a (Å)	13.6876(6)
b (Å)	8.3362(5)
c (Å)	15.0293(8)
α (º)	90
β (º)	110.2487(13)
γ (º)	90
Volume ($Å^3$)	1608.90(15)
Z	2
ρ ($g \cdot cm^{-3}$)	2.278
μ (mm^{-1})	8.945
θ_{max} (º)	33.136
Reflections collected	31164
Independent reflections	5873[R(int) = 0.0610]
Absorption correction	Multi-Scan
Data / restraints /Parameters	5873/ 186/ 273
R1/wR2 [I>2σ(I)]	0.0438/0.1078
R1/wR2 (all data)	0.0499/0.1112
Goodness-of-fit (F^2)	1.061
Peak/hole ($e/Å^{-3}$)	5.629 /−7.360

Table 20. Selected bond lengths (Å) for complex [Pt(Ar^F)(Cl)(cod)] **151**.

Entry	Atoms	Length (Å)	Entry	Atoms	Length (Å)
1	Cl1-Pt1	2.3169(11)	4	Pt1-C13	2.149(5)
2	C1-Pt1	2.020(4)	5	Pt1-C10	2.279(4)
3	Pt1-C14	2.142(4)	6	Pt1-C9	2.292(5)

Table 21. Selected bond angles (°) for complex [Pt(Ar^F)(Cl)(cod)] **151**

Entry	Atoms	Angles (°)	Entry	Atoms	Angles (°)
1	C6-C1-Pt1	121.9(4)	14	C14-Pt1-Cl1	163.18(13)
2	C2-C1-Pt1	119.8(3)	15	C13-Pt1-Cl1	158.52(14)
3	C1-Pt1-C14	88.28(17)	16	C10-Pt1-Cl1	89.18(12)
4	C1-Pt1-C13	93.53(17)	17	C9-Pt1-Cl1	95.57(12)
5	C14-Pt1-C13	38.29(19)	18	C10-C9-Pt1	72.0(3)
6	C1-Pt1-C10	164.74(18)	19	C16-C9-Pt1	109.6(3)
7	C14-Pt1-C10	96.85(17)	20	C9-C10-Pt1	73.0(3)
8	C13-Pt1-C10	81.95(17)	21	C11-C10-Pt1	104.8(3)
9	C1-Pt1-C9	160.04(19)	22	C14-C13-Pt1	70.6(3)
10	C14-Pt1-C9	80.90(17)	23	C12-C13-Pt1	112.2(3)
11	C13-Pt1-C9	88.34(17)	24	C13-C14-Pt1	71.1(3)
12	C10-Pt1-C9	34.99(18)	25	C15-C14-Pt1	109.8(3)
13	C1-Pt1-Cl1	89.94(12)			

Table 22. Selected torsion angles (°) for complex [Pt(Ar^F)(Cl)(cod)] **151.**

Entry	Atoms	Torsion Angles (°)	Entry	Atoms	Torsion Angles (°)
1	Pt1-C1-C2-C3	178.4(3)	6	C11-C12-C13-Pt1	12.6(5)
2	Pt1-C1-C6-C5	−178.4(3)	7	Pt1-C13-C14-C15	101.3(4)
3	Pt1-C9-C10-C11	96.3(4)	8	C12-C13-C14-Pt1	−104.4(4)
4	C16-C9-C10-Pt1	−101.6(5)	9	Pt1-C14-C15-C16	38.2(5)
5	Pt1-C10-C11-C12	39.1(4)	10	Pt1-C9-C16-C15	12.7(5)

Comments to the structure of [Pt(Ar^F)$_2$(cod)] 152: The asymmetric unit contains one molecule of the metal complex.

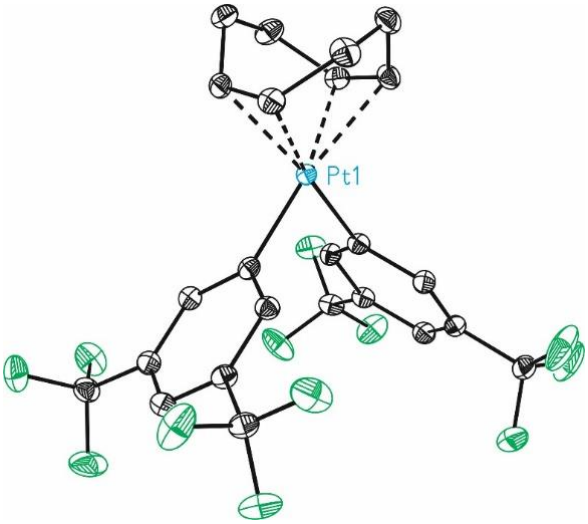

Figure 156. ORTEP drawing (thermal ellipsoids drawn at a 50% probability level) showing the structure model of [Pt(Ar^F)$_2$(cod)] **152**. Hydrogen atoms have been omitted for clarity. Color scheme: C: black, F: light green, Pt: light blue.

Table 23. Crystal data and structural parameters for complex $[Pt(Ar^F)_2(cod)]$ **152**.

Compound	**152**
Formula	$C_{24}H_{18}F_{12}Pt$
Solvent	CH_2Cl_2
Formula weight	728.46
Crystal size (mm^3)	0.50 x 0.20 x 0.20
Temperature (K)	100(2)
Wavelength (Å)	0.71073
Crystal system	Monoclinic
Space group	P21/n
a (Å)	11.0334(11)
b (Å)	10.5588(11)
c (Å)	19.648(2)
α (º)	90
β (º)	93.649(2)
γ (º)	90
Volume ($Å^3$)	2284.3(4)
Z	4
ρ ($g \cdot cm^{-3}$)	2.118
μ (mm^{-1})	6.252
θ_{max} (º)	34.984
Reflections collected	30907
Independent reflections	9398[R(int) = 0.0481]
Absorption correction	Multi-Scan
Data / restraints /Parameters	9398/ 0/ 334
R1/wR2 [I>2σ(I)]	0.0302/0.0757
R1/wR2 (all data)	0.0350/0.0792
Goodness-of-fit (F^2)	1.041
Peak/hole ($e/Å^{-3}$)	2.781 /−4.389

Table 24. Selected bond lengths (Å) for complex [Pt(Ar^F)$_2$(cod)] **152**.

Entry	Atoms	Length (Å)	Entry	Atoms	Length (Å)
1	Pt1-C9	2.018(2)	4	Pt1-C8	2.252(2)
2	Pt1-C17	2.029(2)	5	Pt1-C1	2.274(2)
3	Pt1-C4	2.252(2)	6	Pt1-C5	2.275(2)

Table 25. Selected bond angles (°) for complex [Pt(Ar^F)$_2$(cod)] **152**.

Entry	Atoms	Angles (°)	Entry	Atoms	Angles (°)
1	C9-Pt1-C17	86.44(9)	15	C1-Pt1-C5	86.66(8)
2	C9-Pt1-C4	91.27(9)	16	C8-C1-Pt1	71.36(14)
3	C17-Pt1-C4	160.87(9)	17	C2-C1-Pt1	110.05(16)
4	C9-Pt1-C8	162.96(10)	18	C5-C4-Pt1	73.07(14)
5	C17-Pt1-C8	92.09(9)	19	C3-C4-Pt1	105.49(15)
6	C4-Pt1-C8	95.49(9)	20	C4-C5-Pt1	71.23(13)
7	C9-Pt1-C1	161.44(10)	21	C6-C5-Pt1	110.21(15)
8	C17-Pt1-C1	95.73(8)	22	C1-C8-Pt1	73.05(14)
9	C4-Pt1-C1	80.64(9)	23	C7-C8-Pt1	106.20(16)
10	C8-Pt1-C1	35.59(10)	24	C10-C9-Pt1	120.61(17)
11	C9-Pt1-C5	96.51(9)	25	C14-C9-Pt1	122.72(17)
12	C17-Pt1-C5	163.40(9)	26	C18-C17-Pt1	121.52(17)
13	C4-Pt1-C5	35.70(9)	27	C22-C17-Pt1	121.40(15)
14	C8-Pt1-C5	80.30(9)			

Table 26. Selected torsion angles (°) for complex [Pt(Ar^F)$_2$(cod)] **152**.

Entry	Atoms	Torsion Angles (°)	Entry	Atoms	Torsion Angles (°)
1	Pt1-C1-C2-C3	12.5(3)	7	C2-C1-C8-Pt1	−101.9(2)
2	C2-C3-C4-Pt1	42.8(2)	8	C6-C7-C8-Pt1	43.1(3)
3	Pt1-C4-C5-C6	−102.0(2)	9	Pt1-C9-C10-C11	179.95(17)
4	C3-C4-C5-Pt1	97.1(2)	10	Pt1-C9-C14-C13	179.98(17)
5	Pt1-C5-C6-C7	13.3(3)	11	Pt1-C17-C18-C19	−178.93(16)
6	Pt1-C1-C8-C7	97.8(2)	12	Pt1-C17-C22-C21	178.82(17)

Comments to the structure of XBPhos-Pt 142: The asymmetric unit contains one molecule of the metal complex. Two of the CF_3 groups in the $[B(Ar^F)_3(Cl)]$ group show rotational disorder.

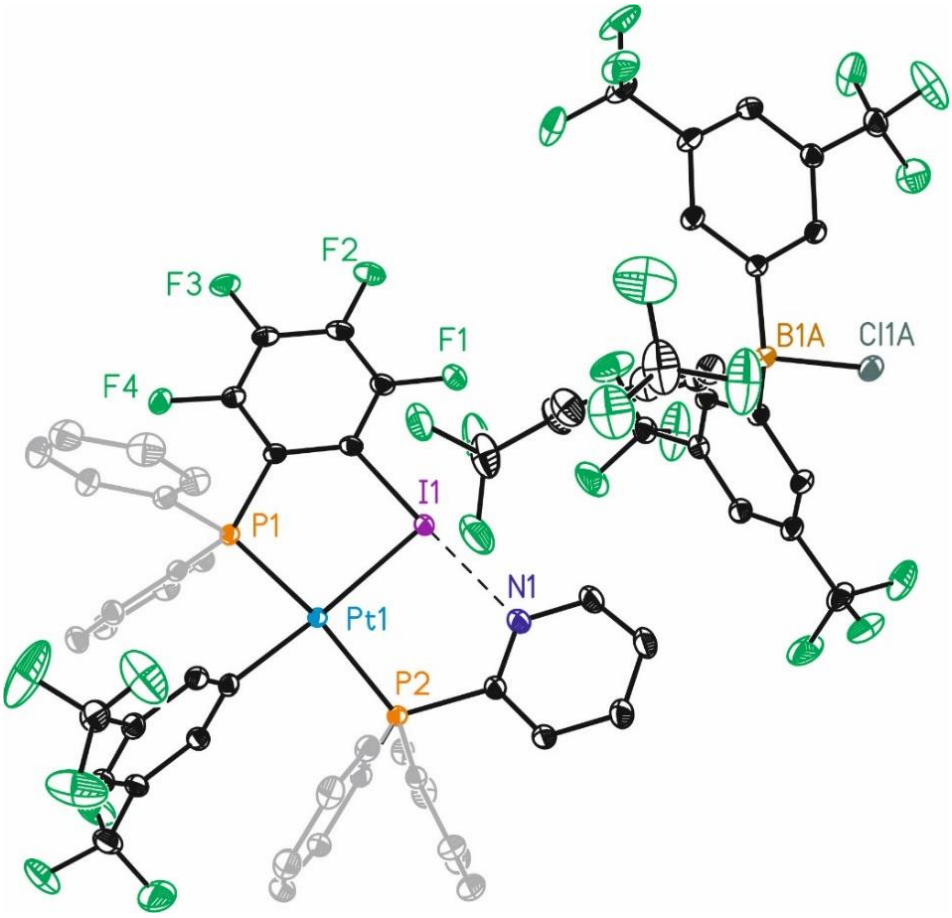

Figure 157. ORTEP drawing (thermal ellipsoids drawn at a 50% probability level) showing the structure model of XBPhos-Pt **142**. Hydrogen atoms have been omitted for clarity. Color scheme: C: black and grey, N: dark blue, P: orange, B: light brown, Cl: dark green, F: light green, I: purple, Pt: light blue.

Table 27. Crystal data and structural parameters for complex XBPhos-Pt **142**.

Compound	**142**
Formula	$C_{67}H_{36}BClF_{28}INP_2Pt$
Solvent	CH_2Cl_2
Formula weight	1817.16
Crystal size (mm^3)	0.50 x 0.20 x 0.10
Temperature (K)	100(2)
Wavelength (Å)	0.71073
Crystal system	Triclinic
Space group	P−1
a (Å)	12.5239(4)
b (Å)	13.5194(5)
c (Å)	19.1388(7)
α (º)	93.0800(10)
β (º)	91.7210(10)
γ (º)	97.2410(10)
Volume ($Å^3$)	3207.8(2)
Z	2
ρ ($g \cdot cm^{-3}$)	1.881
μ (mm^{-1})	2.886
θ_{max} (º)	33.165
Reflections collected	55095
Independent reflections	22235[R(int) = 0.0155]
Absorption correction	Multi-Scan
Data / restraints /Parameters	22235/ 286/ 1013
R1/wR2 [I>2σ(I)]	0.0212/0.0521
R1/wR2 (all data)	0.0222/0.0525
Goodness-of-fit (F^2)	1.058
Peak/hole ($e/Å^{-3}$)	1.331 /−0.811

Table 28. Selected bond lengths (Å) for complex XBPhos-Pt **142**.

Entry	Atoms	Length (Å)	Entry	Atoms	Length (Å)
1	Pt1-C36	2.0302(16)	5	Cl1A-B1A	1.9387(18)
2	Pt1-P1	2.2950(4)	6	C1A-B1A	1.630(2)
3	Pt1-P2	2.3172(4)	7	C9A-B1A	1.627(2)
4	Pt1-I1	2.61349(13)	8	C17A-B1A	1.627(2)

Table 29. Selected bond angles (°) for complex XBPhos-Pt **142**.

Entry	Atoms	Angles (°)	Entry	Atoms	Angles (°)
1	C36-Pt1-P1	87.03(4)	15	C41-C36-Pt1	118.98(12)
2	C36-Pt1-P2	86.77(4)	16	C6A-C1A-B1A	123.10(14)
3	P1-Pt1-P2	172.479(14)	17	C2A-C1A-B1A	120.35(13)
4	C36-Pt1-I1	175.61(5)	18	C10A-C9A-B1A	122.81(14)
5	P1-Pt1-I1	90.592(10)	19	C14A-C9A-B1A	120.38(13)
6	P2-Pt1-I1	95.865(10)	20	C18A-C17A-B1A	122.77(15)
7	C2-I1-Pt1	94.80(4)	21	C22A-C17A-B1A	120.58(14)
8	C7-P1-Pt1	113.65(5)	22	C17A-B1A-C9A	111.72(13)
9	C13-P1-Pt1	114.00(5)	23	C17A-B1A-C1A	110.98(13)
10	C1-P1-Pt1	110.67(5)	24	C9A-B1A-C1A	111.30(13)
11	C24-P2-Pt1	114.06(5)	25	C17A-B1A-Cl1A	108.59(11)
12	C30-P2-Pt1	111.90(5)	26	C9A-B1A-Cl1A	108.13(10)
13	C19-P2-Pt1	115.91(5)	27	C1A-B1A-Cl1A	105.88(11)
14	C37-C36-Pt1	122.39(12)			

Table 30. Selected torsion angles (°) for complex XBPhos-Pt **142**.

Entry	Atoms	Torsion Angles (°)	Entry	Atoms	Torsion Angles (°)
1	Pt1-P1-C1-C6	−177.56(12)	8	Pt1-P2-C24-C25	−78.10(13)
2	Pt1-P1-C1-C2	0.16(15)	9	Pt1-P1-C13-C14	−90.30(13)
3	Pt1-P1-C7-C8	36.84(15)	10	Pt1-P2-C24-C29	94.53(13)
4	Pt1-P1-C7-C12	−143.92(13)	11	Pt1-P2-C30-C31	−168.28(12)
5	Pt1-P1-C13-C18	86.04(13)	12	Pt1-C36-C37-C38	179.01(12)
6	Pt1-P2-C19-N1	−25.35(15)	13	Pt1-C36-C41-C40	−179.03(12)
7	Pt1-P2-C19-C20	159.86(13)			

Comments to the structure of complex 149: The sample measured is a multicomponent crystal. Two crystals could be identified (ratio 80:20) which were processed with TWINABS taking in account overlapping reflections.[36] The asymmetric unit contains one molecule of the cationic metal complex and one molecule of the $[B(Ar^F)_3Cl]$ anion. The metal complex is slightly disordered in a second orientation with a ratio 98.4:1.6. Due to this disorder, the iodine atom was refined in two positions with the previously mentioned ratio. The disordered light atoms could not be refined properly and were maintained with a 1:0 ratio.

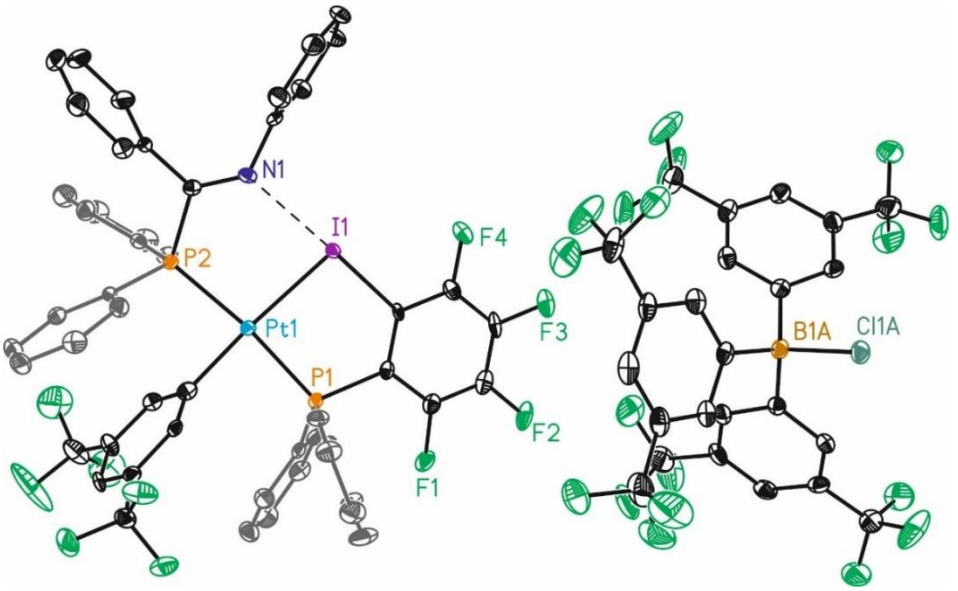

Figure 158. ORTEP drawing (thermal ellipsoids drawn at a 50% probability level) showing the structure of complex **149**. Hydrogen atoms have been omitted for clarity. Color scheme: C: black and grey, N: dark blue, P: orange, B: light brown, Cl: dark green, F: light green, I: purple, Pt: light blue.

Table 31. Crystal data and structural parameters for complex **149**.

Compound	149
Formula	$C_{75}H_{42}BClF_{28}INP_2Pt$
Solvent	CH_2Cl_2
Formula weight	1919.28
Crystal size (mm^3)	0.20 x 0.20 x 0.20
Temperature (K)	100(2)
Wavelength (Å)	0.71073
Crystal system	Triclinic
Space group	P −1
a (Å)	13.6694(8)
b (Å)	14.3677(8)
c (Å)	20.8467(12)
α (º)	100.001(2)
β (º)	104.343(2)
γ (º)	108.779(2)
Volume ($Å^3$)	3609.3(4)
Z	2
ρ ($g \cdot cm^{-3}$)	1.766
μ (mm^{-1})	2.570
θ_{max} (º)	35.301
Reflections collected	300397
Independent reflections	30039 [R(int) = 0.0456]
Absorption correction	Multi-Scan
Data / restraints /Parameters	30039/ 12/ 994
R1/wR2 [I>2σ(I)]	0.0614/0.0821
R1/wR2 (all data)	0.1048/0.0879
Goodness-of-fit (F^2)	2.389
Peak/hole ($e/Å^{-3}$)	7.323 /−3.544

Table 32. Selected bond lengths (Å) for complex **149**.

Entry	Atoms	Length (Å)	Entry	Atoms	Length (Å)
1	I1-Pt1	2.6063(3)	5	B1A-C9A	1.609(5)
2	P1-Pt1	2.2836(8)	6	B1A-C1A	1.619(5)
3	Pt1-C19	1.989(4)	7	B1A-C17A	1.622(5)
4	Pt1-P2	2.3105(8)	8	B1A-Cl1A	1.938(4)

Table 33. Selected bond angles (°) for complex **149**.

Entry	Atoms	Angles (°)	Entry	Atoms	Angles (°)
1	C6-I1-Pt1	94.44(8)	14	C20-C19-Pt1	123.9(3)
2	C13-P1-Pt1	115.40(11)	15	C9A-B1A-C1A	116.8(3)
3	C7-P1-Pt1	111.77(10)	16	C9A-B1A-C17A	105.9(3)
4	C1-P1-Pt1	110.95(10)	17	C1A-B1A-C17A	111.9(3)
5	C19-Pt1-P1	86.63(10)	18	C9A-B1A-Cl1A	107.8(2)
6	C19-Pt1-P2	86.65(10)	19	C1A-B1A-Cl1A	104.8(2)
7	P1-Pt1-P2	173.08(3)	20	C17A-B1A-Cl1A	109.5(2)
8	C19-Pt1-I1	176.22(11)	21	C6A-C1A-B1A	124.5(3)
9	P2-Pt1-I1	96.77(2)	22	C2A-C1A-B1A	119.3(3)
10	C33-P2-Pt1	113.54(11)	23	C10A-C9A-B1A	122.3(3)
11	C27-P2-Pt1	111.09(10)	24	C14A-C9A-B1A	121.4(3)
12	C39-P2-Pt1	114.63(11)	25	C18A-C17A-B1A	117.6(3)
13	C24-C19-Pt1	119.9(3)	26	C22A-C17A-B1A	125.9(3)

Table 34. Selected torsion angles (°) for complex **149**.

Entry	Atoms	Torsion Angles (°)	Entry	Atoms	Torsion Angles (°)
1	C2-C1-P1-Pt1	−171.5(3)	9	Pt1-P2-C27-C32	65.7(3)
2	C6-C1-P1-Pt1	13.1(3)	10	Pt1-P2-C27-C28	−103.0(3)
3	Pt1-P1-C7-C12	157.2(3)	11	Pt1-P2-C33-C34	−11.9(3)
4	Pt1-P1-C7-C8	−24.6(3)	12	Pt1-P2-C33-C38	168.8(2)
5	Pt1-P1-C13-C18	−86.1(3)	13	Pt1-P2-C39-N1	24.2(3)
6	Pt1-P1-C13-C14	87.5(3)	14	Pt1-P2-C39-C40	−163.2(2)
7	Pt1-C19-C20-C21	−177.9(3)	26	C1A-B1A-C9A-C14A	154.8(3)
8	Pt1-C19-C24-C23	−179.5(2)	27	C17A-B1A-C9A-C14A	−79.9(4)

Comments to the structure of XBPhos-Pd 150: The asymmetric unit contains one molecule of the palladium metal complex, a BArF anion and one molecule of dichloromethane (disordered in two positions, occupancy 88:12). In the main molecule the iodine atom is disordered in three different orientations with a ratio of 90:05:05. In the BArF anion some of the CF_3 groups are disordered in two orientations. The I1···N1 contact is represented in the Figure that follow with a discontinuous line.

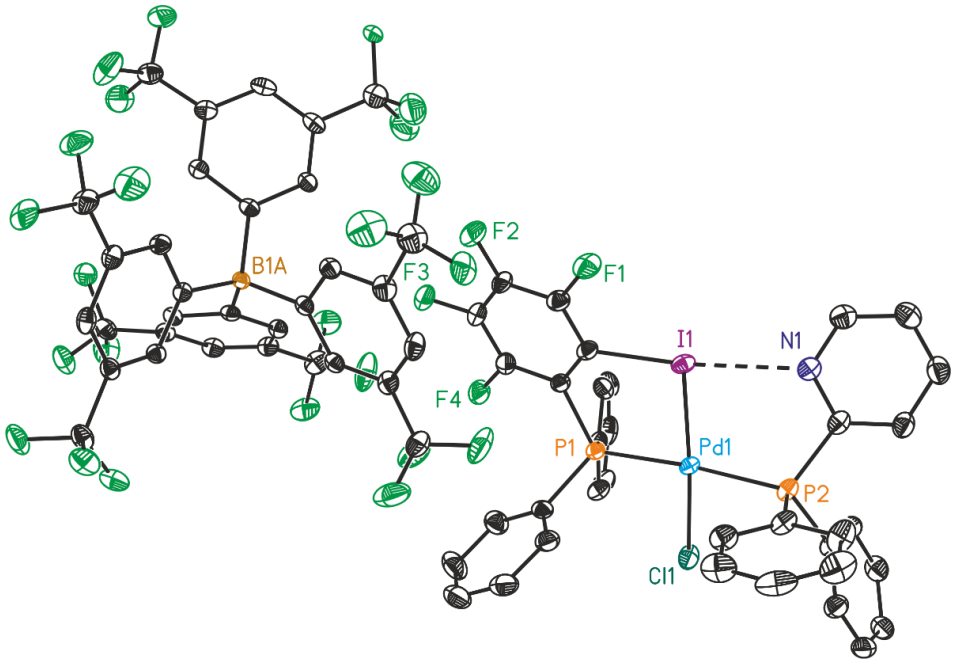

Figure 159. ORTEP drawing (thermal ellipsoids drawn at a 50% probability level) showing the structure of XBPhos-Pd **150**. Hydrogen atoms have been omitted for clarity. Color scheme: C: black, N: dark blue, P: orange, B: light brown, Cl: dark green, F: light green, I: purple, Pd: light blue.

Table 35. Crystal data and structural parameters for complex XBPhos-Pd **150**.

Compound	**150**
Formula	$C_{68}H_{38}BCl_3F_{28}INP_2Pd$
Solvent	CH_2Cl_2
Formula weight	1813.39
Crystal size (mm^3)	0.50 x 0.20 x 0.040
Temperature (K)	100(2)
Wavelength (Å)	0.71073
Crystal system	Triclinic
Space group	P−1
a (Å)	12.8628(3)
b (Å)	16.1728(4)
c (Å)	18.1311(4)
α (º)	107.4434(7)
β (º)	105.1533(7)
γ (º)	91.5654(8)
Volume ($Å^3$)	3450.25(14)
Z	2
ρ ($g \cdot cm^{-3}$)	1.746
μ (mm^{-1})	0.998
θ_{max} (º)	32.715
Reflections collected	67367
Independent reflections	24152[R(int) = 0.0368]
Absorption correction	Multi-Scan
Data / restraints /Parameters	24152/ 1219/ 1206
R1/wR2 [I>2σ(I)]	0.0485/0.1061
R1/wR2 (all data)	0.0778/0.1190
Goodness-of-fit (F^2)	1.031
Peak/hole ($e/Å^{-3}$)	1.657 /−1.921

Table 36. Selected bond lengths (Å) for complex XBPhos-Pd **150**.

Entry	Atoms	Length (Å)	Entry	Atoms	Length (Å)
1	I1-Pd1	2.5478(3)	7	Pd1-P2	2.3411(8)
2	I1'-Pd1	2.436(4)	8	C1A-B1A	1.644(4)
3	I1"-Pd1	2.689(4)	9	C9A-B1A	1.647(4)
4	Pd1-Cl1'	2.20(2)	10	C17A-B1A	1.651(4)
5	Pd1-P1	2.3119(7)	11	C25A-B1A	1.635(4)
6	Pd1-Cl1	2.3342(7)			

Table 37. Selected bond angles (°) for complex XBPhos-Pd **150**.

Entry	Atoms	Angles (°)	Entry	Atoms	Angles (°)
1	C14-I1-Pd1	94.88(8)	12	P1-Pd1-I1	91.008(19)
2	C1'-I1'-Pd1	102.2(18)	13	Cl1-Pd1-I1	175.93(2)
3	C12-I1"-Pd1	96.64(16)	14	P2-Pd1-I1	92.98(2)
4	N1"-I1"-Pd1	87.6(12)	15	P1-Pd1-I1"	84.32(8)
5	Cl1'-Pd1-P1	92.1(8)	16	P2-Pd1-I1"	93.02(8)
6	P1-Pd1-Cl1	86.58(3)	17	C1-P1-Pd1	113.04(10)
7	Cl1'-Pd1-P2	90.8(8)	18	C7-P1-Pd1	113.31(10)
8	P1-Pd1-P2	175.46(3)	19	C13-P1-Pd1	110.24(10)
9	Cl1-Pd1-P2	89.31(3)	20	C25-P2-Pd1	116.00(10)
10	P1-Pd1-I1'	103.08(11)	21	C19-P2-Pd1	110.08(11)
11	P2-Pd1-I1'	81.21(11)	22	C31-P2-Pd1	114.01(9)

Table 38. Selected torsion angles (°) for complex XBPhos-Pd **150**.

Entry	Atoms	Torsion Angles (°)	Entry	Atoms	Torsion Angles (°)
1	Pd1-P1-C1-C2	−91.1(2)	9	Pd1-P2-C19-C20	8.9(3)
2	Pd1-P1-C1-C6	84.8(2)	10	Pd1-P2-C19-C24	−173.5(2)
3	Pd1-P1-C7-C8	−153.3(2)	11	Pd1-P2-C25-C26	−102.6(2)
4	Pd1-P1-C7-C12	30.4(2)	12	Pd1-P2-C25-C30	71.9(3)
5	Pd1-P1-C13-N1'	−6.4(2)	13	Pd1-P2-C31-C1'	41(5)
6	Pd1-P1-C13-C18	178.6(2)	14	Pd1-P2-C31-N1	33.1(5)
7	Pd1-P1-C13-C14	−6.8(3)	15	Pd1-P2-C31-C32	−148.5(2)
8	Pd1-P2-C19-N1"	11(5)			

Comments to the structure of Xantphos-Pt 153: The asymmetric unit contains one molecule of the metal complex. In the $[B(Ar^F)_3(Cl)]$ group, several of the CF_3 substituents show rotational disorder. Also, one of the CF_3 groups in the 3,5-bis(trifluoromethyl)phenyl ligand is disordered in two orientations.

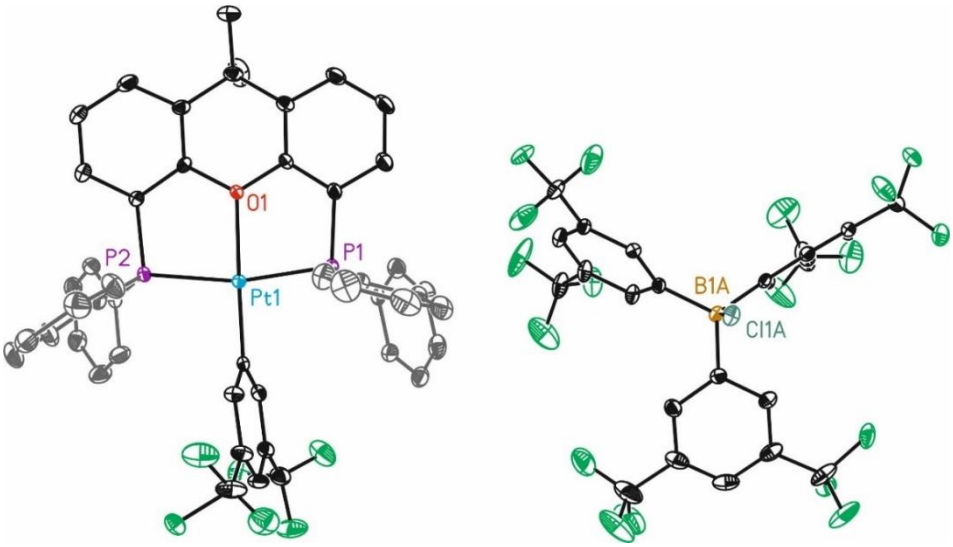

Figure 160. ORTEP drawing (thermal ellipsoids drawn at a 50% probability level) showing the structure of Xantphos-Pt **153**. Hydrogen atoms have been omitted for clarity. Color scheme: C: black and grey, O: red, P: purple, B: light brown, Cl: dark green, F: light green, Pt: light blue.

Table 39. Crystal data and structural parameters for complex Xantphos-Pt **153**.

Compound	**153**
Formula	$C_{71}H_{44}BClF_{24}OP_2Pt$
Solvent	CH_2Cl_2
Formula weight	1672.35
Crystal size (mm^3)	0.40 x 0.40 x 0.20
Temperature (K)	100(2)
Wavelength (Å)	0.71073
Crystal system	monoclinic
Space group	P 21/n
a (Å)	12.5658(6)
b (Å)	24.1230(12)
c (Å)	21.9300(11)
α (º)	90
β (º)	94.3688(14)
γ (º)	90
Volume ($Å^3$)	6628.2(6)
Z	4
ρ ($g \cdot cm^{-3}$)	1.676
μ (mm^{-1})	2.318
θ_{max} (º)	35.079
Reflections collected	124217
Independent reflections	27644[R(int) = 0.0456]
Absorption correction	Multi-Scan
Data / restraints /Parameters	27644/ 525/ 1089
R1/wR2 [I>2σ(I)]	0.0366/0.0737
R1/wR2 (all data)	0.0543/0.0792
Goodness-of-fit (F^2)	1.049
Peak/hole ($e/Å^{-3}$)	3.451 /−2.189

Table 40. Selected bond lengths (Å) for complex Xantphos-Pt **153**.

Entry	Atoms	Length (Å)	Entry	Atoms	Length (Å)
1	Pt1-C40	1.984(2)	5	Cl1A-B1A	1.938(2)
2	Pt1-O1	2.1705(14)	6	C1A-B1A	1.622(3)
3	Pt1-P1	2.2643(5)	7	C9A-B1A	1.637(3)
4	Pt1-P2	2.2684(5)	8	C17A-B1A	1.627(3)

Table 41. Selected bond angles (°) for complex Xantphos-Pt **153**.

Entry	Atoms	Angles (°)	Entry	Atoms	Angles (°)
1	C40-Pt1-O1	176.97(7)	13	C1-O1-Pt1	118.39(12)
2	C40-Pt1-P1	94.85(6)	14	C13-O1-Pt1	118.22(11)
3	O1-Pt1-P1	84.03(4)	15	C45-C40-Pt1	123.23(16)
4	C40-Pt1-P2	97.75(6)	16	C41-C40-Pt1	118.47(15)
5	O1-Pt1-P2	83.68(4)	17	C2A-C1A-B1A	123.04(18)
6	P1-Pt1-P2	165.97(2)	18	C6A-C1A-B1A	120.66(18)
7	C16-P1-Pt1	117.29(7)	19	C10A-C9A-B1A	124.07(19)
8	C22-P1-Pt1	117.38(8)	20	C14A-C9A-B1A	119.84(19)
9	C12-P1-Pt1	100.32(7)	21	C22A-C17A-B1A	123.78(19)
10	C34-P2-Pt1	118.73(7)	22	C18A-C17A-B1A	119.5(2)
11	C28-P2-Pt1	116.20(8)	23	C1A-B1A-C17A	113.52(18)
12	C2-P2-Pt1	99.63(7)	24	C1A-B1A-C9A	111.16(16)

Table 42. Selected torsion angles (°) for complex Xantphos-Pt **153**.

Entry	Atoms	Torsion Angles (°)	Entry	Atoms	Torsion Angles (°)
1	Pt1-O1-C1-C6	173.27(15)	10	Pt1-P1-C16-C21	−78.75(18)
2	Pt1-O1-C1-C2	−5.5(2)	11	Pt1-P1-C22-C27	−27.9(2)
3	Pt1-P2-C2-C3	−168.81(19)	12	Pt1-P1-C22-C23	153.63(17)
4	Pt1-P2-C2-C1	11.35(18)	13	Pt1-P2-C28-C33	−135.59(19)
5	Pt1-P1-C12-C11	175.77(18)	14	Pt1-P2-C28-C29	44.4(2)
6	Pt1-P1-C12-C13	−0.72(18)	15	Pt1-P2-C34-C35	−113.82(19)
7	Pt1-O1-C13-C8	−174.58(15)	16	Pt1-P2-C34-C39	63.5(2)
8	Pt1-O1-C13-C12	5.4(2)	17	Pt1-C40-C41-C42	176.00(17)
9	Pt1-P1-C16-C17	94.71(19)	18	Pt1-C40-C45-C44	−175.40(17)

2.5.3. Synthesis of ligands L3 and L5

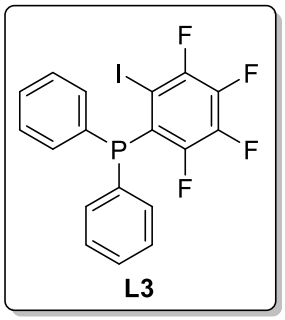

L3

The preparation of **L3** was performed adapting a reported procedure.[12] In a flame-dried Schlenk under inert atmosphere, a solution of 1,2-diiodotetrafluorobenzene **143** (3.0 g, 7.47 mmol) in anhydrous tetrahydrofuran (30.0 mL) was cooled to −78 °C. To the stirred solution, a solution of ^{n}BuLi (2.5 M in hexane, 2.0 mL, 4.98 mmol) was added dropwise. After stirring the reaction mixture for 30 minutes, a solution of chlorodiphenylphosphine **144** (1.0 mL, 4.98 mmol) was slowly added. The pale yellow solution was stirred for an additional 45 minutes and then allowed to warm to room temperature. After stirring for 1 hour at room temperature, the reaction mixture was quenched with deionized water (10.0 mL). The aqueous phase was extracted with dichloromethane (3 x 25.0 mL) and the combined organic phases were then dried over anhydrous $MgSO_4$, filtered and concentrated under reduced pressure. The crude mixture was purified by silica gel column chromatography using cyclohexane as the eluent to yield the ligand **L3** as a pale yellow solid (1.56 g, 68% yield). Spectroscopic data were in agreement with those previously reported.[9a] ^{1}H NMR (400 MHz, $CDCl_3$) δ: 7.44 - 7.34 (m, 10H) ppm; $^{13}C\{^{1}H\}$ NMR (126 MHz, $CDCl_3$) δ: 148.9 (ddm, $J_{C–F}$ = 252.7 Hz, $J_{C–P}$ = 9.8 Hz, C), 147.6 (dtd, $J_{C–F}$ = 245.1 Hz, $J_{C–P}$ = 10.3 Hz, J = 0.3 Hz, C), 141.0 (dm, $J_{C–F}$ = 259.4 Hz, C), 134.3 (dd, $J_{C–P}$ = 12.0 Hz, J = 3.5 Hz, C), 132.9 (dd, $J_{C–P}$ = 20.9 Hz, J = 1.3 Hz, C), 131.7 (tm, $J_{C–P}$ = 9.4 Hz, C), 129.4 (CH), 128.9 (d, $J_{C–P}$ = 6.6 Hz, C), 125.5 - 125.2 (m, CH), 90.0 (ddt, $J_{C–F}$ = 52.0 Hz, $J_{C–P}$ = 22.7 Hz, J = 3.9 Hz, C) ppm; $^{19}F\{^{1}H\}$ NMR (376 MHz, $CDCl_3$) δ: −110.2 - −110.4 (m, 1F), −118.8 - −119.0 (m, 1F), −148.9 - −149.0 (m, 1F), −151.9 - −152.1 (m, 1F) ppm; $^{31}P\{^{1}H\}$ NMR (162 MHz, $CDCl_3$) δ: 20.1 (ddd, $J_{P–F}$ = 23.5, 11.8, 3.9 Hz) ppm.

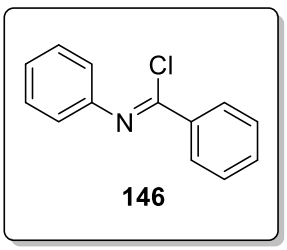

146

The preparation of **146** was performed adapting a reported procedure.[18a] In a flame-dried Schlenk under inert atmosphere, a solution of *N*-phenylbenzamide **145** (6.0 g, 30.00 mmol) in thionyl chloride (9.4 mL, 129.00 mmol) was heated at 70 °C for 2 hours, which resulted in the evolution of HCl and SO_2 gases (neutralization using an aqueous KOH-scrubber). Then, the reaction mixture was cooled to room temperature and the remaining

thionyl chloride was removed under reduced pressure. Product **146** was obtained as a pale brown solid (6.4 g, quantitative yield). Spectroscopic data were in agreement with those previously reported.[18a] ^{1}H NMR (500 MHz, $CDCl_3$) δ: 8.21 - 8.18 (m, 2H), 7.58 - 7.54 (m, 1H), 7.51 - 7.48 (m, 2H), 7.45 - 7.41 (m, 2H), 7.25 - 7.21 (m, 1H) and 7.05 - 7.03 (m, 2H) ppm; ^{13}C{^{1}H} NMR (126 MHz, $CDCl_3$) δ: 147.8 (C), 143.4 (C), 135.6 (C), 132.2 (CH), 129.6 (CH), 129.0 (CH), 128.6 (CH), 125.2 (CH) and 120.6 (CH) ppm.

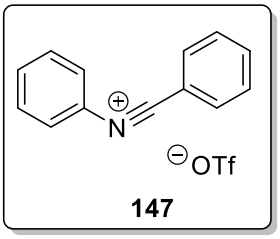

147

The preparation of **147** was performed adapting a reported procedure.[18a] In a flame-dried Schlenk under inert atmosphere, a solution of trimethylsilyl trifluoromethanesulfonate (TMSOTf) (7.1 mL, 39.00 mmol) was slowly added to a solution of *N*-phenylbenzimidoyl chloride **146** (6.5 g, 30.00 mmol) in CH_2Cl_2 (25.0 mL) at −78 ºC. Then, the reaction mixture was allowed to warm to room temperature and stirred for 2 hours (the solution turned to reddish-brown solution). Then, the volatiles were removed under reduced pressure and the pale brown solid was dissolved in a minimum amount of CH_2Cl_2 and pentane (5.0 mL of a 1:1 v/v ratio). The mixture was allowed to crystallize at 7 ºC for 12 hours and pale brown crystals were formed. The crystals were filtered, washed with cold pentane (5.0 mL) and dried under reduced pressure. The product **147** was obtained as a pale brown solid (3.7 g, 38% yield). Spectroscopic data were in agreement with those previously reported.[18a] ^{1}H NMR (400 MHz, $CDCl_3$) δ: 8.45 - 8.43 (m, 2H), 8.06 - 8.04 (m, 2H), 7.98 - 7.94 (m, 1H), 7.70 - 7.66 (m, 3H) and 7.59 - 7.55 (m, 2H) ppm; ^{13}C{^{1}H} NMR (101 MHz, $CDCl_3$) δ: 139.3 (CH), 136.6 (CH), 134.3 (CH), 130.5 (CH), 130.3 (CH), 129.3 (C), 128.5 (CH), 119.5 (q, J_{C-F} = 319.4 Hz, C) and 102.7 (C) ppm.

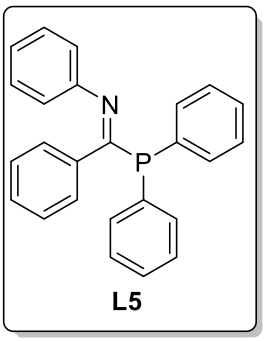

L5

The preparation of ligand **L5** was performed adapting a reported procedure.[18b] In a flame-dried Schlenk under inert atmosphere, a solution of diphenylphosphine **148** (1.5 mL, 8.28 mmol) was slowly added to a solution of (*N*-phenyl)(phenyl)carbonitrilium triflate **147** (3.0 g, 9.11 mmol) in CH_2Cl_2 (25.0 mL) at −78 °C. The reaction mixture was stirred for 15 minutes and the solution was allowed to warm to room temperature generating an orange suspension, which turned into an orange solution in 5 minutes. After stirring the reaction mixture for 30 minutes,

the product H^+•**L5** was obtained as mixture of the *E*- and *Z*-isomers in a 0.8:1.0 ratio. Then, a solution of triethylamine (2.8 mL, 20.10 mmol) was added, which turned the reaction mixture into a red/brown solution. After stirring the reaction mixture for 30 minutes, the volatiles were removed under reduced pressure and the mixture was extracted with methyl *tert*-butyl ether (MTBE) (3 x 20.0 mL). The combined organic fractions were filtered over Celite® and concentrated under reduced pressure. The reaction mixture was filtered over neutral alumina eluting with MTBE. A mixture of *E*-**L5** and *Z*-**L5** was obtained as a yellow solid (2.3 g, 76% yield) in a 1.0:0.5 ratio, respectively, according to $^{31}P\{^1H\}$ NMR spectroscopy.[40] Spectroscopic data were in agreement with those previously reported.[18b] ^1H NMR (400 MHz, $CDCl_3$) δ: 7.55 - 6.65 (m, 20H) ppm; $^{13}C\{^1H\}$ NMR (126 MHz, $CDCl_3$) δ: 178.6 (C), 151.7 (C), 151.4 (C), 140.6 (C) 137.8 (d, $J_{C–P}$ = 27.3 Hz, C), 134.9 (d, $J_{C–P}$ = 18.2 Hz, CH), 135.1 (CH), 134.3 (CH), 129.9 (CH), 127.9 (CH), 123.4 (CH), 120.8 (CH) and 119.3 (CH) ppm; $^{31}P\{^1H\}$ NMR (162.0 MHz, $CDCl_3$) δ: 11.1 (*E*-**L5**) and 1.6 (*Z*-**L5**) ppm.

[40] In the ^1H and $^{13}C\{^1H\}$ NMR spectra *E* and *Z* isomers could not be discriminated; therefore one set of signals is reported for both isomers.

2.5.4. Synthesis of Platinum(II) and Palladium(II) complexes derived from ligands L3, L4, L5 and L6

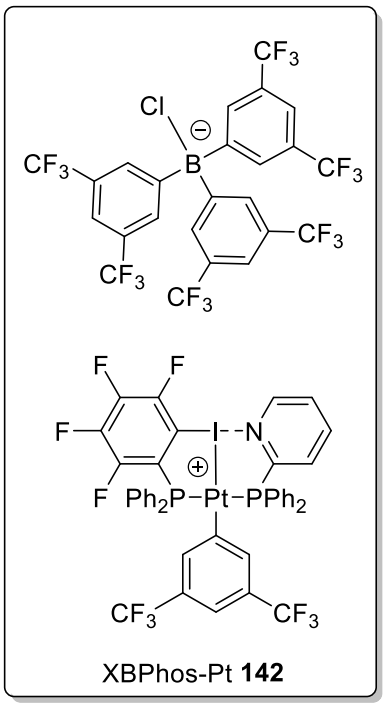

XBPhos-Pt **142**

The preparation of XBPhos-Pt **142** was performed adapting a reported procedure.[9a] In a glove box filled with N_2, $[Pt(Cl)_2(cod)]$ (40.0 mg, 0.11 mmol) was weighted in a glass vial provided with a magnetic stirrer and dissolved in toluene (2.0 mL). Then, NaBArF (97.7 mg, 0.11 mmol) was added to the $[Pt(Cl)_2(cod)]$ solution and the mixture was diluted in toluene (0.8 mL). The reaction mixture was stirred for 1 hour at room temperature. In parallel, a solution of 2-pyridyldiphenylphosphine **L4** (29.2 mg, 0.11 mmol) and 2-iodo-3,4,5,6-tetrafluorophenyldiphenylphosphine **L3** (50.7 mg, 0.11 mmol) in toluene (1.5 mL) was prepared and stirred for 1 hour at room temperature. Then, the solution containing **L3** and **L4** was added dropwise to the solution containing the platinum complexes. The reaction mixture was stirred for 1 hour at room temperature. The mixture was then filtered with a nylon filter to remove the precipitated NaCl. The resulting solution was mixed with pentane (10.0 mL). The solid obtained was washed with pentane (3 x 2.0 mL) and finally dried under reduced pressure. XBPhos-Pt **142** was obtained as a white solid (121.4 mg, 62% yield). ^{1}H NMR (500 MHz, CD_2Cl_2) δ: 8.94 (dm, J = 4.7 Hz, 1H), 7.86 - 7.84 (m, 7H), 7.70 (ddm, J = 7.7 Hz, J = 2.9 Hz, 1H), 7.64 - 7.56 (m, 6H), 7.48 (tm, J = 7.7 Hz, 2H), 7.44 - 7.40 (m, 4H), 7.37 - 7.25 (m, 12H), 7.14 - 7.12 (m, 1H) and 6.77 (t, J = 32.6 Hz, 2H) ppm; ^{13}C{^{1}H} NMR (126 MHz, CD_2Cl_2) δ: 150.1 (dd, $J_{C–P}$ = 76.7 Hz, $J_{C–Pt}$ = 5.3 Hz, C), 148.5 (d, $J_{C–P}$ = 17.8 Hz, CH), 142.0 - 141.9 (m, CH), 139.0 (d, $J_{C–P}$ = 5.0 Hz, CH), 134.9 - 134.7 (m, CH), 133.6 - 133.4 (m, CH), 133.3 (dm, $J_{C–P}$ = 11.8 Hz, CH), 132.9 (dm, $J_{C–P}$ = 48.4 Hz, C), 132.2 (dm, $J_{C–P}$ = 11.8 Hz, CH), 130.2 (q, $J_{C–F}$ = 32.5 Hz, C), 129. 5 (ddm, $J_{C–P}$ = 11.8 Hz, J = 5.8 Hz, CH), 129.3 - 129.2 (m, CH), 128.8 (CH), 128.7 (q, $J_{C–F}$ = 31.6 Hz, C), 128.0 (CH), 127.8 - 127.6 (m, CH), 125.1 (CH), 124.8 (d, $J_{C–P}$ = 58.5 Hz, C), 124.4 (q, $J_{C–F}$ = 272.3 Hz, C), 123.4 (d, $J_{C–P}$ = 61.0 Hz, C), 122.4 (q, $J_{C–F}$ =

272.8 Hz, C), 118.4 - 118.3 (m, CH) and 117.6 - 117.4 (m, CH) ppm; $^{19}F\{^{1}H\}$ NMR (376 MHz, CD_2Cl_2) δ: −62.8 (s, 18F), −63.8 (s, 6F), −115.3 - −115.4 (m, 1F), −117.1 - −117.2 (m, 1F), −142.4 - −142.5 (m, 1F) and −147.4 - −147.5 (m, 1F) ppm; $^{11}B\{^{1}H\}$ NMR (128 MHz, CD_2Cl_2) δ: −6.6 ppm; $^{31}P\{^{1}H\}$ NMR (162 MHz, CD_2Cl_2) δ: 65.2 (tdd, J_{P-Pt} = 1368.2 Hz, J_{P-P} = 376.2 Hz, J_{P-F} = 12.8 Hz) and 48.4 (td, J_{P-Pt} = 1416.4 Hz, J_{P-P} = 376.2 Hz) ppm. IR (neat): 2143, 1502, 1441, 1359, 1345, 1274, 1119, 1029, 999, 889, 691, 679, 512 cm^{-1}; HRMS (ESI) *m/z*: calcd for $C_{43}H_{27}F_{10}INP_2Pt$ $[M]^+$ 1131.0146, found 1131.0143.

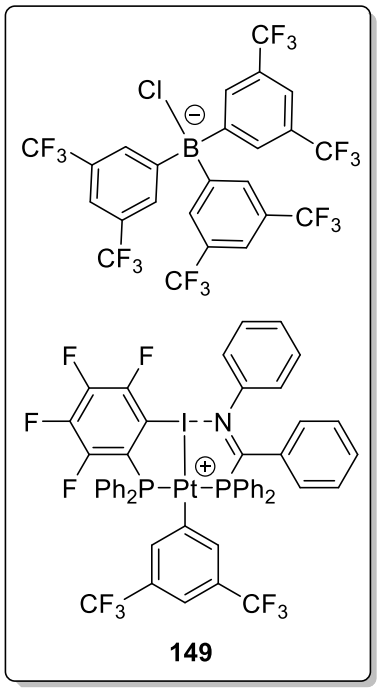

149

The preparation of **149** was performed adapting a reported procedure.[9a] In a glove box filled with N_2, $[Pt(Cl)_2(cod)]$ (24.2 mg, 0.06 mmol) was weighted in a glass vial provided with a magnetic stirrer and dissolved in toluene (1.0 mL). Then, NaBArF (59.9 mg, 0.06 mmol) was added to the $[Pt(Cl)_2(cod)]$ solution and the mixture was diluted in toluene (0.8 mL). The reaction mixture was stirred for 1 hour at room temperature. In parallel, a solution of ligand **L5** (25.1 mg, 0.06 mmol) and 2-iodo-3,4,5,6-tetrafluorophenyldiphenylphosphine **L3** (31.3 mg, 0.07 mmol) in toluene (1.5 mL) was prepared and stirred for 1 hour at room temperature. Then, the solution containing **L3** and **L5** was added dropwise to the solution containing the platinum complexes. The mixture was stirred for 1 hour at room temperature. The reaction mixture was then filtered with a nylon filter to remove the precipitated NaCl. The resulting solution was mixed with pentane (10.0 mL). The solid obtained was washed with pentane (3 x 2.0 mL) and dried under reduced pressure. Complex **149** was obtained as a pale yellow solid (52.7 mg, 42 % yield). ^{1}H NMR (400 MHz, CD_2Cl_2) δ: 7.86 (s, 6H), 7.61 - 7.53 (m, 7H), 7.43 - 7.36 (m, 8H), 7.35 - 7.16 (m, 12H), 7.11 (t, *J* = 7.5 Hz, 1H), 6.96 - 6.89 (m, 4H), 6.57 (t, *J* = 31.3 Hz, 2H) and 6.25 (d, *J* = 7.8 Hz, 2H) ppm; $^{13}C\{^{1}H\}$ NMR (126 MHz, CD_2Cl_2) δ: 135.7 (s, CH), 133.5 (s, CH), 133.4 - 133.1 (m, CH), 132.4 - 132.1 (m, CH), 130.0 (s, CH), 129.6 (s, C), 129.5 (s, C), 129.4 (s, CH), 128.8 (q, J_{C-F} = 31.6 Hz, C), 128.3 (s, CH), 128.2 (s, CH), 127.3 (s, C), 124.4 (q, J_{C-F} = 272.6 Hz, C), 121.2 (s, CH) and 118.5 - 118.3 (m, CH)

ppm; $^{19}F\{^{1}H\}$ NMR (376 MHz, CD_2Cl_2) δ: −62.8 (s, 18F), −63.8 (s, 6F), −115.0 - −115.1 (m, 1F), −116.9 - −117.0 (m, 1F), −142.1 - −142.2 (m, 1F) and −147.0 - −147.1 (m, 1F) ppm; $^{11}B\{^{1}H\}$ NMR (128 MHz, CD_2Cl_2) δ: −6.6 ppm; $^{31}P\{^{1}H\}$ NMR (162 MHz, CD_2Cl_2) δ: 66.8 (tdd, J_{P-Pt} = 1385.1 Hz, J_{P-P} = 376.5 Hz, J_{P-F} = 11.1 Hz) and 63.3 (td, J_{P-Pt} = 1396.5 Hz, J_{P-P} = 376.5 Hz) ppm. IR (neat): 2968, 1500, 1441, 1359, 1274, 1120 cm^{-1}; HRMS (ESI) *m/z*: calcd for $C_{51}H_{33}F_{10}INP_2Pt$ $[M]^+$ 1232.0595, found 1232.0602.

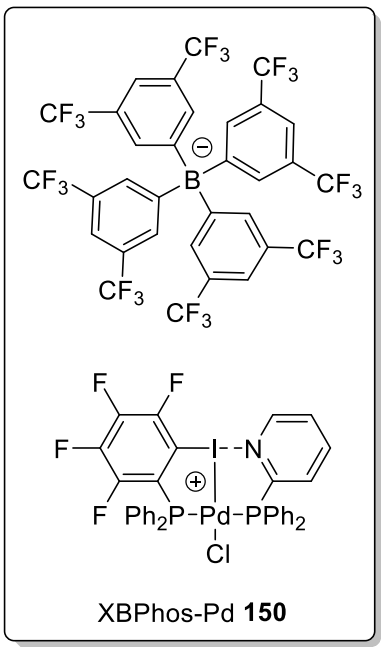

XBPhos-Pd **150**

The preparation of XBPhos-Pd **150** was performed adapting a reported procedure.[9a] In a glove box filled with N_2, $[Pd(Cl)_2(cod)]$ (19.6 mg, 0.07 mmol) was weighted in a glass vial provided with a magnetic stirrer and dissolved in toluene (1.0 mL). Then, NaBArF (63.3 mg, 0.07 mmol) was added to the $[Pd(Cl)_2(cod)]$ solution and the mixture was diluted in toluene (0.8 mL). The reaction mixture was stirred for 1 hour at room temperature. In parallel, a solution of 2-pyridyldiphenylphosphine **L4** (18.3 mg, 0.07 mmol) and 2-iodo-3,4,5,6-tetrafluorophenyldiphenylphosphine **L3** (32.6 mg, 0.07 mmol) in toluene (1.5 mL) was prepared and stirred for 1 hour at room temperature. Then, the solution containing **L3** and **L4** was added dropwise to the solution containing the palladium complexes. The reaction mixture was stirred for 1 hour at room temperature. The reaction mixture was then filtered with a nylon filter to remove the precipitated NaCl. The resulting solution was mixed with pentane (10.0 mL). The solid obtained was washed with pentane (3 x 2.0 mL) and finally dried under reduced pressure. XBPhos-Pd **150** was obtained as a yellow solid (34.6 mg, 29% yield). ^{1}H NMR (500 MHz, CD_2Cl_2) δ: 8.98 (d, *J* = 5.0 Hz, 1H), 7.96 (tm, *J* = 7.8 Hz, 1H), 7.76 - 7.70 (m, 18H), 7.69 - 7.58 (m, 3H), 7.57 - 7.54 (m, 8H), 7.53 - 7.36 (m, 4H) and 7.29 - 7.23 (m, 1H) ppm; $^{13}C\{^{1}H\}$ NMR (126 MHz, CD_2Cl_2) δ: 161.6 (q, J_{C-B} = 50.0 Hz, C), 148.5 (d, J_{C-P} = 18.8 Hz, CH), 139.1 (d, J_{C-P} = 4.7 Hz, CH), 134.7 (s, CH), 134.0 (d, J_{C-P} = 11.5 Hz, CH), 133.7 (d, J_{C-P} = 11.5 Hz, CH), 133.4 (d, J_{C-P} = 11.4 Hz, CH), 133.3 (d, J_{C-P} = 11.5 Hz, CH), 132.8 (d, *J* = 2.7 Hz, CH), 129.4 (t, J_{C-P} = 11.4 Hz, CH), 128.7

(qm, J_{C-F} = 31.3 Hz, C), 127.7 (s, CH), 124.7 (s, CH), 124.4 (q, J_{C-F} = 272.4 Hz, C) and 117.4 - 117.2 (m, CH) ppm; $^{19}F\{^1H\}$ NMR (376 MHz, CD_2Cl_2) δ: −63.0 (s, 24F), −116.5 - −116.6 (m, 1F), −117.1 - −117.2 (m, 1F), −141.3 - −141.4 (m, 1F) and −146.2 - −146.3 (m, 1F) ppm; $^{11}B\{^1H\}$ NMR (128 MHz, CD_2Cl_2) δ: −6.6 ppm; $^{31}P\{^1H\}$ NMR (162 MHz, CD_2Cl_2) δ: 72.1 (dd, J_{P-P} = 488.2 Hz, J_{P-F} = 14.8 Hz) and 52.7 (d, J_{P-P} = 488.2 Hz) ppm. IR (neat): 3361, 3180, 2961, 2922, 2852, 2162, 1633, 1501, 1354, 1274, 1113, 1029, 801, 681, 509 cm^{-1}; HRMS (ESI) *m/z*: calcd for $C_{35}H_{24}F_4INP_2PdCl$ $[M]^+$ 863.9083, found 863.9103.

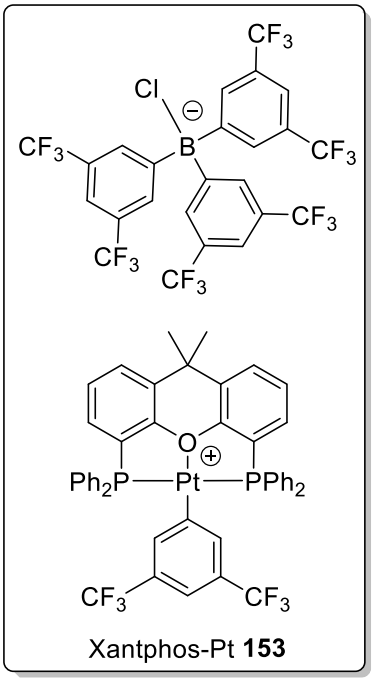

Xantphos-Pt **153**

The preparation of Xantphos-Pt **153** was performed adapting a reported procedure.[9a] In a glove box filled with N_2, $[Pt(Cl)_2(cod)]$ (20.0 mg, 0.05 mmol) was weighted in a glass vial provided with a magnetic stirrer and dissolved in CH_2Cl_2 (2.0 mL). Then, NaBArF (48.9 mg, 0.05 mmol) was added to the $[Pt(Cl)_2(cod)]$ solution and the mixture was diluted in CH_2Cl_2 (0.8 mL). The reaction mixture was stirred for 1 hour at room temperature. Then, a solution of 9,9'-dimethyl-4,5-bis(diphenylphosphino) xanthene **L6** (33.5 mg, 0.05 mmol) in CH_2Cl_2 (1.0 mL) was added dropwise to the solution containing the platinum complexes. The reaction mixture was stirred for 1 hour at room temperature. The reaction mixture was then filtered with a nylon filter to remove the precipitated NaCl. The resulting solution was mixed with pentane (10.0 mL). The solid obtained was washed with pentane (3 x 2.0 mL) and dried under reduced pressure. Xantphos-Pt **153** was obtained as a white solid (63.2 mg, 71% yield). ^1H NMR (400 MHz, CD_2Cl_2) δ: 7.84 - 7.83 (m, 7H), 7.63 - 7.32 (m, 31H) and 1.81 (s, 6H) ppm; $^{13}C\{^1H\}$ NMR (126 MHz, CD_2Cl_2) δ: 154.5 - 154.2 (m, C), 135.0 (s, CH), 133.8 (s, CH), 133.6 (s, C), 133.3 (s, CH), 132.8 (s, C), 132.2 (s, C), 129.8 - 129.5 (m, CH), 128.8 (q, J_{C-F} = 31.2 Hz, C), 128.4 - 128.2 (m, CH), 125.1 (t, J_{C-P} = 28.2 Hz, CH), 124.5 (q, J_{C-F} = 272.4 Hz, C), 122.8 (q, J_{C-F} = 273.3 Hz, C), 119.2 (t, J_{C-P} = 25.7 Hz, CH), 118.5 - 118.4 (m, CH), 117.9 - 117.7 (m, CH), 34.6 (s, C) and 33.4 (s, CH_3) ppm; $^{19}F\{^1H\}$ NMR (376 MHz, CD_2Cl_2) δ: −62.8 (s, 18F) and −63.6 (s, 6F) ppm; $^{11}B\{^1H\}$ NMR (128 MHz,

CD_2Cl_2) δ: −6.7 ppm; $^{31}P\{^1H\}$ NMR (162 MHz, CD_2Cl_2) δ: 30.7 (t, J_{P-Pt} = 1420.9 Hz). IR (neat): 2964, 1438, 1402, 1346, 1275, 1121, 890, 792, 736, 680, 527, 512 cm^{-1}; HRMS (ESI) *m/z*: calcd for $C_{47}H_{35}F_6OP_2Pt$ $[M]^+$ 985.1689, found 985.1659.

2.5.5. Study of the reaction pathway leading to XBPhos-Pt 142

2.5.5.1. General procedure for the preparation of 151 and 152

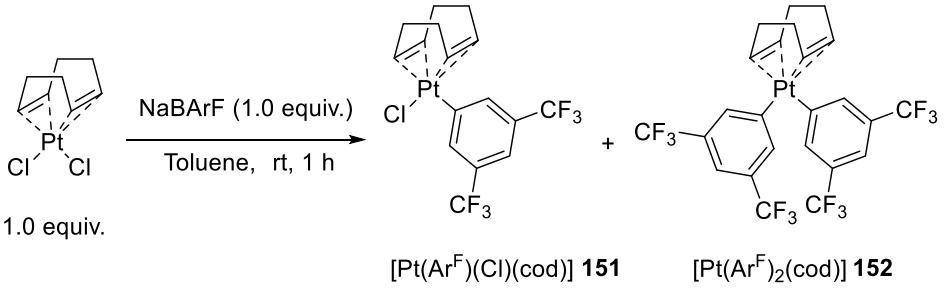

Scheme 63. General procedure of the formation of [Pt(Ar^F)(Cl)(cod)] **151** and [Pt(Ar^F)$_2$(cod)] **152**.

In a glove box filled with N_2, [Pt$(Cl)_2$(cod)] (40.0 mg, 0.11 mmol) was weighted in a glass vial provided with a magnetic stirrer and dissolved in toluene (2.0 mL). Then, NaBArF (97.7 mg, 0.11 mmol) was added to the [Pt$(Cl)_2$(cod)] solution and the mixture was diluted in toluene (0.8 mL). The reaction mixture was stirred for 1 hour at room temperature. The mixture was then filtered with a nylon filter and the resulting solution was dried under reduced pressure. The solid obtained was analyzed by ^1H, $^{19}F\{^1H\}$ and ^{195}Pt NMR. Spectroscopic data were in agreement with the platinum precursor [Pt$(Cl)_2$(cod)] and the platinum complexes [Pt(Ar^F)(Cl)(cod)] **151** and [Pt(Ar^F)$_2$(cod)] **152** (compare Figure 146 and Figure 198, Figure 200; compare Figure 147 and Figure 199, Figure 202).

2.5.5.2. Characterization of single crystal of [Pt(Ar^F)(Cl)(cod)] 151 and [Pt(Ar^F)$_2$(cod)] 152 by NMR techniques

The complexes [Pt(Ar^F)(Cl)(cod)] **151** and [Pt(Ar^F)$_2$(cod)] **152** were prepared following the general procedure indicated in the 2.5.5.1 section. The resulting solid was allowed to crystallize at −30 ºC for 12 hours. Crystals were grown by slow diffusion of pentane in toluene under inert atmosphere. The crystals for complexes **151** and **152** that were subjected to X-ray analysis (see Figure 155

and Figure 156, respectively) were subsequently characterized by NMR techniques.

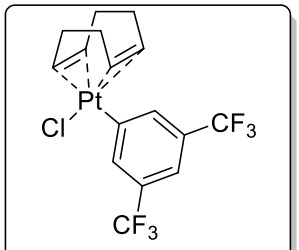

[Pt(Ar^F)(Cl)(cod)] **151**

^{1}H NMR (500 MHz, CD_2Cl_2) δ: 7.75 (t, *J* = 22.8 Hz, 2H), 7.49 (s, 1H), 5.87 - 5.83 (tm, *J* = 17.0 Hz, 2H), 4.66 - 4.52 (tm, *J* = 35.6 Hz, 2H), 2.73 - 2.68 (m, 2H), 2.62 - 2.56 (m, 2H) and 2.45 - 2.39 (m, 4H) ppm; ^{19}F{^{1}H} NMR (376 MHz, CD_2Cl_2) δ: −62.8 ppm.

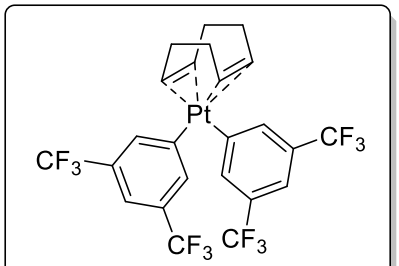

[Pt(Ar^F)$_2$(cod)] **152**

^{1}H NMR (500 MHz, CD_2Cl_2) δ: 7.75 (t, *J* = 34.4 Hz, 4H), 7.37 (s, 2H), 5.13 (t, *J* = 18.3 Hz, 4H) and 2.68 - 2.54 (m, 8H) ppm; ^{13}C{^{1}H} NMR (126 MHz, CD_2Cl_2) δ: 155.7 (t, $J_{C–Pt}$ = 545.4 Hz, C), 134.1 (s, CH), 129.6 (q, *J* = 31.7 Hz, C), 124.0 (q, *J* = 272.8, C), 117.1 - 117.0 (m, CH), 106.8 (t, *J* = 25.0 Hz, CH) and 29.8 (s, CH_2) ppm; ^{19}F {^{1}H} NMR (376 MHz, CD_2Cl_2) δ: −62.9 ppm.

2.5.5.3. NMR experiments of the reaction mixture between [Pt(Cl)$_2$(cod)] and NaBArF

DOSY NMR experiment

Diffusion Ordered SpectroscopY (DOSY) NMR spectra were recorded at 25 ºC in a 500 MHz spectrometer equipped with a cryoprobe. ^{19}F DOSY experiment was obtained with a longitudinal eddy-current delay (LED) bipolar gradient pulse pair and two spoil gradients pulse sequence (ledbpgp2s) in the standard Bruker pulse sequence library.[41] All experiments were processed with standard Bruker 1D and 2D DOSY software. CD_2Cl_2 was used as solvent and the concentration of the mixture was chosen to be 0.05 M. The reaction mixture between [Pt(Cl)$_2$(cod)] and NaBArF was obtained as indicated in section 2.5.5.1, but employing CD_2Cl_2 as solvent.

[41] Bruker User Library (accessed 23 October 2018). https://www.bruker.com/service/information-communication/nmr-pulse-program-lib/bruker-user-library.html

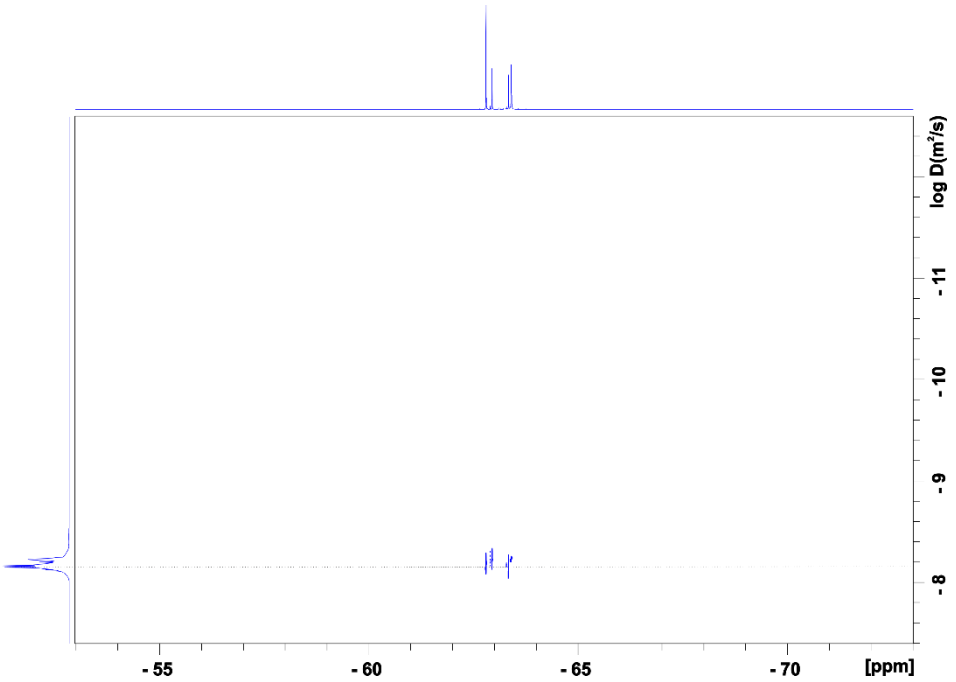

Figure 161. 2D DOSY spectrum of the reaction mixture between $[Pt(Cl)_2(cod)]$ and NaBArF. Log D = −8.17±0.04 → D = 6.76±0.04·10^{-9} m^2/s.

EXSY NMR experiment

EXchange SpectroscoPY (EXSY) NMR spectra were recorded at 25 ºC in a 500 MHz spectrometer equipped with a cryoprobe. ^{19}F EXSY experiment was obtained with a longitudinal eddy-current delay (LED) bipolar gradient pulse pair and two spoil gradients pulse sequence (ledbpgp2s) in the standard Bruker pulse sequence library.[41] All experiments were processed with standard Bruker 1D and 2D EXSY software. The reaction mixture between $[Pt(Cl)_2(cod)]$ and NaBArF was obtained as indicated in section 2.5.5.1, but employing CD_2Cl_2 as solvent ([Pt-complexes] = 0,05 M).

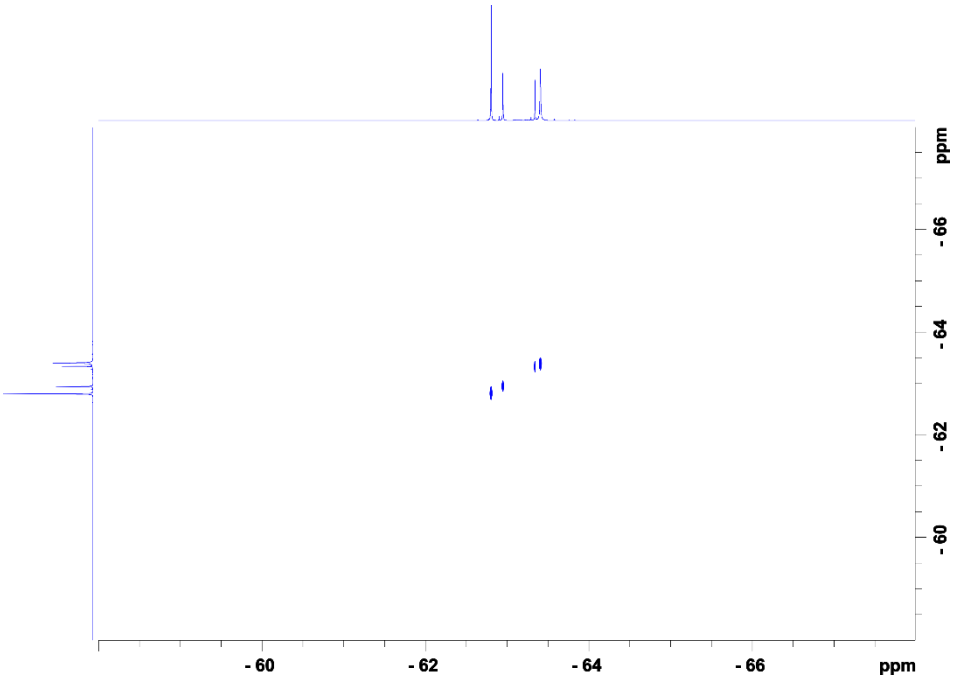

Figure 162. 2D EXSY spectrum of the reaction mixture between $[Pt(Cl)_2(cod)]$ and NaBArF.

2.5.6. Preparation of complex 152

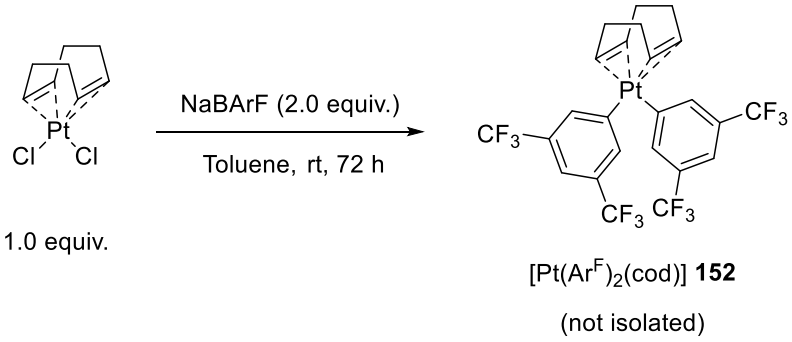

Scheme 64. General procedure for the preparation of complex **152**.

In a glove box filled with N_2, $[Pt(Cl)_2(cod)]$ (20.0 mg, 0.05 mmol) was weighted in a glass vial provided with a magnetic stirrer and dissolved in toluene (1.0 mL). Then, NaBArF (97.7 mg, 0.11 mmol) was added to the $[Pt(Cl)_2(cod)]$ solution and the mixture was diluted in toluene (0.8 mL). The reaction mixture was stirred for 72 hours at room temperature. The mixture was then filtered with a nylon filter and the resulting solution was dry under reduced

pressure. The solid obtained was analyzed by ^{1}H and ^{195}Pt NMR spectroscopic techniques. Spectroscopic data were in agreement with the platinum intermediate $[Pt(Ar^{F})_2(cod)]$ **152** (See Figure 151 and Figure 152).

2.5.7. $^{19}F\{^{1}H\}$ reaction monitoring of the formation of XBPhos-Pt 142

The monitoring of the reaction between $[Pt(Cl)_2(cod)]$ and NaBArF by $^{19}F\{^{1}H\}$ NMR at different reaction times was performed. Following the general procedure (see section 2.5.5.1), a solution of $[Pt(Cl)_2(cod)]$ (10.0 mg, 0.03 mmol) and NaBArF (24.2 mg, 0.03 mmol) in CD_2Cl_2 (0.7 mL) was prepared. This solution was immediately transferred to a screw-capped NMR tube provided with a septum. $^{19}F\{^{1}H\}$ NMR spectra were recorded at 25 ºC in a 400 MHz spectrometer every 5 minutes within 1 hour. In parallel, in a 1.0 mL vial, a solution of 2-pyridyldiphenylphosphine **L4** (7.3 mg, 0.03 mmol) and 2-iodo-3,4,5,6-tetrafluorophenyldiphenylphosphine **L3** (12.4 mg, 0.03 mmol) in CD_2Cl_2 (0.4 mL) was prepared and stirred for 1 hour at room temperature. After 1 hour, the solution containing **L3** and **L4** was added dropwise to the solution containing the platinum complexes in the screw-capped NMR tube. $^{19}F\{^{1}H\}$ NMR were recorded at 25 ºC in a 400 MHz spectrometer every 5 minutes within 1 hour. The formation of the platinum complexes **151** and **152**, and the consumption of NaBArF was monitored. After the addition of the ligands, the formation of the XBPhos-Pt **142** was also monitored. The resulting stacked plots are shown in Figure 150.

2.5.8. Synthesis of substrate 162

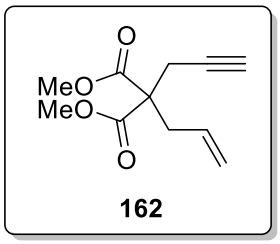

162

The preparation of **162** was performed adapting a reported procedure.[25] In a flame-dried Schlenk under inert atmosphere, a solution of dimethyl 2-(prop-2-ynyl)malonate (1.0 mL, 6.25 mmol) was added to a suspension of NaH (275.0 mg, 6.87 mmol) in THF (80.0 mL) at 0 ºC. The reaction mixture was allowed to warm to room temperature and stirred for 15 minutes. Then, a solution of allyl bromide (0.6 mL, 6.87 mmol) was added to the reaction mixture and the solution was stirred for an additional 16 hours. After stirring for 16 hours at room temperature, the reaction mixture was diluted with ether (60.0 mL). The organic phase was washed with a saturated solution of NH_4Cl (3 x 100.0 mL) and the aqueous phase was extracted with ether (3 x 80.0 mL). Then, the combined organic phases were dried over anhydrous

$MgSO_4$, filtered and concentrated under reduced pressure. The crude mixture was purified by distillation (52 ºC, 0.06 mbar) to yield **162** as a colorless oil (1.19 g, 91% yield). The spectroscopic data were in agreement with those previously reported.[42] ^{1}H NMR (400 MHz, $CDCl_3$) δ: 5.64 - 5.50 (m, 1H). 5.16 - 5.06 (m, 2H), 3.69 (s, 6H), 2.76 - 2.74 (m, 4H) and 1.99 (t, *J* = 2.6 Hz, 1H) ppm; ^{13}C{^{1}H} NMR (101 MHz, $CDCl_3$) δ: 170.3 (C), 131.8 (CH), 120.1 (CH_2), 78.9 (C), 71.6 (CH), 57.0 (C), 52.9 (CH_3), 36.6 (CH_2) and 22.8 (CH_2) ppm.

2.5.9. Screening of reactivity for XBPhos-Pt 142 catalyst

2.5.9.1. Platinum-catalyzed the 1,6-enyne cyclization reaction

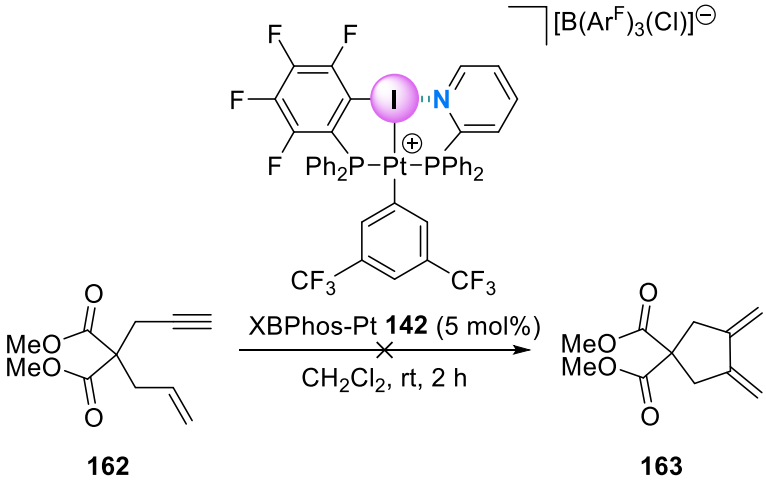

162 **163**

Scheme 65. General procedure for the cyclization of **162** with XBPhos-Pt **142** as catalyst.

In a glove box filled with N_2, dimethyl 2-allyl-2-(prop-2-yn-1-yl)malonate **162** (46.3 mg, 0.22 mmol) and XBPhos-Pt **142** (20.0 mg, 0.01 mmol) were weighted in a 10.0 mL vial provided with a magnetic stirrer. The mixture was dissolved in CH_2Cl_2 (2.5 mL). The solution was stirred at room temperature for 2 hours.[43] Then, the reaction mixture was filtered through a short pad of Celite® and the solvent was removed under reduced pressure. The crude mixture was analyzed by ^{1}H NMR.

[42] Miura, K.; Saito, H.; Fujisawa, N.; Hosomi, A. *J. Org. Chem.* **2000**, *65*, 8119-8122.
[43] The reaction time was extended to 24 hours and the reaction temperature was increased to 60 ºC. No changes in the outcome were detected.

2.5.9.2. Platinum-catalyzed the hydrophenylation of ethylene reaction

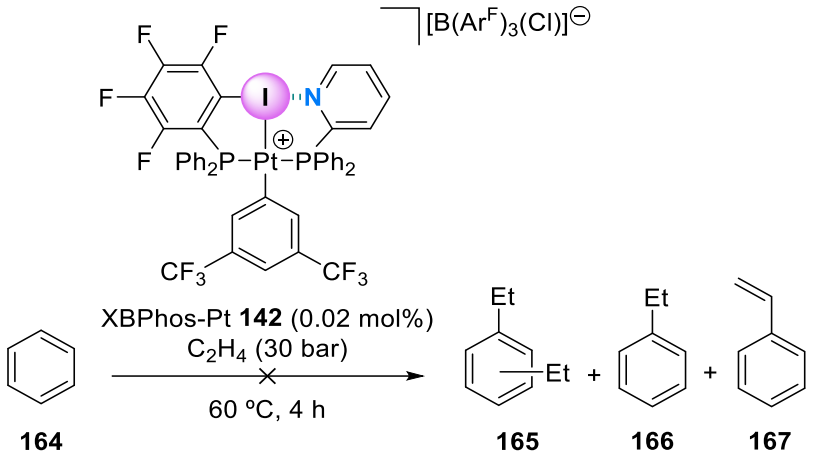

Scheme 66. General procedure for the hydrophenylation of ethylene with XBPhos-Pt **142** as catalyst.

In a glove box filled with N_2, a solution of XBPhos-Pt **142** (6.4 mg, 0.01 mmol) in benzene (3.1 mL, 35.10 mmol) containing 0.01 mol% of the internal standard (*i.e.*, hexamethylbenzene (HMB)) relative to benzene were placed into a 5.0 mL vial equipped with a magnetic stirrer. The vial was transferred into an autoclave reactor. The reactor was charged with ethylene (30 bar), pressurized to 38 bar with N_2 and heated to 60 °C. After 6 hours, the reaction mixture was cooled to room temperature and analyzed by GC-MS.

2.5.10. Cleavage or functionalization of the Pt–Ar^F bond in XBPhos-Pt

2.5.10.1. Attempted cleavage of the Pt–Ar^F bond with HCl

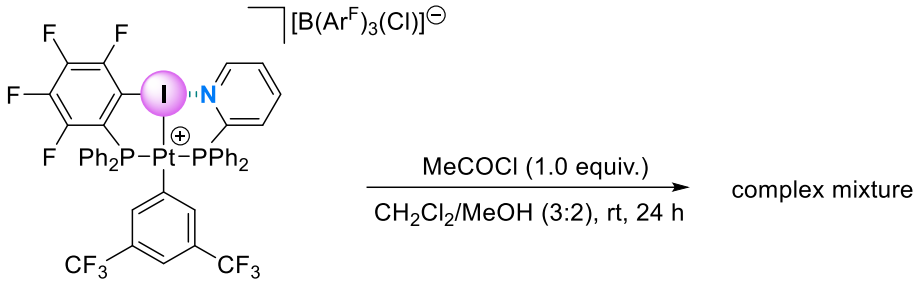

XBPhos-Pt **142**

Scheme 67. Attempted cleavage of the Pt–Ar^F bond with HCl.

In a glove box filled with N_2, a solution of XBPhos-Pt **142** (41,1 mg, 0.02 mmol) in a CH_2Cl_2/MeOH (3:2) mixture (0.6 mL) was stirred in a 3.0 mL glass vial until the complete solubilization. Then, acetyl chloride (1.6 µL, 0.02 mmol) was added and the solution was stirred for 24 hours at room temperature.[44] The crude mixture was analyzed by spectroscopic techniques. The outcome of the reaction was a complex mixture of products.

[44] The temperature of the reaction was increased to 60 °C. The outcome of the reaction was a complex mixture of products.

2.5.10.2. Attempted cleavage of the Pt–Ar^F bond with fluorinating reagents

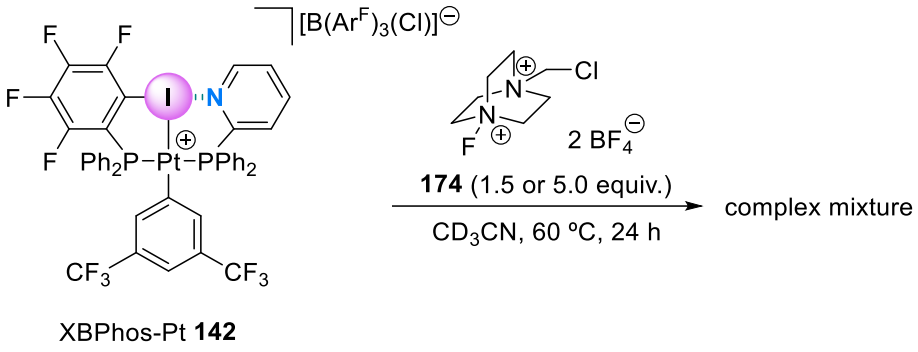

Scheme 68. Attempted cleavage of the Pt–Ar^F bond with a fluorinating reagent.

In a glove box filled with N_2, a solution of XBPhos-Pt **142** (41,2 mg, 0.02 mmol) in CD_3CN (0.6 mL) was placed into a 5.0 mL Schlenk equipped with a magnetic stirrer. Then, a solution of a fluorinating reagent **174** (0.03 or 0.10 mmol) in CD_3CN (0.3 mL) was added to the platinum solution. The solution was heated to 60 ºC for 24 hours, and then, the mixture was analyzed by spectroscopic techniques. The outcome of the reaction was a complex mixture of products.

2.5.10.3. CO insertion into the Pt–Ar^F bond of XBPhos-Pt 142

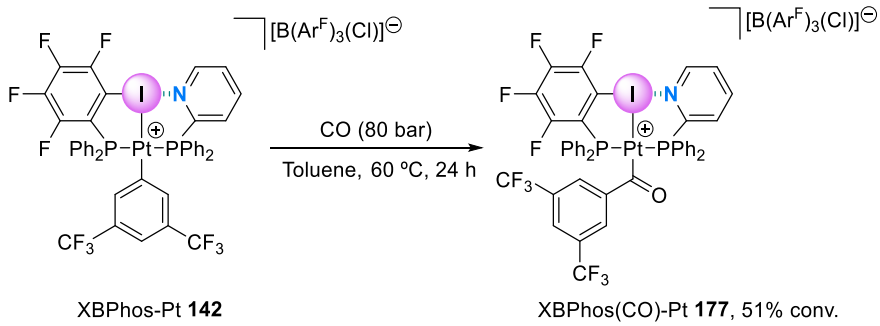

Scheme 69. General procedure for the CO insertion into the Pt–Ar^F bond of XBPhos-Pt **142**.

In a glove box filled with N_2, a solution of XBPhos-Pt **142** (13.3 mg, 0.01 mmol) in toluene (3.0 mL) was placed into a 10.0 mL vial equipped with a magnetic stirrer. The vial was transferred into an autoclave reactor. The autoclave was pressurized with CO to 80 bar. The reaction mixture was stirred

at 60 ºC for 24 hours. The crude mixture was analyzed by low resolution MS-ESI. This technique revealed that complex **177** had been formed (*ca.* 51% conversion, calculated with MS-ESI). MS (ESI) *m/z*: calcd for $C_{43}H_{27}F_{10}INP_2Pt$ $[M]^+$ 1131.01, found 1130.9. MS (ESI) *m/z*: calcd for $C_{44}H_{27}F_{10}INOP_2Pt$ $[M]^+$ 1159.01, found 1158.8.

2.5.11. Copies of NMR spectra

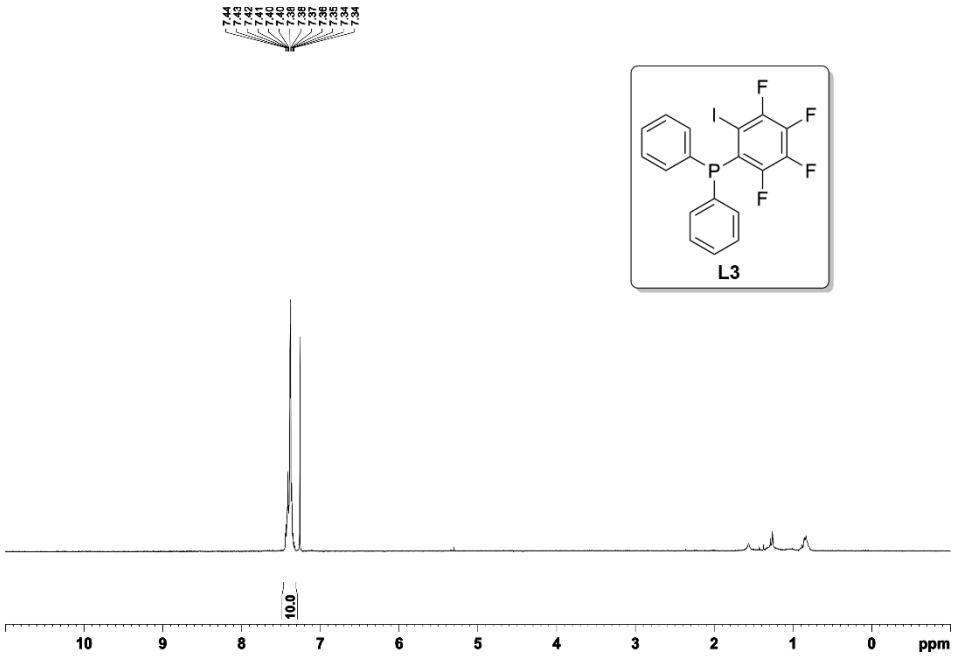

Figure 163. ^{1}H NMR spectrum (400 MHz, $CDCl_3$) of **L3**.

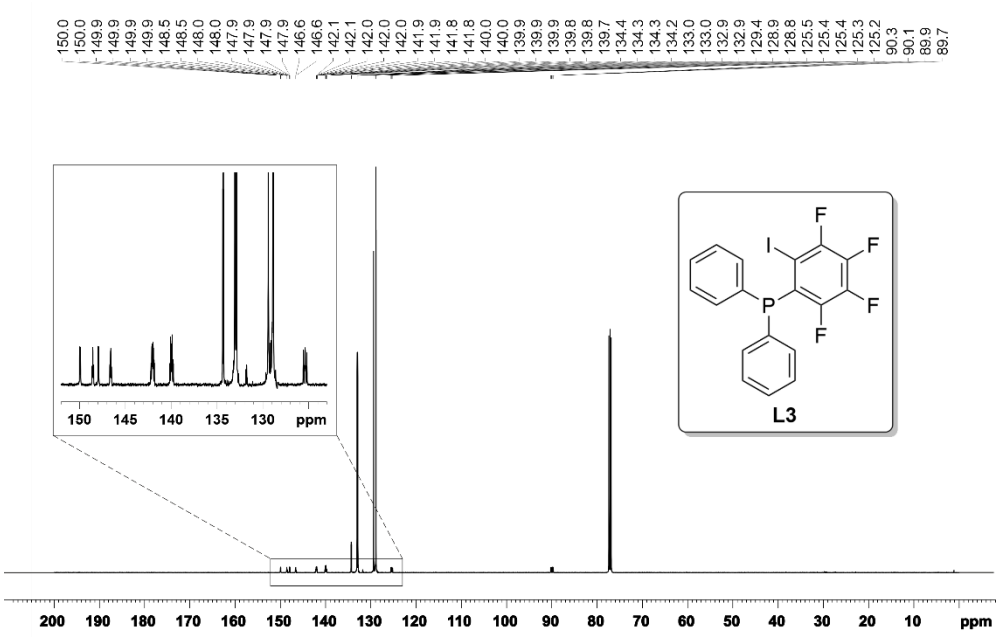

Figure 164. $^{13}C\{^{1}H\}$ NMR spectrum (126 MHz, $CDCl_3$) of **L3**.

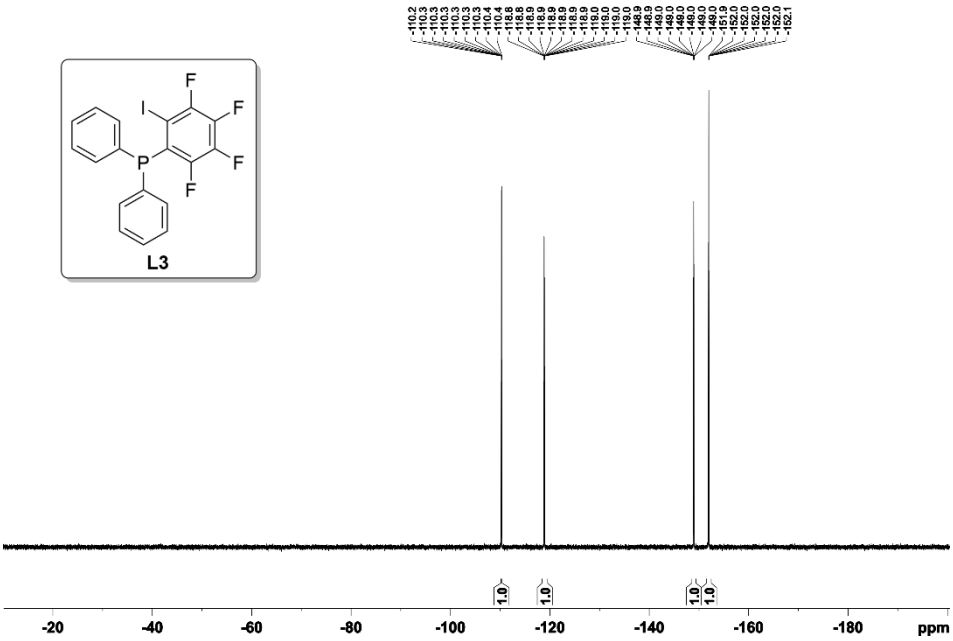

Figure 165. $^{19}F\{^{1}H\}$ NMR spectrum (376 MHz, $CDCl_3$) of **L3**.

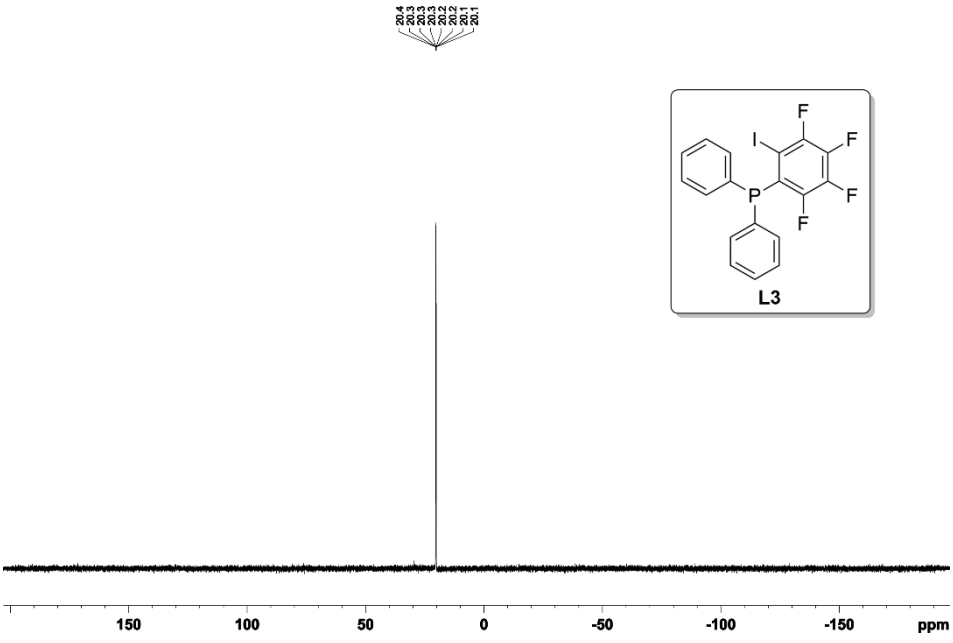

Figure 166. $^{31}P\{^{1}H\}$ NMR spectrum (162 MHz, $CDCl_3$) of **L3**.

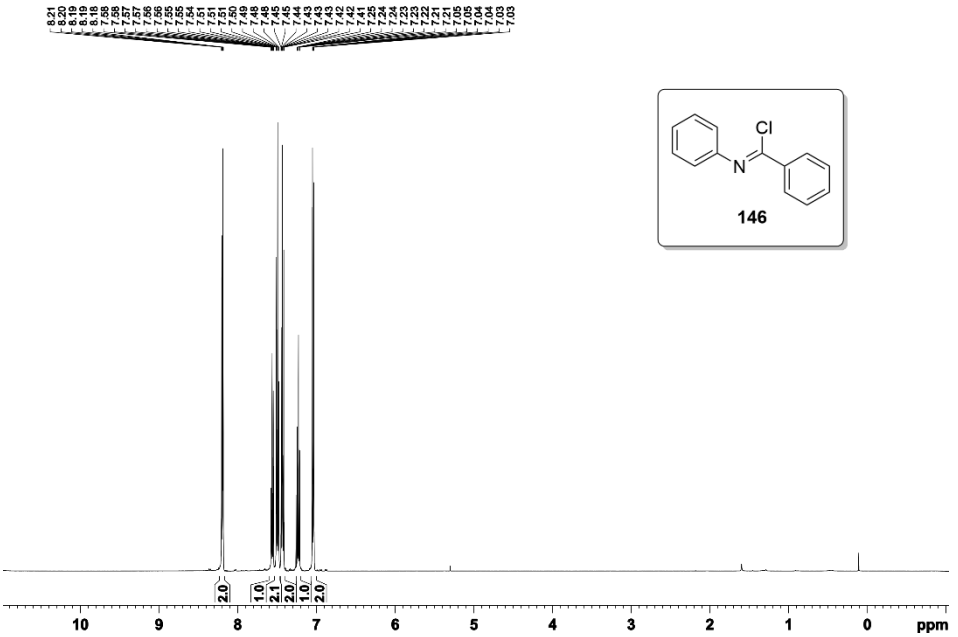

Figure 167. ^{1}H NMR spectrum (500 MHz, $CDCl_3$) of **146**.

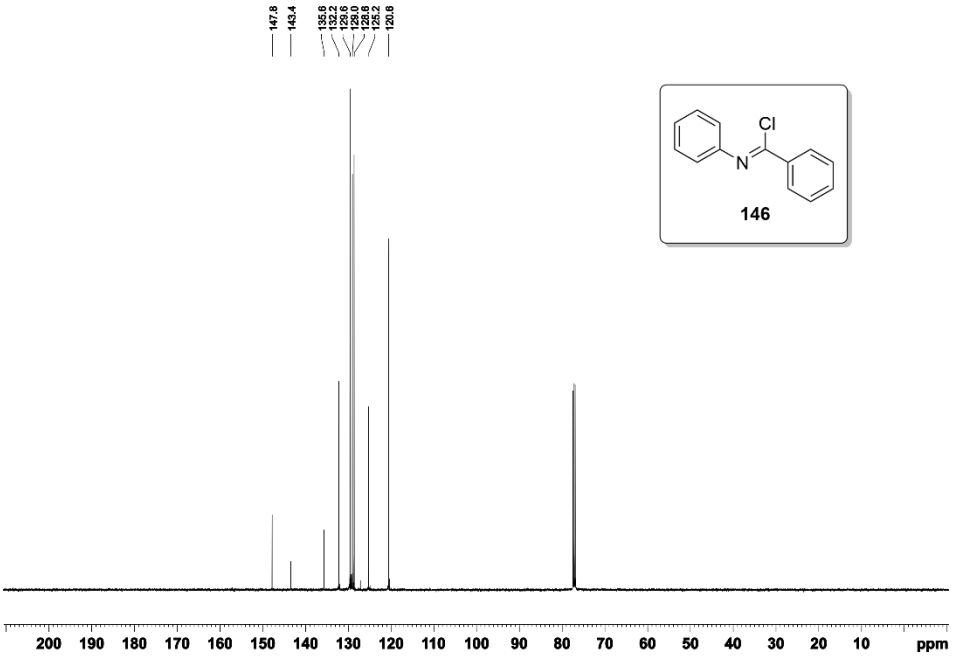

Figure 168. $^{13}C\{^{1}H\}$ NMR spectrum (126 MHz, $CDCl_3$) of **146**.

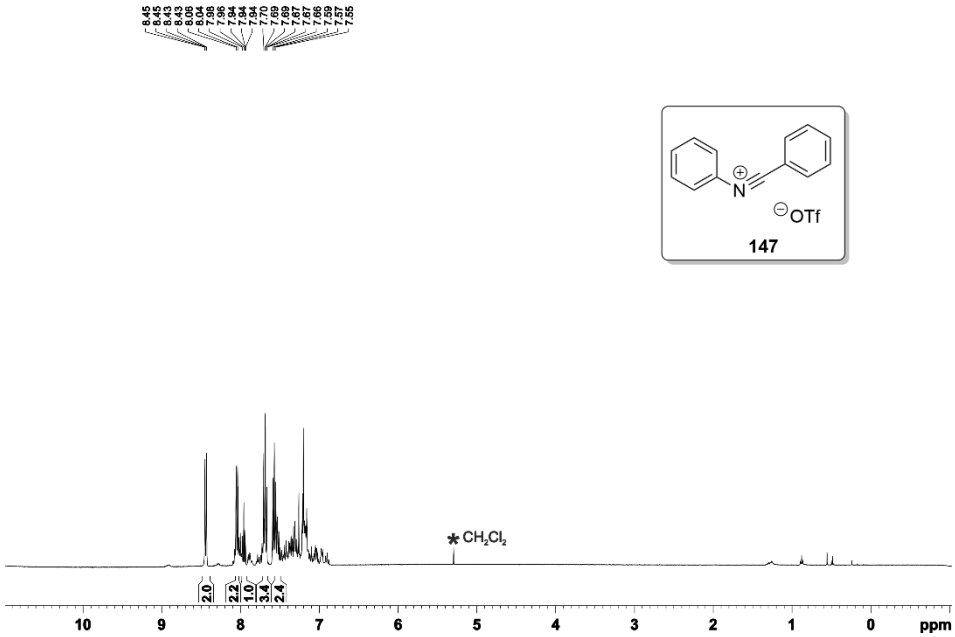

Figure 169. ^{1}H NMR spectrum (400 MHz, $CDCl_3$) of **147**.

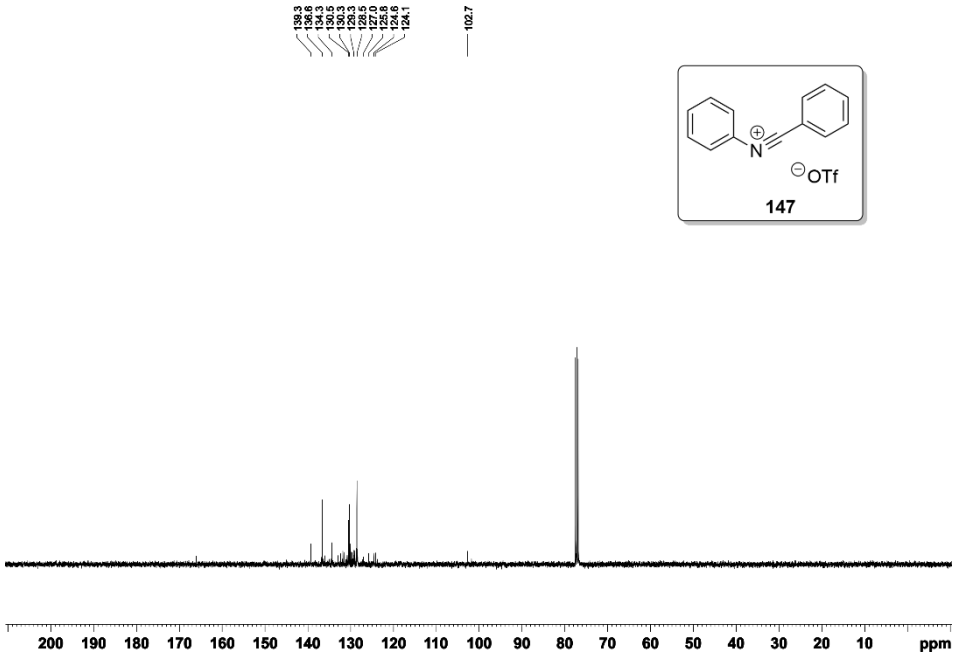

Figure 170. $^{13}C\{^{1}H\}$ NMR spectrum (101 MHz, $CDCl_3$) of **147**.

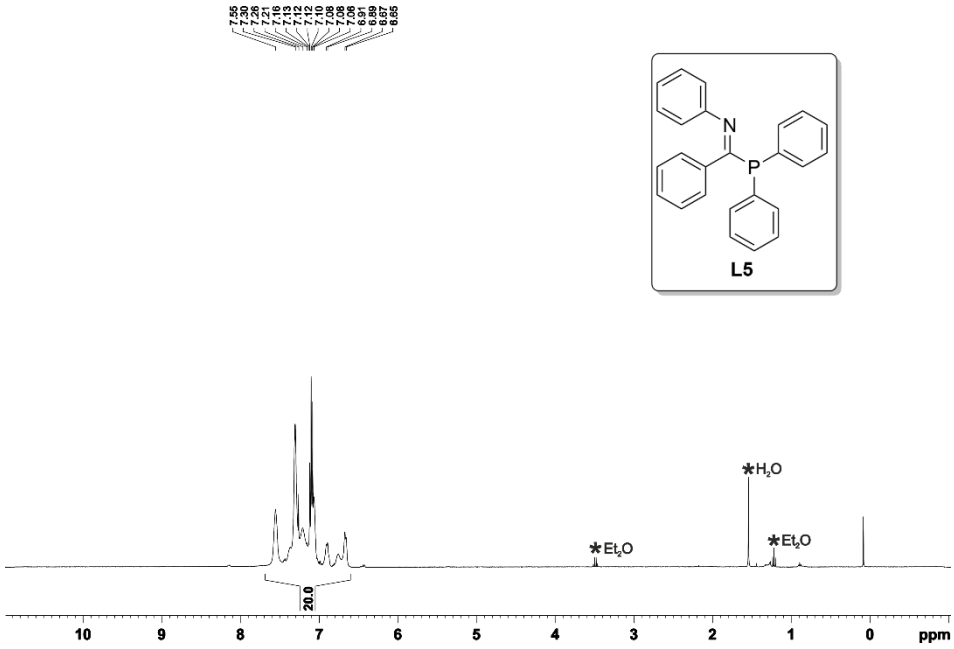

Figure 171. ^{1}H NMR spectrum (400 MHz, $CDCl_3$) of **L5**.

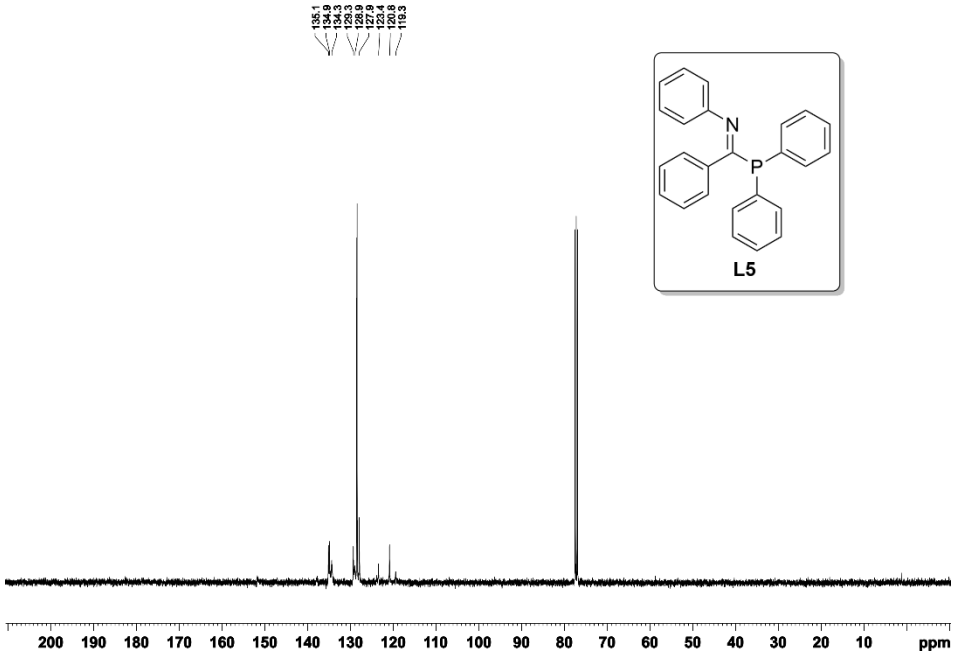

Figure 172. $^{13}C\{^{1}H\}$ NMR spectrum (126 MHz, $CDCl_3$) of **L5**.

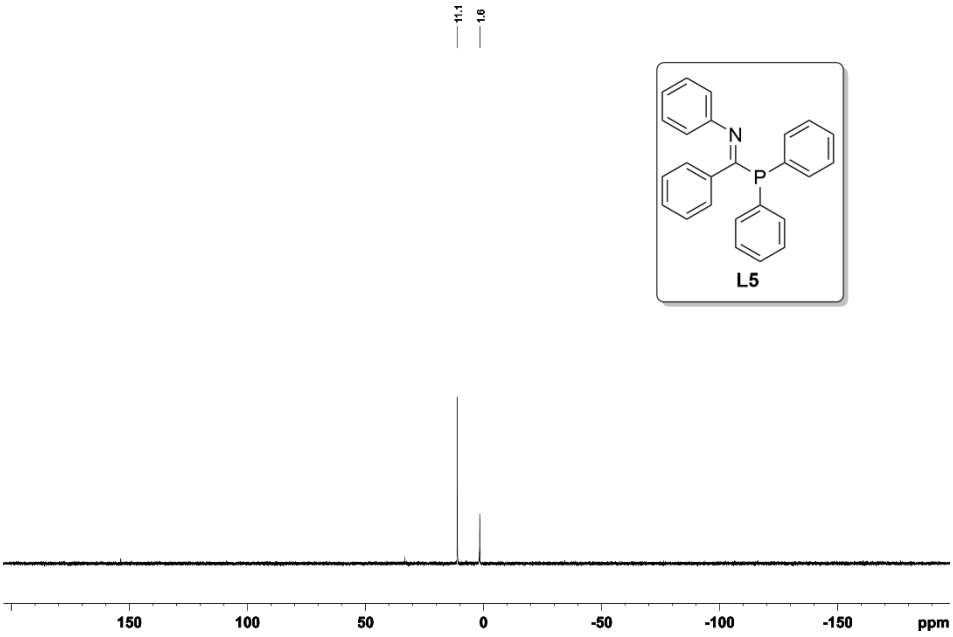

Figure 173. $^{31}P\{^{1}H\}$ NMR spectrum (162 MHz, $CDCl_3$) of **L5**.

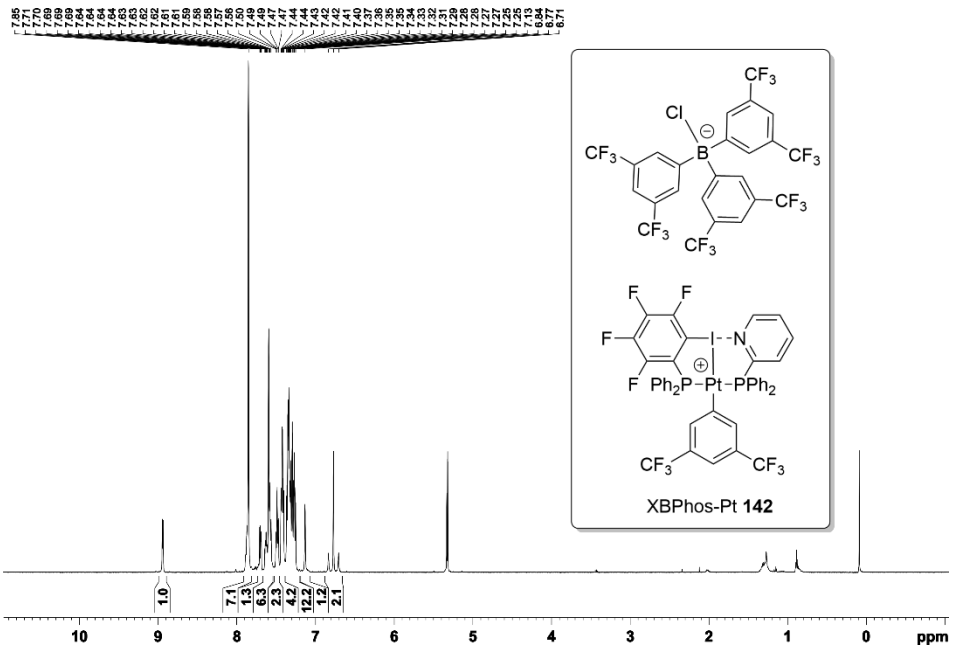

Figure 174. ^{1}H NMR spectrum (500 MHz, CD_2Cl_2) of XBPhos-Pt **142**.

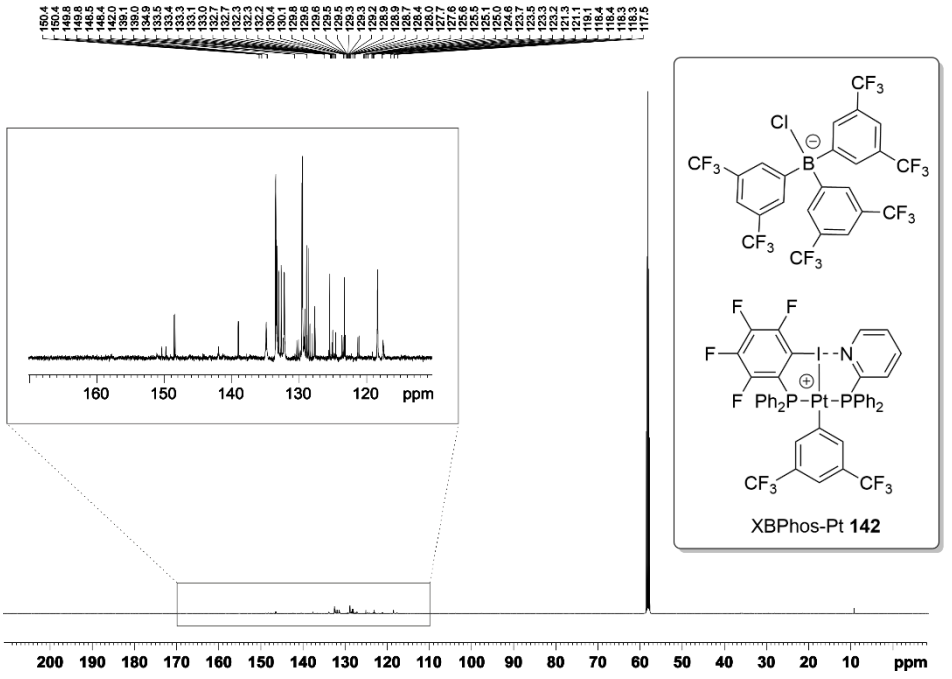

Figure 175. $^{13}C\{^{1}H\}$ NMR spectrum (126 MHz, CD_2Cl_2) of XBPhos-Pt **142**.

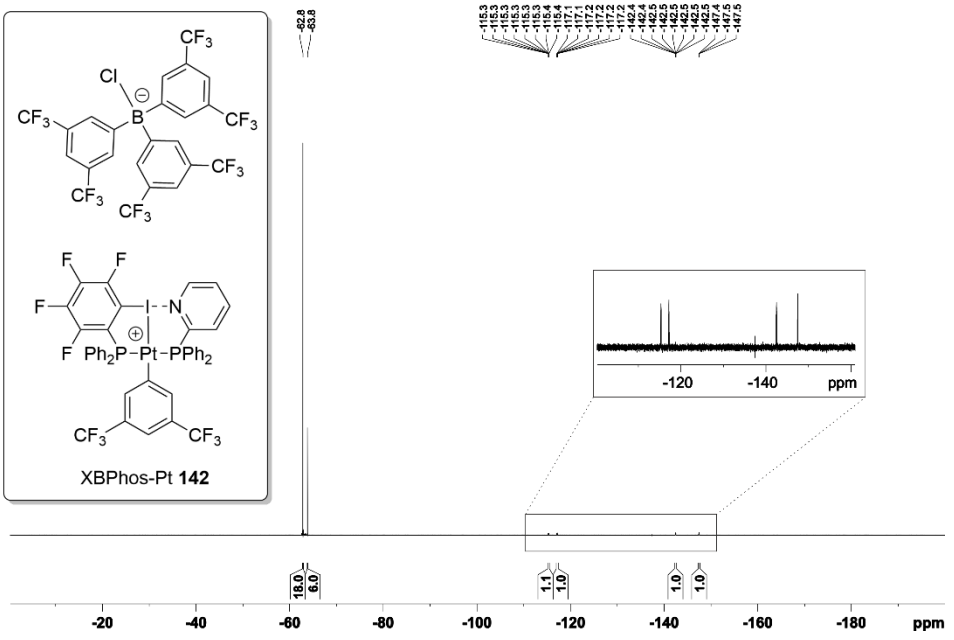

Figure 176. $^{19}F\{^{1}H\}$ NMR spectrum (376 MHz, CD_2Cl_2) of XBPhos-Pt **142**.

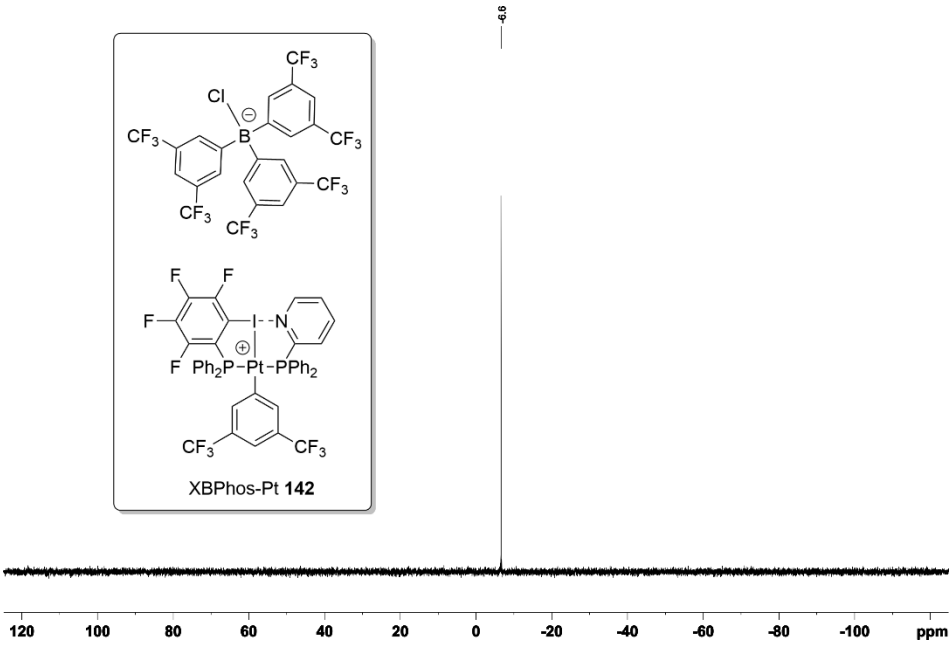

Figure 177. $^{11}B\{^{1}H\}$ NMR spectrum (128 MHz, CD_2Cl_2) of XBPhos-Pt **142**.

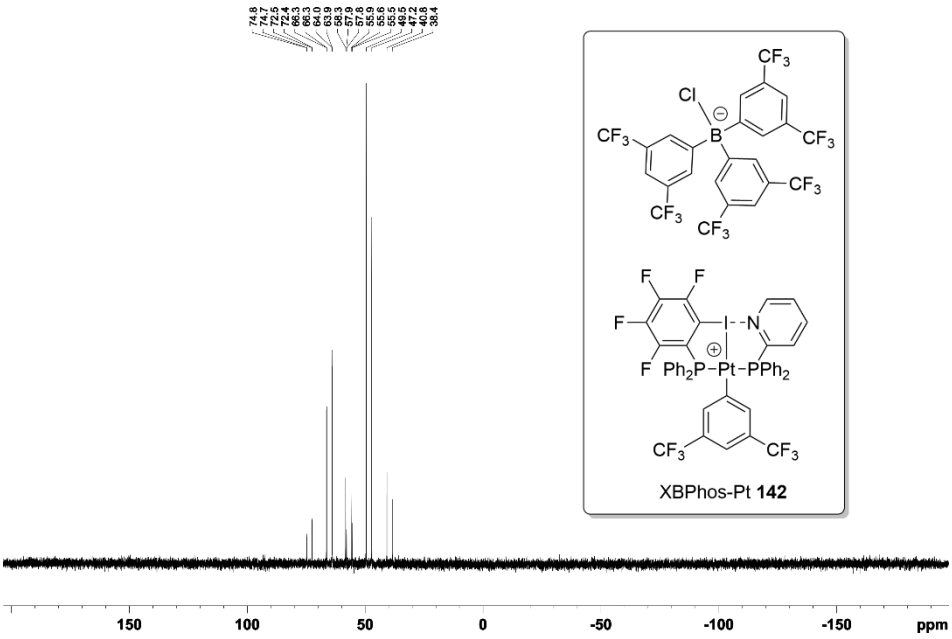

Figure 178. $^{31}P\{^{1}H\}$ NMR spectrum (162 MHz, CD_2Cl_2) of XBPhos-Pt **142**.

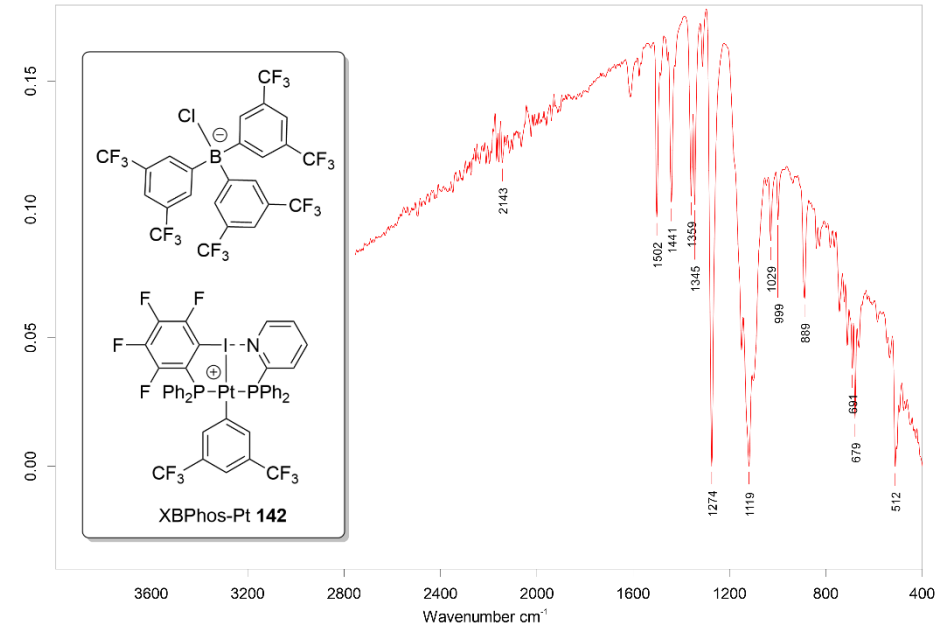

Figure 179. IR spectrum of XBPhos-Pt **142.**

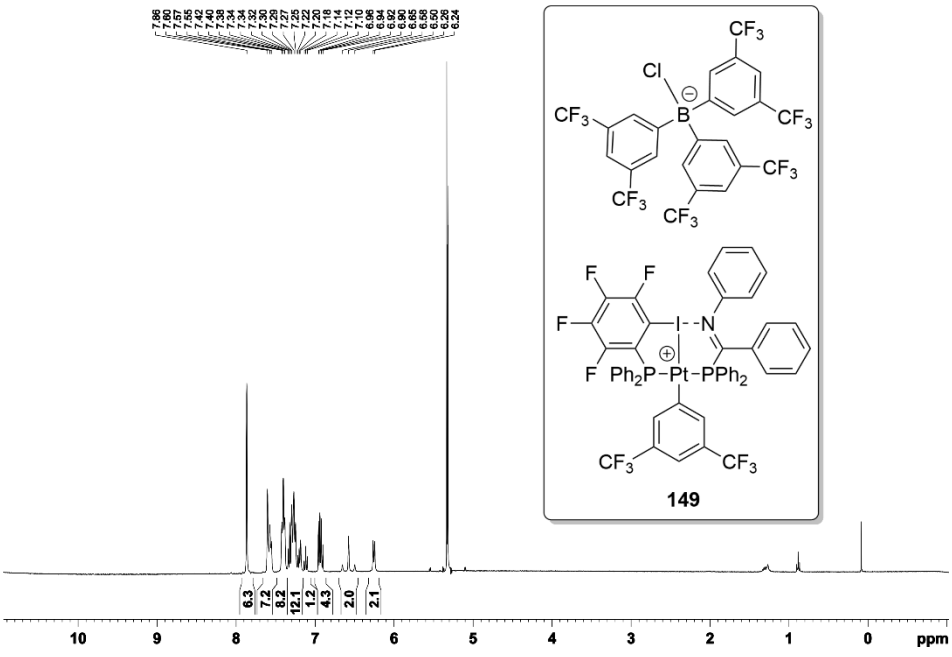

Figure 180. ^{1}H NMR spectrum (400 MHz, CD_2Cl_2) of **149**.

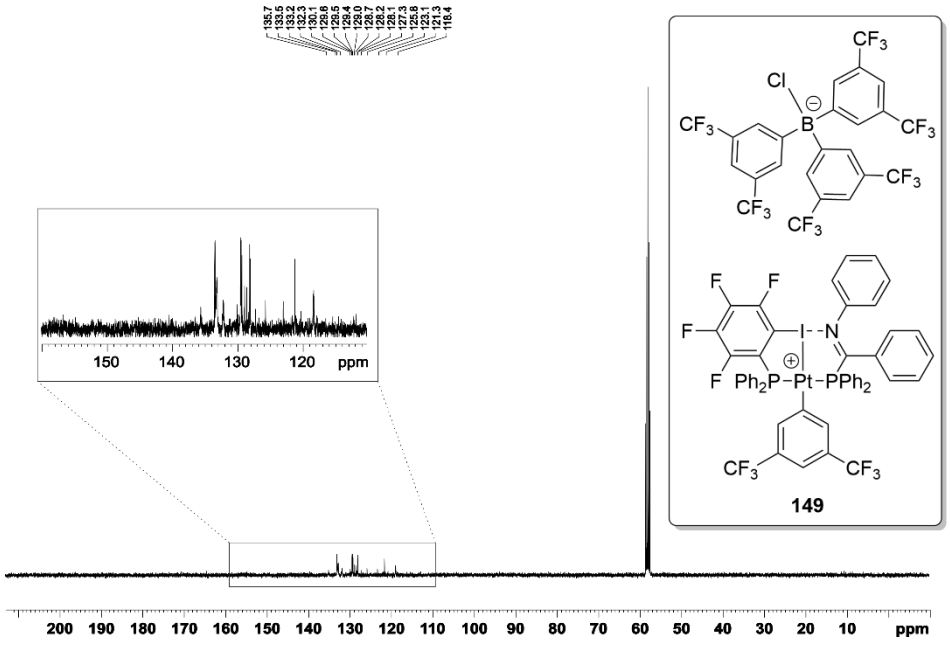

Figure 181. $^{13}C\{^{1}H\}$ NMR spectrum (126 MHz, CD_2Cl_2) of **149**.

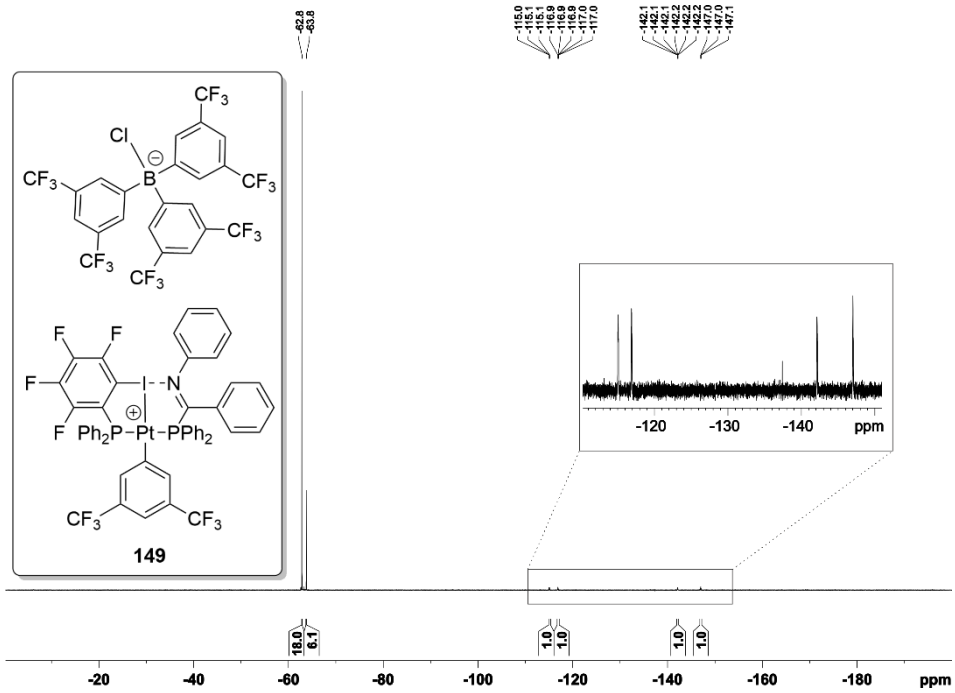

Figure 182. $^{19}F\{^{1}H\}$ NMR spectrum (376 MHz, CD_2Cl_2) of **149**.

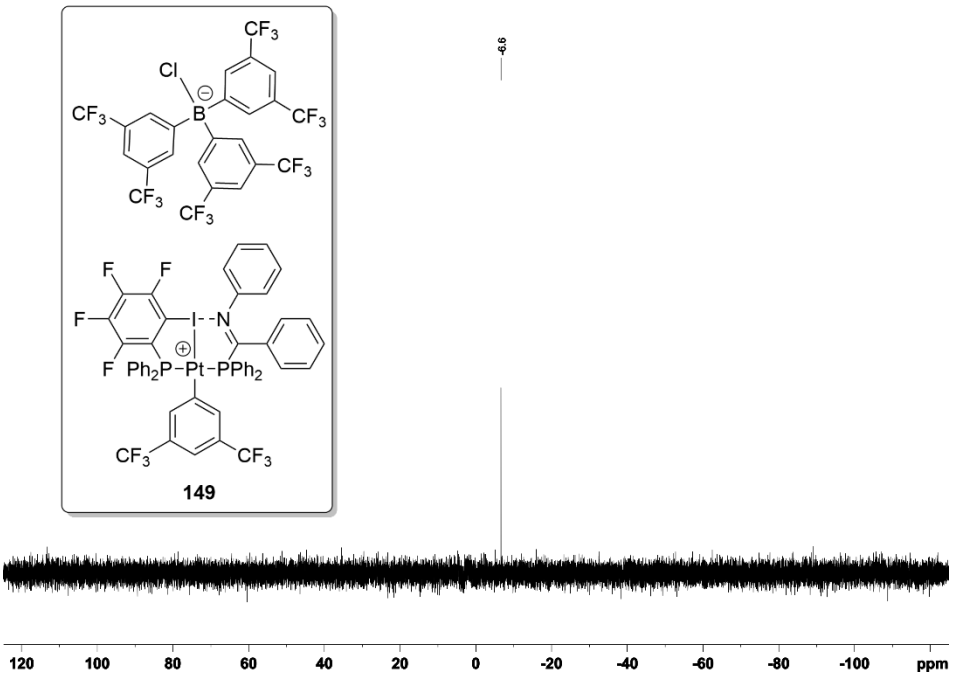

Figure 183. $^{11}B\{^{1}H\}$ NMR spectrum (128 MHz, CD_2Cl_2) of **149**.

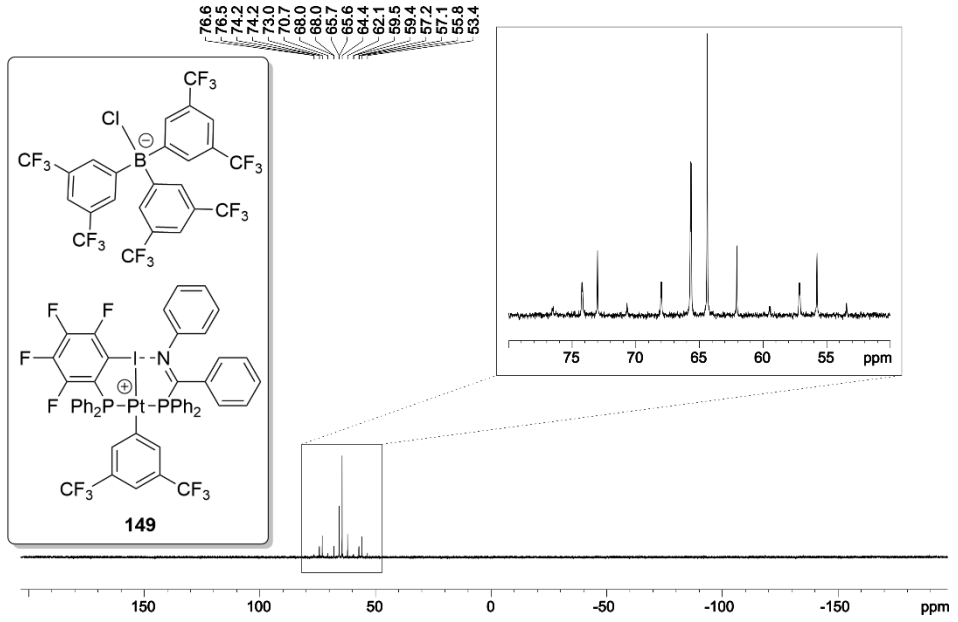

Figure 184. $^{31}P\{^{1}H\}$ NMR spectrum (162 MHz, CD_2Cl_2) of **149**.

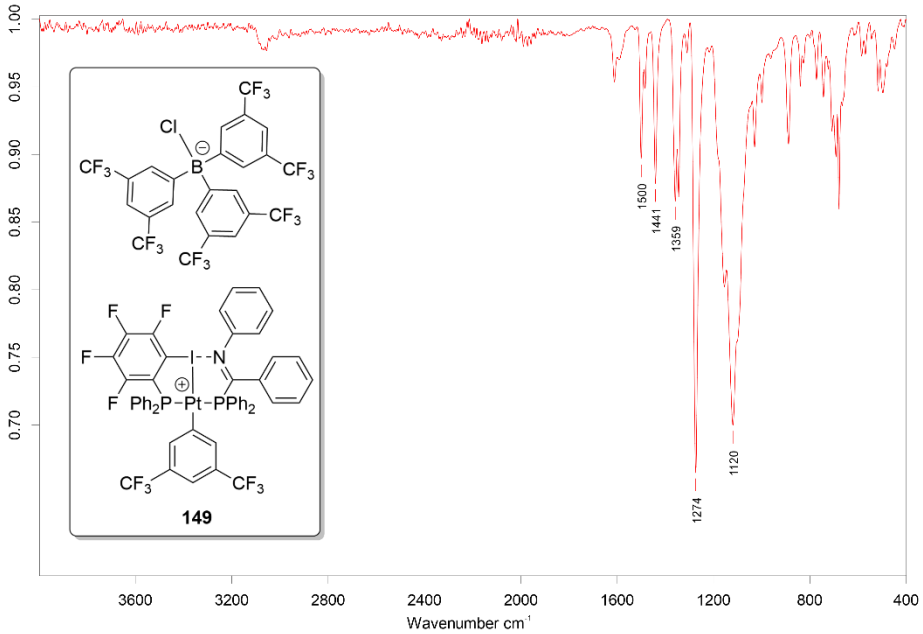

Figure 185. IR spectrum of **149.**

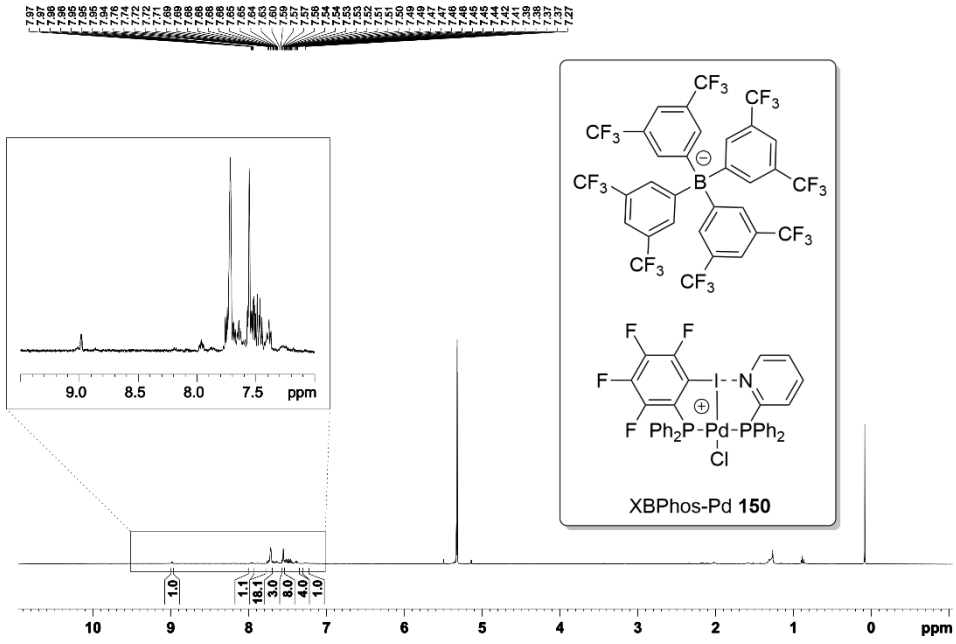

Figure 186. ^{1}H NMR spectrum (500 MHz, CD_2Cl_2) of XBPhos-Pd **150**.

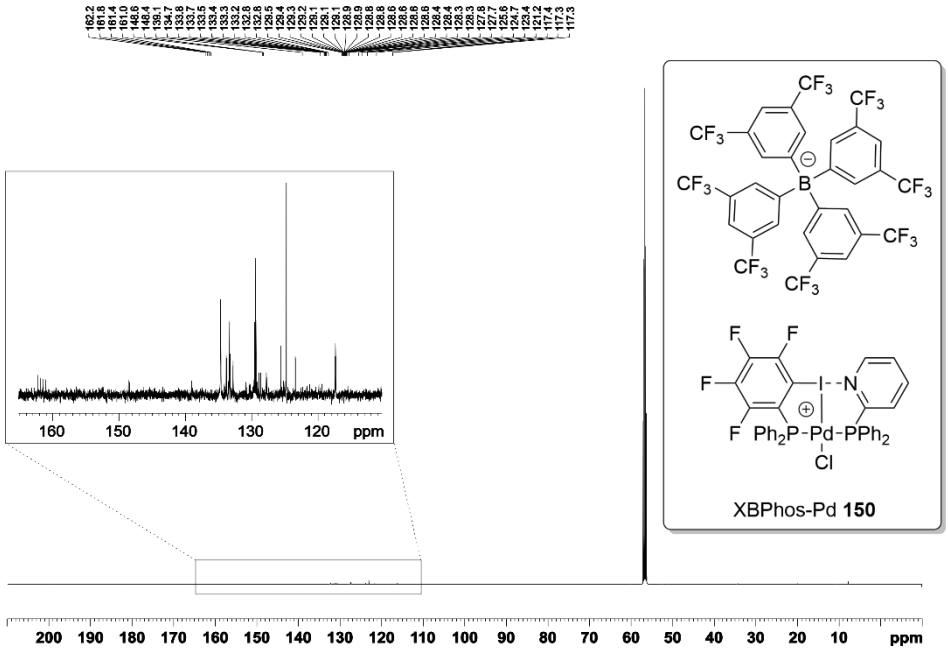

Figure 187. $^{13}C\{^{1}H\}$ NMR spectrum (126 MHz, CD_2Cl_2) of XBPhos-Pd **150**.

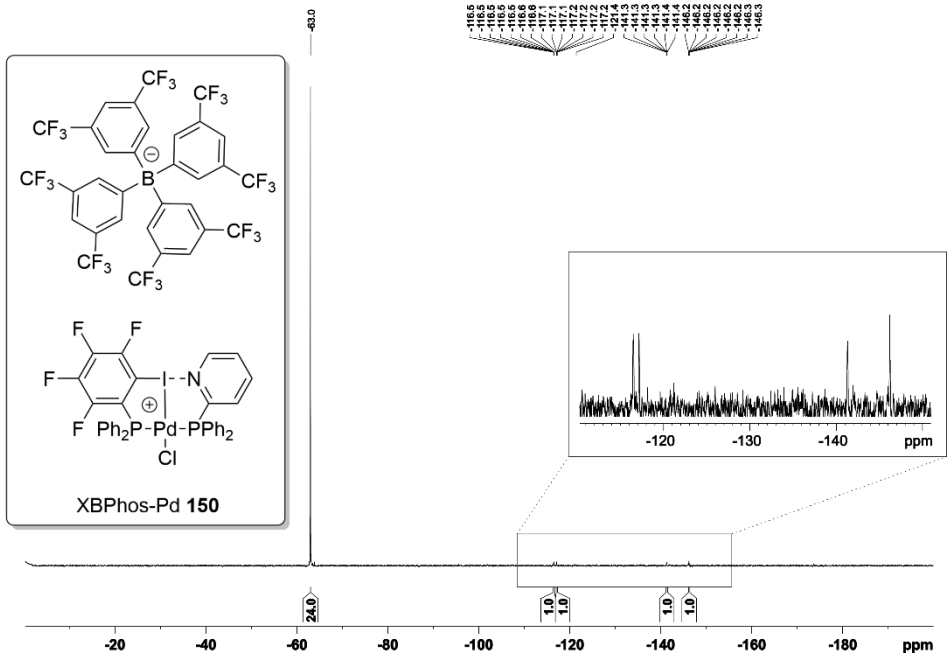

Figure 188. $^{19}F\{^{1}H\}$ NMR spectrum (376 MHz, CD_2Cl_2) of XBPhos-Pd **150**.

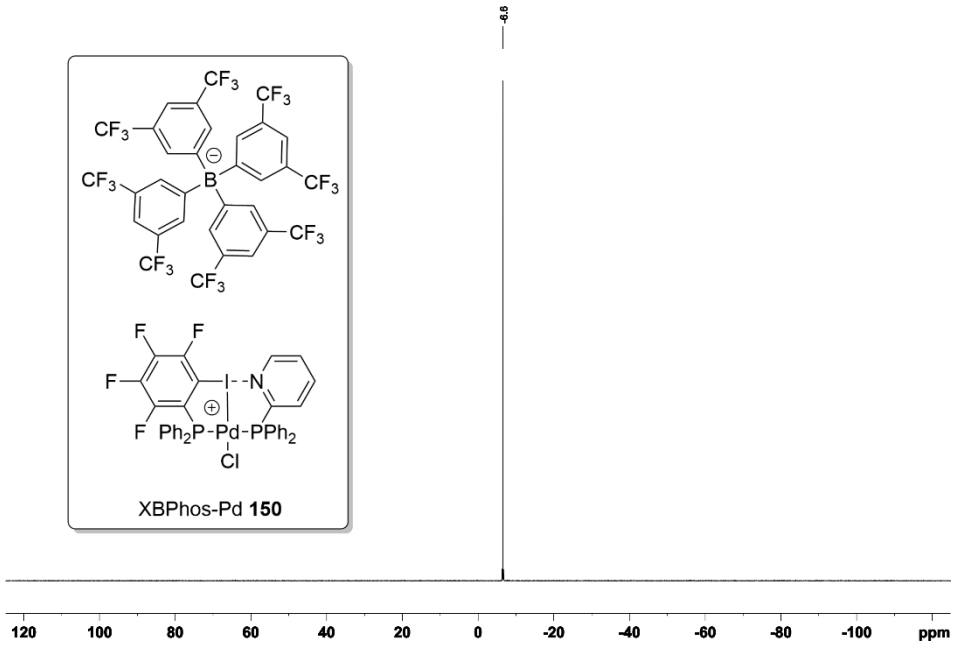

Figure 189. $^{11}B\{^{1}H\}$ NMR spectrum (128 MHz, CD_2Cl_2) of XBPhos-Pd **150**.

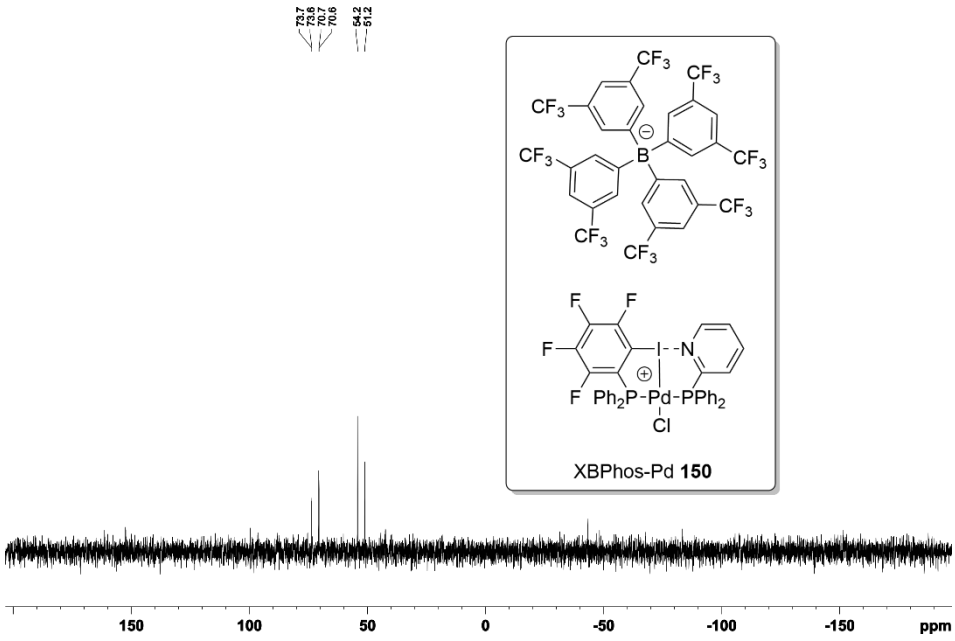

Figure 190. $^{31}P\{^{1}H\}$ NMR spectrum (162 MHz, CD_2Cl_2) of XBPhos-Pd **150**.

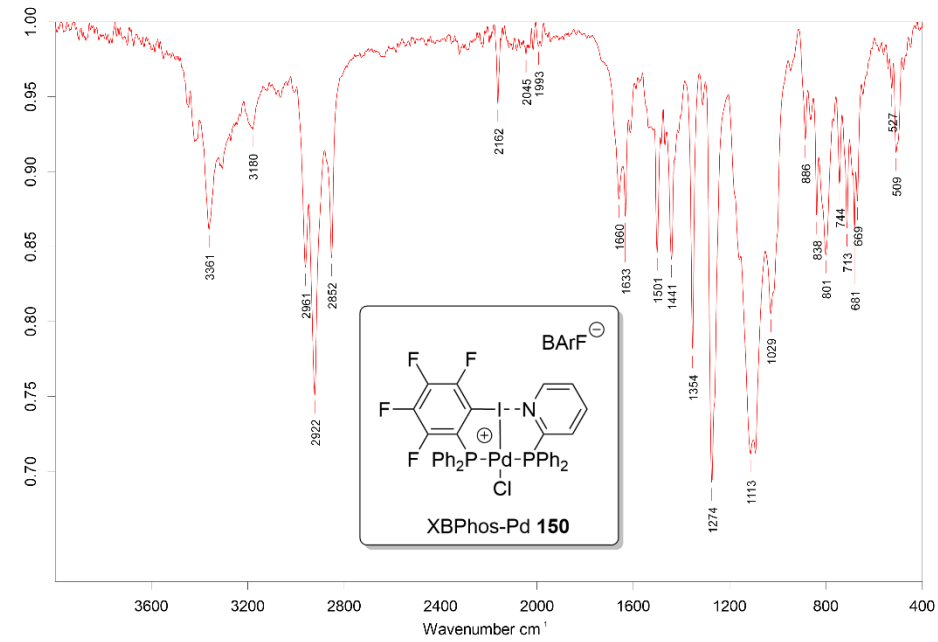

Figure 191. IR spectrum of XBPhos-Pd **150.**

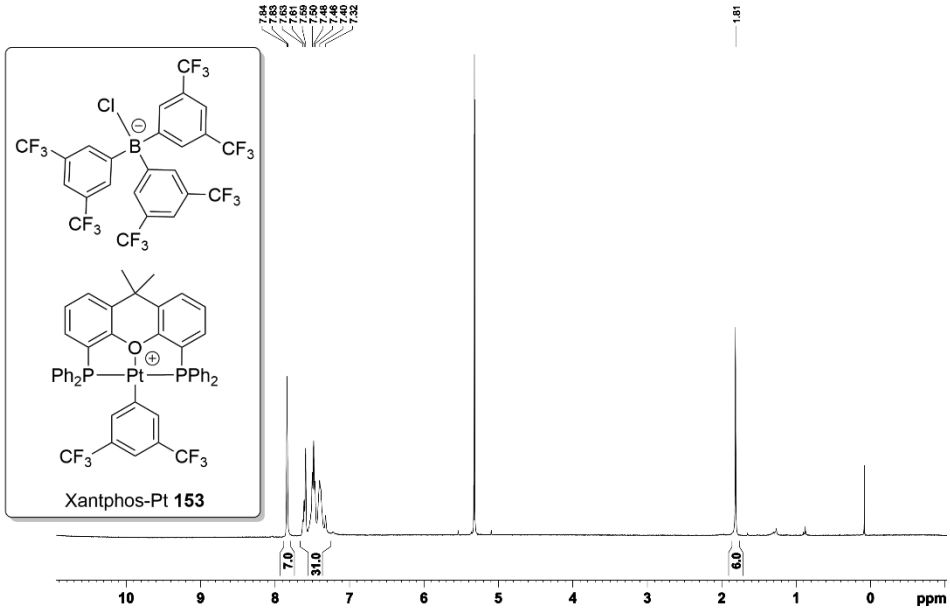

Figure 192. ^{1}H NMR spectrum (400 MHz, CD_2Cl_2) of Xantphos-Pt **153**.

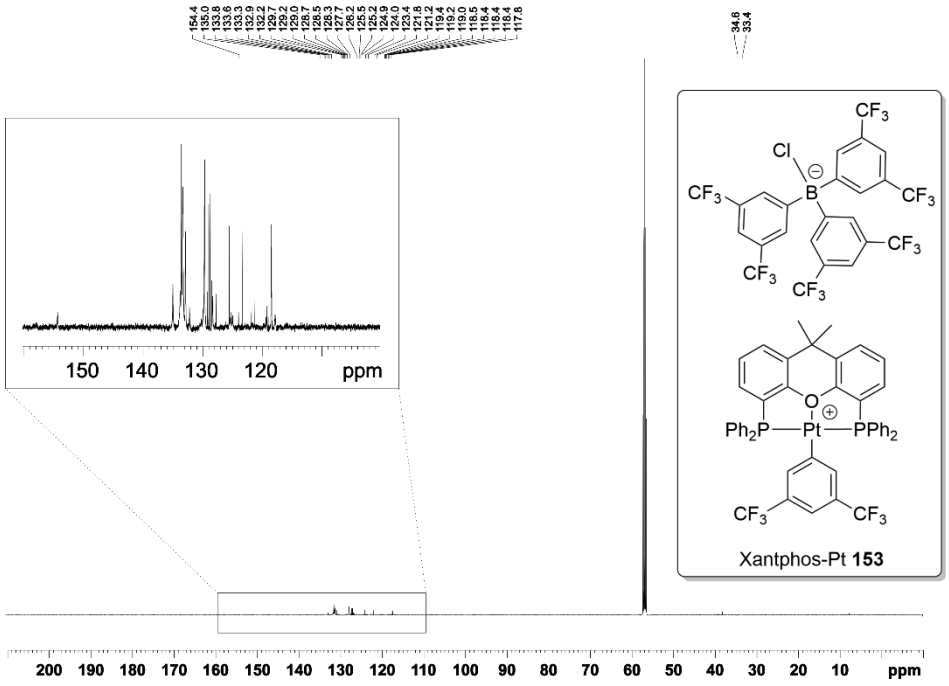

Figure 193. $^{13}C\{^{1}H\}$ NMR spectrum (126 MHz, CD_2Cl_2) of Xantphos-Pt **153**.

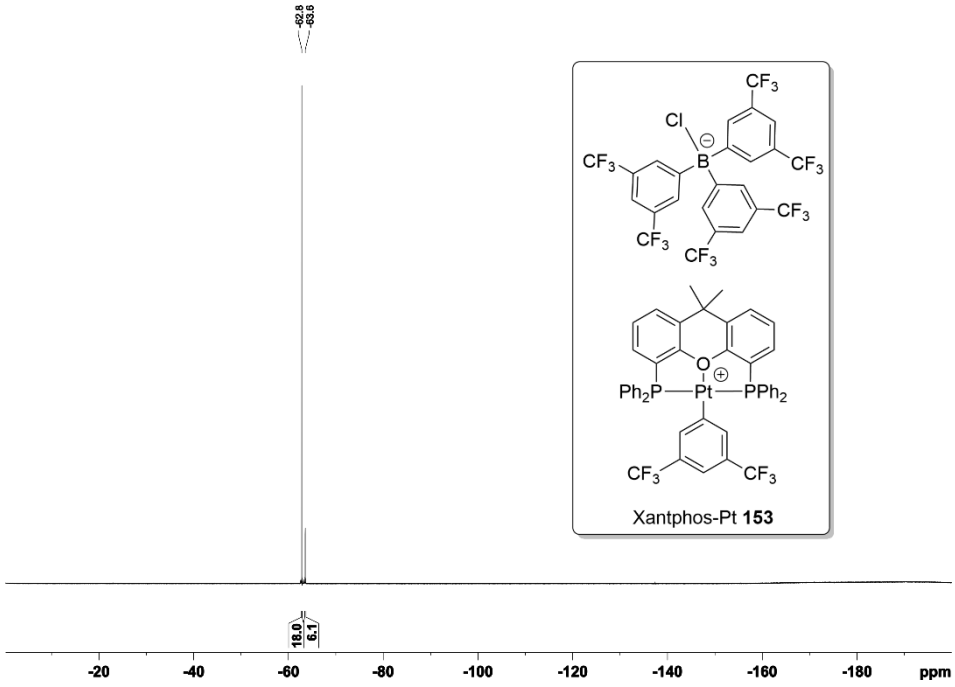

Figure 194. $^{19}F\{^{1}H\}$ NMR spectrum (376 MHz, CD_2Cl_2) of Xantphos-Pt **153**.

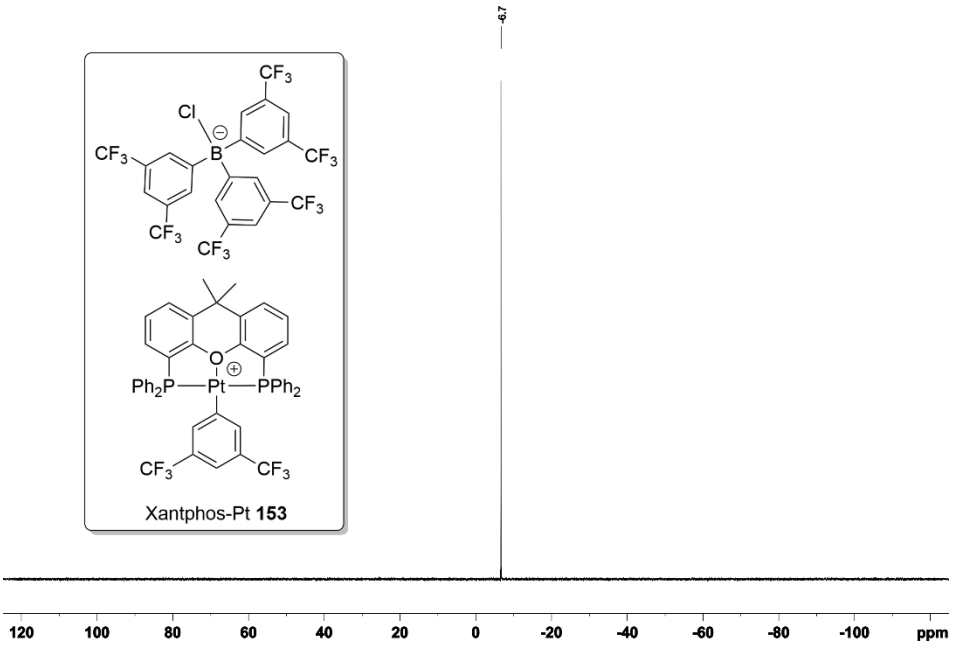

Figure 195. $^{11}B\{^{1}H\}$ NMR spectrum (128 MHz, CD_2Cl_2) of Xantphos-Pt **153**.

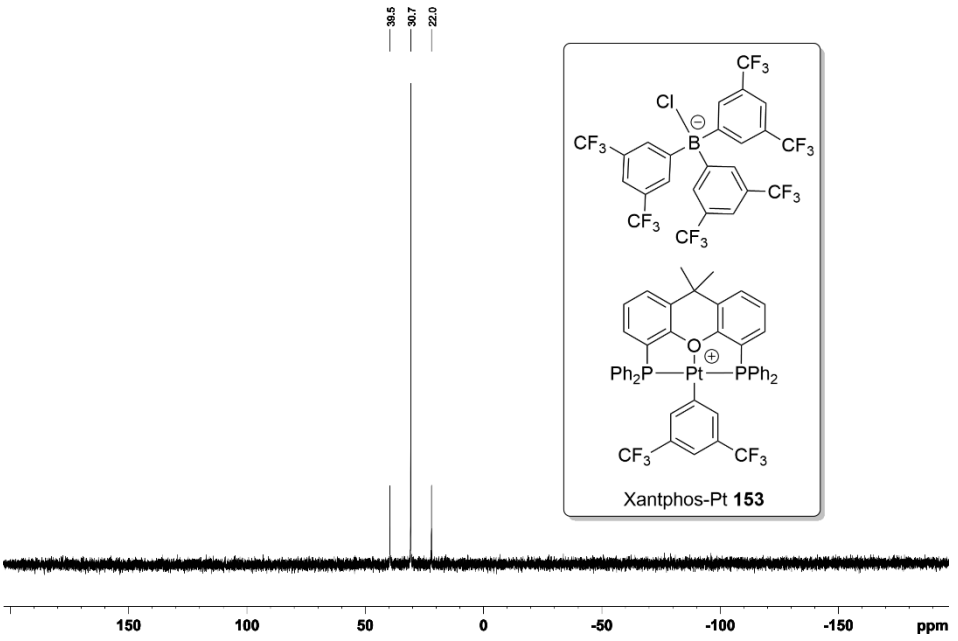

Figure 196. $^{31}P\{^{1}H\}$ NMR spectrum (162 MHz, CD_2Cl_2) of Xantphos-Pt **153**.

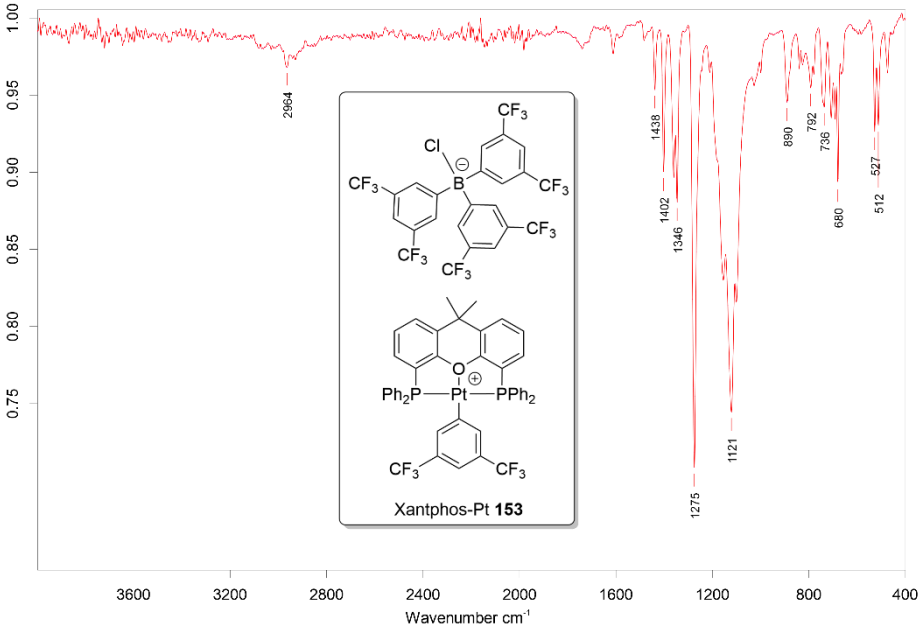

Figure 197. IR spectrum of Xantphos-Pt **153.**

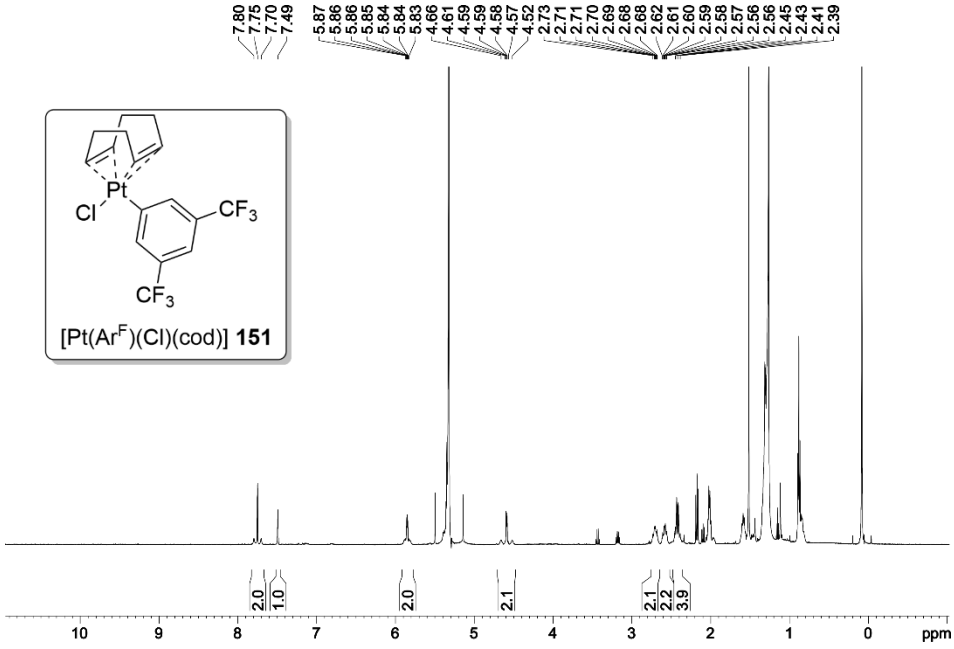

Figure 198. ^{1}H NMR spectrum (500 MHz, CD_2Cl_2) of [Pt(Ar^F)(Cl)(cod)] **151**.

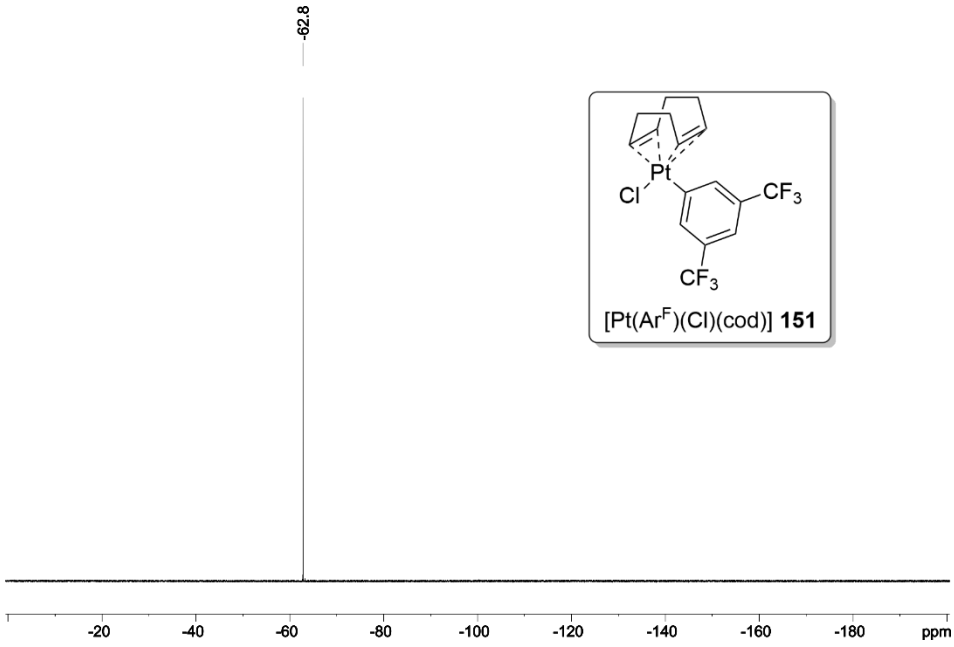

Figure 199. $^{19}F\{^{1}H\}$ NMR spectrum (376 MHz, CD_2Cl_2) of $[Pt(Ar^F)(Cl)(cod)]$ **151**.

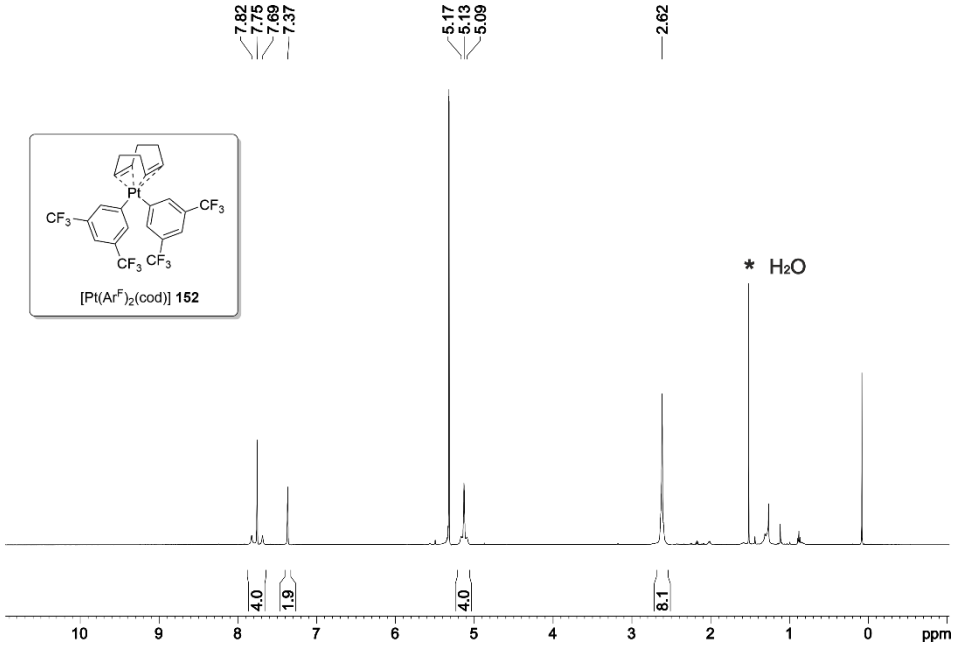

Figure 200. ^{1}H NMR spectrum (500 MHz, CD_2Cl_2) of $[Pt(Ar^F)_2(cod)]$ **152**.

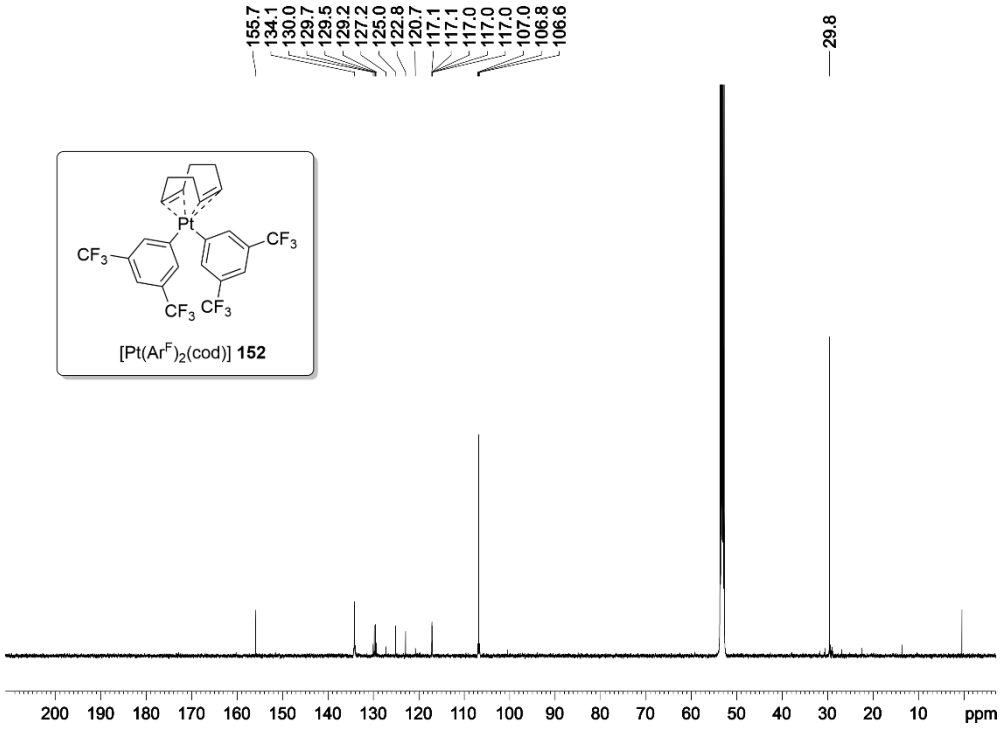

Figure 201. $^{13}C\{^{1}H\}$ NMR spectrum (126 MHz, CD_2Cl_2) of $[Pt(Ar^F)_2(cod)]$ **152**.

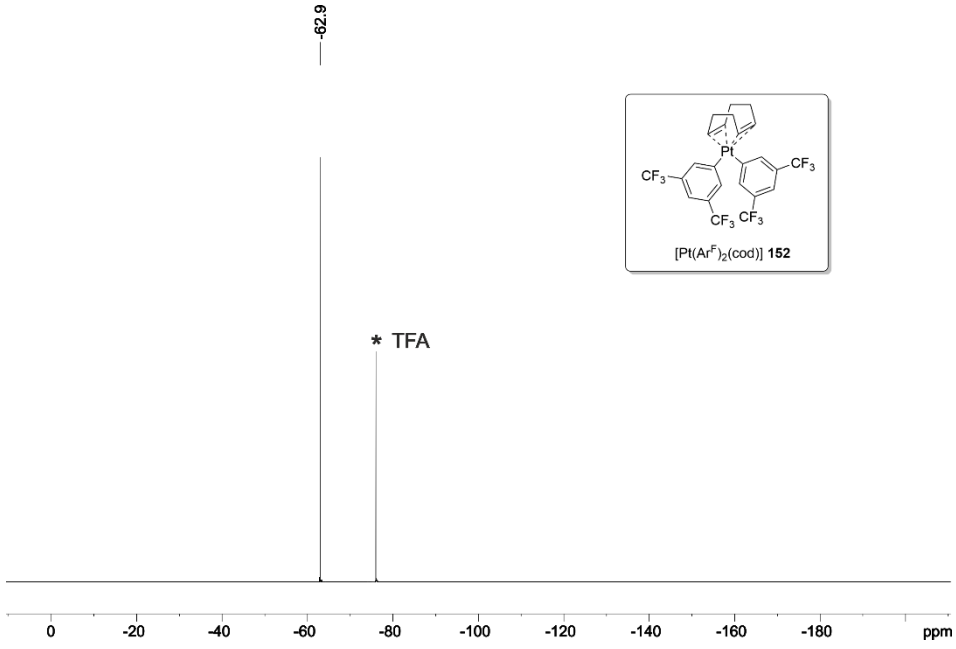

Figure 202. $^{19}F\{^{1}H\}$ NMR spectrum (376 MHz, CD_2Cl_2) of $[Pt(Ar^F)_2(cod)]$ **152**.

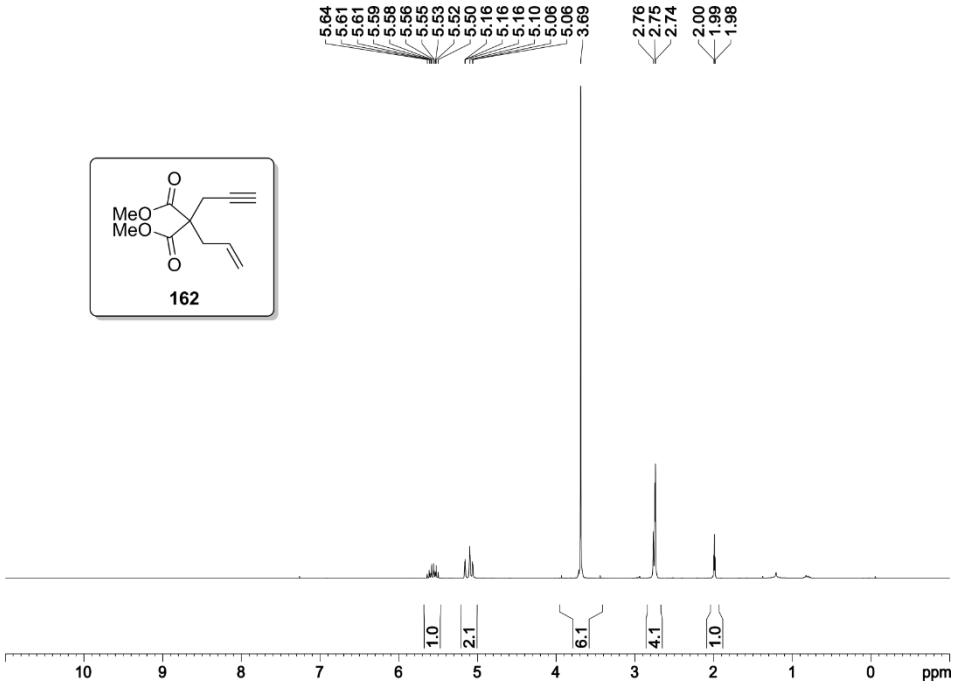

Figure 203. ^{1}H NMR spectrum (400 MHz, CD_2Cl_2) of **162**.

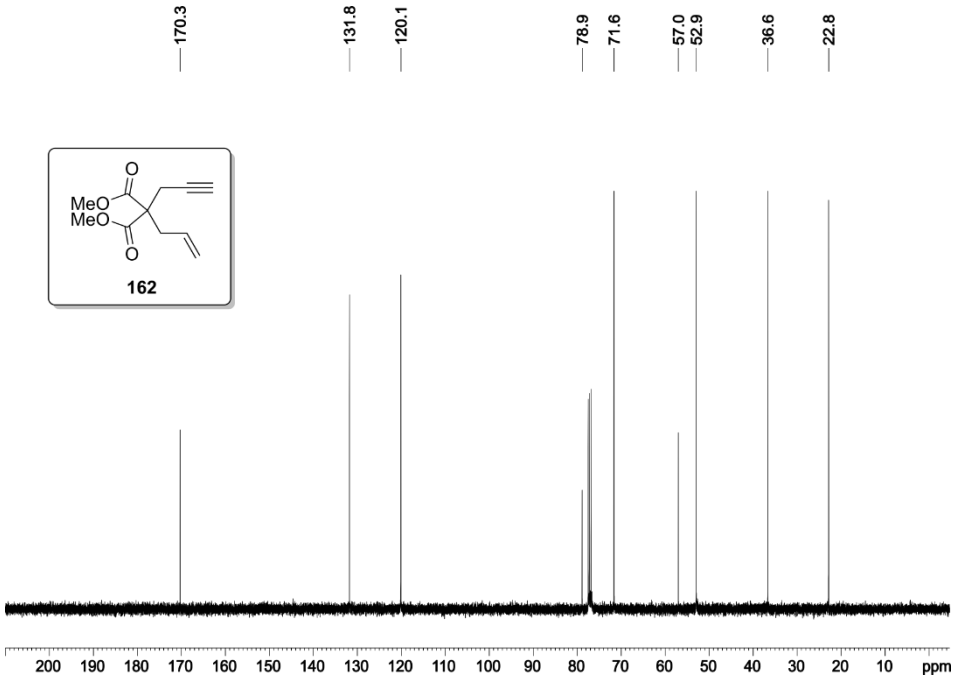

Figure 204. $^{13}C\{^{1}H\}$ NMR spectrum (126 MHz, CD_2Cl_2) of **162**.

CONCLUSIONS

- Catalysts containing linear polyethyleneoxy chains as supramolecular regulation sites and oxazoline units as coordinating groups for copper(I) centers have been designed, prepared and characterized. These supramolecular copper complexes have found application in the catalyzed insertion of copper carbenoids into the O–H groups of an array of structurally diverse alcohols to afford synthetically useful α-alkyl/aryl-α-alkoxy/aryloxy derivatives in yields ranging from 39% to 99% (seventeen examples). Our regulation approach, which consists of screening a set of regulation agents to obtain the highest yield for the substrate of interest, has been demonstrated. The rapid tailoring of the catalyst system to each substrate has been achieved and the practicality of this transformation employing our supramolecularly regulated catalysts has been expanded by preparing advanced synthetic intermediates of relevant APIs.

- The design, synthesis and characterization of new supramolecular platinum(II) and palladium(II) complexes derived from halogen-bonded diphosphines are described. The assembly of two building blocks that incorporate P-containing ligating groups, as well as complementary binding motifs for the assembly process through halogen bonding, efficiently led to new supramolecular platinum(II) and palladium(II) complexes. These new complexes were thoroughly characterized in solution (standard spectroscopic techniques) and in the solid state (single crystal X-ray diffraction). In contrast to the analogous supramolecular rhodium complexes previously reported by our group, the supramolecular platinum complexes prepared (*i.e.*, [Pt(Ar^F)(κ^3*I,P,P*-(**L3•L4**))][$B(Ar^F)_3$(Cl)] and [Pt(Ar^F)(κ^3*I,P,P*-(**L3•L5**))][$B(Ar^F)_3$(Cl)]) incorpora-ted an Ar^F (3,5-bis(trifluoromethyl)phenyl) ligand, which arose from the BArF counterion through a platinum mediated B–Ar^F bond cleavage. A broad study of the reaction intermediates and reaction pathway that led to the final platinum(II) complexes has been performed. A tentative mechanistic rationalization for the formation of the platinum(II) complex **142** is proposed (oxidative addition of a B–C bond from the BArF counterion to [$Pt(Cl)_2$(cod)], subsequent B–Cl reductive elimination, coordination of the phosphine ligands with concomitant displacement of the cod ligand and NaCl elimination). The

complex XBPhos-Pt has proved to be unreactive as a supramolecular catalyst in carbocyclizations of enynes and the hydrophenylation of ethylene. Strategies towards the activation of the complex XBPhos-Pt and analogues for new chemistries are presented.

SUMMARY

The present doctoral thesis encompasses the design, development, characterization and application of supramolecular catalytic systems based on regulation strategies and on halogen bonding as a tool to construct the skeleton of transition metal-based catalysts. The regulation approach has been applied to transformations of interest, such as the insertion of carbenoids species into O–H bonds, leading to synthetically useful α-alkyl/aryl-α-alkoxy/aryloxy derivatives and related compounds that could be used for the preparation of molecules with biological relevance.

Research efforts initially focused on the development of supramolecularly regulated copper(I) catalysts (Chapter 1). The modular design incorporated a linear polyethyleneoxy chain as the supramolecular regulation site and oxazoline units as ligating groups to the copper(I) center. Our regulation mechanism is triggered by the addition of a regulation agent (RA), capable of interacting with the regulation site *via* ion-dipole interactions. The binding of the regulation agent to the polyethyleneoxy moiety not only serves to bring together the two terminal ligating groups, but also to modify the geometry and flexibility of the catalytic site. The choice of regulation agent determined the rigidity and conformational flexibility of the whole catalytic system, which ultimately translated into a modulation of the activity and selectivity of the supramolecular catalyst.

Our investigations began with the preparation of the bisoxazoline ligands, which were straightforwardly synthesized from a monooxazoline derivative by efficient synthetic protocols. After successfully preparing an array of bisoxazoline ligands, binding affinities between the ligand and alkali metal BArF salts (RAs) were evaluated. Binding constants *K* were found to be higher than 10^3 M^{-1} at 25 ºC in $CDCl_3$, for all the BArF salts tested.

With the ligands in hand, copper(I) catalysts were prepared and assayed in the insertion of carbenoids species into O–H bonds. The utility of rapid tailoring of the catalytic system for each substrate through the regulation approach was clearly demonstrated, with yields being improved by the addition of the matched regulation agent for each substrate. The effectiveness of the approach was tested by functionalizing an array of electronically and structurally diverse alcohols to afford synthetically useful α-alkyl/aryl-α-alkoxy/aryloxy derivatives in yields

ranging from 39% to 99%. The greatest improvements were observed for the *p*-fluoro-substituted product with an increase of 55% in the yield (32% yield in the absence of the RA and 87% yield with NaBArF as RA). Quantitative yields were obtained with electron rich phenols (for instance 99% yield for the reaction between *p*-methoxy phenol and ethyl 2-diazo-2-phenylacetate). On the contrary, when the aromatic ring was substituted by electron-withdrawing groups, the yield dropped to 41% yield (for instance with *p*-nitro phenol as substrate). The utility of the approach was further demonstrated by extending the scope of the reaction to challenging substrates, such as tertiary cycloalkanols, whose reaction products are frequently present in drug candidates. The practicality of our catalytic system was also demonstrated by the preparation of advanced synthetic intermediates of biologically relevant compounds, as for instance advanced synthetic intermediates of Prozac® and Benadryl®.

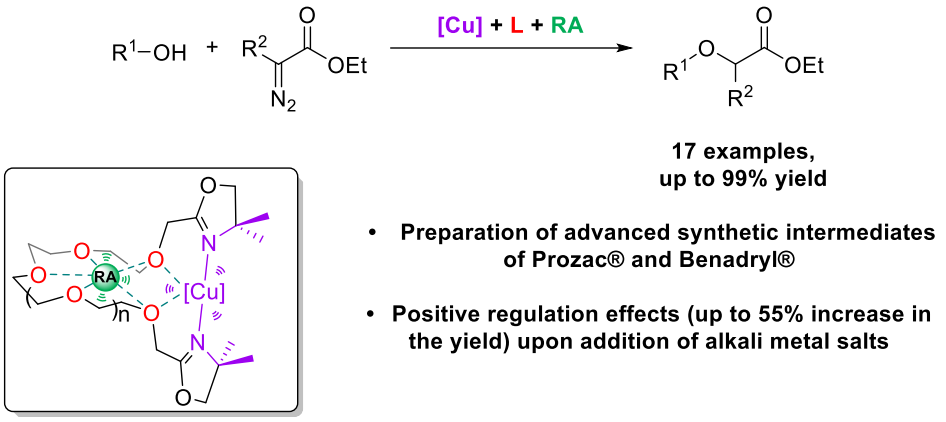

Scheme 70. Supramolecularly regulated insertion of Cu-carbenoids into O–H bonds.

Research efforts also focused on the use of halogen bonding interactions to construct the skeleton of group 10 metal complexes derived from halogen-bonded diphosphines (Chapter 2). New supramolecular platinum(II) and palladium(II) complexes were synthesized by assembling two building blocks that incorporated phosphines as ligating groups, as well as complementary binding motifs for the assembly of a supramolecular diphosphine ligand through halogen bonding. The corresponding platinum(II) and palladium(II) complexes were characterized in solution with standard spectroscopic techniques, which pointed to the formation of metal complexes with a *trans*-coordinated supramolecular diphosphine to a square planar metal center. X-ray diffraction analysis allowed for: (i) the unequivocal determination of the structures of the

complexes; (ii) the determination of the *P*,*I*,*P*-pincer-type nature of the resulting complexes; and (iii) the characterization of the halogen bonding interaction in the solid state (I···N distances ranging from 2.6544 to 2.7210 Å; C–I···N bond angles ranging from 169.74 to 178.17° and normalized interaction ratios (R_{XB}) ranging from 0.75 to 0.77) in the palladium and platinum complexes.

The supramolecular platinum complexes prepared (*i.e.*, [Pt(Ar^F)(κ^3*I*,*P*,*P*-(**L3•L4**))][B(Ar^F)$_3$(Cl)] and [Pt(Ar^F)(κ^3*I*,*P*,*P*-(**L3•L5**))][B(Ar^F)$_3$(Cl)]) incorporated a platinum-bound Ar^F ligand (Ar^F = 3,5-bis(trifluoromethyl)phenyl), which came from the BArF counterion through a platinum-mediated B–Ar^F bond cleavage process. A study of the reaction intermediates and reaction pathways leading to the final platinum(II) complexes was performed. These studies determined that the C–B bonds were cleaved and the Ar^F moieties transferred from the BArF anion to the platinum centers prior to the coordination of the phosphine ligands. Moreover, a tentative mechanistic rationalization for the formation of the complex [Pt(Ar^F)(κ^3*I*,*P*,*P*-(**L3•L4**))][B(Ar^F)$_3$(Cl)] has been proposed (oxidative addition of a B–C bond from the BArF counterion to [Pt(Cl)$_2$(cod)], subsequent B–Cl reductive elimination, coordination of the phosphine ligands with concomitant displacement of the cod ligand and NaCl elimination).

The complex XBPhos-Pt has proven to be unreactive as a supramolecular catalyst in the carbocyclization of enynes and the hydrophenylation of ethylene. Strategies towards the activation of the complex XBPhos-Pt and analogues as catalysts for new chemistries have been also presented.

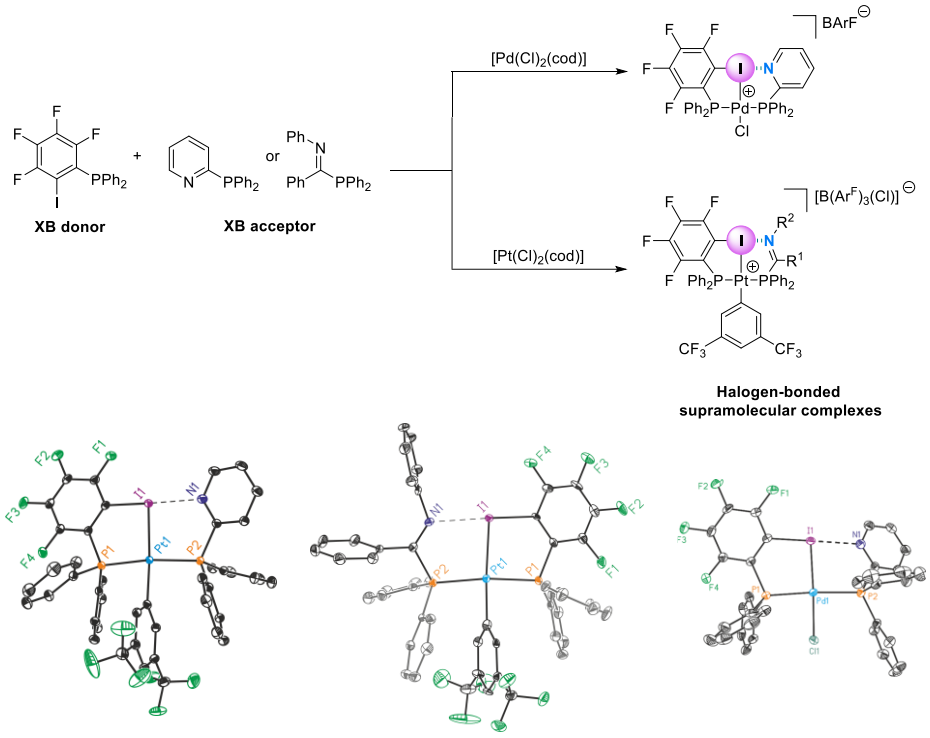

Scheme 71. Preparation of halogen-bonded supramolecular complexes.

RESUM

Aquesta tesi doctoral abasta el disseny, desenvolupament, caracterització i aplicació de sistemes catalítics supramoleculars basats en estratègies de regulació i en l'ús d'interaccions de tipus halogen com a eina per formar l'esquelet de catalitzadors basats en metalls de transició. L'aproximació de regulació s'ha aplicat en transformacions d'interès com la inserció de carbenoids metàl·lics a enllaços O–H que generen derivats α-alquil/aril-α-alcoxi/ariloxi sintèticament útils i utilitzables per a la síntesi de molècules amb rellevància biològica.

En aquest context, les activitats d'investigació es van centrar inicialment en el desenvolupament de catalitzadors de coure(I) regulats supramolecularment (Capítol 1). El disseny modular incorpora cadenes polioxietilèniques lineals com a centres de regulació i unitats d'oxazolina com a grups coordinants pel coure(I). El mecanisme de regulació es desencadena mitjançant l'addició d'un agent de regulació (AR), capaç d'interactuar amb el centre de regulació a través d'interaccions supramoleculars de tipus ió-dipol. La coordinació de l'agent de regulació amb la cadena polioxietilènica no sols s'utilitza per apropar els dos grups terminals, sinó que també serveix per a modificar la geometria i flexibilitat del centre catalític associat. L'elecció de l'agent de regulació determina la rigidesa i la flexibilitat conformacional de tot el sistema catalític, la qual cosa es tradueix finalment en una modulació de l'activitat i selectivitat del catalitzador supramolecular.

Les activitats de recerca van començar amb la preparació de lligands bisoxazolina, que es van sintetitzar directament a partir d'un derivat de monooxazolina mitjançant protocols sintètics eficients. Després de preparar amb èxit una sèrie de lligands bisoxazolina, es van avaluar les constants d'associació entre els lligands i les sals de BArF de metalls alcalins (ARs). Els valors de les constants d'associació K per a totes les sals de BArF estudiades van ser més elevats que 10^3 M^{-1} a 25 °C en $CDCl_3$.

Una vegada sintetitzats els lligands, es van preparar els catalitzadors de coure(I) i aquests es van assajar en la inserció de carbenoids metàl·lics a enllaços O–H. Es va demostrar una ràpida adaptació del sistema catalític a cadascun dels substrats mitjançant l'estratègia de regulació establerta i es van millorar els rendiments de reacció amb l'addició de l'agent de regulació adequat

per a cadascun dels substrats. L'eficiència d'aquesta aproximació es va demostrar estudiant la reacció sobre una sèrie d'alcohols electrònica i estructuralment diversos per a l'obtenció de derivats α-alquil/aril-α-alcoxi/ariloxi sintèticament útils amb rendiments que van oscil·lar entre el 39% i el 99%. El major increment de l'activitat catalítica es va observar per al producte *p*-fluoro-substituït amb un augment del rendiment del 55% (32% de rendiment en absència de AR i 87% de rendiment amb l'ús de NaBArF com AR). Així mateix, es van obtenir rendiments quantitatius per a substrats que tenien una alta densitat electrònica en l'anell aromàtic (per exemple, 99% de rendiment per a la reacció entre *p*-metoxifenol i 2-diazo-2-fenilacetat d'etil). Contràriament, quan l'anell aromàtic estava substituït per grups electroatraients, el rendiment va disminuir fins a un 41% (per exemple, en emprar *p*-nitrofenol com a substrat). La utilitat de l'aproximació es va demostrar estenent l'abast de la reacció a substrats complexos, com ara els cicloalcanols terciaris, els productes de reacció dels quals estan sovint present en productes farmacològics. La utilitat del sistema catalític desenvolupat també es va demostrar mitjançant la preparació d'intermedis sintètics avançats de compostos biològicament rellevants, com per exemple intermedis sintètics avançats de Prozac® i Benadryl®.

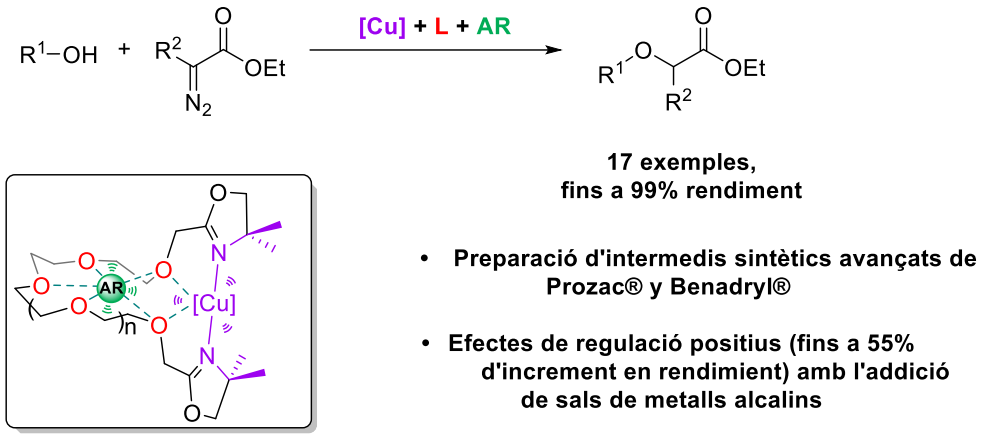

Esquema 72. Inserció de carbenoids de coure a enllaços O–H regulats supramolecularment.

Altres activitats d'investigació es van centrar en l'ús d'interaccions de tipus halogen per formar l'esquelet de complexos metàl·lics del grup 10 derivats de difosfines supramoleculars (Capítol 2). Es van sintetitzar nous complexos

supramoleculars de platí(II) i pal·ladi(II) mitjançant l'assemblatge de dos blocs constituents que contenien fosfines com a grups coordinants, així com grups complementaris capaços de formar enllaços de tipus halogen. Els corresponents complexos de platí(II) i pal·ladi(II) es van caracteritzar en dissolució mitjançant tècniques d'espectroscòpia estàndard, que van apuntar a la formació de complexos metàl·lics amb lligands supramoleculars difosfina *trans*-coordinats a un centre metàl·lic pla quadrat. L'anàlisi de difracció de raigs-X va permetre: (i) la determinació inequívoca de les estructures dels complexos; (ii) la determinació de la naturalesa dels complexos tipus pinça *P,I,P* resultants; (iii) la caracterització de les interaccions d'enllaç d'halogen en estat sòlid (distàncies I···N que van oscil·lar entre 2.6544 i 2.7210 Å; angles d'enllaç C–I···N que van oscil·lar entre 169.74 i 178.17° i els ràtios de la interacció normalitzada (R_{XB}) que van oscil·lar entre 0.75 i 0.77) per als complexos de pal·ladi i platí.

Els complexos supramoleculars de platí preparats ([Pt(Ar^F)(κ^3*I,P,P*-(**L3•L4**))][B(Ar^F)$_3$(Cl)] i [Pt(Ar^F)(κ^3*I,P,P*-(**L3•L5**))][B(Ar^F)$_3$(Cl)]) van incorporar un lligand Ar^F (Ar^F = 3,5-bis(trifluorometil)fenil) unit al platí, el qual provenia del contraió BArF a través d'un procés de ruptura d'un enllaç B–Ar^F mediat pel platí. Es va realitzar un ampli estudi dels intermedis de reacció i dels camins de reacció que conduïen als complexos de platí(II) finals. Aquests estudis van determinar que tant la ruptura de l'enllaç C–B com la transferència del grup Ar^F de l'anió BArF als centres de platí es produïa abans de la coordinació dels lligands fosfina. A més, es va proposar la racionalització mecanística per a la formació del complex [Pt(Ar^F)(κ^3*I,P,P*-(**L3•L4**))][B(Ar^F)$_3$(Cl)] (addició oxidativa de l'enllaç B–C del contraió BArF cap al [Pt(Cl)$_2$(cod)], subsegüent eliminació reductora, coordinació dels lligands fosfina amb desplaçament simultani del lligand cod i eliminació de NaCl).

El complex XBPhos-Pt va resultar ser inactiu com catalitzador en reaccions de ciclació d'enins i d'hidrofenilació de l'etilè. Es van presentar estratègies d'activació del complex XBPhos-Pt i anàlegs per a noves transformacions químiques.

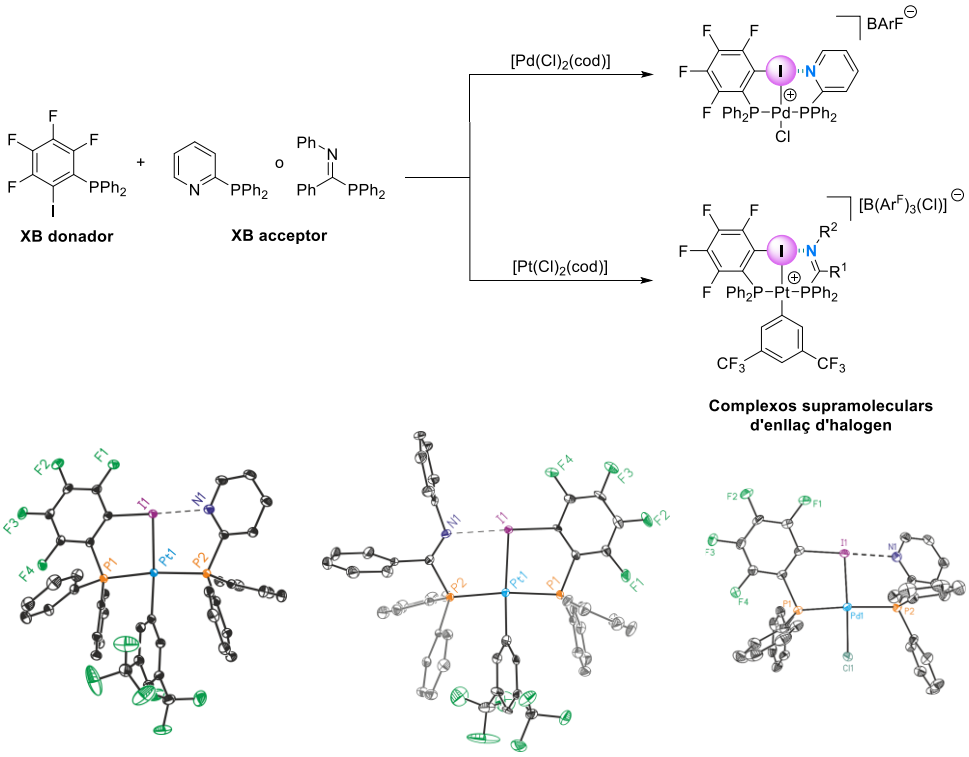

Esquema 73. Preparació dels complexos supramoleculars d'enllaç d'halogen.

RESUMEN

Esta tesis doctoral abarca el diseño, desarrollo, caracterización y aplicación de sistemas catalíticos supramoleculares basados en estrategias de regulación y en el uso de interacciones de tipo halógeno como herramienta para formar el esqueleto de catalizadores basados en metales de transición. La aproximación de regulación se ha aplicado en transformaciones de interés como la inserción de carbenoides metálicos a enlaces O–H, generando derivados α-alquilo/arilo-α-alcoxi/ariloxi sintéticamente útiles y que se puedan utilizar para la síntesis de moléculas con relevancia biológica.

En este contexto, las actividades de investigación se centraron inicialmente en el desarrollo de catalizadores de cobre(I) regulados supramolecularmente (Capítulo 1). El diseño modular incorpora cadenas polioxietilénicas lineales como centros de regulación supramolecular y unidades de oxazolina como grupos coordinantes al cobre(I). Nuestro mecanismo de regulación se desencadena mediante la adición de un agente de regulación (AR), capaz de interactuar con el centro de regulación a través de interacciones supramoleculares de tipo ion-dipolo. La coordinación del agente de regulación con la cadena polioxietilénica no solo se utiliza para acercar los dos grupos coordinantes terminales, sino que también sirve para modificar la geometría y flexibilidad del centro catalítico asociado. La elección del agente de regulación determina la rigidez y la flexibilidad conformacional de todo el sistema catalítico, lo que finalmente se traduce en una modulación de la actividad y selectividad del catalizador supramolecular.

Nuestras investigaciones comenzaron con la preparación de ligandos bisoxazolina, que se sintetizaron directamente a partir de un derivado de monooxazolina mediante protocolos sintéticos eficientes. Después de preparar con éxito una serie de ligandos bisoxazolina, se evaluaron las constantes de asociación entre los ligandos y las sales de BArF de metales alcalinos (ARs). Los valores de las constantes de asociación *K* para todas las sales de BArF estudiadas fueron más altos que 10^3 M^{-1} a 25 ºC en $CDCl_3$.

Una vez sintetizados los ligandos, se prepararon los catalizadores de cobre(I) y éstos se ensayaron en la inserción de carbenoides metálicos a enlaces O–H. Se demostró una rápida adaptación del sistema catalítico a cada uno de los sustratos mediante la estrategia de regulación establecida, mejorando los rendimientos de

reacción con la adición del agente de regulación adecuado para cada sustrato. La eficiencia de esta aproximación se demostró estudiando la reacción sobre una serie de alcoholes electrónica y estructuralmente diversos para la obtención de derivados α-alquilo/arilo-α-alcoxi/ariloxi sintéticamente útiles con rendimientos que oscilaron entre el 39% y el 99%. El mayor incremento de la actividad catalítica se observó para el producto *p*-fluoro-sustituido con un aumento del rendimiento del 55% (32% de rendimiento en ausencia de AR y 87% de rendimiento con el uso de NaBArF como AR). Así mismo, ~~s~~e obtuvieron rendimientos cuantitativos para sustratos que tenían una alta densidad electrónica en el anillo aromático (por ejemplo, 99% de rendimiento para la reacción entre *p*-metoxifenol y 2-diazo-2-fenilacetato de etilo). Por el contrario, cuando el anillo aromático estaba sustituido por grupos electroatrayentes, el rendimiento disminuyó hasta un 41% (por ejemplo, utilizando *p*-nitrofenol como sustrato). La utilidad de la aproximación se demostró extendiendo el alcance de la reacción a sustratos complejos, tales como los cicloalcanoles terciarios, cuyos productos de reacción están frecuentemente presentes en productos farmacológicos. La utilidad de nuestro sistema catalítico también se demostró mediante la preparación de intermedios sintéticos avanzados de compuestos biológicamente relevantes, como por ejemplo intermedios sintéticos avanzados de Prozac® y Benadryl®.

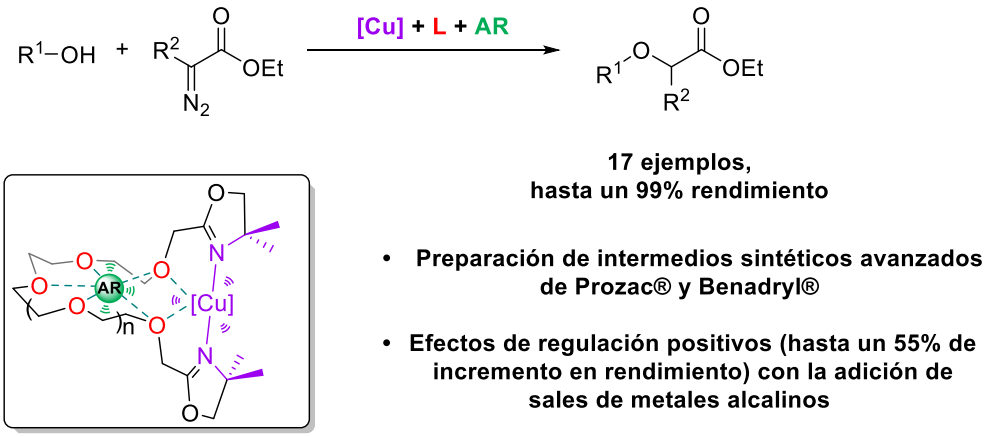

Esquema 74. Inserción de carbenoides de cobre a enlaces O–H reguladas supramolecularmente.

Otras actividades de investigación se centraron en el uso de interacciones de tipo halógeno para formar el esqueleto de complejos metálicos del grupo 10 derivados de difosfinas (supramoleculares) (Capítulo 2). Se sintetizaron nuevos complejos supramoleculares de platino(II) y paladio(II) mediante el ensamblaje de dos bloques constituyentes que contenían fosfinas como grupos coordinantes, así como grupos complementarios capaces de formar enlaces de tipo halógeno. Los correspondientes complejos de platino(II) y paladio(II) se caracterizaron en disolución mediante técnicas de espectroscopia estándar, que apuntaron a la formación de complejos metálicos con ligandos supramoleculares difosfina *trans*-coordinados a un centro metálico plano cuadrado. El análisis de difracción de rayos-X permitió: (i) la determinación inequívoca de las estructuras de los complejos; (ii) la determinación de la naturaleza de los complejos tipo pinza *P,I,P* resultantes; (iii) la caracterización de la interacción por enlace de halógeno en estado sólido (distancias I···N que oscilaron entre 2.6544 y 2.7210 Å; ángulos de enlace C–I···N que oscilaron entre 169.74 y 178.17° y los ratios de la interacción normalizada (R_{XB}) que oscilaron entre 0.75 y 0.77) para los complejos de paladio y platino.

Los complejos supramoleculares de platino preparados ([Pt(Ar^F)(κ^3*I,P,P*-(**L3•L4**))][B(Ar^F)$_3$(Cl)] y [Pt(Ar^F)(κ^3*I,P,P*-(**L3•L5**))][B(Ar^F)$_3$(Cl)]) incorporaron un ligando Ar^F (Ar^F = 3,5-bis(trifluorometil)fenilo) unido al platino, que provenía del contraión BArF a través de un proceso de ruptura del enlace B–Ar^F mediado por platino. Se realizó un amplio estudio de los intermedios de reacción y de los caminos de reacción conducentes a los complejos de platino(II) finales. Estos estudios determinaron que tanto la ruptura del enlace C–B como la transferencia del grupo Ar^F del anión BArF a los centros de platino se producía antes de la coordinación de los ligandos fosfina. Además, se propuso la racionalización mecanística para la formación del complejo [Pt(Ar^F)(κ^3*I,P,P*-(**L3•L4**))][B(Ar^F)$_3$(Cl)] (adición oxidativa del enlace B–C del contraión BArF hacia el [Pt(Cl)$_2$(cod)], subsiguiente eliminación reductora, coordinación de los ligandos fosfina con el simultáneo desplazamiento del ligando cod y eliminación de NaCl).

El complejo XBPhos-Pt fue inactivo como catalizador supramolecular en reacciones de ciclación de eninos e hidrofenilación del etileno. Se presentaron estrategias de activación del complejo XBPhos-Pt y análogos para nuevas transformaciones químicas.

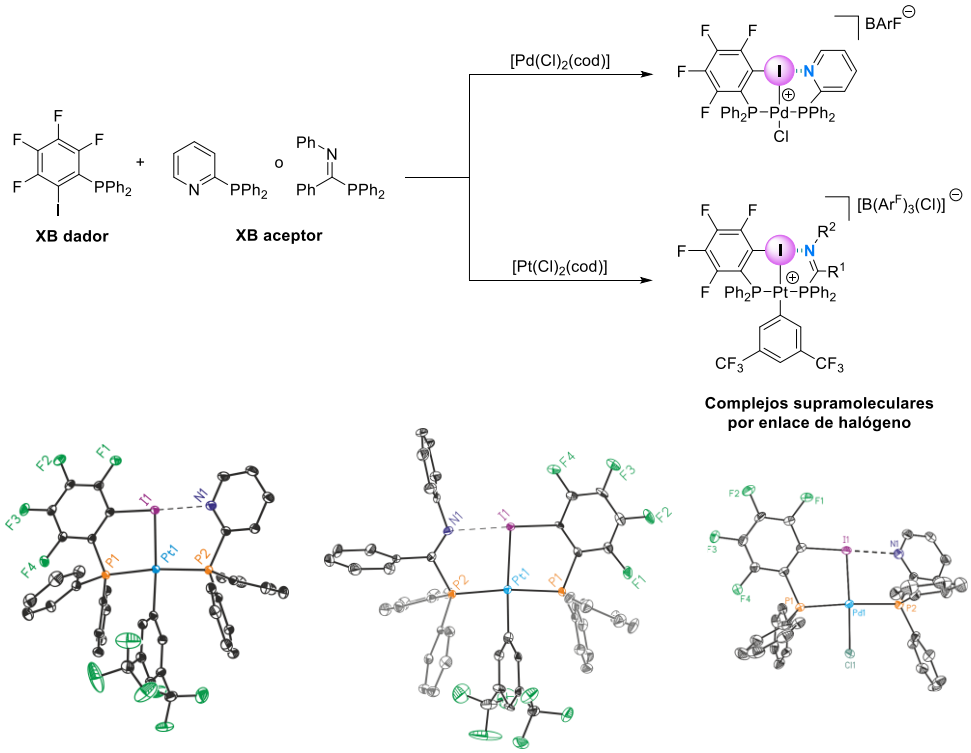

Esquema 75. Preparación de los complejos supramoleculares por enlace de halógeno.

UNIVERSITAT ROVIRA I VIRGILI
SUPRAMOLECULAR CATALYTIC SYSTEMS: SYNTHESIS, CHARACTERIZATION AND APPLICATION IN CATALYSIS
Ester Iniesta Beteta

UNIVERSITAT
ROVIRA i VIRGILI

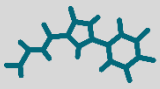

ICIQ

Institut
Català
d'Investigació
Química